ECOLOGICAL IMPACTS OF DEGRADING PERMAFROST

EDITED BY: Dongliang Luo, Guo Donglin, Huijun Jin, Sizhong Yang, Marcia Katharina Phillips and Beat Frey

PUBLISHED IN: Frontiers in Earth Science

frontiers Research Topics

frontiers

ISSN 1664-8714
ISBN 978-2-88976-986-5
DOI 10.3389/978-2-88976-986-5

About Frontiers

Frontiers is more than just an open-access publisher of scholarly articles: it is a pioneering approach to the world of academia, radically improving the way scholarly research is managed. The grand vision of Frontiers is a world where all people have an equal opportunity to seek, share and generate knowledge. Frontiers provides immediate and permanent online open access to all its publications, but this alone is not enough to realize our grand goals.

Frontiers Journal Series

The Frontiers Journal Series is a multi-tier and interdisciplinary set of open-access, online journals, promising a paradigm shift from the current review, selection and dissemination processes in academic publishing. All Frontiers journals are driven by researchers for researchers; therefore, they constitute a service to the scholarly community. At the same time, the Frontiers Journal Series operates on a revolutionary invention, the tiered publishing system, initially addressing specific communities of scholars, and gradually climbing up to broader public understanding, thus serving the interests of the lay society, too.

Dedication to Quality

Each Frontiers article is a landmark of the highest quality, thanks to genuinely collaborative interactions between authors and review editors, who include some of the world's best academicians. Research must be certified by peers before entering a stream of knowledge that may eventually reach the public - and shape society; therefore, Frontiers only applies the most rigorous and unbiased reviews.
Frontiers revolutionizes research publishing by freely delivering the most outstanding research, evaluated with no bias from both the academic and social point of view. By applying the most advanced information technologies, Frontiers is catapulting scholarly publishing into a new generation.

What are Frontiers Research Topics?

Frontiers Research Topics are very popular trademarks of the Frontiers Journals Series: they are collections of at least ten articles, all centered on a particular subject. With their unique mix of varied contributions from Original Research to Review Articles, Frontiers Research Topics unify the most influential researchers, the latest key findings and historical advances in a hot research area! Find out more on how to host your own Frontiers Research Topic or contribute to one as an author by contacting the Frontiers Editorial Office: frontiersin.org/about/contact

ECOLOGICAL IMPACTS OF DEGRADING PERMAFROST

Topic Editors:
Dongliang Luo, Northwest Institute of Eco-Environment and Resources, Chinese Academy of Sciences (CAS), China
Guo Donglin, Zhan Kezhen Nansen International Research Center, Institute of Atmospheric Physics, Chinese Academy of Sciences (CAS), China
Huijun Jin, Northeast Forestry University, China
Sizhong Yang, GFZ German Research Centre for Geosciences, Germany
Marcia Katharina Phillips, Swiss Federal Institute for Forest, Snow and Landscape Research (WSL), Switzerland
Beat Frey, Swiss Federal Institute for Forest, Snow and Landscape Research (WSL), Switzerland

Citation: Luo, D., Donglin, G., Jin, H., Yang, S., Phillips, M. K., Frey, B., eds. (2022). Ecological Impacts of Degrading Permafrost. Lausanne: Frontiers Media SA.
doi: 10.3389/978-2-88976-986-5

Table of Contents

frontiers | Frontiers in Earth Science

TYPE Editorial
PUBLISHED 08 August 2022
DOI 10.3389/feart.2022.967530

OPEN ACCESS

EDITED AND REVIEWED BY
Michael Lehning,
Swiss Federal Institute of Technology Lausanne, Switzerland

*CORRESPONDENCE
Dongliang Luo,
luodongliang@lzb.ac.cn

SPECIALTY SECTION
This article was submitted to Cryospheric Sciences, a section of the journal Frontiers in Earth Science

RECEIVED 13 June 2022
ACCEPTED 01 July 2022
PUBLISHED 08 August 2022

CITATION
Luo D, Guo D, Jin H, Yang S, Phillips MK and Frey B (2022), Editorial: Ecological impacts of degrading permafrost. *Front. Earth Sci.* 10:967530. doi: 10.3389/feart.2022.967530

Editorial: Ecological impacts of degrading permafrost

Dongliang Luo[1]*, Donglin Guo[2], Huijun Jin[3], Sizhong Yang[4,5], Marcia K. Phillips[6] and Beat Frey[7]

[1]State Key Laboratory of Frozen Soil Engineering, Northwest Institute of Eco-Environment and Resources, Chinese Academy of Sciences, Lanzhou, China, [2]Nansen-Zhu International Research Centre, Institute of Atmospheric Physics, Chinese Academy of Sciences, Beijing, China, [3]School of Civil Engineering and Permafrost Institute, Northeast Forestry University, Harbin, China, [4]GFZ German Research Centre for Geosciences, Potsdam, Germany, [5]State Key Laboratory of Cryospheric Sciences, Northwest Institute of Eco-Environment and Resources, Chinese Academy of Sciences, Lanzhou, China, [6]WSL Institute for Snow and Avalanche Research SLF, Davos, Switzerland, [7]Swiss Federal Institute for Forest, Snow and Landscape Research (WSL), Birmensdorf, Switzerland

KEYWORDS

permafrost, engineering impacts of permafrost, ecological impacts of permafrost, permafrost modeling, climate change

Editorial on the Research Topic
Ecological impacts of degrading permafrost

As one of the major cryospheric components, permafrost covers approximately a quarter of the currently exposed land surfaces of the Northern Hemisphere, extending from the Arctic, Subarctic and Boreal zones at high latitudes to the alpine, high-plateau, and mountainous regions at mid-to-low latitudes. In the meantime, the regions of seasonal frost and the near-surface soil layers that undergo seasonal and annual freeze-thaw cycles account for more than one-half of the world's exposed land surfaces.

In general, the spatial distribution and thermal stability of permafrost are primarily controlled by the balance of geothermal flows and redistribution of solar energy at macro-scales, and at local scales by surface characteristics, such as vegetation and snow covers, hydrology, lithology, and geology. The complicated multi-interactions between permafrost and geo-environmental and climatic factors have attracted generations of scientists and engineers to investigate, monitor, and simulate these processes and mechanisms with various methods. In particular, since the 1980s, the extensive and accelerating degradation of permafrost has been increasingly reported for regions at both high latitudes and high elevations. Recently, under the combined influences of climate warming and increasing anthropogenic activities, the degradation of permafrost has been accelerated as manifested by ground surface subsidence and thaw settlement of permafrost soils, rising ground temperature, thickening active layer, disappearance of isolated patches of permafrost, the emergence, expanding or connecting of taliks, as well as shrinking in areal continuity of permafrost. The degradation of permafrost would extensively, profoundly, and inevitably influence the ecological environment and engineering infrastructures in cold regions. However, so far the ecological impacts of the rapidly degrading permafrost have not yet been sufficiently appreciated and evaluated.

In particular, in the context of continuous climate warming and increasing anthropogenic activities, the degradation of permafrost may pose significant risks to sustainable development because of the key roles of permafrost in regulating the carbon pool and ecosystems and freshwater resources, and the safety of engineering facilities. Permafrost acts as a large organic carbon pool as a result of a very slow decomposition rate and extremely low microbial activity caused by subzero temperatures. The soil organic carbon stored in permafrost regions is approximately 1,672 Pg (Tarnocai et al., 2009), outweighing that in the atmosphere and vegetation. In addition, as a potential freshwater reservoir in solid forms, permafrost stores a large amount of ground ice (Zhang et al., 2008), which is likely to be melted as a result of permafrost degradation. Moreover, the successful construction and safe operation of a variety of engineering infrastructures and foundations, such as the railways, highways, airports, dams, and bridges in cold regions (Hjort et al., 2022), require knowledge about the thermophysical and mechanical properties of the frozen soils.

This research collection provides a forum for researchers to share the latest findings on the ecological and engineering impacts of degrading permafrost. In total, there are 17 high-quality original research papers and one review article on this Research Topic, which are contributed by 112 authors. These papers could be roughly categorized into four aspects: 1), Changes of permafrost; 2), Ecological impacts of changing permafrost; 3) Engineering impacts of degrading permafrost, and; 4) Model studies of permafrost distribution and changes.

This collection includes three papers about permafrost changes. In the past, most studies about the degradation of permafrost were generally characterized by melting of ground ice and deepening of the active layer around the top of active permafrost, Dobiński and Kasprzak proposed a new perspective that permafrost degrades from the permafrost base upwards by presenting a special case of such degradation from Hornsund, Svalbard. Based on continuous monitoring of permafrost temperatures in 2013–2020, Yin et al. concurrently found a bottom-up degradation pattern and a complete disappearance of permafrost in 2018 in one island permafrost near the northern lower limit of permafrost in Xidatan along the Qinghai-Tibet Highway on the interior Qinghai-Tibet Plateau (QTP). This is caused by unusually warm summers in the previous 2 years. The degradation of permafrost could be monitored through surface deformation, Du et al. detected the ground deformation in the eastern Tianshan Mountains, China using the small baseline subset interferometric synthetic aperture radar (SBAS-InSAR). They stated that the areas with elevations of 3,150 to 4,275 m a.s.l., slopes of 15–50°, and aspects of southwest, west, and northwest are geologic hazard-prone regions and should receive more attention and field monitoring.

There are nine papers concerning the ecological influences of permafrost, mainly referring to vegetation dynamics, hydrology, dissolved organic carbon (DOC), as well as methane emissions. Carbon storage in the permafrost region is an important component of ecosystem services, attracting a wide range of concerns recently. Li et al. demonstrated tremendous changes to land use/land cover (LULC) induced by climate warming and human activities, and the changes in the LULC accelerated permafrost degradation, leading to obvious changes in the total carbon storage in Heilongjiang Province, Northeast China. Yang et al. clarified that the decomposition and leaching of DOC from organic soil layers and surrounding permafrost sediments were the important carbon sources in ground ice at the top of permafrost. Ma et al. concluded that the permafrost dynamics dominated the aquatic DOC distribution, and permafrost thaw would alter aquatic DOC budgets, eventually adding to atmospheric carbon emissions. Yang et al. examined the cumulative methane emissions under simulated diurnal freeze-thaw cycle (FTC) scenarios, and highlighted the importance of FTCs in stimulating methane emissions and the export of DOC for peat soils collected from the Zoîgé peatlands, the largest peatland complex on the QTP. Regional degradation of permafrost results in many eco-environmental problems under a persistently warming climate and increasing human activities. Jin et al. comprehensively reviewed climate changes, and the distribution and degradation of alpine permafrost, and permafrost degradation-induced changes in hydrology, wetlands, thermokarst lakes, ponds, and vegetation in the source area of the Yellow River, a key water tower of China, and further described the relationship between the lowering permafrost table and succeeding alpine vegetation. To clarify the relationship between permafrost degradation and ecosystem implications, Hu et al. modeled the variations of net primary productivity (NPP) in the Three-River Headwaters Region (TRHR) and found that the increase of NPP in permafrost regions (1.43 g C m^{-2} yr^{-2}) is much higher than that in regions of seasonal frost (0.67 g C m^{-2} yr^{-2}). Wang et al. confirmed the importance of climate and permafrost regimes on vegetation phenological processes by correlating the dynamics of vegetation phenology (the start of the growing season, the end of the growing season, and the growing season length) and freezing index for the three parallel rivers region (TPRR) on the eastern QTP. The surface characteristics cause varied influences on the hydrothermal processes of near-surface soils. Ma et al. emphasized that vegetation acted as a thermal buffer, had a good thermal insulation effect on the ground surface, and was conducive to rainwater infiltration, which were evidenced by the larger annual range of surface temperature and the ground-air temperature difference at

denser vegetation sites in regions of seasonally frozen ground. Ni et al. identified adverse/hazardous impacts of the thawing permafrost on human activities on the QTP in the background of climate warming and concluded a doubled human activity index in regions of seasonally frozen ground in comparison with that in the permafrost region.

There are four papers about the engineering impacts of permafrost degradation. Mao et al. evaluated the engineering stability of the National Highway 214 in Qinghai province, China by categorizing permafrost wetlands on the QTP into 15 types in terms of engineering characteristics, permafrost type, waterlogged area ratio, meadow development degree, and then evaluated the engineering stability of the National Highway 214 in Qinghai province, China. Niu et al. proposed the mitigative methods for frost hazards, including strict control of fine grains content and soil moisture content, prioritizing the use of poorly graded filling, and timely and proper drainage of locally accumulated water in the filling layer for the high-speed railbed along the Harbin-Dalian route in Northeast China. Shang et al. found that the cast-in-place pile foundation enhanced the heat exchange between the atmosphere and soil, expanded the annual range of the surrounding ground temperature, and raised the permafrost table. Using the COMSOL model, He et al. quantitatively studied the influencing factors of thermal recovery after backfilling the coal mine pits and suggested that a composite configuration of organic soil, crush-rock layer, and proper re-vegetation measures could effectively cool the backfilled ground and even offset the climate warming at the Gulian Strip Coal Mine near Mo'he in Northeast China.

Permafrost modeling has attracted a wide range of concerns in the past, as the monitoring of permafrost is insufficient to account for the impacts of permafrost changes on the eco-environments. There are two papers about permafrost modeling in this research collection. Peng et al. developed a thermal calculation model and analyzed the thermal impact of water accumulation on the underlying and ambient permafrost. Yang et al. reviewed the modeling progress of the groundwater-surface water interactions under the influences of snow cover and frozen soil and summarized the current status of hydrologic models suitable for cold environments.

Author contributions

All authors listed have made a substantial, direct, and intellectual contribution to the work and approved it for publication.

Funding

This study was supported by the Western Young Scholars project of the Chinese Academy of Sciences of China (DL), and the National Natural Science Foundation of China (Grant Nos. U2243214 and 41671060).

Acknowledgments

We warmly appreciate Academician Fahu Chen, Professor Zhenhua Zhang, and Tommaso Tesi for editing and supporting this research collection, and sincerely appreciate the Editorial Board and Editorial Office of the *Frontiers in Earth Science* for the kind invitation to edit this Research Topic and their timely support in organizing and managing the selected topic.

Conflict of interest

The authors declare that the research was conducted in the absence of any commercial or financial relationships that could be construed as a potential conflict of interest.

Publisher's note

References

Hjort, J., Streletskiy, D., Doré, G., Wu, Q., Bjella, K., Luoto, M., et al. (2022). Impacts of permafrost degradation on infrastructure. *Nat. Rev. Earth Environ.* 3, 24–38. doi:10.1038/s43017-021-00247-8

Tarnocai, C., Canadell, J. G., Schuur, E. A. G., Kuhry, P., Mazhitova, G., Zimov, S., et al. (2009). Soil organic carbon pools in the northern circumpolar permafrost region. *Glob. Biogeochem. Cycles* 23, GB2023. doi:10.1029/2008gb003327

Zhang, T., Barry, R. G., Knowles, K., Heginbottom, J. A., and Brown, J. (2008). Statistics and characteristics of permafrost and ground-ice distribution in the Northern Hemisphere. *Polar Geogr.* 31, 47–68. doi:10.1080/10889370802175895

frontiers in Earth Science

ORIGINAL RESEARCH
published: 19 July 2021
doi: 10.3389/feart.2021.708630

Thermal Regime and Variations in the Island Permafrost Near the Northern Permafrost Boundary in Xidatan, Qinghai–Tibet Plateau

Guoan Yin, Jing Luo, Fujun Niu, Zhanju Lin and Minghao Liu*

State Key Laboratory of Frozen Soil Engineering, Northwest Institute of Eco-Environment and Resources, Chinese Academy of Sciences, Lanzhou, China

Although the thermal regime and degradation of permafrost on the Qinghai-Tibet Plateau (QTP) have been widely documented, little information exists regarding the island permafrost in the area. Ground temperatures were therefore measured for 8 years (2013–2020) at a permafrost island and at two contrasting sites in the Xidatan region to elucidate the permafrost in this area. Results indicate that the ground temperatures in the island permafrost were markedly higher than those at the same depth in the nearby marginal permafrost and the interior continuous permafrost. In addition, a distinct increasing trend was observed in the ground temperature of the island permafrost over the past 8 years, and warming was signficanty faster in the deep soil than in the topsoil, indicating a bottom–up degradation pattern in the island permafrost. Moreover, due to the persistent increase in the thickness of the active-layer and the decrease in the depth of permafrost table, the permafrost island abruptly disappeared in 2018, which may be attributed to the anomalously high air temperatures that occurred in 2016 and 2017. The results of this study may provide references for understanding of the thermal regime and degradation process of island permafrost on the QTP.

Keywords: frozen ground, active layer, ground temperature, climate change, permafrost degradation, permafrost warming

OPEN ACCESS

Edited by:
Sizhong Yang,
German Research Centre for Geosciences, Helmholtz Centre Potsdam, Germany

Reviewed by:
Liming Jiang,
State Key Laboratory of Geodesy and Earth's Dynamics, Institute of Geodesy and Geophysics (CAS), China
Masato Sato,
National Research Institute for Earth Science and Disaster Resilience (NIED), Japan

****Correspondence:***
Jing Luo
luojing@lzb.ac.cn

Specialty section:
This article was submitted to Cryospheric Sciences, a section of the journal Frontiers in Earth Science

Received: *12 May 2021*
Accepted: *23 June 2021*
Published: *19 July 2021*

Citation:
Yin G, Luo J, Niu F, Lin Z and Liu M (2021) Thermal Regime and Variations in the Island Permafrost Near the Northern Permafrost Boundary in Xidatan, Qinghai–Tibet Plateau. Front. Earth Sci. 9:708630. doi: 10.3389/feart.2021.708630

INTRODUCTION

The global degradation of permafrost has been confirmed by field measurements of the ground tempertures (Biskaborn et al., 2019). This degradation is the result of persistent increases in air temperature, which are likely to continue in the future decades (Serreze et al., 2000; Chadburn et al., 2017; Peng et al., 2018). The permafrost on the Qinghai-Tibet Plateau (QTP) is particularly sensitive to climate change and has undergone noticeable warming over the past several decades (Cheng and Wu, 2007; Ran et al., 2018; Xu et al., 2017; Zhao et al., 2020). Marginal and island permafrost is generally characterized by high ground temperatures and shallow depths. Several studies have pointed out that these types of permafrost degrade more quickly than continuous or discontinuous permafrost (Liu and Chen, 2000; Wu et al., 2005; Jin et al., 2006). The distribution and changes associated with marginal and island permafrost are generally considered important; however, the presence and thermal regimes of permafrost are also strongly affected by local conditions, such as topography, vegetation, and hydrologic factors, which cannot easily be estimated or mapped by the traditional simulation models that are used in the interior permafrost regions of the QTP (Cheng,

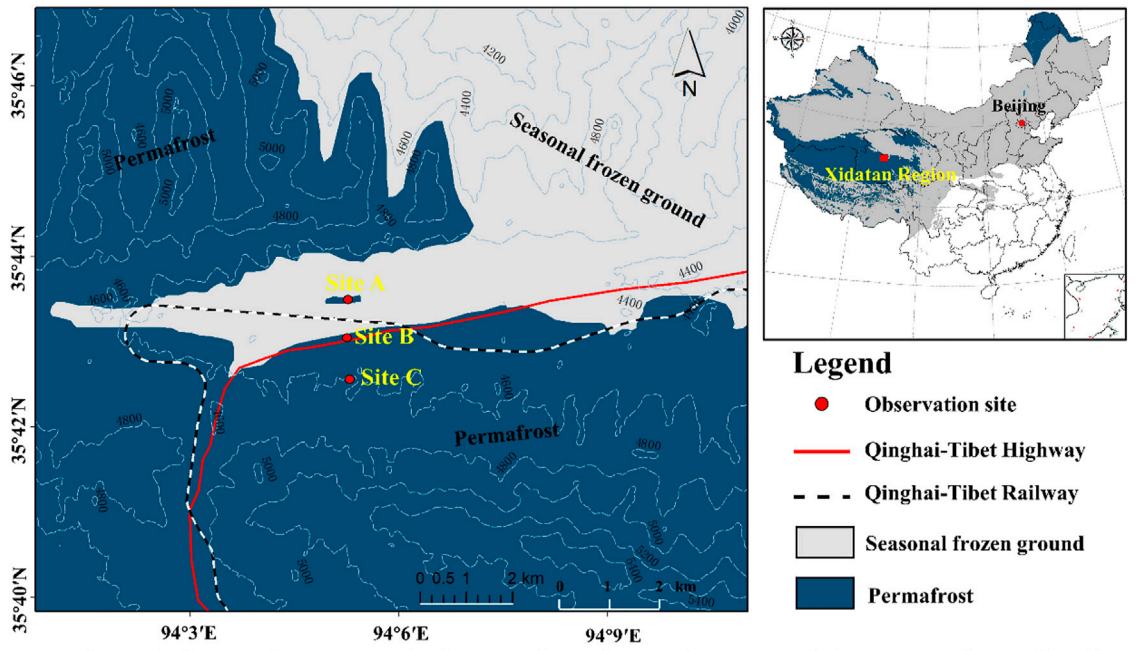

FIGURE1 | Location of the study area and observation sites. The map of the permafrost distribution in Xidatan was revised from Luo et al. (2018).

1984; Zhao et al., 2007; Zou et al., 2016). Several studies focusing on the variation and thermal regimes of the marginal permafrost of the QTP have recently been conducted (Luo et al., 2018; Liu et al., 2020), but investigations characterizing the island permafrost are still limited. A comprehensive investigation of the thermal state of island permafrost is, therefore, essential for a full evaluation of the degradation and changes occurring in the permafrost on the QTP.

The Xidatan region is located within the northern limit of the continuous permafrost on the QTP. The first investigation of the permafrost distribution in this region was conducted *via* borehole drilling and geophysical methods in 1975, and two permafrost islands were found on the west side of the Xidatan basin during this survey (Nan et al., 2003). Using ground penetrating radar (GPR) and borehole validation, the second reported investigation of the permafrost distribution in this region was accomplished in September 2012 (Luo et al., 2018). The results of the second investigation revealed that one of the permafrost islands observed in 1975 had disappeared, whereas the other one was still present; however, the area of the island had significantly decreased over the last four decades. Although the above studies have demonstrated the marked degradation of the island permafrost on the QTP, the specific variation and degradation pattern of the island permafrost and the mechanism by which it responds to climate changes are still unknown. Long-term field observation data are, therefore, required to clarify these issues.

In 2012, ground temperature monitoring boreholes were set up in the island permafrost and two contrasting regions in Xidatan. Using air temperature observations and ground temperature measurements taken between 2013 and 2020, the variation process and the ground thermal regime of the island permafrost can be detailed. The primary goals of this study are to 1) characterize the thermal regime of the island permafrost in the Xidatan region, 2) evaluate the variation process of the island permafrost and examine the differences between marginal and continuous permafrost, and 3) clarify the pattern by which island permafrost degrades and provide information about its response to climate change.

STUDY AREA AND METHODS

Study Area and Observation Sites

The Xidatan region is a down-faulted valley that is located on the northern side of the Eastern Kunlun Mountains, approximately 120 km southwest of Golmud (**Figure 1**). Some major transport arteries such as the Qinghai-Tibet Highway (QTH) and the Qinghai-Tibet Railway pass through this valley. The elevation in this region ranges from 4,000 m in the east to 5,700 m in the west. Except for the surrounding mountainous, the topographic relief in the majority of this region is minimal, with slopes lower than 5° accounting for more than 90% of the area (Yue et al., 2013). Several glaciers that are distributed on the northern slope of Kunlun Mountain form glacial runoffs in the region. The spatial heterogeneity of the surface conditions in this region mainly include flood land, alluvial fans, and alpine steppe. The vegetation is mainly sparse alpine grassland with numerous bare areas. According to observations taken at the meteorological station in the study area, the annual accumulated precipitation has been relatively stable over the last 10 years, with an average of 393 mm (±45 mm standard deviation) (Liu et al., 2020). Xidatan

region is the northern boundary of the permafrost for the QTP (Luo et al., 2018). Isolated permafrost exists in this region (**Figure 1**) and is undergoing degradation (Luo et al., 2018).

Three 15 m-deep boreholes were drilled at site A (a permafrost island that is isolated from the continuous permafrost), site B (marginal to the continuous permafrost), and site C (within the interior of the continuous permafrost). Site A lies approximately 2 km from site C, and the relative difference in elavation at the two sites is almost 20 m. According to the borehole data, the soil in both site A and site B consists of fluvial sand that reaches a thickness of 10 m, which overlies sandy cobble that is 2–4 m thick. The soil profiles in site C are dominantly composed of sand, with some organic matter observed in the top 2.2 m, large amounts of ground ice between 2.2 and 7.0 m, clay from 7.0 to 9.0 m, and weathered mudstone below 9.0 m. Both site A and site B are covered by alpine grassland with a coverage of approxiamtely 40 and 20%, whereas site C is characterized by alpine meadow that covers more than 80% of the surface in this area.

Data Acquisition and Methods

Air Temperature Monitoring

A HOBO Pro v2 (U23-004) logger manufactured by the Onset Computer Corporation, Bourne, MA, United States was used to record the air temperature. The device was installed in a radiation shield near monitoring site C and mounted on a steel pipe at a height of 2.0 m. The logger is accurate to ±0.21°C from 0 to 50°C. Temperatures were recorded at 30 min intervals. The daily mean air temperatures were calculated by averaging the recordes in one day. To assess the changes of the summer and winter temperatures, the thawing degree days (TDDs/°C days, effective temperature sum of the daily temperatures above 0°C) and freezing degree days (FDDs/°C days, effective temperature sum of the daily temperatures below 0°C) were respectively calculated based on the daily temperatures (Frauenfeld et al., 2007).

Ground Temperature Measurements

Thermistor probes linked by cables were used to measure the ground temperature in each borehole, with data acquisition starting in November 2012. The thermistor probe was assembled by the State Key Laboratory of Frozen Soil Engineering, Chinese Academy of Sciences. Each thermistor cable consisted of 25 thermistor sensors at 0.5 m intervals from the surface to a depth of 10 m and at 1 m intervals from 10 to 15 m. A thermistor sensor was placed at a depth of 5 cm (where the impacts of weather and solar radiation can be removed) at each site to measure the ground surface temperature with an accuracy of ±0.05°C. A CR3000 data logger (Campbell Scientific, Edmonton, AB, Canada) with a solar panel capable of recharging a 12 V battery was used to acquire data at each site. Logging was carried out once every 4 h, and data was acquired from November 2012 to December 2020. In addition, the records were timely continuous. The daily, monthly, and mean annual ground temperatures were calculated based on this data.

Calculation of Active Layer Thickness, Permafrost Base, and the Depth of Zero Annual Amplitude

The depth at which the annual maximum ground temperature drops to 0°C is considered the active layer thickness (ALT). Linear interpolation was used to calculate the depth corresponding to 0°C as the ground temperature was measured at a 0.5 m or 1.0 m intervals, and this depth is regarded as the ALT for the year in which the measurement was made. Similarly, because the ground temperature generally presents a linear trend with increasing depth in permafrost, a linear fitting method was used to determine the depth at which the annual mean temperature was close to 0°C, and this depth is identified as the base of the permafrost.

The depth of the zero annual amplitude (DZAA) is defined as the depth at which the seasonal amplitude of the ground temperature is almost zero. However, in most cases, the approximate DZAA is equivalent to the depth at which the seasonal amplitude is diminished to 0.1°C (Isaksen et al., 2007; Liu et al., 2020). In this study, the DZAA is determined as the depth at which the difference between the maximum and minimum annual ground temperature is less than 0.1°C.

RESULTS

Variation in Ground Temperature

Ground Surface Temperatures and Relation With Climate

According to the monitoring results from the HOBO device near site C, the mean annual air temperature at a height of 2 m varied from −3.58 to −2.61°C from 2013 to 2020, with a mean value of −3.26°C. The variations in the daily mean air temperature are presented in **Figure 2A**, with results indicating that there has been a slight increasing trend in the air temperature over the last eight years. In addition, based on the ground temperatures obtained *via* monitoring during the period 2013–2020, the calculated mean annual ground surface temperatures (at 0.05 m depth) were −1.85, −1.91, and −2.08°C at site A, site B, and site C, with results in a surface offset of 1.41, 1.35, and 1.08°C, respectively, for the three sites. Moreover, the calculated TDDs shown an increasing trend while the FDDs shown a decrasing trend during the period from 2013 to 2020 (**Table 1**), which futher demonstrated the gradual warming in the study area.

The relationship curves between the monthly ground surface temperature at a depth of 0.05 m and monthly air temperatures at a height of 2 m at each site are shown in **Figures 2B–D**. The results indicate a strong correlation between the ground surface temperature and the air temperature at all sites. The coefficients of determination (R^2) at sites A, B, and C are 0.94, 0.95, and 0.92, respectively. Snow cover and ground surface conditions are the two main factors that can influence the thermal conduction between the air and surface. However, lower amounts of snowfall and strong winds can lead to an absence of snow or a short period of snow cover in the study area. Therefore, the differences in the correlation between these three sites may result from differences in the type of ground surface present. The higher

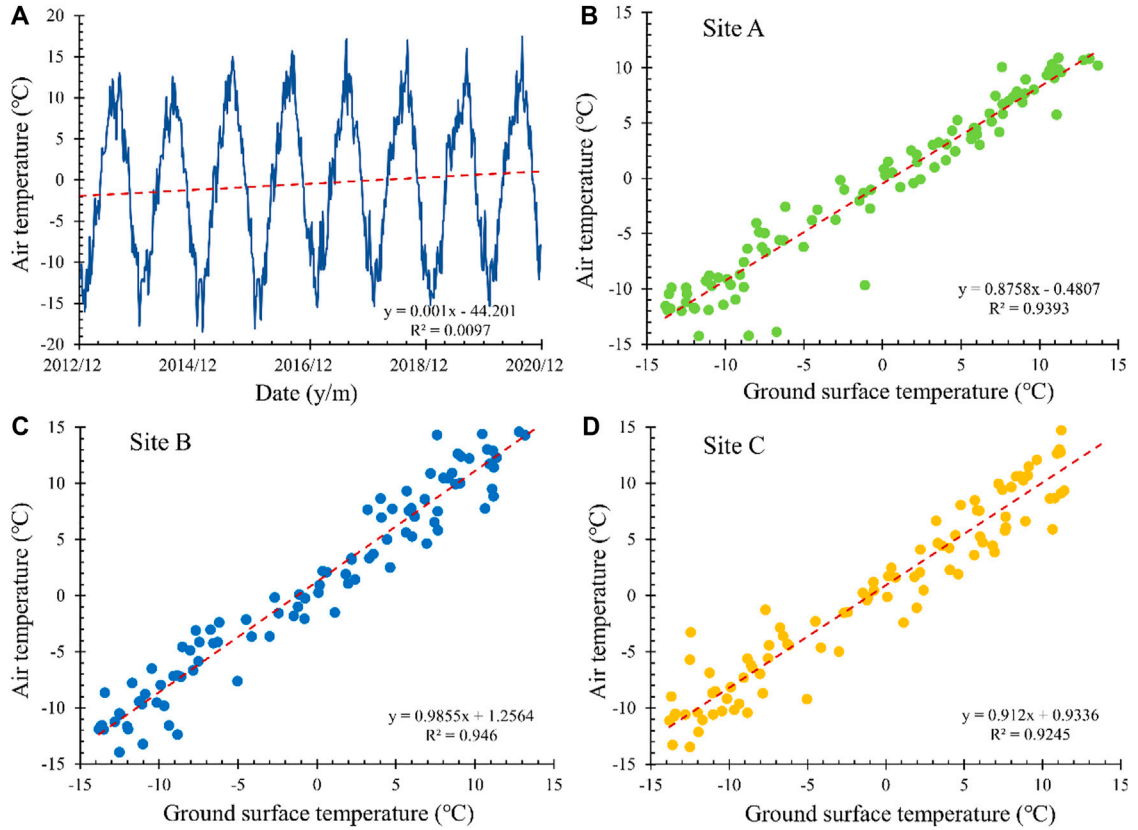

FIGURE 2 | Daily mean air temperature at the study site **(A)**, and mean monthly ground surface temperature (0.05 m depth) vs. mean monthly air temperature during the period from December 2012 to November 2020 at **(B)** Site A, **(C)** Site B, and **(D)** Site C. The linear regression coefficients and coefficient of determination (R^2) are also shown in this figure.

TABLE 1 | Thawing degree days (TDDs/°C days) and freezing degree days (FDDs/°C days in the study area from 2013 to 2020.

Items	2013	2014	2015	2016	2017	2018	2019	2020	Mean
TDDs/°C days	781.3	662.2	858.5	899.6	958.3	946.8	874.9	946.8	866.1
FDDs/°C days	1794.9	1761.8	1702.1	1,634.2	1,577.9	1,693.1	1707.3	1,694.2	1,695.7

correlation in site B can be explained by the fact that this site is nearly vegetation free with gravel of different grain sizes covering the surface. The lower correlation at site C may result from the existence of a significant boundary layer consisting of vegetation and organic material. The considerable vegetation cover and negligible amounts of organic matter in the ground surface layer at the permafrost island area (site A) may result in the moderate correlation observed at this site.

Ground Temperature in Active Layer

The variations in the annual mean ground temperatures observed within the active layer at depths of 1.0 and 2.0 m are shown in **Figure 3**. Although the air temperature was nearly the same at the three sites, the ground temperature in the active layer varied significantly, with the mean value in the island permafrost (site A) being markedly higher than that in the marginal permafrost (site B) and the interior continuous permafrost area (site C), which might be attributed to the difference in the ground surface conditions and the thermal regime of the underlying permafrost. The results in **Figure 3** also indicate that, except for site C, the ground temperature at different depths of the active layer at site A and site B all appear to follow an increasing trend for the period 2013–2020. In addition, the annual variation in the trend of the ground temperature within the active layer at all three sites is significantly influenced by air temperature, and such influence appeared to decrease with depth.

Ground Temperature Near the Permafrost Table and at the Depth of Zero Annual Amplitude

The variations in mean annual ground temperatures near the permafrost table and the DZAA are two important indicators that are usually used to estimate the degradation and the thermal state

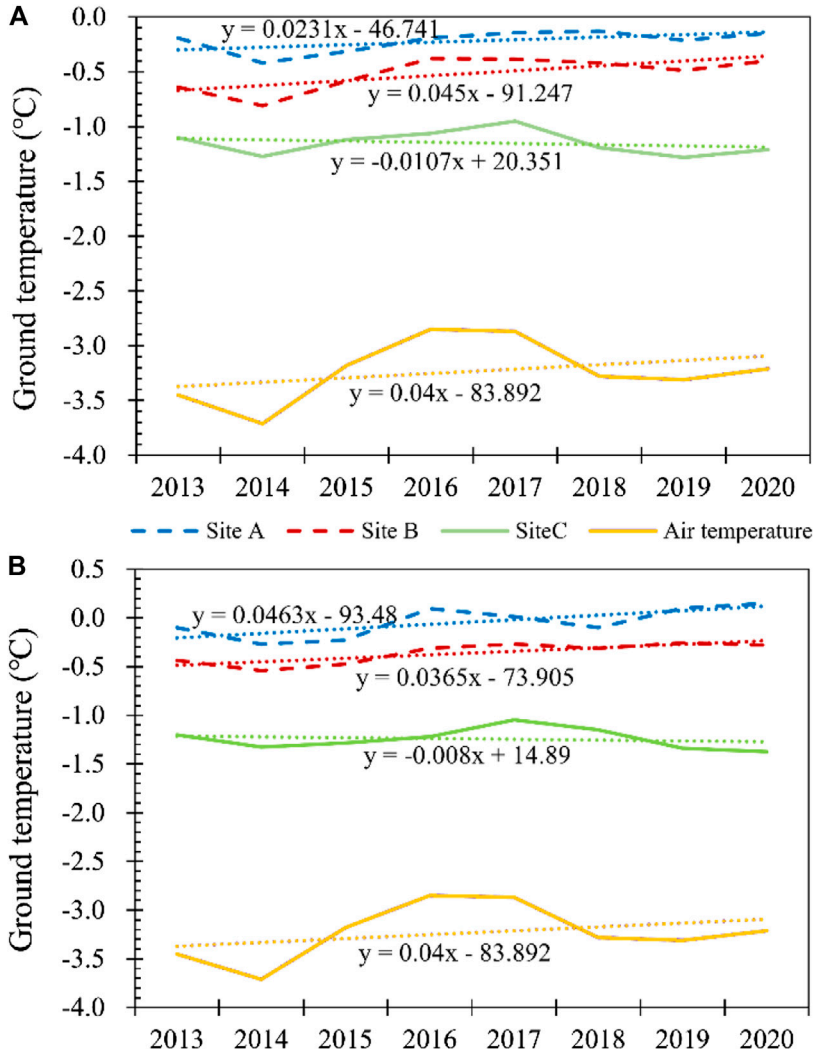

FIGURE 3 | Annual mean ground temperatures in the active layer at the three sites from 2013 to 2020. **(A)** 1.0 m depth, and **(B)** 2.0 m depth. The annual mean air temperatures during the same period are also shown.

of permafrost. The monthly and annual mean ground temperatures at depths near the permafrost table (4.0 m at site A, 3.0 m at site B, and 2.5 m at site C) and the DZAA (11.0 m at site A, 13.0 m at site B, and 12 m at site C), based on the ground temperature at each site, are shown in **Figure 4** and **Table 2**.

The mean annual ground temperature near the permafrost table is −0.09°C for the island permafrost (site A), which is obviously higher than that observed in the marginal permafrost (site B, −0.39°C) or the interior continuous permafrost (site C, −1.27°C) (**Table 2**). In addition, the soil near the permafrost table in site A warms at a faster rate than that at site C but at a slower rate than the soil at site B. The reason for the diversity in the warming rate among the three sites may be the low vegetation cover that accelerates the warming process at site B and the high ice content near the permafrost table that absorbs much of the heat produced when the permafrost thaws at site C. The results in **Figure 4A** indicate that the temperature of the permafrost lying near the permafrost table undergoes obvious seasonal fluctuations in response to changes in the air temperature. The fluctuations were less obvious at site A than at the other two sites, which can be attributed to the much deeper permafrost table. Moreover, the difference in the maximum temperature near the permafrost table at site A, as compared to the other two sites, varied within 0.5°C, whereas the difference in the minimum ground temperature was significantly higher (nearly 3.0°C). Therefore, the high ground temperature in the cold season resulted in the high mean annual ground temperature that was observed near the permafrost table at site A.

The DZAA at site A lies at a depth of approximately 11.0 m, which exceeds the depth of the permafrost base at this site, whereas the DZAA lies within the permafrost at sites B and C. Therefore, the mean annual ground temperature at the DZAA is positive at site A and is noticeably higher than that at sites B and C (**Figure 4B**, **Table 2**). Moreover, the long-term variation in the

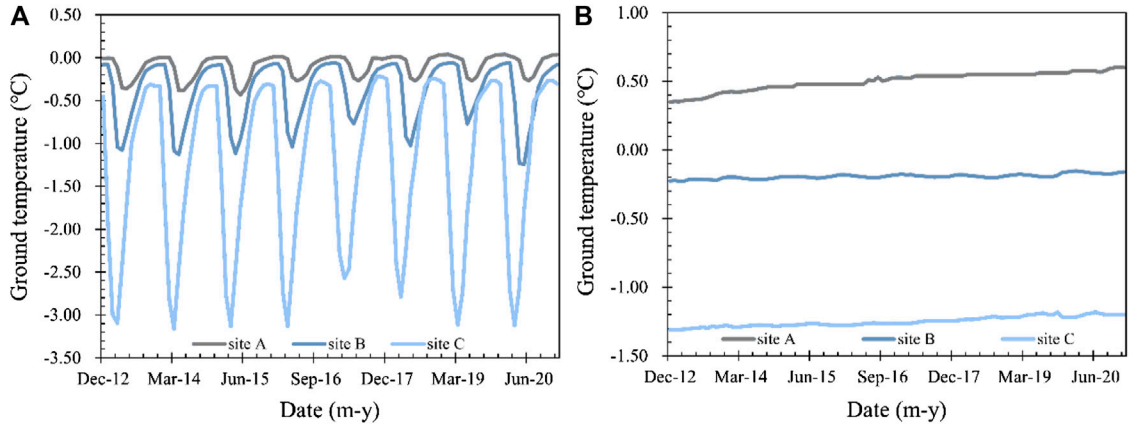

FIGURE 4 | Variation in monthly mean ground temperatures near the permafrost table and the depth of zero annual amplitude. **(A)** Ground temperatures near the permafrost table (site A: 4.0 m, site B: 3.0 m, site C:2.5 m); **(B)** Ground temperatures at the depth of zero annual amplitude (site A: 11.0 m, site B: 13.0 m, site C:12 m).

TABLE 2 | Annual mean ground temperatures near the permafrost table (site A: 4.0 m, site B: 3.0 m, site C: 2.5 m) and the depth of zero annual amplitude (site A: 11.0 m, site B: 13.0 m, site C:12 m) from 2013 to 2020.

Items	Depth/m	Site	2013	2014	2015	2016	2017	2018	2019	2020	Mean	RW/°C·a^{-1}
T_{PT}/°C	4.0	A	−0.14	−0.14	−0.14	−0.09	−0.08	−0.06	−0.05	−0.05	−0.09	0.016
	3.0	B	−0.43	−0.45	−0.43	−0.39	−0.33	−0.39	−0.34	−0.36	−0.39	0.017
	2.5	C	−1.31	−1.34	−1.29	−1.28	−1.22	−1.21	−1.27	−1.27	−1.27	0.012
T_{DZAA}/°C	11.0	A	0.38	0.44	0.48	0.50	0.54	0.55	0.56	0.58	0.50	0.027
	13.0	B	−0.24	−0.22	−0.20	−0.19	−0.19	−0.18	−0.16	−0.16	−0.19	0.011
	12.0	C	−1.30	−1.28	−1.27	−1.27	−1.25	−1.23	−1.20	−1.20	−1.25	0.014

T_{PT}, mean annual ground temperature near the permafrost table.
T_{DZAA}, mean annual ground temperature at the depth of zero annual amplitude.
RW, rate of permafrost warming.

monthly mean ground temperatures in **Figure 4** indicates that the soil warmed faster at site A than at the other two sites over eight years. The specific warming rate at site A is 0.027°C a^{-1}, which is nearly twice the rate at sites B and C (**Table 2**).

Ground Temperature Profiles

A similar pattern is observed in the annual mean ground temperature profiles between 2013 and 2020 for all three sites (**Figure 5**). The annual mean ground temperature in the island permafrost (site A) showed an increasing trend in the top soil layers (0–2 m) in 2013, after which it decreased with depth between 2 m and 4 m. The annual mean ground temperature from 4 to 15 m in site A noticeably increased with depth. Such patterns in the ground temperature profile indicate a net input of heat from both the top and bottom soil layers and resulted in the degradation of the permafrost in the permafrost island. However, except for the top layer, the annual mean ground temperature at site A was obviously higher in 2020 than it was in 2013, especially the negative temperature at 3–8 m, which increased toward 0°C, accompanied by permafrost degradation, over the eight years.

The annual mean ground temperatures at site B and site C in the two years 2013 and 2020 all show a markedly increasing trend with depth in the top soil layers (0–3 m) and remain constant or show a slight increase with depth from 3 to 15 m. The annual mean ground temperatures in the upper part of the soil profile were generally lower than those in the lower parts at these two sites, which is indicative of relatively stable permafrost. When comparing the annual mean ground temperature profiles between 2013 and 2020, the deep soil temperatures in site B and site C increased by 0.02–0.08°C from 2013 to 2020, which is significantly lower than the value observed at site A (0.1–0.2°C).

Long-Term Variation in the Permafrost Thermal Regime

Ground temperature contour maps for depths between 0 and 15 m below the surface at the three sites are shown in **Figure 6**. The thermal regime of the soil layer in the island permafrost (Site A) has changed significantly over the eight year period (**Figure 6A**). Although the maximal depth of the 0°C isotherm near the permafrost table in the summer season remained almost unchanged from 2013 to 2017, the location of the 0°C isotherm near the base of the permafrost markedly increased during this period, resulting in the gradual reduction of the area,

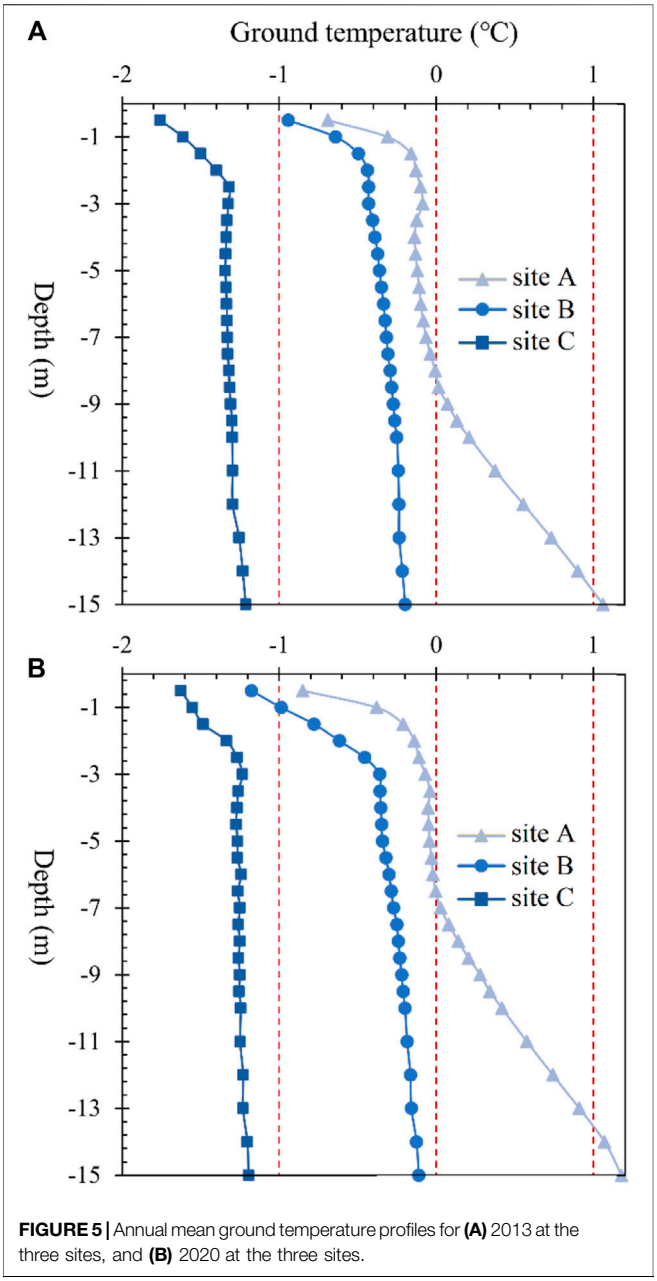

FIGURE 5 | Annual mean ground temperature profiles for **(A)** 2013 at the three sites, and **(B)** 2020 at the three sites.

demonstrating negative ground temperatures. However, this negative ground temperature area disappeared in the warm seasons of 2018–2020, which was accompanied by the disappearance of the permafrost from Site A in the year 2018. In addition, the gradual rise of the 0.5°C isotherm indicated noticeable warming in the deep soil layers at site A, and the rate of warming somewhat increased after the permafrost layer disappeared in 2018. This may be a result of the heat in the warm season after 2018 being fully utilized to heat the deep soil layers rather than being consumed by the hydrothermal phase change associated with the thawing of permafrost.

Permafrost warming also occurred in the marginal permafrost and the interior continuous permafrost during this period, as seen in the ground temperature contour maps in **Figures 6B,C**. The variation in the 0.2°C isotherm in the marginal permafrost (site B) indicates that the thermal regime of the permafrost at this site is the result of slight warming at the top of the permafrost and more noticeable warming in the deep permafrost. However, clear permafrost warming occurred at both the surface and at depth in the interior continuous permafrost permafrost at site C from 2013 to 2020, especially after 2018.

Variations in Active Layer Thickness and Permafrost Base

According to the results of ground temperature monitoring, the ground surface in the study area begins to thaw at the beginning of May and reaches the maximum thaw at the end of August. Therefore, the ALT in this study was determined by linear interpretation from the ground temperature at the end of August at each site. **Table 3** shows the calculated ALT for the three sites from 2013 to 2020. The average ALT in the island permafrost (site A) is 4.26 m, which is significantly higher than the value observed in the marginal permafrost (2.95 m) and the interior continuous permafrost (2.38 m). **Figure 7A** indicates a measurable increasing trend over the last several years at the three sites. The rate of increase at site A is 3.5 cm a^{-1}, which is slightly higher than that at site C and markedly lower than that at site B. In addition, the extremely high air temperature in 2016 meant that the maximum increase in ALT also occurred at all three sites in this year, with the specific increases in ALT from 2015 to 2016 reaching 10 cm at site A, 20 cm at site B, and 11 cm at site C.

The variation in the depth of the permafrost base at the three sites over the period 2013 to 2017 or 2020 are shown in **Table 2** and **Figure 7B**. The depth of the permafrost base ranged from 8.42 to 7.64 m with an average of 7.88 m in the island permafrost (site A), whereas the mean depths of the permafrost base at sites B and C were 17.13 and 80.37 m, which are considerably deeper than that observed at site A (**Table 3**). The variation in the depth of the permafrost base is shown in **Figure 7B**, and the results of this figure show a significant linear decreasing trend in the depth of the permafrost base at all three sites. The decreasing rate of permafrost base was 0.187 m at site A, which is less than that observed at sites B and C.

DISCUSSION

Factors Contributing to the Thermal Differences at the Three Sites

The above results indicate significant variation in the distribution of the permafrost and the thermal regime among the three sites (island permafrost, marginal permafrost, and the interior continuous permafrost). Possible reasons for these differences include differences in the elevation and the local conditions. Elevation is a key factor that determines the permafrost temperatures on the QTP, and the statistical results from 190 boreholes along the Qinghai-Tibet Highway/Railway revealed that the mean annual permafrost temperature at 15 m depth generally decrease by 0.57°C when elevation increases by 100 m

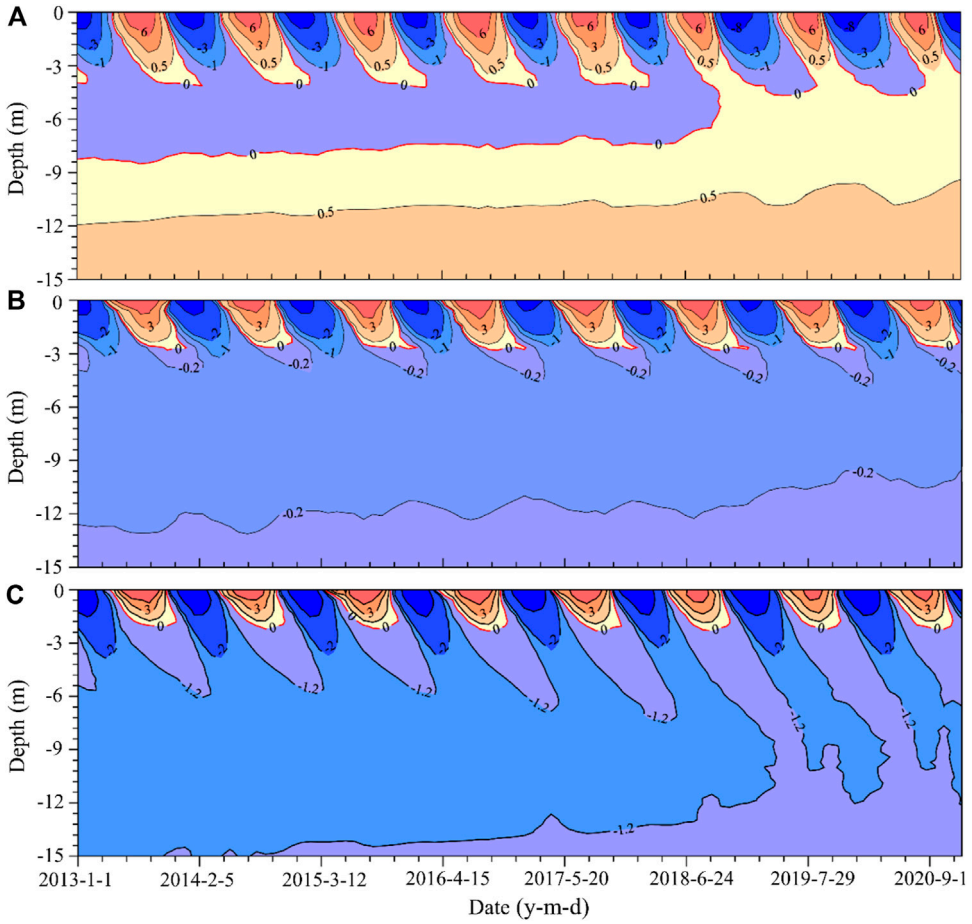

FIGURE 6 | Ground temperatures (°C) as a function of time and depth in **(A)** island permafrost (site A), **(B)** marginal permafrost (site B), and **(C)** interior continuous permafrost (site C). Red isolines represent 0°C and the blue areas represent ground temperatures that are lower than 0°C with time and depth.

TABLE 3 | Thickness of the active layer and the base of the permafrost at the three sites (Site A, Site B, and Site C) from 2013 to 2020. Due to the disappearance of permafrost at site A from 2018, neither the thicknss of the active layer or the depth of the permafrost base are available for the period 2018 to 2020 in the table.

Year	Active layer thickness (m)			Permafrost base (m)		
	Site A	Site B	Site C	Site A	Site B	Site C
2013	4.21	2.81	2.21	8.42	18.21	81.13
2014	4.22	2.78	2.30	7.93	17.62	80.91
2015	4.21	2.82	2.31	7.81	17.44	80.80
2016	4.31	3.02	2.42	7.62	17.12	80.64
2017	4.34	3.04	2.51	7.64	17.03	80.33
2018	–	3.05	2.42	–	16.62	80.02
2019	–	3.03	2.43	–	16.52	79.64
2020	–	3.04	2.43	–	16.50	79.51
Average	4.26	2.95	2.38	7.88	17.13	80.37

(Wu et al., 2010). However, the maximum difference in the elevation of the island permafrost (site A) and the interior continuous permafrost (site C) is approximately 20 m. Such minor differences in altitude cannot explain the signficant differences observed in the ground temperature, 2.38°C at 15 m depth, and the permafrost depth of approximately 74 m between the two sites. Therefore, besides the influence of elevation, the local conditions could might be the main reason that explain the diversity in the permafrost thermal regime observed between the permafrost island and the other sites.

The results of the GPR profiles in the field investigation together with the borehole verification in 2012 indicate that the lowest elevation at which permafrost occurs is 4,369 m in the Xidatan region (Luo et al., 2018), whereas the elevation of site A (within the island permafrost) of approximately 4,490 m is significantly higher than the lowest permafrost limit in this region. Therefore, the permafrost island as well as the nearby seasonally frozen ground at site A should be susceptible to continuous permafrost if the local conditions do not change. The presence of rivers or running water will exert thermal degradation on the permafrost and may result in the permafrost thawing after a long period. According to our investigation, a seasonal river is located at the north side of site A, and a dried-up channel lies between site A and site B. In addition, the seasonal river has led to the formation of a vast area of banked floodplain in this region. Flooding of the floodplain is beneficial to the input of heat into permafroat (Brosten et al., 2009). Therefore, the thermal influence of the river and the fluvial affected surface

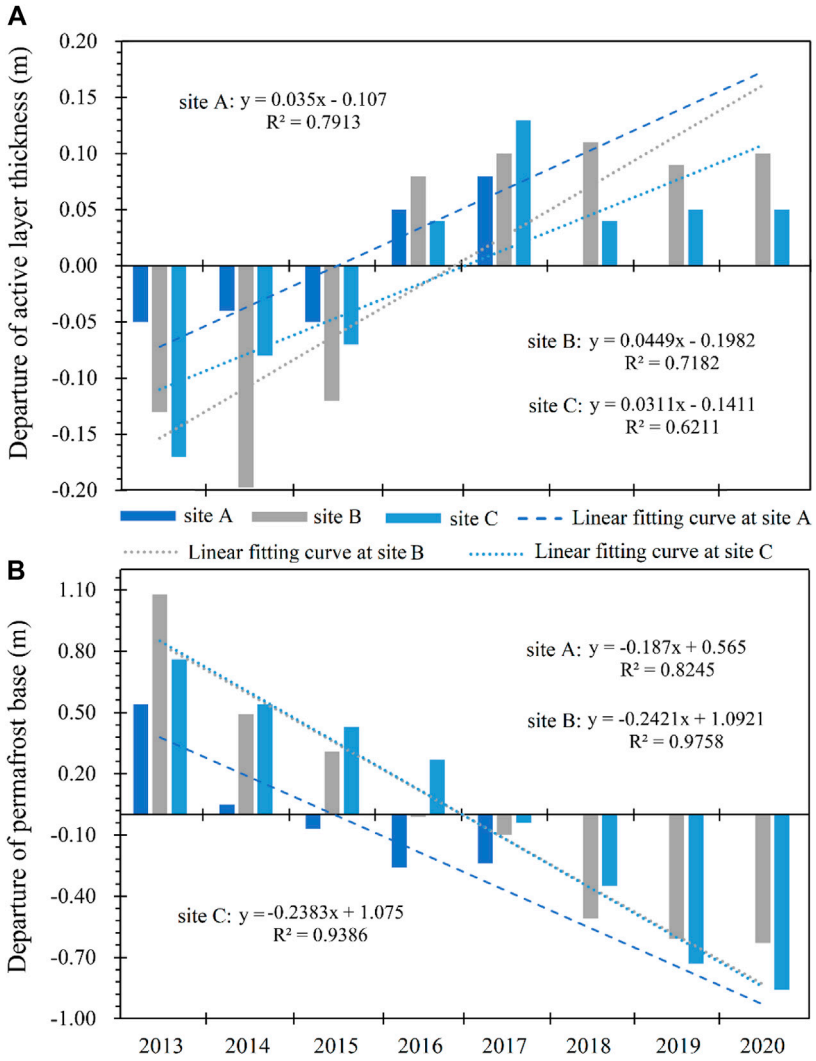

FIGURE 7 | Changes in the thickness of the active layer **(A)** and the depth of the permafrost base **(B)** at the three sites (Site A, Site B, and Site C) from 2013 to 2020. The linear regression coefficients and coefficient of determination (R^2) are shown in figure.

conditions are key factors that may have contributed to the significant difference in the distribution of the permafrost and the thermal regime at the three sites. Meanwhile, warm water of the seasonal river can transport laterally or vertically heat into permafrost, leading to the warming and thawing of permafrost beneath and around the river (Zheng et al., 2019). The thermal impacts of groundwater flow on permafrost is often assumed to be negligible on the QTP. However, presence of groundwater flow may enhance permafrost degradation (Mckenzie and Voss, 2013), especially the lateral heat transfer to isolated permafrost bodies (McClymont et al., 2013; Kurylyk et al., 2016; Sjöberg et al., 2016).

Moreover, differences in the vegetation cover might also have significant effects on the permafrost thermal regime. Vegetation can prevent solar radiation from reaching the topsoil; thus, ground surfaces with high vegetation cover on the QTP are generally at lower temperatures than ground surface with sparse vegetation in summer (Jin et al., 2008). In addition, the existence of organic matter beneath the vegetation cover also reduces the thermal conductivity of shallow soil in summer, thereby reducing the amount of heat reaching the deep soil. However, vegetation becomes withered and organic matter is frozen in winter, which provides a channel for cold air to enter the lower soil layers. Therefore, the high coverage of alpine meadow and the layer of considerable organic material at site C might result in the low ground temperature observed in this region as compared to the other two sites. This is a result of the ground surface at both site A and site B being covered only by sparse alpine grassland with gravelly soil in the top layer.

Possible Reasons for the Abrupt Disappearance of the Permafrost Island

According to the borehole data, the soil layers within the permafrost island are mainly dominated by fluvial deposits,

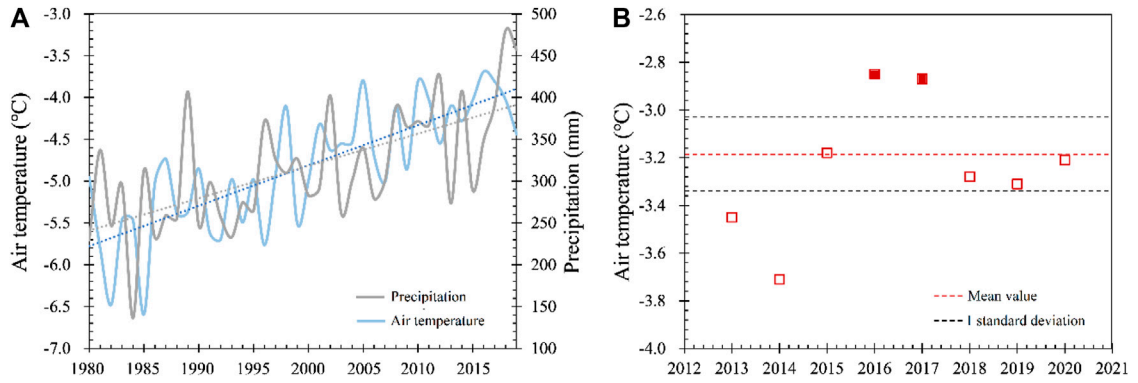

FIGURE 8 | Changes in the local climatic conditions over time. **(A)** Annual mean air temperature and annual accumulated precipitation at Wudaoliang national weather station from 1980 to 2019; **(B)** Annual mean air temperature in the Xidatan region from 2013 to 2020.

and it can therefore be inferred that the permafrost island formed when the river erosion process weakened or the river courses altered. The permafrost island was discovered in 1972 and existed for more than 40 years until its disappearance in 2018. The surface conditions and hydrological process within and near the permafrost island area have not changed noticeably during the past few decades, especially in the last 10 years. Moreover, the seasonal river at the north side of the permafrost island moved northward by approximately 10 m from 2012 to 2020, according to field observations. Therefore, local conditions may not be the main reason for the degradation and ultimate disappearance of the permafrost island.

The annual mean air temperature and accumulated precipitation recorded at a national weather station (Wudaoliang station) near the Xidatan region is shown in **Figure 8A**, with results indicating that both the air temperature and the amount of precipitation in the area have noticeably increased over the past 40 years. Recent studies have demonstrated that the occurrence of a wet climate on the QTP can reduce the thermal responses of permafrost to warming, thereby preventing the degradation of permafrost, especially in arid and semiarid zones (Zhang et al., 2021), however, the extreme precipitation events in summer can have a thermal impact on permafrost (Zhu et al., 2017). Meanwhile, persistent climate warming is also the reason for the enhanced permafrost degradation in this region. The monitored air temperatures in Xidatan indicate that the years 2016 and 2017, immediately before the disappearance of the island permafrost, were both anomalously warm years with annual mean air temperatures that were significantly higher than the average over the period 2013 to 2020 (**Figure 8B**). Such anomalously high air temperatures may have accelerated the phase change in the island permafrost, resulting in the rapidly increasing soil temperature in 2018. Therefore, seasonal climatic changes and extreme events combinatively impact the permfrost thermal dynamics (Marmy et al., 2013).

Degradation Pattern and Warming Rate of the Island Permafrost

The results in **Figure 6** show that the deep soil in the island permafrost warmed more than the top soil, with a specific warming rate of 0.016°C a^{-1} at 4.0 m depth (near the permafrost table), whereas warming rate is 0.027°C a^{-1} at a depth of 11.0 m (the DZAA) (**Table 1**). However, a much smaller difference was observed in the warming rate between the shallow and deep soil in marginal permafrost and interior continuous permafrost than that observed in the island permafrost, especially in the interior continuous permafrost area, which warmed by only 0.002°C a^{-1}. The above analysis indicates that warm island permafrost mainly degrades from bottom to top, which might be attributed to the existence of ground-ice in the top permafrost that obsorbs lots of heat when it melt and the lateral thermal impacts of the season river near the permafrost island.

In addition, when comparing the warming rate of shallow permafrost (6.0 m depth) in the island permafrost with the interior continuous permafrost on the QTP, the warming rate of the island permafrost (0.008°C a^{-1}) is much smaller than that in the other regions of the QTP (Wu et al., 2012). Several studies have confirmed that an increase in the ground temperature of warm permafrost will induce phase change and that a considerable proportion of the heat produced is then absorbed by melting ground ice during this process, resulting in the lower warming rate in warm permafrost (Riseborough, 1990; Romanovsky et al., 2010; Sun et al., 2020). The lower warming rate of the shallow island permafrost can be explained by the above mechanism. Such phenomena have also been also widely reported in many other permafrost regions, such as Northern Europe, southern Siberia, the Mackenzie corridor, and the Tien Shan mountains (Marchenko et al., 2007; Christiansen et al., 2010; Romanovsky et al., 2010; Smith et al., 2010).

CONCLUSION

A case study of a permafrost island in the Xidatan region was conducted based on ground temperature measurement and air temperature observation to reveal variations in the thermal regime and the degradation process of island permafrost on

the QTP with persistent climate warming. According to the results presented herein, the following conclusions can be drawn:

1) Field observation results from 2013 to 2020 indicated that both the ground temperature near the ground surface, within the active layer, near the permafrost table and the DZAA were notably higher in the island permafrost than that in the marginal permafrost and the interior continuous permafrost, which may be attributed to the difference in ground surface conditions and the thermal regime of the underlying permafrost.
2) The patterns of mean ground temperature profiles revealed that a net input of heat from both the top and bottom soil layers resulted in the degradation of the permafrost in the permafrost island. However, the annual mean ground temperatures in the upper permafrost were generally lower than that in the lower areas of marginal permafrost and the interior continuous permafrost, which is indicative of relatively stable permafrost.
3) The ALTs in the island permafrost showed a measurable increasing trend over the past few years, and the average ALT in the island permafrost is significantly higher than the value in the marginal permafrost and the interior continuous permafrost. However, the depth of the permafrost base in the island permafrost showed significant linear decreasing trends from 2013 to 2017, and is shallower than in the depths observed in the marginal permafrost and the interior continuous permafrost.
4) Long-term climate warming has contributed to the persistent degradation of the island permafrost, and the anomalously high air temperatures in 2016 and 2017 accelerated the phase change and resulted in the abrupt disappearance of the permafrost island. In addition, the degradation pattern of the island permafrost is characterized as bottom to top, and the warming rate in the deep soil was obviously higher than that in the topsoil.

DATA AVAILABILITY STATEMENT

The raw data supporting the conclusions of this article will be made available by the authors, without undue reservation.

AUTHOR CONTRIBUTIONS

JL designed the study. GY led the manuscript writing. FN and ZL contributed to data analysis. ML produced the figures.

FUNDING

This research was supported by the Second Tibetan Plateau Scientific Expedition and Research (STEP) program (Grant No. 2019QZKK0905), National Science Foundation of China (Grant Nos. 42071097 and 41801015), and the Youth Innovation Promotion Association of Chinese Academy of Sciences (2020421).

ACKNOWLEDGMENTS

We thank the two reviewers for their valuable comments and suggestions that helped to improve the manuscript.

REFERENCES

Biskaborn, B. K., Smith, S. L., Noetzli, J., Matthes, H., Vieira, G., Streletskiy, D. A., et al. (2019). Permafrost is Warming at a Global Scale. *Nat. Commun.* 10, 264. doi:10.1038/s41467-018-08240-4

Brosten, T. R., Bradford, J. H., McNamara, J. P., Gooseff, M. N., Zarnetske, J. P., Bowden, W. B., et al. (2009). Estimating 3D Variation in Active-Layer Thickness Beneath Arctic Streams Using Ground-Penetrating Radar. *J. Hydrol.* 373, 479–486. doi:10.1016/j.jhydrol.2009.05.011

Chadburn, S. E., Burke, E. J., Cox, P. M., Friedlingstein, P., Hugelius, G., and Westermann, S. (2017). An Observation-Based Constraint on Permafrost Loss as a Function of Global Warming. *Nat. Clim Change.* 7, 340–344. doi:10.1038/nclimate3262

Cheng, G. D. (1984). Problems on Zonation of High-Altitudinal Permafrost. *Acta Geogr. Sin.* 39, 185–193. (in Chinese). doi:10.11821/xb198402006

Cheng, G., and Wu, T. (2007). Responses of Permafrost to Climate Change and Their Environmental Significance, Qinghai-Tibet Plateau. *J. Geophys. Res.* 112, F02S03. doi:10.1029/2006JF000631

Christiansen, H. H., Etzelmüller, B., Isaksen, K., Juliussen, H., Farbrot, H., Humlum, O., et al. (2010). The Thermal State of Permafrost in the Nordic Area During the International Polar Year 2007-2009. *Permafrost Periglac. Process* 21, 156–181. doi:10.1002/ppp.687

Frauenfeld, O. W., Zhang, T., and Mccreight, J. L. (2007). Northern Hemisphere Freezing/Thawing Index Variations Over the Twentieth Century. *Int. J. Climatol.* 27, 47–63. doi:10.1002/joc.1372

Isaksen, K., Sollid, J. L., Holmlund, P., and Harris, C. (2007). Recent Warming of Mountain Permafrost in Svalbard and Scandinavia. *J. Geophys. Res.* 112, F02S04. doi:10.1029/2006JF000522

Jin, H., Sun, L., Wang, S., Ruixia, H., and Shaopeng, Y. (2008). Dual Influences of Local Environmental Variables on the Interior-Eastern Qinghai-Tibet Plateau (I). Vegetation and Snow Cover. *J. Glaciol. Geocryol.* 30, 535–545.

Jin, H., Zhao, L., Wang, S., and Jin, R. (2006). Thermal Regimes and Degradation Modes of Permafrost Along the Qinghai-Tibet Highway. *Sci. China Ser. D.* 49, 1170–1183. doi:10.1007/s11430-006-2003-z'

Kurylyk, B. L., Hayashi, M., Quinton, W. L., McKenzie, J. M., and Voss, C. I. (2016). Influence of Vertical and Lateral Heat Transfer on Permafrost Thaw, Peatland Landscape Transition, and Groundwater Flow. *Water Resour. Res.* 52, 1286–1305. doi:10.1002/2015WR018057

Liu, G., Xie, C., Zhao, L., Xiao, Y., Wu, T., Wang, W., et al. (2020). Permafrost Warming Near the Northern Limit of Permafrost on the Qinghai–Tibetan Plateau During the Period From 2005 to 2017: A Case Study in the Xidatan Area. *Permafrost Periglacial Processes* 2021, 1–12. doi:10.1002/ppp.2089

Liu, X., and Chen, B. (2000). Climatic Warming in the Tibetan Plateau During Recent Decades. *Int. J. Climatol.* 20, 1729–1742. doi:10.1002/1097-0088(20001130)20:14<1729::aid-joc556>3.0.co;2-y

Luo, J., Niu, F.-j., Lin, Z.-j., Liu, M.-h., and Yin, G.-a. (2018). Variations in the Northern Permafrost Boundary Over the Last Four Decades in the Xidatan Region, Qinghai-Tibet Plateau. *J. Mt. Sci.* 15, 765–778. doi:10.1007/s11629-017-4731-2

Marchenko, S. S., Gorbunov, A. P., and Romanovsky, V. E. (2007). Permafrost Warming in the Tien Shan Mountains, Central Asia. *Glob. Planet. Change.* 56, 311–327. doi:10.1016/j.gloplacha.2006.07.023

Marmy, A., Salzmann, N., Scherler, M., and Hauck, C. (2013). Permafrost Model Sensitivity to Seasonal Climatic Changes and Extreme Events in Mountainous Regions. *Environ. Res. Lett.* 8, 035048. doi:10.1088/1748-9326/8/3/035048

McClymont, A. F., Hayashi, M., Bentley, L. R., and Christensen, B. S. (2013). Geophysical Imaging and Thermal Modeling of Subsurface Morphology and Thaw Evolution of Discontinuous Permafrost. *J. Geophys. Res. Earth Surf.* 118, 1826–1837. doi:10.1002/jgrf.20114

Mckenzie, J. M., and Voss, C. I. (2013). Permafrost Thaw in a Nested Groundwater-Flow System. *Hydrogeol J.* 21, 299–316. doi:10.1007/s10040-012-0942-3

Nan, Z. T., Gao, Z. S., and Li, S. X. (2003). Permafrost Changes in the Northern Limit of Permafrost on the Qinghai-Tibet Plateau in the Last 30 Years. *Acta Geogr. Sin.* 58, 817–823. (in Chinese). doi:10.11821/xb200306003

Peng, X., Zhang, T., Frauenfeld, O. W., Wang, K., Luo, D., Cao, B., et al. (2018). Spatiotemporal Changes in Active Layer Thickness Under Contemporary and Projected Climate in the Northern Hemisphere. *J. Clim.* 31 (1), 251–266. doi:10.1175/JCLI-D-16-0721.1

Ran, Y., Li, X., and Cheng, G. (2018). Climate Warming over the Past Half century Has Led to Thermal Degradation of Permafrost on the Qinghai-Tibet Plateau. *The Cryosphere.* 12, 595–608. doi:10.5194/tc-12-595-2018

Riseborough, D. W. (1990). "Soil Latent Heat as a Filter of the Climate Signal in Permafrost," in Proceedings of the Fifth Canadian Permafrost Conference (Quebec City, QC: Centre d'études nordiques. Nordicana) 54, 199–205.

Romanovsky, V. E., Drozdov, D. S., Oberman, N. G., Malkova, G. V., Kholodov, A. L., Marchenko, S. S., et al. (2010). Thermal State of Permafrost in Russia. *Permafrost Periglac. Process.* 21, 136–155. doi:10.1002/ppp.683

Serreze, M. C., Walsh, J. E., Chapin III, F. S., Osterkamp, T., Dyurgerov, M., Romanovsky, V., et al. (2000). Observational Evidence of Recent Change in the Northern High-Latitude Environment. *Clim. Change.* 46, 159–207. doi:10.1023/a:1005504031923

Sjöberg, Y., Coon, E., K. Sannel, A. B., Pannetier, R., Harp, D., Frampton, A., et al. (2016). Thermal Effects of Groundwater Flow through Subarctic Fens: A Case Study Based on Field Observations and Numerical Modeling. *Water Resour. Res.* 52, 1591–1606. doi:10.1002/2015WR017571

Smith, S. L., Romanovsky, V. E., Lewkowicz, A. G., Burn, C. R., Allard, M., Clow, G. D., et al. (2010). Thermal State of Permafrost in North America: a Contribution to the International Polar Year. *Permafrost Periglac. Process.* 21, 117–135. doi:10.1002/ppp.690

Sun, Z., Zhao, L., Hu, G., Qiao, Y., Du, E., Zou, D., et al. (2020). Modeling Permafrost Changes on the Qinghai-Tibetan Plateau From 1966 to 2100: A Case Study From Two Boreholes Along the Qinghai-Tibet Engineering Corridor. *Permafrost and Periglac Process.* 31, 156–171. doi:10.1002/ppp.2022

Wu, Q., Zhang, T., and Liu, Y. (2010). Permafrost Temperatures and Thickness on the Qinghai-Tibet Plateau. *Glob. Planet. Change.* 72 (1-2), 32–38. doi:10.1016/j.gloplacha.2010.03.001

Wu, Q., Zhang, T., and Liu, Y. (2012). Thermal State of the Active Layer and Permafrost along the Qinghai-Xizang (Tibet) Railway From 2006 to 2010. *The Cryosphere.* 6, 607–612. doi:10.5194/tc-6-607-2012

Wu, T., Li, S., Cheng, G., and Nan, Z. (2005). Using Ground-Penetrating Radar to Detect Permafrost Degradation in the Northern Limit of Permafrost on the Tibetan Plateau. *Cold Regions Sci. Technology.* 41, 211–219. doi:10.1016/j.coldregions.2004.10.006

Xu, X., Zhang, Z., and Wu, Q. (2017). Simulation of Permafrost Changes on the Qinghai-Tibet Plateau, China, Over the Past Three Decades. *Int. J. Digital Earth.* 10, 522–538. doi:10.1080/17538947.2016.1237571

Yue, G. Y., Zhao, L., Zhao, Y. H., Du, E. J., Wang, Q., Wang, Z. W., et al. (2013). Relationship between soil properties in permafrost active layer and surface vegetation in Xidatan on the Qinghai-Tibetan Plateau. *J. Glaciol. Geocryol.* 35 (3), 565–573.

Zhang, G., Nan, Z., Zhao, L., Liang, Y., and Cheng, G. (2021). Qinghai-Tibet Plateau Wetting Reduces Permafrost thermal Responses to Climate Warming. *Earth Planet. Sci. Lett.* 562 (1), 116858. doi:10.1016/j.epsl.2021.116858

Zhao, L., Zou, D., Hu, G., Du, E., Pang, Q., Xiao, Y., et al. (2020). Changing Climate and the Permafrost Environment on the Qinghai–Tibet (Xizang) Plateau. *Permafrost Periglac.* 31 (3), 396–450. doi:10.1002/ppp.2056

Zhao, S. M., Cheng, W. M., and Chai, H. X. (2007). Research on the Information Extraction Method of Periglacial Geomorphology on the Qinghai-Tibet Plateau Based on Remote Sensing and SRTM: A Case Study of 1:1,000,000 Lhasa Map Sheet H46. *Gegraphical Res.* 26, 1175–1185. (in Chinese). doi:10.11821/yj2007060012

Zheng, L., Overeem, I., Wang, K., and Clow, G. D. (2019). Changing Arctic River Dynamics Cause Localized Permafrost Thaw. *J. Geophys. Res. Earth Surf.* 124, 2324–2344. doi:10.1029/2019JF005060

Zhu, X., Wu, T., Li, R., Xie, C., Hu, G., Qin, Y., et al. (2017). Impacts of Summer Extreme Precipitation Events on the Hydrothermal Dynamics of the Active Layer in the Tanggula Permafrost Region on the Qinghai-Tibetan Plateau. *J. Geophys. Res. Atmos.* 122 (21), 549–611. doi:10.1002/2017JD026736

Zou, D., Zhao, L., Sheng, Y., Chen, J., Hu, G., Wu, T., et al. (2016). A New Map of Permafrost Distribution on the Tibetan Plateau. *Cryosphere* 11 (6), 2527–2542. doi:10.5194/tc-11-2527-2017

Conflict of Interest: The authors declare that the research was conducted in the absence of any commercial or financial relationships that could be construed as a potential conflict of interest.

frontiers in Earth Science

ORIGINAL RESEARCH
published: 30 July 2021
doi: 10.3389/feart.2021.678655

Studies for Frost Heave Characteristics and the Prevention of the High-Speed Railway Roadbed in the Zoige Wetland, China

Fujun Niu[1,2,3], *He Hu*[1,2]*, *Minghao Liu*[3]*, *Qinguo Ma*[1,2] *and Wenji Su*[1,2]

[1]State Key Laboratory of Subtropical Building Science, South China University of Technology, Guangzhou, China, [2]South China Institution of Geotechnical Engineering, School of Civil Engineering and Transportation, South China University of Technology, Guangzhou, China, [3]State Key Laboratory of Frozen Soil Engineering, Northwest Institute of Eco-Environment and Resources, Chinese Academy of Sciences, Lanzhou, China

The Xining–Chengdu high-speed railway crosses the Zoige Wetland, located on the northeast edge of the Qinghai-Tibet Plateau and the upper reaches of the Yellow River. The cold climate and frost-heave-sensitive subgrade soil cause a large frost heave deformation of the roadbed, threatening the safety of trains. This article systematically studied the ground temperature development, frost heave characteristics, soil water content, and groundwater level variations by field investigation and monitoring. The maximum frost heave deformations of the natural flat ground and hillslope reached 25.64 and 3.17 mm, respectively, and this significant discrepancy was mainly caused by the groundwater supply conditions. Future roadbed stability on the flat ground may be compromised by frost heave deformation. To solve this problem, contrasting indoor tests were conducted to analyze the frost heave characteristics of natural ground clay and replacement coarse-grained soil (CGS). It was shown that the absorbed external water mainly changed into dispersed pore ice in the freezing CGS, while it mainly changed into the layered ice lens in the freezing clay. Further tests showed that the frost susceptibility of the CGS was proportional to the fines content and initial water content. The poorly graded CGS had weaker frost susceptibility than the well-graded CGS. The results suggest that anti-frost methods should be fully considered, including strict control of fines content and water content, prioritizing the use of poorly graded filling, and disruption of local water accumulation in the filling layer.

Keywords: zoige wetland, high-speed railway, frost heave prevention, coarse-grained soil, field monitoring

OPEN ACCESS

Edited by:
Guo Donglin,
Institute of Atmospheric Physics (CAS), China

Reviewed by:
Yanhu Mu,
Chinese Academy of Sciences (CAS), China
Alan Rempel,
University of Oregon, United States
Qingbai Wu,
Chinese Academy of Sciences (CAS), China

***Correspondence:**
He Hu
1204071132@qq.com
Minghao Liu
liuminghao@lzb.ac.cn

Specialty section:
This article was submitted to Cryospheric Sciences, a section of the journal Frontiers in Earth Science

Received: *10 March 2021*
Accepted: *28 June 2021*
Published: *30 July 2021*

Citation:
Niu F, Hu H, Liu M, Ma Q and Su W (2021) Studies for Frost Heave Characteristics and the Prevention of the High-Speed Railway Roadbed in the Zoige Wetland, China. Front. Earth Sci. 9:678655. doi: 10.3389/feart.2021.678655

INTRODUCTION

High-speed railways (HSRs) have been constructed to improve traffic congestion and develop local economies in China in recent years. It has been reported that the total length of HSR in China will reach 38,000 km by 2025. In northwest China, particularly in and around the Qinghai–Tibet Plateau, undeveloped transportation infrastructure seriously restricts local economic development. Therefore, HSR construction is essential and necessary. Long-distance railway and complex geo-engineering conditions make HSR construction extremely difficult. Among the difficulties, thaw settlement in permafrost regions and frost heave in the seasonally frozen ground should be paid

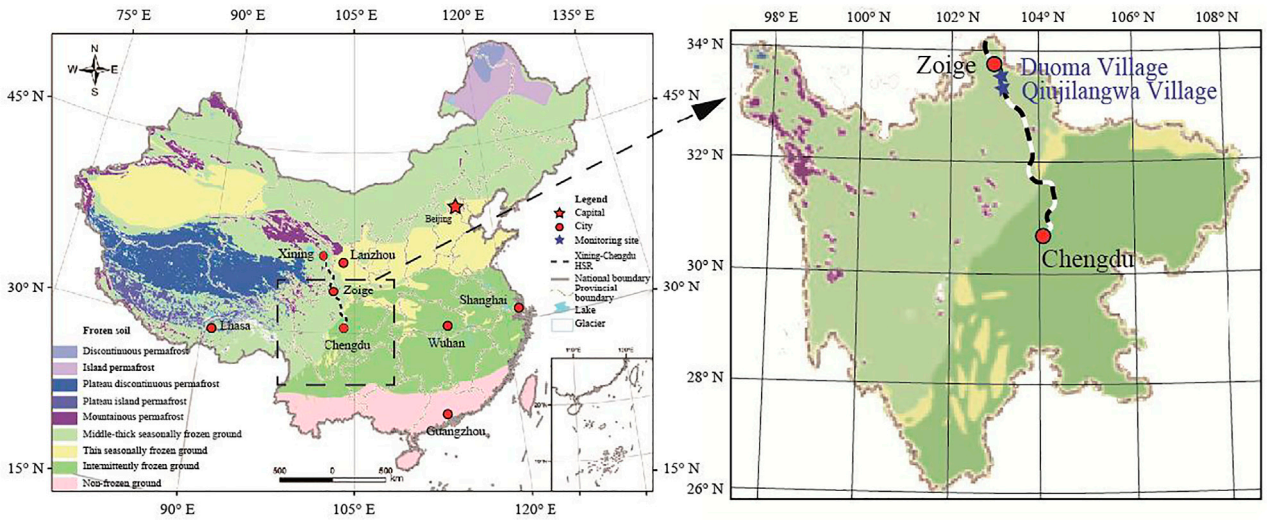

FIGURE 1 | Frozen ground distribution in China and the monitoring site along the Xining-Chengdu HSR.

particular attention to because these regions largely consist of permafrost and seasonally frozen soils (Jin, 2007; Yue et al., 2007; Li et al., 2008; Song et al., 2014; Wang et al., 2020). The cold climate and frost heaving of the subgrade significantly affect the safety and stability of railway lines. A new high-speed railway between Xining (Capital of the Qinghai Province) and Chengdu (Capital of the Sichuan Province) began construction in 2020 and is planned to be completed in 2027. The whole line passes through vast areas of seasonally frozen ground, especially the Zoige section of the swamp wetland located in the northeast part of the Qinghai–Tibet Plateau and the upper reaches of the Yellow River (**Figure 1**). Wet soils, shallow groundwater, and lower temperatures in this area seriously threaten railway stability through frost heaving.

Frost heaving was first investigated by Taber (1929) and has been widely studied using indoor freezing tests and numerical analyses (Everett, 1961; Gilpin, 1980; Konrad, 2008; Thomas et al., 2009; Jin et al., 2019; Xu et al., 2020). Many models have been developed to predict frost heave deformation, including the hydrodynamic model (Harlan, 1973), the rigid-ice model (O'Neill and Miller 1985), the segregation potential model (Konrad and Morgenstern, 1981), and the discrete ice lens model (Nixon, 1991). It is widely agreed that ice lenses caused by water transportation dominate soil deformation. Therefore, eliminating ice lenses is the most effective measure for preventing frost heaving. The formation of ice lenses is closely related to soil type, water content and water migration conditions, temperature and temperature differences, freezing rate, and load (Taber, 1929; Miller, 1972; Gilpin, 1980; Konrad and Morgenstern, 1982; Peppin and Style, 2012; Mao et al., 2014).

The common HSR embankment filling is coarse-grained soil (CGS), which consists of coarse grains and a certain content of fine grain soil. The particle size of the fine grain is less than 0.075 mm. For the freezing CGS, the low unfrozen water content and large void volume make it difficult for ice lenses to form. However, based on field observations along the Harbin–Dalian HSR (HDHR) and Lanzhou–Xinjiang HSR, frost heave still occurred (Liu et al., 2016; Lin et al., 2018). Niu et al. (2017) reported the measured soil water, ground temperatures, and deformation variations of embankments and cut sections in the HDHR. The frost heave deformation discrepancy between two different types of subgrade indicated that soil water content was the primary factor controlling the frost heave amount, while frost depth was the secondary factor. Zhang et al. (2016) and Sheng et al. (2014) proposed the three most likely frost heave mechanisms in the HSR foundation: the high fine content caused by poor quality control of the coarse filling, the top-down water supply mechanism resulting from the flow of rainfall water and other surface water, and the bottom-up water supply mechanism caused by mud pumping under train cyclic loads. A corresponding one-dimensional frost heave model was developed to verify these mechanisms (Sheng et al., 1995; Sheng et al., 2013). It was concluded that the three mechanisms interacted with each other, and their synergetic action caused the observed frost heave deformation of the HSR embankment. Wang et al. (2016) demonstrated that moisture content was the most significant contributing factor to the frost heave ratio of the CGS. If the moisture content was maintained at less than 5%, the frost heave development of the CGS could be prevented. Based on these studies, it is widely agreed that the fines content, water content, and filling type have significant influences on the frost susceptibility of the CGS. However, previous studies mainly focused on the relationships between frost heave deformation and content of the fine grain and ignored the important role of grain size distribution in CGS. Therefore, the impact of soil gradation should be investigated further.

The purpose of this research was to study the frost heave characteristics of HSR roadbeds in the Zoige Wetland and corresponding prevention. To achieve this, a comprehensive

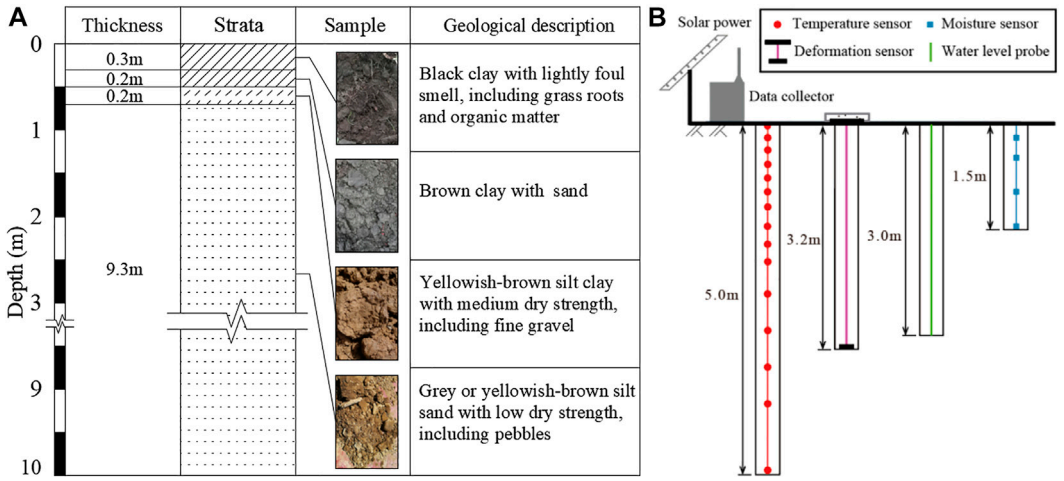

FIGURE 2 | Geotechnical condition and field-monitoring system at the study sites. **(A)** Geotechnical condition; **(B)** schematic diagram of monitoring system.

field-monitoring system was installed to monitor the variations in ground temperature, ground deformation, soil moisture, and groundwater table. Based on the monitoring data and local ecological environment, a soil-replacement method with CGS was proposed to reduce the frost heave deformation of the embankment. Then, the effectiveness of this method was tested in terms of the frost heave amount and frost heave ratio using indoor experiments. Moreover, further experiments were performed to study the influences of various typical factors on the anti-frost effect of the replacement method, including the fine content, initial water content, and grain size distribution of coarse particles. Finally, the frost heave characteristics of filling were studied to provide potential engineering treatments for HSR embankments in cold regions. The results can provide useful guidance for frost heave prevention in road construction in seasonally frozen ground.

FIELD MONITORING OF NATURAL GROUND

Study Site Condition

The construction of the Xining–Chengdu HSR began in March 2020, and the planned construction period was 7.5 years. To observe the frost heave characteristics of the soils underlying the railway line, two monitoring systems were installed at Qiujilangwa village and Duoma village, near the city of Zoige, Sichuan Province (**Figure 1**). The Qiujilangwa village monitoring site is located on flat ground approximately 48 km southeast of Zoige city. The Duoma village monitoring site is located on a hillslope approximately 11 km southeast of Zoige city. Field investigations showed that the natural shallow strata of these two monitoring sites were the same. The strata are composed of black clay with grass roots and organic matter at a depth of 0–0.3 m, brown clay with sand at a depth of 0.3–0.5 m, yellowish-brown silt clay with fine gravel at a depth of 0.5–0.7 m, and yellowish-brown silt sand with pebbles at depths below 0.7 m. The corresponding field photos of the samples are shown in **Figure 2A**.

Monitoring System

Field monitoring was performed under a natural surface. The monitoring system consisted of an automatic data collector, a power supply system, temperature sensors, moisture sensors, deformation sensors, and a water level probe (**Figure 2B**). The variations in soil temperature, moisture content, groundwater table, and deformation caused by freezing and thawing were collected. The temperature sensors were designed and produced by the State Key Laboratory of Frozen Soil Engineering, and the normal measurement range of the sensor was −25 to +80°C. In total, 16 temperature sensors with an accuracy of ±0.02°C were installed in a 5 m-deep borehole with a thermistor string (Wu et al., 2018; Miao et al., 2020). The spacing of the temperature sensors was 0.2 m in the top, 1.0 m, 0.25 m from 1.0 to 2.0 m in depth, and 0.5 m from 2.0 to 5.0 m in depth.

The volumetric water content of the soil was measured using four QSY8909A soil-moisture sensors (Sichuan Stone Edge Science and Technology Co., Ltd.) at depths of 0.2, 0.5, 1.0, and 1.5 m. The moisture sensors had a measurement range of 0–100% and an accuracy of 3% (Lin et al., 2018). In addition, a QSY8907C-200 frost heave sensor (produced by Sichuan Stone Edge Science and Technology Co., Ltd) was used to measure the frost heave amount. The maximum frost depth of natural ground is less than 1.0 m (The National Standards Compilation Group of the People's Republic of China, 2011). The soil layers deeper than 3.2 m are far from the frost front, and the corresponding deformation can be negligible. Thus, a depth of 3.2 m can be taken as a benchmark. The frost heaving sensor was embedded into the soil through a plastic pipe. This sensor measured the relative deformations between the top and bottom plates, as shown in **Figure 2B**. The bottom plate was fixed to a designated depth of 3.2 m by concrete, and the top plate was fixed to the natural ground surface. During the freezing season, the top plate moves up as frost heave occurs. The frost heave

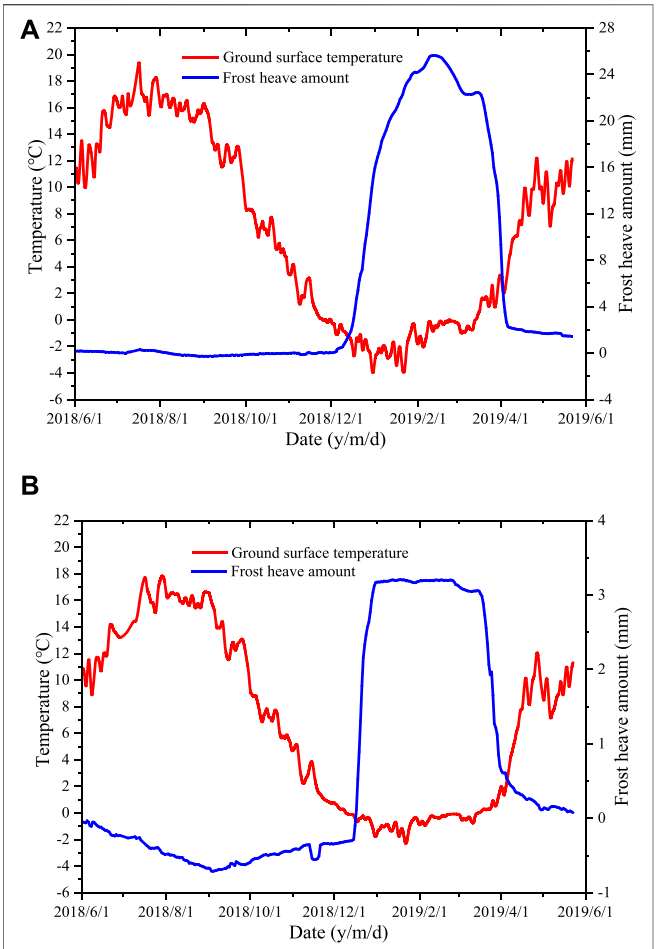

FIGURE 3 | Variations of the ground surface temperature and frost heave amount. **(A)** Data from the Qiujilangwa village monitoring site; **(B)** data from the Duoma village monitoring site.

amount of natural ground can be determined by measuring the displacement of the top plate. The measurement accuracy and measurement range of the heave sensor are 0.01 mm and from −100 mm to +100 mm, respectively. Finally, a HOBO U20-001-01 water level probe was installed in a 3.0 m-deep borehole to record the groundwater table variation automatically. All sensors were connected to a QSY300Z-64CH automatic data collector. The monitored data were automatically collected and transmitted wirelessly. All instruments in this monitoring system were powered by a combination of solar panels and storage batteries. Monitoring data were recorded every 4h from June 2018 through May 2019.

Soil Temperature and Frost Heave Amount

The Qiujilangwa village monitoring site is located on flat ground. According to the monitored data, the ground surface temperature reached a maximum value of 19.4°C in late July 2018 and a lowest value of −4.1°C in late January 2019, as shown in **Figure 3A**. The annual range of surface temperature and mean annual surface temperature were 23.5 and 6.6°C, respectively. The surface temperature dropped to less than 0°C on November 26 and continued until March 13. The freezing period of the ground was approximately 107 days. At this time, the rapid frost heave developed and reached a maximum value of 25.64 mm on February 13, 2019. Following this period of rapid heave, the displacement decreased from February 13 to March 13 to a stable value of 22.44 mm accompanied by the approach of 0°C isotherm. As the temperature further increased and the soil continued thawing, the displacement rapidly decreased to 2.28 mm within 20 days. The final deformation amount was approximately 1.66 mm during the next thaw period. The melting amount was less than the frost heave amount after the freeze–thaw action. We infer that this was because the soil resisted the thaw settlement because of its cohesion. If the number of freeze–thaw cycles increases, the soil cohesion strength will decrease due to water migration. Eventually, the thaw settlement amount would be close to the frost heave amount.

The frost heave ratio is defined as the proportion that the heave amount accounts for frozen depth:

$$\eta = \frac{\Delta h}{H_f} \times 100\% \quad (1)$$

where η is the frost heave ratio, Δh is the frost heave amount (mm), and H_f is the frozen depth (mm).

The contour graphs of the subsurface temperature show temperature distribution using the time as the X-axis, the stratum depth as the *Y*-axis (**Figure 4**). The unmeasured temperatures were obtained based on the least-squares method according to the measured temperatures. According to the current code for engineering geological investigation of frozen ground in China (The National Standards Compilation Group of the People's Republic of China, 2014), the grades of the frost-susceptible silt clay can be classified as grade Ⅰ non-frost soil with a frost heave ratio less than 1%, grade Ⅱ weakly frost-susceptible soil with a frost heave ratio larger than 1% and less than 3.5%, grade Ⅲ frost-susceptible soil with a frost heave ratio larger than 3.5% and less than 6%, grade Ⅳ highly frost-susceptible soil with a frost heave ratio larger than 6% and less than 12%, and grade Ⅴ extra highly frost-susceptible soil with a frost heave ratio larger than 12%. The frozen depth of the Qiujilangwa village monitoring site was 0.42 m when the frost heave amount reached the maximum, based on the contour graph of subsurface temperature shown in **Figure 4A**. At that moment, the frost heave ratio was 6.10%, indicating that the ground soil could be regarded as a grade Ⅳ highly frost-susceptible soil. In addition, the maximum frozen depth (0.54 m) occurred on January 23, 2019, but the heave amount increased until February 23, 2019. This indicates that the frost heave amount was hysteretic to the frost penetration. Owing to the relatively shallow frost penetration and the rapidly rising ground surface temperature after March 13, the frozen depth dropped to zero within four days.

The Duoma village monitoring site is located on a gentle hillslope. The ground surface temperature also began to drop to subzero temperatures on December 10 (**Figure 3B**). Rapid

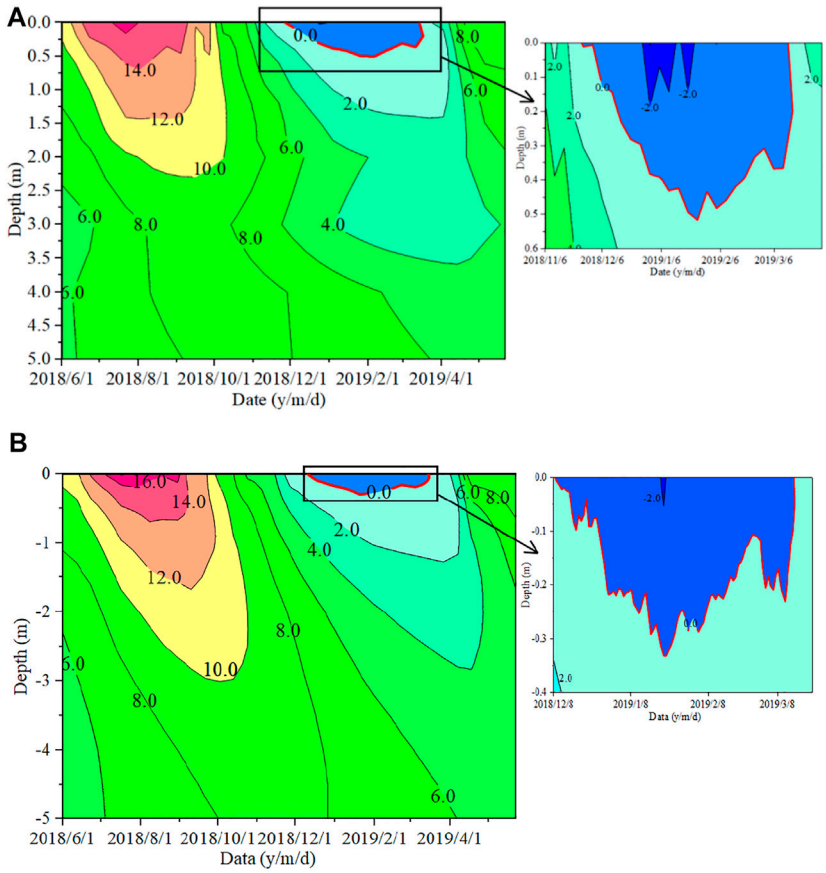

FIGURE 4 | Contour graph of subsurface temperature. **(A)** Data from the Qiujilangwa village monitoring site; **(B)** data from the Duoma village monitoring site.

heaving was recorded immediately accompanied by soil freezing. However, the frost heave amount did not show a successive increasing tendency, but it rapidly reached a maximum value of 3.17 mm on December 31 and then remained stable until the beginning of the thawing season on March 16. The frozen depth on December 31 was 0.22 m, and the corresponding frost heave ratio was 1.45% (**Figure 4B**). The ground soil could be regarded as grade Ⅱ, weakly frost-susceptible soil. The maximum frozen depth (0.33 m) also occurred on January 23, 2019. Furthermore, most thawing settlement occurred over 27 days (March 16 to April 12), reaching 0.34 mm. The highest and lowest ground surface temperatures at the Duoma village monitoring site were 18.5°C and −3.6°C, respectively, similar to the values at the Qiujilangwa village monitoring site (19.4°C and −4.1°C). However, the frost heave displacement at the Duoma village monitoring site was much less than that at the Qiujilangwa village monitoring site.

Soil Moisture Content

The soil moisture content changes with time at different depths for the Qiujilangwa village monitoring site are shown in **Figure 5A**. From July to early September, the moisture content at a depth of 0.2 m gradually decreased to 28.0%, which was attributed to evaporation. This is because the variation of soil moisture content at the shallow surface is related to evaporation, precipitation, vegetation conditions, temperature, and human activity. The Qiujilangwa village monitoring site did not experience any special or large variations of vegetation conditions and human activity from July 2018 to early September 2018. At the same time, the precipitation was small. The subsurface temperature between July and early September was large (**Figure 4**), which was beneficial to water evaporation. Following this process, the water content rapidly increased from September 3 to September 26 to a nearly stable level of approximately 39.2% because of the decrease in subsurface temperature and increase in rainfall. When the surface temperature fell below 0°C, the water content did not rapidly decrease to 9.8% until December 18. This could be because of the phase change of the liquid water into ice. The soil-water sensor only measured the unfrozen liquid water content. In the following frozen period, the unfrozen water content at a 0.2 m depth maintained a stable value of 8%. After March 13, the soil moisture content increased rapidly as the surface temperature increased, and the soils melted during the thawing season.

In the Qiujilangwa village monitoring site, the moisture content variation at a 0.5 m depth was similar to that at a

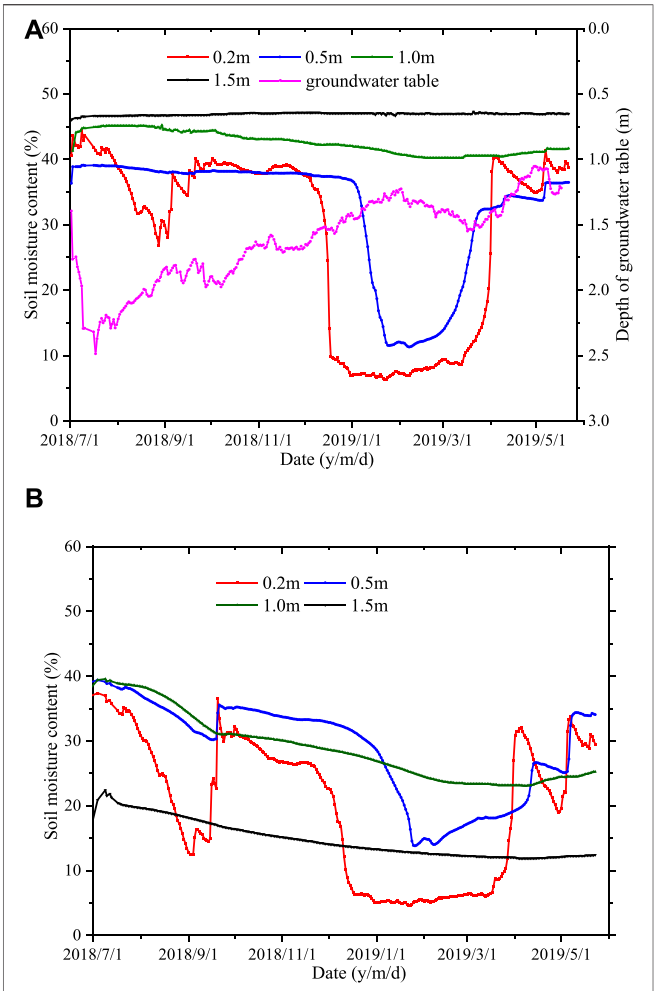

FIGURE 5 | Depth of groundwater table and soil moisture content at various depths. **(A)** Data from the Qiujilangwa village monitoring site; **(B)** data from the Duoma village monitoring site.

0.2 m depth in winter. However, it showed a rapid falling trend on January 6 and a slow rising tendency on February 24, indicating that the corresponding freezing period was less than that at a 0.2 m depth. The steady unfrozen water content during the freezing season was approximately 11.5%. The near-surface soil water content fluctuated acutely with freezing and thawing. Furthermore, the 1.0-m-deep position was far from the frozen depth, but it still showed a slow changing trend in water content from December 2018 to March 2019. The water content changes were caused by moisture migration to the frozen zone and melted ice from the upper-layer frozen soil, respectively. As a result of the approach of the groundwater table (**Figure 5A**), the water content at the 1.5 m depth maintained a steady value of 47.0% during the entire monitoring period. The groundwater table showed a sharply decreasing trend in the initial monitoring time and a slowly growing tendency during the following phase. The groundwater table also varied around a depth of 1.5 m during the freezing season.

The soil water in the Duoma village monitoring site followed nearly the same pattern as that in the Qiujilangwa village monitoring site, as shown in **Figure 5B**. The data of groundwater table variation at the Duoma village monitoring site were not acquired because of the deep groundwater, indicating that the groundwater table was below a depth of 3 m. The maximum frost depth of the Duoma village monitoring site was approximately 0.54 m. The groundwater was far from the upper frozen soil during the freezing season. In other words, no external water was supplied to the near-surface freezing soil during the freezing season. The soil mainly froze in the pattern of *in-situ* frost heave. As a result, the frost heave displacement at the Duoma village monitoring site was much less than that at the Qiujilangwa village monitoring site and showed a stable value during the freezing season. Thus, the underground water supply condition was the primary limiting factor for frost heaving in the Zoige Wetland.

Based on the aforementioned measurement data, it is thought that the Qiujilangwa village had a shallow frost depth but a large frost heave ratio. The Duoma village had a lower frost heave ratio because of the deep groundwater. Therefore, for running safety, corresponding measures must be taken to prevent the frost heave of HSR embankments in sections similar to the Qiujilangwa village site. Groundwater, negative temperature, and frost-susceptible soil are essential conditions for frost heave development. Frost heave can be mitigated or prevented by controlling any one of the three factors. The Zoige Wetland was identified as a National Nature Reserve in 1998 (Zuo et al., 2019). To protect the local ecological environment and underground water source, the method of lowering or cutting off groundwater to prevent frost heave is not allowed. If the insulation board is installed in the embankment foundation, the possible damage under a long-term train dynamic load is difficult to access. The method of replacing natural soil with CGS seems to be the most reliable choice. Therefore, an appropriate indoor test was designed and conducted to distinguish the frost heave ability of natural foundation soil and CSG.

FROST HEAVE ABILITY OF FOUNDATION SOIL AND COARSE-GRAINED SOIL

Test Description

Materials and Experimental Scheme

Natural soil was taken from the Zoige Wetland, and the plastic limit, liquid limit, optimum water content, and maximum dry density were 16.1, 32.5, 17.2%, and 1.98 g/cm^3, respectively. After drying, crushing, and filtering through a 0.075 mm sieve, the clay sample was prepared with an initial water content of 25.0% and a dry density of 1.58 g/cm^3. The density of the fine clay particles was 2.74 g/cm^3. The CGS samples consisted of a certain amount of the above sieved fine clay and coarse particles (>0.075 mm in size). The density of the coarse particles was 2.55 g/cm^3. The soil sample was placed in a cylindrical sample cell. The soil sample was 10 cm in height and 6 cm in diameter, and the corresponding total volume was approximately 282.73 cm^3. The volume of fine

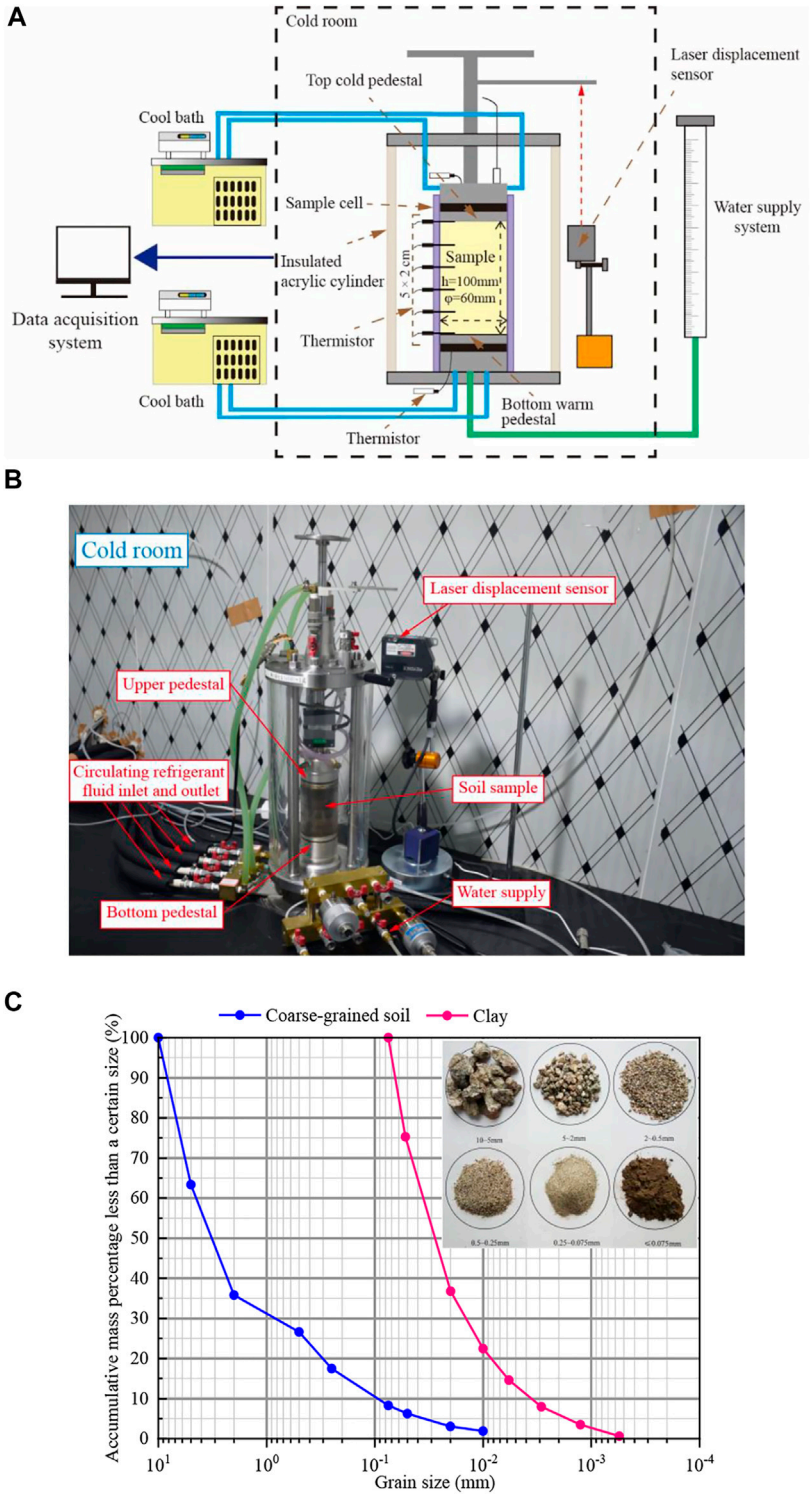

FIGURE 6 | | Frost heave test apparatus and samples. **(A)** Schematic diagram; **(B)** real test devices in the cold room; and **(C)** grain size distribution curves of samples.

clay can be known by dividing its mass by its density. The fines content presented the volume of fine clay as a percentage of the total volume of the sample. The initial water content and fines content of the CGS were 10 and 5.9%, respectively. The dry density of the CGS was 1.95 g/cm^3. The grain size distributions of the CSG and clay are shown in **Figure 6C**.

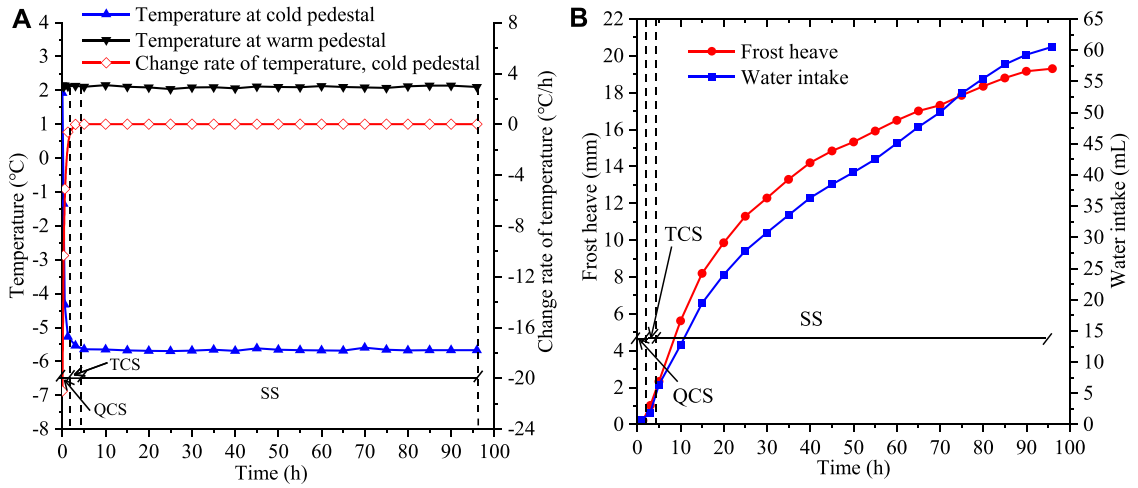

FIGURE 7 | Freezing results of clay sample. **(A)** Variations of temperature and change rate of temperature; **(B)** variations of water intake amount and heave amount.

Test Apparatus and Process

The frost heave test apparatus was composed of six parts: a sample cell, top, and bottom pedestals, two thermal control cool baths, a water supply, a frost heave measuring device, and a data acquisition system (**Figure 6**). The test sample cell was made of organic glass 6 cm in inner diameter, 18.5 cm in height, and 0.75 cm in thickness, and it was used to place the soil sample. Each soil sample was divided into five equal parts, and each part was compacted into a sample cell with a hammer to the target height with a predesigned dry density. At the same time, six Pt 100 thermistors with 2 cm intervals along the sample height were inserted into the soil sample to record the temperature variation at different depths. The sample cell was placed between the fixed bottom pedestal and the vertically movable top pedestal. Two cool baths were connected to the top and bottom pedestals to control the soil temperature. Furthermore, a larger-diameter insulated acrylic cylinder was placed outside the sample cell to reduce heat turbulence from the ambient environment. A Mariotte flask was connected to the bottom pedestal by a plastic tube, and the water level of the Mariotte flask was set at the same height as the bottom of the soil sample to achieve a no-pressure water supply. The frost heave amount was monitored using a laser displacement sensor. The frost heave instruments were placed in a cold room where the room temperature was held at 1°C to maintain the thermal stability of the sample. The data acquisition system consisted of a data logger located outside the cold room and a personal computer. Displacement and temperature data were automatically collected every 5 min.

First, the top and bottom temperatures of the soil sample were kept at +2°C for 12 h to ensure that the initial temperature of the soil sample was uniform. Then, the top and bottom temperatures of the soil sample were set as constant at −6°C and +2°C, respectively, during the entire freezing process. The Mariotte flask was opened simultaneously to provide a moisture source. The frost heave process lasted 96 h for clay and 144 h for CSG. Because of early test carelessness, the soil temperatures in the freezing clay were not measured, but the top cold pedestal and the bottom pedestal were recorded. Because the aim was to determine the frost heave ability of the frozen clay, the unmeasured soil temperature had no effect on this target.

Test Results and Analysis

Frost Heave Characteristics of Natural Clay

The variations in temperature, frost heave, and water intake of clay soil during the freezing process are shown in **Figure 7**. The temperature at the cold pedestal experienced a rapid decrease in the initial freezing stage, followed by a gradual decrease, and an eventual stable state after a period of time (**Figure 7A**). The cooling process was divided into three stages: the quick cooling stage (QCS), transition cooling stage (TCS), and stable stage (SS). The change rate of temperature at the cold pedestal decreased quickly to nearly zero from the QCS to SS, where a negative sign indicated the decrease of temperature. In the QCS and TCS, the frozen depth increased with the downward moving frost front. The amount of liquid water migration was less (**Figure 7B**), and no ice lens was formed because of the short duration. The frost heave amount in these two stages could be regarded as the *in-situ* frost heave amount. The heave with a high frost heave rate was mainly caused by the internal pore water phase changing into ice. The steady stage started when the temperature decreased to the lowest value, and the temperature remained in a stable state after that moment. The frost front almost remained at a fixed height during this stage. Meanwhile, liquid water migration to the frozen zone caused the formation of segregated ice. The frost heave amount at this stage was regarded as the segregated frost heave amount. The final frost heave and water supply amounts were 19.3 mm and 60.5 ml, respectively.

As the water-ice phase in the frozen zone, negative pore water pressure formed, which resulted in successive liquid water transfers from the unfrozen zone to the frozen zone. Meanwhile, the diminishing water in the unfrozen zone also led to the formation of negative pore water pressure, and liquid water was absorbed from the external water source. A frozen

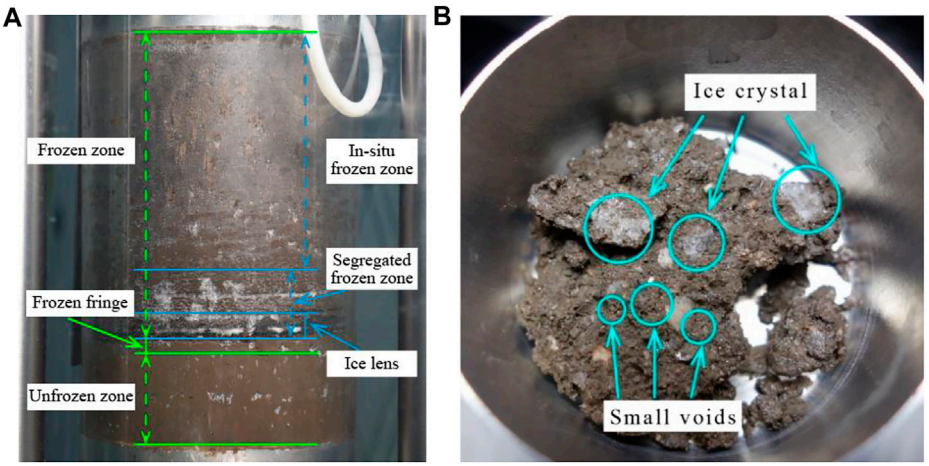

FIGURE 8 | Phase change of migrated water. **(A)** Ice lens formation in the clay; **(B)** large pore ice crystal and small empty voids in the CGS.

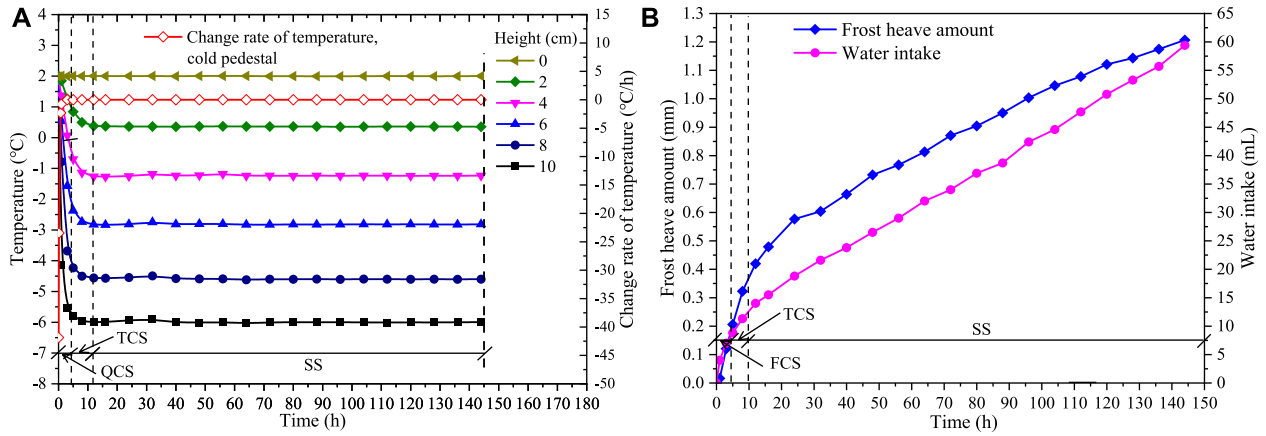

FIGURE 9 | Freezing results of CGS sample. **(A)** Variations of soil temperature and change rate of temperature; **(B)** variations of frost heave and water intake.

fringe of transition existed between the frozen zone and the unfrozen zone, where the phase change of pore water occurred. The frozen fringe temporarily stored the water transferred from the unfrozen zone and provided the water source for upward water migration. The void of clay was small, and easy to fill with pore ice. When the pore pressure exceeded the sum of the overburden pressure and separation pressure, the pore ices were integrated into a whole and formed an ice lens (Nixon, 1991; Thomas et al., 2009). Because of the blocking effect of the ice lens on unfrozen water migration, water that migrated from the unfrozen zone accumulated at the bottom of the ice lens. As a result, the water absorbed from the outside water source further changed into an ice lens, and the frost heave amount progressively increased with the growth of the ice lens. **Figure 8A** shows the typical ice lens formation of freezing clay at 96 h.

Frost Heave Characteristics of Coarse-Grained Soil

The experimental results for the CGS sample are shown in **Figure 9**. Similar to the freezing clay sample, the cooling process of the CGS sample can also be divided into three stages: the QCS, TCS, and SS (**Figure 9A**). The soil bottom temperature was maintained at +2°C, and the soil temperature at other heights decreased as the soil top temperature decreased. The closer to the top, the larger the cooling rate. Increases in the frost heave and water intake rates were observed immediately during freezing. In the SS, the soil temperature of the frozen zone at different heights fluctuated slightly and then remained stable. The frozen depth, frost heave rate, and water intake rate also gradually tended to become stable. The final frozen depth and heave amount were 75.5 and 1.2 mm, respectively. The final water intake and the frost heave ratio were 59.4 ml and 1.60%, respectively.

The states of the CGS column during freezing are shown in **Figure 10**. At the start of freezing, a small amount of water drop was found on the inner surface of the sample cell, which was produced by vapor condensation during the constant-temperature stage. The unfrozen and frozen zones showed no

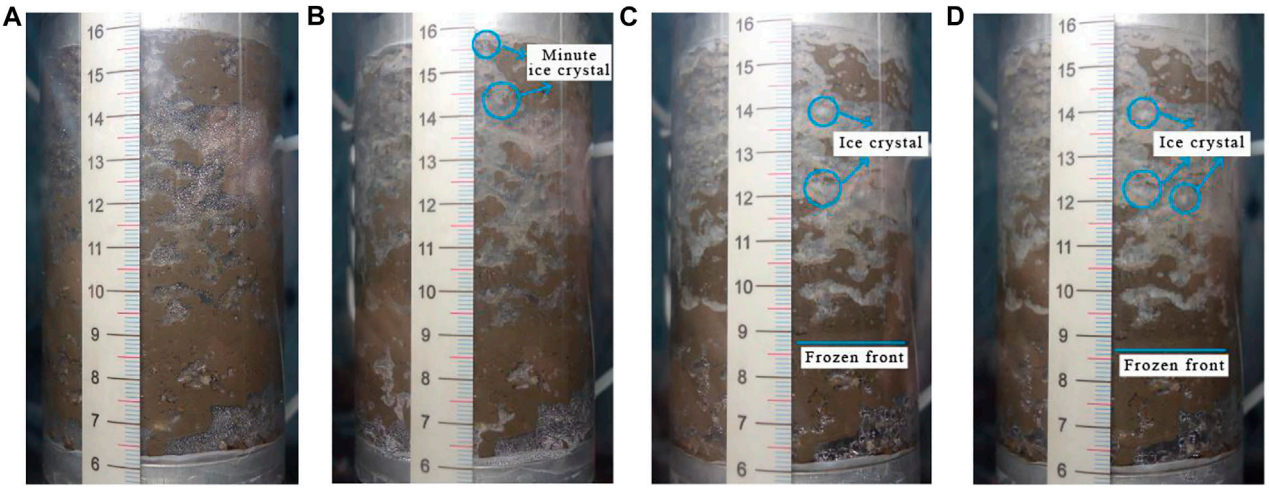

FIGURE 10 | States of CGS sample at **(A)** 0 h; **(B)** 10 h; **(C)** 96 h; and **(D)** 144 h.

distinct difference at 10 h because of the short freezing duration (**Figure 10B**). The liquid water migrated to the frozen zone under temperature gradients, leading to the formation of minute pore ice crystals between the soil particles in the frozen zone. At 96 and 144 h, the ice crystal size further increased with the freezing of migrating liquid water (**Figures 10C,D**). The soil void was filled with ice crystals that changed from migrating water (**Figure 8B**). The pore ice bulk was much less than the CGS particle bulk, leading to the pore pressure being insufficient to resist the sum of the overburden pressure and separation pressure. Even though the large voids were filled with pore ices, partial small voids were still empty without any ice crystals and were interconnected (**Figure 8B**). Ultimately, no visible ice lenses were detected within the frozen fringe.

Comparing the frost heave characteristic diversities between the clay soil and the CGS, it was shown that the water absorbed from outside water source mainly changed into pore ice for CGS, while it mainly changed into an ice lens for clay soil. The pore ice in the CGS was dispersed and not integrated into a whole, which was detrimental to the formation of an ice lens. Thus, the frost heave amount of the CGS was much less than that of the clay soil.

Based on the thermal boundary condition of the CGS sample, it can be concluded the temperature distribution along the soil column depth was nearly linear in the SS. The temperature distribution of the clay sample was similar to that of the CGS sample. One can conclude that the final frozen depth of the clay soil column was approximately 75.0 mm, and the corresponding frozen heave ratio was 25.73%. Under the same temperature conditions, even when the water intake amounts were very close, the frost heave amount and frost heave ratio of the CGS were much lower than those of the natural clay soil. This experimental result shows that replacing natural soil with CGS is a possibility for railway construction. To optimize the anti-frost effect of CGS in HSR embankments, the influence of fines content, initial water content, and grain size distribution of coarse particles on the frost heave ability of the CGS were investigated, as discussed in *Variations in Frost Heave With Soil Composition*.

VARIATIONS IN FROST HEAVE WITH SOIL COMPOSITION

The test samples, apparatuses, and procedures were the same as those in the frost heave test of the CGS, as described in the *Test Description*. The test scheme is listed in **Table 1**. Samples S1–S5 were prepared to study the influence of fines content on the frost susceptibility of CSG, samples S6, S2, and S7 were prepared to study the influence of initial water content, and samples S5 and S8–S10 were prepared to study the influence of the grain size distribution of coarse particles. The mass percentages of the certain-size grains of samples S5 and S8–S10 are presented in **Table 2**. The grain size distributions of the coarse particles of samples S1–S7 are the same. The grain gradation of the other samples with different fines contents can also be determined by combining with the grain gradation of sample S5. Sample S7 is the CGS sample described in *Frost Heave Characteristics of Coarse-Grained Soil*. The uniformity coefficient and coefficient of curvature for samples S5 and S8–S10 are listed in **Table 2**.

Effects of Fines Content and Initial Water Content

The three distribution models of the CGS with a given fines content are presented in **Figure 11**. The CGS without fines grains (**Figure 11A**), owing to its large voids, has a weak water retention ability and low matrix suction; thus, water migration along the coarse grain surface is difficult. In this case, the frost heave deformation is small and mainly in the pattern of *in-situ* frost heave. For the CGS with partial fines (**Figure 11B**), the void size between coarse grains is reduced and the matrix suction increases correspondingly. The external water is absorbed into the frozen soil, leading to the formation of pore ice. When the pore ice size increases to a certain extent, it begins to push the soil aggregate and support the overburden, bringing macroscopic heave of the CGS. Moreover, the void size further decreases, while the matrix suction and water seepage capacity further increase with the

TABLE 1 | Frost heave test schemes for CGS fillings.

Sample	Grain size distribution of coarse particles	Initial water content (%)	Fines content (%)	Porosity (%)	Temperature boundary of soil sample		Well or poorly graded
					Top (°C)	Bottom (°C)	
S1	Size grade I	8	4.0	23.8	−6	2	Well
S2	Size grade I	8	5.9	24.0	−6	2	Well
S3	Size grade I	8	9.3	24.2	−6	2	Well
S4	Size grade I	8	11.9	24.4	−6	2	Well
S5	Size grade I	8	14.2	24.6	−6	2	Poorly
S6	Size grade I	6	5.9	24.0	−6	2	Well
S7	Size grade I	10	5.9	24.0	−6	2	Well
S8	Size grade II	8	14.2	24.6	−6	2	Well
S9	Size grade III	8	14.2	24.6	−6	2	Well
S10	Size grade IV	8	14.2	24.6	−6	2	Poorly

TABLE 2 | Mass percentage of the certain-size grains.

Sample	Grain size distribution of coarse particles	Grain size (mm)										Uniformity coefficient	Coefficient of curvature
		10	5	2	0.5	0.25	0.075	0.05	0.02	0.01	0		
S5	Size grade I	32	24	8	8	8	4.9	7.8	2.8	4.5	0.5	128.57	0.89
S8	Size grade II	40	24	16	4	4	4.9	7.8	2.8	4.5	0.25	178.57	2.57
S9	Size grade III	16	16	16	16	16	4.9	7.8	2.8	4.5	0.25	35.71	1.03
S10	Size grade IV	40	24	16	0	0	4.9	7.8	2.8	4.5	0.075	178.57	1.45

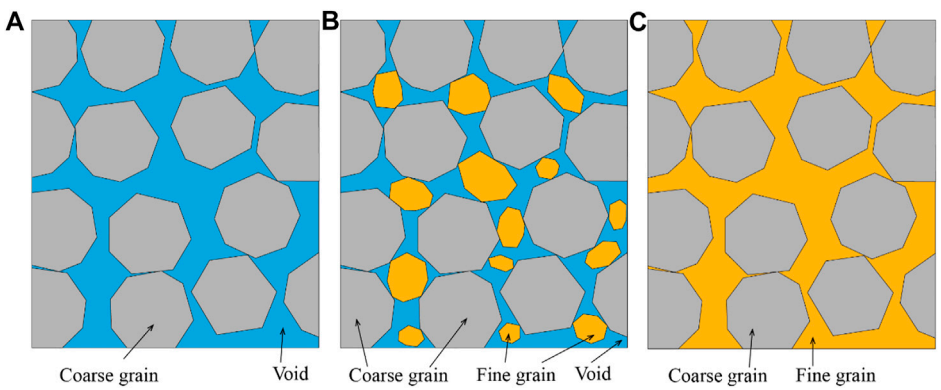

FIGURE 11 | Distribution models of CGS. **(A)** CGS without fines; **(B)** CGS without partial fines; and **(C)** CGS with saturated fines.

TABLE 3 | Frost heave test results for samples S1–S7 after freezing for 144 h.

Sample	Fines content (%)	Initial water content (%)	Frost depth (mm)	Frost heave amount (mm)	Frost heave ratio (%)	Water intake (ml)
S1	4.0	8.0	73.24	0.58	0.79	30.60
S2	5.9	8.0	76.21	0.84	1.10	31.00
S3	9.3	8.0	75.50	1.12	1.48	45.80
S4	11.9	8.0	76.74	1.36	1.77	51.00
S5	14.2	8.0	77.62	1.46	1.88	56.00
S6	5.9	6	77.30	0.68	0.88	40.2
S7	5.9	10	75.50	1.21	1.60	49.4

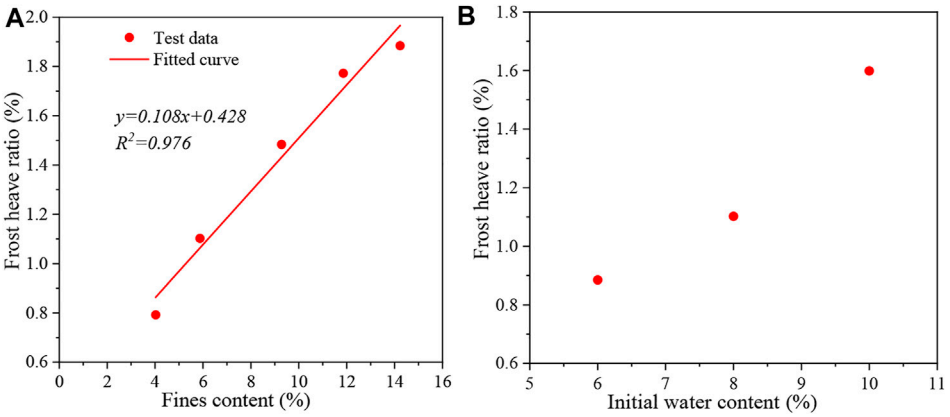

FIGURE 12 | The influence of fines content and initial water content. **(A)** Relationship of frost heave ratio and fines content; **(B)** relationship of frost heave ratio and initial water content.

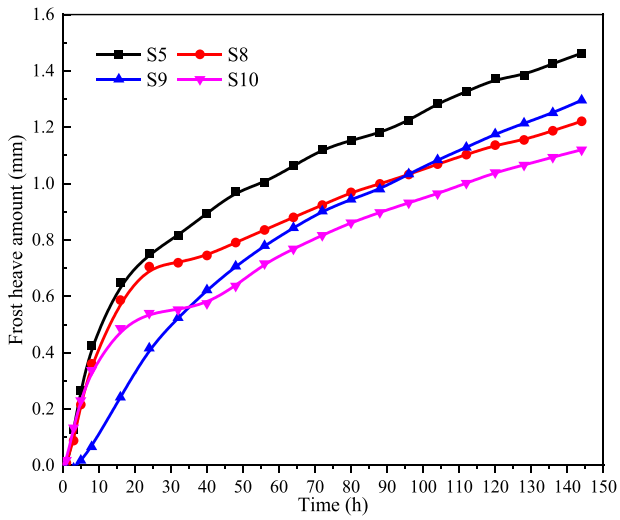

FIGURE 13 | Frost heave for samples with various grain size distributions of coarse particles.

increase in fines content, causing an increase in the water intake amount and pore ice content (**Table 3**). Based on the three models, the experimental results are shown in **Figure 12A**. The frost heave ratio of the CGS in the experiments increased nearly linearly with the increase in fines content. According to the fitting function, the frost heave ratio of the CSG was less than 1% when the fines content was less than 5.3%. At this point, the CSG could be considered a non-frost-susceptible filling. In the case of CGS with saturated fines (**Figure 11C**), where coarse grains were floating in the fine grain, significant frost heave occurred. When the fines content was far more than the coarse grain content, an ice lens formed in the water-saturated freezing CGS (Li et al., 2017).

One can conclude that the fines content strongly affected the water migration, pore ice formation, and frost heave ratio of the CGS, i.e., the fines content improved the frost susceptibility of the CGS, even when it was water unsaturated.

According to the test results of samples S6, S2, and S7, the frost heave ratio increased with initial water content, as shown in **Figure 12B**. The hydraulic conductivity of the unsaturated CGS is (Babu and Srivastava, 2007):

$$K = CD^2 \frac{\gamma_w}{\eta} \frac{e^3}{1+e} \tag{2}$$

$$e = \frac{G_s(1+w)}{\rho} - 1 \tag{3}$$

where K is the hydraulic conductivity of CGS; C is a constant that depends on the compaction method; D is the effective particle size and can be taken as d_{10}; γ_w and η are the unit weight and viscosity coefficient of water, respectively; e is the void ratio; G_s is the specific gravity of soil grains; ρ is the soil density; and w is the water content of soil.

According to **Eq. 2** and **Eq. 3** the hydraulic conductivity of the CGS increases with an increase in water content. As a result, the rate of water migration increases, causing the formation rate of pore ice and the frost heaving rate to increase. Therefore, the total heave amount is expected to increase with increasing water content, as shown in **Table 3**. Meanwhile, the increasing rate of water migration brings more latent heat of the phase change that occurs in the frozen fringe. The increased water content indicates a greater release of latent heat, which inhibits the advancement of the frost front. Therefore, the frozen depth of the CGS is expected to decrease as the water content increases (**Table 3**).

Effect of Grain Size Distribution of Coarse Particles

Figure 13 shows the variations in the frost heave amount for four samples with different grain size distributions of coarse particles during the freezing process. Under the same controlling conditions, the frost heave rate of sample S9 was lower than

TABLE 4 | Test results for samples S5 and S8–S10 after freezing for 144 h.

Sample	Grain size distribution of coarse particles	Frost depth (mm)	Frost heave (mm)	Frost heave ratio (%)
S5	Size grade I	77.62	1.46	1.88
S8	Size grade II	77.95	1.22	1.57
S9	Size grade III	78.13	1.30	1.66
S10	Size grade IV	77.60	1.13	1.45

that of the other samples in the early freezing stage. This was mainly because sample S9 had the highest sand content, especially the medium sand and fine sand. The bound water content was the highest, while the free water content was the lowest. Frost heave mainly occurred in the pattern of *in-situ* frost heave during the early stage. In contrast, the heave rates of samples S5 and S9 were higher than those of samples S8 and S10 in the stable stage. This can be attributed to the lower uniformity coefficient and less difference between neighboring granule group contents in samples S5 and S9 (**Table 2**). The matrix suction increased with the decrease in voids size. As a result, for the porous samples S5 and S9, the water was mainly migrated in the liquid pattern at the stable stage, and the frost heave amounts were larger than those of samples S8 and S10.

The medium sand content and fine sand content of sample S10 were 8% less than those of sample S5. In agreement with this, the frost heave ratio of sample S10 was 0.43% less than that of sample S5 (**Table 4**). It follows that the sand content was another limiting factor for the frost susceptibility of CGS, in addition to the fines content.

DISCUSSION OF EMBANKMENT FROST HEAVE PREVENTION

As discussed in *Test Results and Analysis*, the frost heave ratio of the natural flat ground was much lower than that of the experimental freezing clay. This was because the compacted clay soil in the indoor test had fewer voids and a relatively higher thermal conductivity, which was beneficial for moving the freezing front. Furthermore, the distance between the frozen soil and water supply system in the indoor test was much less than that in the natural ground, meaning that the external water was more easily to be absorbed into the frozen zone and changed into ice. Nevertheless, the frost heave ratio difference between field monitoring and indoor tests did not affect the tests to measure the frost heave ability of the foundation soil and CGS filling.

According to the field monitoring data, under the same temperature and soil type conditions, the groundwater supply was observed to be the primary factor for the frost heave difference between flat ground and hillslope sections. In addition, the infiltration of rainfall is another water supply way water can be supplied for soil segregation frost heaving. When rainfall and snowmelt water accumulate in the embankment fill, even the well-graded A/B group layer can cause obvious frost heaving at negative temperatures. This was verified by the frost heave test. Under suitable water conditions, sample S5 produced a significant frost heave ratio of 1.88%, which was larger than the non-frost-susceptible criterion of 1% (Konrad and Lemieux, 2005). One possible reason for the water accumulation is that water flows from the top surface into the filling layer when the sealing of the track plate fails. Second, the highly compacted CGS filling layer with high fines and sand content has a strong water retention ability and relatively low water seepage capacity. This layer provides a perfect location for water accumulation. Third, the commonly used compound geomembrane in the HSR embankment, which is used to prevent infiltration of groundwater, blocks the rainwater seepage path. As a result, water accumulation may occur above the upper surface of the geomembrane (Miao et al., 2020). Accordingly, two methods have been suggested to disrupt local water accumulation. One is to strictly close the surface and the side of the embankment to prevent external water from seeping into the embankment. The other is to install embankment subdrainage holes to drain the accumulated water from the filling layers.

In the application of the soil-replacement method, fines content and water content are considered the two main influential factors for the frost susceptibility of the CGS. Konrad and Lemieux (2005), Akagawa et al. (2017), and Gao et al. (2018) reported that the frost heave susceptibility of the CGS increased with an increase in fines content and water content. This finding was also confirmed in the above test. The results suggest that CGS filling should strictly control fines content and water content. When the grain size distributions were different, the frost heave amount and frost heave ratio of sample S5 were the largest, while those of sample S10 were the lowest (**Table 4**). The frost heave mitigation effect of the poorly graded CGS was better than that of the well-graded CGS under the same conditions.

However, when the freezing front passes through the CGS filling and infiltrates the frost-susceptible clay, embankment frost heave still can occur in the case of shallow groundwater. Furthermore, rain-induced groundwater level rise further shortens the water migration distance if precipitation is enhanced. Therefore, to reduce the water migration capacity, the depth of soil replacement should not only exceed the maximum frost depth of the CGS filling layer but also include partial natural clay beyond the frost depth.

In short, the frost heave control of the HSR embankment should have three parts: 1) replacing natural clay with weakly frost-susceptible CGS filling; 2) eliminating the local water accumulation in the filling layer; and 3) reducing the water migration capacity of soil between the freezing layer and groundwater as much as possible.

CONCLUSION

In this study, the variations in ground temperature, deformation, soil moisture, and groundwater table were monitored to analyze the frost heave characteristics of the embankment foundation soil in the Zoige Wetland section of the Xining–Chengdu HSR line. Based on these observations and local geological environment data, a subgrade soil-replacement method was proposed to mitigate the frost heave deformation of railway embankments. Two contrasting frost heave tests were conducted on clay soil and CGS to prove the feasibility and validity of this method. Further experiments were performed to optimize the anti-frost effects of the replacement method. The conclusions can be drawn as follows:

- For natural flat ground and hillslope in the Zoige Wetland, the maximum frost heave ratios reached 6.10 and 1.45%, respectively. The groundwater supply condition was the primary factor for the different frost heave at these two sites.
- Under the same conditions, even when the water intake amount was very close, the frost heave ratio of the CGS was far less than that of natural, clay-rich soil. Combined with the local geological environment and engineering construction conditions, the soil-replacement method was proven to be effective in mitigating the frost heave deformation of embankment filling.
- The frost susceptibility of the CGS was proportional to the fines content and initial water content. The frost heave mitigation effect of the poorly graded CGS was better than that of the well-graded CGS under the same conditions. It is suggested that the replacement method should strictly control the fine content and water content, and preferentially use poorly graded CGS filling.
- The replacement of the CGS filling layer should also incorporate other measures to disrupt local rainwater accumulation and reduce the water migration capacity of soil between the freezing filling layer and groundwater.

DATA AVAILABILITY STATEMENT

The original contributions presented in the study are included in the article/**supplementary material**, further inquiries can be directed to the corresponding authors.

AUTHOR CONTRIBUTIONS

FN: Conceptualization, Methodology, Validation, Data curation, Formal analysis, Writing - original draft. HH: Conceptualization, Methodology, Validation, Writing - review & editing. ML: Writing - review & editing. QM: Writing - review & editing. WS: Writing - review & editing.

FUNDING

This research was supported by the Strategic Priority Research Program of the Chinese Academy of Sciences (Grant No. XDA19070504), Science and Technology Service Network Initiative of CAS (No. KFJ-STS-ZDTP-037), National Natural Science Foundation of China (41901074).

SUPPLEMENTARY MATERIAL

The Supplementary Material for this article can be found online at: https://www.frontiersin.org/articles/10.3389/feart.2021.678655/full#supplementary-material

REFERENCES

Akagawa, S., Hori, M., and Sugawara, J. (2017). Frost Heaving in Ballast Railway Tracks. *Proced. Eng.* 189, 547–553. doi:10.1016/j.proeng.2017.05.087

Babu, G. L. S., and Srivastava, A. (2007). A Procedure for the Design of Protective Filters. *Can. Geotech. J.* 44 (4), 490–495. doi:10.1139/t07-005

Everett, D. H. (1961). The Thermodynamics of Frost Damage to Porous Solids. *Trans. Faraday Soc.* 57, 1541–1551. doi:10.1039/tf9615701541

Gao, J., Lai, Y., Zhang, M., and Feng, Z. (2018). Experimental Study on the Water-Heat-Vapor Behavior in a Freezing Coarse-Grained Soil. *Appl. Therm. Eng.* 128, 956–965. doi:10.1016/j.applthermaleng.2017.09.080

Gilpin, R. R. (1980). A Model for the Prediction of Ice Lensing and Frost Heave in Soils. *Water Resour. Res.* 16 (5), 918–930. doi:10.1029/wr016i005p00918

Harlan, R. L. (1973). Analysis of Coupled Heat-Fluid Transport in Partially Frozen Soil. *Water Resour. Res.* 9 (5), 1314–1323. doi:10.1029/wr009i005p01314

Jin, H. W., Lee, J., Ryu, B. H., Shin, Y., and Jang, Y. E. (2019). Experimental Assessment of the Effect of Frozen Fringe Thickness on Frost Heave. *Geomech Eng.* 19 (2), 193–199. doi:10.12989/gae.2019.19.2.193

Jin, Y. (2007). Theory and Application for Retrieval and Fusion of Spatial and Temporal Quantitative Information from Complex Natural Environment. *Front. Earth Sci. China* 1 (3), 284–298. doi:10.1007/s11707-007-0035-0

Konrad, J.-M. (2008). Freezing-induced Water Migration in Compacted Base-Course Materials. *Can. Geotech. J.* 45, 895–909. doi:10.1139/t08-024

Konrad, J.-M., and Lemieux, N. (2005). Influence of Fines on Frost Heave Characteristics of a Well-Graded Base-Course Material. *Can. Geotech. J.* 42 (2), 515–527. doi:10.1139/t04-115

Konrad, J.-M., and Morgenstern, N. R. (1982). Prediction of Frost Heave in the Laboratory during Transient Freezing. *Can. Geotech. J.* 19 (3), 250–259. doi:10.1139/t82-032

Konrad, J.-M., and Morgenstern, N. R. (1981). The Segregation Potential of a Freezing Soil. *Can. Geotech. J.* 18 (4), 482–491. doi:10.1139/t81-059

Li, A., Niu, F., Zheng, H., Akagawa, S., Lin, Z., and Luo, J. (2017). Experimental Measurement and Numerical Simulation of Frost Heave in Saturated Coarse-Grained Soil. *Cold Regions Sci. Techn.* 137, 68–74. doi:10.1016/j.coldregions.2017.02.008

Li, X., Cheng, G., Jin, H., Kang, E., Che, T., Jin, R., et al. (2008). Cryospheric Change in China. *Glob. Planet. Change* 62 (3), 210–218. doi:10.1016/j.gloplacha.2008.02.001

Lin, Z., Niu, F., Li, X., Li, A., Liu, M., Luo, J., et al. (2018). Characteristics and Controlling Factors of Frost Heave in High-Speed Railway Subgrade, Northwest China. *Cold Regions Sci. Techn.* 153, 33–44. doi:10.1016/j.coldregions.2018.05.001

Liu, H., Niu, F., Niu, Y., Xu, J., and Wang, T. (2016). Effect of Structures and Sunny-Shady Slopes on thermal Characteristics of Subgrade along the Harbin-Dalian Passenger Dedicated Line in Northeast China. *Cold Regions Sci. Techn.* 123, 14–21. doi:10.1016/j.coldregions.2015.11.007

Mao, X., Miller, C., Hou, Z., and Khandker, A. (2014). Experimental Study of Soil Water Migration in Freezing Process. *Geotech Test. J.* 37 (3), 436–446. doi:10.1520/gtj20130119

Miao, Q., Niu, F., Lin, Z., Luo, J., and Liu, M. (2020). Comparing Frost Heave Characteristics in Cut and Embankment Sections along a High-Speed Railway in Seasonally Frozen Ground of Northeast China. *Cold Regions Sci. Techn.* 170, 102921. doi:10.1016/j.coldregions.2019.102921

Miller, R. D. (1972). Freezing and Heaving of Saturated and Unsaturated Soils. *Highw. Res. Rec.* 393, 1–11.

Niu, F., Li, A., Luo, J., Lin, Z., Yin, G., Liu, M., et al. (2017). Soil Moisture, Ground Temperatures, and Deformation of a High-Speed Railway Embankment in Northeast China. *Cold Regions Sci. Techn.* 133, 7–14. doi:10.1016/j.coldregions.2016.10.007

Nixon, J. F. (1991). Discrete Ice Lens Theory for Frost Heave in Soils. *Can. Geotech. J.* 28 (6), 843–859. doi:10.1139/t91-102

O'Neill, K., and Miller, R. D. (1985). Exploration of a Rigid Ice Model of Frost Heave. *Water Resour. Res.* 21 (3), 281–296.

Peppin, S. S. L., and Style, R. W. (2012). The Physics of Frost Heave and Ice-Lens Growth. *Vadose Zone J.* 12 (1), 1–12. doi:10.2136/vzj2012.0049

Sheng, D., Axelsson, K., and Knutsson, S. (1995). Frost Heave Due to Ice Lens Formation in Freezing Soils. *Nordic Hydrol.* 26 (2), 125–146. doi:10.2166/nh.1995.0008

Sheng, D., Zhang, S., Niu, F., and Cheng, G. (2014). A Potential New Frost Heave Mechanism in High-Speed Railway Embankments. *Géotechnique* 64 (2), 144–154. doi:10.1680/geot.13.p.042

Sheng, D., Zhang, S., Yu, Z., and Zhang, J. (2013). Assessing Frost Susceptibility of Soils Using PCHeave. *Cold Regions Sci. Techn.* 95, 27–38. doi:10.1016/j.coldregions.2013.08.003

Song, L., Li, H., Wang, K., Wu, D., and Wu, H. (2014). Ecology of Testate Amoebae and Their Potential Use as Palaeohydrologic Indicators from Peatland in Sanjiang Plain, Northeast China. *Front. Earth Sci.* 8 (4), 564–572. doi:10.1007/s11707-014-0435-x

Taber, S. (1929). Frost Heaving. *J. Geol.* 37 (5), 428–461. doi:10.1086/623637

The National Standards Compilation Group of the People's Republic of China (2014). *GB 50324—2014 Code for Engineering Geological Investigation of Frozen Ground*. Beijing, China: China Planning Press. (in Chinese).

The National Standards Compilation Group of the People's Republic of China (2011). *JGJ 118—2011 Code for Design of Soil and Foundation of Building in Frozen Soil Region*. Beijing, China: China Architecture Publishing. (in Chinese).

Thomas, H. R., Cleall, P., Li, Y.-C., Harris, C., and Kern-Luetschg, M. (2009). Modelling of Cryogenic Processes in Permafrost and Seasonally Frozen Soils. *Géotechnique* 59 (3), 173–184. doi:10.1680/geot.2009.59.3.173

Wang, Q., Liu, J., Zhu, X., Liu, J., and Liu, Z. (2016). The experiment Study of Frost Heave Characteristics and gray Correlation Analysis of Graded Crushed Rock. *Cold Regions Sci. Techn.* 126, 44–50. doi:10.1016/j.coldregions.2016.03.003

Wang, T., Zhou, G., Wang, J., and Wang, D. (2020). Impact of Spatial Variability of Geotechnical Properties on Uncertain Settlement of Frozen Soil Foundation Around an Oil Pipeline. *Geomech Eng.* 20 (1), 19–28. doi:10.12989/gae.2020.20.1.019

Wu, X. Y., Niu, F. J., Lin, Z. J., Luo, J., Zheng, H., and Shao, Z. J. (2018). Delamination Frost Heave in Embankment of High Speed Railway in High Altitude and Seasonal Frozen Region. *Cold Regions Sci. Techn.* 153, 25–32. doi:10.1016/j.coldregions.2018.04.017

Xu, X., Bai, R., Lai, Y., Zhang, M., and Ren, J. (2020). Work Conjugate Stress and Strain Variables for Unsaturated Frozen Soils. *J. Hydrol.* 582, 124537. doi:10.1016/j.jhydrol.2019.124537

Yue, Z., Ge, J., Li, Z., and Liu, Y. (2007). Study on Settlement of Unprotected Railway Embankment in Permafrost. *Cold Regions Sci. Techn.* 48 (1), 24–33. doi:10.1016/j.coldregions.2006.09.003

Zhang, S., Sheng, D., Zhao, G., Niu, F., and He, Z. (2016). Analysis of Frost Heave Mechanisms in a High-Speed Railway Embankment. *Can. Geotech. J.* 53 (3), 520–529. doi:10.1139/cgj-2014-0456

Zuo, D., Luo, P., Yang, H., Mou, C., Li, Y., Mo, L., et al. (2019). Assessing the Space Neighborhood Effects and the protection Effectiveness of a Protected Area - a Case Study from Zoige Wetland National Nature Reserve. *Chin. J. Appl. Environ. Biol.* 25 (4), 0854–0861. (in Chinese).

Conflict of Interest: The authors declare that the research was conducted in the absence of any commercial or financial relationships that could be construed as a potential conflict of interest.

The reviewer QW declared a shared affiliation with one of the authors, ML, to the handling editor at time of review.

frontiers in Earth Science

ORIGINAL RESEARCH
published: 03 November 2021
doi: 10.3389/feart.2021.729454

SBAS-InSAR-Based Analysis of Surface Deformation in the Eastern Tianshan Mountains, China

Qingsong Du[1,2,3], Guoyu Li[1,2], Dun Chen[1,2,4], Yu Zhou[1,2,3], Shunshun Qi[1,2,3], Gang Wu[1,2,3], Mingtang Chai[5], Liyun Tang[6], Hailiang Jia[6] and Wanlin Peng[7]*

[1]State Key Laboratory of Frozen Soil Engineering, Northwest Institute of Eco-Environment and Resources, Chinese Academy of Sciences, Lanzhou, China, [2]Da Xing'anling Observation and Research Station of Frozen-Ground Engineering and Environment, Northwest Institute of Eco-Environment and Resources, Chinese Academy of Sciences, Jiagedaqi, China, [3]College of Resources and Environment, University of Chinese Academy of Sciences, Beijing, China, [4]State Key Laboratory for Geomechanics and Deep Underground Engineering, China University of Mining and Technology, Xuzhou, China, [5]School of Civil and Hydraulic Engineering, Ningxia University, Yinchuan, China, [6]Architecture and Civil Engineering School, Xi'an University of Science and Technology, Xi'an, China, [7]The Third Geological Brigade of Xinjiang Geological and Mineral Exploration and Development Bureau, Korla, China

OPEN ACCESS

Edited by:
Guo Donglin,
Institute of Atmospheric Physics (CAS), China

Reviewed by:
Wenyu Gong,
China Earthquake Administration, China
Wang Lingxiao,
Nanjing University of Information Science and Technology, China

***Correspondence:**
Guoyu Li
guoyuli@lzb.ac.cn

Specialty section:
This article was submitted to Cryospheric Sciences, a section of the journal Frontiers in Earth Science

Received: 23 June 2021
Accepted: 30 September 2021
Published: 03 November 2021

Citation:
Du Q, Li G, Chen D, Zhou Y, Qi S, Wu G, Chai M, Tang L, Jia H and Peng W (2021) SBAS-InSAR-Based Analysis of Surface Deformation in the Eastern Tianshan Mountains, China. Front. Earth Sci. 9:729454. doi: 10.3389/feart.2021.729454

Due to the unique geographical characteristics of cold alpine and high-altitude regions, glaciers, permafrost, ground ice, rock glaciers, and other periglacial geomorphology have developed with fragile habitats, and these areas are often the birthplaces of many river basins and natural hazards. With global warming and the extensive cryogenesis and physical weathering, the thermal state of permafrost and the mass balance of glaciers have been changed, and thus it can be deduced that the surface deformation is of great concern. To obtain ground subsidence or uplift over a large area to understand local surface changes, the small baseline subset interferometric synthetic aperture radar (SBAS-InSAR) technique was applied to process 89-scene of Sentinel-1A images ranging from December 25, 2017 to January 2, 2021 to obtain surface deformation for these 3 years for the eastern Tianshan Mountains, China. The surface deformation characteristics of the area were analyzed to provide a basic dataset for environmental protection policies and mitigation or reduction of natural hazards in this region, and to verify the applicability of SBAS-InSAR technology in alpine and high-altitude areas. The results show that the SBAS-InSAR technique processing with sentinel-1A dataset cannot be effectively used to acquire ground deformation in areas covered by trees, scrub/shrub, glaciers, snow, and ground ice, where the decohered phenomenon is serious. In other regions, SBAS-InSAR can effectively measure surface subsidence or uplift. Surface deformation is significant throughout the study area, with rates ranging from −70.7 to 50.8 mm/a and with an average rate of 1.1 mm/a. There are obvious regions of uplift in the northwest, northeast, and central sections of the study area, with uplift greater than 155.73 mm in 3 years, and three obvious regions of subsidence in the northeast and west sections of the study area, with subsidence of at least −125.20 mm in 3 years. The remaining areas of deformation are scattered, with smaller amounts of settlement and uplift and with an isolated and sporadic distribution. Areas with elevations of 3,150 to 4,275 m.a.s.l., slopes of 15°–50°, and southwest, west, and northwest aspects are geologic disaster-prone regions and should

receive more attention and more field monitoring. The results of this study have important implications for local environmental protection and hazard prevention.

Keywords: surface deformation, Eastern Tianshan Mountains, SBAS-InSAR, environmental impact, cold alpine and high-altitude regions, disaster prevention and mitigation

INTRODUCTION

Cold alpine and high-altitude regions are characterized by fragile ecosystem habitats where periglacial geomorphology such as glaciers, permafrost, rock glaciers, and subsurface ice is richly developed due to the perennial low-temperature environment (Du et al., 2021a). In recent years, with global warming (Hansson et al., 2021), the periglacial geomorphology of high alpine-altitude regions has been put at great risk. This warming will accelerate the degradation of glaciers, permafrost, rock glaciers, snow cover, and subsurface ice (Zhu et al., 1996; Shan et al., 2015; Cheng et al., 2019; Zhao et al., 2019), exposing their subsurface land and touching off continuous uneven subsidence (Qin et al., 2018). This may lead to geologic hazards such as landslides, collapses, and debris flows (Metternicht et al., 2005; Shan et al., 2014), which may entail huge economic losses.

Interferometric synthetic aperture radar (InSAR) technology has been developed by many researchers (Massonnet anf Feigl, 1998; Hanssen et al., 1999; Hanssen, 2001; Simons and Rosen, 2007; Lu and Dzurisin, 2014) since its introduction from microwave remote sensing (Rosen et al., 2000; Rott, 2009; Bamler and Hartl, 2010; Ye, 2010; Moreira et al., 2013; Ouchi, 2013; Monserrat et al., 2014) in the 1950s and has become a scientifically effective method of Earth observation (Massonnet and Feigl, 1998; Lu and Dzurisin, 2014), with correspondingly great achievements (Amelung et al., 1999; Mora et al., 2002; Hooper et al., 2004; Metternicht et al., 2005; Hooper, 2008; Ge et al., 2021; Kursah et al., 2021). Compared with traditional optical remote sensing, the advantage of InSAR technology lies in its ability to acquire phase information from ground objects and to be relatively less affected by weather, which in theory enables all-day, all-weather (Liu et al., 2019; Du et al., 2021a; Du et al., 2021b). Earth observation. Moreover, it costs less time and money than manual measurements with comparable precision. Differential interferometric synthetic aperture radar (D-InSAR) (Massonnet and Feigl, 1998; Hanssen, 2001; Simons and Rosen, 2007; Lu and Dzurisin, 2014) has been developed based on InSAR technology, and multi-temporal InSAR (MT-InSAR) (Pepe and Calò, 2017; Zhu et al., 2019; Gatsios et al., 2020; Shahzad et al., 2020) including persistent scatterer InSAR (PS-InSAR) (Ferretti et al., 2001; Colesanti et al., 2003; Zhang et al., 2013; Li et al., 2020; Ge et al., 2021), small baseline subset InSAR (SBAS-InSAR) (Ferretti et al., 2001; Mora et al., 2002; Colesanti et al., 2003; Hu et al., 2021a; Du et al., 2021b), and distributed scatterer InSAR (DS-InSAR) (Zhu et al., 2018; He and Zhao, 2020; Du et al., 2021d; Hu et al., 2021a) have been developed based on D-InSAR. Their practical scope varies, and each has its own advantages and disadvantages. Compared with PS-InSAR, SBAS-InSAR can eliminate the influence of the atmosphere to the greatest extent (Du et al., 2021b). Currently, as more and more SAR satellites are launched, more and more SAR image data are being used for InSAR processing to monitor ground surface changes.

The eastern Tianshan Mountains in China are located in a typical alpine and high-altitude region with a developed periglacial geomorphology and an abundance of minerals (Du et al., 2020a; Du et al., 2021c). To ensure safe conduct of mining and to understand the subsidence of the regional surface, 89 acquisitions of Sentinel-1A images covering the study area from December 25, 2017 to January 2, 2021 were selected and processed by SBAS-InSAR to obtain the ground deformation of the study area during this period. The results can provide a theoretical basis for the formulation of regional development policies, as well as safety recommendations for mining activities within the region.

OUTLINE OF STUDY AREA

The study area is situated in the eastern section of the Tianshan Mountains in China (**Figure 1**) and belongs to the Xinjiang Uyghur Autonomous Region, with a geographical location of 43.25–43.62°N, 84.87–85.49°E, an area of 1,590.78 km^2, and an altitude of 2,549–5,250 m above sea level (m.a.s.l.), with an average altitude of 3,839 m.a.s.l. (**Figure 1B**), making this a typical cold-alpine, high-altitude region (Du et al., 2020a; Du et al., 2021a). According to a land-cover dataset, Esri 2020 Global Land Cover (Karra et al., 2021) (**Figure 1D**), and site inspection, the ground surface cover of the study area is mainly bare land, followed by snow/ice and glaciers (**Figures 1C,D**) and grass (**Figure 1D**). In addition, there are also some other land cover types including water, scrub/shrub, trees, crops, and built areas. The terrain is generally high in the north and low in the south, with snow cover and ice developing in the alpine-mountain areas in the north (3,971–5,250 m.a.s.l.) and grassland widely distributed in the lower, flatter areas in the south (2,549–3,628 m.a.s.l.) and mostly accompanied by rivers, wetlands (scrub/shrub) and trees in the southeast section.

The amount of thawing of snow cover and ice affects the succession and growth of the local grassland ecosystem (Du et al., 2020b), which has a significant influence on the standard of living of pastoralists living in this area. Snow cover and ice are also a source of water resource recharge for many rivers in the adjacent low-altitude areas, and their phase behavior change is a guarantee of water supply for people living and working downstream along the rivers. As global warming accelerates the thawing of snow and ice (Qin et al., 2018), the exposed subsurface land will accelerate subsidence of the regional ground surface. Excessive melting in till sedimentation (moraine) can alter local topography, thereby affecting regional runoff and the water cycle. The amount of surface

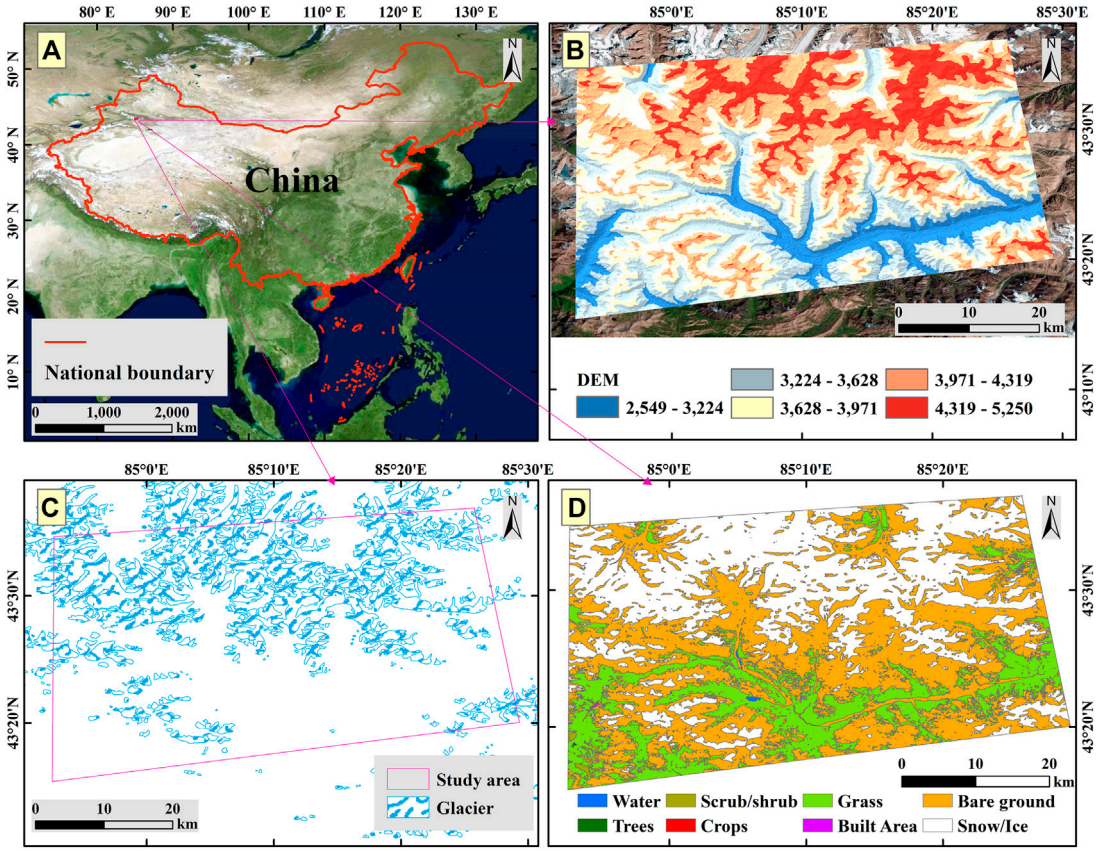

FIGURE 1 | Overview map of the study area [**(A)** location of study area in China; **(B)** digital elevation model (DEM) of the study area; **(C)** distribution of glaciers within the study area; **(D)** surface land cover of the study area derived from the Esri 2020 Global Land Cover dataset (Karra et al., 2021)].

subsidence or uplift is also related to the frequency of natural disasters such as landslides, collapses, and debris flows.

Du et al. (2021b) obtained deformation information from the open-pit mining zone in the lower right corner of the study area (43.28–43.35°N, 84.95–85.12°E) using the SBAS-InSAR technique and compared the results with field GNSS monitoring data. This effort demonstrated the outstanding measurement capability of SBAS-InSAR in this region and obtained credible results. Based on this work, the parameters involved in the SBAS-InSAR processing for this paper were consistent with their settings in the literature (Mora et al., 2002; Hu et al., 2021a; Du et al., 2021b; Kursah et al., 2021), ensuring the reliability of the results, and therefore it was unnecessary to verify the accuracy of the measurement results in this study. This paper focuses on obtaining surface settlement information through SBAS-InSAR processing and analyzing settlement or uplift characteristics to understand the deformation features of the study area over a 3-year period, which will provide basic data for regional development policy formulation. The obtained surface deformation information can be used as an input risk assessment dataset for natural disasters and other studies, thus offering great significance and usefulness.

DATASET AND METHODOLOGY

Dataset

The 89-scene of Sentinel-1A ascending (satellite travelling south to north) acquisitions from December 25, 2017 to January 2, 2021 were downloaded from the ASF website (https://vertex.daac.asfalaska.edu/), along with the precise orbital data corresponding to each acquisition as obtained from the ESA website (https://qc.sentinel1.eo.esa.int/). In general, long-wavelength (low-frequency) bands have good long-range performance and easy access to high-power transmitters and huge antennas (Ferretti et al., 2007). Short-wavelength (high-frequency) bands generally give precise distances and positions, but have a short range of action (Liu et al., 2019). Sentinel-1A has been acquiring data since October 2014 and Sentinel-1B since September 2016 with c-band (4–8 GHz) (Zhu et al., 2019), which has some penetration while maintaining good monitoring capability (high spatial accuracy). Each sentinel-1 constellation is in a near-polar, sun-synchronous orbit, with a 12-day repeat cycle and the two-satellite constellation offers a 6-day repeat cycle, which ensures excellent monitoring capability (high temporal resolution). They are very commonly used as SAR image data and are free and open-source, with multiple modes

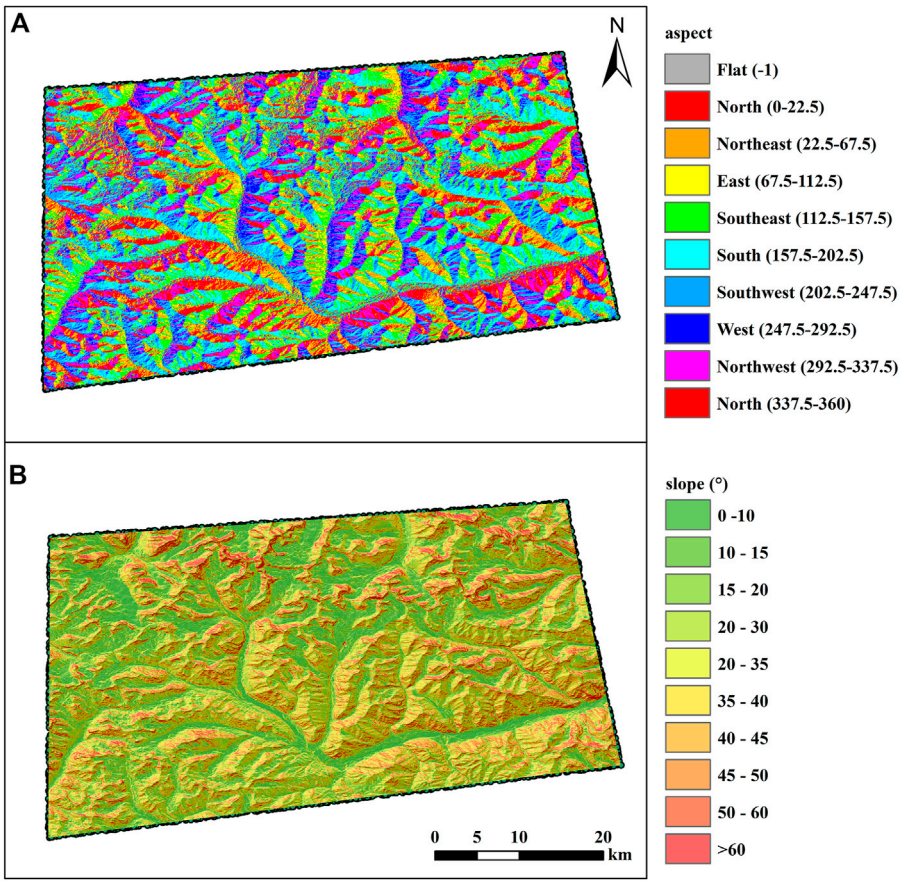

FIGURE 2 | Ground surface topographical information of study area [**(A)** shows the aspect information and **(B)** is the slope data, and all are produced from the DEM dataset].

(Stripmap, SM; Interferometric Wide swath, IW; Extra Wide swath, EW; Wave, WV) and multi-polarization (HH, VV, HH + HV, VV + VH) (Yang et al., 2015).

The data used in this paper were the single-look complex (SLC) Level 1 product in IW mode, which acquires 250 km of surface data at a spatial resolution of 5 × 20 m (single scene) (Yang et al., 2015) and contains both phase and amplitude information. Phase is a function of time, and distance measurements can be obtained based on phase and velocity information (Liu et al., 2019). Based on this, SAR images can be used for distance measurement and deformation observation (Ye, 2010; Hu et al., 2021b). To reduce the time spent on data processing, only the extent of images containing the study area was selected for processing in this paper.

DEM data were provided by the Shuttle Radar Topography Mission (SRTM) 1 Arc-Second Global DEM from the USGS Earth Explorer website (https://earthexplorer.usgs.gov/) with a spatial resolution of 30 m, which can be used to produce aspect and slope dataset products (**Figure 2**) and extract contour lines. Glacier distribution data were derived from the Second Glacier Inventory of China, which can be obtained from the National Tibetan Plateau/Third Pole Environment Data Center (TPDC) (https://data.tpdc.ac.cn/) in vector format.

A ground-surface land coverage dataset (**Figure 1D**), Esri 2020 Global Land Cover (Karra et al., 2021) is based on the dataset produced for the Dynamic World Project by National Geographic Society in partnership with Google and the World Resources Institute. The map is derived from ESA Sentinel-2 imagery at 10 m resolution. It is a composite of LULC predictions for 10 classes throughout the year in order to generate a representative snapshot of 2020 and was produced by a deep learning model trained using over five billion hand-labeled Sentinel-2 pixels, sampled from over 20,000 sites distributed across all major biomes of the world. This dataset is now officially available for global public access and can be downloaded freely through the Land Cover Downloader Map website page (https://www.arcgis.com/apps/instant/media/index.html?appid=fc92d38533d440078f17678ebc20e8e2 or https://ai4edataeuwest.blob.core.windows.net/io-lulc/io-lulc-model-001-v01-composite-v03-supercell-v02-clip-v01.zip). Compared to FROM-GLC10 dataset (Gong et al., 2019), Esri 2020 Global Land Cover is closer to the date of acquisition of the SAR images (December 25, 2017 to January 2, 2021) of the study area and has a higher accuracy of ground features classification.

TABLE 1 | Main purposes and parameter settings of SBAS-InSAR workflow steps.

Workflow step	Purpose	Parameter setting
DEM format conversion	Converting DEM format to binary for easy software recognition	Type: DEM; Unit: m
SAR data read-in	Converting Sentinel-1A format data to software-readable data	Input: Sentinel-1A, orbital data, converted DEM; Mapping resolution, slant range, azimuth: 20, 5, 1
Data reduction and connection	Reducing image extent by study area to reduce data processing time and creating an.xml file of cropped SAR images	Conversion of geographical coordinates to SAR coordinates
Baseline estimation	Determining master and slave images for SAR datasets	Temporal baseline threshold: 18 days, spatial baseline threshold: 2% of the critical baseline
Interferogram generation and flattening	Interference map generation and removal of flatland effects	Consistent with baseline estimation settings
Adaptive filter and coherence generation	Filtering and generation of coherence coefficient graph	Goldstein adaptive filter
Phase unwrapping	Unwrapping the wrapped fuzzy phase	Minimum cost flow method and 3D unwrapping, coherence threshold: 0.35
Edit connection diagram	Removing decohered images	Main reference coherence diagram
Refinement and re-flattening	By selecting ground control points (GCPs) to refine the unwrapped phase and remove the residual phase	GCPs within half a pixel of error
First inversion	Estimating deformation rate and residual	Product coherence threshold: 0.35; Wavelet number of levels: 2
Second inversion	Removing atmospheric phase error	Refinement method: Polynomial refinement
Geocoding	Converting results to geographical coordinates	Coordinate parameters are set in line with DEM

SBAS-InSAR

Since its introduction in 2002 (Mora et al., 2002), SBAS-InSAR technology has been used in many surface deformation monitoring studies. The principles, processing procedures, and other features of SBAS-InSAR have been extensively described in the literature (A. J. Hooper, 2008; Liu et al., 2019; Hu et al., 2021b) and will not be repeated in this paper. In this study, the SBAS-InSAR process was implemented on the SARscape 5.2.1 software platform, and its parameter settings and process were consistent with those in the literature (Chen et al., 2013; Du and Zhao, 2020; Reinosch et al., 2020; Du et al., 2021a; Du et al., 2021b; Du et al., 2021d). **Table 1** gives the parameter settings of each step.

The annual rate (mm/a) for the study area during the 3-year period from December 25, 2017 to January 2, 2021 and the surface cumulative deformation information (mm) will be available once the SBAS-InSAR processing has been completed. Deformation includes subsidence and uplift and represents cumulative deformation information describing ground surface changes for each relevant period starting on December 25, 2017 and ending with the date of image acquisition. Many important intermediate files used during processing will also be available, such as the coherence coefficient graphs, deformation maps of the first estimate, deformation maps after the second estimate, and other important reference files. In the InSAR process, the coherence coefficient is an important parameter ranging from 0 to 1 that determines the accuracy of the measurement results. The magnitude of the coherence coefficient indicates the extent of decohered, and the coherence coefficient can also be used as a threshold to remove low-coherence areas to improve the accuracy of the monitoring results.

Generally, if the coherence is less than 0.2 (Liu et al., 2019; Hu et al., 2021b), there may be few decohered regions, but the accuracy of the measurement results will be reduced. The coherence threshold will mask the areas where the coherence is less than the threshold value. Masked regions will be shown as blank in the result maps. In this study, the threshold was set to 0.35 to ensure the precision of the results.

Deformation Characterization

Deformation velocity maps and cumulative deformation maps were analyzed using the ArcGIS 10.6 software platform to identify the spatial and temporal deformation variation characteristics of the study region, focusing on the consistency and heterogeneity of the study area at overall and local scales. Regions with intense subsidence or uplift changes within the study area were analyzed and zoned in detail, and a set of observation points (OPs) was selected to extract the cumulative deformation for every period. Based on the Land Cover dataset, we have statistically analyzed the surface deformation characteristics of each type of ground feature, including the velocity range, decohered area, and decohered area percentage. This involved reclassifying the deformation velocity and transforming the raster results to vector format to extract the areas of each class, followed by reanalysis and counting of the land-cover area in each class.

The *Raster to Point* tool was used to transfer the acquired deformation velocity result to vector format points which were used as a baseline to extract other corresponding values including slope, aspect, elevation, and surface feature using the *Extract Values to Points* tool. The velocity map can also be transferred to vector polygon for area calculation using the *Raster to Polygon* tool. However, as the *Raster to Polygon* tool only supports data in integer, it is necessary to convert the results of the data type float to integer before raster to polygon processing. The extraction and processing of the relevant data corresponding to each ground cover data is similar.

The overlay method was used to analyze the relationship between deformation and land cover, as well as to collect deformation information for each land-cover type. More attention was paid to areas with intense variation and steep

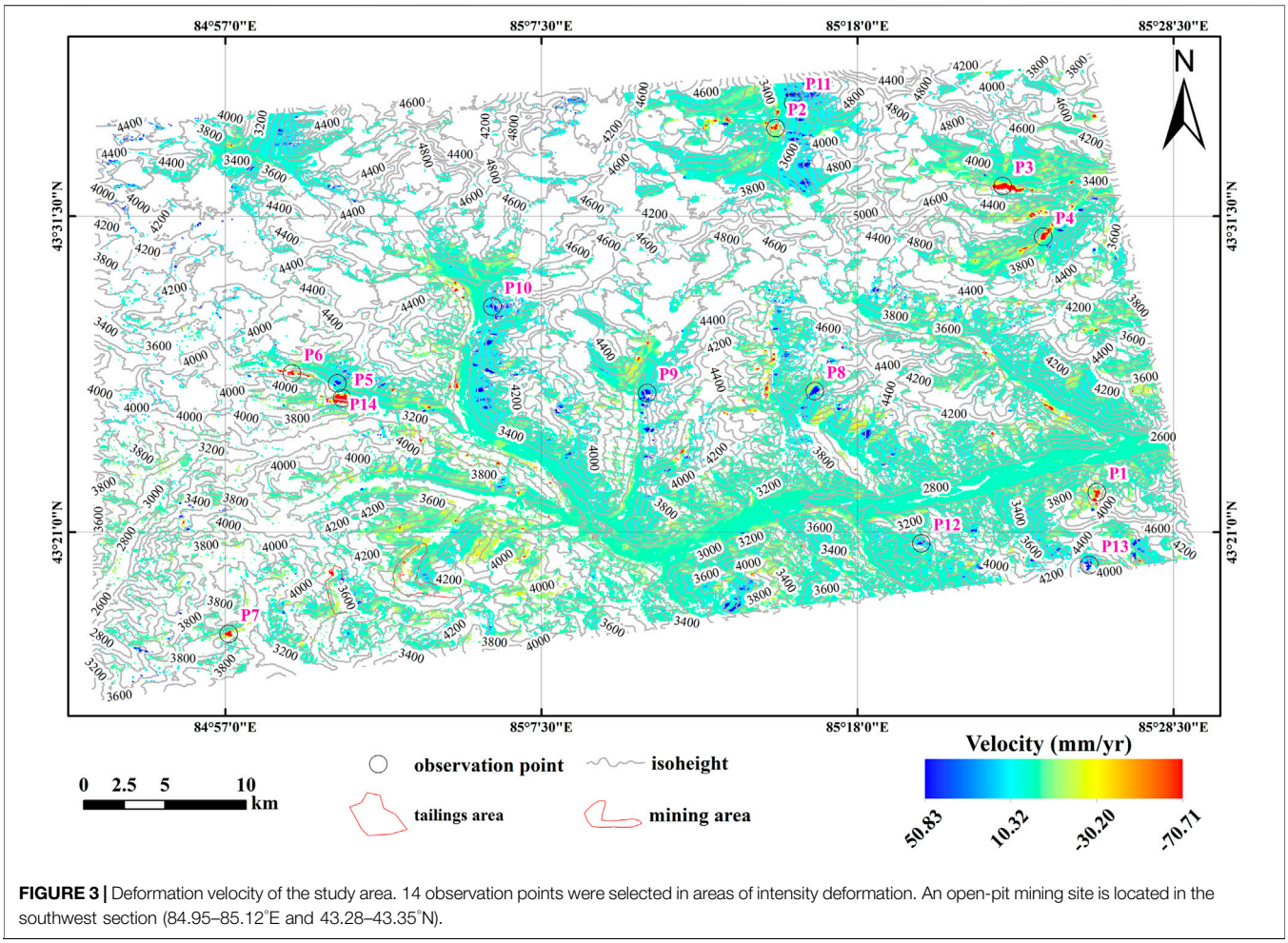

FIGURE 3 | Deformation velocity of the study area. 14 observation points were selected in areas of intensity deformation. An open-pit mining site is located in the southwest section (84.95–85.12°E and 43.28–43.35°N).

slopes to explore the intrinsic relevance between them. Slope data were obtained by calculating the DEM.

During the analysis, all the processes just described were not separate, but rather intertwined with each other. These analyses provided an understanding of the ground surface change characteristics of the study area and a preliminary analysis of deformation factors. The results provide a theoretical basis for formulating regional development policies as well as basic data for physical geological hazard prevention.

RESULTS

Deformation Velocity and Cumulative Deformation

A velocity map (**Figure 3**) and cumulative deformation maps (**Figures 5**–**7**) for the 3 years were created once SBAS-InSAR processing had been completed. Warm colors indicate surface deformation away from the sensor line-of-sight (LOS) direction, whereas cool colors indicate surface deformation toward the sensor LOS direction. Blank regions represent missing data due to decohered. All the deformation descriptions information including the uplift and subsidence about the velocity and cumulative deformation in this paper are based on the sensor (LOS) direction.

Figure 3 shows regions of significant subsidence in the northeastern, southwestern, and southeastern sections of the study area, with rates of subsidence of −30.2 mm/a or more. The northern, central, and southern parts of the study area contain regions of significant uplift, with uplift rates greater than 15.6 mm/a. Areas with obvious deformation are isolated and sporadic. In the southwestern section, there is an open-pit mine, where Du et al. (2021b) have analyzed the associated ground deformation and obtained results in accord with the velocity results comparing with the situ global navigation satellite system (GNSS) measurements. The processing and parameter settings in this paper are identical to those of the literature (Du et al., 2021b), which ensures the reliability and scientific validity of the SBAS-InSAR measurements results in this paper. The maximum settlement rate in the study area was −71.7 mm/a, and the maximum uplift rate was 50.8 mm/a. Settlement rates in other valuable areas mostly ranged from −15.4 to 15.6 mm/a (**Figure 4**).

The areas of cumulative deformation change in 2018 are concentrated at P11, P10, P9, and P8 (marked with small rectangles, pentagrams, ellipses, and large rectangles

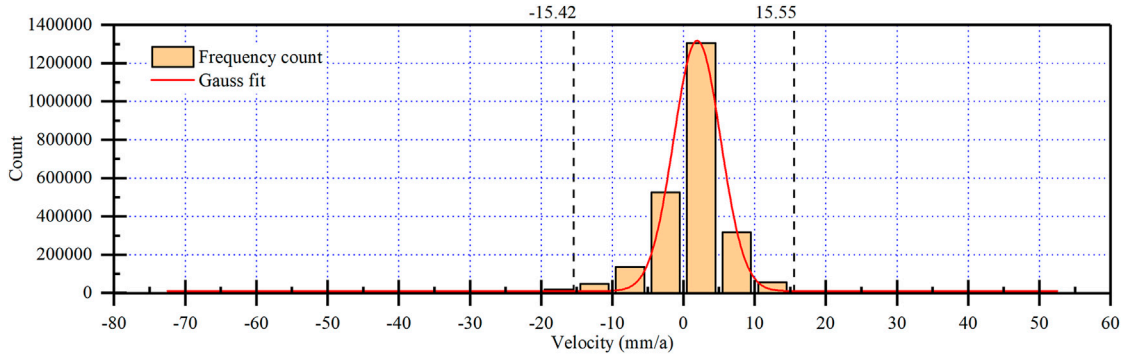

FIGURE 4 | Deformation velocity statistics in the study area. All the velocity values are obtained by applying the *Raster to point* tool based on the velocity raster data.

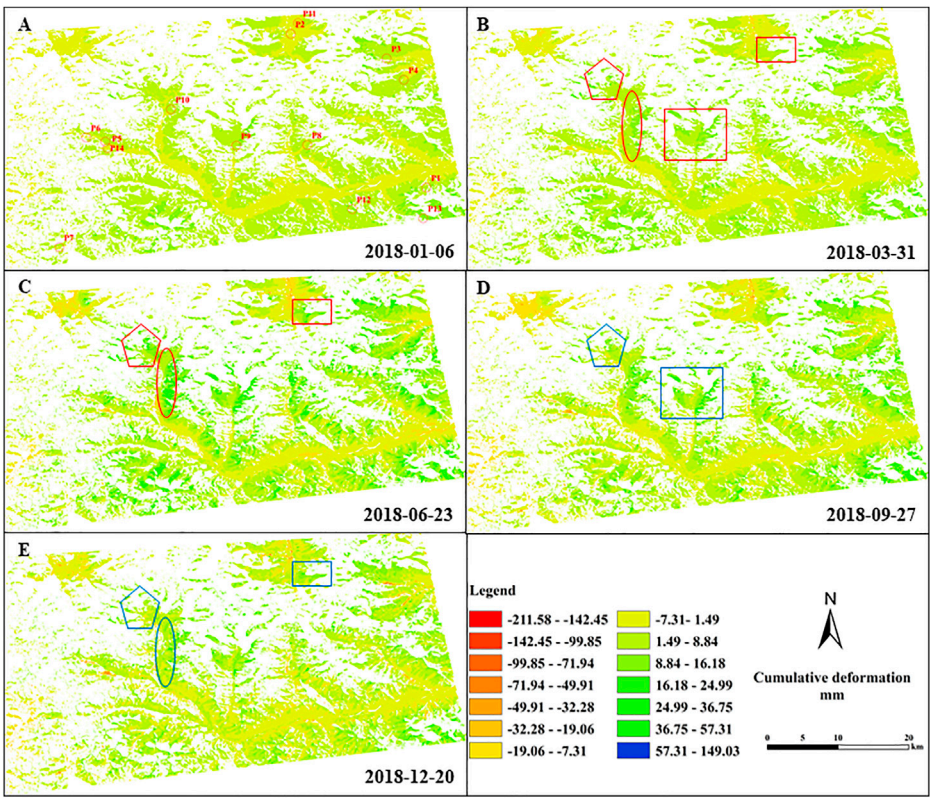

FIGURE 5 | Cumulative deformation (mm) during 2018 [**(A–F)** are the dates of 2018-01-06, 2018-03-31, 2018-06-23, 2018-09-27, and 2018-1220, respectively]. The small red circles in **(A)** show the areas with evident deformation rate (14 observations). Other geometric labels indicate areas of significant change, with red indicating subsidence and blue indicating uplift.

respectively in **Figure 5**, respectively). All four sites are in the subsidence zone and the changes are mainly reflected in an increase in the area of subsidence and an acceleration of subsidence rate. However, there are also some seasonal fluctuations, with an increase in subsidence from January to June and a slowdown in subsidence from June to December. The reason for this phenomenon may be due to the lifting of the ground surface caused by freeze-thaw action.

The change from 2018 to 2019 is most evident at P14, P12, P9, and P13, (marked with a triangle, large ellipses, small ellipses, and large circle on **Figure 6**, respectively). By January 1, 2019, subsidence at P14 continued to increase until December 27, 2019 and had expanded in area. Other regional changes were characterized by similar cyclical fluctuations as in 2018. However, between June 30, 2019 and September 22, 2019, small landslides occurred in P13, P9, and the south-central section through the

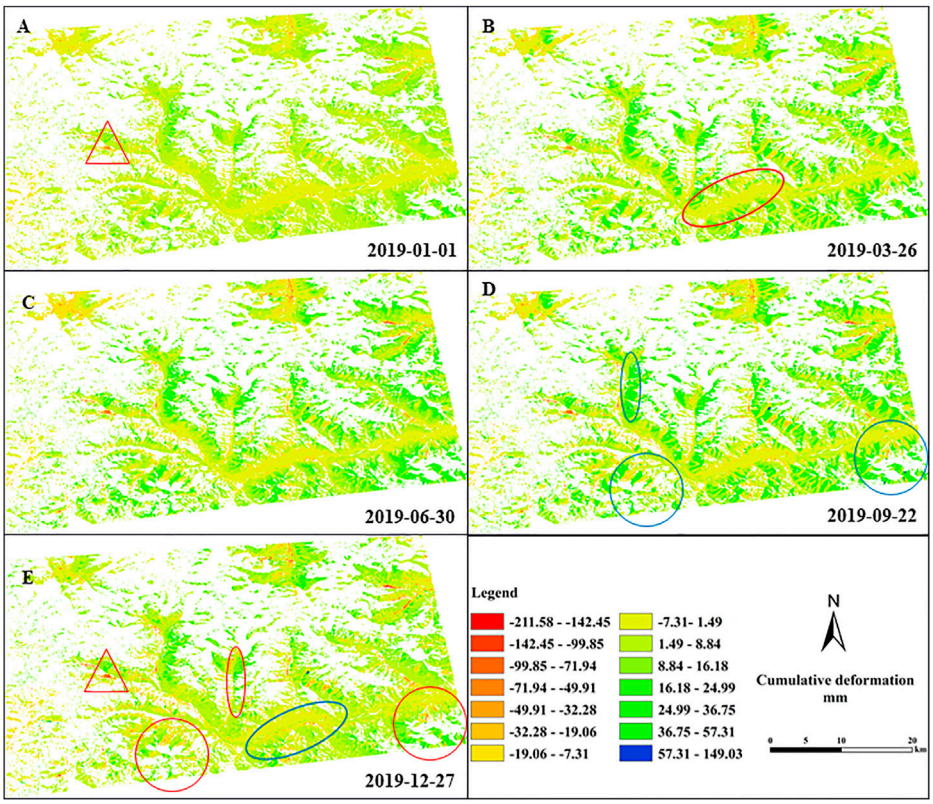

FIGURE 6 | Cumulative deformation (mm) during 2019 [**(A–F)** are the dates of 2019–01-01, 2019-03–26, 2019-06–30, 2019-09–22, and 2019-12–27, respectively]. Geometric labels indicate areas of significant change, with red indicating subsidence and blue indicating uplift.

investigation of historical imageries and information, resulting in greater subsidence during this period, shown as a number of small dark blue dots in **Figure 6**. By the end of 2019, deformation in these three regions had stabilized.

Changes in 2019 are mainly in P14 (marked by a red triangle on **Figure 7**), with continued subsidence and an increase in the area of subsidence. Other areas show little change, mainly due to cyclical variations caused by freeze-thaw action. However, due to landslides during 2018 in P13, P9 and the south-central region, freeze-thaw uplift caused by loose accumulation is greater than that in the past and is shown on the map as a more concentrated darker area (marked with blue ovals and circles on **Figure 7**, respectively).

From **Figures 5**–**7**, we find that the cumulative deformation for each period was based on the starting date of December 25, 2017 and ended with the SAR image acquisition date. It is obvious that as time goes by, the cumulative deformation of the area near P14 (marked with a red triangle in **Figures 6**, **7**) becomes larger. From January 6, 2018 to December 20, 2018, the maximum uplift varied from 26.80 to 50.47 mm, with a growth rate of 88.32%. The maximum settlement varied from −28.15 to −65.73 mm, with an added value up to 37.58 mm. In 2019, the added values of uplift and settlement were 48.29 and 66.41 mm, with growth rates of 93.01 and 96.38%, respectively. In 2020, uplift varied from 102.23 to 149.03 mm, representing an addition of 46.8 mm, and settlement changed from −137.69 to −211.58 mm, with a 53.67% growth rate.

According to velocity maps (**Figure 2**) and cumulative deformation graphs (**Figures 5**–**7**), the regions with violent settlement or uplift are relatively scattered. Settlement regions are distributed in the northeast, southwest, and southeast sections of the study area, whereas uplift is obvious in the north and central areas. All these zones are isolated and sporadic.

Area Statistics and Quantitative Analysis

In order to understand the deformation characteristics corresponding to each land cover type, we took the land cover raster dataset as a baseline and converted it to vector data using the Raster to Polygon tool. The vector data were then used to calculate the area of each ground land cover and the area of decohered regions (blank area in **Figures 3**, **5**–**7**). Statistical indicators were calculated for each land cover, including the proportion of decohered area, velocity range, mean, media number, and standard deviation (SD). The results are shown in **Table 2**.

After the calculation,the entire area of the entire research region is 1,590.78 km^2. Bare ground occupied the largest area with 772.63 km^2 or 45.45%. This is followed by snow/ice and grass with 35.18% (559.47 km^2) and 18.82% (299.21 km^2), respectively. The other 0.55% were scrub/shrub (6.23 km^2),

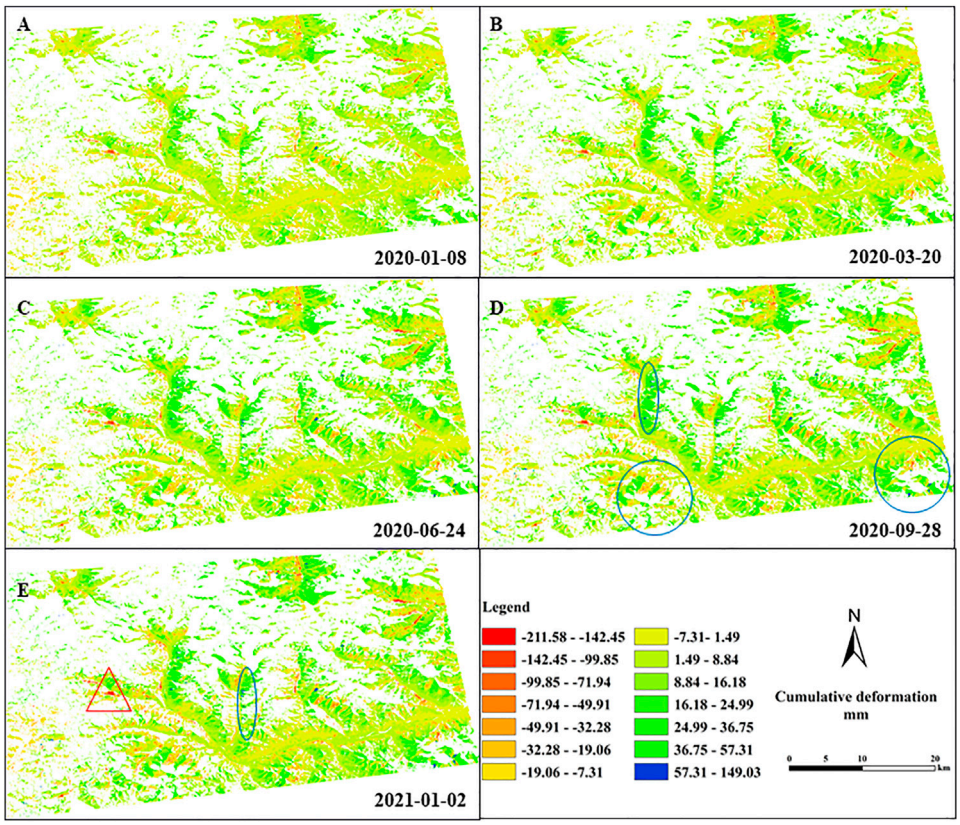

FIGURE 7 | Cumulative deformation (mm) during 2020 [**(A–F)** are the dates of 2020–01-08, 2020-03–20, 2020-06–24, 2020-09–28, and 2021-01–02, respectively]. Geometric labels indicate areas of significant change, with red indicating subsidence and blue indicating uplift.

TABLE 2 | Statistics on deformation velocities corresponding to different land covers.

Land cover	Decohered area (km^2)	Decohered proportion (%)	Velocity range (mm/a)	Average	Median number	Standard deviation
Water	0.99	54.14	−15.3–9.2	1.7	1.6	1.96
Trees	0.25	100	—	—	—	—
Grass	140.76	47.05	−70.7–33.9	0.2	1.0	4.76
Crops	0.03	45.35	−9.0–6.9	−1.4	−2.0	4.16
Scrub/shrub	5.71	91.75	−16.1–24.9	1.7	1.6	3.15
Built area	0.14	38.70	−12.9–6.5	−1.0	−0.9	2.45
Bare ground	324.25	44.87	−70.3–50.8	1.1	1.6	5.52
Snow/ice	511.02	91.34	−27.4–27.3	3.9	3.5	3.33

water (1.83 km^2), built-up areas (0.35 km^2), trees (0.25 km^2), and crops (0.06 km^2) respectively. From **Table 2** and statistical calculations, the results indicate that the decohered phenomenon is serious within the entire study area, with the area of decorrelation being 984.11 km^2 and accounting for 61.87% of total area. The effective measurement area is only 38.13%, with an area of 606.67 km^2. And bare ground, grass, and snow/ice are 398.38, 158.44, and 48.45 km^2, respectively. The areas of other land cover types are all less than 0.6 km^2.

Of the eight land cover types from **Table 2**, bare ground has the greatest range of velocity variation at −70.3–50.8 mm/a and crops have the smallest range of velocity variation at −9.0–6.9 mm/a. This result is due to the large area of bare ground and landslides occurring within. The area of crops is small and does not vary much. The settlement rate of grassland is significantly greater than the uplift rate, which is due to the fact that part of the area where the landslide is close to grassland, resulting in an increase in the settlement rate of grassland. Snow/ice deformation rates ranged from −27.4–27.2 mm/a relatively symmetrically, with sedimentation rates slightly greater than uplift rates due to seasonal freeze-thaw. But the mean and median rates are positive, indicating the presence of localised widespread subsidence at snow/ice. Scrub/shrub rates varied mainly due to environmental succession caused by seasonal

TABLE 3 | Basic information for the observation points.

OP	Longitude E (°)	Latitude N (°)	Altitude (m)	Velocity (mm/a)	Aspect	Slope (°)	Land cover
P1	85.43	43.37	3,451	−32.4	North	9.28	Bare land
P2	85.25	43.57	3,475	−28.2	Northeast	17.77	Bare land
P3	85.38	43.54	3,731	−49.9	Northeast	17.08	Grass
P4	85.40	43.51	3,519	−31.9	Southeast	18.13	Bare land
P5	85.01	43.42	3,343	−47.1	North	25.04	Bare land
P6	84.99	43.44	3,498	−37.7	Northeast	18.54	Bare land
P7	84.95	43.29	3,344	−31.8	Southeast	19.07	Bare land
P8	85.28	43.43	3,701	42.9	West	10.55	Bare land
P9	85.18	43.43	3,460	19.4	West	23.66	Bare land
P10	85.10	43.47	3,566	19.6	Southwest	35.51	Bare land
P11	85.26	43.59	3,453	25.1	West	16.19	Grass
P12	85.34	43.34	3,735	18.1	Southwest	41.15	Bare land
P13	85.43	43.33	4,176	21.6	Southwest	34.88	Bare land
P14	85.01	43.43	3,448	17.9	West	28.68	Bare land

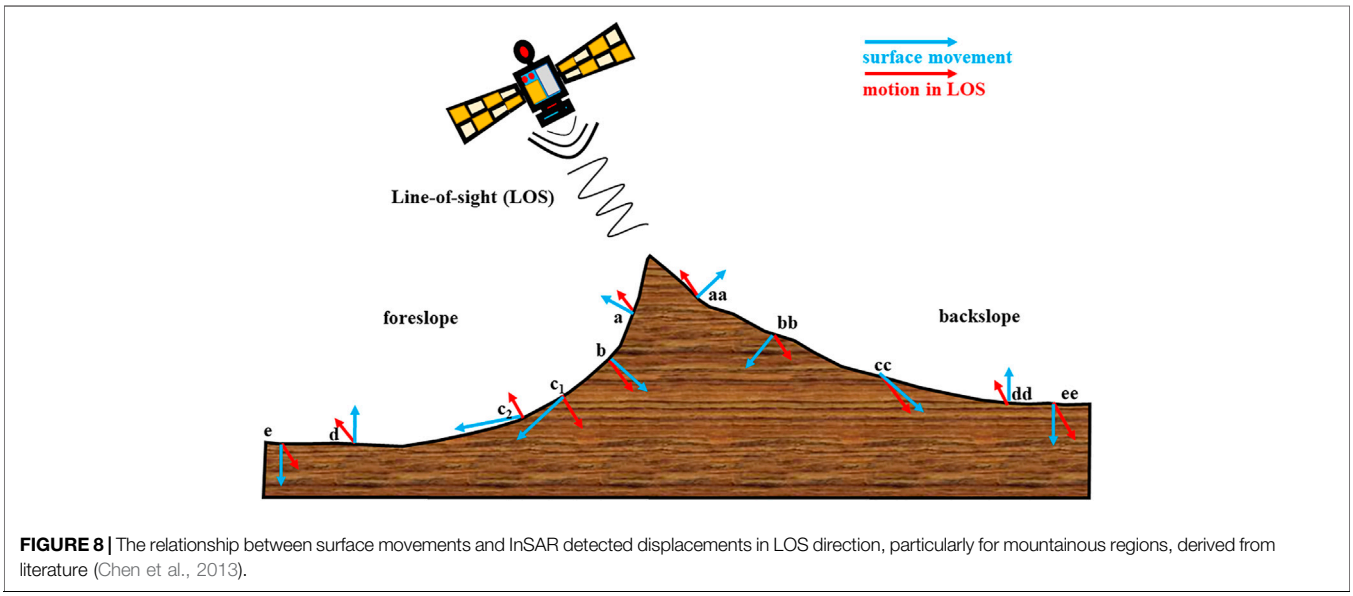

FIGURE 8 | The relationship between surface movements and InSAR detected displacements in LOS direction, particularly for mountainous regions, derived from literature (Chen et al., 2013).

freeze-thaw and snow/ice thawing, ranging from −16.1–24.9 mm/a with an average rate of 1.7 mm/a.

The built area is dominated by a subsidence trend with an average rate of −1.0 mm/a, mainly due to the thawing of the ground ice and permafrost, and more care should be taken to prevent the risk of collapse in the future. Water changes are somewhat fortuitous and the results are not very meaningful. The region of trees is completely decohered and cannot be effectively monitored for surface deformation.

The statistical analysis revealed that the study area was severely decohered. The severity of the decorrelation was found to be in trees, scrub/shrub, snow/ice, water, grass, crops, bare ground, and built area with the area decohered proportion of 100, 91.75, 91.34, 54.14, 47.05, 45.35, 44.87, and 38.7%, respectively.

Time-Series Variation Characteristics of Cumulative Deformation

To determine the variation characteristics of cumulative deformation, 14 observation points (OPs) (**Table 3**, **Figures 3**, **6A**) were selected in areas with dramatic variation, and the cumulative deformation was extracted for each point. **Figure 8** shows the results.

Due to the posture limitations of the SAR satellite when observing, the deformation information obtained through InSAR processing is usually not the real deformation of surface ground, instead the LOS direction. The effectiveness of the deformation results obtained is closely related to the terrain (slope and aspect) (see **Figure 8**), especially in mountainous areas. Specifically, with a few exceptions, the direction of surface movements fits expectations: the parallel movement, caused by widespread slope processes (e.g., general creep), was dominant in the middle section of slopes; for other portions, the rotational motion was prevalently caused by the alluvial accumulation or the combination dynamics of permafrost and the overlaid active layer (Chen et al., 2013). In addition, the occurrence of landslide will form a serious deformation area in a short time.

Figure 8 shows a high agreement between the real surface deformation and the motion in the LOS direction, both at the top of the mountain and at the foot of the mountain, fore and back the

TABLE 4 | Characteristic statistics of areas with the deformation rate greater than 15.0 mm/a.

Aspect		North	Northeast	East	Southeast	South	Southwest	West	Northwest
Ratio (%)		3.75	1.19	0.74	2.22	6.04	29.54	37.71	18.83
Velocity range (mm/a)		15.0–37.6	15.1–22.6	15.0–25.7	15.0–32.1	15.0–44.1	15.0–49.9	15.0–50.8	15.0–43.8
25–75% ranges of velocity (mm/a)		16.1–22.1	15.8–19.3	15.5–17.1	15.5–17.2	15.8–21.1	15.9–20.2	15.9–50.8	16.2–21.1
Media of velocity		18.3	17.0	16.2	16.0	17.3	17.3	17.4	18.1
Mean of velocity		19.6	17.6	16.8	17.2	19.5	19.1	18.6	19.3
Slope range (°)		0.9–53.6	1.3–42.2	4.2–59.1	0.9–63.2	0.6–63.7	0.4-57.7	2.1-60.7	1.8-57.3
25–75% ranges of slope (°)		12.4–28.2	9.1–16.2	14.8–30.1	14.8–36.4	13.3–30.5	19.8–35.3	21.5–34.5	17.1–32.1
Media of slope		18.9	12.1	21.0	27.3	20.6	27.2	28.7	24.3
Mean of slope		21.8	14.2	24.0	27.1	22.5	27.4	27.9	10.3
The ratio of land cover (%)	Bare ground	42.64	56.69	54.43	56.12	71.83	82.03	80.74	69.36
	Grass	38.90	23.62	6.33	4.64	17.03	12.66	17.03	25.67
	Snow/ice	17.96	19.69	39.24	39.24	11.15	5.19	2.13	4.82
	Scrub/shrub	0.50	—	—	—	—	0.13	0.10	0.15

The symbol "—" indicates that the data does not exist.

slope (a, aa, b, bb, c_1, cc, d, dd, e, and ee in **Figure 8**). Ground heave shows as uplift in LOS and surface settlement as subsidence in LOS. It is only when the slope faces satellite and slope gradient is greater than satellite incidence angle that the inconsistency is shown. In **Figure 8**, c2 marks a slope process (blue line), and an uplift signal is manifested in the LOS direction (red line).

The incidence angle of Sentinel-1A images used in this study is 39.08°. For ascending orbit, the west aspect is the satellite-facing slope and the east aspect is the satellite-away slope (Schaufler et al., 2018). Combining the slope and aspect dataset (**Figure 2**), the deformation velocity map (**Figure 3**), and the slope-velocity and aspect-velocity statistics (**Figures 11A,B**), we recognize that most uplift signals are located on satellite-facing slopes (west) and extensive subsidence signals are located on the east aspect. The signals (uplift and subsidence) are more likely caused by slope processes/land sliding.

To further understand the relationship between deformation rate and slope, slope orientation and vegetation, we counted the percentage of each element in the area with deformation rate greater than 15.0 mm/a. The results showed that, except for trees, the deformation rates of bare ground, grassland, snow, and wetland were all greater than 15.0 mm/a among the remaining seven types of ground features, with the percentages of 75.99, 17.91, 5.98, and 0.12%, respectively, and the deformation rates were concentrated between 16.0 and 21.5 mm/a. More statistical information is shown in **Table 4**.

It can be found from **Table 4** that the areas with deformation velocity greater than 15.0 mm/a in the study area are mostly concentrated in the west, southwest, and northwest sides of the slope direction, accounting for 37.71, 29.54, and 18.83%, respectively. The west aspect is the satellite-facing slope and ascending orbits show a positive shift in backscatter for slopes facing west (Schaufler et al., 2018), so that the landslide accumulation phenomenon can be well observed in this area. Moreover, the slope of the hills sloping to the west is also relatively large, concentrated between 17.1 and 35.3°, and the average slope is all greater than 24.3°. In addition, the area is mostly covered with bare land, followed by grassland, with little snow/ice and scrub/shrub coverage, which is more likely to cause landslides and should be paid special attention.

The cumulative deformation of the OPs shows that points P1–P7 are situated in a settlement area, whereas P9–P14 are situated in an uplift area. Over time, the cumulative deformation becomes greater, involving both settlement and uplift. The slope of the cumulative deformation curves shows the velocity of deformation, and P3 and P8 have the maximum values of settlement and uplift, respectively, which agrees with the velocities in **Table 3**. Compared with settlement curves, uplift curves show more volatility, especially those for P13 and P14. However, some anomalies were observed in settlement curves, such as P2 on August 22, 2018 and September 16, 2019 and P7 on April 19, 2019. The sudden jumps that appeared in **Figure 9** were very likely due to unwrapping errors or other noises.

By investigating historical imagery data, mainly *via* comparing Esri satellite maps and Google searching historical images, we found that the location where P7 is located originally had significant amounts of snow cover and ice, which has now largely thawed with global warming (**Figure 10**). The seasonal freezing and thawing of snow cover and ice, as well as the effects of solid winter precipitation, have induced small seasonal fluctuations changes in the cumulative deformation chart at point P7, but the overall trend is settlement.

According to close-up shots of the 14 OPs based on Esri satellite image maps (**Figure 9**), the settlement areas are mostly at the foot of mountains, which have an abundance of broken rocks or areas covered with snow and ice, especially on steep ridges where the landslides are prone to occur. Uplift regions occur mostly in the basins between ridges with relatively flat terrain, near the runoff points, so that changes in river discharge may modify the cumulative deformation process.

Relationship Between Deformation and Topographical Elements

Raster to Point tool was used to create the monitoring points (MPs) consistent with the deformation velocity raster grids within the area and extract the velocity, DEM, aspect, and slope of each point. Aspect and slope dataset for the study area (**Figure 2**) were produced from DEM data. Decohered

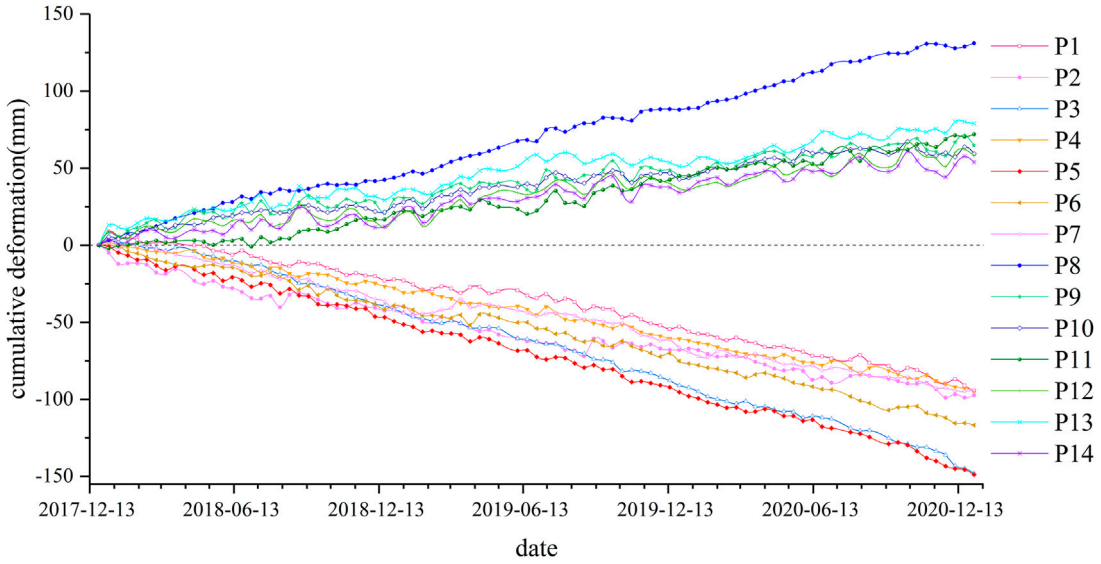

FIGURE 9 | Cumulative deformation (mm) of the observation points. And P1-P7 (cool color), P8-P14 (warm color) are uplift and subside toward the LOS direction, respectively. Slope of the curve shows the deformation velocity (mm/a).

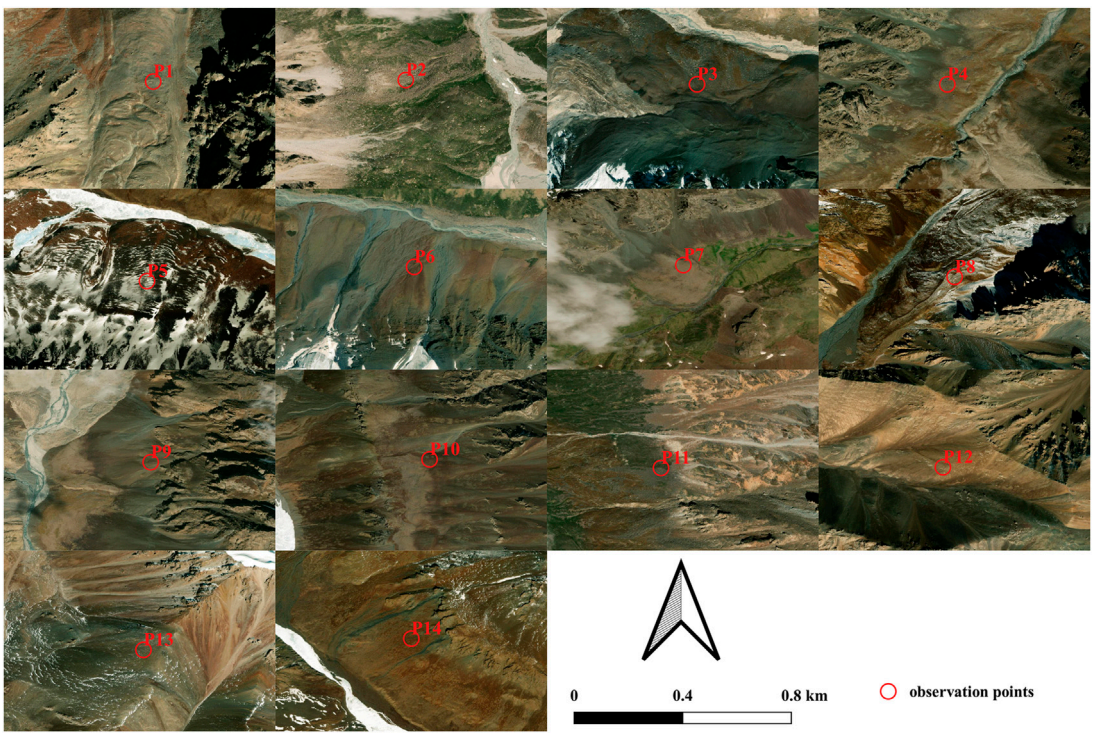

FIGURE 10 | The close-up shots around the observation points based on Esri satellite image maps on a scale of 1:380,000.

areas without a deformation rate were rejected, and a total of 242,778 points were generated.

The statistical analysis addressed the distribution of effective MPs and the relationships between velocity and aspect, slope, and elevation. The results are shown in **Figure 11**. Most of the MPs are distributed in the areas toward the southeast, south, and southwest (112.5–247.5), with slopes ranging from 15° to 50° and altitudes ranging from 3,150 m.a.s.l. to 4,275 m.a.s.l. MPs are less prevalent in areas with slopes greater than 60° and altitudes higher than 4,275 m.

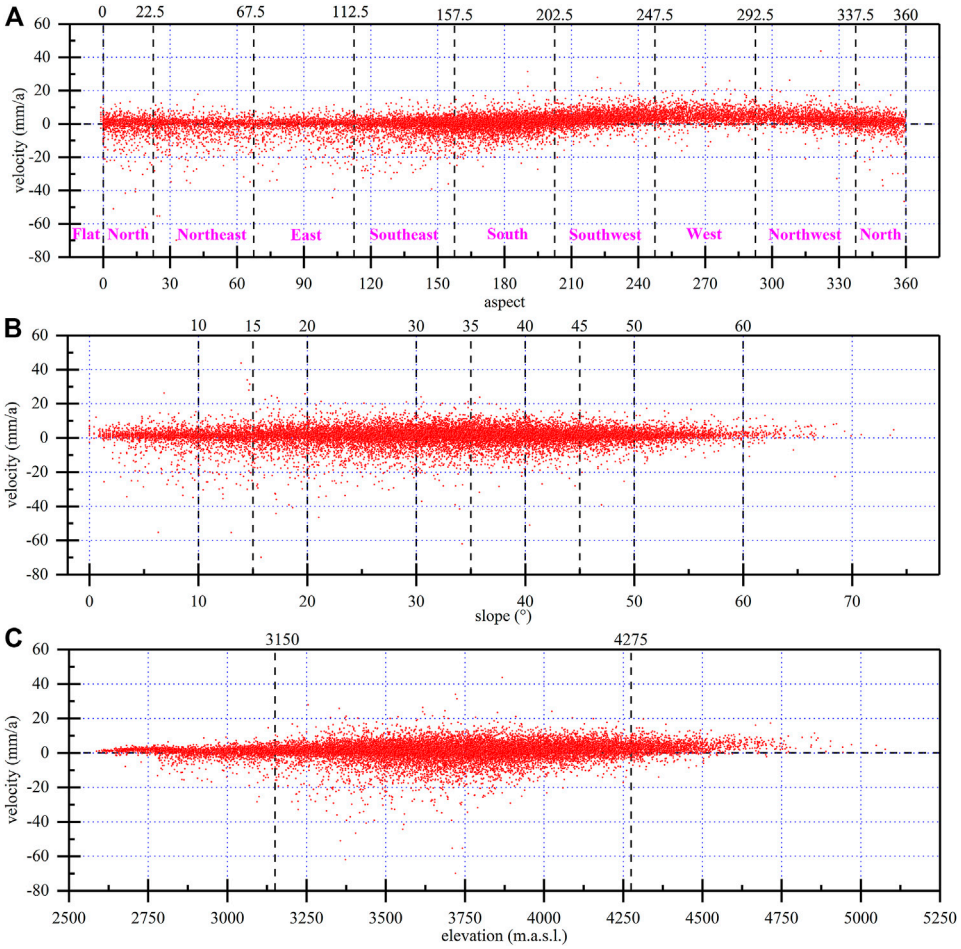

FIGURE 11 | Statistical distribution of terrain factors and deformation [**(A,B,C)** show the relationship between aspect, slope, and elevation, respectively].

Therefore, most of the deformation occurs in areas with slopes of 15–50° and elevations of 3,150–4,275 m.a.s.l., especially in regions with southwest, west, and northwest aspects. Ground areas with severe deformation may induce some secondary geological disasters, such as landslides, collapses, and mud-rock flows.

DISCUSSION

Due to the inherent limitations of InSAR measurements, certain areas lack deformation data due to decorrelation. In this study, significant incoherent regions covered with glaciers, snow cover, and ice were observed within the study area. In addition to the shortcomings of InSAR itself, this phenomenon is also related to the fact that degeneration of glaciers and snow cover not only occurs abruptly, but also in large amounts. Effective solutions for areas with missing values include field surveys, which can then be supplemented by spatial interpolation (Zhang, 2010). Alternatively, InSAR measurements can be processed from multiple SAR image sources and the results combined (Wang, 2019; Zhu et al., 2019). Sources of SAR images include products taken by different sensors, at different orientations, or in different time periods. In addition, reducing the coherence threshold is an effective method.

The deformation data obtained are of great significance, despite the large number of decoherent zones in the study area. The measurement results can provide basic advice and information for later continuous observations, and use of a sequential adjustment method (Wang et al., 2021) ensures that the long time series of SBAS-InSAR measurement data can be supplemented at a later stage. At the same time, current deformation values can provide a theoretical basis for environmental development by the local government. More importantly, the deformation data can provide a general picture over large areas and long time series of the distribution of mines and the degeneration of snow cover and ice in the area.

There are some differences regarding land cover between the close-up shots of OPs P5–P7 in **Figure 9** and the land-cover data in **Table 3**; these may have been caused by the different dates of the images obtained. Land-cover data is derived from ESA Sentinel-2 imagery at 10 m resolution. And it is a composite of LULC predictions for 10 classes throughout the year in order to

generate a representative snapshot of 2020. Whereas the close-up shots were based on the 2020 Esri image maps, which were the integrated product of various satellite images.

The question of whether the deformation in the LOS direction reflects the true displacement of the ground surface has been addressed in many papers (Chen et al., 2013; Liu et al., 2019; Hu et al., 2021b; Ge et al., 2021). As the monitoring results in this paper are obtained based on a single data source and a single InSAR processing method, it is difficult to obtain the real 3-D ground surface deformation. However, combining the available relevant theories (Chen et al., 2013; Reinosch et al., 2020) and the geometric relationship between SAR satellites and monitoring sites (mainly concerning slope and aspect), we found that there are almost no anomalies (the deformation in the LOS direction does not coincide with the true surface displacement) in this study area and the deformation values of the monitoring points are highly consistent with the real surface displacement. The reliability of results in this paper is also supported by the high agreement between the InSAR deformation monitoring values and the actual monitoring values for the mine sites located within the study area (Du et al., 2021b). The correlation between slope and deformation velocity needs to be investigated in depth in the follow-up to propose slope threshold of slope when the anomalies occurred, which will allow us to better analyze the real surface displacements.

CONCLUSION

1) The maximum subsidence velocity in the study area was -70.7 mm/a in the western, northeastern, and southeastern regions, and the maximum uplift rate was 50.8 mm/a in the northern and central regions. The areas with intense subsidence and uplift were isolated and sporadic.
2) The maximum cumulative subsidence in the study area for the 3-year period from December 25, 2017 to January 2, 2021 was −211.58 mm, and the maximum cumulative uplift was 149.03 mm, which was consistent with the deformation velocity.
3) The study area was severely decohered, with a decorrelation area of 984.11 km^2, accounting for 61.87% of the total area. The severity of the decorrelation is trees, scrub/shrub, snow/ice, water, grass, crops, bare ground and built area,with decohered percentage of own area 100, 91.75, 91.34, 54.14, 47.05, 45.35, 44.87, and 38.7%, respectively.
4) There were correlations between deformation and slope, slope direction, and elevation. Specifically, deformation was obvious in areas with elevations between 3,150 and 4,275 m.a.s.l., slopes of 15°–50°, and southwest, west, and northwest aspects, which are disaster-prone regions.

DATA AVAILABILITY STATEMENT

The original contributions presented in the study are included in the article/supplementary material, further inquiries can be directed to the corresponding author.

AUTHOR CONTRIBUTIONS

QD and GL conceived this research. QD prepared the data and wrote the manuscript. All other co-authors reviewed and supervised the manuscript and all authors listed approved it for publication.

FUNDING

This study was funded by the National Natural Science Foundation of China (No. U1703244), the Second Tibetan Plateau Scientific Expedition and Research Program (No.2019QZKK0905), the Foundation of the State Key Laboratory of Frozen Soil Engineering (No. SKLFSE-ZY-20), the Foundation of the State Key Laboratory for Geomechanics and Deep Underground Engineering (No. SKLGDUEK 1904).

ACKNOWLEDGMENTS

Thanks to the teams of organizations and individuals for providing the open and free source data involved in this paper. We express our deepest gratitude to the reviewers, whose careful work and thoughtful suggestions have greatly helped to improve this paper substantially.

REFERENCES

Amelung, F., Galloway, D. L., Bell, J. W., Zebker, H. A., and Laczniak, R. J. (1999). Sensing the Ups and Downs of Las Vegas: InSAR Reveals Structural Control of Land Subsidence and Aquifer-System Deformation. *Geology* 27 (6), 483–486. doi:10.1130/0091-7613(1999)027<0483:STUADO>2.3.CO;2

Bamler, R., and Hartl, P. (2010). Synthetic Aperture Radar Interferometry. *Sci. Geodesy - Adv. Future Dir.* 1, 415–474. doi:10.1007/978-3-642-11741-1_11

Chen, F., Lin, H., Zhou, W., Hong, T., and Wang, G. (2013). Surface Deformation Detected by ALOS PALSAR Small Baseline SAR Interferometry Over Permafrost Environment of Beiluhe Section, Tibet Plateau, China. *Remote Sensing Environ.* 138, 10–18. doi:10.1016/j.rse.2013.07.006

Cheng, G., Zhao, L., Li, R., Wu, X., Sheng, Y., Hu, G., et al. (2019). Characteristic, Changes and Impacts of Permafrost on Qinghai-Tibet Plateau. *Chin. Sci. Bull.* 64 (27), 2783–2795. doi:10.1360/TB-2019-0191

Colesanti, C., Ferretti, A., Prati, C., and Rocca, F. (2003). Monitoring Landslides and Tectonic Motions with the Permanent Scatterers Technique. *Eng. Geology.* 68 (1–2), 3–14. doi:10.1016/S0013-7952(02)00195-3

Du, Q., Li, G., Li, J., and Zhou, Y. (2020a). Research on the River Extration Based on the DEM Data in the Centeral West Tianshan Mountains. *China Rural Water and Hydropower* 456 (10), 29–33+40.

Du, Q., Li, G., Peng, W., Chai, M., Zhou, Y., and Chen, D. (2020b). Land Use Changes in High Cold-Altitude Mining Area Based on Remote Sensing Technology. *Environ. Sci. Technol.* 43 (12), 185–194. doi:10.19672/j.cnki.1003-6504.2020.12.025

Du, Q., Li, G., Peng, W., Zhou, Y., Chai, M., and Li, J. (2021a). Acquiring High-Precision DEM in High Altitude and Cold Area Using InSAR Technology. *Bull. Surv. Mapp.* 528 (03), 44–49. doi:10.13474/j.cnki.11-2246.2021.0076

Du, Q., Li, G., Zhou, Y., Chai, M., Chen, D., Qi, S., et al. (2021b). Deformation Monitoring in an Alpine Mining Area in the Tianshan Mountains Based on SBAS-InSAR Technology. *Adv. Mater. Sci. Eng.* 2021, 1–15. doi:10.1155/2021/9988017

Du, Q., Li, G., Zhou, Y., Wu, G., Chai, M., and Li, F. (2021c). Distribution Characterization Study of the Heavy Metals for a Mining Area of East Tianshan Mountain in Xinjiang Based on the Kriging Interpolation Method. *IOP Conf. Ser. Earth Environ. Sci.* 719 (4), 042063. doi:10.1088/1755-1315/719/4/042063

Du, Q., and Zhao, R. (2020). The Production of DEM in SARscape Format. *Comput. Knowledge Technol.* 16 (07), 238–239. doi:10.14004/j.cnki.ckt.2020.0838

Du, Y., Yan, S., Yang, H., Jiang, J., and Zhao, F. (2021d). Investigation of Deformation Patterns by DS-InSAR in a Coal Resource-Exhausted Region with Spaceborne SAR Imagery. *J. Asian Earth Sci. X* 5, 100049. doi:10.1016/j.jaesx.2021.100049

Ferretti, A., Montiguarnieri, A., Prati, C., Rocca, F., and Massonet, D. (2007). InSAR Principles: Guidelines for SAR Interferometry Processing and Interpretation. *J. Financial Stab.* 10 (10), 156–162. doi:10.1287/ited.1100.0047

Ferretti, A., Prati, C., and Rocca, F. (2001). Permanent Scatterers in SAR Interferometry. *IEEE Trans. Geosci. Remote Sensing* 39 (1), 8–20. doi:10.1109/36.898661

Gatsios, T., Cigna, F., Tapete, D., Sakkas, V., Pavlou, K., and Parcharidis, I. (2020). Copernicus sentinel-1 MT-InSAR, GNSS and Seismic Monitoring of Deformation Patterns and Trends at the Methana Volcano, Greece. *Appl. Sci.* 10 (18), 6445–6523. doi:10.3390/APP10186445

Ge, W., Li, Y., Wang, Z., Zhang, C., and Yang, H. (2021). Spatial-Temporal Ground Deformation Study of Baotou Based on the PS-InSAR Method. *Acta Geologica Sinica - English Edition* 95 (2), 674–683. doi:10.1111/1755-6724.14651

Gong, P., Liu, H., Zhang, M., Li, C., Wang, J., Huang, H., et al. (2019). Stable Classification with Limited Sample: Transferring a 30-m Resolution Sample Set Collected in 2015 to Mapping 10-m Resolution Global Land Cover in 2017. *Sci. Bull.* 64 (6), 370–373. doi:10.1016/j.scib.2019.03.002

Hanssen, R. F. (2001). *Radar Interferometry Data Interpretation and Error Analysis*. Dordrecht, Netherlands: Springer Science and Business Media.

Hanssen, R. F., Weckwerth, T. M., Zebker, H. A., and Klees, R. (1999). High-Resolution Water Vapor Mapping from Interferometric Radar Measurements. *Science* 283 (5406), 1297–1299. doi:10.1126/science.283.5406.1297

Hansson, A., Anshelm, J., Fridahl, M., and Haikola, S. (2021). Boundary Work and Interpretations in the IPCC Review Process of the Role of Bioenergy with Carbon Capture and Storage (BECCS) in Limiting Global Warming to 1.5°C. *Front. Clim.* 3, 1–14. doi:10.3389/fclim.2021.643224

He, M., and Zhao, Y. (2020). Study on the Application Prospect of DS-InSAR Technology in Landslide Deformation Monitoring in Complex and Dangerous Mountainous Areas. *Geomatics Sci. Technol.* 08 (03), 106–113. doi:10.12677/gst.2020.83013

Hooper, A. (2008). A Multi-Temporal InSAR Method Incorporating Both Persistent Scatterer and Small Baseline Approaches. *Geophys. Res. Lett.* 35 (16), 1–5. doi:10.1029/2008GL034654

Hooper, A., Zebker, H., Segall, P., and Kampes, B. (2004). A New Method for Measuring Deformation on Volcanoes and Other Natural Terrains Using InSAR Persistent Scatterers. *Geophys. Res. Lett.* 31 (23), 1–5. doi:10.1029/2004GL021737

Hu, J., Ge, Q., Liu, J., Yang, W., Du, Z., and He, L. (2021a). Constructing Adaptive Deformation Models for Estimating DEM Error in SBAS-InSAR Based on Hypothesis Testing. *Remote Sensing* 13 (10), 2006. doi:10.3390/rs13102006

Hu, J., Li, Z., Zhu, J., and Liu, J. (2021b). *Theory and Application of Monitoring 3-D Deformation with InSAR*. Beijing, China: Science Press.

Karra, K., Kontgis, C., Statman-Weil, Z., Mazzariello, J., Mathis, M., and Brumby, S. (2021). "Global Land Use/land Cover with Sentinel-2 and Deep Learning," in IGARSS 2021-2021 IEEE International Geoscience and Remote Sensing Symposium, Brussels, Belgium, June 11–July 16, 2021 (IEEE).

Kursah, M. B., Wang, Y., Bayoh, H. D., David Bayoh, H., Tarawally, M., and Leone, S. (2021). A Comparative Study on the Predictive Ability of Archived and SBAS-InSAR Inventories for Landslide Susceptibility Using Frequency Ratio Model in Western Area, Sierra Leone. *Environ. Earth Sci.* 80, 387. doi:10.1007/s12665-021-09663-x

Li, Q., Zhou, C., Zheng, L., Liu, T., and Yang, X. (2020). Monitoring Evolution of Melt Ponds on First- Year and Multiyear Sea Ice in the Canadian Arctic Archipelago with Optical Satellite Data. *Ann. Glaciology* 61 (82), 1–10. doi:10.1017/aog.2020.24

Liu, G., Chen, Q., Chen, X., and Cai, G. (2019). *InSAR Principles and Applications*. Beijing, China: Science Press.

Lu, Z., and Dzurisin, D. (2014). *InSAR Imaging of Aleutian Volcanoes: Monitoring a Volcanic Arc from Space*. Chichester, United Kingdom: Springer Praxis Books.

Massonnet, D., and Feigl, K. L. (1998). Radar Interferometry and its Application to Changes in the Earth's Surface. *Rev. Geophys.* 36 (4), 441–500. doi:10.1029/97RG03139

Metternicht, G., Hurni, L., and Gogu, R. (2005). Remote Sensing of Landslides: An Analysis of the Potential Contribution to Geo-Spatial Systems for hazard Assessment in Mountainous Environments. *Remote Sensing Environ.* 98 (2–3), 284–303. doi:10.1016/j.rse.2005.08.004

Monserrat, O., Crosetto, M., and Luzi, G. (2014). A Review of Ground-Based SAR Interferometry for Deformation Measurement. *ISPRS J. Photogrammetry Remote Sensing* 93, 40–48. doi:10.1016/j.isprsjprs.2014.04.001

Mora, O., Lanari, R., Mallorquí, J. J., Berardino, P., and Sansosti, E. (2002). "A New Algorithm for Monitoring Localized Deformation Phenomena Based on Small Baseline Differential SAR Interferograms," in International Geoscience and Remote Sensing Symposium (IGARSS), Toronto, ON, June 24–28, 2002, 1237–1239. doi:10.1109/igarss.2002.1025900

Moreira, A., Prats-Iraola, P., Younis, M., Krieger, G., Hajnsek, I., and Papathanassiou, K. P. (2013). A Tutorial on Synthetic Aperture Radar. *IEEE Geosci. Remote Sens. Mag.* 1 (1), 6–43. doi:10.1109/MGRS.2013.2248301

Ouchi, K. (2013). Recent Trend and advance of Synthetic Aperture Radar with Selected Topics. *Remote Sensing* 5 (2), 716–807. doi:10.3390/rs5020716

Pepe, A., and Calò, F. (2017). A Review of Interferometric Synthetic Aperture RADAR (InSAR) Multi-Track Approaches for the Retrieval of Earth's Surface Displacements. *Appl. Sci.* 7 (12), 1264. doi:10.3390/app7121264

Qin, D., Yao, T., Ding, Y., and Ren, J. (2018). *Introduction to Cryospheric Science*. Beijing, China: Science Press.

Reinosch, E., Buckel, J., Dong, J., Gerke, M., Baade, J., and Riedel, B. (2020). InSAR Time Series Analysis of Seasonal Surface Displacement Dynamics on the Tibetan Plateau. *The Cryosphere* 14 (5), 1633–1650. doi:10.5194/tc-14-1633-2020

Rosen, P. A., Hensley, S., Joughin, I. R., Li, F. K., Madsen, S. N., Rodriguez, E., et al. (2000). Synthetic Aperture Radar Interferometry. *Proc. IEEE* 88 (3), 333–382. doi:10.1109/5.838084

Rott, H. (2009). Advances in Interferometric Synthetic Aperture Radar (InSAR) in Earth System Science. *Prog. Phys. Geogr. Earth Environ.* 33 (6), 769–791. doi:10.1177/0309133309350263

Schaufler, S., Bauer-Marschallinger, B., Hochstöger, S., and Wagner, W. (2018). Modelling and Correcting Azimuthal Anisotropy in sentinel-1 Backscatter Data. *Remote Sensing Lett.* 9 (8), 799–808. doi:10.1080/2150704X.2018.1480071

Shahzad, N., Ding, X., Wu, S., and Liang, H. (2020). Ground Deformation and its Causes in Abbottabad City, pakistan from sentinel-1a Data and Mt-Insar. *Remote Sensing* 12 (20), 1–18. doi:10.3390/rs12203442

Shan, W., Guo, Y., Zhang, C., Hu, Z., Jiang, H., and Wang, C. (2014). "Climate-Change Impacts on Embankments and Slope Stability in Permafrost Regions of Bei'an-Heihe Highway," in *Landslide Science for a Safer Geoenvironment*. Editors K. Sassa, P. Canuti, and Y. Yin (London, United Kingdom: Springer International Publishing), 155–160. doi:10.1007/978-3-319-04999-1_18

Shan, W., Hu, Z., Guo, Y., Zhang, C., Wang, C., Jiang, H., et al. (2015). The Impact of Climate Change on Landslides in southeastern of High-Latitude Permafrost Regions of China. *Front. Earth Sci.* 3, 1–11. doi:10.3389/feart.2015.00007

Simons, M., and Rosen, P. A. (2007). Interferometric Synthetic Aperture Radar Geodesy. *Treatise Geophys.* 3, 391–446. doi:10.1016/B978-044452748-6.00059-6

Wang, H., Zeng, Q., Jiao, J., and Chen, J. (2021). InSAR Time Series Analysis Technique Combined with Sequential Adjustment Method for Monitoring of Surface Deformation. *Beijing Daxue Xuebao (Ziran Kexue Ban)/Acta Scientiarum Naturalium Universitatis Pekinensis* 57 (2), 241–249. doi:10.13209/j.0479-8023.2021.002

Wang, Z. (2019). Research on Resolving of Three-Dimensional Dispalcement from Multi-Source InSAR Data. *Acta Geodaetica et Cartographica Sinica* 48 (9), 1206. doi:10.11947/j.AGCS.2019.20180490

Yang, K., Yang, J., and Jiang, B. (2015). Sentinel-1 Satellite Overview. *Urban Geotechnical Invest. Surv.* 8262 (02), 24–27.

Ye, X. (2010). *Synthetic Aperture Radar Interferometry*. London, United Kingdom: Springer Berlin Heidelberg. doi:10.1007/978-3-642-11741-1

Zhang, J., Huang, H., Liu, Y., and Liu, Y. (2013). Monitoring and Analysis of Ground Subsidence in the Modern Yellow River Delta Area Based on PSInSAR Technique. *Scientia Geographica Sinica* 33 (07), 831–836. doi:10.13249/j.cnki.sgs.2013.07.008

Zhang, J. (2010). InSAR Data Post-processing Based on GIS. M.A. Thesis. Xi'an: Changan University.

Zhao, L., Hu, G., Zou, D., Wu, X., Ma, L., Sun, Z., et al. (2019). Permafrost Changes and its Effects on Hydrological Processes on Qinghai-Tibet Plateau. *Bull. Chin. Acad. Sci.* 34 (11), 1233–1246. doi:10.16418/j.issn.1000-3045.2019.11.006

Zhu, J., Yang, Z., and Li, Z. (2019). Recent Progress in Retrieving and Predicting Mining-Induced 3D Displacement Using InSAR. *Acta Geodaetica et Cartographica Sinica* 48 (02), 135–144. CNKI:SUN:CHXB.0.2019-02-002.

Zhu, L., Wu, Z., Liu, Y., and Li, D. (1996). Permafrost Degeneration in the East of Qinghai-Xizang Plateau. *Chin. Geograph.Sc.* 6 (3), 231–238. doi:10.1007/s11769-996-0025-2

Zhu, X., Wang, Y., Montazeri, S., and Ge, N. (2018). A Review of Ten-Year Advances of Multi-Baseline SAR Interferometry Using terraSAR-X Data. *Remote Sensing* 10 (9), 1374–1405. doi:10.3390/rs10091374

Conflict of Interest: The authors declare that the research was conducted in the absence of any commercial or financial relationships that could be construed as a potential conflict of interest.

Publisher's Note: All claims expressed in this article are solely those of the authors and do not necessarily represent those of their affiliated organizations, or those of the publisher, the editors and the reviewers. Any product that may be evaluated in this article, or claim that may be made by its manufacturer, is not guaranteed or endorsed by the publisher.

frontiers in Earth Science

ORIGINAL RESEARCH
published: 10 November 2021
doi: 10.3389/feart.2021.733483

Establishment and Verification of a Thermal Calculation Model Considering Internal Heat Transfer of Accumulated Water in Permafrost Regions

Erxing Peng[1], Xiaoying Hu[2], Yu Sheng[1], Fansheng Zhou[2], Jichun Wu[1] and Wei Cao[1]*

[1]State Key Laboratory of Frozen Soil Engineering, Northwest Institute of Eco-Environment and Resources, Chinese Academy of Sciences, Lanzhou, China, [2]School of Civil Engineering, Lanzhou University of Technology, Lanzhou, China

Water accumulation in permafrost regions causes a heavy thermal impact on the frozen layer, thereby leading to its degeneration. First, based on the real heat transfer process, this study proposes relevant hypotheses and governing equations for heat calculation models involving completely melted water, ice-bearing water, water–soil interface, and soil under water. The models consider the water surface as a thermal boundary on account of the natural buoyancy convection mechanism in water and the phase transition process. Second, this study verifies the accuracy of the calculation models regarding the measured water and permafrost temperatures. The four seasonal vertical temperature changes in the water according to this model are found to be consistent with the actual temperature-change trend, and the permafrost temperature under water is also consistent with the actual temperature field. This study thus provides theoretical support for the thermal impact analysis of water in permafrost regions.

Keywords: accumulated water, permafrost, ground temperature, thermal impact, calculation model

OPEN ACCESS

Edited by:
Huijun Jin,
Northeast Forestry University, Harbin, China

Reviewed by:
Bin Cao,
Institute of Tibetan Plateau Research (CAS), China
Zhaohui Yang,
University of Alaska Anchorage, United States

****Correspondence:***
Xiaoying Hu
xiaoyinghu@lzb.ac.cn

Specialty section:
This article was submitted to Cryospheric Sciences, a section of the journal Frontiers in Earth Science

Received: *30 June 2021*
Accepted: *30 September 2021*
Published: *10 November 2021*

Citation:
Peng E, Hu X, Sheng Y, Zhou F, Wu J and Cao W (2021) Establishment and Verification of a Thermal Calculation Model Considering Internal Heat Transfer of Accumulated Water in Permafrost Regions. Front. Earth Sci. 9:733483. doi: 10.3389/feart.2021.733483

INTRODUCTION

The gradual expansion of construction works in permafrost regions of the Qinghai–Tibet Plateau has triggered several engineering problems, and in particular the accumulation of water along the roads. A field survey of the Qinghai–Tibet highway revealed that water accumulation along its sides has aggravated in recent years, that is, a tenfold increase in the number of ponds within 100 m of the highway on both sides from 2007 to 2009 (Jin et al., 2000; Lin et al., 2010; Luo et al., 2015; Xu and Wu, 2019). Such accumulation of water may exhibit a severe thermal impact on the permafrost in the surrounding areas, even leading to its melting (Karlsson et al., 2012; Kokelj and Jorgenson, 2013). In particular, the melting of permafrost with high ice content increases the depth of accumulated water and may even lead to thawing disasters in the surrounding regions (Langer et al., 2016). Thus, the most important effect of water accumulation on permafrost and its embankment is the thermal impact attributed to the special thermal sensitivity of permafrost (Calmels et al., 2008; Ling et al., 2012; Huang et al., 2013; Baranskaya et al., 2021). The permafrost suffers thermal erosion that results in decrease in the bearing capacity and stability of embankment, thereby causing uneven settlement, tumbling, or even cracking of the road surface (Niu et al., 2014; Wen et al., 2016; Lin et al., 2017; Sun et al., 2018). Hence, this study focuses on the effect of water accumulation on ground temperature and permafrost table change.

At present, the most important research on accumulated water in permafrost regions pertains to thermokarst lakes (Jorgenson et al., 2012). The main influence of these lakes on the environment and engineering works in permafrost regions is their thermal impact, which generally results in the conduction of vertical and lateral heat transfer to the surrounding permafrost. This transference can cause degradation of permafrost and decrease its stability (Hinkel et al., 2010; Kokelj et al., 2010; Samuelsson et al., 2010). The annual average ground temperature under a lake center is significantly higher in comparison to the temperature under a natural surface (Lin et al., 2011; Niu et al., 2011). This is mainly because a thermokarst lake can be a heat source and transfer energy to the surrounding permafrost, causing thermal erosion, and even transfer more heat downwards than the lateral transfer (Niu et al., 2018). This thermal erosion causes the permafrost under and around the lake to thaw, generating a gradually growing melting zone, and shows degradation effects such as temperature rise and decrease in the permafrost table (Pan et al., 2014; Wang et al., 2017; You et al., 2017). Moreover, lake temperature has been studied as the dominant factor of thermal influence (Burn, 2002). Stepanenko (2005) analyzed the heat and water exchanges between accumulated water and soil and suggested that the temperature gradient of lake water is the main factor affecting the thermal diffusion, freezing, and thawing of the surrounding permafrost.

Fang and Stefan (1996) proposed an accumulated water modified model that takes into account the heat exchange between water and bottom sediments, showing that the bottom water temperature change can affect soil temperature to a depth of 10 m. Water depth and the water–soil contact field have been found to directly affect the influence and extent of external changes on soil temperature. Lin et al. (2011) used a two-dimensional calculation model to assess the heat flux density between a thermokarst lake and its embankment and found that the former causes lateral thermal erosion of the latter. In conclusion, the current thermal calculation models for water accumulation in permafrost regions generally regard the bottom of the accumulated water as the thermal boundary and neglect the heat transfer process inside the water body, despite its significance. In alpine and cold environments, as in permafrost areas, the relationship between water depth and its maximum freezing depth also impacts the degree to which the lower soil layer is affected by water heat, and the temperature at the bottom of the water determines the development of the lower permafrost melting zone (Romanovsk and Osterkamp, 2000; Jorgenson and Shur, 2007; Gao et al., 2017). In the case of completely frozen water, the long-term observed temperature at the bottom of the water will be below 0°C. However, when the water depth is greater than or equal to the freezing thickness, the water does not completely freeze in winter, or only the bottom is frozen at the end of the cold season, and the temperature of the underlying soil continues to be above 0°C. The long-term effects of the above two scenarios will also drive the soil layer at the bottom of the water to gradually form a thawing layer (Hinkel et al., 2007; Wang et al., 2014). Therefore, the depth of the water and heat transfer in it constitute imperatives that cannot be neglected.

Mainly, the research and analysis about thermokarst lakes in permafrost regions are qualitative; the research methods are either site-measured data analysis or numerical calculation models, and heat transfer processes in the accumulated water are ignored. Moreover, water accumulations in permafrost regions are not exclusive of thermokarst lakes, and a large number of them are non-thermal water bodies with shorter formation times. In addition, limitations due to actual conditions render it difficult to study the thermal influence of various types of accumulated water on permafrost using measured data. Thus, this study establishes a calculation model that considers the water surface as the thermal boundary, the natural buoyancy convection mechanism of water, and the phase change process of water and its surrounding permafrost. The accuracy and feasibility of this calculation model were further verified by measured field temperature data. Hence, this study extends theoretical support for research on the influence of accumulated water in permafrost regions.

GOVERNING EQUATION AND THE THEORETICAL MODEL

The model calculation was based on the separate heat transfer characteristics of water, ice, and soil because of the heat transfer difference in different media. In addition, the phase transition process of water and soil was also considered in permafrost regions. The model medium distributions in water and soil are shown in **Figure 1**.

Ice-Free Water Body

In order to simplify the heat calculation of a completely melted water body in a permafrost region, the study considered the following assumptions:

1) The cross section of the accumulated water at different depths is equal.
2) Water is incompressible and isotropic, and mass exchange is regardless. The water density only depends on temperature.
3) The water temperature stratification is mainly reflected in vertical direction, and the heat exchange only occurs in vertical direction. Moreover, the water temperature in horizontal direction is equal.
4) Regardless of the external water supplement and heat exchange between the water surface and air caused by the wind speed, heat convection in the water body is only vertical natural buoyant convection caused by density difference.

As such, this study employed the equivalent heat conduction model based on the thermal diffusion theory, and the thermal diffusion coefficient in the traditional heat conduction equation represents the heat transfer caused by convection (Banimahd et al., 2013; Hondzo and Stefan, 2015). The heat transfer in accumulated water only occurs in vertical direction, and as such, using the theory of thermal diffusion, the convective heat transfer effect in vertical direction can be represented by thermal diffusivity in the model. Moreover, the governing equation of heat transfer in water can adopt the one-dimensional thermal diffusion equation (Banimahd and Zand-Parsa, 2013):

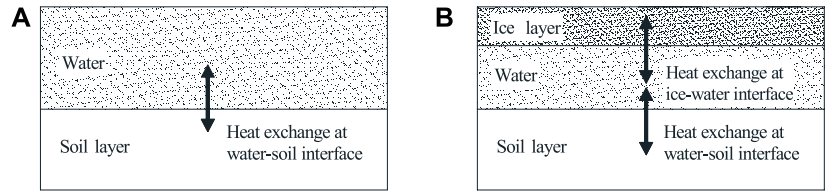

FIGURE 1 | Model medium distribution. **(A)** Completely melted water body. **(B)** Water body with an ice layer.

$$\frac{\partial T_w}{\partial t} = \frac{\partial}{\partial y}\left[(k_w + k_e)\frac{\partial T_w}{\partial y}\right] + \frac{1}{C_{liq}}\frac{d\varphi_y}{dy} 0 \le z \le H, \quad (1)$$

$$\varphi_y = (1-\beta)S(1-\alpha)exp(-\lambda h), \quad (2)$$

$$\rho = \rho_0\left(1.02\times10^{-3} + 6.78\times10^{-8}T - 9.05\times10^{-9}T^2 + 8.64\times10^{-11}T^3 - 6.42\times10^{-13}T^4 + 1.05\times10^{-18}T^7 - 1.05\times10^{-29}T^8\right), \quad (3)$$

where T_w is the water temperature (°C); H is the depth of water (m); k_w is the thermal diffusivity of water molecules, usually 0.57 (m^2/s); k_e is the eddy diffusion coefficient (m^2/s), shown in **Eqs 4**, **5** (Hondzo and Stefan, 2015); C_{liq} is the volumetric heat capacity of water (J/(m^3·°C)), generally 4,182 ρ, the expression of ρ is shown in **Eq. 3**, and the specific heat of water is 4,182 (J/(kg·°C)); and φ_y is the excess heat absorbed at depth y, mainly the solar radiant heat transferred to the water layer. The detailed calculation method is shown in **Eq. 2**; t is time (s); y is the depth of accumulated water (m).

$$k_e = \alpha(N^2)^{-r}, \quad (4)$$

$$N^2 = -\frac{g}{\rho}\frac{\partial \rho}{\partial y}, \quad (5)$$

where α is the coefficient determined by the degree of turbulence; N^2 is the stability coefficient; g is the gravitational acceleration (kg/m^3); ρ is the water density (kg/m^3), which is expressed as follows (3); $\frac{\partial \rho}{\partial y}$ is the vertical density gradient of water body, showing the degree of stability in water body, which is determined by water temperature stratification in vertical direction; and γ is determined by the turbulence formation mode in water body, such as wide or narrow internal waves and shear waves. The value range of γ in the past empirical formula is 0.4–0.6 (Hondzo and Stefan, 2015).

Water Body With Ice Layer

Accumulated water showed a phase change when the temperature drops below 0°C. This process is affected by meteorological factors, water temperature under the ice layer, and thermal characteristics of the ice layer. In order to calculate this phase change process in water body, the study considered the following assumptions:

1) There is no mass exchange with the external environment during the ice freezing and thawing process.
2) Ice layer freezes and thaws along vertical direction of water, and water body at the same depth freezes and thaws at the same time, and heat exchange only occurs in vertical direction.
3) The heat conduction process in the ice layer follows the Fourier thermal conductivity theory.
4) The water–ice conversion process is carried out in a small temperature range, −0.1–0°C.
5) The thermophysical parameters of the ice layer, such as specific heat capacity, thermal conductivity, and density, are all constant.

In this study, governing equations of the solid phase region and the liquid phase region were established based on the temperature method and the energy conservation theory. The governing equations of liquid accumulated water are described in **Eq. 1**. Besides, the governing equations in the solid phase, the ice layer, and water–ice interface equations are described as follows.

Governing equations in the ice layer (Fang et al., 1996) is given as follows:

$$\frac{\partial T_{ice}}{\partial t} = \frac{k_i}{\rho_i C_i}\frac{\partial^2 T_{ice}}{\partial y^2} + \varphi_y. \quad (6)$$

The governing equation at the water–ice interface (Fang et al., 1996) is given as follows:

$$k_i\frac{\partial T_{ice}}{\partial y} - q = \rho_i L_i\frac{dh}{dt}, \quad (7)$$

where T_{ice} is the ice temperature (°C); k_i is the thermal conductivity of ice, generally taken as 2.2 (J/(m·°C·s)); t is the time (s); ρ is the density of ice (kg/m^3); C_i is the specific heat of ice, generally taken as 2,117 (J/(kg·°C)); y is the vertical depth (m); and φ_y is the extra heat absorbed by the water body per unit volume (J/m^3); here, it is mainly the solar short-wave radiation heat transmitted into the ice layer. The detailed calculation method is shown in **Eq. 2**; q is the heat exchange between water and ice (W/m^2); L is the latent heat of dissolution of ice, generally taken as 336,000 (J/kg).

Water–Soil Interface

The heat exchange at the interface between accumulated water and lower soil affects the thermal state of the underlying permafrost, and as such the study considered the following assumptions: because the convective heat transfer between the bottom of the accumulated water and the lower soil is much smaller than heat transfer at the interface, so it is ignored. Therefore, it should be treated as a solid heat transfer problem.

Thus, the governing equation at the water–soil interface is (Shen, 2010) as follows:

$$\frac{\partial T_{\text{bottom}}}{\partial t} = \frac{k_{\text{soil}}}{\rho_{\text{soil}} C_{\text{soil}}} \frac{\partial^2 T_{\text{soil}}}{\partial y^2}\Big|_{y=bottom}, \quad (8)$$

where T_{bottom} is the temperature at the water bottom (°C); t is the calculation time (s); k_{soil} is the thermal conductivity of soil in contact with water (J/(m·°C·s)); ρ_{soil} is the density of soil in contact with water (kg/m^3); C_{soil} is the specific heat of soil in contact with water (J/(kg·°C)); y is the vertical depth of water (m); and T_{soil} is the temperature of soil is in contact with water (°C).

Soil Area

Heat convection, mass migration, and other effects were neglected in the heat calculation of the permafrost under water, and in contrast, only the heat conduction of the soil and the phase change was considered. Assuming that the phase change of the aqueous medium in the model occurred in the temperature range ($T_m \pm \Delta T$), the heat transfer control equation was simplified to (Zhang et al., 2012; Zhang et al., 2019):

$$\rho_{\text{soil}} \mathcal{C}_{\text{soil}} \frac{\partial T}{\partial t} = \frac{\partial}{\partial y}\left(\lambda_{\text{soil}} \frac{\partial T}{\partial y}\right), \quad (9)$$

$$\mathcal{C}_{\text{soil}} = \begin{cases} \mathcal{C}_{\text{u}} & (T > T_{\text{m}} + \Delta T) \\ \dfrac{L}{2\Delta T \rho} + \dfrac{\mathcal{C}_{\text{u}} + \mathcal{C}_{\text{f}}}{2} & (T_{\text{m}} - \Delta T \le T \le T_{\text{m}} + \Delta T_2), \\ \mathcal{C}_{\text{f}} & (T < T_{\text{m}} - \Delta T_1) \end{cases} \quad (10)$$

$$\lambda_{\text{soil}} = \begin{cases} \lambda_{\text{u}} & (T > T_{\text{m}} + \Delta T) \\ \lambda_{\text{f}} + \dfrac{\lambda_{\text{u}} - \lambda_{\text{f}}}{2\Delta T} [T - (T_{\text{m}} - \Delta T)] & (T_{\text{m}} - \Delta T \le T \le T_{\text{m}} + \Delta T), \\ \lambda_{\text{f}} & (T < T_{\text{m}} - \Delta T) \end{cases} \quad (11)$$

where ρ_{soil} is the density of soil (kg/m^3); C_{soil} is the apparent specific heat of soil (J/(kg·°C)); $\mathcal{C}_{\text{u}}$ and λ_{u} are the specific heat of soil (J/(kg·°C)) and thermal conductivity (J/(m·°C·s)) when it melts, respectively; $\mathcal{C}_{\text{f}}$ and λ_{f} are the specific heat (J/(kg·°C)) and thermal conductivity (J/(m·°C·s)) when soil is frozen, respectively; L is the latent heat of phase change per unit mass of aqueous medium 336,,000 (J/kg) (Subin et al., 2012); T is the temperature (°C); t is the time variable (s); and x and y are spatial variables (m).

VERIFICATION OF A THERMAL CALCULATION MODEL CONSIDERING INTERNAL HEAT TRANSFER OF ACCUMULATED WATER IN PERMAFROST REGIONS

Verification Method

First, in this experimental study, the researchers determined the water surface boundary of the model according to the thermal condition of the monitoring site. Then according to the control equation mentioned in *The Governing Equation and Theoretical Model*, the thermal calculation model for the permafrost with accumulated water was established considering the heat transfer process inside water. Finally, the reliability and feasibility of the model were verified by natural ground temperature, water temperature, and ground temperature under water at the monitored site.

Model Parameters

Permafrost models without and with accumulated water were calculated in the study at this stage. The former verified the rationality of the calculation method by comparing it with the natural ground temperature of the monitoring site, whereas the latter verified the rationality and feasibility of the model, considering the interaction between the accumulated water and the permafrost. The soil layer distributions in the models were inferred to be consistent with that of the monitoring field, which is located near the Gonghe–Yushu expressway in the Qinghai–Tibet Plateau of China, shown in **Figure 2**. In the monitoring field, permafrost was observed to be a well-developed, mainly ice-rich permafrost, and soil–ice layer. The permafrost table of natural ground is about −0.8 to −3.5 m, the thickness of permafrost is about 60–100 m, and the annual average temperature of permafrost is about −2.0 to −1.5°C. Silty clay with an ice content of 15% distributes in −3 m of the upper layer, silty clay with ice content of 35% distributes in −3 m to −20 m, and gravel silty clay locates below −20 m.

The size of the thermokarst lake in the monitored field is 40 × 50 m, and its maximum depth is 1 m. The monitoring time within which the study was conducted was from November 2013 to March 2015. During this time, the average air temperature was about −2.5°C, and the average annual cumulative precipitation was about 374 mm. The lowest temperature and highest temperature in a year usually occur in January and July, respectively. The measured temperatures of natural ground and lake center in the monitoring site were used for model verification. The probes were arranged in the same position for monitoring the temperature of the natural ground and lake center. The probes were arranged at −0.2, −0.5, −1.0, −1.5, −2.0, −2.5, −3.0, −3.5, −4.0, −5.0, −6.0, −7.0, −8.0, −10, −12, −14, −16, −18, and −20.0 m. The maximum depth of thaw in the natural ground and lake bottom was about −3.2 and −14 m in 2014. The temperature probe was installed in a steel pipe of 40 mm diameter, and the temperature measured in the steel pipe was regarded as the temperature of soil and water at the corresponding depth. The measurement accuracy and the resolution of temperature probe were ±0.05 and 0.01°C, respectively.

The geometric calculation model and the soil layer distribution are shown in **Figure 3**, and the corresponding thermal parameters are shown in **Table 1**. These thermal parameters were obtained from the reference Cao (2015). The soil depth was set to 60 m, and the water depth was set to 1 m, which is the same as the maximum depth of the measured thermokarst lake. The vertical and horizontal dimension of model geometry was 60 and 0.01 m. For the model of permafrost with accumulated water, the depth of water was 1 m and the depth of soil was 59 m under water in

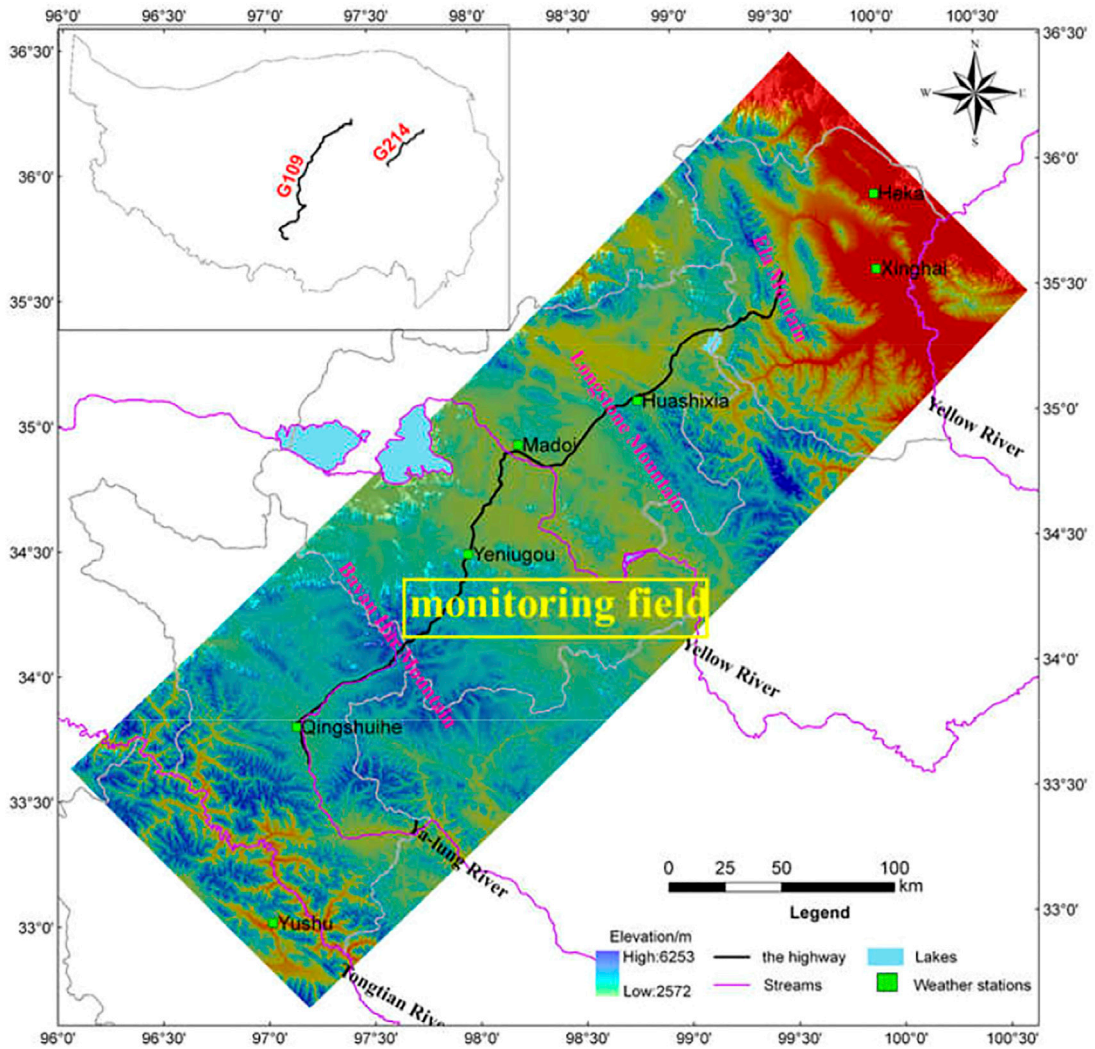

FIGURE 2 | Location of monitoring field.

the vertical direction. The finite differential method was used for discretization calculation, and the difference between the calculation results of adjacent time steps was used as the accurate judgment. Time step was set to 1 h and, notably, the spin-up setting was different for the natural ground model and accumulated water model. For the natural ground model, geothermal gradient was obtained through the initial steady state calculation, and then the instant state was calculated for 300 years in order to obtain the initial temperature field. For the model of permafrost with accumulated water, the calculation method of the initial ground temperature field was the same as the natural ground model. After obtaining the initial ground temperature field, the accumulated water area was activated, and the initial temperature of the water was set to 4°C, which constituted the initial water temperature field.

Temperature Boundary at the Monitored Site

For the simulation of the monitoring site, true temperature boundary conditions are very important. The temperature data of the Madoi meteorological station were applied because there is no weather station at the monitored site. Based on the theory that when the altitude increases by 100 m, the temperature decreases by 0.6°C; the boundary layer theory, the air temperature and ground surface boundary of the monitored site were obtained as shown in **Eqs. 12**, **15–18**. The temperature boundary of the monitored site water surface such as **Eq. 13** was obtained based on the air temperature conditions and the measured data of the water surface temperature (Luo et al., 2016). The air temperature of the Madoi meteorological station is presented in the following equation:

$$T_{air} = T_0 + C \cdot t + A \sin(\omega t + \varphi), \tag{12}$$

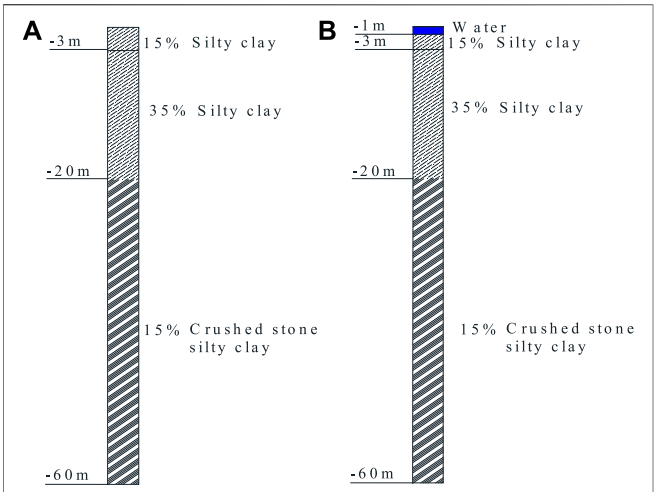

FIGURE 3 | Geometric diagram and soil distribution of calculation models. **(A)** Natural ground. **(B)** Permafrost with accumulated water.

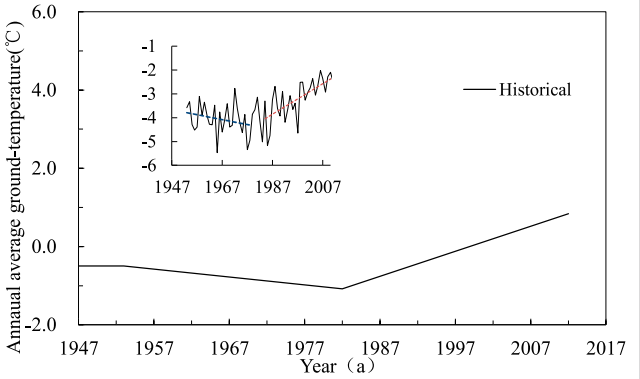

FIGURE 4 | Temperature changes in Madoi from 1947 to 2014.

where T_0 is the initial annual average temperature (°C); c is the average annual temperature change rate (°C/s), a constant, determined by the temperature change trend of the Madoi meteorological station; t is the calculation time corresponding to the temperature change rate segment (s); A is the annual temperature amplitude (°C), according to the temperature record data of the Madoi meteorological station in the past 60 years (**Figure 4**), A = 12; ω is the constant that determines the function period, generally taken as 2π; and φ is the initial phase, which determines the calculation model in this study, and October 1 is used as the initial calculation time of the model calculation, so the initial phase value is π.

Based on the measured water surface temperature and the air temperature, the empirical formula for water surface temperature as a function of air temperature is fitted, as follows:

$$T_{\text{watersurface}} = 0.56T_{\text{air}} - 0.39, R^2 = 0.95, \tag{13}$$

where $T_{\text{water surface}}$ is the water surface temperature (°C) and T_{air} is the air temperature.

Taking π as the initial phase of temperature field calculations, from the previous periodic function of air temperature in **Eq. 12**, it can be seen that the calculation boundary starts from October 1 every year, so the initial water temperature was set as 4°C as per the measured average water temperature in October. The lower boundary always takes the constant heat flux of 0.0474 J/(m^2·s) at the depth of −60 m (Cao, 2015), and the rest of the boundary is adiabatic.

Model Verification

The calculation accuracy of the natural ground model can be verified by measured data of the permafrost table, the permafrost thickness, and the ground temperature at a depth of −15 m, and, the calculation accuracy of the accumulated water model can be determined by measured data of the water and ground temperature changes and the thawing depth of permafrost under the water. As such, model verification is primarily divided into two parts. The acceptable calculation error of numerical simulation is 2–3°C (Banimahd and Zand-Parsa, 2013). Moreover, the Nash coefficient was also used to evaluate the model as follows:

$$E = 1 - \frac{\sum_{t=1}^{T}\left(Q_0^t - Q_m^t\right)^2}{\sum_{t=1}^{T}\left(Q_0^t - \overline{Q_0}\right)^2}, \tag{14}$$

where E is the Nash coefficient. When the value of E is closer to 1, the model reliability is higher. T is the calculation time (s); Q_0^t is observed result at time of t; Q_m^t is simulated result at the time of t; and $\overline{Q_0}$ is an overall average of observed results.

1) Natural ground model

Combined with local temperature and permafrost conditions, the initial steady state was inferred as follows:

TABLE 1 | Thermal parameters of water and soil (Xu, 2001; Cao, 2015).

Classification	ρ_d kg/m^3	L J/kg	λ_f W/(m·°C)	C_f J/(kg·°C)	λ_u W/(m·°C)	C_u J/(kg·°C)
Water	$917_{ice}/\rho(T)_{liq}$	336,000	2.2	2,117	0.57	4,182
15% Silty clay	1840	44,000	1.02	1,276	1.11	1,589
35% Silty clay	1890	158,000	1.93	1,694	1.18	2,300
Crushed stone	1,600	44,000	1.45	1,129	1.28	1,464

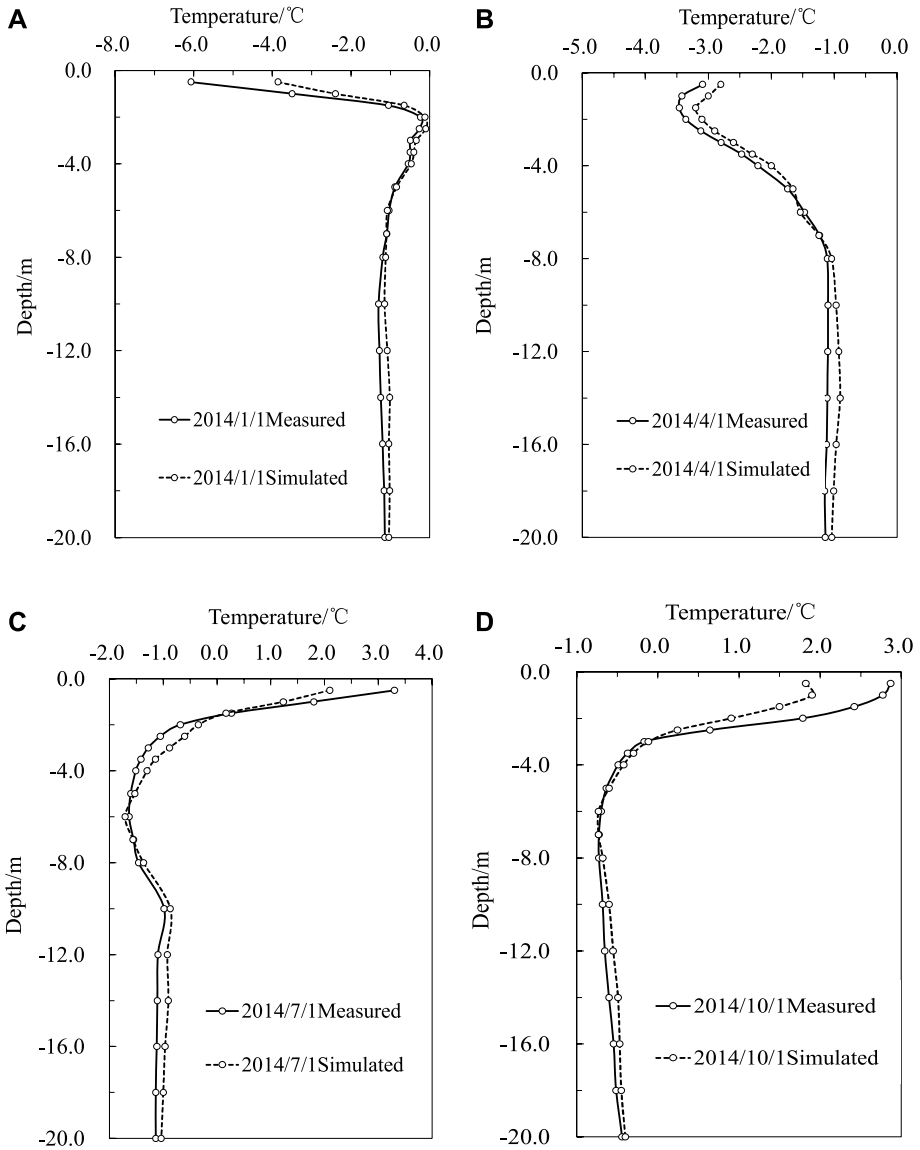

FIGURE 5 | Comparisons of ground temperature between the monitored and the simulated. **(A)** January. **(B)** April. **(C)** July. **(D)** October.

$$T_{ground} = -2.2. \tag{15}$$

Instant state 300a is calculated to obtain the initial temperature field, and a is the abbreviation of annual, so 300a means 300 years.

$$T_{ground} = -2.2 + 12\sin\left(\frac{2\pi t}{31104000} + \pi\right). \tag{16}$$

According to the air temperature trend of Madoi, the calculation should be divided into three parts. Instant state 33a from 1914 to 1946 is shown as **Eq. 17**. Because recording of temperature data of the Madoi weather station began in 1947, the calculation period did not consider the change of annual average temperature.

$$T_{ground} = -2.2 + 12\sin\left(\frac{2\pi t}{31104000} + \pi\right). \tag{17}$$

Instant state 35a from 1947 to 1981 is as follows:

$$T_{ground} = -2.2 + 12\sin\left(\frac{2\pi t}{31104000} + \pi\right), \\ -0.016\left(\frac{t}{31104000} - 300\right). \tag{18}$$

Instant state 33a from 1982 to 2014 is as follows:

$$T_{ground} = -2.78 + 12\sin\left(\frac{2\pi t}{31104000} + \pi\right), \\ +0.065\left(\frac{t}{31104000} - 335\right). \tag{19}$$

The comparison of simulated and measured ground temperature is shown in **Figure 5**, which indicates that the simulated results are consistent with the measured data. For example, the figure shows that the calculated permafrost table on October 1, 2014, is about −2.6 m, which is similar to the permafrost table measure of −2.7 m at the monitored site. The permafrost thickness simulated at this time is almost the same as the actual permafrost thickness, both are about 17 m. The simulation and the measured permafrost temperatures demonstrate the same change trend along with the depth, and the annual average ground temperature of −15 m is −1.27°C and −1.30°C, respectively, and the Nash coefficient of permafrost temperature at the depth of −15 m is 0.71. Therefore, it can be safely inferred that the numerical simulation is in good agreement with the measured data, and it is optimally reflective of the law of the ground temperature change of permafrost at the monitored site, thereby indicating the robust feasibility of this simulation method.

2) Accumulated water model

The permafrost model was used before the accumulation of water, and the calculated frozen ground temperature was used as the initial temperature field of the permafrost part in the interaction model of accumulated water and the permafrost. Because the calculation start time was set as October 1, according to the actual measured water temperature in October, the initial water temperature in the calculation of the accumulation water was set to 4°C. For the calculation models, the ground and water surface boundary conditions were altered and suitably modified with time, as follows:

Initial Steady State

$$T_{ground} = -2.2. \tag{20}$$

Instant state 300a is calculated to obtain the initial temperature field before the existence of accumulated water as follows:

$$T_{ground} = -2.2 + 12\sin\left(\frac{2\pi t}{31104000} + \pi\right). \tag{21}$$

Calculation of water temperature should be divided into three parts when accumulated water exists. Instant state 33a from 1914 to 1946 is presented in **Eq. 22**. Because recording of temperature data of the Madoi weather station began in 1947, the calculation period did not consider the change of annual average temperature.

$$\begin{aligned} T_{\text{water}} &= 0.56T_{\text{air}} - 0.39, \\ &= -3.02 + 6.72\sin\left(\frac{2\pi t}{31104000} + \pi\right). \end{aligned} \tag{22}$$

Instant state 35a from 1947 to 1981 is presented in **Eq. 23**. The temperature data from the Madoi meteorological station show that the annual temperature experienced a small drop during the said period, and the temperature drop rate was −0.016°C/a, so the annual average temperature change is considered.

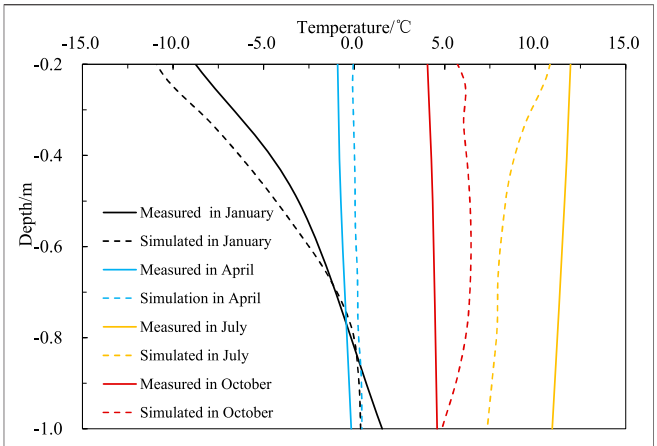

FIGURE 6 | Contrast of water temperature law (1, 4, 7, and 10) in 2014.

$$\begin{aligned} T_{\text{water}} &= 0.56T_{\text{air}} - 0.39, \\ &= -3.02 + 6.72\sin\left(\frac{2\pi t}{31104000} + \pi\right) - 0.009\left(\frac{t}{30114000} - 335\right). \end{aligned} \tag{23}$$

Instant 33a from 1982 to 2014 is presented in **Eq. 24**. The temperature rise rate during this period was 0.065°C/a.

$$\begin{aligned} T_{\text{water}} &= 0.56T_{\text{air}} - 0.39 \\ &= -3.19 + 6.72\sin\left(\frac{2\pi t}{31104000} + \pi\right) \\ &\quad + 0.035\left(\frac{t}{30114000} - 368\right). \end{aligned} \tag{24}$$

Figure 6 shows the comparison of average water temperature between the measured water and the simulated one in 2014. The simulated water temperature was found to be consistent with the measured water temperature variation, and as such, the model reflects the actual variation of water temperature. Moreover, the difference between the simulated and actual values at each measured depth was less than 2°C. This calculation is based on the acceptable calculation error of the numerical simulation proposed by Banimahd and Zand-Parsa (2013), which is 2–3°C, and the Nash coefficient of water temperature at the depth of −1 m is 0.79. Therefore, it is considered that this calculation method can constitute a reliable computation to consider the accumulated water temperature change in the permafrost region.

Figure 7 shows the variation of permafrost temperature under the accumulated water in 5 years (1914, 1934, 1964, 2004, and 2014). It shows that the thawing depth of the permafrost gradually increases under the accumulated water along with the ground temperature rising. The average declining rate of the thawing depth was about 0.16 m/a before 1934, about 0.08 m/a from 1934 to 1964, and about 0.04 m/a from 1934 to 2014. The decrease of the maximum thawing depth of the lower permafrost gradually weakened, which can be essentially attributed to the increase in soil

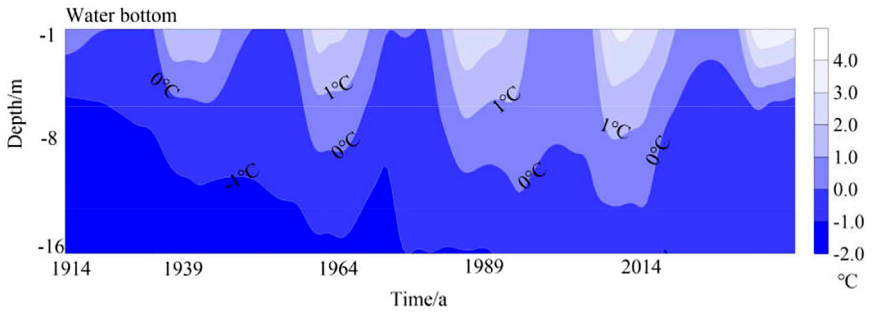

FIGURE 7 | Variations of ground temperature under the accumulated water in years 1914, 1939, 1964, 1989, and 2014 during the calculation time.

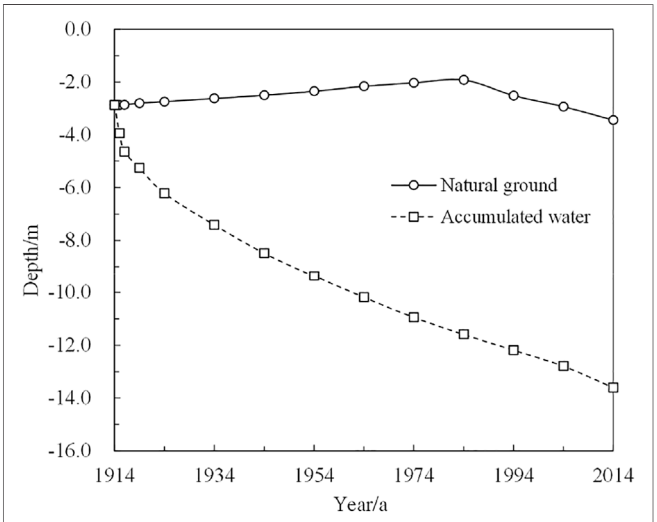

FIGURE 8 | Comparison of the thaw depth for the natural ground and the permafrost underlying accumulated water body during the calculation time.

temperature. The temperature difference between the water bottom temperature and the lower soil temperature gradually decreased with time, and the amount of heat exchange between water and permafrost decreased, correspondingly weakening the thermal influence of water. **Figure 7** also shows that the thermal transmission from the accumulated water caused a melting interlayer in the permafrost. The permafrost development is in conformance with the actual degradation phenomenon.

The ground temperatures under the accumulated water increased by about 0.8°C at −15 m in the past 100a. Compared with the natural ground temperature of 2014 in **Figure 5**, the low-temperature permafrost under the accumulated water degenerated into extremely high-temperature permafrost. Considering that the thawing interlayer formed after 90 years of water accumulation, as shown in **Figure 7**, it is consistent with the development rule of the thermokarst lake (Luo et al., 2015). Moreover, the permafrost table and the variation of ground temperature under accumulated water also meet the thermal erosion characteristics of thermokarst lake (Peng et al., 2020). Therefore, this heat calculation model can be safely used in research and analysis of the thermal influence of accumulated water, and even thermokarst lakes, on permafrost.

Figure 8 shows the variation of the maximum thawing depth of the permafrost under the natural ground and the accumulated water in a calculation time of 100 years. It can be seen from this figure that the permafrost table under the accumulated water is decreasing year by year. The change rate of the permafrost table over time was initially rapid; however, it subsequently slowed down, varying from −3 to −14 m. Therefore, the findings indicate that the accumulated water can cause permafrost degradation.

The comparison of the measured and simulated values of the permafrost temperature under the thermokarst lake in 2014 is shown in **Figure 9**. The Nash coefficient of permafrost temperature at the depth of −15 m was 0.68. Moreover, notably, the numerical simulation is in good agreement with the measured data and well reflects the change law and development trend of the permafrost temperature under water in the monitoring site. In addition, there was a melted interlayer with a thickness of about 13 m under the water. Under the simulation and measurement, the average annual ground temperatures were at −15 m are −0.18 and −0.20°C, respectively. The temperature at the interface between thermokarst lake water and permafrost showed seasonal changes. The temperature change trend is studied to be similar to the air temperature change at the site, and it was the highest in July and the lowest in April, in the study period. However, the amplitude at this interface was smaller than that of the air. It is because the specific heat of water is higher. Moreover, the average value of annual temperature at this interface is larger than that of air because water can accumulate heat in it. Therefore, the thermal calculation of the model between water and permafrost in permafrost regions is feasible and reliable.

CONCLUSION

The equivalent heat conduction model calculation method offers a robust inference regarding the characteristics of water temperature change within a year. Also, the heat transfer effect formed by the buoyant flow caused by the

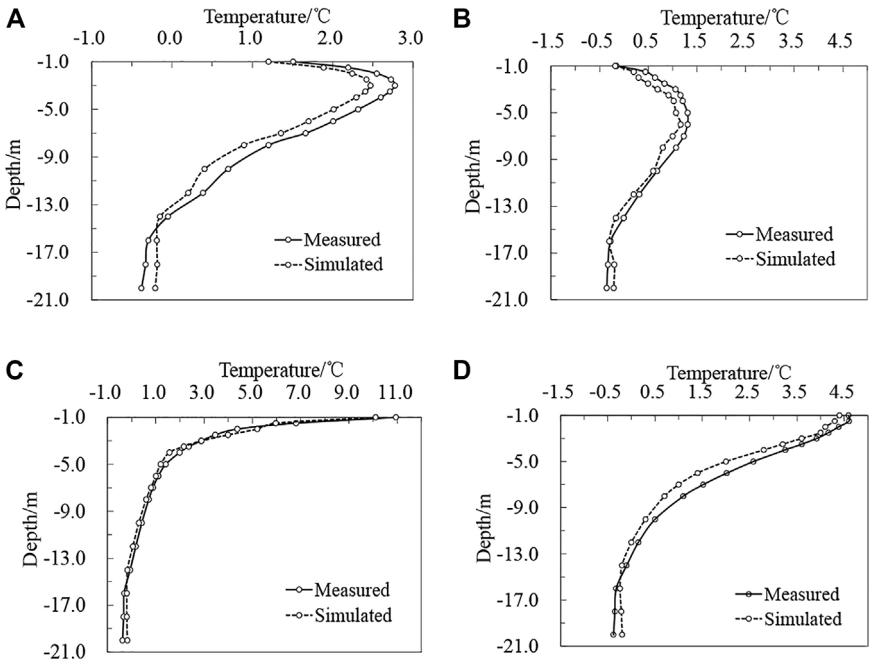

FIGURE 9 | Comparison of the measured and simulated values of the permafrost temperature under the thermokarst lake water in January, April, July, and October, 2014. **(A)** January. **(B)** April. **(C)** July. **(D)** October.

density difference is directly expressed by the change of water thermal conductivity. In addition, the number of calculation equations is reduced, which improves the convergence speed of the calculation. Therefore, the equivalent heat conduction model is sufficient to meet the calculation need, wherein the calculation speed is faster, and is deemed more suitable for the accumulation of water on permafrost.

The thermal erosion of permafrost from accumulated water increases the ground temperature and reduces the thickness of permafrost. The change of temperature at the interface between water and soil is consistent with the air temperature, but the amplitude is smaller. The accumulated water can cause permafrost degradation, even forming a melting interlayer.

The degree of the thermal impact of accumulated water on the underlying permafrost demonstrates an association with the changes in the external climate. The thermal impact in the early stage of water accumulation is found to be greater. As the permafrost table decreases, and the temperature difference between water and permafrost underlying decreases, consequently, the thermal influence of accumulated water on the lower permafrost gradually weakens.

DATA AVAILABILITY STATEMENT

The original contributions presented in the study are included in the article/**Supplementary Material**; further inquiries can be directed to the corresponding author.

AUTHOR CONTRIBUTIONS

EP: writing–original draft preparation and methodology. XH: writing—reviewing and visualization. YS: conceptualization and supervision. FZ: writing—reviewing and editing. JW: writing—reviewing and editing. WC: methodology.

FUNDING

This work was funded by the National Natural Science Foundation of China (41901079, 41971093), Province Natural Science Foundation of Gansu Youth Fund (20JR5RA435), CAS Youth talent growth Fund (Y9510608), Hongliu Excellent Youth Project of Lanzhou University of Technology (062006) and Gansu University innovation Fund Project (2020A-026). The observations in field were supported by Beiluhe Observation and Research Station on Frozen Soil Engineering and Environment in Qinghai-Tibet Plateau, Northwest Institute of Eco-Environment and Resources, Chinese Academy of Sciences.

SUPPLEMENTARY MATERIAL

The Supplementary Material for this article can be found online at: https://www.frontiersin.org/articles/10.3389/feart.2021.733483/full#supplementary-material

REFERENCES

Banimahd, S. A., and Zand-Parsa, S. (2013). Simulation of Evaporation, Coupled Liquid Water, Water Vapor and Heat Transport through the Soil Medium. *Agric. Water Manage.* 130, 168–177. doi:10.1016/j.agwat.2013.08.022

Baranskaya, A., Novikova, A., Shabanova, N., Belova, N., Maznev, S., Ogorodov, S., et al. (2021). The Role of Thermal Denudation in Erosion of Ice-Rich Permafrost Coasts in an Enclosed Bay (Gulf of Kruzenstern, Western Yamal, Russia). *Front. Earth Sci.* 8, 566227. doi:10.3389/feart.2020.566227

Burn, C. R. (2002). Tundra Lakes and Permafrost, Richards Island, Western Arctic Coast, Canada. *Can. J. Earth Sci.* 39 (8), 1281–1298. doi:10.1139/e02-035

Calmels, F., Delisle, G., and Allard, M. (2008). Internal Structure and the thermal and Hydrological Regime of a Typical Lithalsa: Significance for Permafrost Growth and Decay. *Can. J. Earth Sci.* 45 (1), 31–43. doi:10.1139/e07-068

Cao, Y.-B. (2015). *Evolution and Engineering Geology Evaluation of Permafrost along Gonghe-Yushu Highway*. Beijing: University of Chinese Academy of Sciences Press.

Fang, X., Ellis, C. R., and Stefan, H. G. (1996). Simulation and Observation of Ice Formation (Freeze-over) in a lake. *Cold Regions Sci. Technol.* 24 (2), 129–145. doi:10.1016/0165-232x(95)00022-4

Fang, X., and Stefan, H. G. (1996). Long-term lake Water Temperature and Ice Cover Simulations/measurements. *Cold Regions Sci. Technol.* 24 (3), 289–304. doi:10.1016/0165-232x(95)00019-8

Gao, Z., Niu, F., Wang, Y., Luo, J., and Lin, Z. (2017). Impact of a Thermokarst lake on the Soil Hydrological Properties in Permafrost Regions of the Qinghai-Tibet Plateau, China. *Sci. Total Environ.* 574, 751–759. doi:10.1016/j.scitotenv.2016.09.108

Hinkel, K. M., Frohn, R. C., Nelson, F. E., Eisner, W. R., and Beck, R. A. (2010). Morphometric and Spatial Analysis of Thaw Lakes and Drained Thaw lake Basins in the Western Arctic Coastal Plain, Alaska. *Permafrost. Periglac.* 16 (4), 327–341. doi:10.1002/ppp.532

Hinkel, K. M., Jones, B. M., Eisner, W. R., Cuomo, C. J., Beck, R. A., and Frohn, R. (2007). Methods to Assess Natural and Anthropogenic Thaw Lake Drainage on the Western Arctic Coastal Plain of Northern Alaska. *J. Geophys. Res.* 112 (F2), 1–9. doi:10.1029/2006jf000584

Hondzo, M., and Stefan, H. G. (2015). Lake Water Temperature Simulation Model. *J. Hydraul. Eng.* 119 (11), 1251–1273. doi:10.1061/(ASCE)0733-9429(1993)119:11(1251)

Huang, W., Han, H., Shi, L., Niu, F., Deng, Y., and Li, Z. (2013). Effective thermal Conductivity of Thermokarst lake Ice in Beiluhe Basin, Qinghai-Tibet Plateau. *Cold Regions Sci. Technol.* 85 (JAN.), 34–41. doi:10.1016/j.coldregions.2012.08.001

Jin, H., Li, S., Cheng, G., Shaoling, W., and Li, X. (2000). Permafrost and Climatic Change in China. *Glob. Planet. Change* 26 (4), 387–404. doi:10.1016/s0921-8181(00)00051-5

Jorgenson, M. T., Kanevskiy, M., Shur, Y., Osterkamp, T., Fortier, D., Cater, T., and Miller, P. (2012). "Thermokarst lake and Shore Fen Development in Boreal Alaska", in Proceedings of the Tenth International Conference on Permafrost, Salekhard, Russia: The Northern Publisher.

Jorgenson, M. T., and Shur, Y. (2007). Evolution of Ponds and Basins in Northern Alaska and Discussion of the Thaw Pond Cycle. *J. Geophys. Res.* 9 (6), 441–446. doi:10.1029/2006jf000531

Karlsson, J. M., Lyon, S. W., and Destouni, G. (2012). Thermokarst lake, Hydrological Flow and Water Balance Indicators of Permafrost Change in Western Siberia. *J. Hydrol.* 464-465 (none), 459–466. doi:10.1016/j.jhydrol.2012.07.037

Kokelj, S. V., and Jorgenson, M. T. (2013). Advances in Thermokarst Research. *Permafrost Periglac. Process.* 24, 108–119. doi:10.1002/ppp.1779

Kokelj, S. V., Lantz, T. C., Kanigan, J., Smith, S. L., and Courts, R. (2010). Origin and Polycyclic Behaviour of Tundra Thaw Slumps, Mackenzie Delta Region, Northwest Territories, Canada. *Permafrost. Periglac. Process.* 20 (2), 173–184. doi:10.1002/ppp.642

Langer, M., Westermann, S., Boike, J., Kirillin, G., Grosse, G., Peng, S., et al. (2016). Rapid Degradation of Permafrost underneath Waterbodies in Tundra Landscapes-Toward a Representation of Thermokarst in Land Surface Models. *J. Geophys. Res. Earth Surf.* 121 (12), 2446–2470. doi:10.1002/2016jf003956

Lin, Z.-J., Niu, F.-J., Ge, J.-J., Wang, P., and Dong, Y.-H. (2010). Variation Characteristics of the Thawing Lake in Permafrost Regions of the Tibetan Plateau and Their Influence on the Thermal State of Permafrost. *J. Glaciol.* 32 (2), 341–350. doi:10.3724/SP.J.1231.2010.06586

Lin, Z.-J., Niu, F.-J., Xu, Z.-Y., Xu, J., and Wang, P. (2011). Thermal Regime of a Thermokarst Lake and its Influence on Permafrost, Beiluhe Basin, Qinghai-Tibet Plateau. *Permafrost. Periglac.* 21 (4), 315–324. doi:10.1002/ppp.692

Lin, Z. J., Niu, F. J., Fang, J. H., Luo, J., and Yin, G. A. (2017). Interannual Variations in the Hydrothermal Regime Around a Thermokarst lake in Beiluhe, Qinghai-Tibet Plateau. *Geomorphology* 276 (JAN.1), 16–26. doi:10.1016/j.geomorph.2016.09.035

Ling, F., Wu, Q., Zhang, T., and Niu, F. (2012). Modelling Open-Talik Formation and Permafrost Lateral Thaw under a Thermokarst Lake, Beiluhe Basin, Qinghai-Tibet Plateau. *Permafrost Periglac. Process.* 23 (4), 312–321. doi:10.1002/ppp.1754

Luo, D.-L., Jin, H.-J., Lu, L.-Z., and Zhou, J. (2016). Spatiotemporal Changes in Extreme Ground Surface Temperatures and the Relationship with Air Temperatures in the Three-River Source Regions during 1980–2013. *Theor. Appl. Climatol.* 123 (3-4), 885–897. doi:10.1007/s00704-015-1543-6

Luo, J., Niu, F., Lin, Z., Liu, M., and Yin, G. (2015). Thermokarst lake Changes between 1969 and 2010 in the Beilu River Basin, Qinghai-Tibet Plateau, China. *Sci. Bull.* 60 (5), 556–564. doi:10.1007/s11434-015-0730-2

Niu, F.-J., Lin, Z.-J., Liu, H., and Lu, J.-H. (2011). Characteristics of Thermokarst Lakes and Their Influence on Permafrost in Qinghai–Tibet Plateau. *Geomorphology* 132 (3), 222–233. doi:10.1016/j.geomorph.2011.05.011

Niu, F.-J., Luo, J., Lin, Z.-J., Liu, M.-H., and Yin, G.-A. (2014). Morphological Characteristics of Thermokarst Lakes along the Qinghai-Tibet Engineering Corridor. *Arct. Antarct. Alp. Res.* 46 (4)–303. doi:10.1657/1938-4246-46.4.963)

Niu, F.-J., Wang, W., Lin, Z.-J., and Luo, J. (2018). Study on Environmental and Hydrological Effects of Thermokarst Lakes in Permafrost Regions of the Qinghai-Tibet Plateau. *Adv. Earth. Sci.* 33 (4), 335–342. doi:10.11867/j.issn.1001-8166.2018.04.0335

Pan, X., You, Y., Roth, K., Guo, L., Wang, X., and Yu, Q. (2014). Mapping Permafrost Features that Influence the Hydrological Processes of a Thermokarst Lake on the Qinghai-Tibet Plateau, China. *Permafrost Periglac. Process.* 25 (1), 60–68. doi:10.1002/ppp.1797

Peng, E.-X., Sheng, Y., Hu, X.-Y., Wu, J.-C., and Cao, W. (2020). Thermal Effect of Thermokarst lake on the Permafrost under Embankment. *Adv. Clim. Chang. Res.* 12 (1), 76–82. doi:10.1016/j.accre.2020.10.002

Romanovsky, V. E., and Osterkamp, T. E. (2000). Effects of Unfrozen Water on Heat and Mass Transport Processes in the Active Layer and Permafrost. *Permafrost Periglac. Process.* 11 (3), 219–239. doi:10.1002/1099-1530(200007/09)11:3<219::aid-ppp352>3.0.co;2-7

Samuelsson, P., Kourzeneva, E., and Mironov, D. (2010). The Impact of Lakes on the European Climate as Stimulated by a Regional Climate Model. *Boreal. Environ. Res.* 15 (2), 113–129. doi:10.1016/j.apcata.2010.02.027

Shen, H. T. (2010). Mathematical Modeling of River Ice Processes. *Cold Regions Sci. Technol.* 62 (1), 3–13. doi:10.1016/j.coldregions.2010.02.007

Stepanenko, V. M. (2005). Numerical Modeling of Heat and Moisture Transfer Processes in a System lake – Soil. *Russ. Meteorol. Hydro.* 3, 95–104.

Subin, Z. M., Riley, W. J., and Mironov, D. (2012). An Improved lake Model for Climate Simulations: Model Structure, Evaluation, and Sensitivity Analyses in CESM1. *J. Adv. Model. Earth. Sy.* 4 (1). doi:10.1029/2011ms000072

Sun, Z.-Z., Ma, W., Zhang, S.-J., Mu, Y.-H., Yun, H.-B., and Wang, H.-L. (2018). Characteristics of Thawed Interlayer and its Effect on Embankment Settlement along the Qinghai-Tibet Railway in Permafrost Regions. *J. Mt. Sci-engl.* 15 (005), 1090–1100. doi:10.1007/s11629-017-4643-1

Wang, H., Liu, H., and Ni, W. (2017). Factors Influencing Thermokarst lake Development in Beiluhe basin, the Qinghai-Tibet Plateau. *Environ. Earth. Sci.* 76 (24), 816. doi:10.1007/s12665-017-7143-2

Wang, Y.-B., Gao, Z.-Y., Wen, J., Liu, G.-H., Geng, D., and Li, X.-B. (2014). Effect of a Thermokarst lake on Soil Physical Properties and Infiltration Processes in the Permafrost Region of the Qinghai-Tibet Plateau. *China. Sci. China.* 57 (010), 2357–2365. doi:10.1007/s11430-014-4906-4

Wen, Z., Yang, Z., Yu, Q., Wang, D., Ma, W., Niu, F., et al. (2016). Modeling Thermokarst lake Expansion on the Qinghai-Tibetan Plateau and its thermal

Effects by the Moving Mesh Method. *Cold Regions Sci. Technol.* 121, 84–92. doi:10.1016/j.coldregions.2015.10.012

Xu, X.-M., and Wu, Q.-B. (2019). Impact of Climate Change on Allowable Bearing Capacity on the Qinghai-Tibetan Plateau. *Adv. Clim. Change Res.* 10 (2), 99–108. doi:10.1016/j.accre.2019.06.003

Xu, X.-Z., Wang, J.-C., and Zhang, L.-X. (2001). *Physics of Frozen Soil*. Beijing: Science Publish House.

You, Y., Yu, Q., Pan, X., Wang, X., Guo, L., and Wu, Q. (2017). Thermal Effects of Lateral Supra-permafrost Water Flow Around a Thermokarst lake on the Qinghai-Tibet Plateau. *Hydrol. Process.* 31 (13), 2429–2437. doi:10.1002/hyp.11193

Zhang, M., Min, K.-H., Wu, Q., Zhang, J., and Harbor, J. (2012). A New Method to Determine the Upper Boundary Condition for a Permafrost Thermal Model: An Example from the Qinghai-Tibet Plateau. *Permafrost Periglac. Process.* 23 (4), 301–311. doi:10.1002/ppp.1755

Zhang, M., Wang, J., and Lai, Y. (2019). Hydro-thermal Boundary Conditions at Different Underlying Surfaces in a Permafrost Region of the Qinghai-Tibet Plateau. *Sci. Total Environ.* 670 (JUN.20), 1190–1203. doi:10.1016/j.scitotenv.2019.03.090

Conflict of Interest: The authors declare that the research was conducted in the absence of any commercial or financial relationships that could be construed as a potential conflict of interest.

frontiers in Earth Science

REVIEW
published: 01 December 2021
doi: 10.3389/feart.2021.721009

Integrated Hydrologic Modelling of Groundwater-Surface Water Interactions in Cold Regions

Xiaofan Yang[1], Jinhua Hu[1], Rui Ma[2] and Ziyong Sun[2]*

[1]State Key Laboratory of Earth Surface Processes and Resource Ecology, Faculty of Geographical Science, Beijing Normal University, Beijing, China, [2]School of Environmental Studies and State Key Laboratory of Biogeology and Environmental Geology, China University of Geoscience, Wuhan, China

Groundwater-surface water (GW-SW) interaction, as a key component in the cold region hydrologic cycle, is extremely sensitive to seasonal and climate change. Specifically, the dynamic change of snow cover and frozen soil bring additional challenges in observing and simulating hydrologic processes under GW-SW interactions in cold regions. Integrated hydrologic models are promising tools to simulate such complex processes and study the system behaviours as well as its responses to perturbations. The cold region integrated hydrologic models should be physically representative and fully considering the thermal-hydrologic processes under snow cover variations, freeze-thaw cycles in frozen soils and GW-SW interactions. Benchmarking and integration with scarce field observations are also critical in developing cold region integrated hydrologic models. This review summarizes the current status of hydrologic models suitable for cold environment, including distributed hydrologic models, cryo-hydrogeologic models, and fully-coupled cold region GW-SW models, with a specific focus on their concepts, numerical methods, benchmarking, and applications across scales. The current research can provide implications for cold region hydrologic model development and advance our understanding of altered environments in cold regions disturbed by climate change, such as permafrost degradation, early snow melt and water shortage.

Keywords: groundwater-surface water interaction, cold region hydrology, integrated hydrologic modelling, snow cover, frozen soil, flow and heat transfer

OPEN ACCESS

Edited by:
Dongliang Luo,
Northwest Institute of Eco-Environment and Resources (CAS), China

Reviewed by:
Yingying Yao,
Xi'an Jiaotong University, China
Hongkai Gao,
East China Normal University, China

****Correspondence:***
Xiaofan Yang
xfyang@bnu.edu.cn

Specialty section:
This article was submitted to Cryospheric Sciences, a section of the journal Frontiers in Earth Science

Received: *05 June 2021*
Accepted: *29 October 2021*
Published: *01 December 2021*

Citation:
Yang X, Hu J, Ma R and Sun Z (2021) Integrated Hydrologic Modelling of Groundwater-Surface Water Interactions in Cold Regions. Front. Earth Sci. 9:721009. doi: 10.3389/feart.2021.721009

INTRODUCTION

Cold regions are headwaters of many prominent rivers around the world and considered as the water towers of inland river basins in arid/semi-arid regions (Yao et al., 2012; Qin et al., 2017; Immerzeel et al., 2020). As unique and critical elements of the terrestrial cryosphere, frozen soil and snow cover not only have significant influences on the hydrologic processes in cold regions (Ding et al., 2020; Wang et al., 2020; Gao et al., 2021a; McKenzie et al., 2021), but they are also extremely sensitive to seasonal (short-term, from day to month) and climate changes (long-term, from year to decade) (Kang et al., 2020; IPCC, 2019 SROCC). The pronounced global warming has led to permafrost degradation due to increased ground temperature, permafrost thawing, thickening of the active layer, shortening of the freezing period, and prolonged snowmelting period, which directly affect groundwater recharge, runoff, and promote

groundwater-surface water (GW-SW) interactions (Nitze et al., 2018; Cheng et al., 2019; Teufel and Sushama, 2019; Zhao et al., 2019; Evans et al., 2020; Lemieux et al., 2020). Meanwhile, the snow-induced changes, such as shortened snow duration, reduction of the snow cover area, earlier snowmelt, and more frequent extreme snowfall events, have significantly altered the surface albedo and runoff, and indirectly affect the groundwater hydrothermal conditions, the GW-SW interactions, and the energy exchange by changing the surface temperature and soil water infiltration (Barnett et al., 2005; Barnhart et al., 2016; Wu et al., 2018; Che et al., 2019). Therefore, GW-SW interaction is one of the key components in the cold region hydrologic cycle (Ge et al., 2011; Liljedahl et al., 2016). Comprehensive research on GW-SW interactions in cold regions under seasonal and climate changes, their driving factors, and the associated mechanisms is essential to understanding the source and mechanisms of runoff and the response of the hydrologic processes in cold regions. Those insights would provide fundamental evidence for the scientific management of inland basin water resources and promote inter-disciplinary research (i.e., cryosphere science, atmospheric science, hydrology, hydrogeology, etc.).

Seasonal and climate changes significantly affect the hydrologic and energy cycles in cold regions. The dynamic flow and heat transfer processes in such a complex system are driven by the interplay between snow cover, soil freeze-thaw cycles (FTC), surface water and groundwater flow, which should be fully considered in an integrated framework (Flerchinger and Saxton, 1989; Winter et al., 1998; Atchley et al., 2016; Hubbard et al., 2018). However, due to the harsh environment, the measuring range, frequency, and precision of hydrometeorological and geophysical field observations are quite limited (Schilling et al., 2019a; Che et al., 2019). Yet it is difficult to predict the hydrologic processes through field/site control experiments (i.e., soil warming experiments and snow cover control experiments, Melillo et al., 2002; Fu et al., 2018) and indoor snowmelt and freeze-thaw experiments (Waldner et al., 2004; Costa and Pomeroy, 2019; Riviere et al., 2019; Deprez et al., 2020) due to constrained spatio-temporal scales (Tokunaga et al., 2019; Chiasson-Poirier et al., 2020). Therefore, under the scenario of seasonal and climate changes, establishing an integrated hydrologic model to quantitatively simulate and predict the coupled processes of flow and heat transfer, their influencing factors and mechanisms, and most importantly, investigating the dynamics of GW-SW interactions under freeze-thaw cycles and snow cover variations in cold regions are emerging and Frontier topics of cryosphere, hydrology, and hydrogeology research. This paper provides an advanced review on the current research status of integrated hydrologic models of cold regions with future perspectives. The rest of the paper is organized as follows. The research progress in numerical models, benchmarking, and simulations are summarized in *Research Progress in Integrated Hydrologic Modeling of Groundwater-Surface Water Interactions in Cold Regions*, followed by future research and perspectives on model development and potential applications in *Challenges and Future Research Needs*. A brief summary is given in *Summary*.

RESEARCH PROGRESS IN INTEGRATED HYDROLOGIC MODELING OF GROUNDWATER-SURFACE WATER INTERACTIONS IN COLD REGIONS

Surface water (SW) and groundwater (GW), which are essential elements in the global and regional hydrologic cycles, are strongly coupled and dynamically interactive. However, surface water and groundwater are often considered to be separate entities and are investigated individually because the physical, chemical, and biological properties of surface water and groundwater are largely varied (Yang et al., 2012). Under seasonal and climate changes, snow cover and frozen soil poses additional challenges in studying GW-SW interactions in cold regions, and thus, the fundamental processes become more unique, complex, and uncertain (**Figure 1**, Ireson et al., 2013). The temperature variations caused by seasonal and climate changes influence the snow accumulation and melting processes first. Decreasing temperature in autumn and winter provide feasible conditions for snowfall and promote the accumulation of snow cover. Deep snow cover has a heat conservation effect on the soil while shallow snow cover decreases the soil temperature (Rasouli et al., 2019; Mazzotti et al., 2020). Rising air temperature also leads to enlarged areas of snow melting, increasing the surface water flow velocity and water depth as the snowmelt flows into surface runoff, leading to more surface water infiltration and accelerated interaction with groundwater (Barnhart et al., 2016; Chen et al., 2017). Since the surface temperature and evapotranspiration in spring are low in some mountainous and plateau areas, the snow melt even becomes an important source of groundwater recharge (Carroll et al., 2019; Li et al., 2019). Snow melting, radiation, reflection, and blowing snow also strongly alter the local and regional surface energy balance, thus affecting the thermal conditions of the groundwater (Kinar and Pomeroy, 2015). Furthermore, permafrost can act as a barrier in the soil system, which affects the spatial-temporal heterogeneity of the aquifer, thus regulating the preferential flow path of groundwater and influencing groundwater recharge, runoff, and outflow (Xu et al., 2001; Bense et al., 2009). In addition, hydrometeorological factors, such as precipitation, temperature, and evapotranspiration, evidently have impacts on the hydrothermal conditions and moisture transport in the active layer, leading to periodic thawing (Woo, 2012; McKenzie and Voss, 2013). Soil freeze-thaw processes not only result in the phase change between ice and liquid water in groundwater systems, but they also lead to the frequent transport of groundwater in different layers of aquifers and between subsurface and surface systems, affecting the amount of water involved in the regional hydrologic cycle. Moreover, this also changes the structure of the aquifers, thus affecting the preferential flow path of groundwater and making the GW-

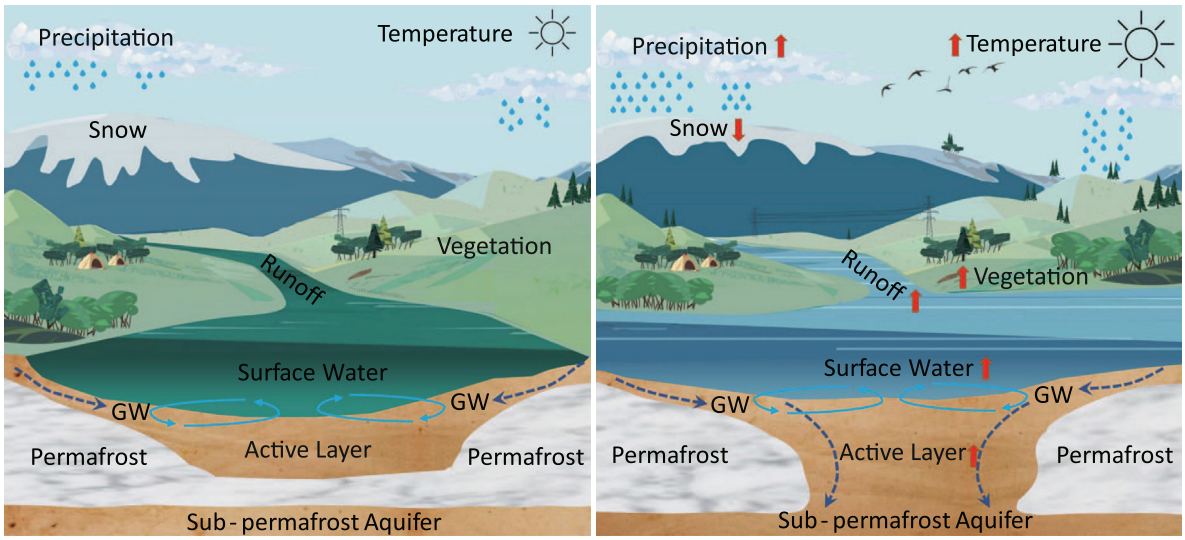

FIGURE 1 | Cold region GW-SW interactions before **(A)** and after **(B)** climate change.

SW interactions more complex in cold regions (Walvoord and Kurylyk, 2016).

With the rapid development of numerical algorithms, computers, and scientific computing techniques, numerical models have become important tools for investigating the hydrologic cycle in cold regions under seasonal and climate changes (Kurylyk et al., 2014a; Ding et al., 2017; Yang et al., 2019). As the connection between the subsurface and surface components of the hydrologic cycle in cold regions, the major problem of modelling GW-SW interactions in cold regions is to accurately describe the coupled thermal-hydrologic (TH) processes in such a complex system consisting of snow cover, surface water, groundwater, and frozen soil under disturbances. Under the influence of temperature, precipitation, and evapotranspiration, the flow and heat transport within the snow cover and the phase change between water and ice are dynamically coupled and complex, the key processes of which include snow accumulation, snowmelt, snow sublimation, blowing snow, and the radiation and reflection from the snow cover (Domine et al., 2019). Surface hydrothermal conditions also affect the flow and heat transport processes in frozen soils, including multiphase flow, heat conduction and convection, water vapour diffusion, and phase changes between ice, liquid water, and vapour. It is noted that different phases and moisture distributions in the soil pores are strongly correlated with temperature during the FTCs, which has a significant impact on the soil physical properties, such as the porosity and permeability. As a result, the constitutive equations describing the coupled TH processes are highly nonlinear in groundwater-permafrost systems (Kurylyk and Watanabe, 2013). Despite these difficulties, the dynamic interactions between the surface and groundwater make it more difficult for hydrologic modeling and simulations (Maxwell et al., 2015). Therefore, it is extremely

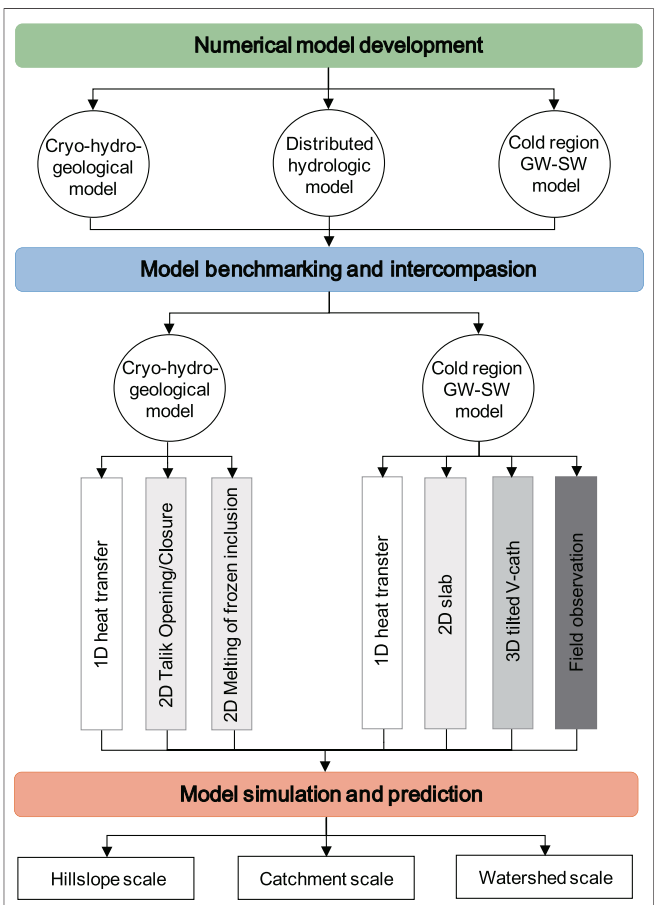

FIGURE 2 | The current research status of modelling GW-SW interactions in cold regions.

TABLE 1 | Summary of cold region integrated hydrologic models.

Category	Model	Developer	Simulated dimension	Reference
Distributed hydrologic models of cold regions	CBHM	Chinese Academy of Sciences (China)	3D	Chen et al. (2018)
	CRHM	University of Saskatchewan (United States)	3D	Marsh et al. (2020)
	GBEHM	Tsinghua University (China)	3D	Li et al. (2019)
	VIC	University of Washington and University of California, Berkeley and Princeton University (United States)	3D	Hamman et al. (2018)
	HydroSiB2-SF	Chinese Academy of Sciences (China)	1D	Wang et al. (2017b)
	WEB-DHM-pF	University of Chinese Academy of Sciences (China)	3D	Song et al. (2020)
Cryo-hydrogeological models	SUTRA (or SUTRA-ICE, modified SUTRA)	U.S. Geological Survey (United States)	2D, 3D	McKenzie et al. (2007); Rushlow et al. (2020)
	Cast3M	Climate Science and Environmental Laboratory (France)	2D	www-cast3m.cea.fr
	FEFLOW	DHI Group	2D, 3D	DHI (2016) Huang et al. (2020) Langford et al. (2020)
	PFLOTRAN-ICE	Los Alamos and Sandia National Laboratories (United States)	3D	Karra et al. (2014) Kumar et al. (2016)
	DarcyTools	Computer-aided Fluid Engineering AB (Sweden)	2D	Svensson et al. (2010); Svensson and Ferry, 2014
	GEOAN	Golder Associates	3D	Holmén (2019)
	MELT	Desert Research Institute (United States)	2D	Frederick and Buffett (2014)
	HEATFLOW/SMOKER	Université Laval and University of Waterloo (Canada)	2D	Molson and Frind (2019)
	FlexPDE	University of East Anglia (UK)	2D	Bense et al. (2009)
	PermaFOAM	Université Paul Sabatier (France)	2D	Orgogozo et al. (2019)
	COMSOL	COMSOL Group	2D	Scheidegger et al. (2017); Scheidegger et al. (2019)
Cold region GW-SW models	GeoTop	University of Zurich (Switzerland)& Eurac Research (Italy)	3D	Endrizzi et al. (2014) Rigon et al. (2006)
	GSFLOW	U.S. Geological Survey (United States)	3D	Markstrom et al. (2008)
	ATS	Los Alamos and Oak Ridge National Laboratories (United States)	3D	Atchley et al. (2015); Painter et al. (2016) Coon et al. (2019)
	HGS	University of Waterloo (Canada)	3D	Aquanty (2017)

challenging to establish an integrated GW-SW model in such a way that all the aforementioned processes are fully considered and precisely described based on fundamental phenomena, including, but not limited to, multi-phase flow in porous media, phase changes, and the coupled thermal-hydrologic processes and interactions between groundwater and surface water (Coon et al., 2016; Painter et al., 2016).

There are a growing number of theoretical and numerical models that are capable of describing the integrated surface and subsurface flow and heat processes in cold regions. These models have been validated through benchmark cases, laboratory experiments, and field observations, and have been applied to predict future trends and responses of the hydrologic system under different seasonal and climate change scenarios (**Figure 2**). Studies of integrated hydrologic models and numerical simulations of cold regions can be divided into three categories: 1) numerical model development, 2) model benchmarking and validation, and 3) model simulation and application.

Numerical Model Development

Most existing hydrologic models are developed for general purposes, including: 1) distributed hydrologic models based on terrestrial hydrology (Yang et al., 2015), 2) groundwater/hydrogeological models based on hydrogeology (Yao et al., 2014; Tian et al., 2018), and 3) physically-based and fully-coupled GW-SW models (Kuffour et al., 2020). In order to fundamentally understand and precisely describe the hydrologic cycle in cold regions, it is natural to modify/improve selected previously developed hydrologic models in order to facilitate the characteristics of the study area and the research needs, leading to three groups of cold region integrated hydrologic models (**Table 1**): 1) distributed hydrologic models of cold regions, 2) cryo-hydrogeological models, and 3) cold region GW-SW models.

The concept of modular-based hydrologic models and distributed hydrologic models based on terrestrial hydrology in cold regions is to establish sub-models/modules for all the sub-processes/subunits in the hydrologic cycle then integrate them into a unified modelling framework. In distributed hydrologic models, such as CBHM (Chen et al., 2018), CRHM (Marsh et al., 2020), GBEHM (Li et al., 2019), VIC (Hamman et al., 2018), HydroSiB2-SF (Wang G. X. et al., 2017), WEB-DHM-pF (Song et al., 2020), different sub-models/modules are "stitched" and tuned before being used to simulate and predict certain processes in selected research areas. For example, the module-based cold regions hydrologic model (CRHM, Marsh et al., 2020), which was developed at the University of Saskatchewan in Canada,

integrates the most complete snow model composed of a series of snow cover-related modules, including radiation, reflection, snow sublimation, snow melting, and blowing snow. Although such module-based distributed hydrologic models integrate all the possible components of the hydrologic cycle in cold regions, they mainly focus on the surface hydrologic process and the water and energy balances, which subsequently simplifies the groundwater by adopting a parameterized scheme or 1D bucket model, ignoring processes such as lateral flow and heat transfer. Moreover, the spatial resolution of these models is usually low (at the kilometer level), so they cannot be used to investigate smaller-scale processes. At present, distributed and module-based hydrologic models of cold regions are mostly used to simulate the effects of seasonal and climate changes on frozen soil, surface hydrologic processes, and vegetation in large-scale watersheds (Zhou et al., 2014; Chen et al., 2018; Gao et al., 2018; Qi et al., 2019).

In theory, the main idea of the cryo-hydrogeological model, which considers the groundwater, hydrogeology, and permafrost, is to establish the constitutive equations of multiphase groundwater flow and heat transfer (based on the theories of flow and heat transfer in porous media), which characterizes the effects of the FTCs on the pore water, soil porosity, and permeability using the soil freeze-thaw curve or a physical process-based constitutive relationship (such as the Clausius-Clapyeron equation). Furthermore, they simulate the soil moisture and temperature, groundwater runoff, and its recharge from surface runoff in the basin (Kurylyk and Watanabe, 2013). If considering surface hydrologic processes in cold regions, such models mostly use temperature, precipitation, evapotranspiration, and snowmelt as the boundary conditions and forcing data, or one-way coupling (weak coupling) with surface hydrologic process models (such as simultaneous heat and water, SHAW models) (Voss et al., 2018). In particular, the cryo-hydrogeological models use snow accumulation and ablation (key elements in snow hydrology) as the upper boundary of the simulation domain by altering the surface temperature, while ignoring the physical processes of moisture and energy transport during snowmelt and its impact on the runoff and GW-SW interactions. Therefore, hydrogeological models in cold regions are mostly used to study the hydrogeological response of frozen soil or the effects of seasonal and annual changes on surface processes (i.e., soil moisture, temperature, and dynamic changes in the groundwater) (Evans et al., 2018; Jafarov et al., 2018). The models that have been reported for hydrogeological research in cold regions include but not limited to SUTRA (or modified SUTRA, SUTRA-ICE, McKenzie et al., 2007; McKenzie and Voss, 2013), Cast3M (www-cast3m.cea.fr), GSFLOW (Markstrom et al., 2008), FEFLOW (DHI, 2016), and PFLOTRAN-ICE (Karra et al., 2014), DarcyTools (Svensson et al., 2010; Svensson and Ferry, 2014), GEOAN (Holmén, 2019), Ginette (Rivière et al., 2019), MELT (Frederick and Buffet, 2014), SMOKER (Molson and Frind, 2019), FlexPDE (Bense et al., 2009), PermaFOAM (Orgogozo et al., 2019), COMSOL (Scheidegger et al., 2017).

In recent years, to accurately and efficiently describe the hydrologic processes in cold regions, the cold region GW-SW model has gradually emerged on the basis of the original GW-SW models and cryo-hydrogeological models (Jan et al., 2020). Such models are considered as the extensions of the cryo-hydrogeological models, while the groundwater-frozen soil modules still follow or directly adopt the cryo-hydrogeological models. The difference is that the surface hydrologic processes (i.e., snowfall, snow accumulation and melt, runoff, and evapotranspiration) are no longer simply presented as boundary conditions, but rather, they are included in the form of governing equations (Schilling et al., 2019b). In this type of models, the constitutive equations of each hydrologic process are simultaneously solved and coupled in an interactive way (two-way coupling or strong coupling). Such models constitute the transient partial differential equations (PDEs) that are iteratively solved using numerical discretization and high-performance computing techniques. Moreover, soil hydrologic properties (e.g., the soil water content and infiltration rate) are directly used to help identify the water flow and energy transport processes under saturated/unsaturated conditions (Painter et al., 2016; Jan et al., 2018). Recently developed models include but not limited to the integrated cryohydrologic model GeoTop (Rigon et al., 2006; Endrizzi et al., 2014), the Advanced Terrestrial Simulator (ATS; Atchley et al., 2015; Painter et al., 2016; Coon et al., 2019)—a hydro-ecological model for cold regions developed by the U.S. Department of Energy (US DOE), and the HydroGeoSphere (HGS; Aquanty, 2017) - an integrated hydrologic model developed by the University of Waterloo in Canada. The cold region GW-SW models combine the advantages of the previous two types of models. Physical processes in frozen soil and snow are both been taken into consideration in the cold region GW-SW models, which use a two-way coupling numerical method to connect and simultaneously simulate the dynamic GW-SW processes. In addition, their spatial resolutions are quite high (~cm), which is suitable for simulating small-scale processes. Although such models have a great potential for future development and applications, the model structure, coupling algorithms, and parallel computing efficiency still need to be improved. In addition, most of the current cold region GW-SW models are mostly in-house developed or commercialized software, which makes it difficult for community development that greatly limits the scope and promotion of such models. It is also noted that the aforementioned models are often assigned with prior assumptions on permafrost hydrological behavior as well as the subsequent impacts on catchment hydrology (Walvoord and Kurylyk, 2016; Gao et al., 2021a). Such models follow a "bottom-up" modeling approach with most of the process understanding obtained from *in-situ* observations, which have limited spatial and invariably limited temporal coverage (Lindstrom et al., 2002; Niu and Yang, 2006; Brutsaert and Hiyama, 2012). In recent years, "top-down" modeling methodology learned from data has emerged, such as soil temperature–based water saturation function (Wang L. et al., 2017), HBV (Osuch et al., 2019), FLEX-Topo (Gao et al., 2021b), etc. Undoubtedly, these "top-down" modeling approaches provide new insights on the

TABLE 2 | Summary of the model benchmarking studies.

Intercomparison project	Benchmark test cases	Participated models	Reference
IH-MIP Maxwell et al. (2014)	(1) Excess infiltration	CATHY	Bixio et al. (2002) Camporese et al. (2010)
	(2) Excess saturation	HGS	Aquanty (2017)
	(3) Tilted V-catchments	OGS	Delfs et al. (2009) Delfs et al. (2012)
	(4) Return flow	PIHM	Kumar et al. (2009)
	(5) Slabs	PAWS	Shen and Phanikumar (2010)
		ParFlow	Kollet and Maxwell (2006)
		tRIBS-VEGGIE	Ivanov et al. (2004)
IH-MIP2 Kollet et al. (2017)	(1) Ttilted V-catchment with 3D subsurface	ATS	Atchley et al. (2015) Painter et al. (2016) Coon et al. (2019)
	(2) Superslab case with additional horizontal subsurface eterogeneity	Cast3M	www-cast3m.cea.fr
	(3) The Borden site rainfall-runoff experiment	CATHY	Bixio et al. (2002) Camporese et al. (2010)
		GEOtop	Endrizzi et al. (2014) Rigon et al. (2006)
		HGS	Delfs et al. (2009) Delfs et al. (2012)
		MIKE-SHE	Abbott et al. (1986) Butts et al. (2004)
		ParFlow	Kollet and Maxwell (2006)
InterFrost project (wiki.lsce.ipsl.fr/interfrost) in 2015 Rühaak et al. (2015)	(1) 1D analytical solution	Cast3M	www-cast3m.cea.fr
	(2) Melting of a frozen inclusion	SUTRA-ICE	McKenzie et al. (2007)
	(3) Talik opening/closure	SMOKER	Bense et al. (2009)
		FEFLOW	DHI (2016)
InterFrost project (wiki.lsce.ipsl.fr/interfrost) in 2018 Grenier et al. (2018)	(1) Frozen inclusion thaw	SUTRA	McKenzie et al. (2007); McKenzie and Voss (2013)
	(2) Talik opening/closure	Cast3M	www-cast3m.cea.fr
		GSFLOW	Markstrom et al. (2008)
		FEFLOW	DHI (2016)
		PFLOTRAN-ICE	Karra et al. (2014)
		DarcyTools	Svensson et al. (2010); Svensson and Ferry, 2014
		GEOAN	Holmén (2019)
		MELT	Frederick and Buffett (2014)
		SMOKER	Molson and Frind (2019)
		FlexPDE	Bense et al. (2009)
		PermaFOAM	Orgogozo et al. (2019)
		Ginette	Rivière et al. (2019)
		COMSOL	Scheidegger et al. (2017)

impact of permafrost on catchment hydrology, which also have strong potential in future model development. In this paper, we are mainly focused on "bottom-up" modeling approach.

Model Benchmarking and Intercomparison

The representation of the physical processes, parameterization schemes, numerical discretization schemes, and grid types of the same type of numerical models are often diverse, and their accuracy and physical realism is quite uncertain. This motives research on model testing, intercomparison, and validation using benchmark cases in order to comprehensively evaluate the physical accuracy, completeness, calculation accuracy, and efficiency of these models (Kurylyk and Watanabe, 2013). A summary of the model benchmarking and intercomparison studies is given in **Table 2**.

With the recent advancement of integrated GW-SW modelling frameworks, Maxwell et al. (2014) identified the need for a formalized Integrated Hydrologic Model Intercomparison Project (IH-MIP), and to this end, they established standard procedures and benchmark test cases for coupled surface-subsurface models and presented the results of an intercomparison study of seven coupled surface-subsurface models, which included the CATHY (Bixio et al., 2002; Camporese et al., 2010), HGS, OGS (Delfs et al., 2009; Delfs et al., 2012), PIHM (Kumar et al., 2009), PAWS (Shen and Phanikumar, 2010), ParFlow (Kollet and Maxwell, 2006) and tRIBS-VEGGIE (Ivanov et al., 2004) models. These seven integrated hydrologic models were intercompared using a standard set of benchmark test cases (i.e., excess infiltration, excess saturation, tilted V-catchments, slabs, and return flow). Kollet et al. (2017) introduced the

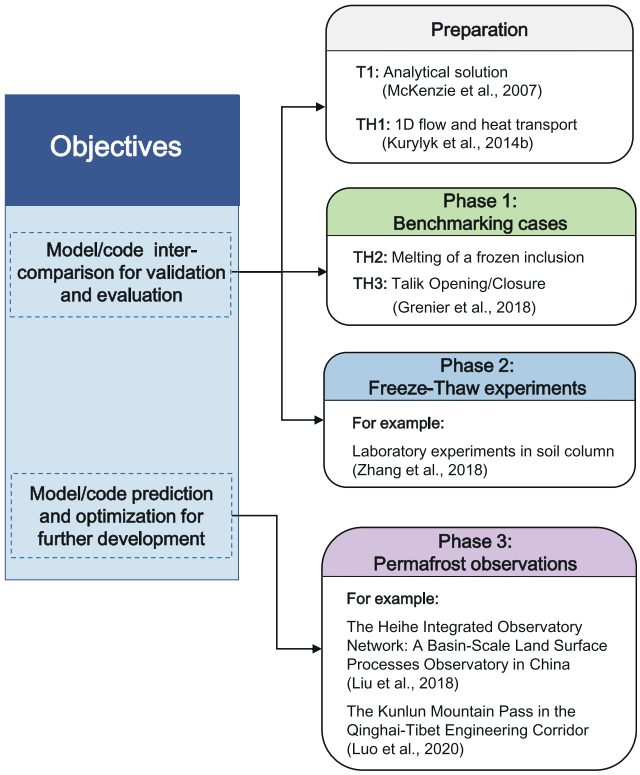

FIGURE 3 | The flowchart and examples of cold region hydrologic model benchmarking.

results of the second phase of the Integrated Hydrologic Model Intercomparison Project (IH-MIP2). ATS, Cast3M, CATHY (Bixio et al., 2002; Camporese et al., 2010), GEOtop, HGS, MIKE-SHE (Abbott et al., 1986; Butts et al., 2004), and ParFlow (Kollet and Maxwell, 2006) were investigated in the IH-MIP2. Compared with the first phase, the complexity of the benchmarking tests was increased in IH-MIP2, which include a tilted V-catchment with 3D subsurface, a superslab case with additional horizontal subsurface heterogeneity, and the Borden site rainfall-runoff experiment. Parameters such as saturated, unsaturated, and ponded storages, discharge, as well as velocity profiles in the superslab and Borden site benchmarking tests were intercompared among seven integrated hydrologic models.

McKenzie et al. (2007) first considered an analytical solution of the 1D Stefan heat transfer equation in model benchmarking and proposed a 2D thawing case in an ideal frozen soil medium. Kurylyk et al. (2014b) revisited the 1D analytical solution and suggested that heat conduction and phase change should be considered for cryo-hydrogeological code benchmarking. In order to comprehensively verify and optimize the integrated hydrologic model of cold regions, the InterFrost project (wiki.lsce.ipsl.fr/interfrost) was launched at the end of 2014. The objective of the InterFrost project was to propose a series of simple to complex, practical, representative benchmarking cases for model comparison and benchmark verification and to further optimize and develop these models. Identical input and setups were configured in each of the models investigated, and the numerical simulation results were inter-compared with the 1D analytical solution, results from 2D benchmark cases, measured data from laboratory experiments, and observation data collected from cold region watersheds. By using the 1D analytical solution and the 2D benchmark cases, Rühaak et al. (2015) attempted to compare the evolution of temperature simulated by 4 of the codes assessed by the InterFrost project. Grenier et al. (2018) introduced 13 cryo-hydrogeology codes/softwares that participated in the first phase of the InterFrost project, comprehensively evaluated and analysed the performance of the models using the analytical solution of the 1D Stefan equation and results from 2D ideal benchmark cases (frozen inclusion thaw and talik opening/closure) using a series of indicators, and finally, they proposed a path to develop and verify cryo-hydrogeology models (**Figure 3**). It is worth noting that the InterFrost project is still actively advancing, and the next two phases will continue to discuss more practical benchmarking verification and evaluation based on laboratory freezing-thawing experiments and field observations in cold regions.

Nevertheless, the current research on integrated hydrologic models of cold regions largely lacks benchmarking verification, also the sub-models (e.g., snow cover and frozen soil

representation) and algorithms (e.g., GW-SW coupling and phase change) still need to be verified. In particular, the constitutive equations, parameter selections, and calibrations need to be assessed for groundwater flow and heat transport in frozen soil and the snow accumulation and ablation processes. The integration and coupling method of these sub-models also needs to be evaluated. In addition, the current benchmarking problems are too simple and mostly focus on the verification of freeze-thaw models. It is essential to evaluate models based on field data (e.g., soil moisture and temperature, snow depth and snow water equivalent, Schilling et al., 2019b; Chen et al., 2017; Gao et al., 2017; Gao et al., 2020) and control experiments.

Model Simulation and Prediction

Distributed hydrologic models of cold regions are mostly used to simulate and predict surface hydrologic processes in larger-scale watersheds, but they may not be feasible to simulate the dynamic processes of GW-SW interactions in cold regions due to their over-simplification of subsurface processes. Cryo-hydrogeological models are mainly used to simulate and predict the hydrogeological response of frozen soil affected by climate and seasonal changes, without fully considering the physical processes of snow cover and its influence on the interaction between groundwater and surface water in cold regions. The fully-coupled cold region GW-SW model can accurately simulate the dynamic processes of GW-SW interactions; however, it is still in development and has limited applications, especially in the field. In recent years, research on modelling GW-SW interactions in cold regions included, but was not limited to, describing the dynamic processes of GW-SW interactions at multiple scales (e.g., hillslope scale (Woo, 2012), catchment scale (Evans et al., 2015), watershed scale (Lemieux et al., 2020)) and predicting their temporal and spatial changes, quantitatively analyzing groundwater lateral flow and heat transfer, local-scale permafrost heterogeneity (e.g., taliks), micro-surface processes (e.g., micro-topography), the impact of snow accumulation and melting, frozen soil on the hydrologic processes, and GW-SW interactions in cold regions under seasonal and climate changes (**Table 3**).

Hillslope Scale

At the hillslope scale, SUTRA (including SUTRA-ICE and modified versions of SUTRA), developed by the US Geological Survey (USGS) has been extensively utilized in various studies. Ge et al. (2011) established a two-dimensional conceptual model of the slope using SUTRA-ICE, which motivated the study of GW-SW interactions in cold regions. The model was used to simulate the subsurface TH processes in the permafrost region of the Qinghai-Tibetan Plateau (QTP) and to calculate the subsurface runoff and its recharge of the surface runoff in the basin. Wellman et al. (2013) applied SUTRA-ICE to address the development of sub-lake and supra-permafrost talik under climate change. A 2D cylindrical cross section (1800 m in radius and 500 m in height) in Yukon Flats, Alaska (United States) was designed to study the evolution of sub-lake talik evolution and supra-permafrost near a lake under various environmental conditions over 1,000 years. Evans and Ge (2017) applied SUTRA to establish a 2D slope model in the Alaska permafrost area, the northern QTP, the seasonal permafrost in the Colorado Rockies, United States, and New Brunswick, Canada. Different hydrogeological effects of permafrost and seasonal frozen ground degradation on groundwater flow were comprehensively explored under climate change scenarios. Simulated results revealed that there is greater groundwater flow in hillslopes with permafrost than seasonal frozen ground under warming scenario. Lamontagne-Hallé et al. (2018) used SUTRA and an improved set of boundary conditions to simulate the distribution of the frozen soil and the dynamic groundwater discharge in permafrost regions under climate warming. Zipper et al. (2018) employed the modified version of SUTRA to study groundwater-permafrost interactions under the influence of wildfire in a 2D transect (200 m width, 20–25 m height) that simply represented the Anaktuvuk River field sites. To examine active-layer dynamics and perennial thaw zones in boreal hillslopes, Walvoord et al. (2019) applied the enhanced version of SUTRA to an idealized 2D hillslope model (100 m long) under fully-saturated condition. Various idealized boundary conditions subjected to seasonal air-temperature variation in a long-term warming trend were superimposed. The enhanced version of SUTRA could simulate coupled fluid-flow and heat transport incorporating the nonlinear phase change between ice and liquid water. Model results indicated that perennial thaw zones serve as a detectable precursor to accelerated permafrost degradation. Rushlow et al. (2020) investigated the effects of snow cover and air temperature on the active layer, the freeze-thaw states, and the groundwater flow near water tracks using SUTRA.

The Advanced Terrestrial Simulator (ATS), developed by Los Alamos and Oak Ridge National Laboratories (USA), is an ecosystem hydrology code focusing on solving problems of integrated surface/subsurface hydrology that involve with vegetation, surface energy balance, snow, and other environmental interactions. HEATFLOW/SMOKER, developed by Université Laval and University of Waterloo (Canada), is a finite element numerical model for solving complex density-dependent groundwater flow, contaminant transport, groundwater age, and thermal energy transport problems. Both codes are open-source and have emerged as powerful tools in solving flow and heat transport problems within partially frozen ground in cold regions. Sjöberg et al. (2016) employed the ATS to estimate the thermal effects of groundwater flow in permafrost environments. Numerical simulations were configured using 1D vertical columns and 2D vertical (10 m long × 5 m deep) cross-sections of the subsurface using data from a subarctic fen in northern Sweden. Shojae Ghias et al. (2017) developed a conceptual model in the Iqaluit Airport taxiway, Nunavut, Canada. A corresponding 100 m wide and 50 m high vertical cross-section was calibrated *via* HEATFLOW/SMOKER. Simulated results were compared with the observed ground temperature, and the impacts of future climate-warming on the thermal regime and flow system under climate scenarios

TABLE 3 | Summary of cold region integrated hydrologic models and their applications.

Scale	Reference	Model	Category	Study area and configuration
Slope	Ge et al. (2011)	SUTRA	Cryo-hydrogeological models	2D conceptual slope in the QTP
	Wellman et al. (2013)			2D cylindrical cross section (1800 m in radius and 500 m in height) in Yukon Flats, Alaska, United States
	Evans and Ge (2017)			Alaska permafrost area; northern QTP, China; Colorado Rockies, United States; New Brunswick, Canada
	Lamontagne-Hallé et al. (2018)			An idealized 500 m long, 2D homogeneous cross-section with a 2% land surface slope
	Zipper et al. (2018)			2D transect (200 m width, 20–25 m height) that simply represented the Anaktuvuk River field sites
	Walvoord et al. (2019)			2D hillslope model (100 m long) near the West Fork of the Dall River in interior Alaska
	Rushlow et al. (2020)			3D half-hillslope (500 m long, 40 m wide, 60 m thickness, 0.08 slope in *x* direction and 0.05 slope in *y* direction) in Alaska, United States
	Sjöberg et al. (2016)	ATS	Cold region GW-SW models	2D vertical cross-sections (10 m long × 5 m depth) from a subarctic fen in northern Sweden
	Jafarov et al. (2018)			A 45 m deep, 1 km wide 2D domain hillslope on the southern Seward Peninsula
	Sjöberg et al. (2021)			The slopes near the streams in the Agashashok basins and the Cutler-Imelyak basins located in the Noatak National Preserve in northwestern Alaska
	Hamm and Frampton (2021)			Two idealized hillslopes (50 m in *x*-direction, 1 m in *y*-direction and 20 m in *z*-direction) with inclinations (22°, 11°) that can be found in Adventdalen, Svalbard
	Shojae Ghias et al. (2017)	HEATFLOW/ SMOKER	Cryo-hydrogeological models	A corresponding vertical cross-section with 100 m width and 50 m height from the Iqaluit Airport taxiway, Nunavut, Canada
	Dagenais et al. (2020)			A vertical cross-section (600 m long × 200 m height) extracted from a 3D geological model (0.8 km long × 2.6 km wide × 200 m height) in Nunavik (Québec), Canada
	Bense et al. (2012)	FlexPDE	Cryo-hydrogeological models	A topography-driven, 10 km long and 0.6 km high groundwater flow system in the Northwest Territories, Canada
	Wicky and Hauck (2017)	GeoStudio	Cryo-hydrogeological models	170 m long slope with a talus thickness of 17 m and a constant slope angle of 33° in the Valais Alps, Western Swiss Alps
	Orgogozo et al. (2019)	PermaFOAM	Cryo-hydrogeological models	Two 2,500 m-long 2D transects in a permafrost-dominated forested watershed in Central Siberia
	Scheidegger et al. (2019)	COMSOL	Cryo-hydrogeological models	Two contrasting geological settings (20 km long × 3 km high and 300 km long ×1.5 km high) in Great Britain
	Huang et al. (2020)	FEFLOW	Cryo-hydrogeological models	Shady and sunny slope (200 m long × 250 m high) in the QTP, China
Catch-ment	Endrizzi et al. (2014)	GEOtop 2.0	Cold region GW-SW models	A synthetic catchment (two 160 m long × 200 m width hillslopes forming a convergent topography)
	Evans and Ge (2017)	STUTA	Cryo-hydrogeological models	The mountainous Hulugou catchment with 8 km long, 3 km width and elevation range from 2,970 to 4,470 m on the QTP
	Kumar et al. (2016)	PFLOTRAN	Cryo-hydrogeological models	Ice-wedge polygons extracted from four sites near Barrow, Alaska
	Painter et al. (2016)	ATS	Cold region GW-SW models	Benchmarking case: The "tilted open book" catchment Field data: An ice wedge polygon at Barrow Alaska
	Schilling et al. (2019b)	HGS	Cold region GW-SW models	Analytical solution: 1D Stefan heat transfer equation Benchmarking case: Classical 3D V-catchment Field data: the Borden site in Canada
	Evans et al. (2020)	STUTA	Cryo-hydrogeological models	550 m × 100 m × 60 m hillslope measurements from the Upper Kuparuk River watershed on the North Slope of Alaska, United States
	Jan et al. (2020)	ATS	Cold region GW-SW models	The ice-wedge polygon area of Alaska, United States
Water-Shed	Wang et al. (2009)	WEB-DHM	Distributed hydrologic models of cold regions	The Binngou watershed (30.48 km^2) of the upper reaches of the Heihe River Basin, China
	Holmén et al. (2011)	GEOAN	Cryo-hydrogeological models	The entire Paris Basin, France
	Zhang et al. (2013)	SHAWDHM	Distributed hydrologic models of cold regions	The Binggou watershed
	Yang et al. (2015)	GBHM	Distributed hydrologic models of cold regions	The upper reaches of the Heihe River Basin
	Carroll et al. (2019)	GSFLOW	Cold region GW-SW models	The Copper Creek watershed (24 km^2) of the upper Colorado River in the United States
	Cochand et al. (2019)	HGS	Cold region GW-SW models	The Saint-Charles River catchment, Quebec, Canada
	Langford et al. (2020)	FEFLOW	Cryo-hydrogeological models	The Scotty Creek Basin in Northwestern Territories of Canada
	Marsh et al. (2020)	CHM	Distributed hydrologic models of cold regions	The Marmot Creek Research Basin of the Kananaskis River Valley of the Canadian Rockies
	Yao et al. (2017)	MODFLOW-NWT	Cryo-hydrogeological models	The Qilian Mountains on the QTP, China

(Continued on following page)

TABLE 3 | (*Continued*) Summary of cold region integrated hydrologic models and their applications.

Scale	Reference	Model	Category	Study area and configuration
	Yao et al. (2021)			The Yarlung Zangbo basin on the northern Himalayan mountainous region, China

proposed by the Intergovernmental Panel on Climate Change (IPCC) were analyzed. To better understand the thermal-hydrologic controls and consequences of taliks, Jafarov et al. (2018) used the ATS to simulate the evolution of taliks developed under preferentially distributed snow. The numerical simulations were conducted in a hillslope transect (45 m deep, 1 km wide, 2D domain) on the southern Seward Peninsula. Dagenais et al. (2020) adopted the cryo-hydrogeological numerical model HEATFLOW to study the flow and heat transfer processes in an ice-rich permafrost mound. First, the HEATFLOW model was verified using a vertical cross-section (600 m long × 200 m high) extracted from a 3D geological model (0.8 km long × 2.6 km wide × 200 m high) of the Tasiapik valley, near Umiujaq, Nunavik (Québec), Canada. Numerical simulations were then performed for future projection under a regional climate-change scenario. Based on the "Umiujaq model" provided in Dagenais et al. (2020), Albers et al. (2020) performed HEATFLOW-SMOKER to investigate the sensitivity of the model to changes in the thermal and hydraulic properties of the system. It was demonstrated that the model was quite sensitive to the near-surface thermal and hydraulic parameters, and to those parameters which define the characteristics of the active layer. Sjöberg et al. (2021) applied ATS to investigate if the impact of permafrost on flow path depth could cause the same pattern in temperatures of groundwater discharging from hillslopes to streams. The model domain was 1,000 m in the horizontal (x) direction, 8 m thick (z), and had a slope of 0.1, which represents the slopes near the streams in the Agashashok basins and the Cutler-Imelyak basins located in the Noatak National Preserve in northwestern Alaska. Hamm and Frampton (2021) used ATS to simulate two idealized hillslopes (50 m in *x*-direction, 1 m in *y*-direction, and 20 m in *z*-direction) with inclinations (22°, 11°) that can be found in Adventdalen, Svalbard, and compare them to a baseline case (0°). Results show that hillslope inclination causes differences in ground temperature uphill and downhill and highlight the relevance of considering lateral flow of water in the subsurface combined with heat flux for modelling arctic catchments with permafrost.

Other in-house developed or commercial software were also used in simulating groundwater flow and heat transport in cold regions. Bense et al. (2012) studied the climate change-induced hydraulic evolution of aquifers and the consequent increase in baseflow in idealized permafrost environments using the FlexPDE (developed using the finite element method). Wicky and Hauck (2017) used the commercially available GeoStudio software to model the air flow and heat transfer in a natural talus slope and studied the ground thermal regime. The entire domain represented an idealized 170 m long talus slope with a talus thickness of 17 m and a constant slope angle of 33°. Orgogozo et al. (2019) developed the cryo-hydrogeological numerical model (permaFOAM) in the open-source CFD environment, OpenFOAM (https://openfoam.com). Based on permafrost observation in central Siberia in Russia, seasonal changes in soil moisture and temperature were simulated in a 2D transect. The permaFOAM accurately described the phase change between the pore water and ice in frozen soils and quantitatively analysed the influence of surface evapotranspiration on the coupled TH processes in the groundwater in frozen soils. Scheidegger et al. (2019) applied the commercial software COMSOL to simulate the impact of long-term climatic variability on groundwater flow and permafrost dynamics in two contrasting geological settings (20 km long × 3 km high and 300 km long ×1.5 km high) in Great Britain. The sensitivity of simulated permafrost thickness to a variety of climatic and subsurface conditions was also evaluated. Using FEFLOW, Huang et al. (2020) established an ideal 2D slope model of the central part of the QTP and predicted the hydrogeological processed in high altitude areas in the context of future climate change. The impacts of the slope aspect, land surface temperature, FTCs, and permeability were all analysed, and finally, the land surface temperature was identified as the main factor controlling the seasonal dynamics of the shallow groundwater systems in permafrost regions.

Catchment Scale

At the catchment scale, Endrizzi et al. (2014) applied GEOtop 2.0 to a synthetic catchment (two 160 m long and 200 m wide hillslopes forming a convergent topography) and simulated the GW-SW interactions with frozen soil and snow cover under different meteorological forcings. Evans et al. (2015) used SUTRA to describe the groundwater flow in mountainous headwater catchments and evaluated the impact of permafrost on groundwater. The model was applied to a representative mountainous Hulugou catchment (8 km long, 3 km wide. elevation range from 2,970 m to 4,470 m) on the QTP, China, and then, they obtained predictions under a warming scenario with a mean annual surface temperature increase of 2°C. Kumar et al. (2016) applied a multiphase subsurface thermal hydrology model (PFLOTRAN; http://www.pflotran.org/) to study the thermal regimes of 3D ice-wedge polygons extracted

from four sites near Barrow, Alaska. A high-resolution (25 cm) LiDAR (light detection and ranging) digital elevation model (DEM) was used to characterize the microtopographic features of the landscape, which were characterized and represented as a high-resolution grid. Painter et al. (2016) developed the ATS model by combing a surface energy balance model to simulate the surface water flows and snow distribution in the microtopography. The tilted open book catchment was used to conduct fully integrated thermal hydrology simulations, and a cross section across a low-centered, ice-wedge polygon in Barrow, Alaska, in a fine-scale 100-years projected future warming climate was also presented. Schilling et al. (2019b) improved the GW-SW flow model HydroGeoSphere (HGS) by adding a surface flow model with snowmelt and the degree-day model in an attempt to simultaneously balance the computational efficiency and accuracy. First, the analytical solution of the 1D Stefan heat transfer equation was simulated to verify the accuracy of the freeze-thaw parameterization scheme in the integrated GW-SW model, and then the classical 3D V-catchment benchmark case was calculated to determine the impact of the snow melt and FTCs on the GW-SW interactions. Furthermore, the model was directly used to simulate the GW-SW interactions of the Borden site in Canada, whose feasibility was evaluated based on the snow depth, snow water equivalent, and groundwater and surface water flow under different precipitation and temperature conditions. Evans et al. (2020) employed SUTRA in a 3D domain (550 m × 100 m × 60 m) with a horizontal spatial resolution of 3 m × 3 m and a vertical resolution of 20 cm. The model was representing a small catchment adopted from the Upper Kuparuk River watershed on the North Slope of Alaska, United States. The effect of surface temperature variation on groundwater discharge with water tracks was investigated. Jan et al. (2020) evaluated the GW-SW interaction in the ice-wedge polygon area of Alaska, United States, and analysed the effects of the microtopography on the TH processes using the ATS. The model was driven by on-site meteorological data with a 25 cm horizontal spatial resolution, and the simulation results exhibited a high degree of consistency with the snow depth, water table, and soil temperature observed in the Next Generation Ecosystem Experiments (NGEE) Arctic Program of the U.S. Department of Energy (US DOE), which demonstrated the accuracy of the fully-coupled GW-SW models in cold regions.

Watershed Scale

At the watershed scale, Wang et al. (2009) incorporated a frozen soil parameterization into a distributed hydrological model (WEB-DHM) and applied the model to the Binngou watershed (30.48 km^2) of the upper reaches of the Heihe River Basin for evaluation with the *in-situ* observations. WEB-DHM was subsequently developed into WEB-DHM-SF by incorporating the enthalpy-based coupled snow and frozen ground physics (Qi et al., 2019; Song et al., 2020). Holmén et al. (2011) developed the GEOAN model to study the impact of climate and permafrost on groundwater in the entire Paris Basin (approx. 163,400 km^2). This large-scale 3D hydrogeological model had the highest numerical resolution (333 m × 333 m) in the cross-cutting plane, and the vertical resolution ranged from a few meters up to more than 100 m. It included geological layers from the Triassic to the Tertiary (a total of 34 geological layers represented by 58 numerical layers). The model was calibrated using the actual TH conditions, and then, the future groundwater flow for the next 130,000 years was calculated. Zhang et al. (2013) used SHAWDHM in the Binggou watershed and the results showed that the model was able to predict soil freezing and thawing, unfrozen soil water content, and snow depth reasonably well. Yang et al. (2015) developed a distributed scheme (GBHM) for eco-hydrological simulation in the upper Heihe River, which has been subsequently developed into the distributed Geomorphology-Based Eco-hydrological Model (GBEHM) (Gao et al., 2016) and a physical process and machine learning combined hydrological model GBHM-ANN-CA-CV (Yang et al., 2020). The results identified that the soil freezing and thawing process would significantly influence the runoff generation. Yao et al. (2017) used regional groundwater model MODFLOW-NWT (Niswonger et al., 2011) to explore the partitioning between baseflow and mountain block recharge in the QTP. The model was first calibrated using mountain stream baseflows and then run with multiple scenarios in the Qilian Mountains. Carroll et al. (2019) comprehensively used high-quality field snow observations and the GSFLOW model to study the GW-SW interactions under seasonal and climate changes in the Copper Creek watershed (24 km^2) of the upper Colorado River in the United States from 1987 to 2018. The driving and verification data for GSFLOW was obtained from two SNOTEL site observations (i.e., snow area, snow depth, snow water equivalent, during snow, and snowmelting periods), high-precision (3 m) LiDAR-based Airborne Snow Observatory data, and hydrometeorological data. Their results indicate that seasonal snowmelt and vegetation water consumption are the main factors controlling the hydrologic processes in the low-altitude areas of the basin, while the runoff is completely controlled by snowmelt in the high-altitude mountains. Cochand et al. (2019) used a modified the HGS model to assess the potential impact of climate change on the GW-SW interactions in the 553 km^2 Saint Charles River Basin in Quebec, Canada. First, the model was developed and calibrated to reproduce the observed streamflow and the hydraulic heads from 1970 to 2000, and then, it was used with three different temperature and precipitation scenarios to simulate the surface flow and groundwater dynamics from 2070 to 2100. The simulations predict that the warmer winters will cause more precipitation (rain and snow), which will increase the winter stream discharges and the water table. Conversely, the summer stream discharges will decrease due to an increase in the evapotranspiration, demonstrating that winter processes play a key role in the seasonal modifications anticipated for surface and subsurface flow dynamics. Langford et al. (2020) used the piFreeze plug-in to one-way couple the surface water heat balance SHAW model with the FEFLOW groundwater model based on the Scotty Creek Basin in Northwestern Territories of

Canada. This study not only explored the importance of the initial conditions but also demonstrated the critical role that the variations in the microtopography of the land surface and permafrost table and talik development play in permafrost degradation. Based on the model CRHM developed by Pomeroy et al. (2007), Marsh et al. (2020) presented a new distributed model, the Canadian Hydrological Model (CHM). The model was further used in the Marmot Creek Research Basin of the Kananaskis River Valley of the Canadian Rockies and focused on the role of cold region processes in hydrology. Yao et al. (2021) used MODFLOW-NWT to evaluate the annual and seasonal contributions of groundwater discharge to total river flow in the Yarlung Zangbo basin on the northern Himalayan mountainous region. Results indicated that the groundwater recharge and discharge would increase with projected increasing ratio of recharge to precipitation, and thawing permafrost would increase groundwater recharge and discharge.

In summary, due to the complexity in simulating cold region hydrologic cycles and lack of high-quality data, although some cutting-edge research has emerged in recent years, many scientific issues are still unclear, and more advanced model developments are needed for quantitative analysis and accurate prediction. For now, due to computational limitations and complexities, 2D slope models have been more commonly employed than 3D catchment and watershed models. In addition, conceptual domains are often adopted instead of realistic terrains in cold regions, especially in the 2D slope scale. Also, the assumptions and setups of the models are quite simple (e.g., ignoring microtopography and heterogeneities, simplified subsurface aquifer layers, the assignment of hydraulic and thermal boundary conditions) that cannot accurately reflect the actual situations. Therefore, even the aforementioned models have improved our theoretical understanding of cold region hydrologic processes, but there are still limitations and uncertainties in solving practical problems (Lamontagne-Hallé et al., 2020). Future model development should focus on describing the dynamic processes on multiple scales (i.e., 3D groundwater flow, heat transfer, groundwater-frozen soil, snowmelt-groundwater, and GW-SW interactions), quantitatively analyzing the influencing mechanisms and factors, and predicting the temporal and spatial evolution of GW-SW interactions in cold regions under seasonal and climate change.

CHALLENGES AND FUTURE RESEARCH NEEDS

GW-SW Interactions in Cold Regions

With projections of rapid and abrupt warming for the foreseeable future, surface water-groundwater interactions are considered as critical elements in cold-region hydrologic processes. As a key link in the hydrologic cycle in cold regions, the interactions between groundwater and surface water are unique, complex, and uncertain. The core issue is the dynamic processes of water and energy transport between the surface and the subsurface, especially in regions with snow cover and frozen soil. Therefore, the physics of surface water-groundwater interactions should be accurately represented in hydrologic models.

Future Model Development

However, the existing integrated hydrologic models of cold regions still have room to develop in several aspects:

a) The physical processes are not completely considered in the existing integrated hydrologic models of cold regions. In the distributed hydrologic models based on terrestrial hydrology, the surface hydrologic processes are well considered, but the groundwater processes are often simplified, and even lateral flow and heat transfer processes are directly neglected. In contrast, in the cryo-hydrogeological models, the interactions between soil and groundwater are accurately simulated, but the surface hydrologic processes are often described by simple parameterization or one-way coupling.
b) Compared with the previous models, the coupled GW-SW models of cold regions consider both the surface and subsurface hydrologic processes. Since incorporating more processes can potentially increase the uncertainty and computational time, the coupling algorithms and parallel computing efficiency of the coupled GW-SW models of cold regions still need to be improved. Moreover, most coupled GW-SW models of cold regions are not open source, which inhibits its further development and community applications.
c) In addition, various models have been developed and applied in recent years, while rigorous and systematic benchmark verifications are relatively rare. The physical processes and solution strategies behind various models vary among codes, and their accuracies and physical realism are unknown, which limits their practical application and prediction capabilities.

Perspectives

Therefore, it is vital to develop the next generation integrated GW-SW models. Not only should a complete description of GW-SW processes be ensured, but the integrated GW-SW models should achieve a better balance between accuracy and computational efficiency. Furthermore, to evaluate and optimize the present models of cold regions, it is urgent that more code validation and intercomparison efforts should be initiated across multi-disciplinaries. The next-generation GW-SW models are expected to fundamentally explain the hydrologic process in cold regions and address the challenges of climate change.

SUMMARY

Integrated hydrologic models of cold regions have emerged as promising tools to simulate the impacts of pronounced climate warming and seasonal changes on the groundwater-surface water (GW-SW) interactions and groundwater resources. This review revealed the current state-of-the-art integrated hydrologic models of cold regions and subsequently prospected the future development. We first introduced different types of numerical models and explained the cons and pros of simulating GW-SW interactions if using these models. Selected intercomparison project and benchmarking cases for testing the accuracy of the numerical models were

also reviewed. It should be highlighted that the research on rigorous and systematic benchmark validations should be largely promoted for benefiting the next generation models. Recent research on modelling GW-SW interactions in cold regions were summarized from hillslope scale to watershed scale, with aspects in temporal and spatial changes of the hydrologic cycle, and quantitatively analyzing groundwater lateral flow and heat transfer, local-scale permafrost heterogeneity, micro-surface roughness, the impact of snow accumulation and melting and frozen soil on the GW-SW interactions in cold regions, and the prediction under seasonal and climate changes. In conclusion, more efforts are absolutely needed to further develop integrated hydrologic models, specifically for applications in cold regions, as suggested in future research perspectives.

AUTHOR CONTRIBUTIONS

XY designed the research; JH and XY wrote the initial draft of the manuscript; RM, ZS, XY, and JH revised the manuscript; all authors agreed to its submission.

FUNDING

The current research is supported by the National Natural Science Foundation of China (NSFC, Grant No. 42077172, 41730854), the Second Tibetan Plateau Scientific Expedition and Research Program (STEP, Grant No. 2019QZKK0306), and the Strategic Priority Research Program of Chinese Academy of Sciences (Grant No. XDA20100104).

REFERENCES

Abbott, M. B., Bathurst, J. C., Cunge, J. A., O'Connell, P. E., and Rasmussen, J. (1986). An Introduction to the European Hydrological System – Systeme Hydrologique Europeen, "She". 1: History and Philosophy of a Physically-Based, Distributed Modeling System. *J. Hydrol.* 87 (1-2), 45–59. doi:10.1016/0022-1694(86)90114-9

Albers, B. M. C., Molson, J. W., and Bense, V. F. (2020). Parameter Sensitivity Analysis of a Two-Dimensional Cryo-Hydrogeological Numerical Model of Degrading Permafrost Near Umiujaq (Nunavik, Canada). *Hydrogeol. J.* 28, 905–919. doi:10.1007/s10040-020-02112-2

Aquanty (2017). *HydroGeoSphere: A Three-Dimensional Numerical Model Describing Fully-Integrated Subsurface and Surface Flow and Solute Transport*. WaterlooCanada: University of Waterloo.

Atchley, A. L., Coon, E. T., Painter, S. L., Harp, D. R., and Wilson, C. J. (2016). Influences and Interactions of Inundation, Peat, and Snow on Active Layer Thickness. *Geophys. Res. Lett.* 43 (10), 5116–5123. doi:10.1002/2016gl068550

Atchley, A. L., Painter, S. L., Harp, D. R., Coon, E. T., Wilson, C. J., Liljedahl, A. K., et al. (2015). Using Field Observations to Inform thermal Hydrology Models of Permafrost Dynamics with ATS (v0.83). *Geosci. Model. Dev.* 8 (9), 3235–3292. doi:10.5194/gmd-8-2701-2015

Barnett, T. P., Adam, J. C., and Lettenmaier, D. P. (2005). Potential Impacts of a Warming Climate on Water Availability in Snow-Dominated Regions. *Nature* 438, 303–309. doi:10.1038/nature04141

Barnhart, T. B., Molotch, N. P., Livneh, B., Harpold, A. A., Knowles, J. F., and Schneider, D. (2016). Snowmelt Rate Dictates Streamflow. *Geophys. Res. Lett.* 43 (15), 8006–8016. doi:10.1002/2016gl069690

Bense, V. F., Ferguson, G., and Kooi, H. (2009). Evolution of Shallow Groundwater Flow Systems in Areas of Degrading Permafrost. *Geophys. Res. Lett.* 36 (22), L22401. doi:10.1029/2009gl039225

Bense, V. F., Kooi, H., Ferguson, G., and Read, T. (2012). Permafrost Degradation as a Control on Hydrogeological Regime Shifts in a Warming Climate. *J. Geophys. Res. -Earth. Surf.* 117 (F3), F03036. doi:10.1029/2011jf002143

Bixio, A. C., Gambolati, G., Paniconi, C., Putti, M., Shestopalov, V. M., Bublias, V. N., et al. (2002). Modeling Groundwater–Surface Water Interactions Including Effects of Morphogenetic Depressions in the Chernobyl Exclusion Zone. *Environ. Geol.* 42 (2-3), 162–177. doi:10.1007/s00254-001-0486-7

Brutsaert, W., and Hiyama, T. (2012). The Determination of Permafrost Thawing Trends from Long-Term Streamflow Measurements with an Application in Eastern Siberia. *J. Geophys. Res.* 117, D2211. doi:10.1029/2012jd018344

Butts, M. B., Payne, J. T., Kristensen, M., and Madsen, H. (2004). An Evaluation of the Impact of Model Structure on Hydrological Modelling Uncertainty for Streamflow Simulation. *J. Hydrol.* 298 (1-4), 242–266. doi:10.1016/j.jhydrol.2004.03.042

Camporese, M., Paniconi, C., Putti, M., and Orlandini, S. (2010). Surface-subsurface Flow Modeling with Path-Based Runoff Routing, Boundary Condition-Based Coupling, and Assimilation of Multisource Observation Data. *Water Resour. Res.* 46, W02512. doi:10.1029/2008wr007536

Carroll, R. W. H., Deems, J. S., Niswonger, R., Schumer, R., and Williams, K. H. (2019). The Importance of Interflow to Groundwater Recharge in a Snowmelt-Dominated Headwater Basin. *Geophys. Res. Lett.* 46, 5899–5908. doi:10.1029/2019gl082447

Che, T., Li, X., Liu, S., Li, H., Xu, Z., Tan, J., et al. (2019). Integrated Hydrometeorological, Snow and Frozen-Ground Observations in the alpine Region of the Heihe River Basin, China. *Earth Syst. Sci. Data.* 11 (3), 1483–1499. doi:10.5194/essd-11-1483-2019

Chen, R., Wang, G., Yang, Y., Liu, J., Han, C., Song, Y., et al. (2018). Effects of Cryospheric Change on alpine Hydrology: Combining a Model with Observations in the Upper Reaches of the Hei River, China. *J. Geophys. Res. Atmos.* 123 (7), 3414–3442. doi:10.1002/2017jd027876

Chen, X., Long, D., Hong, Y., Zeng, C., and Yan, D. (2017). Improved Modeling of Snow and Glacier Melting by a Progressive Two-Stage Calibration Strategy with Grace and Multisource Data: How Snow and Glacier Meltwater Contributes to the Runoff of the Upper Brahmaputra River basin. *Water Resour. Res.* 53 (3), 2431–2466. doi:10.1002/2016wr019656

Cheng, G., Zhao, L., Li, R., Wu, X., Sheng, Y., Hu, G., et al. (2019). Characteristic, Changes and Impacts of Permafrost on Qinghai-Tibet Plateau. *Chin. Sci. Bull.* 64 (27), 2783–2795. (in Chinese). doi:10.1360/TB-2019-0191

Chiasson-Poirier, G., Franssen, J., Lafrenière, M. J., Fortier, D., and Lamoureux, S. F. (2020). Seasonal Evolution of Active Layer Thaw Depth and Hillslope-Stream Connectivity in a Permafrost Watershed. *Water Resour. Res.* 56 (1), 025828. doi:10.1029/2019WR025828

Cochand, F., Therrien, R., and Lemieux, J.-M. (2019). Integrated Hydrological Modeling of Climate Change Impacts in a Snow-Influenced Catchment. *Groundwater* 57 (1), 3–20. doi:10.1111/gwat.12848

Coon, E. T., David Moulton, J., and Painter, S. L. (2016). Managing Complexity in Simulations of Land Surface and Near-Surface Processes. *Environ. Model. Softw.* 78, 134–149. doi:10.1016/j.envsoft.2015.12.017

Coon, E. T., Svyatsky, D., Jan, A., Kikinzon, E., Berndt, M., Atchley, A., et al. (2019). Advanced Terrestrial Simulator. Available at: https://www.osti.gov/doecode/biblio/28622 (Accessed October 11, 2019). doi:10.11578/DC.20190911.1

Costa, D., and Pomeroy, J. W. (2019). Preferential Meltwater Flowpaths as a Driver of Preferential Elution of Chemicals from Melting Snowpacks. *Sci. Total Environ.* 662, 110–120. doi:10.1016/j.scitotenv.2019.01.091

Dagenais, S., Molson, J., Lemieux, J.-M., Fortier, R., and Therrien, R. (2020). Coupled Cryo-Hydrogeological Modelling of Permafrost Dynamics Near Umiujaq (Nunavik, Canada). *Hydrogeol. J.* 28, 887–904. doi:10.1007/s10040-020-02111-3

Delfs, J.-O., Blumensaat, F., Wang, W., Krebs, P., and Kolditz, O. (2012). Coupling Hydrogeological with Surface Runoff Model in a Poltva Case Study in Western Ukraine. *Environ. Earth Sci.* 65 (5), 1439–1457. doi:10.1007/s12665-011-1285-4

Delfs, J.-O., Park, C.-H., and Kolditz, O. (2009). A Sensitivity Analysis of Hortonian Flow. *Adv. Water Resour.* 32 (9), 1386–1395. doi:10.1016/j.advwatres.2009.06.005

Deprez, M., De Kock, T., De Schutter, G., and Cnudde, V. (2020). A Review on Freeze-Thaw Action and Weathering of Rocks. *Earth-Science Rev.* 203, 103143. doi:10.1016/j.earscirev.2020.103143

DHI (2016). *PiFreeze, a Freeze/thaw Plug-In for FEFLOW, User Guide*. Denmark: HørsholmDHI.

Ding, Y., Zhang, S., Chen, R., Han, T., Han, H., Wu, J., et al. (2020). Hydrological Basis and Discipline System of Cryohydrology: From a Perspective of Cryospheric Science. *Front. Earth Sci.* 8, 574707. doi:10.3389/feart.2020.574707

Ding, Y., Zhang, S., and Chen, R. (2017). *Introduction to Hydrology in Cold Regions*. Beijing: science press. (in Chinese).

Domine, F., Picard, G., Morin, S., Barrere, M., Madore, J.-B., and Langlois, A. (2019). Major Issues in Simulating Some Arctic Snowpack Properties Using Current Detailed Snow Physics Models: Consequences for the thermal Regime and Water Budget of Permafrost. *J. Adv. Model. Earth Syst.* 11, 34–44. doi:10.1029/2018ms001445

Endrizzi, S., Gruber, S., Dall'Amico, M., and Rigon, R. (2014). GEOtop 2.0: Simulating the Combined Energy and Water Balance at and below the Land Surface Accounting for Soil Freezing, Snow Cover and Terrain Effects. *Geosci. Model. Dev.* 7 (6), 2831–2857. doi:10.5194/gmd-7-2831-2014

Evans, S. G., and Ge, S. (2017). Contrasting Hydrogeologic Responses to Warming in Permafrost and Seasonally Frozen Ground Hillslopes. *Geophys. Res. Lett.* 44 (4), 1803–1813. doi:10.1002/2016gl072009

Evans, S. G., Ge, S., and Liang, S. (2015). Analysis of Groundwater Flow in Mountainous, Headwater Catchments with Permafrost. *Water Resour. Res.* 51, 9564–9576. doi:10.1002/2015wr017732

Evans, S. G., Ge, S., Voss, C. I., and Molotch, N. P. (2018). The Role of Frozen Soil in Groundwater Discharge Predictions for Warming alpine Watersheds. *Water Resour. Res.* 54 (3), 1599–1615. doi:10.1002/2017wr022098

Evans, S. G., Godsey, S. E., Rushlow, C. R., and Voss, C. (2020). Water Tracks Enhance Water Flow above Permafrost in upland Arctic Alaska Hillslopes. *J. Geophys. Res. -Earth. Surf.* 125, e2019JF005256. doi:10.1029/2019jf005256

Flerchinger, G. N., and K. E. Saxton, K. E. (1989). Simultaneous Heat and Water Model of a Freezing Snow-Residue-Soil System I. Theory and Development. *Trans. ASAE* 32 (2), 0565–0571. doi:10.13031/2013.31040

Frederick, J. M., and Buffett, B. A. (2014). Taliks in Relict Submarine Permafrost and Methane Hydrate Deposits: Pathways for Gas Escape under Present and Future Conditions. *J. Geophys. Res. Earth Surf.* 119 (2), 106–122. doi:10.1002/2013jf002987

Fu, Q., Hou, R., Li, T., Jiang, R., Yan, P., Ma, Z., et al. (2018). Effects of Soil Water and Heat Relationship under Various Snow Cover during Freezing-Thawing Periods in Songnen Plain, China. *Sci. Rep.* 8, 1325. doi:10.1038/s41598-018-19467-y

Gao, B., Qin, Y., Wang, Y., Yang, D., and Zheng, Y. (2016). Modeling Ecohydrological Processes and Spatial Patterns in the Upper Heihe basin in China. *Forests* 7 (1), 10. doi:10.3390/f7010010

Gao, B., Yang, D., Qin, Y., Wang, Y., Li, H., Zhang, Y., et al. (2018). Change in Frozen Soils and its Effect on Regional Hydrology, Upper Heihe Basin, Northeastern Qinghai-Tibetan Plateau. *Cryosphere* 12 (8), 657–673. doi:10.5194/tc-12-657-2018

Gao, H., Ding, Y., Zhao, Q., Hrachowitz, M., and Savenije, H. H. G. (2017). The Importance of Aspect for Modelling the Hydrological Response in a Glacier Catchment in Central Asia. *Hydrol. Process.* 31 (16), 2842–2859. doi:10.1002/hyp.11224

Gao, H., Dong, J., Chen, X., Cai, H., Liu, Z., Jin, Z., et al. (2020). Stepwise Modeling and the Importance of Internal Variables Validation to Test Model Realism in a Data Scarce Glacier basin. *J. Hydrol.* 591, 125457. doi:10.1016/j.jhydrol.2020.125457

Gao, H., Han, C., Chen, R., Feng, Z., Wang, K., Fenicia, F., et al. (2021b). Diagnosing the Impacts of Permafrost on Catchment Hydrology: Field Measurements and Model Experiments in a Mountainous Catchment in Western China. *Hydrol. Earth Syst. Sci. Discuss.* [preprint]in review. doi:10.5194/hess-2021-264

Gao, H., Wang, J., Yang, Y., Pan, X., Ding, Y., and Duan, Z. (2021a). Permafrost Hydrology of the Qinghai-Tibet Plateau: A Review of Processes and Modeling. *Front. Earth Sci.* 8 (8), 576838. doi:10.3389/feart.2020.576838

Ge, S., Mckenzie, J., Voss, C., and Wu, Q. (2011). Exchange of Groundwater and Surface-Water Mediated by Permafrost Response to Seasonal and Long Term Air Temperature Variation. *Geophys. Res. Lett.* 38, L14402. doi:10.1029/2011gl047911

Grenier, C., Anbergen, H., Bense, V., Chanzy, Q., Coon, E., Collier, N., et al. (2018). Groundwater Flow and Heat Transport for Systems Undergoing Freeze-Thaw: Intercomparison of Numerical Simulators for 2D Test Cases. *Adv. Water Resour.* 114, 196–218. doi:10.1016/j.advwatres.2018.02.001

Hamm, A., and Frampton, A. (2021). Impact of Lateral Groundwater Flow on Hydrothermal Conditions of the Active Layer in a High Arctic Hillslope Setting. *Cryosphere* 15, 4953–4871. doi:10.5194/tc-15-4853-2021

Hamman, J. J., Nijssen, B., Bohn, T. J., Gergel, D. R., and Mao, Y. (2018). The Variable Infiltration Capacity Model Version 5 (VIC-5): Infrastructure Improvements for New Applications and Reproducibility. *Geosci. Model. Dev.* 11, 3481–3496. doi:10.5194/gmd-11-3481-2018

Holmén, J., Benabderrahmane, H., Buoro, A., and Brulhet, J. (2011). Modelling of Permafrost Freezing and Melting and the Impact of a Climatic Cycle on Groundwater Flow at the Meuse/haute-Marne Site. *Phys. Chem. Earth Parts. A/b/c* 36 (17), 1531–1538. doi:10.1016/j.pce.2011.10.021

Holmén, J. (2019). "Transport of Dissolved Components, Heat Flow, Permafrost and Density Dependent Flow," in *Three-dimensional Coupled Flow and Heat Transport* (Toronto, Canada: Golder Associates). GEOAN, User's Guide, 28.

Huang, K., Dai, J., Wang, G., Chang, J., Lu, Y., Song, C., et al. (2020). The Impact of Land Surface Temperatures on Suprapermafrost Groundwater on the central Qinghai-Tibet Plateau. *Hydrological Process.* 34 (6), 1475–1488. doi:10.1002/hyp.13677

Hubbard, S. S., Williams, K. H., Agarwal, D., Banfield, J., Beller, H., Bouskill, N., et al. (2018). The East River, Colorado, Watershed: a Mountainous Community Testbed for Improving Predictive Understanding of Multiscale Hydrological-Biogeochemical Dynamics. *Vadose Zone J.* 17 (1), 180061. doi:10.2136/vzj2018.03.0061

Immerzeel, W. W., Lutz, A. F., Andrade, M., Bahl, A., Biemans, H., Bolch, T., et al. (2020). Importance and Vulnerability of the World's Water Towers. *Nature* 577, 364–369. doi:10.1038/s41586-019-1822-y

IPCC (2019). Special Report on the Ocean and Cryosphere in a Changing Climate. Available at: https://www.ipcc.ch/srocc/ (Accessed October 11, 2019).

Ireson, A. M., van der Kamp, G., Ferguson, G., Nachshon, U., and Wheater, H. S. (2013). Hydrogeological Processes in Seasonally Frozen Northern Latitudes: Understanding, Gaps and Challenges. *Hydrogeol. J.* 21 (1), 53–66. doi:10.1007/s10040-012-0916-5

Ivanov, V. Y., Vivoni, E. R., Bras, R. L., and Entekhabi, D. (2004). Catchment Hydrologic Response with a Fully Distributed Triangulated Irregular Network Model. *Water Resour. Res.* 40, W11102. doi:10.1029/2004wr003218

Jafarov, E. E., Coon, E. T., Harp, D. R., Wilson, C. J., Painter, S. L., Atchley, A. L., et al. (2018). Modeling the Role of Preferential Snow Accumulation in through Talik Development and Hillslope Groundwater Flow in a Transitional Permafrost Landscape. *Environ. Res. Lett.* 13 (10), 105006. doi:10.1088/1748-9326/aadd30

Jan, A., Coon, E. T., Graham, J. D., and Painter, S. L. (2018). A Subgrid Approach for Modeling Microtopography Effects on Overland Flow. *Water Resour. Res.* 54 (9), 6153–6167. doi:10.1029/2017wr021898

Jan, A., Coon, E. T., and Painter, S. L. (2020). Evaluating Integrated Surface/subsurface Permafrost thermal Hydrology Models in ATS (v0.88) against Observations from a Polygonal Tundra Site. *Geosci. Model. Dev.* 13, 2259–2276. doi:10.5194/gmd-13-2259-2020

Kang, S., Guo, W., Zhong, X., and Xu, M. (2020). Changes in the Mountain Cryosphere and Their Impacts and Adaptation Measures. *Clim. Change Res.* 16 (2), 143–152. (in Chinese). doi:10.12006/j.issn.1673-1719.2019.257

Karra, S., Painter, S. L., and Lichtner, P. C. (2014). Three-phase Numerical Model for Subsurface Hydrology in Permafrost-Affected Regions (PFLOTRAN-ICE v1.0). *The Cryosphere* 8, 1935–1950. doi:10.5194/tc-8-1935-2014

Kinar, N. J., and Pomeroy, J. W. (2015). Measurement of the Physical Properties of the Snowpack. *Rev. Geophys.* 53 (2), 481–544. doi:10.1002/2015rg000481

Kollet, S. J., and Maxwell, R. M. (2006). Integrated Surface-Groundwater Flow Modeling: A Free-Surface Overland Flow Boundary Condition in a Parallel Groundwater Flow Model. *Adv. Water Resour.* 29 (7), 945–958. doi:10.1016/j.advwatres.2005.08.006

Kollet, S., Sulis, M., Maxwell, R. M., Paniconi, C., Putti, M., Bertoldi, G., et al. (2017). The Integrated Hydrologic Model Intercomparison Project, IH-MIP2: a

Second Set of Benchmark Results to Diagnose Integrated Hydrology and Feedbacks. *Water Resour. Res.* 53, 867–890. doi:10.1002/2016wr019191

Kuffour, B. N. O., Engdahl, N. B., Woodward, C. S., Condon, L. E., Kollet, S., and Maxwell, R. M. (2020). Simulating Coupled Surface-Subsurface Flows with ParFlow v3.5.0: Capabilities, Applications, and Ongoing Development of an Open-Source, Massively Parallel, Integrated Hydrologic Model. *Geosci. Model. Dev.* 13 (3), 1373–1397. doi:10.5194/gmd-13-1373-2020

Kumar, J., Collier, N., Bisht, G., Mills, R. T., Thornton, P. E., Iversen, C. M., et al. (2016). Modeling the Spatiotemporal Variability in Subsurface thermal Regimes across a Low-Relief Polygonal Tundra Landscape. *The Cryosphere* 10 (5), 2241–2274. doi:10.5194/tc-10-2241-2016

Kumar, M., Duffy, C. J., and Salvage, K. M. (2009). A Second-Order Accurate, Finite Volume-Based, Integrated Hydrologic Modeling (FIHM) Framework for Simulation of Surface and Subsurface Flow. *Vadose Zone J.* 8 (4), 873–890. doi:10.2136/vzj2009.0014

Kurylyk, B. L., MacQuarrie, K. T. B., and McKenzie, J. M. (2014a). Climate Change Impacts on Groundwater and Soil Temperatures in Cold and Temperate Regions: Implications, Mathematical Theory, and Emerging Simulation Tools. *Earth-Science Rev.* 138, 313–334. doi:10.1016/j.earscirev.2014.06.006

Kurylyk, B. L., McKenzie, J. M., MacQuarrie, K. T. B., and Voss, C. I. (2014b). Analytical Solutions for Benchmarking Cold Regions Subsurface Water Flow and Energy Transport Models: One-Dimensional Soil Thaw with Conduction and Advection. *Adv. Water Resour.* 70, 172–184. doi:10.1016/j.advwatres.2014.05.005

Kurylyk, B. L., and Watanabe, K. (2013). The Mathematical Representation of Freezing and Thawing Processes in Variably-Saturated, Non-deformable Soils. *Adv. Water Resour.* 60, 160–177. doi:10.1016/j.advwatres.2013.07.016

Lamontagne-Hallé, P., Mckenzie, J. M., Kurylyk, B. L., Molson, J., and Lyon, L. N. (2020). Guidelines for Cold-regions Groundwater Numerical Modeling. *Wiley Interdiscip. Rev. Water* 7 (6), e1467. doi:10.1002/wat2.1467

Lamontagne-Hallé, P., McKenzie, J. M., Kurylyk, B. L., and Zipper, S. C. (2018). Changing Groundwater Discharge Dynamics in Permafrost Regions. *Environ. Res. Lett.* 13 (8), 084017. doi:10.1088/1748-9326/aad404

Langford, J. E., Schincariol, R. A., Nagare, R. M., Quinton, W. L., and Mohammed, A. A. (2020). Transient and Transition Factors in Modeling Permafrost Thaw and Groundwater Flow. *Groundwater* 58 (2), 258–268. doi:10.1111/gwat.12903

Lemieux, J.-M., Fortier, R., Murray, R., Dagenais, S., Cochand, M., Delottier, H., et al. (2020). Groundwater Dynamics within a Watershed in the Discontinuous Permafrost Zone Near Umiujaq (Nunavik, Canada). *Hydrogeol. J.* 28, 833–851. doi:10.1007/s10040-020-02110-4

Li, H., Li, X., Yang, D., Wang, J., Gao, B., Pan, X., et al. (2019). Tracing Snowmelt Paths in an Integrated Hydrological Model for Understanding Seasonal Snowmelt Contribution at basin Scale. *J. Geophys. Res. Atmos.* 124 (16), 8874–8895. doi:10.1029/2019jd030760

Liljedahl, A. K., Boike, J., Daanen, R. P., Fedorov, A. N., Frost, G. V., Grosse, G., et al. (2016). Pan-Arctic Ice-Wedge Degradation in Warming Permafrost and its Influence on Tundra Hydrology. *Nat. Geosci.* 9 (4), 312–318. doi:10.1038/ngeo2674

Lindström, G., Bishop, K., and Löfvenius, M. O. (2002). Soil Frost and Runoff at Svartberget, Northern Sweden-measurements and Model Analysis. *Hydrol. Process.* 16, 3379–3392. doi:10.1002/hyp.1106

Liu, S., Li, X., Xu, Z., Che, T., Xiao, Q., Ma, M., et al. (2018). The Heihe Integrated Observatory Network: A Basin-Scale Land Surface Processes Observatory in China. *Vadose Zone J.* 17 (1), 1–21. doi:10.2136/vzj2018.04.0072

Luo, L., Zhuang, Y., Zhang, M., Zhang, Z., Ma, W., Zhao, W., et al. (2020). An Integrated Observation Dataset of the hydrological-thermal-deformation Dynamics in the Permafrost Slopes and Engineering Infrastructure in the Qinghai-Tibet Engineering Corridor. *Earth Syst. Sci. Data* 13 (8), 4035–4052. doi:10.5194/essd-2020-106

Markstrom, S. L., Niswonger, R. G., Regan, R. S., Prudic, D. E., and Barlow, P. M. (2008). *GSFLOW–Coupled Ground-water and Surfacewater Flow Model Based on the Integration of the Precipitation-Runoff Modeling System (PRMS) and the Modular Ground-Water Flow Model (MODFLOW-2005)*. Reston, VA: U.S. Geological Survey Techniques and Methods Report, 6 (D1), 240.

Marsh, C. B., Pomeroy, J. W., and Wheater, H. S. (2020). The Canadian Hydrological Model (CHM) v1.0: a Multi-Scale, Multi-Extent, Variable-Complexity Hydrological Model - Design and Overview. *Geosci. Model. Dev.* 13 (1), 225–247. doi:10.5194/gmd-13-225-2020

Maxwell, R. M., Condon, L. E., and Kollet, S. J. (2015). A High-Resolution Simulation of Groundwater and Surface Water over Most of the continental US with the Integrated Hydrologic Model ParFlow V3. *Geosci. Model. Dev.* 8 (3), 923–937. doi:10.5194/gmd-8-923-2015

Maxwell, R. M., Putti, M., Meyerhoff, S., Delfs, J. O., Ferguson, I. M., Ivanov, V., et al. (2014). Surface-subsurface Model Intercomparison: A First Set of Benchmark Results to Diagnose Integrated Hydrology and Feedbacks. *Water Resour. Res.* 50, 1531–1549. doi:10.1002/2013wr013725

Mazzotti, G., Essery, R., Moeser, C. D., and Jonas, T. (2020). Resolving Small-Scale forest Snow Patterns Using an Energy Balance Snow Model with a One-Layer Canopy. *Water Resour. Res.* 56 (1), 026129. doi:10.1029/2019wr026129

McKenzie, J. M., Kurylyk, B. L., Walvoord, M. A., Bense, V. F., Fortier, D., Spence, C., et al. (2021). Invited Perspective: What Lies beneath a Changing Arctic. *The Cryosphere* 15 (1), 479–484. doi:10.5194/tc-15-479-2021

McKenzie, J. M., and Voss, C. I. (2013). Permafrost Thaw in a Nested Groundwater-Flow System. *Hydrogeol. J.* 21 (1), 299–316. doi:10.1007/s10040-012-0942-3

McKenzie, J. M., Voss, C. I., and Siegel, D. I. (2007). Groundwater Flow with Energy Transport and Water-Ice Phase Change: Numerical Simulations, Benchmarks, and Application to Freezing in Peat Bogs. *Adv. Water Resour.* 30 (4), 966–983. doi:10.1016/j.advwatres.2006.08.008

Melillo, J. M., Steudler, P. A., Aber, J. D., Newkirk, K., Lux, H., Bowles, F. P., et al. (2002). Soil Warming and Carbon-Cycle Feedbacks to the Climate System. *Science* 298, 2173–2176. doi:10.1126/science.1074153

Molson, J. W., and Frind, E. O. (2019). *HEATFLOW-SMOKER User Guide*. WaterlooCanada: Université Laval University of Waterloo, 132.

Niswonger, R. G., Panday, S., and Ibaraki, M. (2011). *MODFLOW-NWT, a Newton Formulation for MODFLOW-2005*. Reston, VA: U.S. Geological Survey Techniques and Methods Report. 6, A37. doi:10.3133/tm6a37

Nitze, I., Grosse, G., Jones, B. M., Romanovsky, V. E., and Boike, J. (2018). Remote Sensing Quantifies Widespread Abundance of Permafrost Region Disturbances across the Arctic and Subarctic. *Nat. Commun.* 9, 5423. doi:10.1038/s41467-018-07663-3

Niu, G.-Y., and Yang, Z.-L. (2006). Effects of Frozen Soil on Snowmelt Runoff and Soil Water Storage at a continental Scale. *J. Hydrometerol.* 7, 937–952. doi:10.1175/jhm538.1

Orgogozo, L., Prokushkin, A. S., Pokrovsky, O. S., Grenier, C., Quintard, M., Viers, J., et al. (2019). Water and Energy Transfer Modeling in a Permafrost-dominated, Forested Catchment of Central Siberia: The Key Role of Rooting Depth. *Permafrost and Periglac Process* 30 (2), 75–89. doi:10.1002/ppp.1995

Osuch, M., Wawrzyniak, T., and Nawrot, A. (2019). Diagnosis of the Hydrology of a Small Arctic Permafrost Catchment Using HBV Conceptual Rainfall-Runoff Model. *Hydrol. Res.* 50 (2), 459–478. doi:10.2166/nh.2019.031

Painter, S. L., Coon, E. T., Atchley, A. L., Berndt, M., Garimella, R., Moulton, J. D., et al. (2016). Integrated Surface/subsurface Permafrost thermal Hydrology: Model Formulation and Proof-Of-Concept Simulations. *Water Resour. Res.* 52 (8), 6062–6077. doi:10.1002/2015wr018427

Pomeroy, J. W., Gray, D. M., Brown, T., Hedstrom, N. R., Quinton, W. L., Granger, R. J., et al. (2007). The Cold Regions Hydrological Model: a Platform for Basing Process Representation and Model Structure on Physical Evidence. *Hydrol. Process.* 21, 2650–2667. doi:10.1002/hyp.6787

Qi, J., Wang, L., Zhou, J., Song, L., Li, X., and Zeng, T. (2019). Coupled Snow and Frozen Ground Physics Improves Cold Region Hydrological Simulations: an Evaluation at the Upper Yangtze River Basin (Tibetan Plateau). *J. Geophys. Res. Atmos.* 124 (23), 12985–13004. doi:10.1029/2019jd031622

Qin, D., Yao, T., Ding, Y., and Ren, J. (2017). *Introduction to Cryospheric Science*. Beijing: Science Press. (in Chinese).

Rasouli, K., Pomeroy, J. W., and Whitfield, P. H. (2019). Are the Effects of Vegetation and Soil Changes as Important as Climate Change Impacts on Hydrological Processes. *Hydrol. Earth Syst. Sci.* 23 (12), 4933–4954. doi:10.5194/hess-23-4933-2019

Rigon, R., Bertoldi, G., and Over, T. M. (2006). GEOtop: A Distributed Hydrological Model with Coupled Water and Energy Budgets. *J. Hydrometeorol.* 7 (3), 371–388. doi:10.1175/jhm497.1

Rivière, A., Jost, A., Gonçalvès, J., and Font, M. (2019). Pore Water Pressure Evolution below a Freezing Front under Saturated Conditions: Large-Scale Laboratory experiment and Numerical Investigation. *Cold Regions Sci. Tech.* 158, 76–94. doi:10.1016/j.coldregions.2018.11.005

Rühaak, W., Anbergen, H., Grenier, C., McKenzie, J., Kurylyk, B. L., Molson, J., et al. (2015). Benchmarking Numerical Freeze/thaw Models. *Energ. Proced.* 76, 301–310. doi:10.1016/j.egypro.2015.07.866

Rushlow, C. R., Sawyer, A. H., Voss, C. I., and Godsey, S. E. (2020). The Influence of Snow Cover, Air Temperature, and Groundwater Flow on the Active-Layer thermal Regime of Arctic Hillslopes Drained by Water Tracks. *Hydrogeol. J.* 28, 2057–2069. doi:10.1007/s10040-020-02166-2

Scheidegger, J. M., Busby, J. P., Jackson, C. R., McEvoy, F. M., and Shaw, R. P. (2017). *Coupled Modelling of Permafrost and Groundwater. A Case Study Approach (No. CR/16/053*. Keyworth, Notthingham: British Geological Survey, 359.

Scheidegger, J. M., Jackson, C. R., McEvoy, F. M., and Norris, S. (2019). Modelling Permafrost Thickness in Great Britain over Glacial Cycles. *Sci. Total Environ.* 666, 928–943. doi:10.1016/j.scitotenv.2019.02.152

Schilling, O. S., Cook, P. G., and Brunner, P. (2019a). Beyond Classical Observations in Hydrogeology: The Advantages of Including Exchange Flux, Temperature, Tracer Concentration, Residence Time, and Soil Moisture Observations in Groundwater Model Calibration. *Rev. Geophys.* 57 (1), 146–182. doi:10.1029/2018rg000619

Schilling, O. S., Park, Y.-J., Therrien, R., and Nagare, R. M. (2019b). Integrated Surface and Subsurface Hydrological Modeling with Snowmelt and Pore Water Freeze-Thaw. *Groundwater* 57 (1), 63–74. doi:10.1111/gwat.12841

Shen, C., and Phanikumar, M. S. (2010). A Process-Based, Distributed Hydrologic Model Based on a Large-Scale Method for Surface-Subsurface Coupling. *Adv. Water Resour.* 33, 1524–1541. doi:10.1016/j.advwatres.2010.09.002

Shojae Ghias, M., Therrien, R., Molson, J., and Lemieux, J.-M. (2017). Controls on Permafrost Thaw in a Coupled Groundwater-Flow and Heat-Transport System: Iqaluit Airport, Nunavut, Canada. *Hydrogeol. J.* 25 (3), 657–673. doi:10.1007/s10040-016-1515-7

Sjöberg, Y., Coon, E., K. Sannel, A. B., Pannetier, R., Harp, D., Frampton, A., et al. (2016). Thermal Effects of Groundwater Flow through Subarctic Fens: a Case Study Based on Field Observations and Numerical Modeling. *Water Resour. Res.* 52 (3), 1591–1606. doi:10.1002/2015wr017571

Sjöberg, Y., Jan, A., Painter, S. L., Coon, E. T., Carey, M. P., O'Donnell, J. A., et al. (2021). Permafrost Promotes Shallow Groundwater Flow and Warmer Headwater Streams. *Water Resour. Res.* 57, e2020WR027463. doi:10.1029/2020wr027463

Song, L., Wang, L., Li, X., Zhou, J., Luo, D., Jin, H., et al. (2020). Improving Permafrost Physics in a Distributed Cryosphere-hydrology Model and its Evaluations at the Upper Yellow River Basin. *J. Geophys. Res. Atmos.* 125 (18), e2020JD032916. doi:10.1029/2020jd032916

Svensson, U., and Ferry, M. (2014). DarcyTools: A Computer Code for Hydrogeological Analysis of Nuclear Waste Repositories in Fractured Rock. *J. Appl. Math. Phy.* 2 (6), 365–383. doi:10.4236/jamp.2014.26044

Svensson, U., Ferry, M., and Kuylenstierna, H. O. (2010). *DarcyTools, Version 3.4. Concepts, Methods and Equation (No. SKB R-07-38*. Stockholm, Sweden: Svensk Kärnbränslehantering AB, 134.

Teufel, B., and Sushama, L. (2019). Abrupt Changes across the Arctic Permafrost Region Endanger Northern Development. *Nat. Clim. Chang.* 9, 858–862. doi:10.1038/s41558-019-0614-6

Tian, Y., Zheng, Y., Han, F., Zheng, C., and Li, X. (2018). A Comprehensive Graphical Modeling Platform Designed for Integrated Hydrological Simulation. *Environ. Model. Softw.* 108, 154–173. doi:10.1016/j.envsoft.2018.08.011

Tokunaga, T. K., Wan, J., Williams, K. H., Brown, W., Henderson, A., Kim, Y., et al. (2019). Depth- and Time-Resolved Distributions of Snowmelt-Driven Hillslope Subsurface Flow and Transport and Their Contributions to Surface Waters. *Water Resour. Res.* 55, 9474–9499. doi:10.1029/2019wr025093

Voss, C. I., Provost, A. M., McKenzie, J. M., and Kurylyk, B. L. (2018). *SUTRA, A Model for Saturated-Unsaturated, Variable-Density Groundwater Flow with Solute or Energy Transport – Documentation of the Freeze-Thaw Capability, Saturation and Relative- Permeability Relations, Spatially Varying Properties, and Enhanced Budget and Velocity Output*. Reston, VA: U.S. Geological Survey Techniques and Methods Report, 150.

Waldner, P. A., Schneebeli, M., Schultze-Zimmermann, U., and Flühler, H. (2004). Effect of Snow Structure on Water Flow and Solute Transport. *Hydrol. Process.* 18 (7), 1271–1290. doi:10.1002/hyp.1401

Walvoord, M. A., and Kurylyk, B. L. (2016). Hydrologic Impacts of Thawing Permafrost—A Review. *Vadose Zone J.* 15 (6), 1–20. doi:10.2136/vzj2016.01.0010

Walvoord, M. A., Voss, C. I., Ebel, B. A., and Minsley, B. J. (2019). Development of Perennial Thaw Zones in Boreal Hillslopes Enhances Potential Mobilization of Permafrost Carbon. *Environ. Res. Lett.* 14 (1), 015003. doi:10.1088/1748-9326/aaf0cc

Wang, G., Lin, S., Hu, Z., Liu, Y., Sun, X., and Huang, K. (2020). Improving Actual Evapotranspiration Estimation Integrating Energy Consumption for Ice Phase Change across the Tibetan Plateau. *J. Geophys. Res. Atmos.* 125, e2019JD031799. doi:10.1029/2019jd031799

Wang, G. X., Mao, T. X., Chang, J., Song, C. L., and Huang, K. W. (2017a). Processes of Runoff Generation Operating during the spring and Autumn Seasons in a Permafrost Catchment on Semi-arid Plateaus. *J. Hydrol.* 550, 307–317.

Wang, L., Koike, T., Yang, K., Jackson, T. J., Bindlish, R., and Yang, D. (2009). Development of a Distributed Biosphere Hydrological Model and its Evaluation with the Southern Great Plains Experiments (SGP97 and SGP99). *J. Geophys. Res.* 114, D08107. doi:10.1029/2008jd010800

Wang, L., Zhou, J., Qi, J., Sun, L., Yang, K., Tian, L., et al. (2017b). Development of a Land Surface Model with Coupled Snow and Frozen Soil Physics. *Water Resour. Res.* 53 (6), 5085–5103. doi:10.1002/2017wr020451

Wellman, T. P., Voss, C. I., and Walvoord, M. A. (2013). Impacts of Climate, lake Size, and Supra- and Sub-permafrost Groundwater Flow on lake-talik Evolution, Yukon Flats, Alaska (USA). *Hydrogeol. J.* 21 (1), 281–298. doi:10.1007/s10040-012-0941-4

Wicky, J., and Hauck, C. (2017). Numerical Modelling of Convective Heat Transport by Air Flow in Permafrost Talus Slopes. *The Cryosphere* 11 (3), 1311–1325. doi:10.5194/tc-11-1311-2017

Winter, T. C., Harvey, J. W., Franke, O. L., and Alley, W. M. (1998). *Ground Water and Surface Water A Single Resource*. Denver, CO: U.S. Government Printing Office.

Woo, M. K. (2012). *Permafrost Hydrology*. Heidelberg: Springer.

Wu, X., Che, T., Li, X., Wang, N., and Yang, X. (2018). Slower Snowmelt in spring along with Climate Warming across the Northern Hemisphere. *Geophys. Res. Lett.* 45 (22), 12331–12339. doi:10.1029/2018gl079511

Xu, X., Wang, J., and Zhang, L. (2001). *Permafrost Physics*. Beijing: Science press. (in Chinese).

Yang, D., Gao, B., Jiao, Y., Lei, H., Zhang, Y., Yang, H., et al. (2015). A Distributed Scheme Developed for Eco-Hydrological Modeling in the Upper Heihe River. *Sci. China Earth Sci.* 58 (1), 36–45. doi:10.1007/s11430-014-5029-7

Yang, L., Song, X., Zhang, Y., Han, D., Zhang, B., and Long, D. (2012). Characterizing Interactions between Surface Water and Groundwater in the Jialu River Basin Using Major Ion Chemistry and Stable Isotopes. *Hydrol. Earth Syst. Sci.* 16 (11), 4265–4277. doi:10.5194/hess-16-4265-2012

Yang, M., Wang, X., Pang, G., Wan, G., and Liu, Z. (2019). The Tibetan Plateau Cryosphere: Observations and Model Simulations for Current Status and Recent Changes. *Earth-Science Rev.* 190, 353–369. doi:10.1016/j.earscirev.2018.12.018

Yang, S., Yang, D., Chen, J., Santisirisomboon, J., Lu, W., and Zhao, B. (2020). A Physical Process and Machine Learning Combined Hydrological Model for Daily Streamflow Simulations of Large Watersheds with Limited Observation Data. *J. Hydrol.* 590 (1), 125206. doi:10.1016/j.jhydrol.2020.125206

Yao, T., Thompson, L., and Yang, W. (2012). Different Glacier Status with Atmospheric Circulations in Tibetan Plateau and Surroundings. *Nat. Clim. Chang.* 1580, 1–5. doi:10.1038/nclimate1580

Yao, Y., Zheng, C., Andrews, C. B., Scanlon, B. R., Kuang, X., Zeng, Z., et al. (2021). Role of Groundwater in Sustaining Northern Himalayan Rivers. *Geophys. Res. Lett.* 48 (10), e2020GL092354. doi:10.1029/2020gl092354

Yao, Y., Zheng, C., Andrews, C., Zheng, Y., Zhang, A., and Liu, J. (2017). What Controls the Partitioning between Baseflow and Mountain Block Recharge in the Qinghai-Tibet Plateau. *Geophys. Res. Lett.* 44 (16), 8352–8358. doi:10.1002/2017gl074344

Yao, Y., Zheng, C., Liu, J., Cao, G., Xiao, H., Li, H., et al. (2014). Conceptual and Numerical Models for Groundwater Flow in an Arid Inland River basin. *Hydro. Process.* 29 (6), 1489–1492. doi:10.1002/hyp.10276

Zhang, X., Wang, Q., Yu, T., Wang, G., and Wang, W. (2018). Numerical Study on the Multifield Mathematical Coupled Model of hydraulic-thermal-salt-

mechanical in Saturated Freezing saline Soil. *Int. J. Geomech.* 18 (7), 04018064. doi:10.1061/(asce)gm.1943-5622.0001173

Zhang, Y., Cheng, G., Li, X., Han, X., Wang, L., Li, H., et al. (2013). Coupling of a Simultaneous Heat and Water Model with a Distributed Hydrological Model and Evaluation of the Combined Model in a Cold Region Watershed. *Hydrol. Process.* 27 (25), 3762–3776. doi:10.1002/hyp.9514

Zhao, L., Hu, G., Zou, D., Wu, X., Ma, L., Sun, Z., et al. (2019). Permafrost Changes and its Effects on Hydrologic Processes on Qinghai-Tibet Plateau. *Bull. Chin. Acad. Sci.* 34 (11), 1233–1246. (in Chinese). doi:10.16418/j.issn.1000-3045.2019.11.006

Zhou, J., Pomeroy, J. W., Zhang, W., Cheng, G., Wang, G., and Chen, C. (2014). Simulating Cold Regions Hydrological Processes Using a Modular Model in the West of China. *J. Hydrol.* 509 (4), 13–24. doi:10.1016/j.jhydrol.2013.11.013

Zipper, S. C., Lamontagne-Hallé, P., McKenzie, J. M., and Rocha, A. V. (2018). Groundwater Controls on Postfire Permafrost Thaw: Water and Energy Balance Effects. *J. Geophys. Res. Earth Surf.* 123 (10), 2677–2694. doi:10.1029/2018jf004611

Conflict of Interest: The authors declare that the research was conducted in the absence of any commercial or financial relationships that could be construed as a potential conflict of interest.

frontiers in Earth Science

ORIGINAL RESEARCH
published: 25 January 2022
doi: 10.3389/feart.2022.806022

Thermal Recovery of Backfilled Pit in the Gulianhe Strip Coalmine in the Hola Basin in Northern Da Xing'Anling Mountains, NE China

Ruixia He[1], Yan Li[1,2], Huijun Jin[1,2,3]*, Hongwei Wang[1], Xiaoying Jin[3], Meiquan Zhu[3], Xinyu Li[4], Yadong Huang[1,2], Doudou Jin[1,2] and Futing Ma[5]*

[1]State Key Laboratory of Frozen Soils Engineering, Da Xing'anling Observation and Research Station of Frozen-Ground Engineering and Environment, Northwest Institute of Eco-Environment and Resources, Chinese Academy of Sciences, Lanzhou, China, [2]School of Resources and Environment, University of Chinese Academy of Sciences, Beijing, China, [3]School of Civil Engineering, Institute of Cold Regions Science and Engineering, Northeast-China Observatory and Research-Station of Permafrost Geo-Environment (Ministry of Education), Northeast Forest University, Harbin, China, [4]School of Civil Engineering, Harbin Institute of Technology, Harbin, China, [5]Gulianhe Strip Coalmine, Heilongjiang, China

OPEN ACCESS

Edited by:
Guo Donglin,
Zhan Kezhen—Nansen International Research Center, Institute of Atmospheric Physics (CAS), China

Reviewed by:
Xiaoqing Peng,
Lanzhou University, China
Wansheng Pei,
Northwest Institute of Eco-Environment and Resources (CAS), China
Xicai Pan,
Institute of Soil Science (CAS), China

***Correspondence:**
Yan Li
liyan1@nieer.ac.cn
Huijun Jin
hjjin@nefu.edu.cn

Specialty section:
This article was submitted to Cryospheric Sciences, a section of the journal Frontiers in Earth Science

Received: *31 October 2021*
Accepted: *04 January 2022*
Published: *25 January 2022*

Citation:
He R, Li Y, Jin H, Wang H, Jin X, Zhu M, Li X, Huang Y, Jin D and Ma F (2022) Thermal Recovery of Backfilled Pit in the Gulianhe Strip Coalmine in the Hola Basin in Northern Da Xing'Anling Mountains, NE China. Front. Earth Sci. 10:806022. doi: 10.3389/feart.2022.806022

In the northern Da Xing'anling Mountains in Northeast China on the southern margin of the Eastern Asia permafrost body, the ground thermal state and boreal ecological environment are sensitive to climate change and human activities. Since the 1980s, the Hola Basin here has been continuously and extensively developed. In particular, open pits and later backfilling in strip coal mining alters land–atmospheric hydrothermal exchanges in permafrost regions, leading to serious damages to the permafrost environment and boreal forest. After mining, pits need to be backfilled timely and properly for hydrothermal recovery of Xing'an permafrost and the boreal ecological environment. In this study, based on the comparative analysis of monitored ground temperatures in backfilled and undisturbed areas, influencing factors of thermal recovery after backfilling were analyzed through numerical simulations. Results show that the thermal recovery of permafrost in the backfilled area is closely related to temperature, depth, material, and soil moisture content of backfill. The warmer, finer, and thicker the backfill soils, the longer the permafrost recovery. Thermal recovery of permafrost also depends on the moisture content of backfill; the shortest recovery occurs at 15–25% in the backfilled soil moisture content. Based on numerical simulations and combined with enlightenments from features of the ecosystem-protected Xing'an permafrost in Northeast China, a composite configuration of organic soil, crush-rock layer, and proper re-vegetation measures is advised. Based on prudent regulation of heat transfer modes, this composite backfilling method can effectively cool the backfilled ground and can even possibly offset the climate warming.

Keywords: strip coalmine, Xing'an permafrost, open-pit, backfilling, thermal recovery, influencing factor

1 INTRODUCTION

Coal is one of the important pillar industries in most northern countries. With the exploitation and transportation of coal resources, some problems of environmental pollution and ecological damage have become increasingly prominent and widely concerned, with serious impacts on the sustainable development of coalmine enterprises and the ecological environment (e.g., Bell et al., 2001; Pandey et al., 2014; Qian et al., 2017). Because of the harsh climate and fragile ecological environment in cold regions, mining activities will consequently alter hydrothermal exchanges and transport processes between the ground and atmosphere, resulting in adverse impacts to the hydrothermal stability of permafrost and a long-established ecological environment (e.g., Ding, 1988; Burov and Gresov, 2011; Cao et al., 2011; Demirel et al., 2011; James et al., 2013; Gao et al., 2017). In particular, strip coal mining disrupts, damages, or even destroys pristine boreal forests, original landforms, and intact surfaces, eventually resulting in land degradation and soil erosion, with mine pits reaching tens or even hundreds of meters in depth and leading to permafrost thinning or thaw; in the areas underlain by cold and thick permafrost, waters from melting ground ice, surface snowmelt and runoff, and precipitation gather at the bottom of mine pits, accelerating permafrost thaw (Zheng et al., 2000; Cao and Sheng, 2013; Li et al., 2014). At the same time, exposed cut slopes formed by strip mining are prone to collapse or landslides due to the thawing permafrost, and saturated gangue piles/hills are also prone to slumps, gelifluctions, debris flows, or mudflows (e.g., Hildebrand 1983; Peretrukhin and Potaueva 1983; Zheng et al., 2000; Jin et al., 2008; Cao and Sheng, 2013; Nauta et al., 2014; Zhang M. et al., 2015; Zhang et al., 2017; Booshehrian et al., 2020). In addition, the permafrost table was locally lowered due to the mining excavation, and the water-retaining properties of the permafrost layer will be dramatically weakened or totally lost; the water table may be lowered substantially and rapidly, and it becomes too deep for water availability for plant growth, leading to the succession of the biological community and the ecological environment (Wang et al., 2004; Quinton et al., 2005; Cao et al., 2011; Quinton and Baltzer, 2013; Gao et al., 2017). Therefore, it is important to protect the natural environment in the processes of coal resource exploitation and to propose reasonable, economical, and effective measures for solving engineering problems in the mining area. At present, pit backfilling is the most effective and economical method for land reclamation after coal mining. It not only reduces geohazard risks and protects the environment but also helps recover surface vegetation after land reclamation (e.g., Moreno-de Las Heras et al., 2009; Erener, 2011; Zhang L. et al., 2015; Wang et al., 2016, 2021a, 2021b). Timely and proper backfilling might also benefit the recovery of ground temperature and the permafrost environment. However, existing research mainly focuses on the influences of the topography and backfill properties of strip coalmines on the re-vegetation in permafrost areas. Only few research works are carried out on the evaluation methods of the permafrost environment and numerical simulations of the impacts of excavation backfilling on the permafrost recovery in strip coal mines. Because of paucity of field monitoring data, the influencing mechanisms for and factors on ground temperature recovery in backfill areas have not yet been studied systematically (e.g., Li et al., 2014; Cao et al., 2016; Gao et al., 2017). In summary, inadequate attention has been paid on thermal recovery processes after backfilling in permafrost regions and their influencing mechanisms and factors. In particular, key influencing factors for the thermal recovery of backfilled soils, such as backfill materials and their properties, are seldom mentioned.

The Gulianhe strip coalmine in the Hola Basin is in the discontinuous permafrost zone in the northern Da Xing'anling Mountains in Northeast China. The region is characterized by extensive and stable winter air temperature inversion, thick surficial deposits, dense vegetation, stable snow cover, and extensive distribution of intermontane wetlands. In the discontinuous permafrost zone in the north, permafrost generally forms in the low-lying and north-facing landscape conditions, and is protected by ecosystems; its distribution displays strong spatial variations. It is thus the ecosystem-protected permafrost (Shur and Jorgenson, 2007). Therefore, this ecosystem-protected permafrost in the northern part of Northeast China is generally referred to as the "Xing'an permafrost" for its distinct developing and the growth environment in boreal forests and wetlands (Zhou et al., 2000; Jin et al., 2008). In comparison with the permafrost on the Qinghai–Tibet Plateau, the Xing'an permafrost are less sensitive to climate changes, but they are more responsive to human activities or other external disturbances that may modify or alter surface covers and drainage conditions (e.g., mining and transportation, land cultivation and reclamation, deforestation, urbanization, and forest fires).

The Gulianhe coalmine has been adopting the strip-mining techniques since it was put into production in 1992. During the mining process, the seasonally thawed layer over permafrost (active layer) was stripped in advance and the permafrost soil was thawed at first, followed by downward digging/stripping layer by layer. Mining activities in combination with the overburden and rock dumping/disposal greatly damaged or destroyed the original natural surface and vegetation cover, leading to damages to the vulnerable permafrost environment and delicate ecological balance of boreal forest. Now, there are dozens of pits in the mining areas in the Hola Basin. These open pits are generally 60,000–100,000 m^2 in areal extent and 25–40 m in depth. Extensive engineering infrastructures, such as open pits, gangue piles, waste banks, and access/trucking roads, have become major drivers for an accelerated degradation of Xing'an permafrost in the Hola Basin (Serban et al., 2021). Evidently, timely restoration of the permafrost environment and maintenance of the local balance of boreal ecology for sustainable development of mining areas are generally mandated, and the hydrothermal responses of the backfilled open pits in frozen ground are worth systematic and in-depth studying. However, due to the chronic thermal recovery of permafrost, studies on changes in ground temperature require long-term monitoring data. Thus, numerical simulations and field monitoring can be combined to analyze the recovery processes of permafrost and their influencing factors.

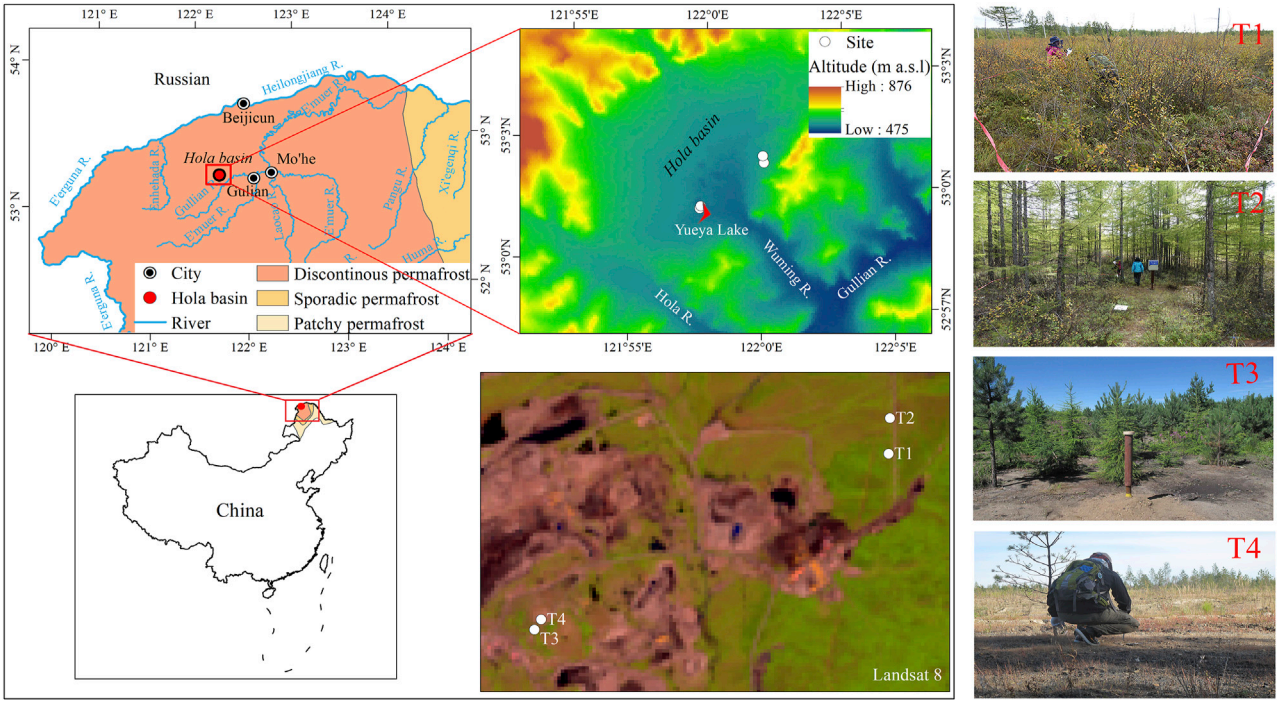

FIGURE 1 | Study region and sites in the Gulianhe Strip coalmine in the Hola Basin in the northern Da Xing'anling Mountains in Northeast China.

In our study, first, two representative backfilled and undisturbed areas were selected for monitoring ground temperatures. Then a numerical model for heat transfer in permafrost regions was established for studying the influencing factors of heat transfer. Finally, through the comparisons of simulated and monitored data of backfill temperature, ground temperatures during backfilling and the backfilling time, we identified the major influencing factors for ground temperature recovery. The study can provide key scientific support for environmental protection and ecological restoration of open pit coalmines in the boreal forest in permafrost zones.

2 MATERIALS AND METHODS

2.1 Study Area

As a representative intermontane basin at relatively high latitudes in the northern Da Xing'anling Mountains, the Hola Basin (52°57′–53°03′N, 121°52′–122°04′E) (**Figure 1**) is encircled by forested low hills, with an areal extent of about 60 km^2, and the peripheral mountains of the Hola Basin, about 130 km^2. The fault-depressed Hola Basin is high in the north, sloping gently southward.

The study area has a cold, continental climate in the northern temperate zone. Due to strong influences of alternating monsoons, regional climate is characterized by long, dry, and cold winters and short, moist, and warm summers, without distinct spring and autumn seasons. According to the data from the Mo'he meteorological station (196,1–2020), the mean annual air temperature (MAAT) was −4.1°C; the recorded minimum and maximum air temperatures reached at −46.7°C (December 27, 1968) and 28.1°C (June 27, 2010), respectively. MAAT was warming at a rate of about 0.035°C/a during 1961–2020. The average annual precipitation was 440 mm.

Before the 1980s, the measured permafrost thickness at the bottom (center) of the Hola Basin was 70–100 m (the maximum at 130 m) and that in the periphery transition zone was 40–50 m; it was finally thinned to 10–20 m at the slope toes of surrounding hills. Ground temperature at the depth of zero annual amplitude (T_{ZAA}) increased from −3.5 ~ −3.0 C at the center to −0.5°C on the margin of the basin. Taliks were mainly distributed on the tops of low hills and gentle sunny slope toes around the Hola Basin (Guo et al., 1989; Wang et al., 1989; He et al., 2015). Prior to the 1980s, the Hola Basin was a pristine boreal forest dominated by Xing'an larch (*Larix gmelinii*) and Scotch pine (*Pinus sylvestris*). The mixed broadleaf–conifer forest extends from the gentle slope toes to the bottom of the basin. The main tree species were Xing'an larch (*Larix gmelinii*), Asian white birch (*Betula platyphylla*), and Scotch pine (*Pinus sylvestris*), and the undergrowth, *Vaccinium uliginosum* Linn. and *Betula fruticose* Pallas. *Carex tato* wetlands and shrub-*Carex tato* wetlands were extensively developed on the bottom of the basin.

The large-scale resource exploitations in the Hola Basin, especially the strip coal mining since the 1990s, have severely disturbed the local ecological environment. Field investigations have found great changes in the surrounding permafrost environment in comparison with that before mining (Serban

TABLE 1 | Detailed information of four boreholes for ground temperature measurements at the backfilled and undisturbed areas in the Gulianhe strip coalmine in the Hola Basin in the northern Da Xing'anling Mountains in Northeast China.

Borehole	T1	T2	T3	T4
Latitude (°N)	53°00.889′	53°00.989′	53°00.463′	53°00.511′
Longitude (°E)	122°00.951′	122°00.928′	121°58.521′	121°58.574′
Elevation(m a. s. l.)	535	532	522	523
Monitoring depth (m)	20	20	20	20
Backfill depth (m)	—	—	2.6	20
Backfill material	—	—	Gravel	Coal gangue/slag
Surface characteristics	*Carex tato* and shrubs	*Larix gmelinii*	Planted *Larix gmelinii*	Bare ground
Time period	2017–2020	2017–2020	2015–2020	2015–2020

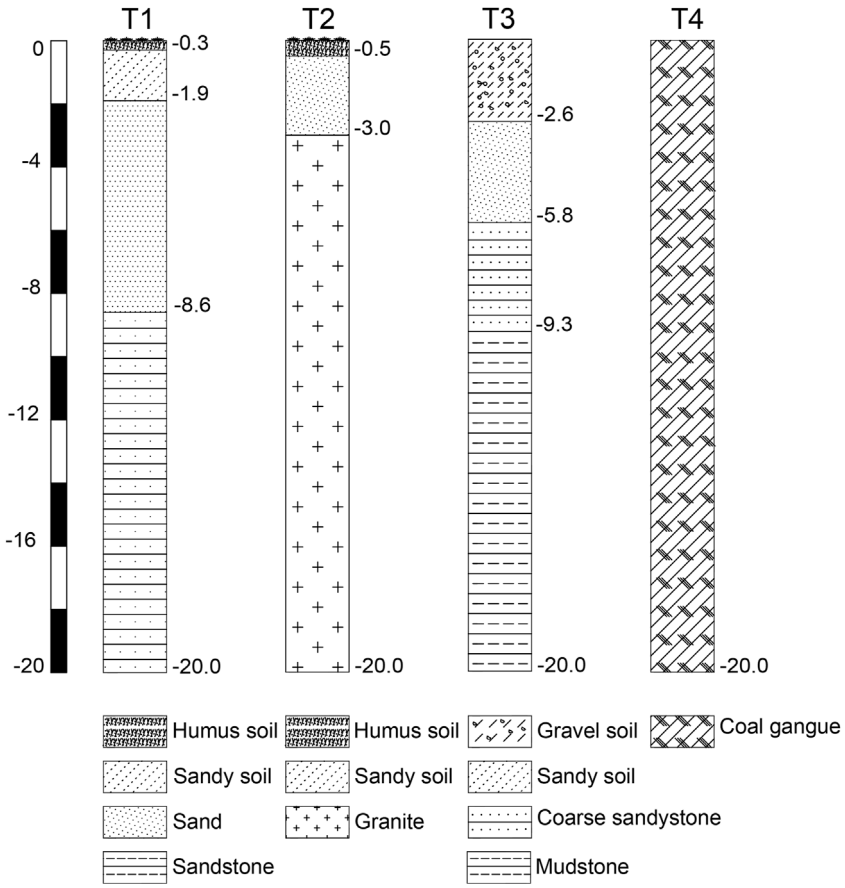

FIGURE 2 | Lithology at the four monitoring boreholes in the backfilled and undisturbed areas in the Gulianhe strip coalmine in the Hola Basin in northern Da Xing'anling Mountains in Northeast China.

et al., 2021). To facilitate the mandated ecological recovery, some open pits were backfilled in 2007.

2.2 Data Monitoring

2.2.1 Site Descriptions and Measurements

Two areas (undisturbed and backfilled) (**Figure 1**) in the Hola Basin were selected to study the influences of pit backfilling in strip coalmines on permafrost recovery. A pristine forestland with minor anthropogenic disturbances in the northern Hola Basin was chosen as the undisturbed area. Two ground temperature boreholes of 20.0 m in depth (**Figure 1**) were established in shrub-*Carex tato* wetland (T1) and *Larix gmelinii* (T2) forest at this undisturbed area in September 2017. In mining areas, some excavated pits were backfilled in summer and autumn 2007 for ecological restoration. The other two boreholes (T3 and T4, both 20.0 m in depth) (**Figure 1**) were established in the backfilled area in August 2014. Borehole T3 was established at the experimental forest plot of Northeast Forestry University, with a 2.6-m thick backfill covered by a dry ground surface re-planted with *Larix gmelinii* and *Betula platyphylla*.

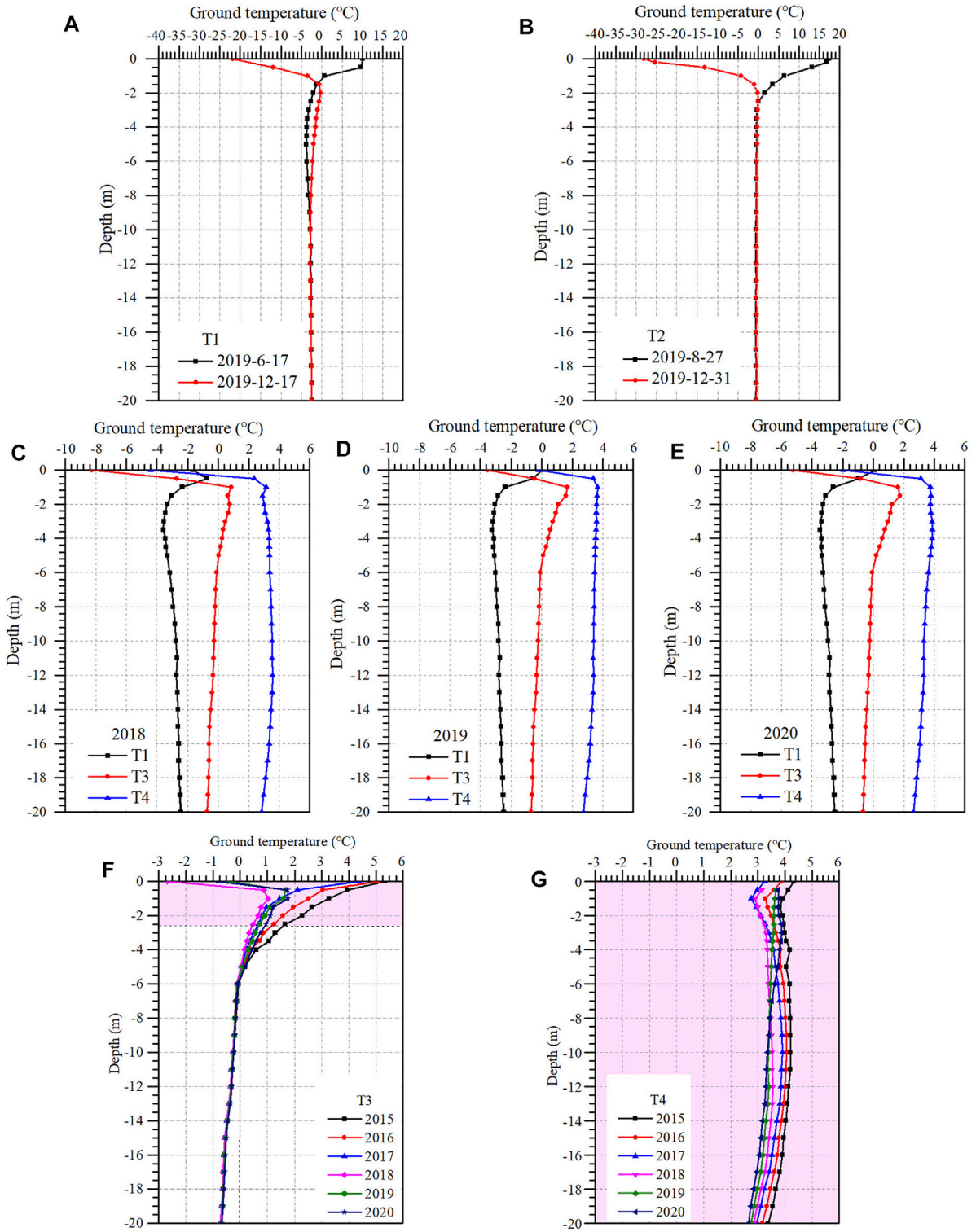

FIGURE 3 | Ground temperatures in the Gulianhe strip coalmine in the Hola Basin in the northern Da Xing'anling Mountains, Northeast China. Notes: **(A,B)** ground temperature–depth profiles in Boreholes T1 and T2 in the undisturbed area, respectively, in 2019; **(C–E)** mean annual temperatures of soil at all measured depths in Boreholes T1 (undisturbed area), T3 (2.6 m backfill), and T4 (20 m backfill), respectively, from 2018 to 2020; and **(F,G)** measured mean annual soil temperature at depths of 0–20 m in Boreholes T3 and T4 in the backfilled area, respectively, in 2015–2020. The rectangles in purple represent the depth of the backfilled layer.

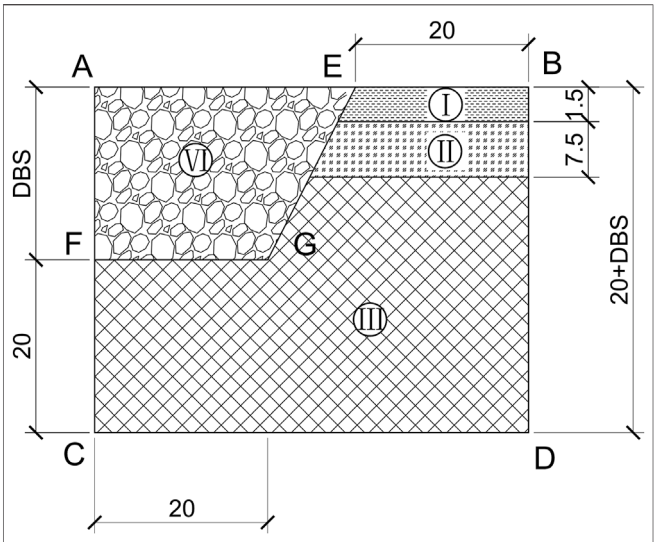

FIGURE 4 | Physical model of the pit backfill domain in the Gulianhe strip coalmine in the Hola Basin in northern Da Xing'anling Mountains, Northeast China.

Borehole T4 was established in the center of the backfilled zone, with a backfill thicker than 20.0 m. The detailed information and lithology of four boreholes are shown in **Table 1** and **Figure 2**.

Thermistor cables (with an accuracy of ±0.05°C in the laboratory), assembled in the State Key Laboratory of Frozen Soils Engineering (SKLFSE), were permanently installed in encased steel tubes every 0.5 m at depths of 0–5 m and every 1.0 m at depths of 5–20 m. Ground temperature was acquired by CR3000 data loggers in the undisturbed area (Boreholes T1 and T2) at a frequency of six times daily since October 2017. Ground temperatures in Boreholes T3 and T4 were manually measured every 10 or 15 days since September 2014.

2.2.3 Monitoring Results and Analysis

Figures 3A,B show the ground temperature–depth profiles of Boreholes T1 and T2 in the warm and cold seasons in 2019. For Borehole T2, the maximum seasonal thaw depth was approximately 2.5 m, and the 3-year average of T_{ZAA}(10 m) was −0.43°C, indicating an area of warm permafrost. At Borehole T1, the maximum seasonal thaw depth was about 1.6 m, and the 3-year average of T_{ZAA} (15 m) was close to −2.83°C.

Boreholes T3 and T4 are in the pit backfilled area after coal mining. **Figures 3C–E** show mean annual soil temperatures in Borehole T1 in the undisturbed area and Boreholes T3 and T4 from 2018 to 2020. Evidently, the thermal influence of coal mining on permafrost temperature is great and increases with backfill thickness.

For Borehole T3, annual maximum thaw depth increased from 2.6 m in 2018 to 6.0 m in 2020. However, after pit backfilling, soil temperatures of the upper layer declined, indicating a rapidly cooling backfill. For Borehole T4, soil temperature was positive at depths of 0–20 m (**Figures 3F,G**), indicating a talik since backfilling. However, after backfilling in 2007, by comparing changes in mean annual soil temperatures in the observed 6 years (2015–2020), ground temperature was declining at an average cooling rate of 0.2°C/a.

Field observations indicate great impacts of coal mining on ground temperature, directly thawing permafrost in the mining area. However, ground temperature lowered after the pit backfilling, indirectly proving the good thermal effect of the backfill on ground thermal regimes.

2.3 Mathematical Model Descriptions

2.3.1 Physical Models

Recovery of permafrost can be evaluated by changes in ground temperature, the single most important indicator of the ground thermal state. **Figure 4** shows the physical model of the backfilled domain. It is built on the actual permafrost distribution, mining status, and coalmine geometry. According to the results of borehole drilling, the original lithology at the backfilled location can be roughly divided into three layers, namely, sandy clay (Layer Ⅰ), sand (Ⅱ), and weathered sandstone (Ⅲ), and layer Ⅳ (backfill) unconformably contacts with three of other layers in the upper boundaries. The surrounding area is assumed infinite in the computation. However, for convenience in calculation, we defined the horizontal and vertical dimensions in the thermally impacted range of mining areas and assumed an adiabatic boundary. The backfill area in the model is thus two-dimensional and symmetrical. Therefore, half of the model domain is taken for calculation. We also assumed the spatial homogeneity for backfilled material and temperature distribution.

The basic assumptions of the numerical model calculation are as follows: 1) the thermal disturbance of the soil at the bottom of the pit is neglected after the pit is mined; that is, the ground temperature at the bottom of the pit is calculated based on the permafrost changes with depth in the natural state; 2) the backfill soil has uniform soil quality, porosity, and water content, regardless of the effect of water flow; and 3) the surface elevation after backfilling is consistent with the natural surface.

2.3.2 Governing Equations

Frozen soil is a relatively discrete porous medium, in which heat is mainly conducted in the soil, and convection, advection, and radiation can be ignored. It is assumed that soil layers are homogeneous and isotropic, without water replenishment and without heat convection due to water migration. For frozen soil with freeze–thaw cycles, the phase changes of ice–water need to be considered; heat convection and advection and other effects are ignored, and the unfrozen water content is only a function of temperature. Therefore, frozen soil undergoes an unsteady heat transfer process with phase change, and the equation of temperature field is governed by the following:

$$C^{*}\frac{\partial T}{\partial t}=\frac{\partial}{\partial x}\left(\lambda^{*}\frac{\partial T}{\partial x}\right)+\frac{\partial}{\partial y}\left(\lambda^{*}\frac{\partial T}{\partial y}\right), \tag{1}$$

where C^{*} and λ^{*} represent the effective volumetric heat capacity and thermal conductivity of soil, respectively, and T is the soil temperature. Considering that the specific heat capacity and thermal conductivity of soil vary under freezing, frozen, thawing, and thawed conditions, and assuming that the

TABLE 2 | Thermal parameters of different media (based on Leng, 2011; Liang et al., 2018; Yang, 2018; Pei et al., 2019; Mu et al., 2020).

Thermal parameters		C_u (In 10^6 J/(m^3·K))	C_f (In 10^6 J/(m^3·K))	λ_u (W/(m·K))	λ_f (W/(m·K))	L (in 10^6 J/m^3)
Silty clay		2.357	1.879	1.125	1.351	60.3
Gravel soil		3.170	2.210	1.060	1.380	132.0
Weathered rock		2.099	1.846	1.474	1.824	37.7
Backfilling soil	Pebbly sand	2.456	1.825	1.450	1.651	20.4
	Crushed rock	1.015	1.015	0.387	0.387	0
	Coal gangue	1.800	1.800	0.251	0.251	0
	Sandy clay	2.677	2.208	1.240	1.380	106.8

ice–water phase changes occur in a temperature range $[\ T_b\ ,\ T_p\ ]$, the effective volumetric heat capacity ($C*$) and effective thermal conductivity ($\lambda*$) can be described as follows (Bonacina et al., 1972; Zhang M. et al., 2015):

$$C^* = \begin{cases} C_f & T < T_b \\ \dfrac{C_f + C_u}{2} + \dfrac{L}{T_p - T_b} & T_b < T < T_p \\ C_u & T > T_p \end{cases}, \quad (2)$$

$$\lambda^* = \begin{cases} \lambda_f & T < T_b \\ \lambda_f + \dfrac{\lambda_u - \lambda_f}{T_p - T_b}(T - T_b) & T_b < T < T_p \\ \lambda_u & T > T_p \end{cases}, \quad (3)$$

where C_f and C_u refer to the volumetric heat capacity of frozen and unfrozen soils, respectively; λ_f and λ_u represent the thermal conductivity coefficient of frozen and unfrozen soils, respectively; and L denotes the latent heat of phase change per unit volume. Thermal parameters of the different layers are listed in **Table 2**.

If the backfill material is crushed rock, the air on the rock layer flows under an unstable pressure gradient, so the convective heat transfer process of the air in the crushed rock should be considered (Pei et al., 2019), and then the governing equation of the crushed rock can be rewritten by the following equation:

$$C_c^* \frac{\partial T}{\partial t} = \frac{\partial}{\partial x}\left(\lambda_c^* \frac{\partial T}{\partial x}\right) + \frac{\partial}{\partial y}\left(\lambda_c^* \frac{\partial T}{\partial y}\right) - C_{air}\rho_{air}\left(V_x \frac{\partial T}{\partial x} + V_y \frac{\partial T}{\partial y}\right), \quad (4)$$

where C_c^* is the effective volumetric heat capacity of crushed rock; λ_c^* is the effective thermal conductivity of crushed rock; C_{air} is the specific heat of air at a constant pressure, the value is taken as $1.004 \times 10^4\ (J/(kg \cdot K))$; ρ_{air} is the density of the air, the value is taken as 0.641 (kg/m^3); and V_x and V_y are the velocity components in the x and y directions, respectively, in the space coordinate system.

2.3.3 Boundary and Initial Conditions

2.3.3.1 Boundary Conditions

For this permafrost temperature numerical model, the boundary conditions are as follows:

1) Upper boundary condition

The upper surface temperature of the model is affected by air temperature, climate warming rate, solar radiation, precipitation, evaporation, and insulation effects of snow and vegetation covers (Wang et al., 2021b). According to Zhu (1988), temperature on the natural ground surface (Plane AB in **Figure 4**) varies as follows:

$$T(t_h) = T_0 + \frac{\Delta T_{warm}}{8760} t_h + A \times \sin\left(\frac{2\pi}{8760} t_h + \frac{\pi}{2} + \alpha_0\right), \quad (5)$$

where T_0 is the mean annual ground surface average temperature, taken as −3.5°C (Luo et al., 2014); ΔT_{warm} represents the warming rate of MAAT, 0.05°C/a (Jin et al., 2008); the annual amplitude of temperature A is 23 °C based on the meteorological record at Mo'he, Heilongjiang Province, China; and t_h is the time in hour.

Assuming a higher MAAT of the atmosphere–backfill boundary (AE) $[T(t_h)]$ than the natural ground surface (AB), $(T(t_h))$ is written as follows:

$$T(t_h) = T_0 + \Delta T + \frac{\Delta T_{warm}}{8760} t_h + A \times \sin\left(\frac{2\pi}{8760} t_h + \frac{\pi}{2} + \alpha_0\right), \quad (6)$$

where ΔT is the temperature increment and the value is 1.0°C.

2) Bottom boundary (Plane CD) condition

The thermal boundary temperature gradient at the bottom of the model domain is small and relatively stable, which is taken as the second type of boundary condition, that is, the Neumann boundary condition of known heat flux density. According to regional geological data (Mu et al., 2020), the geothermal heat flux is taken as $0.04\ W/m^2$.

3) Lateral boundary (Planes AC and BD) conditions

According to the assumptions for the physical model, one of the lateral boundaries, namely, AC, is symmetrical, and the other boundary BD is adiabatic.

2.3.3.2 Initial Conditions

Due to the hydrothermal impacts of coal mining on geothermal fields of the periphery permafrost and active layer, observed values cannot be used as the initial temperature in model simulations. Thus, the initial ground temperature of the model is obtained by long-term transient calculation with the upper boundary conditions (**Eq. 5**) without considering climate

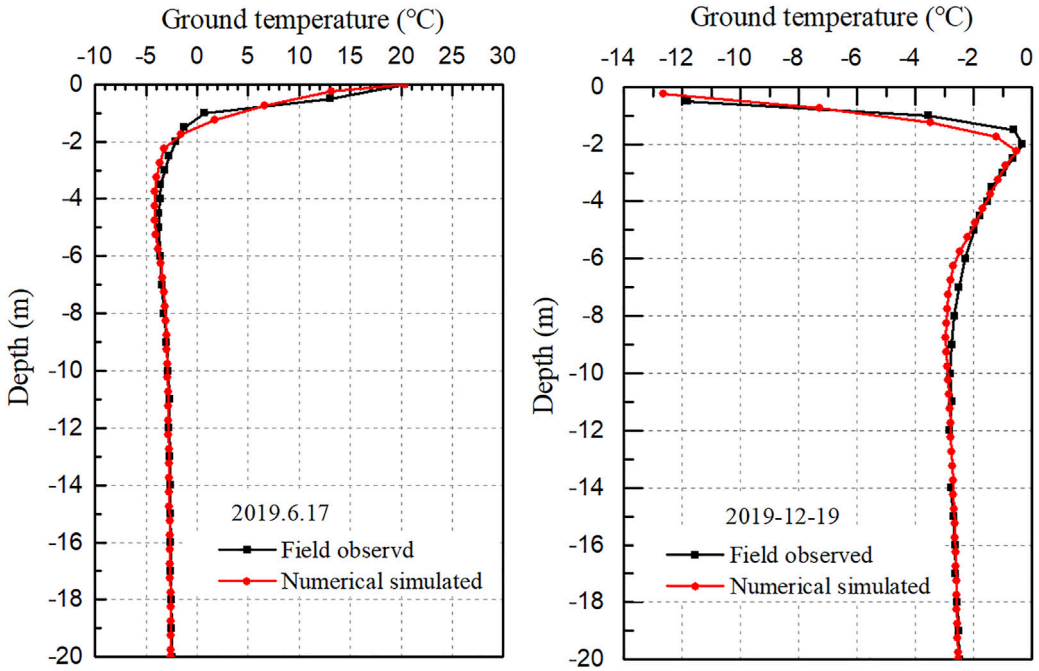

FIGURE 5 | Comparison between field observation data and numerical simulation results for ground temperatures in Borehole T1 at the undisturbed area in the Gulianhe strip coalmine in the Hola Basin in northern Da Xing'anling Mountains, Northeast China.

warming (Zhang et al., 2011) until the temperature field below the annual change layer remains basically unchanged, and ground temperature at the same location above the annual change layer remains the same every year.

3. NUMERICAL SIMULATION RESULTS AND ANALYSES

3.1 Numerical Model and Parameterization Validation

Validation and parameterization of numerical model are based on field monitoring data of ground temperature in Borehole T1. Numerical simulation results of ground temperatures in the permafrost zone are in good agreement with field monitoring data, as indicated in the similar changing trends of simulated and monitored ground temperatures (**Figure 5**). For the active layer, however, ground temperatures differ appreciably between the two (the numerical simulation result is about 0.15°C higher than the measured), which is possibly because of neglecting the insulation effect of surface vegetation and organic soil in the superficial layer in the numerical model. There are also certain deviations in model parameterization. Overall, simulation results are highly consistent with field observed data. Thus, the numerical model could be reliably used to evaluate the thermal influences of the pit backfilling.

3.2 Numerical Simulation Conditions

Strip coal mining activities have disturbed the thermal state of ambient and underlying permafrost. Large mine pits and subsequent water ponding and drainage would thaw the ambient and underlying permafrost of mine pits, possibly forming new taliks or expanding the nearby existing taliks. Therefore, mine pits should be timely backfilled after coal mining to facilitate permafrost and ecological recovery. However, annual average ground (backfill) and air temperatures, properties of backfilled soils, and pit depth are important factors for the hydrothermal recovery of the backfilled ground. Thus, four variables, that is, temperature of backfilling soils (TBS: 0, 2, 5, 10, 15, and 20°C), depth of backfill soils (DBS: 2.6, 5, 10, 15, 20, and 30 m), moisture content of backfilled soils (MCBS: 10, 15, 20, 25, 30, and 35%), and material of backfill soils (MBS: crushed rock, pebbly sand, coal gangue, and sandy clay), were evaluated in model simulations for a time span of over 50 years.

3.3 Influencing Factors for Long-Term Ground Temperature Recovery

3.3.1 Temperature of Backfilling Soil

After pit backfilling, the heat brought into the ground by the backfilled soil cannot dissipate immediately and completely. Heat dissipation would affect the temperature of ambient soils, even leading to the thawing of the underlying and ambient permafrost. TBS is important for the recovery time of ground temperature (Gao et al., 2017). Thus, mine pits should be backfilled timely, preferably in cold seasons, for rapid recovery of ground temperature field. In this study, the modeled pit is 20 m deep and backfilled with pebbly sand. Four cases with different TBS (0, 2, 5, 10, 15, and 20°C) are analyzed and evaluated (**Figure 6**).

Variations in centerline ground temperature of the backfilled ground over the next 50 years are shown in **Figure 6**. Evidently, TBS has an important effect on the

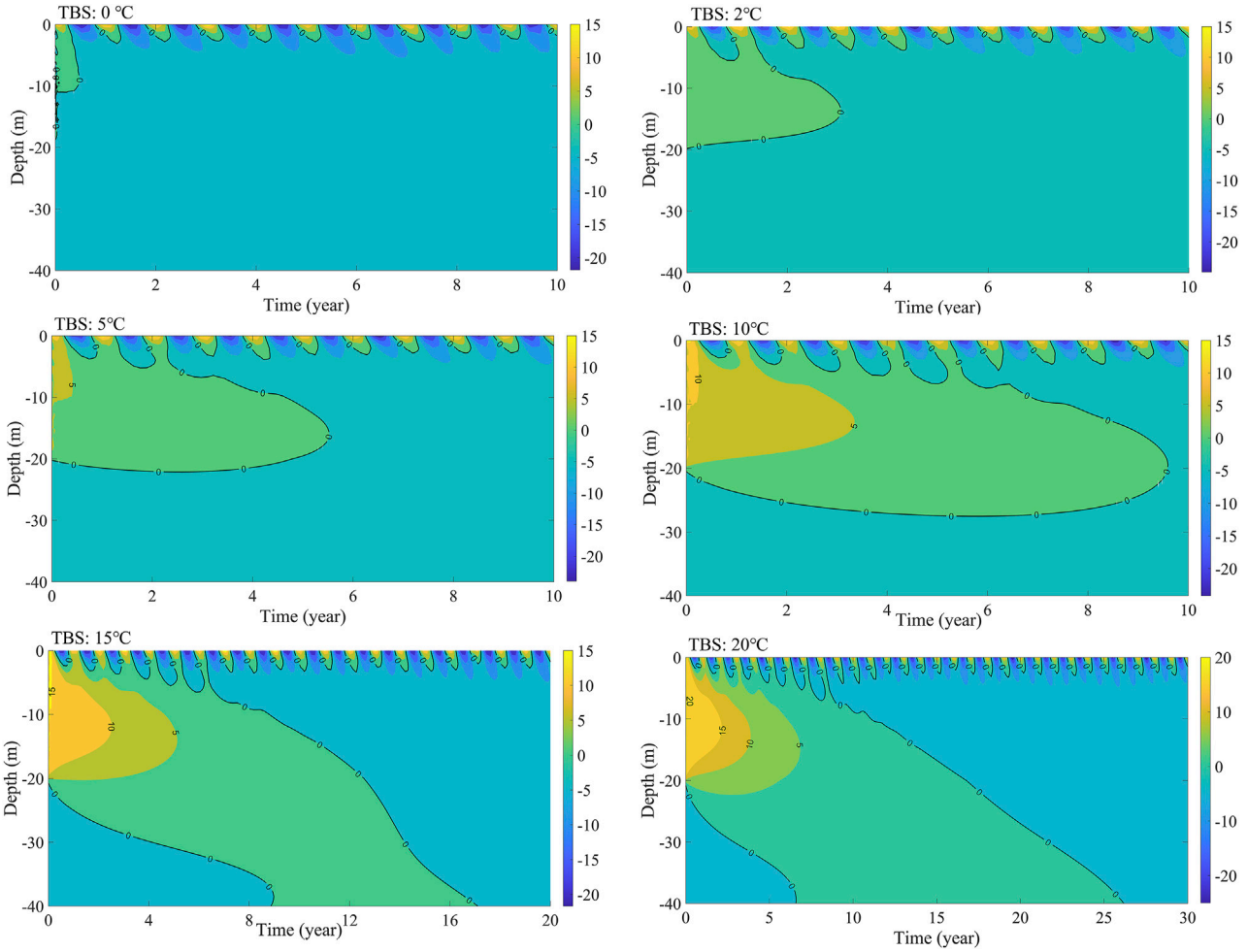

FIGURE 6 | Variations in centerline temperature of the backfilled area under different temperatures of the backfilling soil (TBS) scenarios (0, 2, 5, 10, 15, and 20°C).

thermal recovery. TBS has a negative correlation with the thermal recovery time due to the main conductive mode of heat transfer in soil; to cool the warmer soil, more heat needs to be released. Thus, it takes more time to re-balance with the ambient environment. Clearly, regardless of other factors, when the TBS is 0, 2, 5, 10, 15, and 20°C, the ground temperature recovery time would be 0.3, 3.7, 9, 17, and 26 years, respectively. Notably, as TBS increases, heat transfer between the backfilled ground and ambient permafrost gradually increases; meanwhile, it takes longer to cool and freeze the ground. **Figure 7** shows the non-linear growth relationship between TBS and recovery time of the backfilled pit, and the relationship can be fitted as follows:

$$t_r = 32.05 \times e^{-0.027T} - 30.82, \quad (7)$$

where t_r is the recovery time (a) and T is the TBS (temperature of the backfilling soil).

3.3.2 Depth of Backfilled Soil

The deeper the excavated pit of strip coalmine, the greater scope and scale of thermal impacts on ambient soils. Especially in permafrost regions, it will take longer time for areas with deep pits to freeze back after backfilling. Six cases with different DBS (2.6, 5, 10, 15, 20, and 30 m) were analyzed in this study (**Figure 8**). The simulation parameters (TBS at 15°C and MBS, pebbly sand) are used to analyze and evaluate the ground temperature distribution. As DBS increases, the thermal recovery also prolongs (**Figure 8**). For example, when the DBS is 2.6 m, ground temperature would recover in the second year after backfilling, while when the DBS reaches 30 m, it will take 50 years for ground refreezing. At the same time, after backfilling, permafrost at the lower part of pit is thermally affected by backfilling, and ground temperature rises and permafrost thaws, forming a thawed interlayer.

As shown in **Figure 9**, there is a non-linear growth relationship between the recovery time and DBS, as follows:

$$t_r = 8.021 \times e^{-0.027H} - 8.734, \quad (8)$$

where t_r is the recovery time (a) and T is the DBS (depth of backfilled soil).

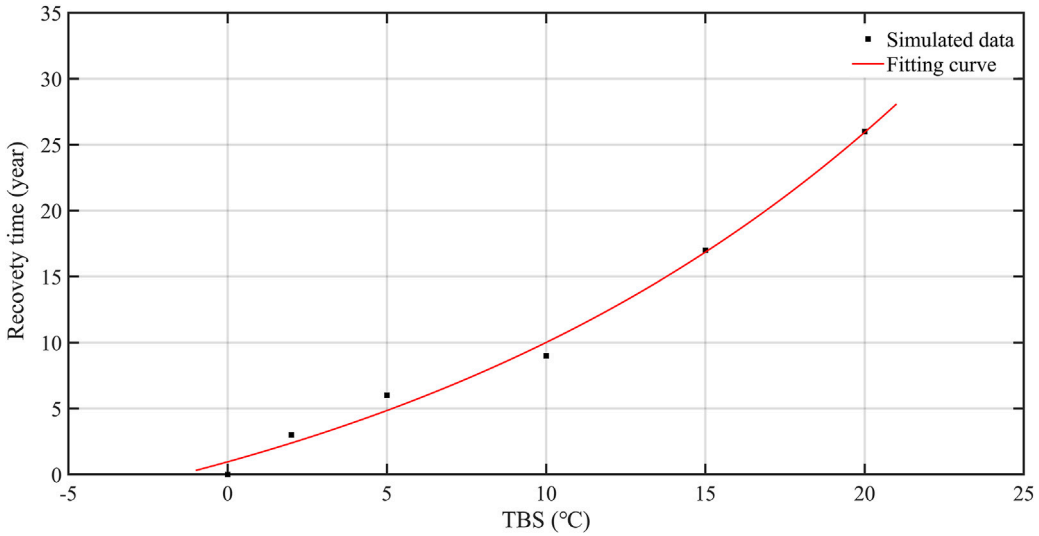

FIGURE 7 | Relationship between temperature of the backfilling soil (TBS) and the recovery time of ground temperature.

3.3.3 Moisture Content of Backfill Soil

Thermophysical parameters of soil, such as heat conductivity, heat capacity, and latent heat, were strongly affected by soil moisture content. **Table 3** shows the thermophysical parameters of sandy clay under different water contents. Thermophysical parameters of soils vary with soil moisture content, and different heat transfer capacities of varied soils affect the thermal recovery of permafrost. Therefore, MCBS needs to be considered for studying the influence factors of pit backfilling on the recovery of ground thermal regimes.

Figure 10 shows variations in ground temperatures of backfill centerline with six ascending MCBS (10, 15, 20, 25, 30, and 35%) under the conditions of 15°C in TBS, 20 m in DBS, and sandy clay in MBS. Apparently, the recovery time of ground temperature is closely related to MCBS (**Figure 10**). When moisture content of sandy clay is 15–25%, it would take about 50 years for the ground to freeze-up and about 95 years for moisture content higher than 25%. However, 75 years would be needed for the thermal recovery with MCBS at lower than 15%. Thus, near the optimal moisture content of sandy clay at 15–25%, permafrost would recover most rapidly.

As shown in **Figure 11**, the recovery time of ground temperature is related to the optimal soil moisture content of backfill. When MCBS is near the optimal soil moisture content, the ground temperature field recovers the most rapidly; otherwise, it takes longer. The relationship between MCBS and recovery time can be fitted as follows:

$$t_r = 0.202 \times (w - 19.62)^2 + 52.91, \quad (9)$$

where t_r is the recovery time (a) and w is the MCBS (moisture content of the backfilling soil, %).

3.3.4 Material of the Backfill Soil

Recovery time of permafrost in the backfilled area differs distinctly because of highly variable thermophysical parameters of different backfilled soils. All four backfill types (crushed rock, pebbly sand, coal gangue, and sandy clay) are simulated under the case of DBS at 20 m and TBS at 15°C (**Figure 12**). As shown in **Figure 12**, it takes the shortest time to recover the permafrost by backfilling with crushed rock, indicating the good cooling effect of crushed rock. Along the Qinghai–Tibet railway, this was also validated in the case of crushed rock subgrade (Lai et al., 2009; Zhang L. et al., 2015; Pei et al., 2019). Compared with crushed rock, the cooling time required for backfilling with pebbly sand would be relatively longer, almost twice that of crushed rock. This is mainly because that the specific surface area, specific heat, and heat conduction of pebbly sand are larger than those of crushed rock. At the same time, the backfilling of pebbly sand may thaw the permafrost at the pit bottom down to about 12 m in depth. The time for coal gangue/slag backfill to restore its ground temperature field would be about 20 years and that of sand clay would be 41 years, and the permafrost 20 m under the backfill would be affected. Among the four simulated materials (MBS), the time required for sandy clay backfilling would be the longest, and the depth of thermal impact on the underlying permafrost would be the largest.

4 DISCUSSION

Due to the sensitivity and vulnerability of the boreal permafrost ecological environment, strip coal mining and ground facility construction inevitably result in environmental damage to varied extents, thus accelerating the degradation of Xing'an permafrost in Northeast China. Particularly, abundant open pits have been dug for coal mining, with substantial impacts on the surrounding and underlying permafrost. According to observations, open pits receive remarkably more solar radiation. Therefore, air temperatures in pits are 0.5–1.2°C higher than those in surrounding areas, forming a distinct local climate in pits and influencing ambient and underlying permafrost (Zheng et al.,

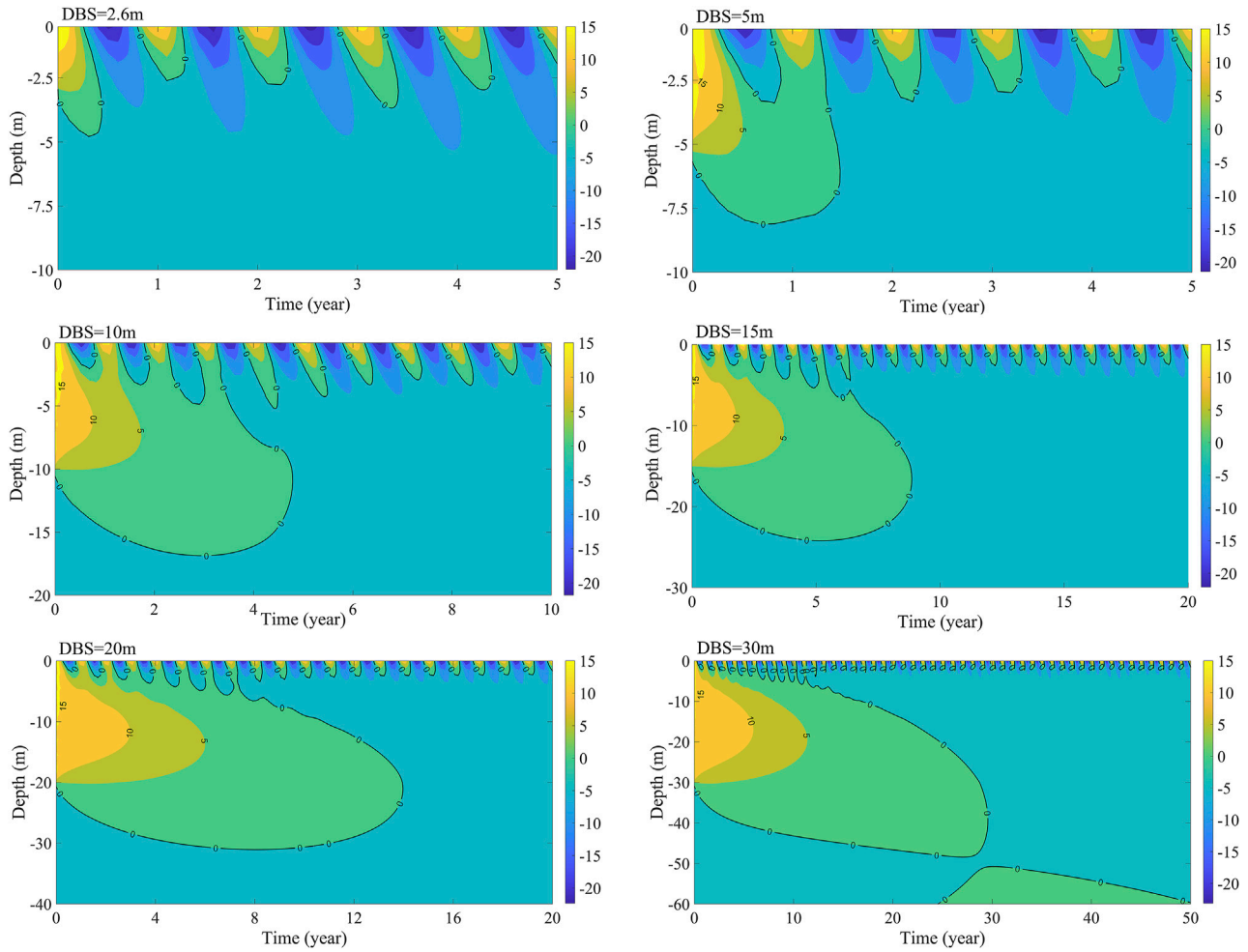

FIGURE 8 | Temporal variations in backfill centerline temperature under different depths of backfill soils (DBS at 2.6, 5, 10, 15, 20, and 30 m).

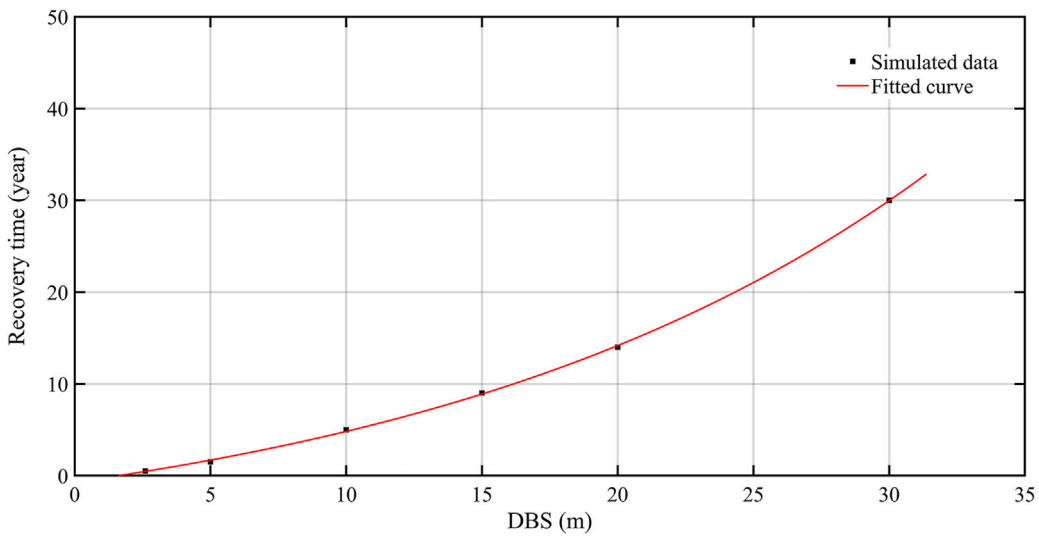

FIGURE 9 | Regression relationship between the depths of backfill soils (DBS) and the recovery time of ground temperature.

TABLE 3 | Physical parameters of sandy clay at different moisture content (Chen et al., 2018; Han et al., 2019; Xu et al., 2001).

Moisture content of sandy clay (%)	Thermal conductivity [W/(m·K)]		Volume heat capacity [in 10^6 J/(m^3·K)]		Latent heat (in 10^6 J/m^3)
	λ_u (unfrozen)	λ_f (frozen)	C_u (unfrozen)	C_f (frozen)	L
10	0.78	0.74	2.426	1.874	53.39
15	1.11	1.02	2.342	2.041	80.08
20	1.24	1.38	2.677	2.208	106.8
25	1.28	1.80	3.011	2.375	133.5
30	1.42	2.12	3.346	2.543	160.2
35	1.54	2.40	3.681	2.710	186.9

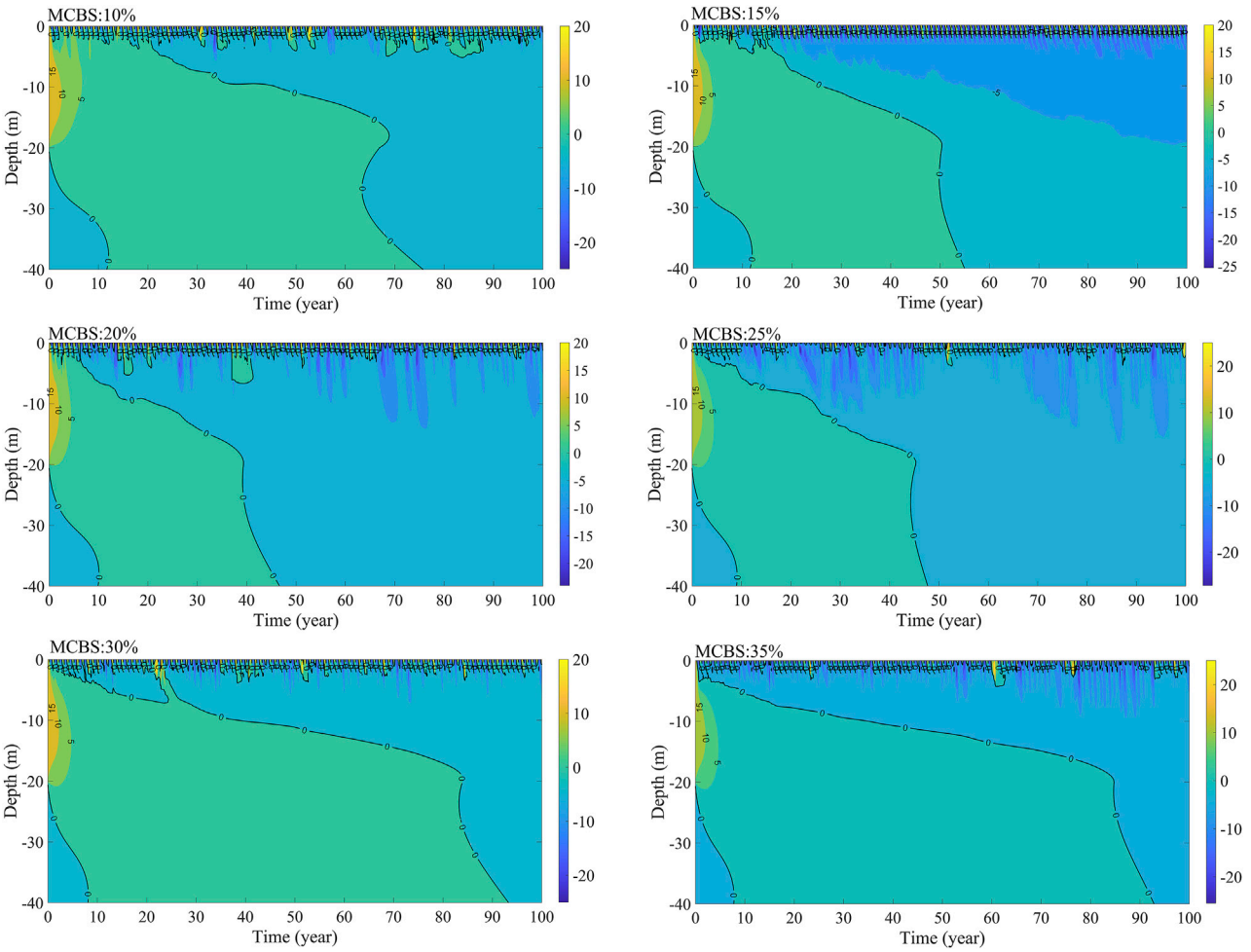

FIGURE 10 | Temporal variations in ground temperature of backfill centerline under different soil moisture content (MCBS) (10, 15, 20, 25, 30, and 35%).

2000). Moreover, excavation of pits in areas with thin permafrost layers may thaw through the underlying permafrost. Therefore, timely and proper backfilling of open pits in the mining area is crucial to the effective recovery of the permafrost ecological environment. However, limited by many factors, slow recovery of the permafrost environment after backfilling, or even the thaw of permafrost, may influence ground temperature and water conditions in the backfilled areas; this surely will further affect the restoration of vegetation and the ecological environment (Wang et al., 2001; Li et al., 2014; Cao et al., 2016; Gao et al., 2017).

In this study, thermal recovery of permafrost after backfilling was analyzed and predicted through numerical simulations. The simulation results show a gradual recovery of ground temperature field in open pits in permafrost regions over time if backfilled timely. Ground temperatures of backfilled pit are affected by

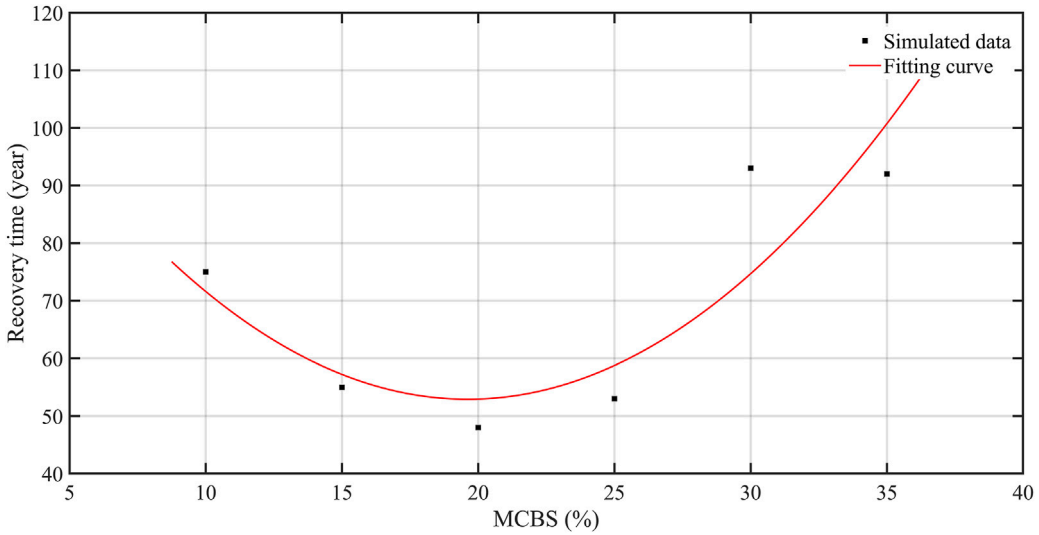

FIGURE 11 | Relationship between soil moisture content (MCBS) and the ground temperature recovery time.

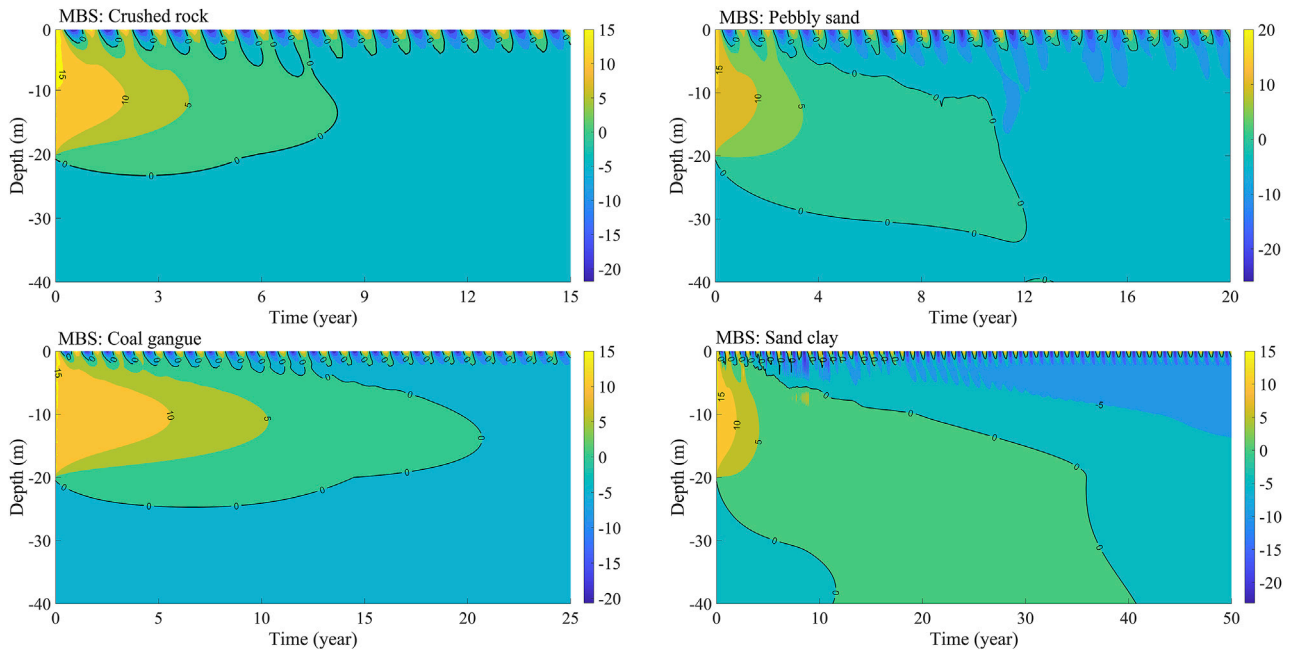

FIGURE 12 | Temporal variations in centerline temperature of different backfill soils (crushed rock, pebbly sand, coal gangue, and sand clay).

temperature, thickness, moisture content, and material types of backfill. The time of ground freeze-up is used to judge the degree of influence factors. First, temperature difference between backfill and surrounding permafrost induces heat transfer. Warm backfill may thaw the surrounding permafrost. In addition, it will take longer time to refreeze the backfilled ground. Then the thicker the backfill, the greater the thermal disturbances to the ambient permafrost, and the longer to refreeze the backfill. Model simulation results in our study are consistent with those in previous studies (e.g., Li et al., 2014; Cao et al., 2016; Gao et al., 2017). Some effective measures have been proposed in previous studies from perspectives of construction seasons, backfilling modes, and backfilling soil temperature. For example, it is advised for backfilling in cold seasons. Moreover, backfill thickness is a high-sensitivity factor, and layered backfilling can be implemented in cold seasons of different years for accelerating the thermal recovery in permafrost regions.

Climate warming is evident in Northeast China (Jin et al., 2008; Luo et al., 2014; Zhang et al., 2021). Under a warming climate, how to recover the temperature in the backfilled areas in permafrost regions in shorter time? The unique or azonal distribution of the ecosystem-protected permafrost and talik at regional to landscape scales in Northeast China gives us some enlightenments. Under certain conditions, local factors affect the occurrence or temperature of permafrost by modifying radiation, convection, and conduction processes in the ground and on the ground surfaces (Cheng, 2004). Simulation results demonstrate that except for backfilling temperature, water content, and depth/thickness of backfilled soil, backfilled soil types are key to the thermal recovery of permafrost. Based on these enlightenments from influencing mechanisms of local geo-environmental factors (Cheng, 2004), changes in backfilling material types and structures and modes in heat transfer, as well as comprehensive regulation measures, can be used for ground cooling in the backfilled areas for offsetting climate warming and for thermal recovery of permafrost in shorter time.

Many observational studies have suggested that the mean annual soil temperature in permafrost regions under crushed rock is 4–7°C lower than that in surrounding permafrost (Romanovskij and Turin, 1986; Harris, 1996; Harris and Pedersen, 1998; Gorbunov and Seversky, 2001). This was attributed to the Balch effect (Blach, 1900; Cheng, 2004). In winter, density of cold air is higher than that of hot air. Hence, cold air drains into stockpiles through large pores of rocks and squeezes out the hot air with small density in pores, forming convection, thereby enhancing heat loss. In summer, hot air occupies the upper spaces, while cold air stays low. There are relatively stable stratification and insignificant convection. Heat exchange is mainly based on heat conduction. Due to the extremely small thermal conductivity of air [only 0.025 W/(m·K)], the heat exchange rate is minor. The annual balance of heat exchange results in stronger heat dissipation than heat absorption, thus cooling the ground. Simulation results in this study also show that compared with sandy clay, pebbly sand, and coal gangues, temperature in the backfilling region recovers more quickly when backfilled with crushed rock. This result confirms those conclusions on the cooling effect of the crushed rock foundation on the Qinghai–Tibet Plateau (e.g., Cheng, 2004; Lai et al., 2009). As a result, taking into account the Balch effect and the principle of convection regulation, crushed rock is more effective for backfilling mine pits to recover permafrost in shorter time.

Furthermore, in this study, only single material backfilling has been considered in numerical simulations. In fact, a new backfilling structure can be conceived. For example, an organic soil layer can be paved atop of the crushed rock layer for vegetation restoration and for maintaining the thermal state of underlying permafrost due to its good water-holding capacity and the thermal diode effect. In summer, the dry organic soil layer has poor thermal conductivity, and it can effectively impede heat conduction, weakening the warming of the underlying soil. In autumn and rainy season, the organic soil layer can be kept water-saturated. In winter, the thermal conductivity of ice-saturated, organic soil increases dramatically (He R. et al., 2021). In a word, it loses heat more effectively from the underlying soil into the atmosphere, effectively cooling and protecting the underlying permafrost. Moreover, due to the different thermal conductivity of organic soil under frozen and thawed states, large thermal offsets occur between the ground surface and at the permafrost table (Smith and Riseborough, 2002; Luo et al., 2018, 2020; Du et al., 2022). Due to the thermal offset, regions with a positive mean annual ground surface temperature, or those beyond permafrost zones, might occasionally generate or preserve permafrost (Smith and Riseborough, 2002; Cheng, 2004; Jin et al., 2008; He R.-X. et al., 2021). From the perspective of heat transfer control, the recovery of permafrost can be accelerated by configuring the structure of the backfilling layer and adding a layer of organic soil on the surface.

Some studies indicate that vegetation can reflect 10–23% of insolation, and green grasses in sedge (*Carex tato*) wetlands and other shrub marshlands can even reflect 23–28% of insolation (Wang et al., 1999). Dense vegetation can shield direct radiation and scattered radiation of solar energy, thus reducing net radiation onto ground surfaces (Tyrtikov, 1956; Kelley et al., 2004). Therefore, it is suggested to adopt reasonable planting in accordance with local situations after backfilling. For example, herb and shrub species can be combined. Herbs protect the ground surface from erosion, and they are beneficial in maintaining water and soils in early stage of backfilled areas. Shrubs not only are characteristics of strong resistance to drought, strong water–soil retention, and prevention of wind erosion but also grow quickly, and they are highly tolerant to and can quickly colonize barren lands. Besides, root sprouts of shrubs can extend into soil parent materials to immobilize weathering soil layers and stabilize slopes while absorbing nutrients. The combined planting of herbs and shrubs can shield direct and scattered solar radiation, and reduce heats into underlying soil, which is beneficial to thermal recovery of permafrost.

In a word, pit backfilling in permafrost regions may choose appropriate season first, such as the cold season. Second, the backfilling materials and structure shall be designed on purpose according to the principle of radiation, convection, and conduction regulation and comprehensive regulation, thus effectively cooling ground and even offsetting the climate warming. However, in this study, only a qualitative discussion was conducted on the feasibility of accelerating permafrost recovery by changing backfilling materials and structures. Specific measures may need a series of tests and practice to further determine key parameters *per se*.

Furthermore, it is worth noting that with strip mining, ambient permafrost is disturbed, accelerating ground thawing. As the mining continues to deepen, permafrost thaw would accelerate. In addition, precipitation and subsequent infiltration, surface runoff, and thawing permafrost will collect water at the pit bottom, affecting the backfill refreezing. However, these factors and climate-induced impacts are not considered in this study. Therefore, our simulation results may have overestimated the time or possibility of permafrost recovery. Thus, more practical and sound conclusions would need more improvement in monitoring and modeling.

5 CONCLUSION

Strip coal mining has caused serious degradation of ambient permafrost. After backfilling, the slow rate of ground re-freezing in the mining area will affect soil moisture distribution, subsequently affecting the vegetation recovery. The recovery of permafrost in the backfilled area after coal mining is important for restoring the permafrost and the ecological environment. This study mainly presents the results of ground temperature monitoring to study influences of pit backfilling in Northeast China; combined with numerical simulation results, influencing factors for backfill temperature were analyzed. The main conclusions were drawn as follows:

1) By comparing ground temperatures at backfilled and undisturbed areas, backfilling has caused serious degradation of permafrost. The results of six-year monitoring data at the backfilled areas in permafrost regions show that a timely backfilling have a good effect on ground temperature recovery.
2) Regardless of the disturbances of ground temperature caused by climate warming and mining activities, the temperature of backfill soil (TBS), depth of backfill soil (DBS), moisture content of backfill soil (MCBS), and material of backfill soil (MBS) have great impacts on the recovery of the ground temperature field. Among them, the higher the backfilling temperature, the greater the backfill depth and the longer the ground temperature recovery time. Permafrost recovery time of backfill with finer particles, such as sandy clay and coal gangues, is longer. In addition, numerical simulations indicate a close relationship of permafrost recovery time and the optimal moisture content of backfill. When MCBS is close to the optimal soil moisture content, the ground re-freezes most rapidly; otherwise, ground freezing would be slow.
3) Based on numerical simulation results and combining with enlightenments from azonal distribution of the ecosystem-protected Xing'an permafrost in Northeast China, it is possible to lower ground temperature and even offset the influences of climate warming by choosing the right backfill material types, configuring new backfill structures, as well as through a heat transfer mode regulation. Therefore, it is recommended that low temperature and composite structure of organic soil and crush rock layers should be used for backfilling after coal mining in permafrost regions, and the backfilled area should be timely and properly re-vegetated.

DATA AVAILABILITY STATEMENT

The raw data supporting the conclusion of this article will be made available by the authors, without undue reservation.

AUTHOR CONTRIBUTIONS

RH, YL, and HJ contributed to the conceptualization and writing of the manuscript. HW, XJ, MZ, XL, YH, DJ, and FM contributed to data collection and data compilation. All authors contributed to the article and approved the submitted version.

FUNDING

This study was financially supported by the National Natural Science Foundation of China (NSFC Grant Nos 41401081 and 41871052), the State Key Laboratory of Frozen Soils Engineering (Grant No. SKLFSE-ZT-41), the Strategic Priority Research Program of the Chinese Academy of Sciences (CAS) (Grant No. XDA20100103), and the Northwest Institute of Eco-Environment and Resources (Grant No. E1550601).

ACKNOWLEDGMENTS

We thank the editor and the two reviewers for constructive and detailed comments on the article.

REFERENCES

Bell, F. G., Bullock, S. E. T., Halbich, T. F.J., and Lindsay, P. (2001). Environmental impacts associated with an abandoned mine in the Witbank Coalfield, South Africa. *International Journal of Coal Geology* 45 (2–5), 195–216. doi:10.1016/S0166-5162(00)00033-1

Blach, E. S. (1990). *Glaciers or Freezing Caverns*. Philadelphia: Allen, Lane and Scott, 1–337.

Bonacina, C., Comini, G., Fasan, A., and Primicerio, M. (1972). Numerical Solution of Phase-Change Problems. *Int. J. Heat Mass. Transf* 16 (10), 1825–1832. doi:10.1016/0017-9310(73)90202-0

Booshehrian, A., Wan, R., and Su, X. (2020). Hydraulic Variations in Permafrost Due to Open-Pit Mining and Climate Change: a Case Study in the Canadian Arctic. *Acta Geotech.* 15, 883–905. doi:10.1007/s11440-019-00786-x

Burov, B. A., and Gresov, A. I. (2011). Influence of Coal Deposits on Permafrost Degradation in the Shelf Zone of Arctic Seas and Methane Emission into the Water Column. *Dokl. Earth Sc.* 440 (1), 1320–1323. doi:10.1134/s1028334x11090157

Cao, W., and Sheng, Y. (2013). Permafrost Environment Problems and Countermeasures in the Process of Coal Mining. *Hydrogeol Eng. Geol.* 40 (5), 91–96. (in Chinese).

Cao, W., Sheng, Y., Qin, Y., Li, J., and Wu, J. (2011). An Application of a New Method in Permafrost Environment Assessment of Muli Mining Area in Qinghai-Tibet Plateau, China. *Environ. Earth Sci.* 63, 609–616. doi:10.1007/s12665-010-0728-7

Cao, W., Sheng, Y., Wu, J., Li, J., Li, J., and Chou, Y. (2016). Simulation Analysis of the Impact of Excavation Backfill on Permafrost Recovery in an Opencast Coal-Mining Pit. *Environ. Earth Sci.* 75 (9), 837. doi:10.1007/s12665-016-5659-5

Chen, L., Yu, W., Yi, X., Hu, D., and Liu, W. (2018). Numerical Simulation of Heat Transfer of the Crushed-Rock Interlayer Embankment of Qinghai-Tibet Railway Affected by Aeolian Sand Clogging and Climate Change. *Cold Regions Sci. Tech.* 155, 1–10. doi:10.1016/j.coldregions.2018.07.009

Cheng, G. (2004). Influences of Local Factors on Permafrost Occurrence and Their Implications for Qinghai-Xizang Railway Design. *Sci. China Ser. D-earth Sci.* 47, 704–709. doi:10.1007/bf02893300

Demirel, N., Emil, M. K., and Duzgun, H. S. (2011). Surface Coal Mine Area Monitoring Using Multi-Temporal High-Resolution Satellite Imagery. *Int. J. Coal Geology.* 86 (1), 3–11. doi:10.1016/j.coal.2010.11.010

Ding, D. W. (1988). Theoretical Study on Thermodynamics of Frozen Ground in China. *J. Glaciol Geocryol* 10 (3), 312–318. (in Chinese).

Du, R., Peng, X., Frauenfeld, O. W., Sun, W., Liang, B., Chen, C., et al. (2022). The Role of Peat on Permafrost Thaw Based on Field Observations. *CatenaCatena* 208, 105772. doi:10.1016/j.catena.2021.105772

Erener, A. (2011). Remote Sensing of Vegetation Health for Reclaimed Areas of Seyitömer Open Cast Coal Mine. *Int. J. Coal Geology.* 86 (1), 20–26. doi:10.1016/j.coal.2010.12.009

Gao, S.-h., He, R.-x., Jin, H.-j., Huang, Y.-d., Zhang, J.-m., and Luo, D.-l. (2017). Thermal Recovery Process of a Backfilled Open-Pit in Permafrost Area at the Gulian Strip Coal Mine in Northeast China. *J. Mt. Sci.* 14 (11), 2212–2229. doi:10.1007/s11629-017-4439-3

Gorbunov, A. P., and Seversky, E. V. (2001). "Influence of Coarsely Fragmental Deposits on Permafrost Formation," in *Extended Abstracts, International Symposium on Mountain and Arid Land Permafrost* (Ulaanbaatar: Urlah Erderm Publishing), 24–25.

Guo, D. X., Huang, Y. Z., Wang, J. C., Wang, B. L., Zeng, Z. G., and He, Y. X. (1989). Function of geologic structure in the formation of permafrost conditions in the Huola River Basin, North Da Hinggan Ling. *J Glaciol Geocryol.* 11 (3), 215–222.(in Chinese)

Han, F., Yu, W., Zhang, X., Yu, F., Yi, X., and Hu, D. (2019). Parameter Sensitivity Analyses of Influence on thermal Regime of Embankment in Permafrost Regions along the Qinghai-Tibet Engineering Corridor. *Cold Regions Sci. Tech.* 166 (10), 102817. doi:10.1016/j.coldregions.2019.102817

Harris, S. A. (1996). "Lower Mean Annual Ground Temperature beneath a Block Stream in the Kunlun Pass, Qinghai Province, China," in Proceedings, 5th Chinese Conference on Glaciology and Geocryology (Lanzhou: Gansu Culture Pres), 227–237.

Harris, S. A., and Pedersen, D. E. (1998). Thermal Regimes beneath Coarse Blocky Materials. *Permafrost Periglac. Process.* 9, 107–120. doi:10.1002/(sici)1099-1530(199804/06)9:2<107:aid-ppp277>3.0.co;2-g

He, R.-X., Jin, H.-J., Luo, D.-L., Li, X.-Y., Zhou, C.-F., Jia, N., et al. (2021b). Permafrost Changes in the Nanwenghe Wetlands Reserve on the Southern Slope of the Da Xing'anling–Yile'huli Mountains, Northeast China. *Adv. Clim. Change Res.* 12 (5), 696–709. doi:10.1016/j.accre.2021.06.007

He, R., Jia, N., Jin, H., Wang, H., and Li, X. (2021a). Experimental Study on thermal Conductivity of Organic-Rich Soils under Thawed and Frozen States. *Geofluids* 2021, 1–12. doi:10.1155/2021/7566669

He, R. X., Jin, H. J., Ma, F. T., Liu, F. C., and Xiao, D. H. (2015). Recent Progress in Studying Permafrost and Regions Environment in the Hola basin of north Greater Khingan Mountains. *J. Glaciol Geocryol* 37 (1), 109–117. (in Chinese).

Hildebrand, E. E. (1983). "Thaw Settlement and Ground Temperature Model for High Design in Permafrost," in Proceedings of the 4th International Conference on Permafrost (Washington DC: National Academy Press), 492–497. doi:10.7522/j.issn.1000-0240.2015.0011

James, M., Lewkowicz, A. G., Smith, S. L., and Miceli, C. M. (2013). Multi-decadal Degradation and Persistence of Permafrost in the Alaska Highway Corridor, Northwest Canada. *Environ. Res. Lett.* 8 (4), 045013. doi:10.1088/1748-9326/8/4/045013

Jin, H., Sun, G., Yu, S., Jin, R., and He, R. (2008). Symbiosis of Marshes and Permafrost in Da and Xiao Hinggan Mountains in Northeastern China. *Chin. Geogr. Sci.* 18 (1), 62–69. doi:10.1007/s11769-008-0062-0

Kelley, A. M., Epstein, H. E., and Walker, D. A. (2004). Role of vegetation and climate in permafrost active layer depth in arctic tundra of northern Alaska and Canada. *Journal of Glaciology and Climatology* 26, 269–274.

Lai, Y., Guo, H., and Dong, Y. (2009). Laboratory Investigation on the Cooling Effect of the Embankment with L-Shaped Thermosyphon and Crushed-Rock Revetment in Permafrost Regions. *Cold Regions Sci. Tech.* 58 (3), 143–150. doi:10.1016/j.coldregions.2009.05.002

Leng, Y. F. (2011). *Experimental Research on Physical Mechanical Properties and Numerical Analysis on Temperature Field of Permafrost of China-Russia Oil Pipeline*. Changchun: Jilin University. (in Chinese).

Li, J. P., Sheng, Y., Cao, W., and Qiu, Y. L. (2014). An Analysis of the Impact of Opencast Coal-Mining Pit Backfill on Permafrost Recovery. *Hydrogeol Eng. Geol.* 41 (4), 125–130. (in Chinese).

Liang, Z. F., Pan, Y. T., Feng, M. Y., Du, Y. S., Li, G. Y., and Ran, Z. (2018). Study on thermal Property of Coal Gangue. *Coal Technol.* 37 (10), 231–233. (in Chinese).

Luo, D., Jin, H., Jin, R., Yang, X., and Lü, L. (2014). Spatiotemporal Variations of Climate Warming in Northern Northeast China as Indicated by Freezing and Thawing Indices. *Quat. Int.* 349, 187–195. doi:10.1016/j.quaint.2014.06.064

Luo, D., Jin, H., Wu, Q., Bense, V. F., He, R., Ma, Q., et al. (2018). Thermal Regime of Warm-Dry Permafrost in Relation to Ground Surface Temperature in the Source Areas of the Yangtze and Yellow Rivers on the Qinghai-Tibet Plateau, SW China. *Sci. Total Environ.* 618, 1033–1045. doi:10.1016/j.scitotenv.2017.09.083

Luo, D., Liu, L., Jin, H., Wang, X., and Chen, F. (2020). Characteristics of Ground Surface Temperature at Chalaping in the Source Area of the Yellow River, Northeastern Tibetan Plateau. *Agric. For. Meteorology* 281, 107819. doi:10.1016/j.agrformet.2019.107819

Moreno-de Las Heras, M., Merino-Martín, L., and Nicolau, J. M. (2009). Effect of Vegetation Cover on the Hydrology of Reclaimed Mining Soils under Mediterranean-Continental Climate. *Catena* 77 (1), 39–47. doi:10.1016/j.catena.2008.12.005

Nauta, A. L., Heijmans, M. M. P. D., Blok, D., Limpens, J., Elberling, B., Gallagher, A., et al. (2014). Permafrost Collapse after Shrub Removal Shifts Tundra Ecosystem to a Methane Source. *Nat. Clim Change* 5 (1), 67–70. doi:10.1038/NCLIMATE2446

Pandey, B., Agrawal, M., and Singh, S. (2014). Coal Mining Activities Change Plant Community Structure Due to Air Pollution and Soil Degradation. *Ecotoxicology* 23 (8), 1474–1483. doi:10.1007/s10646-014-1289-4

Pei, W., Zhang, M., Lai, Y., Yan, Z., and Li, S. (2019). Evaluation of the Ground Heat Control Capacity of a Novel Air-L-Shaped TPCT-Ground (ALTG) Cooling System in Cold Regions. *Energy* 179, 655–668. doi:10.1016/j.energy.2019.04.156

Peretrukhin, N. A., and Potaueva, T. V. (1983). "Laws Governing Interactions between railroad Roadbeds and Permafrost," in Proceedings of 4th international conference on Permafrost (Washington D C: National Academy Press), 984–987.

Qian, D., Yan, C., Xing, Z., and Xiu, L. (2017). Monitoring Coal Mine Changes and Their Impact on Landscape Patterns in an alpine Region: a Case Study of the Muli Coal Mine in the Qinghai-Tibet Plateau. *Environ. Monit. Assess.* 189 (11), 559. doi:10.1007/s10661-017-6284-9

Quinton, W. L., and Baltzer, J. L. (2013). The Active-Layer Hydrology of a Peat Plateau with Thawing Permafrost (Scotty Creek, Canada). *Hydrogeol J.* 21 (1), 201–220. doi:10.1007/s10040-012-0935-2

Quinton, W. L., Shirazi, T., Carey, S. K., and Pomeroy, J. W. (2005). Soil Water Storage and Active-Layer Development in a Sub-alpine Tundra Hillslope, Southern Yukon Territory, Canada. *Permafrost Periglac. Process.* 16 (4), 369–382. doi:10.1002/ppp.543

Romanovskij, N. N., and Turin, A. I. (1986). *Kurums. Biul Peryglac.* 31, 249–259.

Serban, R. D., Serban, M., He, R. X., Jin, H. J., Li, X. Y., and Li, X. Y. (2021). 46-year (1973-2019) Permafrost Landscape Changes in the Ho'la Basin, Northeast China Using Machine Learning and Object-Oriented Classification. *Remot Sens* 13, 1910. doi:10.3390/rs13101910

Shur, Y. L., and Jorgenson, M. T. (2007). Patterns of Permafrost Formation and Degradation in Relation to Climate and Ecosystems. *Permafrost and Periglacial Processes* 18, 7–19. doi:10.1002/ppp.582

Smith, M. W., and Riseborough, D. W. (2002). Climate and the Limits of Permafrost: a Zonal Analysis. *Permafrost Periglac. Process.* 13, 1–15. doi:10.1002/ppp.410

Tyrtikov, A. P. (1959). *Perennially frozen ground and vegetation. In Fundamentals of Geocrylogy*. Moscow: Academy of Science USSR, 399–421.

Wang, J. C., Guo, D. X., Huang, Y. Z., and Zeng, Z. G. (1989). A Study on Seasonally Thawed Layer in the Basin of Huola River in Northern Da Hinggan Ling. *J Glaciol Geocryol* 11 (3), 203–214.

Wang, C. H. (1999). *Freeze-Thaw Processes of Frozen Soils and Cold Regions Development and Construction in Northeast China*. Beijing: Science Press (in Chinese).

Wang, G. X., Cheng, G. D., and Shen, Y. P. (2001). *Research on Ecological Environmental Change in Changjiang-Yellow Rivers Source Regions and Their Integrated Protection*. Lanzhou, China: Lanzhou University Press.

Wang, G. X., Yao, J. Z., Guo, Z. G., Wu, Q. B., and Wang, Y. B. (2004). Human Engineering Activities on Frozen Soil Ecosystem Change and its Effect on

Railway Construction. *Chin. Sci Bull* 49 (15), 1556–1564. doi:10.1007/bf03184309

Wang, J., Wang, H., Cao, Y., Bai, Z., and Qin, Q. (2016). Effects of Soil and Topographic Factors on Vegetation Restoration in Opencast Coal Mine Dumps Located in a Loess Area. *Sci. Rep.* 6, 22058. doi:10.1038/srep22058

Wang, T., Du, B., Li, C. C., Wang, H., Zhou, W., Wang, H., et al. (2021a). Ecological Environment Rehabilitation Management Model and Key Technologies in Plateau alpine Coal Mine. *J. China Coal Soc.* 46 (1), 230–244. (in Chinese).

Wang, T., Peng, E., Xia, L., Zhou, G., and Wang, J. (2021b). Uncertainties of thermal Boundaries and Soil Properties on Permafrost Table of Frozen Ground in Qinghai-Tibet Plateau. *J. Rock Mech. Geotechnical Eng.* 13 (3), 671–681. doi:10.1016/j.jrmge.2020.10.008

Xu, X. Z., Wang, J. C., and Zhang, L. X. (2001). *Frozen Soil Physics*. Beijing, China: Science Press, 86–91.

Yang, Z. W. (2018). *Laboratory Investigation on thermal Conductivity of Typical Soil in the Northeast Inner Mongolia during Freezing and Thawing Processes*. Hoh Hot, Inner Mongolia, China: Inner Mongolia University. (in Chinese).

Yanhu, M., Guoyu, L., Wei, M., Zhengmin, S., Zhiwei, Z., and Wang, F. (2020). Rapid Permafrost Thaw Induced by Heat Loss from a Buried Warm-Oil Pipeline and a New Mitigation Measure Combining Seasonal Air-Cooled Embankment and Pipe Insulation. *Energy* 203, 117919. doi:10.1016/j.energy.2020.117919

Zhang, J., Rao, Y., Geng, Y., Fu, M., and Prishchepov, A. V. (2017). A Novel Understanding of Land Use Characteristics Caused by Mining Activities: A Case Study of Wu'an, China. *Ecol. Eng.* 99, 54–69. doi:10.1016/j.ecoleng.2016.11.026

Zhang, L., Wang, J., Bai, Z., and Lv, C. (2015b). Effects of Vegetation on Runoff and Soil Erosion on Reclaimed Land in an Opencast Coal-Mine Dump in a Loess Area. *Catena* 128, 44–53. doi:10.1016/j.catena.2015.01.016

Zhang, M., Lai, Y., Zhang, J., and Sun, Z. (2011). Numerical Study on Cooling Characteristics of Two-phase Closed Thermosyphon Embankment in Permafrost Regions. *Cold Regions Sci. Tech.* 65 (2), 203–210. doi:10.1016/j.coldregions.2010.08.001

Zhang, M., Pei, W., Zhang, X., and Lu, J. (2015a). Lateral thermal Disturbance of Embankments in the Permafrost Regions of the Qinghai-Tibet Engineering Corridor. *Nat. Hazards* 78 (3), 2121–2142. doi:10.1007/s11069-015-1823-6

Zhang, Z. Q., Wu, Q. B., and Hou, M. T. (2021). Permafrost change in Northeast China in the 1950s-2010s. *Advances in Climate Change Research* 12 (1), 18–28. doi:10.1016/j.accre.2021.01.006

Zheng, H. L., and Ma, F. T. (2000). Effect of Opencast Mining on Permafrost Environment. *Opencast Coal Min Technol* 4, 14–16. (in Chinese)

Zhou, Y. W., Qiu, G. O., Guo, D. X., Cheng, G. D., and Li, S. D. (2000). *Geocryology in China*. Beijing: Science Press–450. (in Chinese).

Zhu, L. N. (1988). Study of the Adherent Layer on Different Types of Ground in Permafrost Regions on the Qinghai-Xizang Plateau. *J. Glaciol Geocryol* 10, 8–14. (in Chinese).

Conflict of Interest: The authors declare that the research was conducted in the absence of any commercial or financial relationships that could be construed as a potential conflict of interest.

The reviewer WP declared a shared affiliation with several of the authors, RH, YL, HW, YH, and DJ, to the handling editor at the time of review.

Publisher's Note: All claims expressed in this article are solely those of the authors and do not necessarily represent those of their affiliated organizations, or those of the publisher, the editors, and the reviewers. Any product that may be evaluated in this article, or claim that may be made by its manufacturer, is not guaranteed or endorsed by the publisher.

frontiers in Earth Science

ORIGINAL RESEARCH
published: 01 February 2022
doi: 10.3389/feart.2021.806309

Hydrothermal Dynamics of Seasonally Frozen Soil With Different Vegetation Coverage in the Tianshan Mountains

Shen Ma[1,2], *Bin Yang*[3], *Jingyi Zhao*[1,2], *Changhai Tan*[3], *Ji Chen*[1,2]*, *Qihang Mei*[1,2] and *Xin Hou*[1,2]

[1]Beiluhe Observation and Research Station on Frozen Soil Engineering and Environment in Qinghai-Tibet Plateau, State Key Laboratory of Frozen Soil Engineering, Northwest Institute of Eco-Environment and Resources, Chinese Academy of Sciences, Lanzhou, China, [2]University of Chinese Academy of Sciences, Beijing, China, [3]Command Center of Comprehensive Natural Resources Survey, China Geological Survey, Beijing, China

The hydrothermal relationship between vegetation and seasonal frozen soil is one of the key research contents in the fields of permafrost ecological environment, hydrology and climate change in alpine mountainous areas. Based on the monitoring data of air temperature, precipitation and soil hydrothermal conditions at the depth of 0–5 m from site TS-04 (with high vegetation coverage) and site TS-05 (with low vegetation coverage) in the alpine grassland of the Tianshan Mountains, this study compared and analyzed the characteristics of freezing-thawing process, temperature and moisture changes of seasonal frozen soil with different vegetation coverage. The results show that the maximum seasonal freezing depth of the two sites is almost comparable, but site TS-04 has a smaller freezing and thawing rate, and a shorter duration of freeze-thaw at all depths. TS-04 also has a smaller annual range of surface temperature and ground-air temperature difference. The analysis indicates that vegetation acts as a thermal buffer and has a good thermal insulation effect on the ground surface. Site TS-04 had high unfrozen water content in the unfrozen period and the water content increased with depth, while the unfrozen water content was low in site TS-05. In addition, the thresholds of soil water content response to rainfall events at 5 cm depth of site TS-04 and site TS-05 were 5 and 11 mm precipitation respectively, which indicated that the high vegetation coverage is conducive to rainwater infiltration, and the underlying soil of the site has a faster response to rainfall events.

Keywords: frozen ground, vegetation coverage, soil freezing-thawing cycle, hydrothermal process, Tianshan Mountains

OPEN ACCESS

Edited by:
Sizhong Yang,
GFZ German Research Centre for Geosciences, Germany

Reviewed by:
Wei Shan,
Northeast Forestry University, China
Shuying Zang,
Harbin Normal University, China

***Correspondence:**
Ji Chen
chenji@lzb.ac.cn

Specialty section:
This article was submitted to Cryospheric Sciences, a section of the journal Frontiers in Earth Science

Received: *31 October 2021*
Accepted: *23 December 2021*
Published: *01 February 2022*

Citation:
Ma S, Yang B, Zhao J, Tan C, Chen J, Mei Q and Hou X (2022) Hydrothermal Dynamics of Seasonally Frozen Soil With Different Vegetation Coverage in the Tianshan Mountains. Front. Earth Sci. 9:806309. doi: 10.3389/feart.2021.806309

INTRODUCTION

Many factors affect the soil hydrothermal state in the alpine ecosystem. The coupling of various factors (e.g., air temperature, precipitation, soil properties) results in variations in the subsurface soil at different temporal-spatial scales (Yang et al., 2007; Wang et al., 2009; Dai et al., 2013). Among these factors, vegetation cover has a significant influence on the soil hydrothermal status over a short period of time (Cheng et al., 2008). The interactions between soil moisture and heat with different vegetation types and amount of coverage are also different. The temperature and moisture conditions of subsurface soil often control many processes of the ecosystem. In cold regions, subsurface soil

often experiences intense seasonal freezing and thawing, which complicates the heat and moisture exchange between soil and the ecosystem (Wu et al., 2003).

The variations in subsurface soil hydrothermal processes in alpine regions can lead to anomalies in the land–air energy and water balance, which can significantly affect surface hydrological processes, the ecological environment, carbon–nitrogen cycles, and climate systems in the Qinghai-Tibet Plateau and its surrounding areas (Groffman et al., 2011; Natali et al., 2011; Li et al., 2016). In permafrost regions, surface vegetation plays a very important role in the development of permafrost by changing the hydrothermal coupling cycle of the underlying soil. Vegetation coverage influences thaw–freeze cycles and thermal states of permafrost. The differences in vegetation type and coverage result in varying heat and water exchange efficiencies in subsurface soil. A deeper understanding of the relationship between soil and vegetation can more accurately describe the interaction between soil hydrothermal processes and vegetation and help establish a more accurate continental ecological model; thus, a more accurate land surface ecological model can be developed (Dickinson, 1986; Sellers et al., 1986). In permafrost regions, due to the unique periodic freeze and thaw of permafrost, there is insufficient understanding of the relationship between frozen soil and overlying vegetation. A numerical model that can accurately simulate the interaction between frozen soil hydrothermal processes and overlying vegetation has not been established. Thus, terrestrial ecological and surface models can not accurately reflect the processes of frozen ground (Nan et al., 2002; Xiao et al., 2013; Chen et al., 2015; Wu et al., 2018). Fully understanding the relationship between frozen soil and vegetation is a key issue to solve in establishing a model that can more accurately reflect the ecology and surface of frozen soil areas.

The Tianshan Mountains are the largest mountain range in Central Asia, where permafrost, seasonal frozen soil, and alpine steppe are prominent in high altitude areas. The Tianshan Mountains and the Qinghai-Tibet Plateau feature different permafrost types. The permafrost areas of the Qinghai-Tibet Plateau have high-plain permafrost, while the permafrost areas of the Tianshan Mountains have mountain-type permafrost. At present, domestic and foreign scholars have done a lot of research on the soil hydrothermal characteristics of the Qinghai Tibet Plateau, but the soil hydrothermal state in the Tianshan area is not yet clear. In the mountainous permafrost region of the Tianshan Mountains, how vegetation impacts the soil water and heat conditions (such as soil freeze–thaw and soil moisture phase changes) is still poorly understood. In this study, we used a large amount of field monitoring data from typical alpine grassland ecosystems in the hinterland of the Tianshan Mountains to study the differences of soil hydrothermal dynamic responses to vegetation coverage changes in typical seasonal frozen regions.

STUDY AREA AND METHODS

Study Area and Observation Sites

The study area is located in the Kuixiandaban area, Tianshan Mountains, Xinjiang Province. This area has a typical continental dry climate (**Figure 1**). The nearest meteorological station is Daxigou station, which is built on the gentle slope of an alpine meadow with an altitude of 3,549 m in the headwater area of the Urumqi River. According to the long-term climatic data, the annual average air temperature of the Daxigou meteorological station was -4.97°C, and the annual average precipitation was 460.5 mm (1961–2016). The slope is 5.7° at the TS-04 site and 8.5° at the TS-05 site. According to field detection data, the lower limit of the permafrost distribution in the source area of the Urumqi River is 3,250 m on the sunny slope and 2,900 m on the shady slope.

The elevations of monitoring points TS-04 (42.97°N, 86.84°E) and TS-05 (42.94°N, 86.84°E) are 3,145 and 2,949 m, respectively. Both stations are located on the southern slope of the watershed between the north and south slopes of the Tianshan Mountains within the source area of the Ulastai River. The TS-04 site is located on the alluvial and diluvial platform in the Wusite Valley, 3.2 km from the Wusite Railway Bridge. On the east and west sides of the site, the rivers flowing southwest and southeast meet at 100 m south of the site, so the water conditions of the site are good. According to the drilling data, the main types and ranges of soil textures at the TS-04 site are black brown clay (0–0.3 m), fine sand (0.3–0.7 m), rock (0.7–1.3 m), sand stone (1.3–2 m), sand (2–3 m); the TS-05 site has fine sandy soil (0–0.3 m), clay (0.3–0.6 m), fine sand (0.6–1.2 m), and coarse sand with gravel (1.2–3 m). Field investigations show that the two study sites are not in the permafrost area, which is typically frozen seasonally.

The vegetation types of both sites are alpine steppe. The dominant plant species are *S. purpurea*, *S. subsessiliflora*, and *S. basiplumosa* of the dense perennial grasses of the genus *Stipa L.* and rhizome type perennial Carex-Qinghai-Tibet *Carex*, *Artemisia wellbyi*, *A. younghusbandii*, and *A. minor*. The vegetation coverage of the TS-04 site is 80–90%, while the vegetation coverage of the TS-05 site is 30–40%.

Methods

Collection of Basic Monitoring Data

The research period spans September 2017 to August 2018. The main observations include air temperature, snow depth, precipitation, soil temperature, and water content (**Table 1**). The snow depth and precipitation were measured by a SR50 snow depth detector (±1 cm) and a T200B precipitation meter (±0.1 mm), respectively. The air temperature at 2 m above the ground was measured by an HMP155A-L air temperature and humidity sensor (±0.2°C). A soil profile was excavated, and soil moisture sensors produced by the Campbell Company in the United States were inserted at depth intervals of 0.05, 0.20, 0.40, 0.80, 1.2, 1.6, and 2.0 m. In addition, soil moisture in this article refers to unfrozen water. The research team drilled a deep hole at each site to place cables produced by the State Key Laboratory of Frozen Soil Engineering to measure soil temperature at depths ranging from 0.05 to 40 m. A heat flux plate was placed at a depth of 5 cm in the soil surface. All sensors collected data at a rate of 30 min per session.

Definition of Precipitation Response Events and Freeze-Thaw Cycles

According to the accuracy of the rain gauge, when the precipitation was greater than 0.2 mm within 6 h, a new

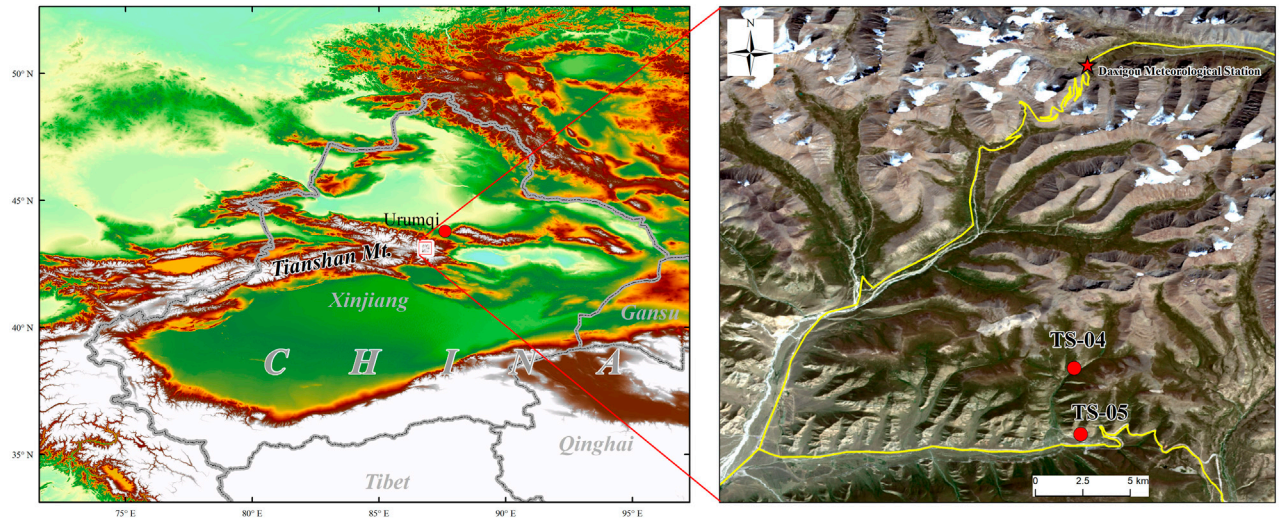

FIGURE 1 | Location of the study area and observation sites.

TABLE 1 | List of measurements used in this study.

Observational elements	Instrument type	Accuracy
Air temperature and relative humidity	HMP155A-L, Vaisala	± 0.2°C; 2%RH
Wind speed and wind direction	05103, R. M. Young	± 0.3 m/s; ± 3°
Atmospheric pressure	CS106, Vaisala	± 1.5 hPa
Percipitation	T-200B, Vaisala	± 0.1 mm
Snow depth	SR50A, Campbell	± 1 cm
Soil heat flux	HFP01-10, HUKSEFLUX	50 μV/W·m-2
Soil temperature	SKLFSE-TS	± 0.05°C
Unfrozen soil water	CS616, Campbell	± 2%

precipitation–soil moisture response process started. Six hours represents the interval between two consecutive precipitation periods; generally 6–8 h is used in the literature (Dunkerley, 2008). The instrument noise threshold was 0.2 mm because precipitation events with an interval of more than 6 h are very frequent, and 0.2 mm is a frequent isolated record that will not produce any soil moisture changes (Lozano-Parra et al., 2015). To study how precipitation events impact soil wetting, we defined the extent, start, and end times of precipitation events.

Diurnal changes in soil temperature may cause soil moisture to increase at a rate of 0.1% every 30 min during the day, so we defined a 0.2% increase in soil moisture within 30 min as the response threshold of soil moisture to precipitation (Lin and Zhou, 2008). To avoid the impact of snowfall on rainfall events, we selected the highest rainfall months of July, August, and September for analysis.

The freeze–thaw process of soil can be divided into four stages, regardless of the soil salinity and texture, according to the daily maximum and minimum temperatures of the soil: thawed period, T_{min}>0°C; frozen period, T_{max}<0°C; freezing period, T_{max} >0°C and T_{min} <0°C; thawing period, T_{max} >0°C and T_{min} <0°C. The freezing and thawing periods are also called the daily freeze–thaw cycle (Yang et al., 2007; Guo et al., 2011).

RESULT

Meteorological Data of TS-04 and TS-05 Stations

The meteorological conditions of the two stations are very similar, and the trend in the data is nearly the same (**Figure 2**). The wind speed near the ground is generally low in summer and high in the cold season. The wind speed near the ground of TS-05 is greater than that of TS-04 (**Figure 2A**). The variations in the daily average temperatures of the two stations are nearly the same, but there is an obvious temperature difference in summer (**Figure 2B**). The summer temperature of the TS-05 station is higher than that of the TS-04 station. There is a close relationship between the air relative humidity and precipitation. When a precipitation event occurs, it is often accompanied by an increase in air humidity. According to **Figure 2C** and **Figure 2D**, there is a good correlation between air humidity change and precipitation. It can also be seen that the precipitation of TS-05 is less than that of TS-04. According to the landform data of the two stations, we know that the vegetation of the TS-04 station is relatively dense due to abundant water and heat in summer. The vegetation grows more easily, and it can reduce the surface wind speed and solar radiation.

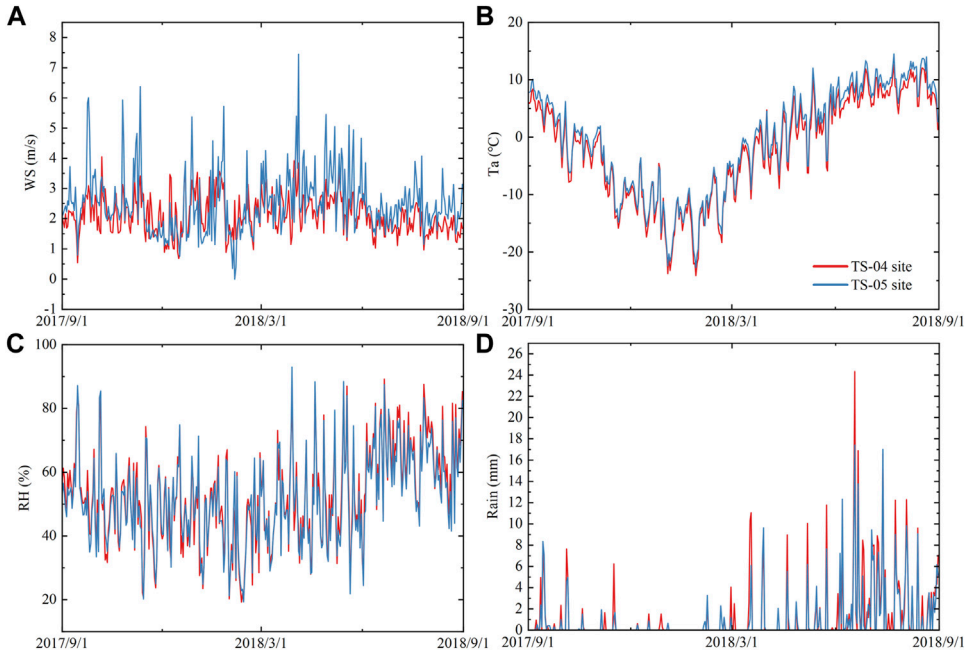

FIGURE 2 | Comparison of meteorological data between TS-04 and TS-05 stations. (WS, Wind Speed; Ta, Air temperature; RH, Relative humidity).

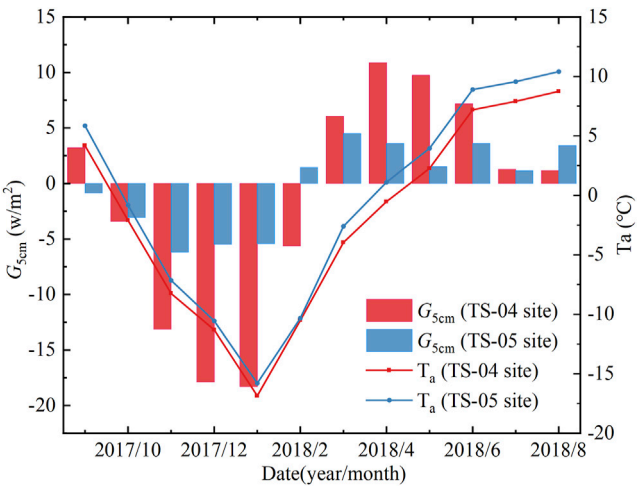

FIGURE 3 | Monthly mean changes of air temperature (Ta) and 5 cm soil heat flux (G_{5cm}) at TS-04 and TS-05 sites.

Soil Thermal Conditions Under Various Amounts of Vegetation Coverage

Soil Heat Flux in Shallow Layers

Soil heat flux is an important thermal index of soil, which can directly reflect the transmission state of soil heat. When the ambient temperature is greater than the soil temperature, the heat passes into the soil from the environment under the action of the temperature gradient, and the soil heat flux is positive. In contrast, when the soil heat flux is negative, the soil releases heat to the environment. The study of heat exchange between soils elucidates the conditions of heat absorption and release in soil and the change of heat storage, which is directly related to the distribution of energy in the atmosphere and soil. These processes also play an important role in the study of climate change. **Figure 3** shows the monthly mean change in soil heat flux and air temperature at TS-04 and TS-05. In the cold season, the soil heat flux at TS-04 varies from −18.31 (w/m^2) to 10.87 (w/m^2), with a range of 29.18 (w/m^2). The minimum value occurs in January 2018, the maximum value occurs in April, and the annual average value is −1.58 w/m^2. The minimum value of the soil heat flux at TS-05 was −6.19 w/m^2 in November 2017, the maximum value was 4.49 w/m^2 in March 2018, and the annual average value was −0.16 w/m^2. The soil heat flux at the two stations was negative for 5 months, therefore the soil released heat to the environment. The soil absorbed heat from the environment in the remaining 7 months. Before the soil heat flux reaches the maximum value, the air temperature and soil heat flux exhibit the same trends. With a gradual increase of temperature, the soil heat flux decreased.

Temperature Change During Soil Freezing-Thawing

At the TS-04 site (**Figure 4A**), a significant daily freeze–thaw cycle occurs from a soil depth of 5–40 cm. The duration of the daily freeze–thaw cycle during the thawing period is significantly longer than the freezing period. As the soil depth increases, the duration of the daily freeze–thaw cycle gradually decreases. In a freeze–thaw cycle, the maximum duration of the daily freeze–thaw cycle at the soil surface (5 cm) is 37 days. In the thawing period, the duration of the daily freeze–thaw cycle is 27 days. There is almost no daily freeze–thaw cycle at 80 cm (it

TABLE 2 | The time of soil freeze-thaw process at different depths.

Site	Soil depth/cm	Thawed		Freezing		Frozen		Thawing	
		Starting and ending time/year-month-day	Duration/day	Starting and ending time/year-month-day	Duration/day	Starting and ending time/year-month-day	Duration/day	Starting and ending time/year-month-day	Duration/day
TS-04	5	2017/9/1–2017/10/11 2018/4/17–2018/8/31	178	2017/10/12–2017/10/21	10	2017/10/22–2018/3/20	150	2018/3/21–2018/4/16	27
	20	2017/9/1–2017/11/11 2018/4/25–2018/8/31	201	2017/11/12–2017/11/19	8	2017/11/20–2018/4/5	137	2018/4/6–2018/4/24	19
	40	2017/9/1–2017/12/4 2018/5/12–2017/8/31	207	2017/12/5–2017/12/6	2	2017/12/7–2018/4/22	137	2018/4/23–2018/5/11	19
	80	2017/9/1–2017/12/27 2018/6/7–2017/8/31	204	2017/12/28	1	2017/12/29–2018/6/4	158	2018/6/5–2018/6/6	2
TS-05	5	2017/9/1–2017/10/7 2018/4/16–2018/8/31	175	2017/10/8–2017/11/15	39	2017/11/16–2018/2/23	100	2018/2/24–2018/4/15	51
	20	2017/9/1–2017/11/11 2018/3/26–2018/8/31	231	2017/11/12	1	2017/11/13–2018/3/21	129	2018/3/22–2018/3/25	4
	40	2017/9/1–2017/11/20 2018/4/2–2017/8/31	233	2017/11/21	1	2017/11/22–2018/3/26	125	2018/3/27–2018/4/1	6
	80	2017/9/1–2017/12/16 2018/4/8–2017/8/31	253	2017/12/17	1	2017/12/18–2018/4/6	110	2018/4/7	1

only occurs in the monitoring period for 3 days). From the beginning and ending times of the daily freeze–thaw cycle, there is a clear lag at each depth. The daily freeze–thaw cycle occurred on October 12, 2017 at the 5-cm layer, while the daily freeze–thaw cycle occurred at a 20-cm depth 1 month later. The daily freeze–thaw cycle appeared at the 80-cm depth on December 28 after 78 days and only lasted for 1 day (**Table 2**).

At the TS-05 site, the depth of the daily soil freeze–thaw cycle is less than that at the TS-04 site. The daily soil freeze–thaw cycle at TS-05 almost only occurs at the 5-cm layer (**Figure 4B**), while the depth of the daily freeze–thaw cycle at TS-04 reached 40 cm. The daily freezing–thawing cycle first occurred at 5 cm on October 8, 2017, and its duration of 39 days was much longer than that of soil under 5 cm. After 69 days, only a day-long freeze–thaw cycle occurred at a depth of 80 cm. The daily freeze–thaw cycle of soil at a depth of 5 cm during the thawing period began on February 24, 2018 and lasted for 51 days. In general, the characteristics of the daily freezing-thawing cycles at TS-05 and TS-04 are as follows: the duration of the daily freezing–thawing cycles in spring is longer than that in autumn, and the duration of the daily freeze–thaw cycle decreases with an increase of depth. In addition, TS-05 has a longer duration freeze–thaw cycle, but TS-04 has a deeper freeze–thaw depth than TS-05. The daily vertical transfer rate of the TS-05 freeze–thaw cycle in the thawing period (1.95 cm/d) is higher than that in freezing period (1.16 cm/d), but both values are higher than those at TS-04 (1.04 cm/d).

The monitoring results of a complete freeze–thaw cycle were analyzed in **Figure 5**. Both sites reflect the characteristics of "one-way freezing and two-way thawing" of seasonal frozen soil. The ground at TS-04 first entered the continuous freezing stage on October 21, 2017 (**Figure 5A**). During this stage, with a decrease of temperature, the soil in the seasonal frozen layer successively entered the frozen state. The freezing rate was relatively slow at the beginning, then with the decrease of temperature, the freezing rate began to accelerate. With the continuous downward movement of the freezing front, the soil reached maximum freezing depth on March 18, 2018. The maximum freezing depth was approximately 2.2 m. As the temperature rises, each layer of soil enters the thawing period, and the surface and the bottom of the seasonal frozen layer begin to absorb heat and thaw almost simultaneously. However, the soil at the bottom of the

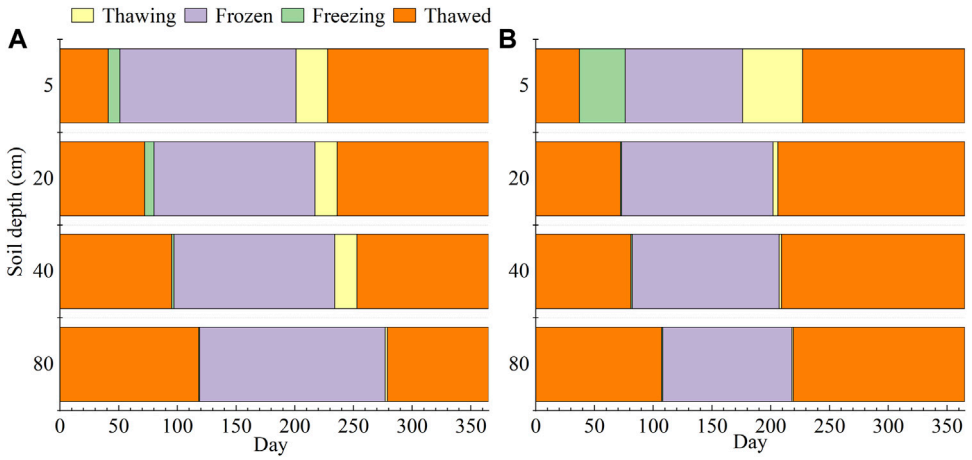

FIGURE 4 | Daily freezing-thawing cycles occurred at 5~80 cm of TS-04 and TS-05 sites (2017.9.1–2018.9.1).

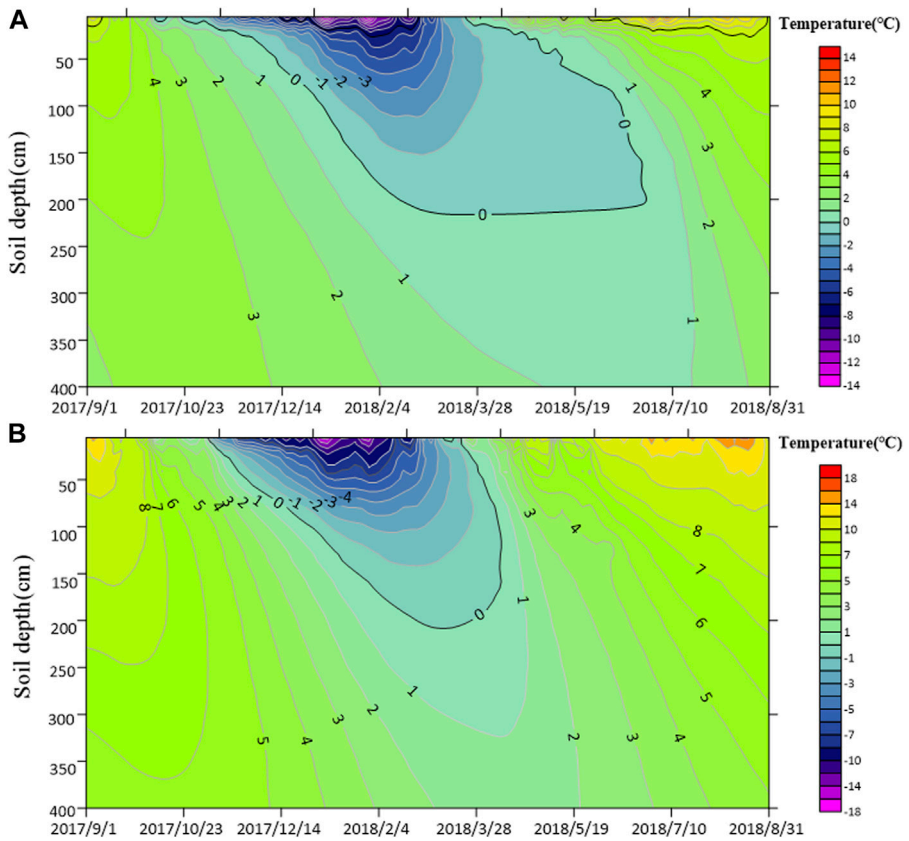

FIGURE 5 | Soil temperature contour map of two sites:**(A)** TS-04 site and **(B)** TS-05 site.

seasonal frozen layer changes very slowly, and the warming rate is only 0.1 cm/d. According to the preliminary analysis, the temperature differences of deep soil are very small such that the temperature gradient is small and leads to the slow soil warming. The thawing process from the surface downward begins at a relatively slow rate. The melting rate of soil begins to accelerate when the melting front reaches a depth of approximately 1 m. The two opposite melting processes (from the surface downward and from the bottom upward) finally met at a depth of 2 m on June 27, 2018. At this point, the seasonal frozen layer was completely melted.

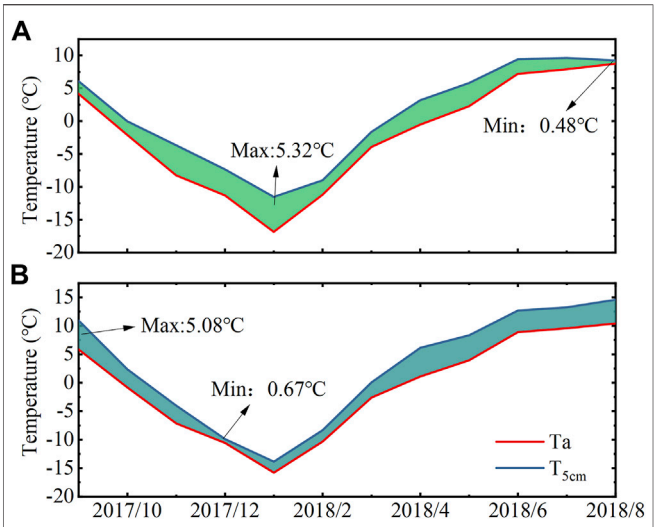

FIGURE 6 | The difference of soil temperature at 5 cm with air temperature:**(A)** TS-04 site and **(B)** TS-05 site.

For TS-05 in **Figure 5B**, the soil temperature at 5 cm began to exhibit negative temperatures continuously on November 6, 2017. Then, as the temperature decreased, the freezing front moved downward. The soil reached its maximum freezing depth (about 2.1 m) on March 8 of the following year, and the freezing rate was 1.74 cm/d. The topsoil and subsoil of the seasonal frozen layer entered the bidirectional thawing stage on March 21 and 9, 2018, respectively. The two melting fronts met at a depth of approximately 160 cm on April 10, and the melting rates were 7.62 cm/d (from top to bottom) and 1.52 cm/d (from bottom to top). After that, the soil entered the warming stage.

Difference Between Air Temperature and Soil Temperature at a 5 cm Depth

Vegetation is the interface of water and heat exchange between Earth and air and plays an important role in energy transfer; the difference in air temperatures can reflect the heat insulation effect of vegetation.

Ground–air temperature difference generally refers to the difference between air temperature and soil temperature at 5 cm; it can accurately reflect the influence of vegetation on the underlying soil temperature. The soil temperature trend at 5 cm was the same as that of air temperature (**Figure 6**). At TS-04 where the vegetation cover is vast, the maximum value of the ground–air temperature difference occurred in January 2018 (5.32°C), and the minimum value was in August 2018 (0.48°C), with an average temperature difference of 2.83°C (**Figure 6A**).

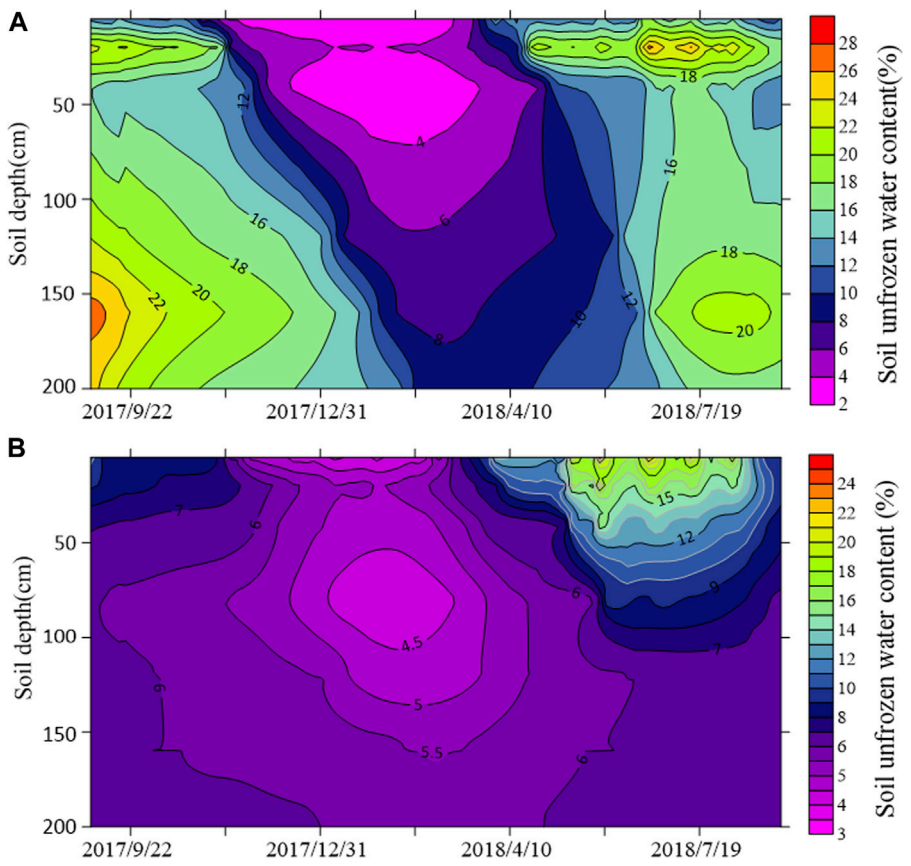

FIGURE 7 | Isoline map of soil unfrozen water content in two sites:**(A)** TS-04 site, **(B)** TS-05 site.

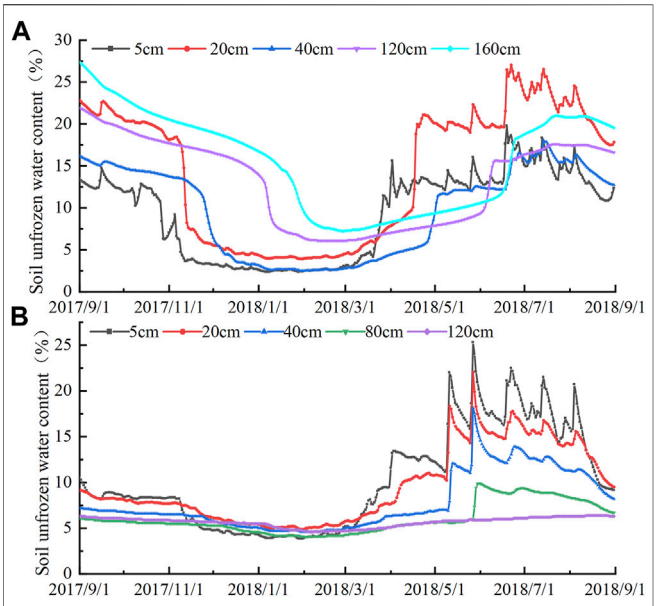

FIGURE 8 | Change curves of soil unfrozen water content at different depths in TS-04 site **(A)** and TS-05 site **(B)**.

However, in contrast to TS-04, the maximum (5.08°C) and minimum (0.67°C) ground-temperature difference at TS-05 (small vegetation coverage) occurred in summer (September) and winter (December), respectively (**Figure 6B**). Compared with TS-04, the average annual temperature difference at TS-05 increased by 0.48–3.31°C: greater vegetation coverage affects the heat balance of air and soil at the site through plant transpiration and water exchange between the atmosphere and soil. Thus, the 5-cm soil temperature at TS-04 (large vegetation coverage) will not dramatically rise or fall during the heating or cooling stage: this temperature helped with insulation in the cold season and cooling in the warm season.

Soil Moisture Under Various Amounts of Vegetation Cover

Variation of Unfrozen Soil Water Content During a Freezing–Thawing Cycle

The variation of soil moisture in the seasonal frozen layer reflects the dry and wet conditions of soil and is an important part of the water cycle in the ground–air system. Through the analysis of unfrozen soil water content during the study period in **Figure 7**, the vertical variation of soil water at TS-04 was evident (**Figure 7A**). In the unfrozen period, there is a low aquifer and two high aquifers in the change curve of unfrozen soil water content. The low aquifer is about 40 cm (about 15% water content), and the high aquifer is about 20 cm (about 25% water content) and 160 cm (about 27% water content), respectively. Due to the frost process of soil, the unfrozen water content of soil at different depths varies greatly in a complete freeze–thaw cycle. With an increase of depth, the change of the soil moisture content has an obvious lag (**Figure 8A**). This is because the soil moisture content of the site is generally high, and sufficient heat needs to be released or absorbed in the freezing and thawing processes to change the soil moisture. The unfrozen water content in the shallow layer (0–20 cm) changed sharply and the fluctuation gradually weakened with an increase of depth. Thus, the soil over 20 cm at the site frequently exchanged water and heat with the atmosphere, and the soil moisture changed dramatically. Meanwhile, the deep soil was less affected by the external environment such that the overall trend was relatively stable.

The content of unfrozen water at TS-05 was analyzed. Based on **Figure 7B**, the soil moisture in the unfrozen period gradually decreased with an increase in depth. The unfrozen water content of the soil at different depths during the freeze–thaw stage shows little variation. The amplitude of the change curve of unfrozen soil water content was relatively small in the cold season, but the change was more intense in the warm season and the shallow layer has a higher unfrozen water content. The soil moisture at TS-05 was generally low, and the unfrozen water content did not change significantly in the freeze–thaw stage (**Figure 8B**). The rainfall has a strong effect on unfrozen soil water content within 1 m in summer when rainfall is greatest. The unfrozen water content at TS-04 is generally much greater than that at TS-05, and the unfrozen water content changes more widely in the phase transition of water.

Soil Moisture Replenishment by Rainfall

In addition to the changes of unfrozen soil water content under freeze–thaw, rainfall also plays an important role in supplementing soil moisture. In the rainfall–soil moisture system, the surface characteristics (especially vegetation) directly affect the soil response time to rainfall and the depth of infiltration. To study the influence of different vegetation coverages on the underlying soil moisture, the response time and depth of soil moisture during rainfall events were selected for analysis. As seen in **Figure 9**, the distribution of precipitation at the two sites is nearly the same; the annual rainfall at TS-04 and TS-05 is 410.18 and 347.27 mm, respectively. Rainfall events are mainly concentrated in June, July, and August, accounting for about 70% of the annual rainfall. The rainfall events from June 2018 to August 2018 were counted. A total of 31 rainfall events occurred at TS-04, 18 of which caused a response of soil moisture. There were seven low-intensity rainfall events (**Figure 10**). A total of 27 rainfall events occurred at TS-05, of which only four rainfall events were able to elicit a response of soil moisture (all occurred in high-intensity rainfall areas). A rainfall of 5.33 mm within 6 h at TS-04 can cause a response of the soil moisture at a depth of 5 cm, while TS-05 needs a continuous 9.5 h of rainfall to reach 12.54 mm. From the point of view of the infiltration depth of rainfall (**Figure 11**), six of the 18 effective rainfall events (i.e., those that can cause a response of soil moisture) at TS-04e could cause a change in the soil moisture at 20 cm; the minimum rainfall was 7.56 mm (lasting for 1.5 h). However, the four effective rainfall events at TS-05 only caused a response of the soil moisture at 5 cm.

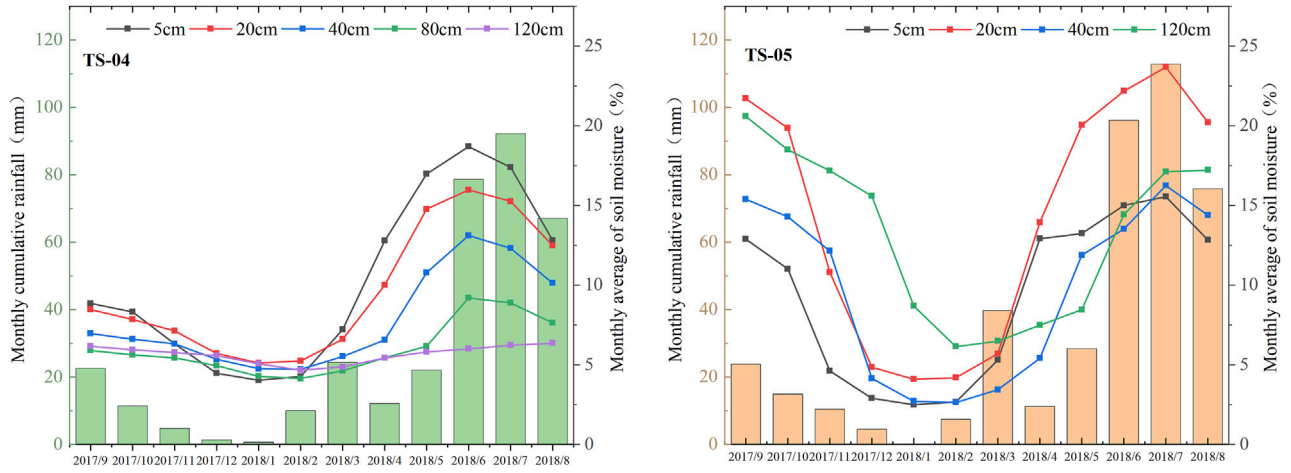

FIGURE 9 | Monthly accumulated precipitation and monthly average unfrozen water content of soil at TS-04 site and TS-05 site.

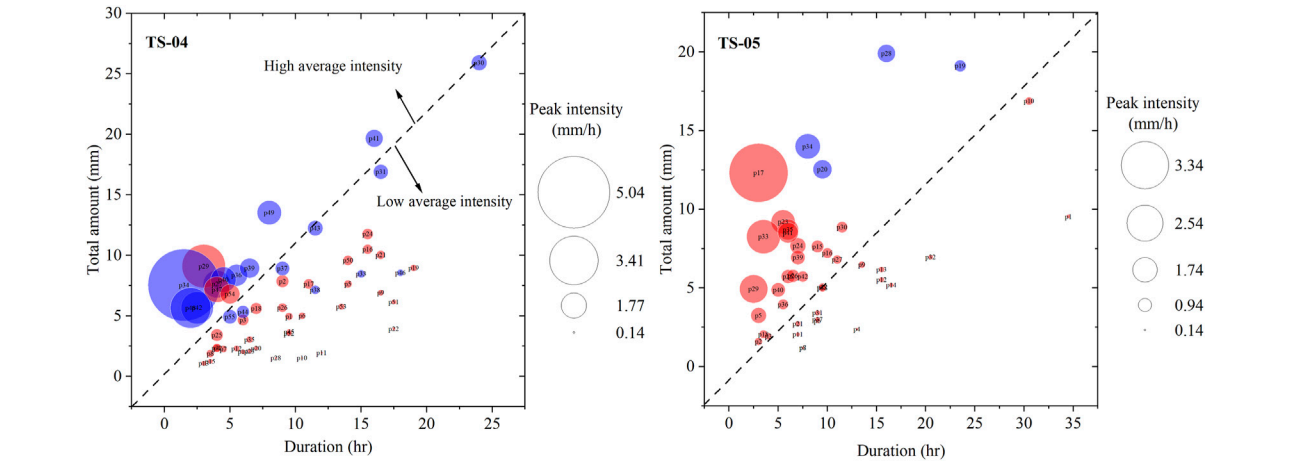

FIGURE 10 | Bubble plots of the intensity of rainfall in the summer and the response of soil moisture at TS-04 and TS-05 sites.

DISCUSSION

Effects of Vegetation Coverage on the Thermal Condition of the Soil

Vegetation is an important component of terrestrial ecosystems, participating in a variety of physical, chemical and biological processes between the atmosphere and soil (Van Hall et al., 2017; Pang et al., 2019; Gu et al., 2020). At high altitudes, intense solar radiation can cause dramatic changes in surface temperature. Vegetation can effectively reduce near-surface radiation through photosynthesis and leaf shielding, thus reducing the range of surface temperature variation, which is very important for frozen soil (Fedorov et al., 2019). The TS-04 site has 90% vegetation coverage, and dense vegetation can greatly reduce solar radiation reaching the ground. Although the radiation of TS-05, where vegetation coverage is relatively smaller, can also be reduced to a certain extent, it is much less of a change than that of TS-04. Thus, the soil temperature at all depths at TS-05 were higher than that at TS-04 (**Figure 12**). However, this difference gradually decreased with the soil depth. When the soil reaches a certain depth, the impact of vegetation on the soil is very weak, and the soil temperature difference between the two stations is very small. In permafrost regions, another factor affecting soil thermal conditions of vegetation is the process of freezing and thawing. Vegetation coverage impacts soil heat transfer efficiency (Domine et al., 2016). Vegetation slows down the heat transfer rate between the ground and air during soil freezing–thawing, resulting in delayed soil heat absorption or heat dissipation. This process delays the initial time of soil freezing and thawing and slows down the freezing–thawing rate (Guo et al., 2011). This further explains the differences in freeze–thaw processes between the two sites in **Figure 5**.

Vegetation covers the surface and has a large impact on the surface soil. The thermal insulation of vegetation inhibits the

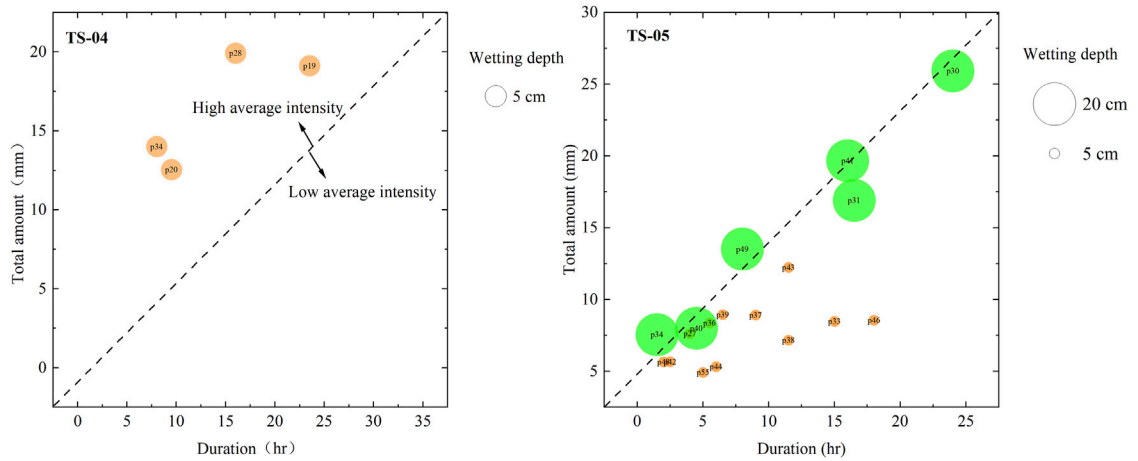

FIGURE 11 | Depth of soil moisture response to rainfall at TS-04 and TS-05 sites.

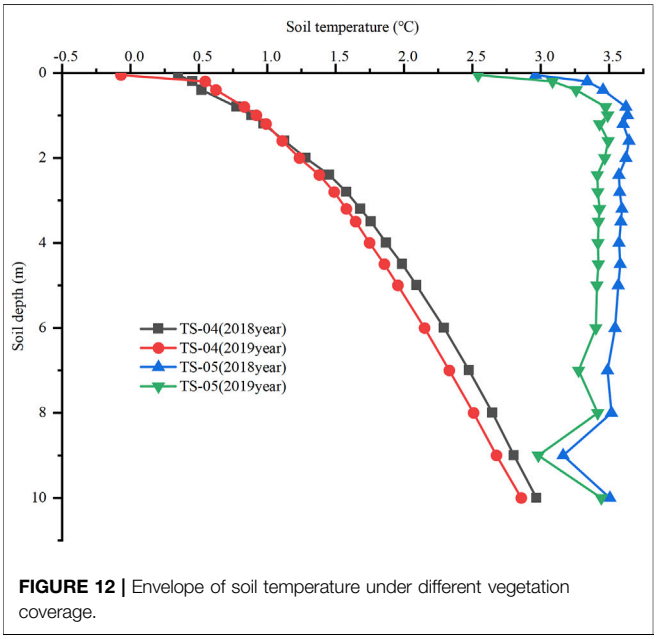

FIGURE 12 | Envelope of soil temperature under different vegetation coverage.

temperature change of shallow soil caused by temperature changes. Some studies show that there is a significant negative correlation between vegetation coverage and surface temperature (Weng et al., 2004). The 5-cm heat flux and ground–air temperature difference at the two stations shows that vegetation coverage has a profound impact on the thermal state of shallow soil. Interestingly, the variation range of the 5-cm soil heat flux at TS-04 was greater than that at TS-05. It is reasonable that the vegetation coverage at TS-04 is higher, so it greatly reduces the heat transfer at the 5-cm soil depth, but the result is the opposite. Soil temperature and soil moisture are not independent variables, and their mutual coupling is a real law. In the frozen soil region, the coupling process is very complex due to the particularity of frozen soil. The phase change of soil moisture has a profound impact on the change of the soil heat flux. The unfrozen soil water content at TS-04 can double that at TS-05. The soil with a higher content of unfrozen water has higher ice content in the cold season, so TS-04 (greater vegetation coverage) will release more heat. In the warm season, because the thermal conductivity of ice is greater than that of soil, ice will preferentially absorb more heat and melt into water. As temperatures and rainfall increase and vegetation enters the growing season, the plant canopy reduces the amount of solar radiation reaching the ground. Therefore, although the air temperature continued to rise, the heat flux at TS-04 decreased. The annual average soil heat flux of the two stations is negative, indicating that the heat transfer direction in this area is from soil to atmosphere, which is more conducive to the development of frozen soil.

The influence of vegetation on soil thermal conditions is multifaceted and complex. Vegetation reduces 1) wind speed near the surface, 2) evaporation of water from the topsoil and 3) the release of heat from the soil to the air. Vegetation can also increase or decrease the heat transfer properties of soil by changing the soil environment. In addition to vegetation, winter snow in Tianshan also affects the thermal conditions of soil. Snow will generally reduce the soil temperature, but a particular snow depth also plays a role in thermal insulation. This paper has not studied the impact of snow on soil thermal conditions in Tianshan, but it is clear that the impact of snow on soil temperature cannot be ignored.

Effects of Vegetation Coverage on Soil Water Content

The soil moisture content in frozen soil areas can determine the degree of soil freezing in the cold season. Vegetation is the main interface of soil water exchange with the outside environment, which will have an important impact on the content of the soil water. Generally, soil water retention is controlled by vegetation characteristics and soil properties. The change of vegetation and soil properties will inevitably lead to a change in soil water retention

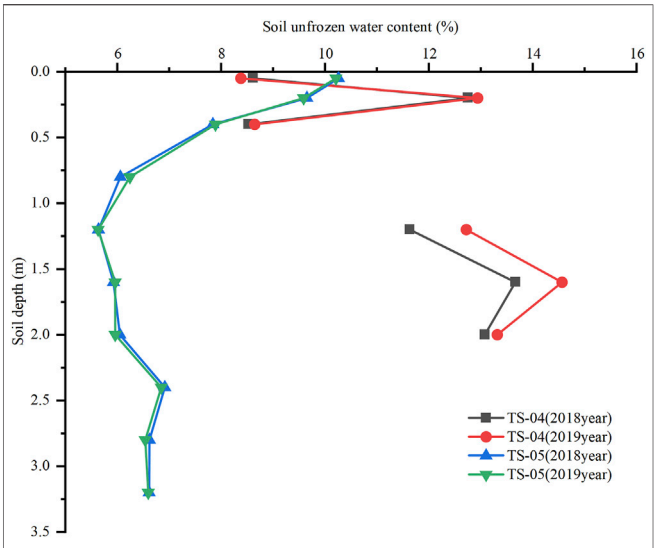

FIGURE 13 | Envelope of soil unfrozen water content under different vegetation coverage.

(Dai et al., 2020). Soil organic matter can increase the adsorption of water and affect the soil water retention, which is the most important factor affecting the soil water of alpine grasslands (Wang et al., 2016). The abundant vegetation at the TS-04 site increases the content of soil organic matter, which changes the distribution of the soil water. At the TS-04 site, plant roots are most concentrated at a soil depth of 20 cm. Plant roots can increase the soil water retention of rhizosphere soil, but more mucus produced by roots will reduce the saturated hydraulic conductivity at a 20-cm depth; thus, it will reduce the soil moisture at adjacent depths. This process explains why the unfrozen water content of soil at a 20-cm depth at the TS-04 site rapidly increases (**Figure 13**). Studies have shown that a higher degradation of grassland produces a lower soil moisture content (Pan et al., 2017). In this study, the overall soil moisture of the TS-04 site, where the vegetation coverage is greater, is higher than that at TS-05.

Importantly, vegetation affects soil moisture content through the response of vegetation to precipitation. Plant roots affect the infiltration capacity and rate by indirectly affecting the characteristics of soil structure and changing soil channels. Therefore, the precipitation infiltration rates of soil with different vegetation types and vegetation coverage vary (Cui et al., 2019). Studies have shown that the infiltration rate of alpine grassland with large vegetation coverage is 125% higher than that with small vegetation coverage. In this study, the response of soil moisture to rainfall at the two sites with different amounts of vegetation coverage was significantly different; large vegetation coverage showed better permeability. Therefore, the soil moisture at the TS-04 site continuously accumulates during rainfall such that the overall moisture content is much greater than that of the TS-05 site. The TS-05 site has small vegetation coverage and a weak water infiltration capacity. Only heavy rainfall events can cause a change in the 5-cm shallow soil water.

Topography also has a great influence on the distribution of soil moisture. The slope of the TS-05 site is steeper than that of the TS-04 site, which is also an important factor affecting the response of soil moisture to rainfall. Sites with steeper slopes have difficulty storing rainwater because most of the rainwater is lost through surface runoff and cannot supplement the soil moisture. This process is also an important explanation of the difference between soil moisture at the two sites.

CONCLUSION

The results showed that the change in vegetation cover significantly affected the soil freeze–thaw process. Because of the heat insulation of vegetation, the start time of soil freezing–thawing was delayed and the rate of soil freezing–thawing decreased at the site with high vegetation coverage. A smaller vegetation coverage correlates to a shallower and longer duration soil daily freeze–thaw cycle. The duration of daily freeze–thaw cycles during the thawing period was significantly longer than that in the freezing period, and the number of days experiencing a daily freeze–thaw cycle significantly decreased with an increase in the soil depth.

The effect of vegetation is mainly reflected in the winter thermal insulation and summer cooling. A greater vegetation coverage correlates to a larger temperature difference between the ground and air in the cold season, a smaller temperature difference between the ground and air in the warm season, and better insulation of the soil. A higher vegetation coverage correlates to a greater impact of the soil moisture on the soil thermal conditions.

Rainfall easily accumulates in areas with high vegetation coverage. The overall soil moisture content at the site with large vegetation coverage is greater than that at the site with small vegetation coverage.

DATA AVAILABILITY STATEMENT

The original contributions presented in the study are included in the article/supplementary material, further inquiries can be directed to the corresponding author.

AUTHOR CONTRIBUTIONS

All authors listed have made a substantial, direct, and intellectual contribution to the work and approved it for publication.

FUNDING

This work was funded by the Independent Project of the State Key Laboratory of Frozen Soils Engineering (Grant No. SKLFSE-ZQ-55).

ACKNOWLEDGMENTS

We thank the reviewers for their valuable comments and suggestions that helped to improve the manuscript.

REFERENCES

Chen, H., Nan, Z., Zhao, L., Ding, Y., Chen, J., and Pang, Q. (2015). Noah Modelling of the Permafrost Distribution and Characteristics in the West Kunlun Area, Qinghai-Tibet Plateau, China. *Permafrost Periglac. Process.* 26 (2), 160–174. doi:10.1002/ppp.1841

Cheng, H., Wang, G., Hu, H., and Wang, Y. (2008). The Variation of Soil Temperature and Water Content of Seasonal Frozen Soil with Different Vegetation Coverage in the Headwater Region of the Yellow River, China. *Environ. Geol.* 54 (8), 1755–1762. doi:10.1007/s00254-007-0953-x

Cui, Z., Wu, G.-L., Huang, Z., and Liu, Y. (2019). Fine Roots Determine Soil Infiltration Potential Than Soil Water Content in Semi-arid Grassland Soils. *J. Hydrol.* 578, 124023. doi:10.1016/j.jhydrol.2019.124023

Dai, L., Yuan, Y., Guo, X., Du, Y., Ke, X., Zhang, F., et al. (2020). Soil Water Retention in alpine Meadows under Different Degradation Stages on the Northeastern Qinghai-Tibet Plateau. *J. Hydrol.* 590, 125397. doi:10.1016/j.jhydrol.2020.125397

Dai, Y., Shangguan, W., Duan, Q., Liu, B., Fu, S., and Niu, G. (2013). Development of a China Dataset of Soil Hydraulic Parameters Using Pedotransfer Functions for Land Surface Modeling. *J. Hydrometeorology* 14 (3), 869–887. doi:10.1175/jhm-d-12-0149.1

Dickinson, R. E. (1986). *Biosphere/Atmosphere Transfer Scheme (BATS) for the NCAR Community Climate Model.* Technical report. NCAR.

Domine, F., Barrere, M., and Sarrazin, D. (2016). Seasonal Evolution of the Effective thermal Conductivity of the Snow and the Soil in High Arctic Herb Tundra at Bylot Island, Canada. *The Cryosphere* 10 (6), 2573–2588. doi:10.5194/tc-10-2573-2016

Dunkerley, D. (2008). Identifying Individual Rain Events from Pluviograph Records: a Review with Analysis of Data from an Australian Dryland Site. *Hydrol. Process.* 22 (26), 5024–5036. doi:10.1002/hyp.7122

Fedorov, A. N., Konstantinov, P. Y., Vasilyev, N. F., and Shestakova, A. A. (2019). The Influence of Boreal forest Dynamics on the Current State of Permafrost in Central Yakutia. *Polar Sci.* 22, 100483. doi:10.1016/j.polar.2019.100483

Genxu, W., Shengnan, L., Hongchang, H., and Yuanshou, L. (2009). Water Regime Shifts in the Active Soil Layer of the Qinghai-Tibet Plateau Permafrost Region, under Different Levels of Vegetation. *Geoderma* 149 (3), 280–289. doi:10.1016/j.geoderma.2008.12.008

Groffman, P. M., Hardy, J. P., Fashu-Kanu, S., Driscoll, C. T., Cleavitt, N. L., Fahey, T. J., et al. (2011). Snow Depth, Soil Freezing and Nitrogen Cycling in a Northern Hardwood forest Landscape. *Biogeochemistry* 102 (1), 223–238. doi:10.1007/s10533-010-9436-3

Gu, C., Mu, X., Gao, P., Zhao, G., Sun, W., and Tan, X. (2020). Distinguishing the Effects of Vegetation Restoration on Runoff and Sediment Generation on Simulated Rainfall on the Hillslopes of the Loess Plateau of China. *Plant Soil* 447 (1), 393–412. doi:10.1007/s11104-019-04392-4

Guo, D., Yang, M., and Wang, H. (2011). Characteristics of Land Surface Heat and Water Exchange under Different Soil Freeze/thaw Conditions over the central Tibetan Plateau. *Hydrol. Process.* 25 (16), 2531–2541. doi:10.1002/hyp.8025

Li, W., Wu, J., Bai, E., Jin, C., Wang, A., Yuan, F., et al. (2016). Response of Terrestrial Carbon Dynamics to Snow Cover Change: A Meta-Analysis of Experimental Manipulation (II). *Soil Biol. Biochem.* 103, 388–393. doi:10.1016/j.soilbio.2016.09.017

Lin, H., and Zhou, X. (2008). Evidence of Subsurface Preferential Flow Using Soil Hydrologic Monitoring in the Shale Hills Catchment. *Eur. J. Soil Sci.* 59 (1), 34–49. doi:10.1111/j.1365-2389.2007.00988.x

Lozano-Parra, J., Schnabel, S., and Ceballos-Barbancho, A. (2015). The Role of Vegetation Covers on Soil Wetting Processes at Rainfall Event Scale in Scattered Tree woodland of Mediterranean Climate. *J. Hydrol.* 529, 951–961. doi:10.1016/j.jhydrol.2015.09.018

Nan, Z. T., Li, S. X., and Liu, Y. Z. (2002). Mean Annual Ground Temperature Distribution on the Tibetan Plateau: Permafrost Distribution Mapping and Further Application. *J. Glaciology Geocryology* 24 (2), 142–148. (in Chinese).

Natali, S. M., Schuur, E. A. G., Trucco, C., Hicks Pries, C. E., Crummer, K. G., and Baron Lopez, A. F. (2011). Effects of Experimental Warming of Air, Soil and Permafrost on Carbon Balance in Alaskan Tundra. 17(3), 1394–1407. doi:10.1111/j.1365-2486.2010.02303.x

Pan, T., Hou, S., Wu, S., Liu, Y., Liu, Y., Zou, X., et al. (2017). Variation of Soil Hydraulic Properties with alpine Grassland Degradation in the Eastern Tibetan Plateau. *Hydrol. Earth Syst. Sci.* 21 (4), 2249–2261. doi:10.5194/hess-21-2249-2017

Pang, Z., Jiang, L., Wang, S., Xu, X., Rui, Y., Zhang, Z., et al. (2019). Differential Response to Warming of the Uptake of Nitrogen by Plant Species in Non-degraded and Degraded alpine Grasslands. *J. Soils Sediments* 19 (5), 2212–2221. doi:10.1007/s11368-019-02255-0

Sellers, P. J., Mintz, Y., Sud, Y. C., and Dalcher, A. (1986). A Simple Biosphere Model (SIB) for Use within General Circulation Models. *J. Atmos. Sci.* 43 (6), 505–531. doi:10.1175/1520-0469(1986)043<0505:asbmfu>2.0.co;2

Van Hall, R. L., Cammeraat, L. H., Keesstra, S. D., and Zorn, M. (2017). Impact of Secondary Vegetation Succession on Soil Quality in a Humid Mediterranean Landscape. *CATENA* 149, 836–843. doi:10.1016/j.catena.2016.05.021

Wang, X., Yi, S., Wu, Q., Yang, K., and Ding, Y. (2016). The Role of Permafrost and Soil Water in Distribution of alpine Grassland and its NDVI Dynamics on the Qinghai-Tibetan Plateau. *Glob. Planet. Change* 147, 40–53. doi:10.1016/j.gloplacha.2016.10.014

Weng, Q., Lu, D., and Schubring, J. (2004). Estimation of Land Surface Temperature-Vegetation Abundance Relationship for Urban Heat Island Studies. *Remote Sensing Environ.* 89 (4), 467–483. doi:10.1016/j.rse.2003.11.005

Wu, Q. B., Shen, Y. P., and Shi, B. (2003). Relationship between Frozen Soil Together with its Water-Heat Process and Ecological Environment in the Tibetan Plateau. *J. Glaciology Geocryology* 25 (3), 250–255.

Wu, X. B., Nan, Z. T., Wang, W. Z., and Zhao, L. (2018). Simulation of the Impact of Vegetation and Soil Characteristics on Permafrost over the Tibetan Plateau Based on the Noah Land Surface Model. *J. Glaciology Geocryology* 40 (2), 279–287. (in Chinese).

Xiao, Y., Zhao, L., Dai, Y., Li, R., Pang, Q., and Yao, J. (2013). Representing Permafrost Properties in CoLM for the Qinghai-Xizang (Tibetan) Plateau. *Cold Regions Sci. Tech.* 87, 68–77. doi:10.1016/j.coldregions.2012.12.004

Yang, M., Yao, T., Gou, X., Hirose, N., Fujii, H. Y., Hao, L., et al. (2007). Diurnal Freeze/thaw Cycles of the Ground Surface on the Tibetan Plateau. *Chin. Sci Bull* 52 (1), 136–139. doi:10.1007/s11434-007-0004-8

Conflict of Interest: The authors declare that the research was conducted in the absence of any commercial or financial relationships that could be construed as a potential conflict of interest.

frontiers in Earth Science

ORIGINAL RESEARCH
published: 11 February 2022
doi: 10.3389/feart.2022.821305

Experimental Study on Thermal Regime and Frost Jacking of Pile Foundation During Operation Period in Permafrost Regions

Yunhu Shang[1,2], *Fujun Niu*[1]*, *Jianhong Fang*[3] *and Libo Wu*[4]

[1]State Key Laboratory of Frozen Soil Engineering, Northwest Institute of Eco-Environment and Resources, Chinese Academy of Sciences, Lanzhou, China, [2]Da Xing'anling Observation and Research Station of Frozen-Ground Engineering and Environment, Northwest Institute of Eco-Environment and Resources, Chinese Academy of Sciences, Jiagedaqi, China, [3]Qinghai Research Institute of Transportation, Xining, China, [4]School of Civil Engineering and Hydraulic Engineering, Ningxia University, Yinchuan, China

The stability of a cast-in-place pile foundation in permafrost region is primarily subject to the thermal regime and tangential frost-heave forces (TFF) during the operation period. However, studies focusing on the thermal and mechanical characteristics of pile foundation during runtime are rare. To investigate the effect of pile foundation on the thermal regime and quantify the magnitude of unit tangential frost-heave forces (UTFF), a field experiment was conducted on the Qinghai–Tibet Plateau, China. Results showed that the cast-in-place pile foundation enhanced the heat exchange between the atmosphere and soil, which expanded the annual range of the surrounding ground temperature. Furthermore, the permafrost table depth was increased by 0.4–0.7 m (0.33–0.58 times the pile diameter). The TFF increased significantly when the soil temperature decreased from 0 to −0.5°C. Meanwhile, the thickness of the frost heaving layer was approximately double that of the active layer, in which the maximum UTFF was higher than 52.04 kPa. The adfreezing bond force of permafrost to pile shaft burdened most of the applied load, and the end bearing contributed relatively little. Findings from this study will benefit the stability maintenance and structure design of pile foundation in permafrost regions.

Keywords: tangential frost-heave forces, cast-in-place pile foundation, thermal regime, permafrost region, frost heaving, frost jacking

OPEN ACCESS

Edited by:
Guo Donglin,
Institute of Atmospheric Physics (CAS), China

Reviewed by:
Yao Xiao,
Northwest Institute of Eco-Environment and Resources (CAS), China
Yinghong Qin,
Guangxi University for Nationalities, China

***Correspondence:**
Fujun Niu
niufujun@lzb.ac.cn

Specialty section:
This article was submitted to Cryospheric Sciences, a section of the journal Frontiers in Earth Science

Received: *24 November 2021*
Accepted: *13 January 2022*
Published: *11 February 2022*

Citation:
Shang Y, Niu F, Fang J and Wu L (2022) Experimental Study on Thermal Regime and Frost Jacking of Pile Foundation During Operation Period in Permafrost Regions. Front. Earth Sci. 10:821305. doi: 10.3389/feart.2022.821305

INTRODUCTION

The cast-in-place pile foundation was first widely adopted in Qinghai–Tibet Plateau permafrost regions. Owing to its superior mechanical stability, more cast-in-place pile foundations will be constructed under the scenarios of the promotion of road grading. More than 80% of the bearing capacity of pile foundation in permafrost regions, irrespective of their types, is provided by adfreezing force between the surrounding frozen soil and the pile shaft (Aksenov and Kistanov, 2008). Adfreezing force is highly sensitive to temperature changes (Goncharov, 1965; Wang et al., 2005; Ma and Wang, 2014); hence, the thermal regime can affect the safety of pile foundation. To understand the stability of pile foundation more effectively during operation in permafrost regions, the interactive thermal effect between the pile foundation and the permafrost environment must be discussed. For the thermal regime of the cast-in-place pile foundation in permafrost, previous studies

have primarily focused on the disturbance of hydration (Jia et al., 2004; Wu et al., 2006; Tang and Yang, 2010), temperature optimization of casting concrete (Wu et al., 2004; Li et al., 2005), and freeze-back time (Wang et al., 2004; Wang et al., 2005; Yuan et al., 2005; Zhang et al., 2010; Wang et al., 2013). Although these studies have emphasized on the thermal characteristics of pile foundation in the construction period, analyses of the thermal regime during the operation period are lacking.

In addition to the thermal regime, the seasonal frost heaving of active layers may threaten the safety of pile foundation in permafrost. It can cause a large uplift force, which contributes to the destructive movement of pile foundation (Andersland and Ladanyi, 2003). Additionally, the heaved pile may not return to its original position at the end of the thaw period owing to the support provided by the adfreezing bond force of the permafrost to the pile shaft. Furthermore, the uplift would be cumulated after several seasonal freeze-thaw cycles (Johnston, 1981). For a pile foundation in permafrost region, the total uplift force is a function of the unit tangential frost-heave forces (UTFF) and the area of the foundation in contact with the active layer. Therefore, to resist the uplift, the precise value of the tangential frost-heave forces (TFF) must be determined. Considering the perimeter of a pile, frost line, and minimum temperature of an active layer, Tsytovich (1959) proposed Dalmatov's equation to estimate the TFF. Subsequently, Penner and Irwin (1969) reported that Dalmatov's equation agreed well with the data acquired from field experiments. Based on the frost heaving deformation theory of foundation soil, He et al. (2015) derived an integral equation for three-dimensional viscoelastic problem of pile frost heaving force computation. Torgersen (1976) summarized the typical limiting tangential adfreezing stress values for several material types. Liu (2018) proposed a model to simulate frost jacking performances of a pile foundation, which was validated by a case study of simplified bridge pile foundation in permafrost region. Vyalov and Porkhaev (1976) recommended the design values of UTFF to be 80 kPa for the soil temperatures above −3°C and 60 kPa for those below −3°C. Liu (1993) discussed the distribution of tangential stress with the penetration of frost line. For the control measures, the screw piles were introduced to reduce frost diseases, and a series of laboratory tests and numerical simulations were conducted to evaluate the frost jacking characteristics of screw piles (Wang et al., 2017a; Wang et al., 2017b; Wang et al., 2018). A fiberglass reinforced plastic cover was proposed to relieve the frost jacking of pile foundation, and the control effect of the frost jack was assessed (Wen et al., 2016). Jiang et al. (2014) determined that two-phase closed thermosyphons can significantly restrain the frost jacking of pile foundation. Zhou et al. (2021) numerically researched the frost jacking behavior of pile foundations with and without two-phase closed thermosyphons in permafrost regions. Few studies have reported the TFF of cast-in-place pile foundation, particularly in permafrost regions. Because many variables are involved and that the material type and surface condition are key factors that govern the TFF, the existing research results barely serve as guides for the design of cast-in-place pile foundation. Hence, it is necessary to conduct field studies to determine the TFF magnitude of cast-in-place pile foundation.

Generally, the thermal regime of cast-in-place pile foundation buried in permafrost during the construction period has been the primary foci of research to date. However, the thermal and mechanical characteristics of pile foundation during operation are less well understood. The purposes of this study are primarily to:

1) Investigate the characteristics of the thermal regime of cast-in-place pile foundation during the operation period;
2) Evaluate the tangential frost-heave forces of cast-in-place pile foundation.

Hence, a field experiment was conducted on a site along the China National Highway 214 (G214) in a permafrost region of the Qinghai–Tibet plateau. Based on monitored data, we analyzed the effect of the cast-in-place pile foundation on the thermal regime and predicted the magnitude of TFF. The results will provide essential references for the structure design and stability maintenance of cast-in-place pile foundation in permafrost regions.

EXPERIMENTAL SITE AND MONITORING STUDIES

The experimental site was located in the Huashixia Area of Maduo County, Qinghai Province, Western China (**Figure 1A**). The elevation was approximately 4,300 m, and the permafrost table was approximately 2.5 m deep. An ice-rich frozen layer existed near the permafrost table. The mean annual ground temperature was about −0.7°C, signifying a region of unstable warm permafrost (Ma et al., 2008), which was highly sensitive to climate change. More precisely, permafrost degradation would more easily weaken the freezing strength and anchorage capacity of pile foundations in this area. Thus, it is representative to conduct the study on thermal regime and frost jacking of pile foundation in this experimental site.

The soil around the piles can be divided into three layers: silty clay (0–2 m), sand with gravel (2–8 m), and weathered mudstone (below 8 m). Two pile foundations, of diameter 1.2 m, were cast with C30 concrete (mixed with silicate cement) on the site in October 2012, and their lengths were 20 and 30 m. The main reinforcement in each pile foundation consisted of 28 ribbed reinforced bars with the diameter of 22 mm. A load exceeding 120 t was applied on each pile foundation on 4 November 2015.

Thermistors were instrumented along the pile sides and fixed on the reinforcement cages, as shown in **Figure 1B**. A borehole more than 10 m from the piles was drilled, and the thermistors were fixed in it to examine the natural ground temperature. Rebar stress gauges were installed in the reinforcement cage, and a protective layer of thickness approximately 7 cm existed between the reinforcement cage and the pile foundation surface. The depths of the monitoring points are summarized in **Table 1** and **Table 2**. Data were collected using data loggers at 2:00, 8:00, 14:00, and 20:00.

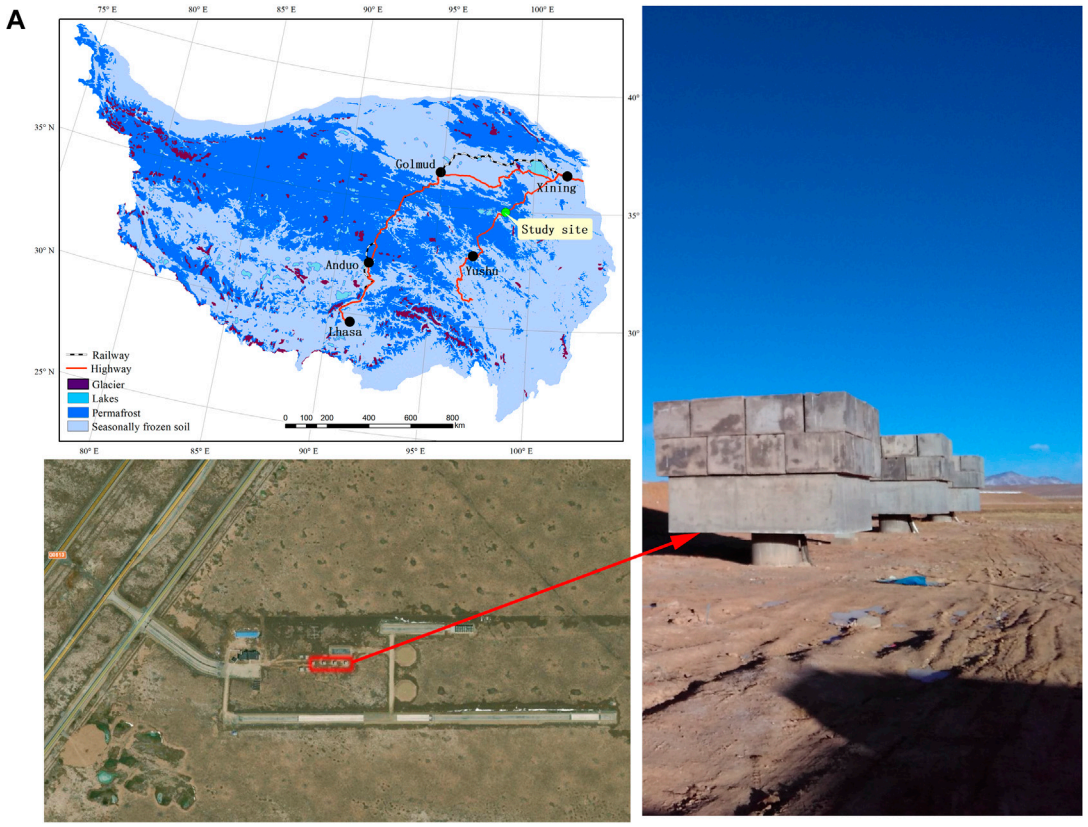

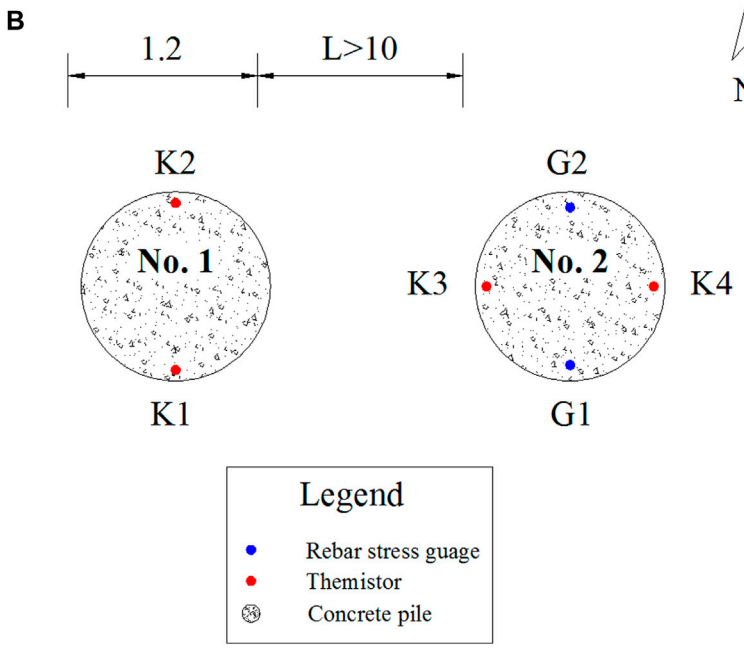

FIGURE 1 | Experimental site.

TABLE 1 | Depths of the thermistors.

	Borehole	Depths (m)
Natural ground	Natural borehole	0, −0.5, −1, −1.5, −2, −2.5, −3, −3.5, −4, −4.5, −5, −6, −7, −8, −9, −10
No. 1	K 1, K 2	0, −0.5, −1, −1.5, −2, −2.5, −3, −3.5, −4, −4.5, −5, −5.5, −6, −6.5, −7, 7.5, −8, −8.5, −9, −9.5, −10,−11, −12, −13, −14, −15, −16, −17, −18, −19, −20
No. 2	K 3, K 4	0, −0.5, −1, −1.5, −2, −2.5, −3, −3.5, −4, −4.5, −5, −5.5, −6, −6.5, −7, 7.5, −8, −8.5, −9, −9.5, −10, −11, −12, −13, −14, −15, −16, −17, −18, −19, −20, −21, −22, −23, −24, −25, −26, −27, −28, −29, −30

TABLE 2 | Depths of the rebar stress gauges.

	Borehole	Depths (m)
No. 2	G 1	−5.2, −10.7, −11.8, −12.9, −16.2, −17.3, −18.4, −21.6, −25.8
	G 2	−5.2, −6.3, −7.4, −9.6, −11.8, −14, −16.2, −17.3, −18.4, −19.5, −21.6, −23.7, −27.9, −30

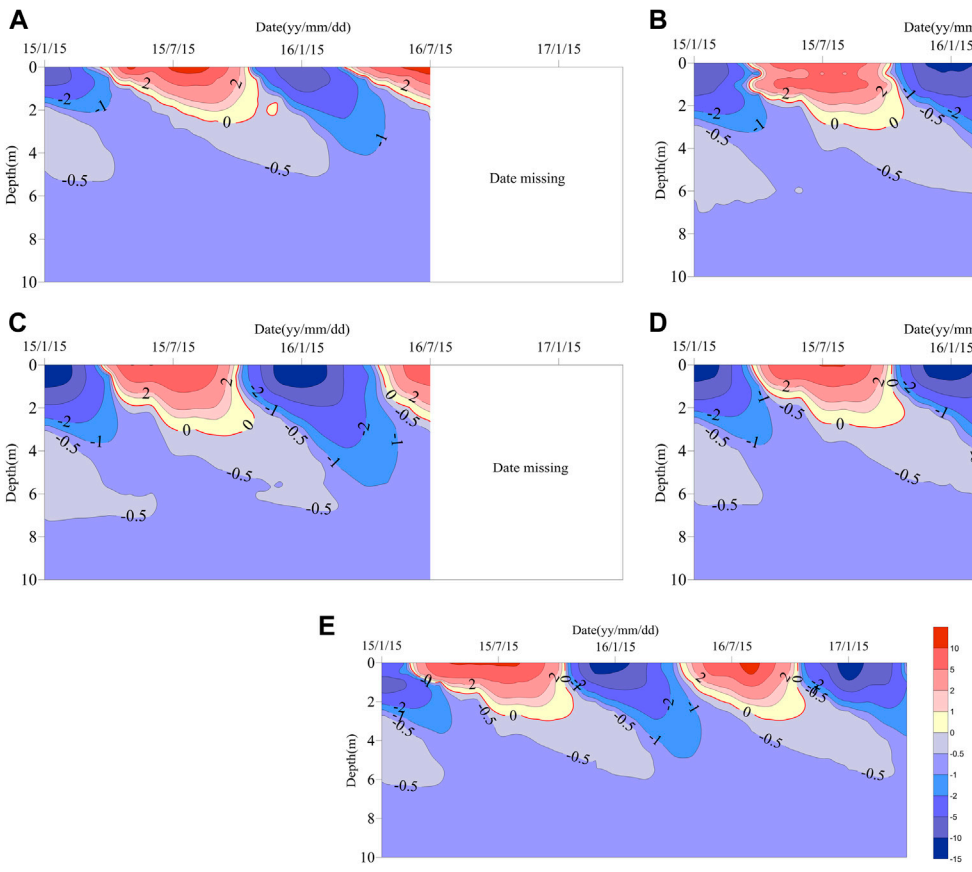

FIGURE 2 | Freeze-thaw process of the boreholes.

RESULTS AND ANALYSIS

Thermal Characteristic of the Pile Foundation

To investigate the effect of the pile foundation, **Figure 2** is presented to depict the freeze-thaw process of the natural ground and pile sides. Little difference between the two cycles in the isotherms of 0 and -0.5°C can be seen in **Figures 2B,D,E**. This phenomenon illustrated the pile foundations had completed the freezeback. As shown, a visible distinction existed between the natural ground and pile sides in the freeze-thaw process. First, the natural permafrost table was at the depth of 2.6 m in 2015

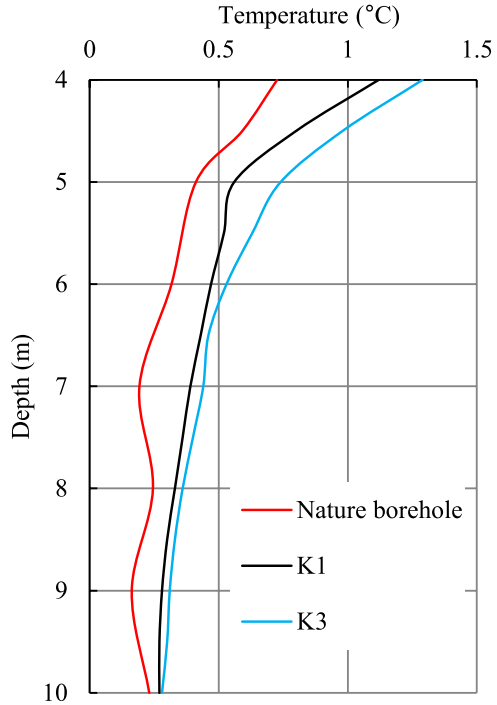

FIGURE 3 | Annual range of ground temperature of pile sides and natural borehole.

(**Figure 2A**); however, for the pile side, it ranged from three to 3.3 m (**Figure 2B–E**). Next, the −0.5°C isotherm of the natural borehole could reach the depth of 5.1 m in March 2016, which was 0.9–1.7 m shallower than that of the boreholes along the pile sides. Subsequently, the area encircled by the −1°C isotherm in the natural borehole was significantly smaller than that in boreholes K1, K2, and K3. The thermal conductivity and thermal capacity of the pile foundation were 2.94 W/(m•°C) and 2,449 kJ/(m3•°C), respectively (National Standards of the People's Republic of China, 2016). The freeze-thaw process of the surrounding soil was significantly affected by the pile foundation. This attributed to the thermal conductivity of the pile, which enhanced the heat transfer between the soil and atmosphere. As shown in **Figure 2B,C** little difference can be seen between the depths of their permafrost tables. This characteristic was also observed on the east and west sides of pile No. 2 (**Figure 2D,E**).

To quantify the effect of the concrete foundation, **Figure 3** shows the annual range of ground temperature (ARGT) along the pile sides and the nature borehole under the depth of 4 m. As shown, the ARGTs of the pile sides were significantly larger than that of the natural borehole. At the depth of 7 m, the ARGTs of boreholes K1 and K3 were more than double that of the natural borehole. Hence, the pile foundation increased the ARGT to a large degree.

The thermal regime difference between the natural ground and pile foundation demonstrated that the pile foundation acted as a heat source for the surrounding soil in warm seasons, and that the soil absorbed more heat through it. However, in the winter, the pile played a role in cooling the ground and pumped heat out of the surrounding soil. In this way, the pile foundation altered the freeze-thaw process.

Table 3 lists the time consumed by the shallow layers (0–3 m) of the boreholes to cool to the target temperatures, and the target temperatures included 0°C and −0.5°C. It is noteworthy that, to cool the active layer below 0°C, the natural borehole consumed 14.25 d, which was approximately double those consumed by boreholes K2 and K3. In addition, before the shallow layer (0–3 m) cooled to below −0.5°C, the cooling rate of the boreholes along the pile sides was more than 1.5 times that of the natural ground. The pile foundation accelerated the freeze rate of the shallow layers and reduced the cooling time significantly, which may alter the frost-heave capacity of the surrounding soil (Xu et al., 2001).

Response of Rebar Axis Force in Pile Foundation to Applied Load and Frost Heaving

Figure 4 shows the variation in rebar axis force (RAF) of pile No. 2 under the loads and the frost heaving. The vertical coordinate F, monitored using rebar stress gauges, did not represent the RAF, and its variation signified the increase or decrease in the RAF. The variation values of the RAF at several depths are listed in **Table 4**. The negative values signified compression, whereas the positive tension. A step decrease occurred 36 h after load application, and the F values of all depths changed in the same manner. Additionally, the absolute value of the variation decreased with depth in the range from 6.3 to 27.9 m. The variation value at the depth of 6.3 m was more than 11 times that at the depth of 27.9 m, indicating that the adfreezing bond force in the deep layer burdened a small percentage of the applied load. In addition, the absolute value of the F variation was larger at the depth of 6.3 m than 5.2 m; this may illustrate that the weight of the pile section exceeded the adfreezing bond force between the two depths.

Subsequently, the RAF increased sharply as the cold season was approaching, which related to the frost heaving of the surrounding active layer. From the variation values (**Table 4**) and ratio (**Figure 5**), it can be seen that the strain, caused by frost heaving, decreased with the depth. Additionally, the adfreezing bond force in the layer between 6 and 10 m alleviated most of the TFF.

To further understand the development process of the TFF, **Figure 6** is presented to show the relationship between the freeze-thaw process and the RAF variation of pile No. 2. Note that the value of F almost had not increased until the 0°C isotherm disappeared. Subsequently, it increased with the thickness decrease of the soil layer above −0.5°C. Furthermore, the F values reached the maximum on March 29, 2016 when the −0.5°C isotherm disappeared. The thickness of the frost heaving layer was approximately double

TABLE 3 | Time consumed by shallow layers (0–3 m) to cool to below 0 °C and −0.5°C during freezing period in late 2015.

Target temperature (°C)	Cooling time (d)			
	Nature borehole	K 1	K 2	K 3
0	14.25	8	7.25	7.25
−0.5	148.83	90.00	89.75	93.00

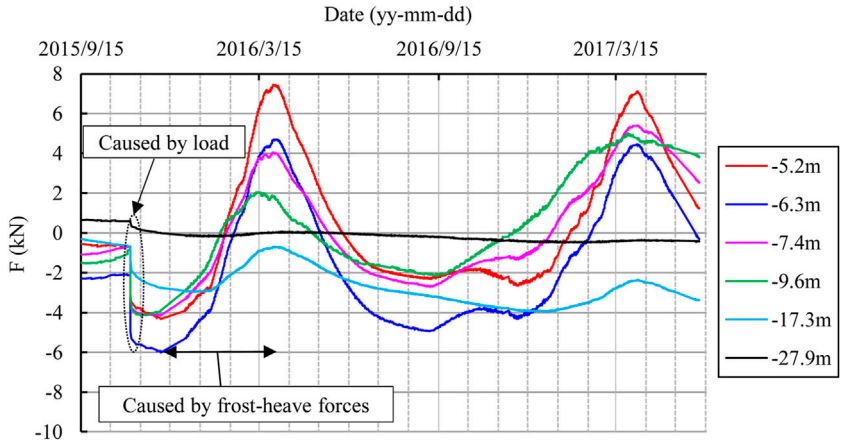

FIGURE 4 | Variations of rebar axis force at different depths of pile No. 2.

TABLE 4 | Variations of rebar axis force caused by load and TFF.

Depth (m)	The variations caused by the load in 35 h (kN)	The variations caused by the TFF (kN)
–5.2	–2.72	11.78
–6.3	–3.18	10.72
–7.4	–3.09	8.19
–9.6	–2.97	6.22
–17.3	–1.21	2.53
–27.9	–0.28	0.83

that of the active layer. This phenomenon may be attributed to the existence and migration of unfrozen water within the soil (Qiu et al., 1994). In other words, the soil first contained both ice and unfrozen water when the temperature dropped below 0°C. The unfrozen water was subjected to the exist temperature gradient, and moved toward the colder direction. It enhanced the ice lens formation and frost heaving. The maximum uplift force occurred when the ground was completely saturated with ice (and little unfrozen water). After that, the heaving almost stopped development. Not only the active layer, but also the permafrost with unfrozen water can cause the TFF in the freezing process.

It is noteworthy that all the F magnitudes under frost heaving were significantly higher than those before load application (**Figure 5**). And the force diagram of shallow pile section is shown in **Figure 7**. Meanwhile, the relationship between the tangential frost-heave forces [$Q(z)$], applied load (P) and axial force of pile shaft at the depth of 6.3 m [N (6.3)] can be described as **Eq. 1**:

$$Q(z) = \pi D \int_0^{6.3} q(z)\mathrm{d}z = P + N(6.3) \tag{1}$$

Where D is the diameter of pile, $q(z)$ is the unit tangential frost-heave forces and the z is the depth.

It can be concluded that the maximum TFF was more than the load (120 t). According to above scenario, the TFF was generated

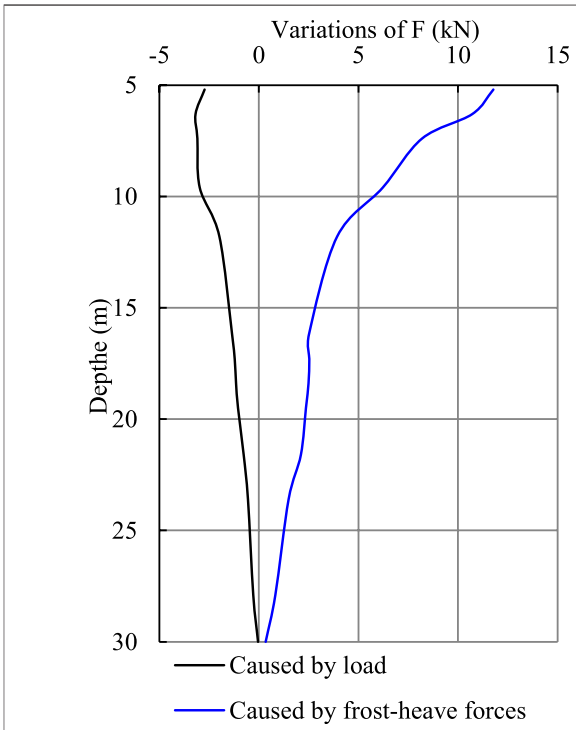

FIGURE 5 | Variations of RAF with depth.

by the frost heaving layer, and its thickness was approximately 6 m. Combining with the load magnitude and the pile diameter, the maximum UTFF should exceed 52.04 kPa.

Distribution of Adfreezing Force Along Pile Under Applied Load and Frost Heaving

Figure 8 shows the force diagram of pile. According to the existing literature (Weaver and Morgenstern, 1981; Tang et al.,

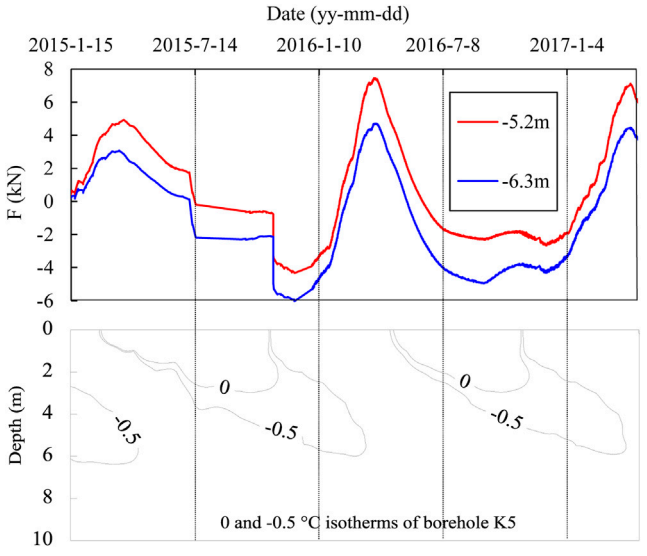

FIGURE 6 | Time series of the freeze-thaw process and seasonal variations of RAFs at depths of –5.2 and –6.3 m of pile No. 2.

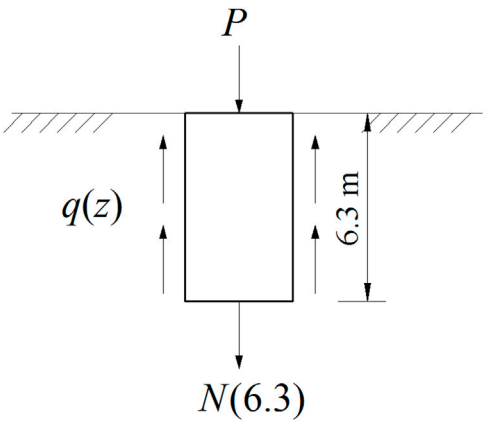

FIGURE 7 | Force diagram of pile section under frost heaving.

2019; Wang et al., 2021), the corresponding profiles of axial force were calculated from strains multiplied by the pile axial rigidity, and can be described as:

$$N = E \cdot A \cdot \varepsilon \tag{2}$$

Where E is the Young's modulus of the pile, and A is the cross-section area.

The shaft resistance can be described as:

$$q(z,t) = \frac{-1}{\pi D} \cdot \frac{\partial N(z,t)}{\partial z} \tag{3}$$

Where t is the time.

The shaft resistance of the *k-th* soil layer were calculated using axial force at each soil layer, based on **Eq. 4**:

$$q_k = \frac{-1}{\pi D} \cdot \frac{N_{k+1} - N_k}{l_k} \tag{4}$$

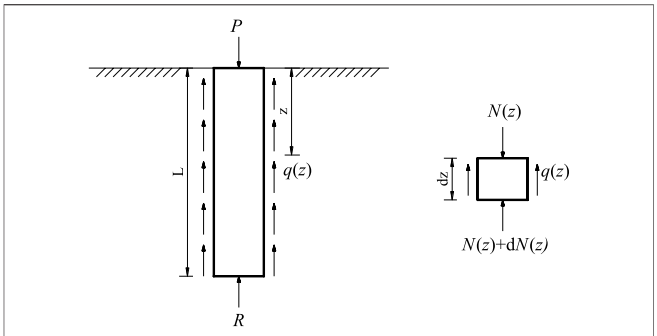

FIGURE 8 | Force diagram of pile **(A)** Variations of RAF with depth **(B)** Distribution of temperature with depth.

Where N_{k+1} and N_k are the axial forces of pile shaft at the bottom and top of the *k-th* soil layer; l_k is the thickness of the *k-th* soil layer.

The Young's modulus of the piles is estimated using **Eq. 5**:

$$E = \frac{(E_c A_c + E_a A_a)}{A} \tag{5}$$

Where E_c and E_a are the Young's modulus of concrete and steel rebar, respectively; A_c, A_a, and A are the cross-sectional areas of concrete, rebars, and pile, respectively.

The relationship between strains of steel rebar and pile can be described as **Eq. 6**, **Eq. 7**, and **Eq. 8**:

$$\varepsilon(z,t) = \varepsilon_a(z,t) \tag{6}$$

$$\frac{N(z,t)}{EA} = \frac{N_a(z,t)}{E_a A_a} \tag{7}$$

$$\frac{\frac{\partial N(z)}{\partial t}}{EA} = \frac{\frac{\partial N_a(z)}{\partial t}}{E_a A_a} \tag{8}$$

To illustrate the response of rebar axial force to the applied load, according to the measured results, **Figure 9** shows the variations of RAF and temperature with depth after load application. It can be seen that the pile side temperature have dropped below 0°C when the load was applied on the pile (**Figure 9B**). The pile shaft experienced a significant compression processes in the initial period (**Figure 9A**). The compression development tendency attenuated, and got into a relatively stable state a month later. The distribution characteristics of variable quantity of the RAF along the pile side were similar at the different times. It should be noted that the compression faded with the depth due to the effect of adfreezing bond force of the permafrost to the pile shaft.

In order to further explain the interaction of the pile-soil interface in an intuitive way, the coefficient $\alpha(z) = \Delta N_a(z)/\Delta N_a(6.3)$ was selected as an index to assess the strain distribution of pile under the depth of 6.3 m according to **Eq. 8**. **Table 5** lists the $\alpha(z)$ with the depth at different times. It can be found that the α under the depth of 18.4 m gradually increase with time in a month after load application, indicating that the deeper pile section needed a considerable period to response to the applied load. Meanwhile, the α (30) range from 1.29% to 5.72% during this

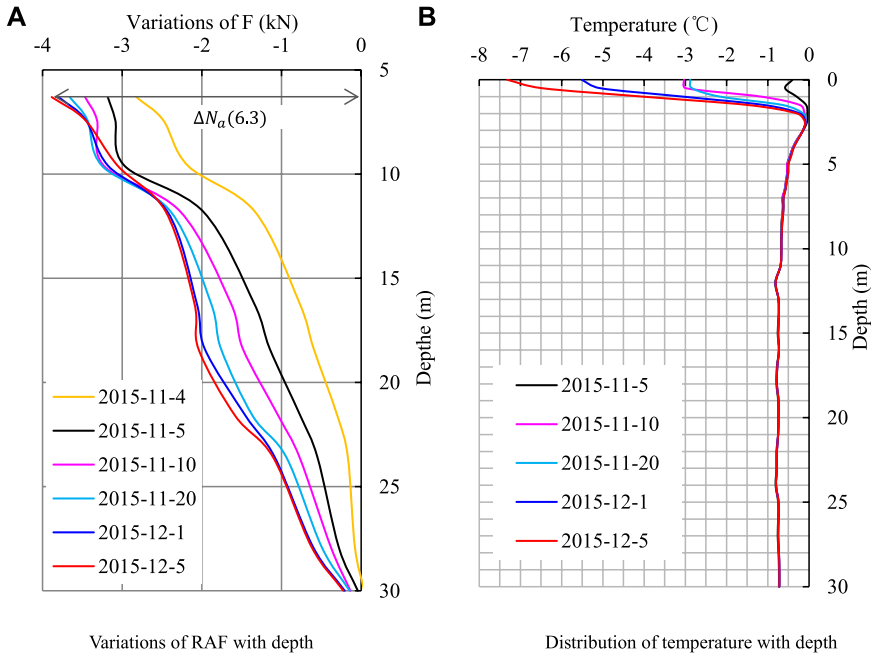

FIGURE 9 | Variations of RAF and temperature with depth after load application **(A)** Variations of RAF with depth **(B)** Distribution of temperature with depth.

TABLE 5 | The coefficient α with depth at different time after load application.

Depths (m)	$\Delta N_a(z)/\Delta N_a(6.3)$ (%)									
	6.3	**7.4**	**9.6**	**11.8**	**16.2**	**18.4**	**21.6**	**23.6**	**27.9**	**30**
2015-11-5	100.00	97.06	93.37	62.32	42.25	36.00	23.97	17.21	8.84	1.29
2015-11-10	100.00	95.70	93.20	65.48	47.18	42.80	29.99	22.28	10.97	3.86
2015-11-20	100.00	93.95	88.92	65.33	51.51	48.05	37.23	25.62	13.51	3.93
2015-12-1	100.00	91.02	83.64	64.02	54.34	51.65	38.21	28.50	15.87	5.40
2015-12-5	100.00	89.19	78.65	63.14	53.87	52.54	40.70	28.40	16.01	5.72

period. In other words, the end-bearing resistance only burdened less than 5.72% of applied load, which was consistent with that reported in Aksenov and Kistanov (2008), Johnston (1981) and Andersland and Ladanyi (2003).

The relationship between the end-bearing resistance and shaft resistance can be described by **Eq. 9**:

$$R = P - \pi D \int_0^L q(z)\mathrm{d}z \tag{9}$$

Thus, the α can also reflect the effect of shaft resistance on the pile axial force. The maximum shaft resistance appeared in the layer 9.6–11.8 m on November 5, 2015, which was approximately 3.9 times that between the depths of 27.9 and 30 m. Furthermore, the shaft resistance took more than 94.28% of the applied load, which was a significant specificity comparing with the pile in unfrozen soil. The shaft resistance was mainly provided by freezing strength of permafrost to the concrete pile, which owned a significant characteristic of temperature-dependent. Thus, a frozen state for the surrounding soil is the key factor that guarantees the stability of pile foundation in permafrost regions. Further investigations on controlling the thermal regime of pile foundation in permafrost are necessary for the operation safety of superstructure.

It can be confirmed that the frost action of active layer subjected a considerably large uplift forces to the pile foundation (**Figure 4**). To explore the effect of frost heaving on the pile foundation, **Figure 10** presents the variations of RAF and temperature with depth during freezing period. A part of pile shaft was stretched under the frost action of active layer on January 25, 2017. Then, this tension of pile shaft further developed as the freezing front saturated downward. Until April 5, 2017, the tension had occurred on the pile section above a depth of 21.6 m, when the uplift forces should reach the maximum. It can be concluded that the influence depth of frost action on the pile foundation may reach a depth of 21.6 m. In other words, the adfreezing bond force of the layer between 6.3 and 21.6 m played a major role in anchoring the pile, which overcame most of adfreezing uplift forces caused by the frost action of shallow layer.

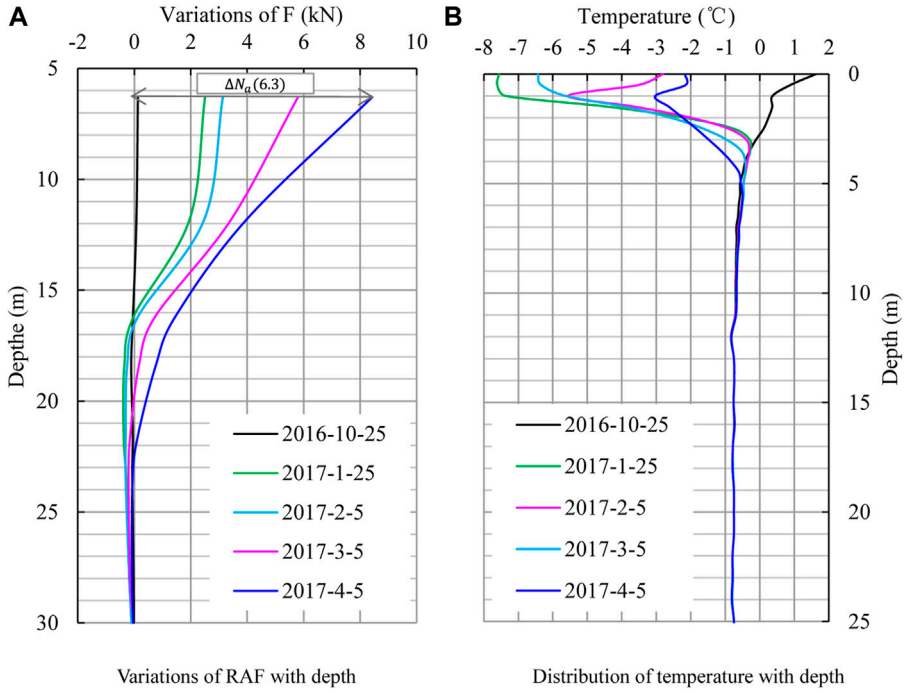

FIGURE 10 | Variations of RAF and pile side temperature with depth during freezing period.

TABLE 6 | The coefficient α with depth at different time under adfreezing uplift forces.

Depths(m)	$\Delta N_a(z)/\Delta N_a(6.3)$ (%)							
	6.3	11.8	16.2	18.4	21.6	23.6	27.9	30
2016-10-25	100.00	59.87						
2017-1-25	100.00	78.31						
2017-2-5	100.00	79.14	4.09			Compression		
2017-3-5	100.00	59.31	12.68	2.84				
2017-4-5	100.00	47.32	17.22	9.04	1.46			

For further exploring the distribution of shaft resistance of permafrost to the pile shaft, **Table 6** lists the coefficient α with depth at different time under adfreezing uplift forces. The thickness of the frost heaving layer was approximately 6 m in view of the above-mentioned facts. The total shaft resistance of the first (6.3–11.8 m) layer overcame approximately 52.68% of the adfreezing uplift forces on April 5, 2017. The unit adfreezing force of this layer was approximately 4.04 times that of the 4th (18.4–21.6 m) layer.

CONCLUSION

A field experiment was conducted in this study. Based on the monitoring data, we discussed the effect of cast-in-place pile foundation on the geotemperature during operation, and quantitatively analyzed the TFF. Based on the results, the following conclusions were obtained:

1) The cast-in-place pile foundation acted as a better thermal conductor in the ground and enhanced the heat exchange between the atmosphere and soil. Furthermore, it increased the annual range of the surrounding ground temperature.
2) The pile foundation increased the permafrost table depth by 0.4–0.7 m in contrast to natural ground, which accounted for 0.33–0.58 times the pile diameter. It should be an important consideration in the stability maintenance of pile foundation during operation.
3) The TFF increased significantly when the soil temperature dropped from 0 to −0.5°C. The thickness of the frost heaving layer was approximately double that of the active layer, and the maximum UTFF should be beyond 52.04 kPa. This lesson will serve as a guide for the design of cast-in-place pile foundation.
4) More than 94.28% of the bearing capacity was contributed by freezing strength for cast-in-place pile foundation in permafrost regions. The adfreezing bond force of

permafrost to pile shaft played an important role in burdening applied load and resisting the frost jacking.

In this study, it was discovered that the cast-in-place pile foundation may negatively affect the stability in the thermal regime. In future experiments, we will propose measures to mitigate this effect. In addition, the soil type and the characteristics of pile structure are two key factors that govern the TFF; therefore, we will discuss the influencing mechanism of the two factors in future publications.

DATA AVAILABILITY STATEMENT

The raw data supporting the conclusion of this article will be made available by the authors, without undue reservation.

AUTHOR CONTRIBUTIONS

YS: Roles/Writing—original draft, Data curation, Formal analysis, Resources, Methodology. FN: Funding acquisition, Writing—review and editing, Supervision. JF: Resources. LW: Visualization.

FUNDING

This work was supported by the Second Tibetan Plateau Scientific Expedition and Research (STEP) program (Grant No. 2019QZKK0905), the State Key Program of National Natural Science of China (Grant Nos. 42001063 and 41961011), the Program of the State Key Laboratory of Frozen Soil Engineering (Grant No. SKLFSE-ZT-202120).

REFERENCES

Aksenov, V. I., and Kistanov, O. G. (2008). Estimation of Resistance Components to an Axial Load on Piles Embedded in Permafrost. *Soil Mech. Found. Eng.* 45 (2), 71–75. doi:10.1007/s11204-008-9001-4

Andersland, O. B., and Ladanyi, B. (2003). *Frozen Ground Engineering*. Hoboken: John Wiley & Sons.

Goncharov, Y. M. (1965). Formation of the Supporting Zone Round a Pile Driven into Thawed Permafrost Ground. *Soil Mech. Found. Eng.* (2), 11–14. doi:10.1007/bf01704772

He, F., Wang, X., Jiang, D. J., Liang, Q. G., and Ren, M. Y. (2015). Research on Three-Dimensional Viscoelastic Frost Heaving Force Problem of Pile Foundation. *Rock Soil Mech.* 36 (9), 2510–2516. doi:10.16285/j.rsm.2015.09.010

Jia, X. Y., Yang, Y. Q., and Li, W. J. (2004). Study of Ground Temperature Field during Pile Foundation Construction in Permafrost Regions. *Rock Soil Mech.* 25 (7), 1139–1142. doi:10.16285/j.rsm.2004.07.029

Jiang, D. J., Wang, X., Liu, D. R., and Xia, Q. (2014). Experimental Study of Stability of Piled Foundation with Thermosyphons of Power Transmission tower along Qinghai—Tibet Railway in Permafrost Regions. *Chin. J. Rock Mech. Eng.* 33 (2), 4258–4263. doi:10.13722/j.cnki.jrme.2014.s2.108

Johnston, G. H. (1981). *Permafrost Engineering Design and Construction*. Hoboken: John Wiley & Sons. Available at: https://kns.cnki.net/kcms/detail/detail.aspx?dbcode=CJFDanddbname=CJFD2005andfilename=BFJT200501003anduniplatform=NZKPTandv=7Dj9mr7fKjNluVA12twfXLfyc5485JVNv7Zrxabnsc4BvoKVkm5VAHM50zFc_sVj

Li, X. H., Yang, Y. P., and Wei, Q. C. (2005). Numerical Simulation of Pile Foundation Conduction at Different Molding Temperature in Permafrost Regions. *J. Beijing Jiaotong Univ.* 29 (1), 10–13.

Liu, H. X. (1993). Discussion on the Distribution of Tangential Frost Heaving Forces along the Lateral Surface of Pile. *J. Glaciol. Geocryol.* 15 (2), 289–292. Available at: https://kns.cnki.net/kcms/detail/detail.aspx?dbcode=CJFDanddbname=CJFD9093andfilename=BCDT199302015anduniplatform=NZKPTandv=H7SBZ8HowYIOv4PpLyfRUaCslsu8-UPF57elX6zPKcGOvnB-4e9olvSWXB_y9RdP

Liu, J., Wang, T., Tai, B., and Lv, P. (2020). A Method for Frost Jacking Prediction of Single Pile in Permafrost. *Acta Geotech.* 15, 455–470. doi:10.1007/s11440-018-0711-0

Ma, W., Feng, G., Wu, Q., and Wu, J. (2008). Analyses of Temperature fields under the Embankment with Crushed-Rock Structures along the Qinghai-Tibet Railway. *Cold Regions Sci. Tech.* 53 (3), 259–270. doi:10.1016/j.coldregions.2007.08.001

Ma, W., and Wang, D. Y. (2014). *Frozen Soil Mechanics*. Beijing: Science Press.

National Standards of the People's Republic of China (2016). *GB 50010-2016 Code for Design of concrete Structures*. Beijing: China Architecture & Building Press.

Penner, E., and Irwin, W. W. (1969). Adfreezing of Leda clay to Anchored Footing Columns. *Can. Geotech. J.* 6 (3), 327–337. doi:10.1139/t69-031

Qiu, G. Q., Liu, J. R., and Liu, H. X. (1994). *Geocryological Glossary*. Lanzhou: Gansu Science and Technology Press.

S. S. Vyalov and G. V. Porkhaev (Editors) (1976). *Handbook for the Design of Bases and Foundations of Building and Other Structures on Permafrost* (Ottawa: Nat. Res. Counc. Can, Tech. Transl. TT), 1865.

Tang, L., Wang, K., Deng, L., Yang, G., Chen, J., and Jin, L. (2019). Axial Loading Behaviour of Laboratory concrete Piles Subjected to Permafrost Degradation. *Cold Regions Sci. Tech.* 166, 102820. doi:10.1016/j.coldregions.2019.102820

Tang, L. Y., and Yang, G. X. (2010). Thermal Effects of Pile Construction on Pile Foundation in Permafrost Regions. *Chin. J. Geotech. Eng.* 32 (9), 1350–1353. Available at: https://kns.cnki.net/kcms/detail/detail.aspx?dbcode=CJFDanddbname=CJFD2010andfilename=YTGC201009009anduniplatform=NZKPTandv=H8NGq_iBN1VQS-dbIP4ZF0ysLl3-pmUsVqkoEdjRuIcxEISGOY21RqMkUrwUGkVS

Torgersen, S. E. (1976). Frost protection with Open Foundations (In Norwegian). *Frost i Jord* 17 (10), 367–373.

Tsytovich, N. A. (1959). *Principles of Geocryology, Part 2, Chap. 3*, 1239. Ottawa: Nat. Res. Counc. Can, Tech. Transl. TT.

Wang, J., Zhu, H.-H., Mei, G.-X., Xiao, T., and Liu, Z.-Y. (2021). Field Monitoring of Bearing Capacity Efficiency of Permeable Pipe Pile in Clayey Soil: A Comparative Study. *Measurement* 186, 110151. doi:10.1016/j.measurement.2021.110151

Wang, T. F., Liu, J. K., Tai, B. W., and ZangLv, P. (2018). Model Tests on Frost Jacking Behaviors of Helical Steel Piles. *Chin. J. Rock Mech. Eng.* 40 (6), 1084–1092. Available at: https://kns.cnki.net/KXReader/Detail?invoice=Ch1%2B6hbk4FUt%2F36dRyx9Tv4aetDPtys1JZVGRwSmBWZ1qYz1wstxOgNXRMBkU8iWVGrOkYDTcSsh1H%2BXbG90sxXKO%2F6B68TyFtt3ChUumAhvLIJWQUNT%2FDhauOTedynbeVlw4CGrHbuxM7B%2BghFhBiKeRW8uGV9YSumpRehkwso%3DandDBCODE=CJFDandFileName=YTGC201806017andTABLEName=cjfdlast2018andnonce=ED75EB94C603454883711AA9EFEA4C29anduid=andTIMESTAMP=1643104086714

Wang, T., Liu, J., Tai, B., Zang, C., and Zhang, Z. (2017b). Frost Jacking Characteristics of Screw Piles in Seasonally Frozen Regions Based on Thermo-Mechanical Simulations. *Comput. Geotechnics* 91, 27–38. doi:10.1016/j.compgeo.2017.06.018

Wang, T., Liu, J., Tian, Y., and Lv, P. (2017a). Frost Jacking Characteristics of Screw Piles by Model Testing. *Cold Regions Sci. Tech.* 138, 98–107. doi:10.1016/j.coldregions.2017.03.008

Wang, X., Jiang, D. J., Liu, D. R., and He, F. (2013). Experimental Study of Bearing Characteristics of Large-Diameter Cast-In-Place Bored Pile under Non-refreezing Condition in Low-Temperature Permafrost Ground. *Chinj. Rock Mech. Eng.* 32 (9), 1807–1812. Available at: https://kns.cnki.net/kcms/detail/detail.aspx?dbcode=CJFDanddbname=CJFD2013andfilename=YSLX201309012anduniplatform=NZKPTandv=Dn4xAiK4szqoyMMq4G-4O8AdO4FY4LnBmVcb2hk2yeesaBZ7zeIiWyl7ncmD0WMh

Wang, X., Jiang, D. J., Zhao, X. Y., and Liu, D. R. (2005). Experimental Study on Bearing Features of Bored Pile under Non-refreezing Condition in Permafrost Region. *Chin. J. Geotech. Eng.* 27 (1), 81–84.

Wang, X., Jiang, D. J., Zhao, X. Y., Shi, C. S., and Wang, C. H. (2004). An Experimental Study on Refreezing Characteristics of Large-Diameter Bored Pile in Different Permafrost Areas of the Qinghai-Tibet Plateau. *Chin. J. Rock Mech. Eng.* 23 (24), 4206–4211.

Weaver, J. S., and Morgenstern, N. R. (1981). Pile Design in Permafrost. *Can. Geotech. J.* 18 (3), 357–370. doi:10.1139/t81-043

Wen, Z., Yu, Q., Ma, W., Dong, S., Wang, D., Niu, F., et al. (2016). Experimental Investigation on the Effect of Fiberglass Reinforced Plastic Cover on Adfreeze Bond Strength. *Cold Regions Sci. Tech.* 131, 108–115. doi:10.1016/j.coldregions.2016.07.009

Wu, Y. P., Guo, C. X., Zhao, S. Y., Zhang, L. X., and Zhu, Y. L. (2004). Influence of Casting Temperature of Single Pile on Temperature Field of Ground in Permafrost of Qinghai-Tibet Plateau. *J. China Railw. Soc.* 6, 81–85.

Wu, Y. P., Su, Q., Guo, C. X., Zhu, Y. L., Zhang, L. X., and Zhao, S. Y. (2006). Nonlinear Analysis of Ground Refreezing Process for Pile Group Bridge Foundation in Permafrost. *China Civ. Eng. J.* 39 (2), 78–84.

Xu, X. Z., Wang, J. C., and Zhang, L. X. (2001). *Frozen Soil Physics*. Beijing: Science Press.

Yuan, X. Z., Ma, W., and Liu, Y. Z. (2005). Study on thermal Regime of High-Temperature Frozen Soil while Construction of Cast-In-Place Pile. *Chin. J. Rock Mech. Eng.* 6, 1052–1055.

Zhang, J. Z., Zhou, Y. J., and Zhou, G. (2010). Study on the Freezing-Back Time of Bridge Pile Foundation in the Permafrost Regions of Qinghai-Tibet Highway. *Highway* 1, 33–38.

Zhou, Y., Wang, X., Niu, F., He, F., Guo, C., Liu, D., et al. (2021). Frost Jacking Characteristics of Transmission Tower Pile Foundations with and without Thermosyphons in Permafrost Regions of Qinghai-Tibet Plateau. *J. Cold Reg. Eng.* 35 (2), 04021004. doi:10.1061/(asce)cr.1943-5495.0000246

Conflict of Interest: The authors declare that the research was conducted in the absence of any commercial or financial relationships that could be construed as a potential conflict of interest.

Publisher's Note: All claims expressed in this article are solely those of the authors and do not necessarily represent those of their affiliated organizations, or those of the publisher, the editors and the reviewers. Any product that may be evaluated in this article, or claim that may be made by its manufacturer, is not guaranteed or endorsed by the publisher.

frontiers in Earth Science

ORIGINAL RESEARCH
published: 14 February 2022
doi: 10.3389/feart.2022.838558

Spatiotemporal Characteristics of NPP Changes in Frozen Ground Areas of the Three-River Headwaters Region, China: A Regional Modeling Perspective

Jianan Hu[1], *Zhuotong Nan*[1,2]* *and Hailong Ji*[1]

[1]Key Laboratory of Ministry of Education on Virtual Geographic Environment, Nanjing Normal University, Nanjing, China, [2]Jiangsu Center for Collaborative Innovation in Geographical Information Resource Development and Application, Nanjing, China

OPEN ACCESS

Edited by:
Dongliang Luo,
Northwest Institute of Eco-Environment and Resources (CAS), China

Reviewed by:
Lihui Luo,
Northwest Institute of Eco-Environment and Resources (CAS), China
Dehua Mao,
Northeast Institute of Geography and Agroecology (CAS), China

***Correspondence:**
Zhuotong Nan
nanzt@njnu.edu.cn

Specialty section:
This article was submitted to Cryospheric Sciences, a section of the journal Frontiers in Earth Science

Received: 17 December 2021
Accepted: 27 January 2022
Published: 14 February 2022

Citation:
Hu J, Nan Z and Ji H (2022) Spatiotemporal Characteristics of NPP Changes in Frozen Ground Areas of the Three-River Headwaters Region, China: A Regional Modeling Perspective. Front. Earth Sci. 10:838558. doi: 10.3389/feart.2022.838558

Permafrost degradation triggered by climate warming can disturb alpine ecosystem stability and further influence net primary productivity (NPP). Known as the "water tower of China", the Three-River Headwaters Region (TRHR) on the eastern Qinghai-Tibet plateau (QTP), is characterized by a fragile alpine meadow ecosystem underlain by large areas of unstable permafrost and has been subject to rapid climate change in recent decades. Despite some site-specific studies, the spatial and temporal changes in NPP in the different frozen ground zones across the TRHR associated with climate change remain poorly understood. In this study, a physically explicit Noah land surface model with multi-parameterization options (Noah-MP) was employed to simulate NPP changes on the TRHR during 1989–2018. The simulation was performed with a spatial resolution of 0.1° and a temporal resolution of 3h, and validated at two sites with meteorological and flux observations. The results show that the average NPP was estimated to be 299.7 g C m^{-2} yr^{-1} in the seasonally frozen ground (SFG) zone and 198.5 g C m^{-2} yr^{-1} in the permafrost zone. NPP in the TRHR increased at a rate of 1.09 g C m^{-2} yr^{-2} during 1989–2018, increasing in 1989–2003 and then decreasing in subsequent years. The NPP in permafrost area increased at a rate of 1.43 g C m^{-2} yr^{-2} during 1989–2018, which is much higher than the rate of change in NPP in the SFG area (0.67 g C m^{-2} yr^{-2}). Permafrost degradation has complicated ecosystem implications. In areas where permafrost degradation has occurred, both increasing and decreasing changes in NPP have been observed.

Keywords: net primary productivity (NPP), NOAH-MP, permafrost, seasonally frozen ground, three-river headwaters region

INTRODUCTION

On the Qinghai-Tibetan Plateau (QTP), carbon cycles occur in a unique way owing to the special geographical features and ecological environment (Lin et al., 2019). From an ecological perspective, the ecosystems of the QTP are extremely vulnerable, and climate changes could pose a great challenge to them (Chen et al., 2014). Climatic warming has been observed across the world and on the QTP during recent decades (Liu and Chen, 2000; Zhao et al., 2004; Trenberth et al., 2013). As a critical ecological barrier for regional sustainable development in China, the Three-River Headwaters

Region (TRHR) is one of the most fragile and sensitive terrestrial ecosystems on the QTP (Tong et al., 2014; Mao et al., 2015; Jiang and Zhang, 2016a). At some monitoring sites, ecosystem degradation has been observed in the TRHR in recent years (Guo et al., 2015).

Net primary productivity (NPP) refers to the amount of net organic matter that plants take up from the atmosphere through photosynthesis, and it plays an important role in regulating the carbon cycle of ecosystems (Melillo et al., 1993). Dynamic changes in NPP can be used to assess the Earth's ability to sustain life and the sustainability of the ecosystem to maintain development in the face of climate change (Zhao and Running, 2010). The TRHR is known as the "Water Tower of China", and the accurate estimation of NPP change in the TRHR is very important and has always been a hot topic in terrestrial carbon cycle and climate change research on the QTP (Zhao et al., 2013; Jiang and Zhang, 2015; Liang et al., 2016). Most existing studies of NPP changes, especially those related to frozen ground, are generally restricted to the site scale. However, there are few monitoring sites, making it difficult to gain complete insights into NPP changes across the region.

Frozen ground is an integral part of the plateau cryosphere and helps preserve a stable microclimate and ecosystem balance by supplying soil moisture and nutrients for vegetation growth. A significant portion of unstable permafrost underlies the TRHR, which is highly sensitive to climate change. Global warming has triggered permafrost degradation over the past several decades, not only in the circum-Arctic (Osterkamp, 2005; Smith et al., 2005) but also in the TRHR (Wu and Zhang, 2008). It has already been demonstrated that permafrost degradation disturbs alpine ecosystem stability through repeated freezing and thawing and further influences NPP accumulation (Qin and Ding, 2010; Schuur and Abbott, 2011; Burke et al., 2013). Previous modeling studies on NPP changes have primarily been conducted using semiempirical, analytical, or ecological models (Zhang et al., 2016; Lin et al., 2017) and different datasets, and reported widely ranging mean annual NPP values (e.g., Wang et al., 2009; Guo et al., 2013). Unfortunately, these models are generally unable to describe the physical processes occurring in frozen ground, so they lack the ability to represent the effects of frozen ground on changes in NPP in terms of sustaining vegetation growth.

Physically explicit numerical models such as the land surface model (LSM) are theoretically superior to empirical models in their ability to describe physical processes within the soil (Abramowitz et al., 2008). At present, most LSMs focus only on the energy and water balance on the surface without considering the carbon cycle (Chen and Dudhia, 2001; Ek et al., 2003). In addition, many LSMs do not simulate vegetation dynamically, but rely on prescribed vegetation indices (Ruddell et al., 2015). This limits the ability of these LSMs to monitor NPP changes and their responses to permafrost changes. Therefore, a general-purpose LSM that incorporates not only water and energy transport processes, but also carbon cycling and dynamic vegetation is usually required to better represent the physiological mechanisms of vegetation and the interplay between vegetation and frozen ground. Recently, the Noah LSM has been extended into a multiphysics simulation platform (Noah-MP) that includes a dynamic vegetation component (Niu et al., 2011). This model has the potential to facilitate the simulation of carbon assimilation processes and permafrost dynamics. Thus, it provides a solid foundation for this study to simulate NPP changes with full interaction with permafrost dynamics over the TRHR.

This study aims to: 1) investigate the spatiotemporal characteristics of NPP over the entire TRHR during 1989–2018; 2) identify the responses of NPP to climate change in different frozen ground zones in the TRHR; and 3) strengthen the understanding of NPP responses to permafrost degradation in the region. This work has the potential to provide a scientific reference for restoring, conserving and developing the local ecological environment in a changing climate in a sustainable way.

MATERIALS AND METHODS

Study Area and Data

The TRHR is bounded by longitude 89°24′–102°27′E and latitude 31°39′–36°10′N (**Figure 1**), with an area of approximately 3.95 × 10^5 km^2. The altitude gradually decreases from the northwest to the southeast, averaging 4,000 m above sea level (a.s.l.). As the source area of the Yellow River, Yangtze River, and Lancang River, the TRHR delivers approximately 40 billion m^3 of water downstream every year (Feng et al., 2017). The main land cover types are grassland, desert, wetland, shrub, and forest, with alpine steppe and alpine meadow being the main grassland types (Liu et al., 2014). The TRHR has a typical high-altitude continental climate, with temperature and precipitation exhibiting considerable spatial variations across the TRHR. The mean annual air temperature over the TRHR ranges from −5.6 to −3.8°C and decreases from southeast to northwest (Yi et al., 2012). Annual precipitation generally falls from the southeast (772 mm) to the northwest (262 mm) and is primarily concentrated between June and September due to the influence of the warm and humid air currents emanating from the southern Bay of Bengal (Shi et al., 2017). The ecosystem in the TRHR is fragile and vulnerable, with low resilience to disturbance (Jiang and Zhang, 2016b). Permafrost is widespread in the upper reaches of the Yangtze River, while in the eastern part permafrost is sporadic and the seasonally frozen ground (SFG) is found at low elevations (Zou et al., 2017). Two flux sites are located in the north and southeast to the THRH: the Damxung flux site (DX; 30.49°N, 91.06°E, 4,286 m a.s.l; covered by alpine meadow; **Figure 1**) and the Haibei flux site (HB; 37.06°N, 101.32°E, 3,205 m a.s.l; covered by alpine shrub-meadow; **Figure 1**).

Vegetation types on the TRHR were extracted from the Vegetation Atlas of China at 1:1 million scale (Hou, 2001). A QTP soil dataset with a resolution of 1 km were used, covering the entire TRHR with 18 soil layers (Wu and Nan, 2016). The gridded Chinese Meteorological Forcing Dataset (CMFD) (0.1° in space and 3 h in time) (He et al., 2020) were used to drive the model. It includes seven meteorological elements such as 2 m air temperature, 10 m wind speed, air pressure, specific humidity,

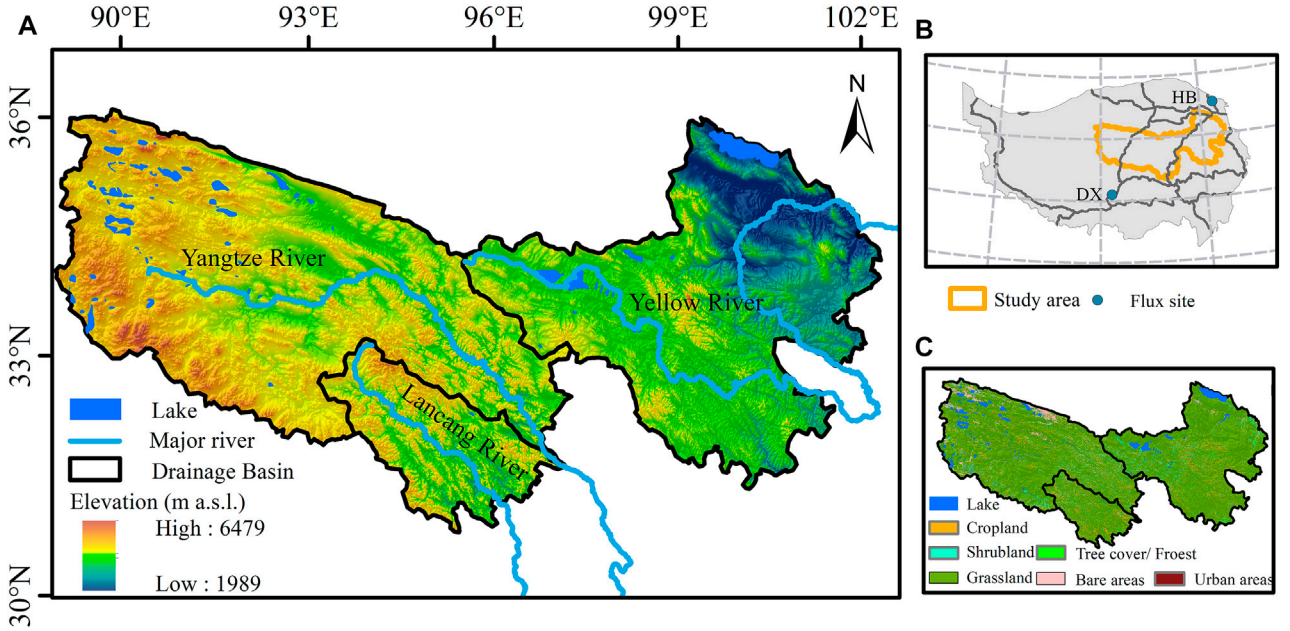

FIGURE 1 | Topography of the Three-River Headwaters Region (TRHR) **(A)**, its location on the Qinghai-Tibet Plateau **(B)**, and the distribution of land cover within this region **(C)**. DX: the Damxung flux site; HB: the Haibei flux site.

precipitation rate, downward shortwave radiation, and longwave radiation.

Model and Setting

The Noah-MP model is a new-generation land surface model based on Noah LSM, extends the physical processes and introduces the latest developments in related parameterization schemes (Niu et al., 2011). In this model, the states of terrestrial energy, water, carbon, and associated flux exchanges between the land surface and the atmosphere are described in detail. Surface temperatures are calculated through an iterative solution of the surface energy balance including solar radiation, longwave radiation, sensible heat, latent heat, and ground heat fluxes. The "semitile" method is employed to address the heterogeneity of the surface. Based on the Clapp-Hornberber water retention relationship, Noah-MP solves the one-dimensional Richards equation to determine vertical soil moisture distribution (Clapp and Hornberger, 1978).

Noah-MP describes the photosynthesis of C3 and C4 plants by a biochemical model (Collatz et al., 1991; Collatz et al., 1992). Specifically, the gross photosynthesis rate is determined by the minimum of three limiting factors: Rubisco limitation, light limitation and transport of photosynthate for C3 plants and PEP-carboxylase limitation for C4 plants. A short-term vegetation phenology model is coupled to Noah-MP, allowing the model to describe carbon assimilation (Dickinson et al., 1998). The carbon budgets are described for various plant parts, such as leaves, wood, and roots, as well as carbon pools (fast and slow). The assimilation of carbon through photosynthesis, the allocation of the assimilated carbon to various biological carbon pools (leaf, stem, wood, root, and soil), and the respiration from each pool are included in the model. The rate of change in leaf carbon mass, C_{leaf} (g m^{-2}), over the time, t, is computed from:

$$\frac{\partial C_{leaf}}{\partial t} = F_{leaf}A - \left(S_{cd} + T_{leaf} + R_{leaf}\right) C_{leaf} \quad (1)$$

where F_{leaf} is the fraction of the assimilated carbon allocated to leaf; A represents the total carbon assimilation rate of the leaves that receive both Sun and shade; S_{cd} represents the mortality due to cold and drought stresses; T_{leaf} represents the rate of leaf turnover caused by senescence, herbivory, or mechanical factors. R_{leaf} represents the rate of both leaf maintenance and growth respiration. The rest of the vegetation is calculated similar to leaf carbon mass. NPP and other carbon fluxes can be derived by calculating the allocation of assimilated carbon in various parts of the vegetation (e.g., leaf, stem, wood and root) and the amount of carbon consumed by each component.

Noah-MP offers a framework for providing multiple options for interpreting and parameterizing a given process (**Table 1**). Two to four different parameterization schemes are available for twelve physical subprocesses of the model. Each subprocess parameterization scheme can be combined within the model depending on the user's needs to perform simulation research. The Noah-MP LSM with improved simulation capability for permafrost over the QTP was employed in this study. The physical options used in this study were basically similar to Li et al. (2020) as presented in **Table 1**. The strength of Noah-MP in simulating thermal and hydrological processes occurring with frozen ground on the QTP was well demonstrated in Li et al. (2020), where more details were also described.

TABLE 1 | Optional Noah-MP parameterization schemes used in this study.

Physical component	Option used	Description
Vegetation model	Dynamic	LAI and shade fraction calculated from dynamic simulation of carbon uptake and partitioning
Canopy stomatal resistance	Ball-Berry	The stomatal resistance for sunlit and shaded leaves related to their photosynthesis rates
Runoff and groundwater	SIMGM	TOPMODEL-based runoff with simple groundwater
Soil moisture factor for stomatal resistance	Noah	A schema based on soil moisture
Radiation transfer	gap = F(3D, cosz)	Two-stream with a 3D canopy structure
Rainfall and snowfall	Jordan91	A one-dimensional temperature model for a snow cover
Snow surface albedo	CLASS	Considering overall snow age
Supercooled liquid water	Koren99	A variant of standard
Frozen soil permeability	Koren99	Use of only liquid water content to compute hydraulic properties
Surface layer drag coefficient	M-O	Accounting for the zero-displacement height, with the same roughness lengths
Lower boundary of soil temperature	Noah	Non-zero heat flux from bottom
Snow/soil temperature time scheme	Semi-implicit	Flux top boundary condition

The model was then forced for the period of January 1989 to December 2018, using the CMFD. Prior to the start of the model run, a 30-year spin-up using the repeat forcing in 1989 was conducted to mitigate the effects of the initial values. The total simulation depth was set to 8 m. The lower temperature boundary was set at 16 m using the annual mean air temperature at 2 m (Niu et al., 2011). The model resolution is 3 h in time and 0.1° in space.

Permafrost was determined from the simulation results following the definition of permafrost, the soil with temperatures below 0°C for more than two consecutive years (Muller, 1943). More specifically, a grid cell was classified as permafrost if the maximum soil temperature of any soil layers was below or equal to 0°C for two consecutive years. The remainder of grid cells was classified as SFG only if the minimum soil temperature of any layer was equal to or below 0°C for the same period. When calculating the areas, the simulation maps were projected into Albers' equal-area projection system and the lakes were excluded from the processing.

Model Calibration and Validation

Restricted by data availability, two monitoring sites (Damxung and Haibei) from the China Flux Network nearby the TRHR with typical alpine vegetation types were selected for model calibration and validation in this study (**Figure 1**). Two nearby flux monitoring sites, i.e., the Golog site covered by alpine shrub meadow and the Maqu site covered by marsh meadow, were not used because no open-access data are currently available. According to previous studies on the sensitivity of Noah-MP parameters (e.g., Arsenault et al., 2018), we selected two most sensitive parameters related to the vegetation dynamics, i.e., max carboxylation rate and optimal growth temperature of vegetation. We followed an error and trial procedure to calibrate the parameters so that the simulated gross primary product (GPP) data best fit the observed GPP data at the two sites by referring to existing studies (Chen et al., 2021; Yang et al., 2021). At the Damxung site, simulation results were validated against the observed time series (2004–2006) of soil temperature and soil moisture content, and of GPP (2004–2005). At the Haibei site, the soil temperature and soil moisture records from 2004–2006 and GPP from 2003–2005 were used for validation. Metrics such as the widely-used Nash-Sutcliffe efficiency coefficient (NSE) and Pearson's correlation coefficient (R) were used to quantify the agreement.

Trend Analysis

Theil-Sen trend analysis is a robust statistical trend analysis method widely used to identify both the trends and magnitudes of hydrometeorological variables (Sen, 1968). We computed the change rate (CR) of NPP and climatic factors using Sen's slope following **Eq. 2**:

$$CR = Median\left(\frac{X_j - X_k}{j - k}\right),\ \mathrm{j} > \mathrm{k} \tag{2}$$

where X_j and X_k are the value of the variable of interest at time j and k ($j > k$), respectively. A positive CR indicates an upward trend of the variable, and the higher the CR value, the more pronounced the trend. Conversely, a negative CR indicates a downward trend, and the lower the CR value, the more pronounced the decline. The spatial distribution of statistical significance of NPP trends was mapped and evaluated using two-tailed significance test of the Mann-Kendall (M-K) test.

The M-K test statistic S is computed as follows:

$$S = \sum_{i=1}^{n-1} \sum_{j=i+1}^{n} sgn\left(x_j - x_i\right) \tag{3}$$

where n is the number of data points, x_i and x_j are the NPP values at the time i and j ($j > i$), respectively, and sgn() is a symbolic function. In cases where the sample size n > 10, the standard normal test statistic (Z_S) of the M-K test is given by:

$$Z_s = \begin{cases} \dfrac{S-1}{\sqrt{Var\,(S)}} & , if\ S > 0 \\ 0 & , if\ S = 0 \\ \dfrac{S+1}{\sqrt{Var\,(S)}} & , if\ S < 0 \end{cases} \tag{4}$$

The null hypothesis, H_0, is rejected when $[Z] > Z_{\alpha/2}$, where α is pre-assigned significance level (α = 0.9) and $Z_{\alpha/2}$ is the $\alpha/2$ quantiles of the standard normal deviation. Positive values of Z_S indicate an increasing trend, while negative Z_S decreasing trend.

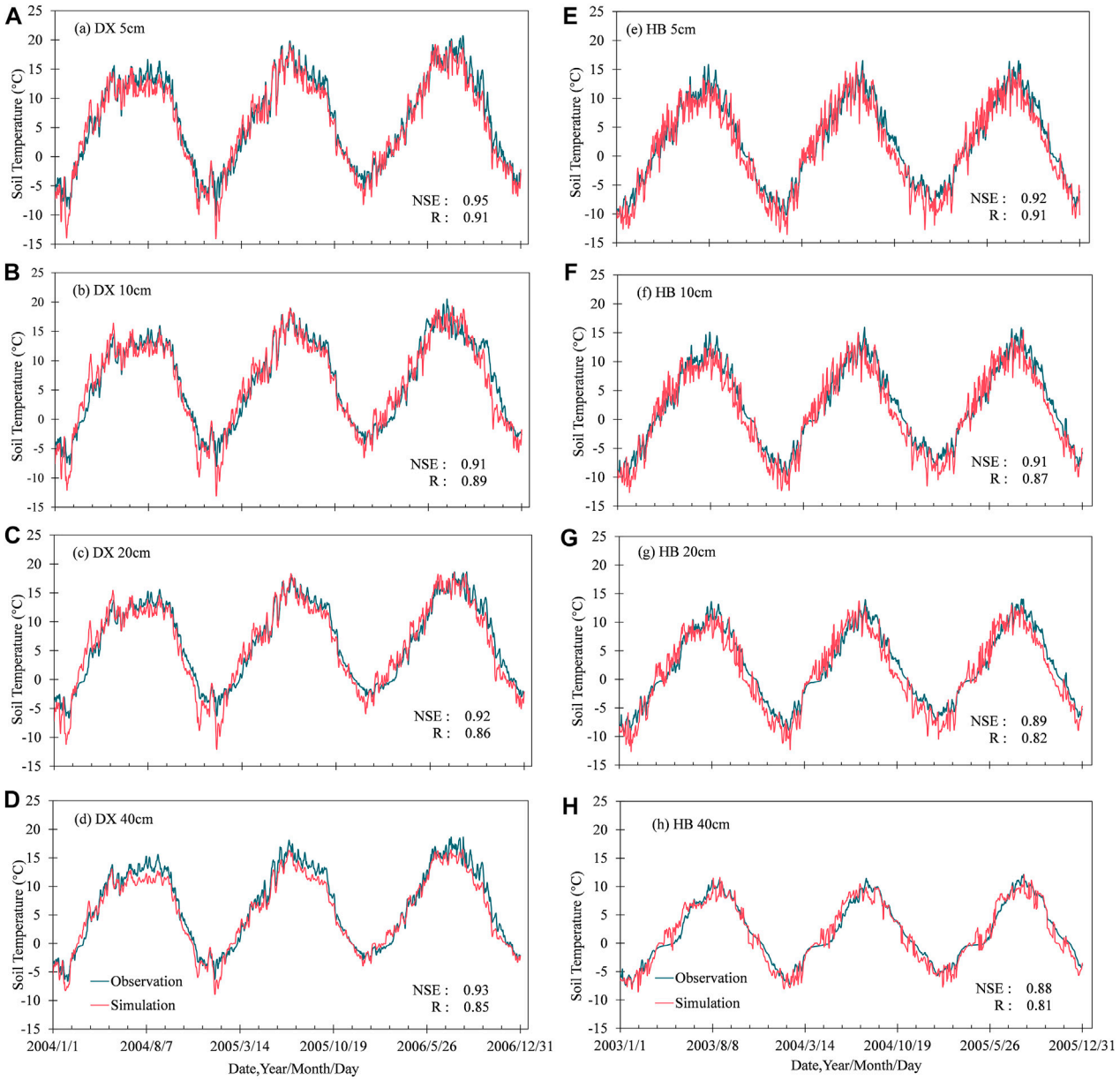

FIGURE 2 | Simulated and observed soil temperatures at different depths at Damxung [DX, **(A–D)**] and Haibei [HB, **(E–H)**] sites. NSE: Nash-Sutcliffe efficiency coefficient; R: Pearson's correlation coefficient.

RESULTS AND DISCUSSION

Model Validation at Two Flux Sites

Figure 2 shows the time series of simulated and observed daily mean soil temperature for differernt soil layers at the Damxung and Haibei sites. The simulated (red lines in **Figure 2**) and observed (dark green lines) soil temperature were in good agreement at both sites. The NSE and R values for soil temperature were above 0.88 and 0.81, respetively, for all depths at two sites. Soil temperature exhibted strong seasonality in these layers, and the amplitude of soil temperature variation decreased with soil depth, as expected. In spite of some discrepancies between simulation and observation, the Noah-MP LSM performed well overall and can capture well the temporal variation of observations at different depths at the two sites.

There was also a good agreement between the simulated (red lines in **Figure 3**) and measured (dark green lines) unfrozen water content. Since no measurements of unfrozen water content were made in deep layers, the comparison was limited to the upper layers. The NSE values for unfrozen water content ranged from 0.80 to 0.83 in all layers at both sites, and the R values exceeded

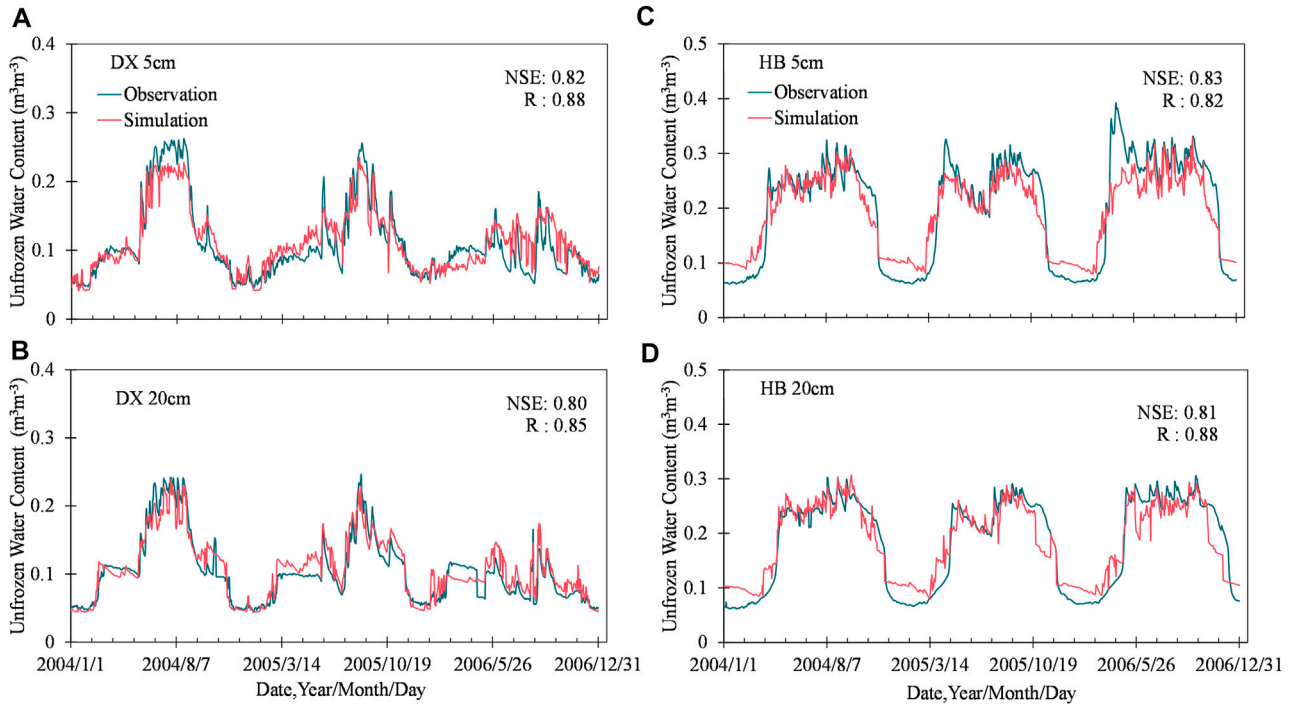

FIGURE 3 | Simulated and observed unfrozen water content at different depths at Damxung [DX, **(A,B)**] and Haibei [HB, **(C,D)**] sites. NSE: Nash-Sutcliffe efficiency coefficient; R: Pearson's correlation coefficient.

0.8 in all layers. The unfrozen water content cyclically fluctuated with the seasons. During the transition periods from the frozen to the thawed state, the simulated unfrozen water content changes rapidly in response to the phase change. At the Haibei site, there was a slight overestimation during the cold seasons (December to March). This could be caused by insufficient consideration of the ice process in the model. Overall, the Noah-MP LSM captured well the dynamics of soil mositure at different depths at the two sites.

The comparisons between the simulations and the corresponding observations in terms of GPP are shown in **Figure 4**. The simulated (orange lines in **Figure 4**) and observed (dark green lines) GPP agreed well at both sites, as indicated by favorable values in NSE (0.79 at Damxung and 0.82 at Haibei) and R (0.75 at Damxung and 0.78 at Haibe). Some discrepancies between the simulation and observation can be observed at the Damxung site. For example, the GPP observations recorded a short-term spike in June 2004, while the GPP simulations showed a trend toward a gradual increase during the same period. According to our knowledge, the growing season at the Damxung site usually occurred in the warm months from May to September each year and vegetation growth generally peaked amidst the growing season (Shen et al., 2015). Since that flux observations are directly measured by the eddy correlation method based on the micrometeorology theory, some error maybe be present in the observations. Despite some discrepancies, the favorable NSE and R scores for both sites are suggestive that the Noah-MP LSM is capable of tracking daily GPP changes over time.

Spatiotemporal Patterns of NPP Over the TRHR

Figure 5A displays NPP distribution averaged over the period 1989 to 2018. The regionally averaged NPP during this study period was 237.86 g C m^{-2} yr^{-1} and ranged from 0 to 750 g C m^{-2} yr^{-1}. The NPP decreased gradually from the southeast to the northwest, which is largely consistent with the temperature and precipitation distributions in the TRHR (**Figures 5B,C**). Similar results have been reported in previous research in the same region based on remote sensing data and the Carnegie–Ames–Stanford model (Zhang et al., 2016).

Large snow mountains and deserts stretch over the Yangtze River headwaters area, and rivers and lakes are scattered throughout the region, which is characterized by a dry and cold climate with less than 300 mm in annual precipitation and a mean air temperature below −5°C. The average annual NPP in the Yangtze River headwaters area was relatively low, mostly ranging from 0–80 g C m^{-2} yr^{-1}, and only in the southeast parts of its headwaters area, where meadows are widespread, reached 200 g C m^{-2} yr^{-1}. In contrast, NPP values in the Lancang River headwaters area and the southeastern parts of the Yellow River headwaters area were much higher due to the favorable climate, abundant rainfall, and diverse vegetation types, and most of them exceeded 300 g C m^{-2} yr^{-1}.

The simulation showed highly variable growth of NPP in the TRHR during the study period (**Figure 6A**), increasing from about 210 g C m^{-2} yr^{-1} in 1989 to 269 g C m^{-2} yr^{-1} in 2018 with a total growth of 59 g C m^{-2} yr^{-1}. A significant increase in NPP was

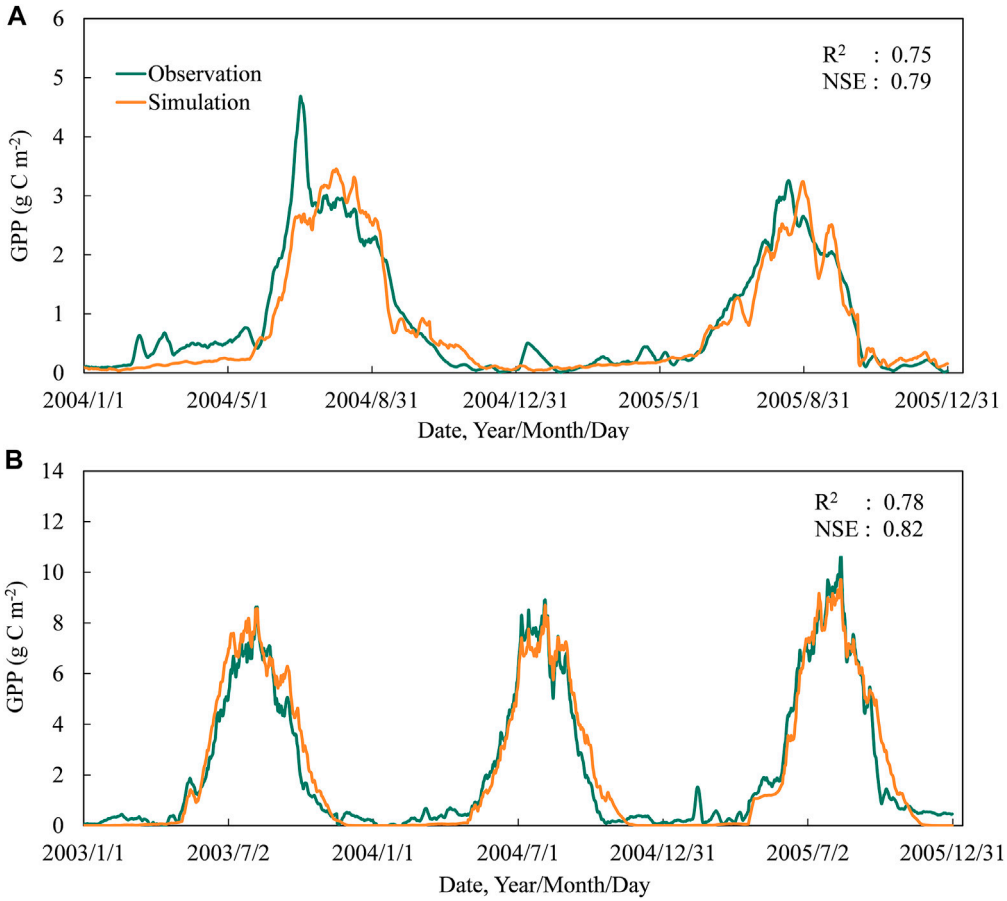

FIGURE 4 | Simulated and observed gross primary product (GPP) values at Damxung **(A)** and Haibei **(B)** sites.

observed during the study period with an estimated rate of change of 1.09 g C m^{-2} yr^{-2} in response to increasing air temperature (0.06°C yr^{-1}) and precipitation (4.08 mm yr^{-1}).

As shown in **Figure 6A**, the interannual variation in NPP across the region from 1981 to 2018 exhibited obvious inter-phase changes. NPP increased rapidly in the first 15 years (1989–2003), but decreased significantly in the next 15 years after 2004. The TRHR has experienced increases in temperature and precipitation over the past 30 years, reflecting a "warming and wetting" trend from 1989 to 2003 (**Figures 6B,C**), with an annual increase in air temperature and precipitation of 0.08°C per year and 5.73 mm per year, respectively. Increased precipitation and temperature provide water and energy availability for vegetation growth and survival. The green-up period of vegetation was advanced and the wilting period was delayed, which facilitated the accumulation of NPP. Over the period of 2004–2018, a steady increase in temperature and a concomitant decrease in precipitation were observed in the TRHR, at rates of change of 0.03°C yr^{-1} and −4.01 mm yr^{-1}, respectively. Due to the continued decline in precipitation, plants do not receive enough water, which has adversely affected their photosynthesis and accumulation of NPP.

A number of previous studies have also reported the mean annual NPP in the TRHR based on different methods and data. Han et al. (2018) estimated mean annual NPP in the TRHR based on a statistical model to be 283.97 g C m^{-2} yr^{-1} from 1988 to 2012, which is slightly higher than our estimate (247.26 g C m^{-2} yr^{-1}) for 1989–2012. Guo et al. (2013) even reported an extremely high estimate for 1960–2011 in the same region using a climate productivity model (Thornthwaite Memorial model), which is 570.35 g C gm^{-2} yr^{-1}. In contrast, Wang et al. (2009) reported a mean annual NPP (143.17 g C m^{-2} yr^{-1}) for the period of 1988–2004 using an ecological model fed with satellite-based GPP data, which is much lower than our estimate (231.72 g C m^{-2} yr^{-1} for 1989–2004). Our simulation reveals an increase-then-decrease trend of NPP in the TRHR, as also found in Zhang et al. (2016). However, their study gave an overall increasing rate of 1.31 g C m^{-2} yr^{-2} using the process-based CASA model driven by remote sensing and climate data, which was a little higher than our result (1.09 g C m^{-2} yr^{-2}). The reasons for these discrepancies

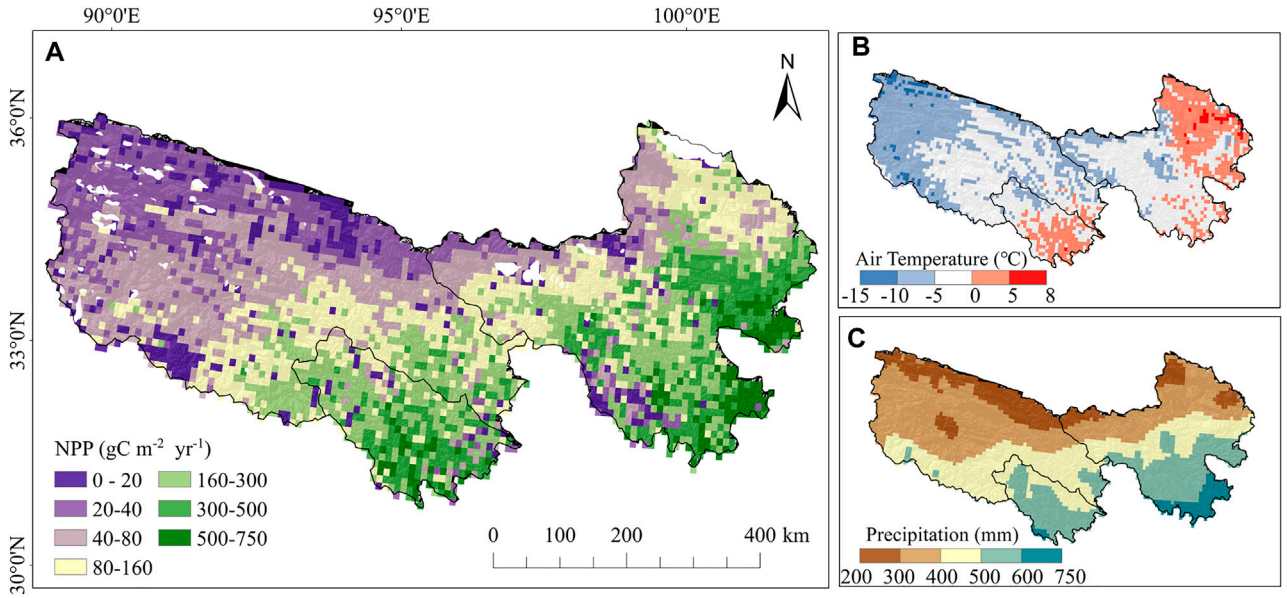

FIGURE 5 | Distribution of net primary product (NPP) **(A)** averaged over the 1989–2018 period in the TRHR, along with spatial distributions of mean annual air temperature **(B)** and mean annual precipitation **(C)** over the same period. Lakes are excluded in **(A)**.

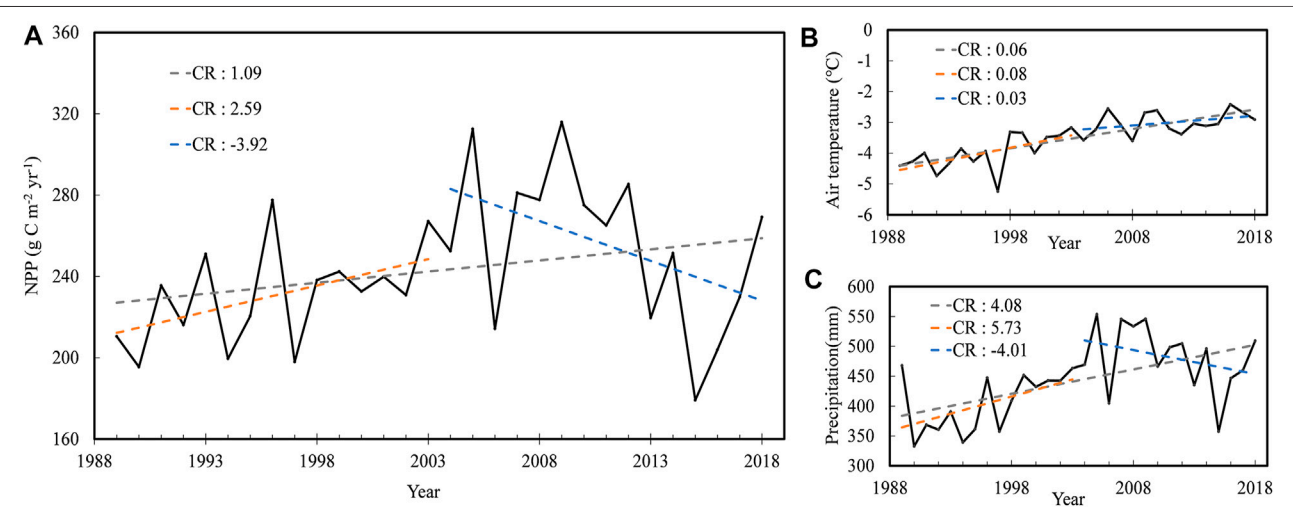

FIGURE 6 | Inter-annual variations of simulated NPP **(A)**, air temperature **(B)** and precipitation **(C)** in the TRHR from 1989 to 2018. Gray, orange and blue dashed lines represent the trend line from 1989 to 2018, 1989 to 2003 and 2004 to 2018, respectively. CR: the change rate of NPP, air temperature and precipitation in a unit of g C m^{-2} yr^{-2} **(A)** °C yr^{-1} **(B)** and mm yr^{-1} **(C)**, respectively.

could be multifaceted, including the special treatment of freeze-thaw dynamics in Noah-MP that is not present in other methods.

Changes of Net Primary Productivity in Different Frozen Ground Zones

The simulation indicates a considerable reduction in permafrost extent in the TRHR during the study period, declining from about 296 × $10^3$$km^2$ in 1989 to about 221 × $10^3$$km^2$ in 2018 with a reduced total area of 75 × $10^3$$km^2$. The trend of decreasing permafrost area was clearly observed throughout the period, with a change rate estimated at 2.87 × 10^3 km^2 yr^{-1}, in parallel to the increasing in air temperature (0.06°C yr^{-1}). Most of the thawed permafrost was converted to SFG, leading to an increase in SFG areas in the TRHR. The rate of change in SFG area was estimated to be 2.17 × $10^3$$km^2$ per year, which is slightly lower than the rate at which permafrost disappeared.

Spatially, permafrost has degraded extensively in the TRHR. In the central portion of the Yangtze River headwaters area and south of the Yellow River headwaters area, permafrost declined sharply during

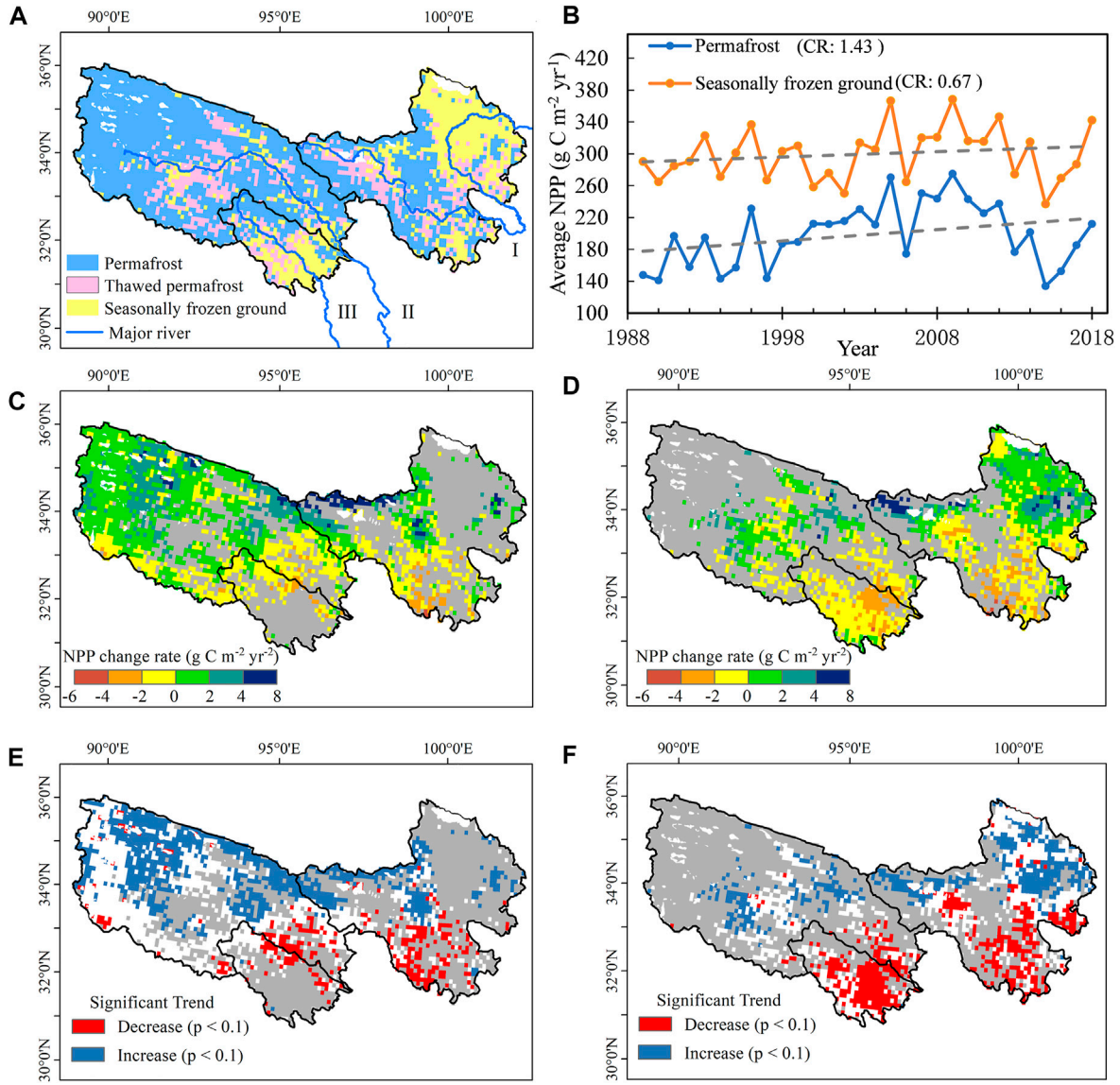

FIGURE 7 | Distribution of frozen ground type in the TRHR in 2018 **(A)**, inter-annual variability of NPP in the TRHR stratified by frozen ground type **(B)**, and the rates of change in NPP in the permafrost zone **(C)** and the seasonally frozen ground (SFG) zone **(D)** in the TRHR from 1989 to 2018 based on a 30-year Noah-MP simulation, as well as significance tests for the trends in the permafrost zone **(E)** and SFG zone **(F)**. The thawed permafrost in **(A)** was identified relative to the beginning of the simulation. I, II, III represent the Yellow River, the Yangtze River and Langcang River, respectively. The gray dashed lines in **(B)** represent the trend from 1989 to 2018. Lakes are excluded from the maps. CR: the rate of change in a unit of g C m^{-2} yr^{-2}. The blank areas in **(E,F)** indicate a *p* value >0.1.

1989–2018 (**Figure 7A**). Permafrost also disappeared during the period in the central portion of the Lancang River headwaters. Those areas where permafrost disappeared consistently show the highest increase in air temperature, resulting in attenuated thickness of permafrost and disappearance of some of those that were already thermally unstable. The loss of permafrost in the TRHR occurred mostly in areas along major rivers.

Based on the distribution of frozen ground (**Figure 7A**) obtained from the simulation, we estimated the inter-annual variability of NPP by stratified frozen ground type, i.e., for the permafrost zone and the SFG zone, respectively. Thawed permafrost areas were specifically identified by contrasting the occurrence of permafrost in 2018 to that in 1989. The mean annual NPP in the SFG zone was estimated as 299.7 g C m^{-2} yr^{-1}, significantly higher than in the permafrost zone (198.5 g C m^{-2} yr^{-1}). We found that the mean annual NPP in both the permafrost zone and the SFG zone showed substantially increasing trends during the study period in relation to climate changes (**Figures 6B,C**). Unlike the magnitude of the mean annual NPP, the rate of change in NPP in the permafrost zone was estimated to be 1.43 g C m^{-2} yr^{-2}, which is significantly greater than the rate of change of NPP in the SFG zone (0.67 g C m^{-2} yr^{-2}). A consistently remarkable reduction in NPP was observed in both the permafrost and SFG zones in 2006, echoing the largest fall in precipitation that year (**Figure 6C**).

The spatial patterns of NPP change rate in the permafrost zone and SFG zone were different, as shown in **Figures 7B,C**. In the permafrost zone, NPP decreased primarily in the southern and central TRHR and increased in the extensive northwestern TRHR. The highest growth in NPP in the permafrost zone was observed in the northwest parts of the Yellow River headwaters area and west of the Yangtze River headwaters area. The growth of NPP occurred primarily in regions that permafrost extensively distributes, while NPP decreased in the areas that permafrost sporadically distributes. In the SFG zone, the NPP decreased in the majority of the Lancang River headwaters area and the southern parts of the Yellow River headwaters area, while it mainly increased in the northeast of the Yellow River headwaters area. The sharpest decreases in NPP in the SFG area occurred in the northeast portion of the Lancang River headwaters area. In the regions where permafrost degraded to SFG, both increases and decreases in NPP were observed. **Figures 7D,E** shows the significance of changes in NPP in the permafrost zone and SFG zone based on the M-K trend test. It indicates that the rates of change greater than 2 g C m^{-2} yr^{-2} and most negative rates of change are significant regardless of frozen ground zone, except for rates of change with modest increases (0–2 g C m^{-2} yr^{-2}), which are insignificant.

Implications for NPP Responses to Permafrost Degradation

Permafrost forms and exists in a low temperature climate. These climate conditions are mainly characterized by long, cold winters and short, relatively dry, cool summer. Plant communities in the alpine permafrost region are dominated by alpine vegetation types that includes meadow, steppe, cold desert and subnival cushion plant. Biomass in permafrost regions is low due to the combined influence of rigid climatic conditions, and NPP accumulation is also impaired. In the SFG zone, climate conditions are relatively better, there is relatively abundant precipitation and moderate temperatures, and vegetation is more diverse and abundant compared to the permafrost zone. The biomass in the SFG zone is relatively high, and NPP can increase more quickly. Therefore, the mean value of NPP in the SFG zone is much higher than that in the permafrost zone. This is consistent with the result of our simulation.

However, contrary to our general understanding, the simulation shows that the rate of change in NPP in the present permafrost zone is significantly greater than that in the SFG zone. Li et al. (2022) calculated the temporal and spatial changes of NPP on the QTP using the random forest and the Biome-BGC model and also found that the NPP change rate in permafrost regions was higher than non-permafrost regions, confirming the same finding from our simulation. Since permafrost is very sensitive to climate change, a small change in air temperature may result in considerable heat disturbance in the ground. A rapid response of permafrost to climate change has contributed to rapid growth of NPP in the permafrost zone. Once the magnitude of climate change exceeds the threshold that permafrost can withstand, permafrost will degrade. Permafrost degradation can lead to changes in vegetation distribution as well as ecosystem productivity.

Permafrost degradation exerts complicated impacts on ecosystems. In areas where permafrost degradation has occurred, both increasing and decreasing changes in NPP have been observed (**Figures 7A,D**). It is generally understood that permafrost degradation causes the conversion of permafrost to SFG, i.e., the conversion from lower NPP to higher NPP. An increase in NPP was observed in central parts of the Yangtze River headwaters area where permafrost has degraded (**Figure 7C**). Climate warming directly affects permafrost by increasing soil temperature. The increased ground temperature creates better thermal conditions for vegetation growth. The growth of plant root is no longer restricted by the low temperature of permafrost, which promotes the decomposition of organic matter and prolongs the growing season of plants, which in turn increases the productivity of the ecosystem (Euskirchen et al., 2006; Chen et al., 2012).

However, in many cases, the direction of NPP changes due to permafrost degradation is the opposite (**Figure 7D**). For example, in the southern parts of the Yellow River headwaters area, NPP showed a decreasing trend in the areas where permafrost degradation occurred (corresponding to the thawed permafrost areas in **Figure 7A**). During the degradation, seasonal melt depth increases and ground ice begins to melt. Soil moisture in the root zone is no longer retained by the frozen soil, but instead percolates and migrates downwards, ultimately leading to a drop in both the soil moisture conditions and ground water levels. Plant growth is inhibited by this reduced water availability, leading to stunted roots and subsequently reduced ecosystem productivity (Torre Jorgenson et al., 2013; Streletskiy et al., 2015).

In contrast to the Arctic and Antarctic regions, strong interactions exist between the atmosphere, cryosphere, hydrosphere, and biosphere in the TRHR (Bibi et al., 2018). Given limited knowledge of biosphere's response to climate change, further modeling studies and long-term field observations are required to understand phenological dynamics and response to climate change. Although the Noah-MP model includes the basic carbon cycle processes, biological community succession and human activities are not included in the model. The simulation results were only a manifestation of the fundamental changes in the natural cycle. Further research needs to incorporate a range of external processes into the model to more realistically simulate NPP changes in this region.

CONCLUSION

Changes in NPP in the TRHR during 1989–2018, stratified by frozen ground type, were simulated using the Noah-MP LSM operating at a spatial resolution of 0.1° and a temporal resolution of 3 h. Results were validated against available meteorological and flux observations at two nearby sites. The following conclusions can be drawn:

1) The validation demonstrated that Noah-MP is able to effectively simulate the spatiotemporal variations of NPP in the TRHR. There was good agreement between the simulation and observations at two sites, with NSE and R values above 0.80 for both soil temperature and soil moisture and above 0.75 for GPP.
2) During 1989–2018, NPP in the TRHR increased at a rate of 1.09 g C m^{-2} yr^{-2}. NPP increased rapidly in the first 15 years

(1989–2003), but decreased significantly in the next 15 years after 2004.

3) The mean annual NPP averaged in the SFG zone (299.7 g C m^{-2} yr^{-1}) was much higher than that in the permafrost zone (198.5 g C m^{-2} yr^{-1}) during 1989–2018, but it was estimated that NPP in the permafrost area increase at a rate of 1.43 g C m^{-2} yr^{-2}, which was much higher than the rate of change in NPP in the SFG zone (0.67 g C m^{-2} yr^{-2}). In areas where permafrost degradation has occurred, both increasing and decreasing changes in NPP have been observed.

Although modeling and validation efforts have been made, long-term *in-situ* monitoring and comprehensive field investigations in the TRHR are still required to validate the simulation results. This study lays the foundation for further research on NPP response to permafrost changes and its feedback in the future.

DATA AVAILABILITY STATEMENT

The original contributions presented in the study are included in the article/Supplementary Material, further inquiries can be directed to the corresponding author.

AUTHOR CONTRIBUTIONS

Conceptualization, ZN and JH; Methodology, JH and ZN; Software, JH and HJ; data collection, JH and HJ; Funding acquisition, ZN; Supervision, ZN; Writing—Original Draft Preparation, JH; Writing—Review and Editing, ZN and JH.

FUNDING

This work was supported by the Second Tibetan Plateau Scientific Expedition and Research (STEP) program (No. 2019QZKK0905-08) and the grants of National Natural Science Foundation of China (Nos 41971074 and 42171125).

ACKNOWLEDGMENTS

The authors would like to thank the China FLUX network (http://www.cnern.org.cn, accessed 15 December 2021) and the National Ecosystem Science Data Center, National Science and Technology Infrastructure of China (http://www.nesdc.org.cn) for providing the data.

REFERENCES

Abramowitz, G., Leuning, R., Clark, M., and Pitman, A. (2008). Evaluating the Performance of Land Surface Models. *J. Clim.* 21 (21), 5468–5481. doi:10.1175/2008jcli2378.1

Arsenault, K. R., Nearing, G. S., Wang, S., Yatheendradas, S., and Peters-Lidard, C. D. (2018). Parameter Sensitivity of the Noah-MP Land Surface Model with Dynamic Vegetation. *J. Hydrometeorology* 19 (5), 815–830. doi:10.1175/jhm-d-17-0205.1

Bibi, S., Wang, L., Li, X., Zhou, J., Chen, D., and Yao, T. (2018). Climatic and Associated Cryospheric, Biospheric, and Hydrological Changes on the Tibetan Plateau: A Review. *Int. J. Climatol* 38, e1–e17. doi:10.1002/joc.5411

Burke, E. J., Jones, C. D., and Koven, C. D. (2013). Estimating the Permafrost-Carbon Climate Response in the CMIP5 Climate Models Using a Simplified Approach. *J. Clim.* 26 (14), 4897–4909. doi:10.1175/jcli-d-12-00550.1

Chen, B., Zhang, X., Tao, J., Wu, J., Wang, J., Shi, P., et al. (2014). The Impact of Climate Change and Anthropogenic Activities on alpine Grassland over the Qinghai-Tibet Plateau. *Agric. For. Meteorology* 189-190, 11–18. doi:10.1016/j.agrformet.2014.01.002

Chen, F., and Dudhia, J. (2001). Coupling an Advanced Land Surface-Hydrology Model with the Penn State-NCAR MM5 Modeling System. Part I: Model Implementation and Sensitivity. *Mon. Wea. Rev.* 129, 569–585. doi:10.1175/1520-0493(2001)129<0569:caalsh>2.0.co;2

Chen, S., Liu, W., Qin, X., Liu, Y., Zhang, T., Chen, K., et al. (2012). Response Characteristics of Vegetation and Soil Environment to Permafrost Degradation in the Upstream Regions of the Shule River Basin. *Environ. Res. Lett.* 7 (4), 045406. doi:10.1088/1748-9326/7/4/045406

Chen, Y., Feng, X., Fu, B., Wu, X., and Gao, Z. (2021). Improved Global Maps of the Optimum Growth Temperature, Maximum Light Use Efficiency, and Gross Primary Production for Vegetation. *J. Geophys. Res. Biogeosci* 126 (4), e2020JG005651. doi:10.1029/2020jg005651

Clapp, R. B., and Hornberger, G. M. (1978). Empirical Equations for Some Soil Hydraulic Properties. *Water Resour. Res.* 14 (4), 601–604. doi:10.1029/WR014i004p00601

Collatz, G. J., Ball, J. T., Grivet, C., and Berry, J. A. (1991). Physiological and Environmental Regulation of Stomatal Conductance, Photosynthesisand Transpiration: A Model that Includes a Laminar Boundary Layer. *Agric. For. Meteorology* 52 (2-4), 107–136. doi:10.1016/0168-1923(91)90002-8

Collatz, G., Ribas-Carbo, M., and Berry, J. (1992). Coupled Photosynthesis-Stomatal Conductance Model for Leaves of C4 Plants. *Funct. Plant Biol.* 19 (5), 519–538. doi:10.1071/PP9920519

Dickinson, R. E., Shaikh, M., Bryant, R., and Graumlich, L. (1998). Interactive Canopies for a Climate Model. *J. Clim.* 11 (11), 2832–2836. doi:10.1175/1520-0442(1998)011<2823:icfacm>2.0.co;2

Ek, M. B., Mitchell, K. E., Lin, Y., Rogers, E., Grunmann, P., Koren, V., et al. (2003). Implementation of Noah Land Surface Model Advances in the National Centers for Environmental Prediction Operational Mesoscale Eta Model. *J. Geophys. Res.* 108 (D22), 8851–8862. doi:10.1029/2002jd003296

Euskirchen, E. S., McGuire, A. D., Kicklighter, D. W., Zhuang, Q., Clein, J. S., Dargaville, R. J., et al. (2006). Importance of Recent Shifts in Soil thermal Dynamics on Growing Season Length, Productivity, and Carbon Sequestration in Terrestrial High-Latitude Ecosystems. *Glob. Change Biol.* 12 (4), 731–750. doi:10.1111/j.1365-2486.2006.01113.x

Feng, A., Li, Y., Gao, J., Wu, S., and Feng, A. (2017). The Determinants of Streamflow Variability and Variation in Three-River Source of China: Climate Change or Ecological Restoration? *Environ. Earth Sci.* 76 (20), 696. doi:10.1007/s12665-017-7026-6

Guo, B., Zhou, Y., Zhu, J., Liu, W., Wang, F., Wang, L., et al. (2015). Spatial Patterns of Ecosystem Vulnerability Changes during 2001-2011 in the Three-River Source Region of the Qinghai-Tibetan Plateau, China. *J. Arid Land* 8 (1), 23–35. doi:10.1007/s40333-015-0055-7

Guo, P., Yang, D., Wang, H., and Cheng, J.-Q. (2013). Climate Change and its Effects on Climatic Productivity in the Three-River Headwaters Region in 1960–2011. *Chin. J. Ecol.* 32 (10), 2806–2814. (in Chinese). doi:10.132992/j.1000-4890.2013.0302

Han, Z., Song, W., Deng, X., and Xu, X. (2018). Grassland Ecosystem Responses to Climate Change and Human Activities within the Three-River Headwaters Region of China. *Sci. Rep.* 8 (1), 9079. doi:10.1038/s41598-018-27150-5

He, J., Yang, K., Tang, W., Lu, H., Qin, J., Chen, Y., et al. (2020). The First High-Resolution Meteorological Forcing Dataset for Land Process Studies over China. *Sci. Data* 7 (1), 25. doi:10.1038/s41597-020-0369-y

Hou, X. (2001). *1:1 Million Vegetation Map of China*. Beijing: National Tibetan Plateau Data Center.

Jiang, C., and Zhang, L. (2015). Climate Change and its Impact on the Eco-Environment of the Three-Rivers Headwater Region on the Tibetan Plateau, China. *Int. J. Environ. Res. Public Health* 12 (10), 12057–12081. doi:10.3390/ijerph121012057

Jiang, C., and Zhang, L. (2016a). Ecosystem Change Assessment in the Three-River Headwater Region, China: Patterns, Causes, and Implications. *Ecol. Eng.* 93, 24–36. doi:10.1016/j.ecoleng.2016.05.011

Jiang, C., and Zhang, L. (2016b). Effect of Ecological Restoration and Climate Change on Ecosystems: A Case Study in the Three-Rivers Headwater Region, China. *Environ. Monit. Assess.* 188 (6), 382. doi:10.1007/s10661-016-5368-2

Li, C., Sun, H., Liu, L., Dou, T., Zhou, M., Li, W., et al. (2022). The Importance of Permafrost in the Steady and Fast Increase in Net Primary Production of the Grassland on the Qinghai-Tibet Plateau. *Catena* 211, 105964. doi:10.1016/j.catena.2021.105964

Li, X., Wu, T., Zhu, X., Jiang, Y., Hu, G., Hao, J., et al. (2020). Improving the Noah-MP Model for Simulating Hydrothermal Regime of the Active Layer in the Permafrost Regions of the Qinghai-Tibet Plateau. *J. Geophys. Res. Atmos.* 125 (16). doi:10.1029/2020jd032588

Liang, T., Yang, S., Feng, Q., Liu, B., Zhang, R., Huang, X., et al. (2016). Multi-Factor Modeling of Above-Ground Biomass in alpine Grassland: A Case Study in the Three-River Headwaters Region, China. *Remote Sensing Environ.* 186, 164–172. doi:10.1016/j.rse.2016.08.014

Lin, S., Wang, G., Feng, J., Dan, L., Sun, X., Hu, Z., et al. (2019). A Carbon Flux Assessment Driven by Environmental Factors over the Tibetan Plateau and Various Permafrost Regions. *J. Geophys. Res. Biogeosci.* 124 (5), 1132–1147. doi:10.1029/2018jg004789

Lin, X., Han, P., Zhang, W., and Wang, G. (2017). Sensitivity of alpine Grassland Carbon Balance to Interannual Variability in Climate and Atmospheric CO 2 on the Tibetan Plateau during the Last century. *Glob. Planet. Change* 154, 23–32. doi:10.1016/j.gloplacha.2017.05.008

Liu, X., and Chen, B. (2000). Climatic Warming in the Tibetan Plateau during Recent Decades. *Int. J. Climatol.* 20, 1729–1742. doi:10.1002/1097-0088(20001130)20:14<1729:aid-joc556>3.0.co;2-y

Liu, X., Zhang, J., Zhu, X., Pan, Y., Liu, Y., Zhang, D., et al. (2014). Spatiotemporal Changes in Vegetation Coverage and its Driving Factors in the Three-River Headwaters Region during 2000-2011. *J. Geogr. Sci.* 24 (2), 288–302. doi:10.1007/s11442-014-1088-0

Mao, T., Wang, G., and Zhang, T. (2015). Impacts of Climatic Change on Hydrological Regime in the Three-River Headwaters Region, China, 1960-2009. *Water Resour. Manage.* 30 (1), 115–131. doi:10.1007/s11269-015-1149-x

Melillo, J. M., McGuire, A. D., Kicklighter, D. W., Moore, B., Vorosmarty, C. J., and Schloss, A. L. (1993). Global Climate Change and Terrestrial Net Primary Production. *Nature* 363 (6426), 234–240. doi:10.1038/363234a0

Muller, S. W. (1943). *Permafrost: or, Permanently Frozen Ground and Related Engineering Problems*. Michigan: U.S. Geological Survey Representative Strategic Engineering Study.

Niu, G.-Y., Yang, Z.-L., Mitchell, K. E., Chen, F., Ek, M. B., Barlage, M., et al. (2011). The Community Noah Land Surface Model with Multiparameterization Options (Noah-MP): 1. Model Description and Evaluation with Local-Scale Measurements. *J. Geophys. Res.* 116 (D12), D12109. doi:10.1029/2010jd015139

Osterkamp, T. (2005). The Recent Warming of Permafrost in Alaska. *Glob. Planet. Change* 49 (3-4), 187–202. doi:10.1016/j.gloplacha.2005.09.001

Qin, D., and Ding, Y. (2010). Key Issues on Cryospheric Changes, Trends and Their Impacts. *Adv. Clim. Change Res.* 1 (1), 1–10. doi:10.3724/sp.J.1248.2010.00001

Ruddell, B. L., Yu, R., Kang, M., and Childers, D. L. (2015). Seasonally Varied Controls of Climate and Phenophase on Terrestrial Carbon Dynamics: Modeling Eco-Climate System State Using Dynamical Process Networks. *Landscape Ecol.* 31 (1), 165–180. doi:10.1007/s10980-015-0253-x

Schuur, E. A. G., and Abbott, B. (2011). High Risk of Permafrost Thaw. *Nature* 480, 32–33. doi:10.1038/480032a

Sen, P. K. (1968). Estimates of the Regression Coefficient Based on Kendall's Tau. *J. Am. Stat. Assoc.* 63, 1379–1389. doi:10.1080/01621459.1968.10480934

Shen, Z.-X., Li, Y.-L., and Fu, G. (2015). Response of Soil Respiration to Short-Term Experimental Warming and Precipitation Pulses over the Growing Season in an alpine Meadow on the Northern Tibet. *Appl. Soil Ecol.* 90, 35–40. doi:10.1016/j.apsoil.2015.01.015

Shi, H., Li, T., and Wei, J. (2017). Evaluation of the Gridded CRU TS Precipitation Dataset with the point Raingauge Records over the Three-River Headwaters Region. *J. Hydrol.* 548, 322–332. doi:10.1016/j.jhydrol.2017.03.017

Smith, S. L., Burgess, M. M., Riseborough, D., and Mark Nixon, F. (2005). Recent Trends from Canadian Permafrost thermal Monitoring Network Sites. *Permafrost Periglac. Process.* 16 (1), 19–30. doi:10.1002/ppp.511

Streletskiy, D. A., Tananaev, N. I., Opel, T., Shiklomanov, N. I., Nyland, K. E., Streletskaya, I. D., et al. (2015). Permafrost Hydrology in Changing Climatic Conditions: Seasonal Variability of Stable Isotope Composition in Rivers in Discontinuous Permafrost. *Environ. Res. Lett.* 10 (9), 095003. doi:10.1088/1748-9326/10/9/095003

Tong, L., Xu, X., Fu, Y., and Li, S. (2014). Wetland Changes and Their Responses to Climate Change in the "Three-River Headwaters" Region of China since the 1990s. *Energies* 7 (4), 2515–2534. doi:10.3390/en7042515

Torre Jorgenson, M., Harden, J., Kanevskiy, M., O'Donnell, J., Wickland, K., Ewing, S., et al. (2013). Reorganization of Vegetation, Hydrology and Soil Carbon after Permafrost Degradation across Heterogeneous Boreal Landscapes. *Environ. Res. Lett.* 8 (3), 035017. doi:10.1088/1748-9326/8/3/035017

Trenberth, K. E., Dai, A., van der Schrier, G., Jones, P. D., Barichivich, J., Briffa, K. R., et al. (2013). Global Warming and Changes in Drought. *Nat. Clim Change* 4 (1), 17–22. doi:10.1038/nclimate2067

Wang, J., Liu, J., Shao, Q., Liu, R-G., Fan, J-W., and Chen, Z-Q. (2009). Spatial-temporal Patterns of Net Primary Productivity for 1988–2004 Based on GLOPEM-CEVSA Model in the "Three-River Headwaters" Region of Qinghai Province, China. *Chin. J. Plant Ecol.* 33 (2), 254–269. (in Chinese). doi:10.3773/j.issn.1005-264x.2009.02.003

Wu, Q., and Zhang, T. (2008). Recent Permafrost Warming on the Qinghai-Tibetan Plateau. *J. Geophys. Res.* 113, D13108. doi:10.1029/2007jd009539

Wu, X., and Nan, Z. (2016). "A Multilayer Soil Texture Dataset for Permafrost Modeling over Qinghai– Tibetan Plateau," in IEEE International Geoscience and Remote Sensing Symposium, Beijing, China, 10-15 July 2016, 4917–4920.

Yang, Q., Dan, L., Lv, M., Wu, J., Li, W., and Dong, W. (2021). Quantitative Assessment of the Parameterization Sensitivity of the Noah-MP Land Surface Model with Dynamic Vegetation Using ChinaFLUX Data. *Agric. For. Meteorology* 307, 108542. doi:10.1016/j.agrformet.2021.108542

Yi, X., Li, G., and Yin, Y. (2012). Temperature Variation and Abrupt Change Analysis in the Three-River Headwaters Region during 1961-2010. *J. Geogr. Sci.* 22 (3), 451–469. doi:10.1007/s11442-012-0939-9

Zhang, Y., Zhang, C., Wang, Z., Chen, Y., Gang, C., An, R., et al. (2016). Vegetation Dynamics and its Driving Forces from Climate Change and Human Activities in the Three-River Source Region, China from 1982 to 2012. *Sci. Total Environ.* 563-564, 210–220. doi:10.1016/j.scitotenv.2016.03.223

Zhao, D., Wu, S., and Yin, Y. (2013). Dynamic Responses of Soil Organic Carbon to Climate Change in the Three-River Headwater Region of the Tibetan Plateau. *Clim. Res.* 56 (1), 21–32. doi:10.3354/cr01141

Zhao, L., Ping, C.-L., Yang, D., Cheng, G., Ding, Y., and Liu, S. (2004). Changes of Climate and Seasonally Frozen Ground over the Past 30 Years in Qinghai-Xizang (Tibetan) Plateau, China. *Glob. Planet. Change* 43 (1-2), 19–31. doi:10.1016/j.gloplacha.2004.02.003

Zhao, M., and Running, S. W. (2010). Drought-Induced Reduction in Global Terrestrial Net Primary Production from 2000 through 2009. *Science* 329 (5994), 940–943. doi:10.1126/science.1192666

Zou, D., Zhao, L., Sheng, Y., Chen, J., Hu, G., Wu, T., et al. (2017). A New Map of Permafrost Distribution on the Tibetan Plateau. *The Cryosphere* 11 (6), 2527–2542. doi:10.5194/tc-11-2527-2017

Conflict of Interest: The authors declare that the research was conducted in the absence of any commercial or financial relationships that could be construed as a potential conflict of interest.

frontiers in Earth Science

ORIGINAL RESEARCH
published: 16 February 2022
doi: 10.3389/feart.2022.802157

Permafrost Base Degradation: Characteristics and Unknown Thread With Specific Example From Hornsund, Svalbard

Wojciech Dobiński[1]* *and Marek Kasprzak*[2]

[1]*Institute of Earth Sciences, University of Silesia, Sosnowiec, Poland,* [2]*Institute of Geography and Regional Development, University of Wroclaw, Wroclaw, Poland*

Permafrost degradation is one of the most pressing issues in the modern cryosphere related to climate change. Most attention is paid to the degradation of the top of the active permafrost associated with contemporary climate. This is the most popular issue because in the subsurface part of it there is usually the greatest accumulation of ground ice in direct relation to the changes taking place. The melting of ground ice is the cause of the greatest changes related to subsidence and other mass-wasting processes. The degradation of the subsurface permafrost layer is also responsible for the increased emission of CO_2 and methane. However, this is not a fully comprehensive look at the issue of permafrost degradation, because depending on its thickness, changes in its thermal properties may occur more or less intensively throughout its entire profile, also reaching the base of permafrost. These changes can degrade permafrost throughout its profile. The article presents the basic principles of permafrost degradation in its overall approach. Both the melting of the ground ice and the thermal degradation of permafrost, as manifested in an increase in its temperature in part or all of the permafrost profile, are discussed. However, special attention is paid to the degradation characteristics from the permafrost base. In the case of moderately thick and warm permafrost in the zone of its sporadic and discontinuous occurrence, this type of degradation may particularly contribute to its disappearance, and surficial consequences of such degradation may be more serious than we expect on the basis of available research and data now. A special case of such degradation is the permafrost located in the coastal zone in the vicinity of the Hornsund Spitsbergen, where a multidirectional thermal impact is noted, also causing similar degradation of permafrost: from the top, side and bottom. Especially the degradation of permafrost from the permafrost base upwards is an entirely new issue in considering the evolution of permafrost due to climate change. Due to the difficulties in its detection, this process may contribute to the threats that are difficult to estimate in the areas of discontinuous and sporadic permafrost.

Keywords: permafrost, permafrost base, active layer, permafrost degradation, hornsund, svalbard

OPEN ACCESS

Edited by:
Dongliang Luo,
Northwest Institute of Eco-Environment and Resources (CAS), China

Reviewed by:
Huijun Jin,
Northeast Forestry University, China
Alexander N. Fedorov,
Melnikov Permafrost Institute (RAS), Russia

***Correspondence:**
Wojciech Dobiński
wojciech.dobinski@us.edu.pl

Specialty section:
This article was submitted to Cryospheric Sciences, a section of the journal Frontiers in Earth Science

Received: *26 October 2021*
Accepted: *12 January 2022*
Published: *16 February 2022*

Citation:
Dobiński W and Kasprzak M (2022) Permafrost Base Degradation: Characteristics and Unknown Thread With Specific Example From Hornsund, Svalbard. Front. Earth Sci. 10:802157. doi: 10.3389/feart.2022.802157

1 INTRODUCTION

Climate warming causes the degradation of all components of the cryosphere that are more or less persistent at the Earth's surface. The permafrost is undoubtedly one of the most stable and the most influencing component of the range of the earth's cryosphere (Lunardini 1995). Its degradation is the subject of attention of many authors in terms of the entire Arctic (e.g., Liljedahl et al., 2016; Shi et al., 2019), within its regional aspects: Alaska (Jorgenson et al., 2001), as a part of the Russian Arctic (Vasiliev et al., 2020), or Tibet (Yang et al., 2010; Yin et al., 2021) and many diverse environments. Predominantly permafrost degradation is described most commonly as process operating from the ground surface downwards (Lawrence and Slater 2005; Delisle 2007; Frey and McClelland 2009; Streletskiy et al., 2015; Oliva et al., 2018; Luo et al., 2018; Luo et al., 2020). It includes the impact on infrastructure (Hjort et al., 2018), where the climatic influence is the most spectacular and often directly visible because the time lag between initial degradation and its further effects is not long. Hence, at the interface between the active layer (AL) and permafrost, the reaction to climate and surface warming will be the strongest and fastest, the most spectacular and at the same time the easiest to identify and measure.

The heat flux into the ground does not stop, however, at the interface between permafrost and the AL, but with a certain delay, penetrating further down. This process depends on various factors, especially heat capacity, heat permeability and amount of ice in the medium. The more complex the geological medium is, the more complicated process related to heat flux in accompany with it and the more difficult it is to describe or model. Stable and much more homogeneous geothermal heat flux is directed opposite to the highly seasonal heat penetrating the AL from the surface. The balance of these opposite heat streams is visible at the semi-stable point of zero annual amplitude (ZAA) in the ground, as the average soil temperature resulting from the influence of heat from these two opposite directions (Lunardini 1995; Lunardini 1996). In the coastal area, there is also the transmission of heat due to the lateral thermal effect of sea water. This is the third important factor in the degradation of permafrost.

In this paper, we want to draw the attention of the reader to that part of the degradation process which is of much less scientific interest and which may play a very important role in this process, especially in the areas of discontinuous and sporadic permafrost. It is about degradation proceeding from the permafrost base. The aim of the study is to present a hypothesis regarding the general properties of permafrost degradation from below, its general relationship with the climate and degradation of upper part of permafrost in contact with the AL, and in particular to determine the probable extent and speed of degradation from bottom up in comparison the downward degradation from surface. We want to pay attention in particular to the scale and likely consequences of the bottom-up degradation of permafrost. This seems to be an even more serious threat than those occurring due to the downward degradation of permafrost from above. We will also pay attention to the role of sea influence on land permafrost and possible dangers related to this process, which are not well understood so far. To this end, we will show an example of geophysical imaging conducted on the coast of the Wedel Jarlsberg Land in southwestern Spitsbergen. This is linked to the possibility of sea water intrusions on Arctic coasts (Kasprzak et al., 2017; Guimond et al., 2021).

2 MODELS OF PERMAFROST DEGRADATION

Overall, 81% of the permafrost regions in the Northern Hemisphere are influenced by ecosystems, indicating the dominant role of ecosystems in permafrost stability here. Permafrost driven solely by climate, such as that on the Qinghai-Tibet Plateau, occupies 19% of permafrost regions (Ran et al., 2021). Northeast China also experienced substantial climate warming over the past 60 years and can be used as an indicator of change. The rises in mean annual air and mean annual ground-surface temperatures were higher in permafrost zones than in the seasonal frost zone (Li et al., 2021). Permafrost degradation leads to deterioration of the ecological environment in this cold region. As a result, the belt of larch forests has shifted northwards and wetland areas with symbiotic relationships with permafrost have decreased significantly. Limits of all latitudinal permafrost zones moved northward significantly (Chen et al., 2020).

Downward permafrost degradation develops always when the maximum depth of seasonal thawing exceeds the maximum depth of seasonal freezing, and it generally results in the formation of a talik disconnecting the permafrost from the seasonal frost layer. This type of degradation is divided into four stages: 1) initial degradation, 2) accelerated degradation, 3) layered talik, and 4) finally the conversion of permafrost to seasonal frost (Jin et al., 2006). Three types of permafrost temperature curves may be attributed to these models: 1) Stable permafrost temperature profiles in the continuous permafrost zone with mean annual ground temperatures (MAGT) colder than −1.5°C and thicker permafrost, 2) The degrading permafrost temperature curves along the margins of the discontinuous permafrost zone and in the island permafrost zones, with MAGTs of −0.5 to −1.5°C This type of permafrost is generally thin and thermally unstable, and 3) Phase-changing transitory permafrost temperature curves on the margins of permafrost islands and around taliks with MAGTs generally higher than −0.5°C. Generally, permafrost in these areas is very thin and unstable (Jin et al., 2006). It is important to know also that on the margins of permafrost islands, because of the higher temperatures of unfrozen soils and zero vertical thermal gradients, heat is more easily transferred laterally to permafrost. Therefore, lateral permafrost degradation is predominant in this case (Jin et al., 2006).

According to Wu et al. (2010), the process of permafrost degradation can be divided into five subsequent stages: 1) starting stage, 2) temperature rising stage, 3) zero geothermal gradient stage, 4) talik layers stage, and 5) disappearing stage. There are two modes of perennially frozen ground thawing: from top to

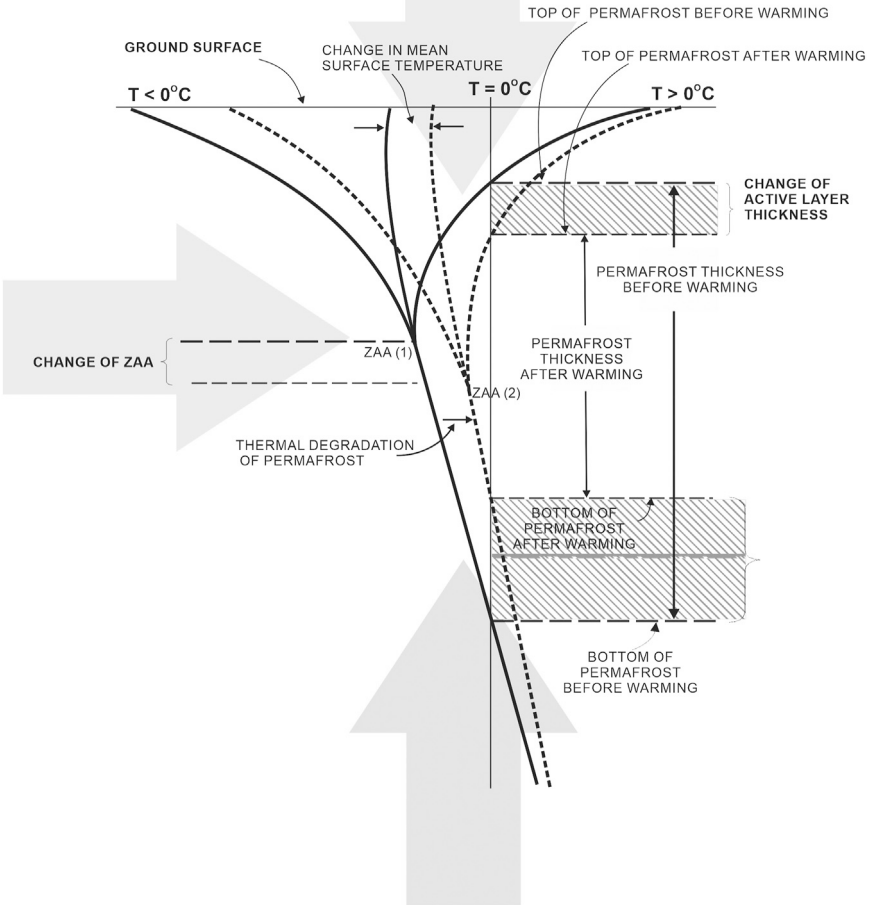

FIGURE 1 | General characteristics of permafrost degradation. When a heat wave passes through the entire permafrost layer, it warms the permafrost layer up throughout the entire profile, causing the permafrost table to lower, the ZAA temperature to rise, and the permafrost base to rise.

bottom and opposite. During the temperature rising stage, when the heat flux in the perennially frozen soil layer is less than that in the unfrozen soil underlying frozen soil layer, the geothermal flux is partly used to thaw the base of permafrost, and permafrost thaws from bottom to top. With the decrease of thermal gradient in the perennially frozen ground, the heat that is used to thaw permafrost base increases, and geothermal heat will be entirely consumed to thaw the base of permafrost until the temperature gradient reaches zero thermal gradient state (Wu et al., 2010). More detailed description of subsurface thermal and hydrogeological processes in permafrost regions and subsurface effects of climate change in cold regions is presented in Kurylyk et al. (2014).

The modes of permafrost degradation are related to the types of permafrost. In the periglacial environment, we can deal with a permafrost medium 1) without ice—frozen rock, or cryotic permafrost, which is not frozen due to increased pressure or mineralization, and 2) with one that contains ice of various origins and in varying amounts. It can be ice-cemented loose sedimentary rock, or massive ice, e.g., of glacial origin.

In the case of ice-free permafrost, its degradation is based on a rise in temperature in the sub-zero temperature range and in decrease in its thickness, followed by a complete disappearance by combining the permafrost base and the permafrost table. In the case of ice-containing permafrost, the degradation process is more complicated and consists not only in the rise in temperature, but also in the melting of the ice it contains, which also causes a variety of mechanical processes involving the material medium which permafrost encompassing, such as thermokarst, landslides, mud flows, and others. These processes are visible on the surface of the ground and they usually cause large changes in the geographical environment, or various threats to human activity. This bipartite process of permafrost degradation has resulted in confusion about assigning them

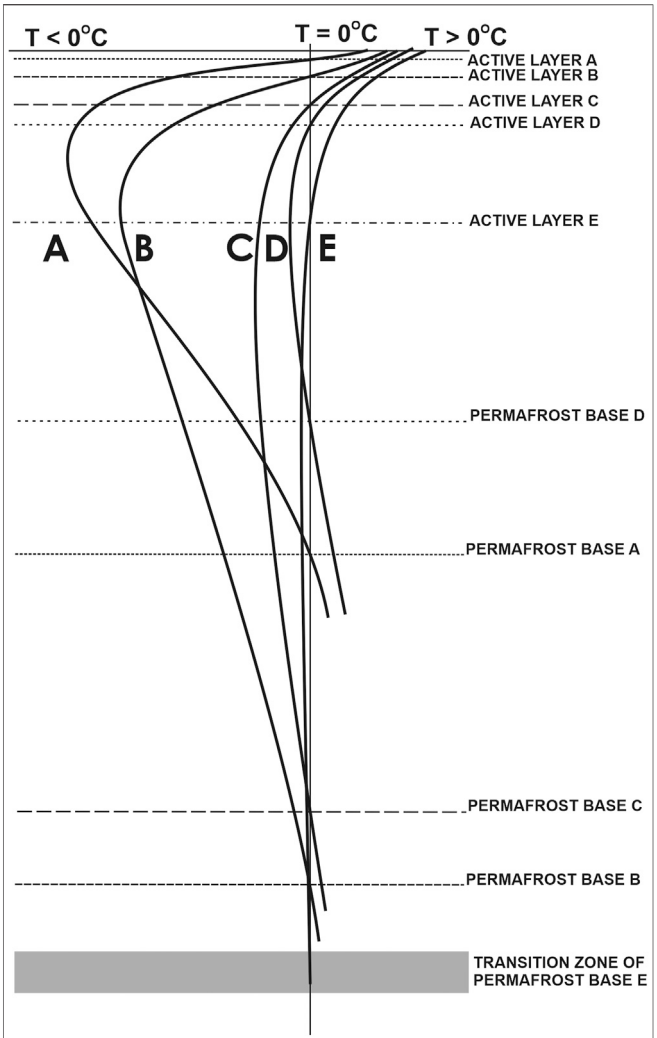

FIGURE 2 | Five selected theoretical permafrost thermal profiles. Notes: **(A)**—cold and thin permafrost layer, high thermal gradients from both directions, **(B)**—cold and thick permafrost layer, low thermal gradient from below, **(C)**—warm and thick permafrost layer with low thermal gradient from both sides, **(D)**—warm and thin permafrost with low thermal gradient from above, and **(E)**—The zero-gradient profile, mean annual ground temperature is basically at 0°C or at the freezing temperature of soil.

the correct name: melting vs thawing (Grosse et al., 2010). Generally speaking, the term thawing is of course correct, but at the same time it is clear that the ice present in the permafrost eventually melts as it degrades.

In general, it can be assumed that the degradation of permafrost occurs simultaneously from the top—by increasing the AL, from the bottom by raising the permafrost base, and in terms of its internal temperature, which rises in the permafrost layer in the range of negative temperatures (Jin et al., 2006; Wu et al., 2010) (**Figure 1**). The entire process is initiated from the top—climatically. The downward degradation occurs with the delay associated with the penetration of the medium by the heat wave that reaches the permafrost boundary, the later the thicker it is. In the case of a small difference in temperature, however, it may extinguish before reaching the permafrost base. Then, the degradation does not encompass the entire permafrost layer.

3 CLIMATIC AND GEOLOGICAL DEPENDENCIES

Since permafrost is a geological phenomenon resulting from climatic influences, defined as the thermal state of the ground (Lunardini 1995; Everdingen van 2005), its temperature characteristics are therefore the only property that fully and completely describes it. Its thermal state will therefore be a derivative of the climatic components that affect the Earth's surface. The most direct is the effect of temperature influence. This impact can be very diverse, leading to the formation of various temperature profiles in the permafrost ranging from almost 0 to 1,600 m in depth. In fact, wherever the mean annual air temperature (MAAT) is negative, permafrost can form. Its temperature profile will, however, vary depending on the specificity of the climate - on the one hand, and the geothermal impact—on the other. Other permafrost types, such as those ecosystem-driven, modified, or protected permafrost, will also depend on geo-environmental conditions, such as interrelations with organic soils and surface canopies. Nevertheless, these relationships do not contradict the general principle that is of key importance to the topic under discussion. Some characteristic theoretical profiles relevant to the content of this article are shown in **Figure 2**.

In a very cold climate but high geothermal gradient, permafrost may be "cold"—its temperature at the depth of ZAA point will be low but the thickness will not be great because both: the "cold" gradient coming from above and the "warm" gradient coming from below will be high. This will result in a profile of permafrost having a "boomerang shape" and a relatively large angle between the permafrost temperature line and the 0°C line as shown in **Figure 2** (line A). Both the determination of the top and the bottom of the permafrost layer in such a system will be the easiest, because the point at the intersection of the 0°C line with the temperature profile is clear and unambiguous.

In the case of permafrost with a large "cold" gradient flowing from the surface and small heat flux from the depths of the Earth, the permafrost temperature at the ZAA point may also be low and slowly increases with depth, permafrost thickness will be the greatest (**Figure 2**, line B). Both the top and bottom of the permafrost can be clearly marked.

Another situation arises when the "cold gradient" in the upper part is not great, as is the case in cold maritime climates (**Figure 2**, line D). Here, the temperature amplitude between winter and summer is much smaller than that in a continental climate. Then, the influence of the cold climate does not produce such a thick layer of permafrost as in the case of B (**Figure 2B**) because the "cold" wave is extinguished at a shallower depth. However, it also depends on the geothermal degree. In general, this type of permafrost is not very cold, the temperature of ZAA is higher than that of A and B above (**Figure 2**). The permafrost temperature line and the 0°C line will intersect at a more

acute angle than in the above cases, and the determination of the upper and especially the base of permafrost will be much more difficult than in cases A and B. It is also worth noting that due to the different temperature on the surface, as well as the different degree of geothermal heat flux in the ground and the capacity and thermal permeability of the medium, the thickness of the AL does not correlate with the depth of permafrost base location.

The most interesting case from the point of view of this paper is the one where the MAAT is not particularly low and the thermal gradient is also not high. This situation creates the conditions for the formation of a relatively thick permafrost, but with relatively "warm" characteristics (**Figure 2C**). Its temperature both at the ZAA point and along the entire temperature line will be quite similar an has "shape of bow." Also, the intersection of the permafrost temperature line with 0°C will have the acute angle. The asymptotic nature of temperature line will make it impossible in practice to unambiguously determine the lower border, i.e., the range of the bottom of permafrost. Such warm permafrost is found especially in the zone of discontinuous and sporadic permafrost occurrence (Smith, 1988).

A particular example of a susceptible permafrost is isothermal permafrost in which there is no temperature gradient (**Figure 2E**). Permafrost has such thermal characteristics in an advanced state of degradation and its complete disappearance is the fastest. It is caused by a sharp decrease in the permafrost table and an elevation of the permafrost base, the determination of which is difficult due to the temperature close to 0°C

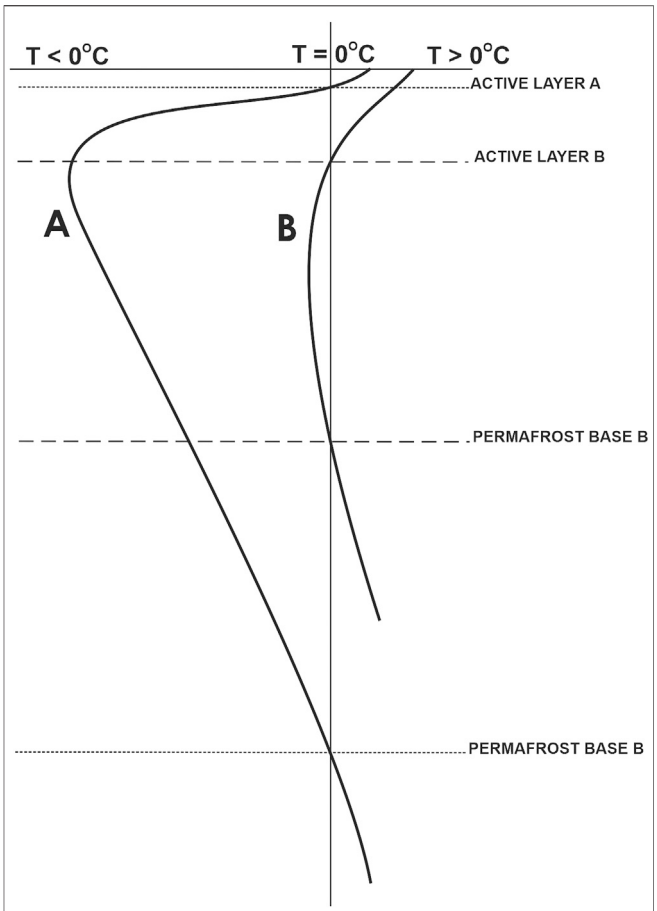

FIGURE 3 | General shape of degrading permafrost profile thermal curve. Notes: **(A)**—initial stage, cold permafrost (boomerang-like shape), **(B)**—degrading permafrost (bow-like shape). Compare the difference between the amount of degradation of the top (AL) and the bottom of permafrost.

4 PERMAFROST DEGRADATION FROM THE SURFACE

As mentioned above, the degradation of permafrost from the surface is the process of particular interest in contemporary research. This process is often limited to the characteristics of the increasing thickness of the AL. Its thickness may increase faster when it includes, for example, coarse rock sediments and the ice content in the permafrost is small. This is because enormous energy is absorbed in the process of permafrost degradation into a phase change—melting of ground ice. The largest amount of such ice is usually near the ground surface. This phase transformation (ice melting) slows down the process of permafrost degradation from the top, i.e., mainly the increase in the thickness of the AL. However, heat penetration into the permafrost is not completely stopped. The released latent heat raises the permafrost temperature also within the negative temperature range, causing the ZAA position to shift towards the positive temperature (**Figure 1**). In this way, first the upper part of the permafrost temperature line, and then the lower part "moves" towards 0°C line, showing the temperature increase in the permafrost in all its thickness. This process may take shorter or longer time depending on the temperature difference, the thickness of the permafrost, or the thermophysical properties of the heat-conducting rocks. The process of permafrost degradation from the surface is the easiest to observe and measure, because such permafrost is basically available just below the seasonally thawing AL, i.e., at a depth of several dozen centimeters to several meters.

5 PERMAFROST DEGRADATION FROM BELOW

Determining the extent of permafrost degradation from bottom is much more difficult and becomes more complicated as increases in permafrost thickness, also increasing difficulties in measuring temperature or observing phase transformation at great depth. So far there are few publications presenting the results of permafrost bottom studies with the use of indirect geophysical methods. Seismic and electrical resistivity methods are used in the study of thin permafrost (You et al., 2013; Sjöberg et al., 2015), and in the study of the AL and subsurface permafrost in high mountain and Arctic environments (Hauck and Kneisel 2008). Recognition of the process of degradation of permafrost from the bottom, however, may in some cases be crucial for determining the

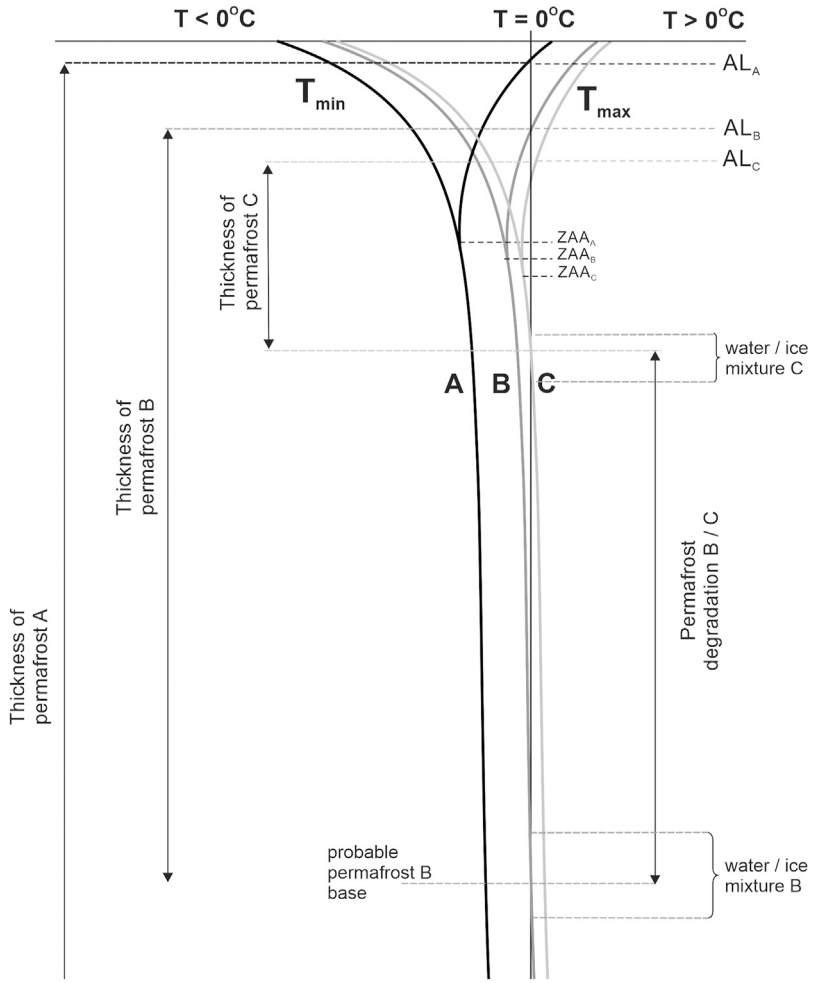

FIGURE 4 | Mode of degradation of thick isothermal warm permafrost, general view. Thermal degradation dominates between permafrost profiles **(A,B)**, physical degradation (thawing, and melting of ice) occurs between permafrost profiles **(B,C)**. Compare difference between amount of degradation between AL and permafrost base.

correct extent of permafrost degradation not only in the surface area, but above all in its thickness.

Based on the existing knowledge, it is first necessary to characterize this process theoretically. After a shorter or longer period of time, which is required for the heat to flow into the soil, the temperature rise is either quenched at a certain depth in the permafrost or reaches its floor. As already mentioned, it depends on the magnitude of the thermal gradient in both directions, the thickness of the permafrost and the thermal properties of the medium.

In the case of thin permafrost and in a situation of high thermal gradients, it is relatively easy to define its base, which may be very similar to the upper limit that exists between the AL and the permafrost. In the sediment material, this will be in the immediate vicinity of the overlying, ice-cemented permafrost layer with a water-saturated, unconsolidated sediment layer underneath.

In a thick layer of permafrost and in the case of small thermal gradients, the degradation of permafrost will be slower. The first phase of degradation will be the increasing the temperature of the entire permafrost layer as a result of the slow penetration of the heat wave into the soil. As a result, due to the warming, the temperature profile will change its shape from a "boomerang" (**Figure 3A**) to an "bow" shape (**Figure 3B**). The permafrost profile will increasingly approximate the isothermal profile with a very slow, asymptotic approach to the intersection with the 0°C line. The intersection of the permafrost profile with the 0°C temperature line will be at a very sharp angle, which in practice manifests itself in the fact that in a relatively wide depth range there will be a temperature close to 0°C on both the positive and negative sides (**Figure 4E**). This situation favors the presence of both ice and liquid water. Determining the permafrost base in such an environment is very difficult and the permafrost base (**Figure 2E**) takes the form of a transition zone rather than a sharp borderline (Elvebakk 2010; Szewczyk and Nawrocki 2011) (**Figure 4**). In solid rock, apart from temperature variations, the phase changes of water will be basically unnoticeable, but it depends on the porosity of the rock.

In an empirical sense, the process of permafrost degradation from the bottom-up of thick permafrost is virtually unknown. Therefore, it is particularly important to understand the degradation of such permafrost, especially occurring in the sedimentary material, as it is likely to occur unexpectedly and violently, with serious risks.

The above-mentioned "asymptotic" intersection of the permafrost profile with the 0°C line shows primarily the uncertainty and zonal character of the permafrost base. It should be noted, however, that such property of this border is caused by its enormous potential for "vertical mobility." When the permafrost profile line is sufficiently close to 0°C line, another heat wave reaching the permafrost base, can move it up greatly, even when the temperature jump is small. Such a rapid degradation process can occur even when the temperature jump is less than 1°C. This move upward of the permafrost base can probably lead to very rapid thawing of the ice included in sedimentary material which may be at phase equilibrium. This process is faster if less ice is used in the earlier cementation of sedimentary material. The latent heat delays the process of the degradation, but depends on amount of water in the ground. We know, however, that in permafrosted ground water/ice is concentrated mainly in its upper subsurface layer rather than its lower part. This is why the disintegration of the sedimentary material on greater depth can take place faster. **Figure 4** shows the theoretical course of this process. As a result, in a relatively short period of time, it is difficult to identify threats may arise, especially in the regions of the fastest degradation of permafrost in thick sedimentary material. The difficulty in detecting them lies in the fact that this process takes place underground, often at considerable depth, and may, in principle, go unnoticed until serious mass processes, such as subsidence or sliding, occur. This process is extremely difficult to estimate and, as far as we know, has never been the subject of research, analysis or modeling in a quantitative sense.

The correctness of the hypothetical model presented here is evidenced by all known thermal profiles of permafrost, in which it is clearly visible that their intersection with the 0°C axis always has a sharp angle and a more asymptotic character at the permafrost base than at the permafrost table (Dobiński 2020a). It is also documented by empirical research (Elvebakk 2010; Szewczyk and Nawrocki 2011). It is also shown by the few results of studies on the variability of the entire permafrost layer (Harris 2001; You et al., 2013; Sjöberg et al., 2015; Kasprzak et al., 2017; Czekirda et al., 2019).

6 PERMAFROST DEGRADATION FROM THE SEA

A large part of the research on permafrost on Arctic coasts is carried out in areas with subsea permafrost, such as in Siberia or Alaska (e.g., Hunter et al., 1988; Rekant et al., 2005; Overduin et al., 2016; Angelopoulos et al., 2020). The presence and conditions of underwater permafrost determines a number of geomorphological processes in this zone. However, the situation is different on those sections of the High Arctic coast where subsea/offshore permafrost is not found. There is a special case of degradation of the terrestrial permafrost both laterally and partially from below, as sea water can directly affect the deeper parts of the substrate. Under favorable conditions, it creates an intrusion of salty and periodically warm water cutting into the land, similarly as it is common in regions of lower latitudes (Cooper et al., 1964; Werner et al., 2012).

This situation was visualized using electrical resistivity tomography (ERT) in 2012 on the west coast of Spitsbergen (Kasprzak et al., 2017) and similarly confirmed by geophysical methods also in other locations (Strzelecki et al., 2017; Kasprzak 2020; Kasprzak et al., 2020; Pedrazas et al., 2020). The presence of sea intrusion leads to the formation of a horizontal "permafrost wedge" subjected to changes under influence of air temperature from above and sea water temperature from below, as shown in **Figure 5**. A cryo-hydrogeological model of seawater intrusion affecting permafrost was recently proposed by Guimond et al. (2021).

Heat transfer from the sea to the inland is favored not only by the strong summer heating of sea water in the bays of the Greenland Sea near Hornsund, but also the observed changes in the extent and frequency of sea ice. The progressive thawing of permafrost and melting of ground ice of this zone and the retraction of the "permafrost wedge" will result in a lower resistance of the sediment material to erosion and the potential dangers of infrastructure located on the seashore.

7 PERMAFROST DEGRADATION IN HORNSUND AREA, SPITSBERGEN

The glacier-free part of the land near the Hornsund Fjord in the southwestern part of Spitsbergen is an area that is particularly exposed to climatic warming. A continuous series of measurements started in 1979 at the Polish Polar Station operating here shows that over 40 years the MAAT increased by over 4°C (**Figure 6**), increasing on average by 1.14°C per decade (Marsz and Styszyńska 2013; Wawrzyniak and Osuch 2020). It is also worth noting that in 2016 the MAAT was positive in Hornsund (**Figure 6**). The data clearly suggest that the warming of the air at the surface has been penetrating the ground for several decades, modifying ground temperature and influencing the shape of the permafrost present here. This is not an isolated situation, but rather an example representative of the entire west coast of Spitsbergen (Nordli et al., 2014).

Permafrost occurring in Svalbard can be divided into two characteristic types (Szafraniec and Dobiński 2020). The first occurs in a very frosty and dry periglacial environment, covering the highest peaks and mountain ridges of Svalbard, which most often appears in the form of nunattacks protruding above the glacial area. The temperature in this area is almost perennially negative, maintaining the occurrence of permafrost, which in this environment reaches 450–500 m deep (Humlum et al., 2003). The second type is permafrost, which includes low-elevation areas of Svalbard, which include coastal areas and the forefields of

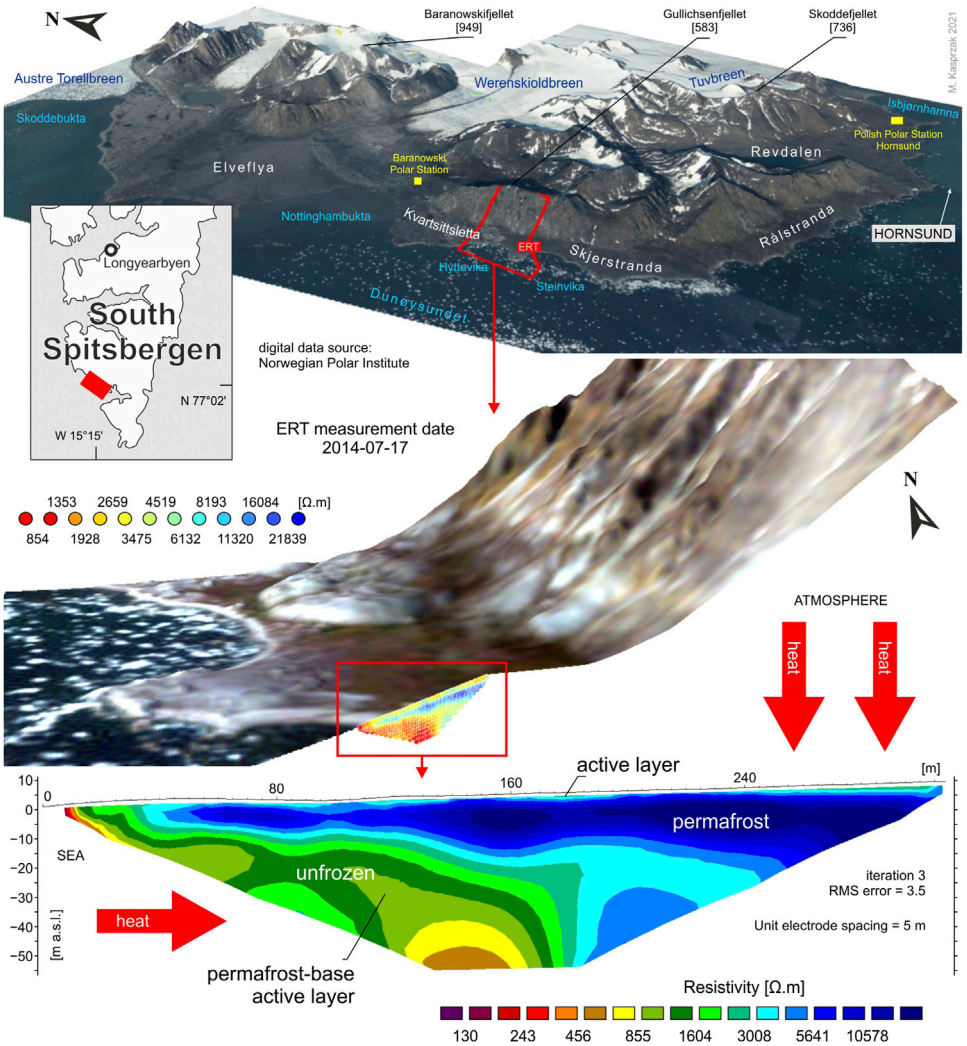

FIGURE 5 | Multidirectional permafrost degradation; dominant change in the electrical resistivity of the ground is caused by the intrusion of seawater. Example from the Gulf of Hytte, Svalbard, August 2014. The geoelectric properties in this case refer directly to the temperature of the ground. Frozen rocks lose their ability to conduct electricity. Deep blue colors shows "permafrost wedge" directing towards the sea-shore.

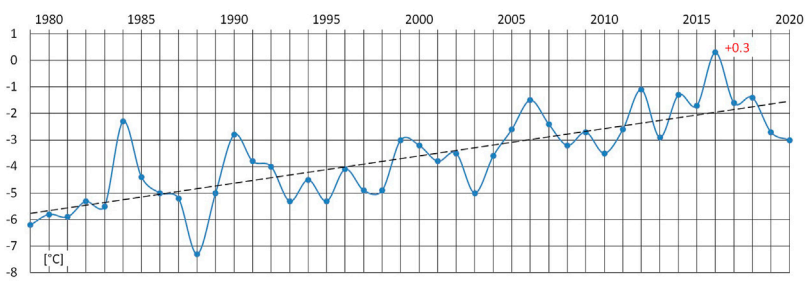

FIGURE 6 | Mean annual air temperature measured at the Polish Polar Station in Hornsund. Data based on: Marsz and Styszyńska (2013), Meteorological Bulletin (2009–2020). The graph also shows the trend line (black dashed line).

retreating glaciers. There is a much milder climate here. MAAT is still negative, which allows permafrost to survive and even aggrade in the proglacial forefields. The permafrost thickness in this region is approx. 100 m (Humlum et al., 2003; Wawrzyniak et al., 2016). The latter, however, does not apply to land in the immediate vicinity of the sea. Geophysical surveys

conducted in the Hornsund region indicate the thermal impact of the sea reaching inland (Kasprzak et al., 2017). As a result, in the summer period, at an average distance of 50–60 m from the shoreline, permafrost ranging from only a few to approx. 20–30 m. This situation depends on the local shape of the shore and is particularly visible on the protruding parts of land, as it was found on the example of the Wilczek Peninsula (Strzelecki et al., 2017).

8 DISCUSSION

Permafrost degradation is one of the most important warming processes in the cryosphere. Due to the extent of permafrost, which covers more than 25% of the land surface (Dobinski, 2011), this process should receive special attention. So far, however, the research has focused on the upper subsurface layer of freezing soil: the AL and shallow permafrost. Indeed, emissions of CO_2 and methane, i.e., gases that can enhance the warming effect, are related to the shallowest (ca. 3 m) layer of soils (Knoblauch et al., 2018). Studies and modeling based on satellite data are particularly popular (e.g., Beck et al., 2015; Jorgenson and Grosse 2016; Trofaier et al., 2017; Hu et al., 2020; Kalinicheva and Shestakova 2021). Unfortunately, this approach is limited and does not include deeper processes. Permafrost degradation, however, in the areas of sporadic and discontinuous permafrost, with favorable climatic conditions may encompass the entire permafrost layer. In the unstable zone permafrost is warming and thinning rapidly. At Xidatan permafrost base has been rising up since 1975, about 20 m in the past 20 years (Jin et al., 1999). The MAGTs at depths of 12–20 m have risen .2–.3°C (Jin et al., 2000). This last publication presents however much more synthetic view on permafrost evolution in China since Quaternary. Therefore, it is worth to remember that permafrost on the Qinghai-Tibet Plateau is largely relict and has been degrading since the Last Glaciation (Wang et al., 2000).

Studies on permafrost degradation in the Russian Arctic by Vasiliev et al. (2020) indicate that since 1970, the average ground temperature at depths of 10–12 m in the zone of continuous permafrost occurrence, has been increasing at an annual average rate of .03–.06°C yr^{-1}. These authors divided permafrost degradation into three main phases. The initial stage of degradation is a gradual increase in AL thickness (ALT) while permafrost temperature remains relatively low. This is due to the protective role of the transition layer, although extremely hot summers can partially thaw it. The second stage, termed "climate-driven, ecosystem-protected permafrost," is where increased permafrost degradation is initiated after the ground ice in the transition layer has completely thawed. The third and final stage of degradation occurs when the progressive lowering of permafrost table converts the permafrost to a seasonally frozen layer, followed by rising temperatures at the ZAA depth to above 0°C.

The use of deep boreholes in Russian Arctic research also provides direct data on the depth of the permafrost base (Duchkov et al., 1994). Its greatest thickness, exceeding 400–500 m, is found in Yakutia. For this area, the thermal evolution of permafrost in the entire profile was forecasted until 2,200 (Balobaev et al., 2009). The observed and progressive increase in MAAT (from 1960 by 2–2.5°C) will cause changes in permafrost temperature reaching 200–250 m. The currently observed trend causes that in the latitude between 60 and 70° N by 2030–2040 the seasonal thawing of the ground from above may reach 10–15 m and the rate of deepening of the AL may be .2–.3 m yr^{-1}. Degradation of Siberian permafrost may lead to its complete disappearance south of the 62°N especially in areas subjected to strong anthropogenic influence (Balobaev 1991).

The quantitative method of reconstruction of palaeocryogenic conditions, proposed by Balobaev (1991), also allowed the determination of the trend of permafrost changes over a longer period of time, reaching from the Last Glaciation Maximum. Since the period 18–20 thousand years ago, when permafrost covered the vast lowland territory of Western Siberia down to 51–52°N latitude its thickness has decreased by 120–170 m as a result of thawing from below.

Monitoring of permafrost degradation along the Bei'an-Heihe Expressway in the eastern part of Northeast China show a lowered permafrost table and an elevated permafrost base whereas the base of permafrost degraded faster than its table. The results shows also that the rising rate of the permafrost base is higher than the lowering rate of the permafrost table, which has remained at the same depth since 2012, whereas the permafrost base has continued its rising. Rising rate of the permafrost base (0.38 m/yr) is larger than the lowering rate of the permafrost table (0.12 m/yr). During summer months, the groundwater heat can be transmitted also to the permafrost base and causes it to rise faster than the lowering of the permafrost table (Guo et al., 2021). Sun et al. (2020) indicated also, that in Xidatan along the Qinghai-Tibet Highway on the interior Qinghai-Tibetan Plateau, the main degradation mode of the site in the discontinuous zone appeared to be upward thawing from the permafrost base. They argued that when heat from the surface transferred to the permafrost base, because the reduced temperature gradient was less than the geothermal gradient from the geothermal heat flux of the deep stratum, it led to the bottom of the permafrost absorbing heat from the underlying unfrozen soil. Therefore, the permafrost base began to thaw and move upward, which resulted in thinning of the permafrost (Sun et al., 2020).

Studies on Canadian permafrost show that the ALT has increased by an average of 0.39 m. since the end of the Little Ice Age (ca. 1850), while the permafrost base has increased by an average of 3 m (Zhang et al., 2006). The simulation results indicate that in the areas of sporadic permafrost the permafrost base increased by an average of 17 m, and in some places by 50 m, in the last ca. 150 years (Zhang et al., 2006). These data and calculations show that the rate of permafrost degradation from the bottom is on average 10 times greater than that from the ground surface in a large territory of southern Canada which is subject to occurrence of discontinuous and sporadic permafrost. The rise in the permafrost base by this size (50 m) corresponds to an increase in mean annual ground temperature by about .9°C (Zhang et al., 2006). This

simulation shows that the thermal response of the permafrost base takes much longer than that of the AL. However, while the AL freezes seasonally and the degradation process is thus stopped, thawing from bottom up can be a continuous process with greater inertia. ALT is determined primarily by summer temperature, while the depth of permafrost base is determined mostly by annual ground temperature as a result; the permafrost base will continue to rise with some lag even if the surface temperature ceases to increase (Zhang et al., 2006).

Thus, it can be seen that while the delay associated with the time needed to penetrate the entire permafrost layer stops the onset of degradation from below, once it has started, the process may be much faster and much more difficult to stop due to the same delay in the surface heat transmission in the permafrost base.

In this respect, the situation is specific on the southern coast of Spitsbergen. As shown in **Figure 6**, this is an area of particularly strong climate warming, which also translates into changes in the thermal state of the permafrost occurring here. Currently, MAAT no longer indicates that climatic conditions for continuous permafrost may persist, because MAAT is too high and this area may be moved into the category of discontinuous permafrost in next years. This probability is additionally justified by the strong influence of sea water from the fjord. The first show that permafrost in the Hornsund region is already isothermal, with a zero geothermal gradient (Wawrzyniak et al., 2016), which means that the first stage of degradation, i.e., increasing the temperature within the entire permafrost layer, has ended. In the next stage, when the climate does not change, ground temperature may quickly rise to above 0°C and permafrost may disappear first in particularly vulnerable places in southern Spitsbergen.

The disappearance of permafrost on the coast of the Hornsund region does not necessarily have to be associated with the violent mass processes of the melting of ground ice. The thickness of marine and glacial sediments on the Hornsund coast is not great, and most of the solid rock of the substrate is subject to freezing. On the other hand, it is worth noting that in solid rock, where the water content is usually minimal, the ground freezes and thaws much faster, because little energy is used for the ice/water phase change and the amount of latent heat used is low. For this reason, the degradation of permafrost and its complete disappearance may be very fast under these conditions. In particular, therefore, under these conditions, the process shown in **Figure 4** may be realized, where, with a slight final rise in soil temperature, the complete disappearance of permafrost may be rapid.

9 CONCLUSION

Permafrost degradation is a process in which two basic changes can be distinguished: 1) the increasing of permafrost temperature in part or all of its thermal profile, within the negative temperature, and 2) the disappearance of permafrost by increasing soil temperature to a positive value i.e., melting ground ice, which significantly delays the degradation process.

The permafrost decay process starts usually at the surface (in volcanic locations it may change) as a result of the warming. Its first result is an increase in the ALT. It differs primarily depending on the thermal conductivity and heat capacity of the medium, accompanied by soil ice/water content. The heat wave that penetrates the AL raises the temperature gradually, delaying ground warming. However, the progress of degradation and disappearance of permafrost at its base may be usually many times greater and faster than that in contact with the AL.

In the particular case when the permafrost on the coast is sufficiently thin and the seasonal temperature changes encompass the entire permafrost layer, its thickness (the distance between the depths of permafrost table and base) may change seasonally. Such seasonal change at the bottom may be called the bottom AL (Kasprzak et al., 2017; Dobiński 2020b). This process is possible when a relatively thin permafrost is thermally active in its entire volume.

The most likely process that can cause the disappearance of permafrost is the multidirectional degradation of warm isothermal permafrost remaining at a temperature just below 0°C, through the climatic impact, and also indirectly due to the thermal properties of sea water. When the heat wave covers the entire permafrost layer crosses the 0°C border, degradation is the fastest from its lower limit (the base of permafrost), and the disappearance of permafrost from the bottom can be rapid.

The land part of the coast, subjected to the thermal influence of sea water from below, is particularly vulnerable to permafrost thawing. The heat wave from the sea, or the physical intrusion of saline water into the land, determine the thermal conditions of the deeper subsoil. Water temperature changing throughout the year, similarly to the air temperature, drives the intensity and direction of heat transfer.

The described processes may lead to dangerous threats of an unknown scale when they involve not a solid rock, but a layer of sediments cemented with ice. The thicker the layer of ice-poorer loose sediment, and the greater the warming, the greater the risk of the disappearance of permafrost.

The authors are convinced of the necessity of wider involvement in the full recognition of the degradation process and the disappearance of permafrost in the world, with particular emphasis on this process proceeding from below (Burn and Nelson, 2006; Dobiński and Leszkiewicz, 2010).

DATA AVAILABILITY STATEMENT

The original contributions presented in the study are included in the article/supplementary material, further inquiries can be directed to the corresponding author.

AUTHOR CONTRIBUTIONS

WD developed the concept of the article, wrote chapters 1–5 and 7 made figures 1–4. Both authors MK compiled sections on coastal permafrost degradation—chapter 6 and provided empirical data. He designed and produced **Figures 5**, **6**. Both

authors contributed to conclusions, manuscript revision, read, and approved the submitted version.

FUNDING

MK's participation in this research was funded by the research project no. 2015/19/D/ST10/02869 of the National Science Center, Poland. Used aerial photographs of the Norwegian Polar Institute were purchased as part of the order ZP. 2420.1.IGRR.ZG.2013 (2013-01-9) financed from statutory funds of the Institute of Geography and Regional Development, University of Wroclaw. Publication partly funded by 'Excellence Initiative - Research University' policy of the University of Wrocław, Poland.

ACKNOWLEDGMENTS

The authors are grateful to the reviewers for the numerous and valuable comments that helped to shape the manuscript better. We are also especially grateful to the editors: Dongliang Luo and Huijun Jin for the valuable discussion of the work, a series of editorial comments and suggestions for further studies of permafrost degradation.

REFERENCES

A. A. Marsz and A. Styszyńska (Editors) (2013). *Climate and Climate Change at Hornsund* (Svalbard. Gdynia: Gdynia Maritime University), 402.

Angelopoulos, M., Overduin, P. P., Miesner, F., Grigoriev, M. N., and Vasiliev, A. A. (2020). Recent Advances in the Study of Arctic Submarine Permafrost. *Permafrost and Periglac Process* 31 (1), 442–453. doi:10.1002/ppp.2061

Balobaev, V. T. (1991). *Geothermy of the Frozen Zone of the Lithosphere of the Asia North*. Novosibirsk: USSR Acad Sci. (in Russian).

Balobaev, V. T., Skachkov, Y. B., and Shender, N. I. (2009). Climate Change and Permafrost Thickness Forecast for Central Yakutia till 2200. *Sci. J. Geogr. Nat. Resour.* 2, 50–56. (in Russian with Eng. abstract).

Beck, I., Ludwig, R., Bernier, M., Lévesque, E., and Boike, J. (2015). Assessing Permafrost Degradation and Land Cover Changes (1986-2009) Using Remote Sensing Data over Umiujaq, Sub-arctic Québec. *Permafrost Periglac. Process.* 26 (2), 129–141. doi:10.1002/ppp.1839

Burn, C. R., and Nelson, F. E. (2006). Comment on "A Projection of Severe Near-Surface Permafrost Degradation during the 21st century" by David M. Lawrence and Andrew G. Slater. *Geophys. Res. Lett.* 33, L21503. doi:10.1029/2006GL027077

Chen, S. S., Zang, S. Y., and Sun, L. (2020). Characteristics of Permafrost Degradation in Northeast China and its Ecological Effects: A Review. *Sci. Cold Arid Reg.* 12 (1), 1–11. doi:10.3724/SP.J.1226.2020.00001

Cooper, H. H., Jr., Kohout, F. A., Henry, H. R., and Glover, R. E. (1964). *Sea Water in Coastal Aquifers*. Washington DC: US Government Printing Office.

Czekirda, J., Westermann, S., Etzelmüller, B., and Jóhannesson, T. (2019). Transient Modelling of Permafrost Distribution in Iceland. *Front. Earth Sci.* 7 (130), 1–23. doi:10.3389/feart.2019.00130

Delisle, G. (2007). Near-surface Permafrost Degradation: How Severe during the 21st century. *Geophys. Res. Lett.* 34, L09503. doi:10.1029/2007GL029323

Dobiński, W., and Leszkiewicz, J. (2010). Active Layer and Permafrost Occurrence in the Vicinity of the Polish Polar Station, Hornsund, Spitsbergen in the Light of Geophysical Research. *Probl. Klimat. Pol.* 20, 129–142. (in Polish with English summary).

Dobinski, W. (2011). Permafrost. *Earth-Science Rev.* 108, 158–169. doi:10.1016/j.earscirev.2011.06.007

Dobiński, W. (2020a). Permafrost Active Layer. *Earth-Science Rev.* 208, 103301. doi:10.1016/j.earscirev.2020.103301

Dobiński, W. (2020b). Northern Hemisphere permafrost extent: Drylands, glaciers and sea floor. Comment to the paper: Obu, J., et al. 2019. Northern Hemisphere permafrost map based on TTOP modeling for 2000-2016 at 1 km2 scale, Earth Science Reviews, 193, 299-316. *Earth-sci. Rev.* 203, 103037. doi:10.1016/j.earscirev.2019.103037

Duchkov, A. D., Balobaev, V. T., and Volodko, B. V. (1994). *Temperature, Permafrost and Radiogenic Heat Production in the Earth's Crust of Northern Asia*. RAS, Novosibirsk: Rus. with Eng. summary..

Elvebakk, H. (2010). *Results of Borehole Logging in Well LYB CO2, Dh4 of 2009, Longyearbyen, Svalbard. NGU Rep. 2010.018*. Trondheim: Geological Survey of Norway, 35.

Everdingen van, R. O. (2005). *Multi-language Glossary of Permafrost and Related Ground-Ice Terms. Definitions*. Calgary, Alberta: U. Calgary, IPA.

Frey, K. E., and McClelland, J. W. (2009). Impacts of Permafrost Degradation on Arctic River Biogeochemistry. *Hydrol. Process.* 23, 169–182. doi:10.1002/hyp.7196

Grosse, G., Romanovsky, V., Nelson, F. E., Brown, J., and Lewkowicz, A. G. (2010). Why Permafrost Is Thawing, Not Melting. *Eos Trans. Am. Geophys. Union* 91 (9), 87. doi:10.1029/2010eo090003

Guimond, J. A., Mohammed, A. A., Walvoord, M. A., Bense, V. F., and Kurylyk, B. L. (2021). Saltwater Intrusion Intensifies Coastal Permafrost Thaw. *Geophys. Res. Lett.* 48, e2021GL09477. doi:10.1029/2021GL094776

Guo, Y., Shan, W., Zhang, C., Hu, Z., Wang, S., and Gao, J. (2021). Monitoring of Permafrost Degradation along the Bei'an-Heihe Expressway in China. *Bull. Eng. Geol. Environ.* 80, 1–10. doi:10.1007/s10064-020-01919-3

Harris, S. A. (2001). Twenty Years of Data on Climate – Permafrost – Active Layer Variations at Lower Limit of alpine Permafrost, Marmot Basin, Jasper National Park, Canada. *Geogr. Ann. Ser. A-phys. Geogr.* 83 A (1–2), 1–13. doi:10.1111/j.0435-3676.2001.00140.x

Hauck, C., and Kneisel, C. (2008). *Applied Geophysics in Periglacial Environment*. Cambridge University Press.

Hjort, J., Karjalainen, O., Aalto, J., Westermann, S., Romanovsky, V. E., Nelson, F. E., et al. (2018). Degrading Permafrost Puts Arctic Infrastructure at Risk by Mid-century. *Nat. Commun.* 9, 5147. doi:10.1038/s41467-018-07557-4

Hu, J., Zhao, S., Nan, Z., Wu, X., Sun, X., and Cheng, G. (2020). An Effective Approach for Mapping Permafrost in a Large Area Using Subregion Maps and Satellite Data. *Permafrost and Periglac Process* 31 (4), 548–560. doi:10.1002/ppp.2068

Humlum, O., Instanes, A., and Sollid, J. L. (2003). Permafrost in Svalbard: a Review of Research History, Climatic Background and Engineering Challenges. *Polar Res.* 22, 191–215. doi:10.3402/polar.v22i2.6455

Hunter, J. A., Mac Aulay, H. A., Pullan, S. E., Gagné, R. M., Burns, R. A., and Good, R. L. (1988). "Thermal Evidence for an Active Layer on the Seabottom of the Canadian Beaufort Sea Shelf," in Proceeding of the Permafrost. Fifth International Conference, Trondheim, August 2–5 1988 (Tapir Pub.), Vol. 2 949–954.

Jin, H., Cheng, G., Li, X., Li, S. X., et al. (1999). Permafrost on the Qinghai-Tibet Plateau under a Warming Climate. *Chin. Sci Bull* 44 (S1), 152–158. doi:10.1007/bf02885940

Jin, H., Li, S., Cheng, G., Shaoling, W., and Li, X. (2000). Permafrost and Climatic Change in China. *Glob. Planet. Change* 26, 387–404. doi:10.1016/s0921-8181(00)00051-5

Jin, H., Zhao, L., Wang, S., and Jin, R. (2006). Thermal Regimes and Degradation Modes of Permafrost along the Qinghai-Tibet Highway. *Sci. China Ser. D* 49 (11), 1170–1183. doi:10.1007/s11430-006-2003-z

Jorgenson, M. T., and Grosse, G. (2016). Remote Sensing of Landscape Change in Permafrost Regions. *Permafrost Periglac. Process.* 27 (4), 324–338. doi:10.1002/ppp.1914

Jorgenson, M. T., Racine, C. H., Walters, J. C., and Osterkamp, T. E. (2001). Permafrost Degradation and Ecological Changes Associated with a Warming Climate in Central Alaska. *Clim. Chang.* 48, 551–579. doi:10.1023/A:1005667424292

Kalinicheva, S. V., and Shestakova, A. A. (2021). Using thermal Remote Sensing in the Classification of Mountain Permafrost Landscapes. *J. Mountain Sci.* 18 (3), 635–645. doi:10.1007/s11629-020-6475-7

Kasprzak, M., Łopuch, M., Głowacki, T., and Milczarek, W. (2020). Evolution of Near-Shore Outwash Fans and Permafrost Spreading under Their Surface: A Case Study from Svalbard. *Remote Sensing* 12 (3), 482. doi:10.3390/rs120304810.3390/rs12030482

Kasprzak, M. (2020). Seawater Intrusion on the Arctic Coast (Svalbard): The Concept of Onshore-Permafrost Wedge. *Geosciences* 10 (349), 349–411. doi:10.3390/geosciences10090349

Kasprzak, M., Strzelecki, M. C., Traczyk, A., Kondracka, M., Lim, M., and Migała, K. (2017). On the Potential for a Bottom Active Layer below Coastal Permafrost: the Impact of Seawater on Permafrost Degradation Imaged by Electrical Resistivity Tomography (Hornsund, SW Spitsbergen). *Geomorphology* 293, 347–359. doi:10.1016/j.geomorph.2016.06.013

Knoblauch, C., Beer, C., Liebner, S., Grigoriev, M. N., and Pfeiffer, E.-M. (2018). Methane Production as Key to the Greenhouse Gas Budget of Thawing Permafrost. *Nat. Clim Change* 8, 309–312. doi:10.1038/s41558-018-0095-z

Kurylyk, B. L., MacQuarrie, K. T. B., and McKenzie, J. M. (2014). Climate Change Impacts on Groundwater and Soil Temperatures in Cold and Temperate Regions: Implications, Mathematical Theory, and Emerging Simulation Tools. *Earth-Science Rev.* 138, 313–334. doi:10.1016/j.earscirev.2014.06.006

Lawrence, D. M., and Slater, A. G. (2005). A Projection of Severe Near-Surface Permafrost Degradation during the 21st century. *Geophys. Res. Lett.* 32, L24401. doi:10.1029/2005GL025080

Li, X., Jin, H., Sun, L., Wang, H., He, R., Huang, Y., et al. (2021). Climate Warming over 1961-2019 and Impacts on Permafrost Zonation in Northeast China. *J. For. Res.* doi:10.1007/s11676-021-01403-y

Liljedahl, A. K., Boike, J., Daanen, R. P., Fedorov, A. N., Frost, G. V., Grosse, G., et al. (2016). Pan-Arctic Ice-Wedge Degradation in Warming Permafrost and its Influence on Tundra Hydrology. *Nat. Geosci* 9, 312–318. doi:10.1038/ngeo2674

Lunardini, V. J. (1996). Climatic Warming and the Degradation of Warm Permafrost. *Permafrost Periglac. Process.* 7, 311–320. doi:10.1002/(sici)1099-1530(199610)7:4<311:aid-ppp234>3.0.co;2-h

Lunardini, V. J. (1995). *Permafrost Formation Time*. CRREL Report 95-8. US Army Corps of Engineers, Cold Regions Research and Engineering Laboratory.

Luo, D., Jin, H., Bense, V. F., Jin, X., and Li, X. (2020). Hydrothermal Processes of Near-Surface Warm Permafrost in Response to strong Precipitation Events in the Headwater Area of the Yellow River, Tibetan Plateau. *Geoderma* 376, 114531. doi:10.1016/j.geoderma.2020.114531

Luo, D., Jin, H., Jin, X., He, R., Li, X., Muskett, R. R., et al. (2018). Elevation-dependent thermal Regime and Dynamics of Frozen Ground in the Bayan Har Mountains, Northeastern Qinghai-Tibet Plateau, Southwest China. *Permafrost and Periglac Process* 29 (4), 257–270. doi:10.1002/ppp.1988

Meteorological Bulletin (2009–2020). *Spitsbergen – Hornusnd, Summary of the Years 2009–2020. Polish Polar Station*. Warszawa: Institute of Geophysics, Polish Academy of Sciences. Available from: https://hornsund.igf.edu.pl/Biuletyny/(Accessed September 1, 2021).

Nordli, Ø., Przybylak, R., Ogilvie, A. E. J., and Isaksen, K. (2014). Long-term Temperature Trends and Variability on Spitsbergen: the Extended Svalbard Airport Temperature Series, 1898-2012. *Polar Res.* 33 (1), 21349. doi:10.3402/polar.v33.21349

Oliva, M., Pereira, P., and Antoniades, D. (2018). The Environmental Consequences of Permafrost Degradation in a Changing Climate. *Sci. Total Environ.* 616-617, 435–437. doi:10.1016/j.scitotenv.2017.10.285

Overduin, P. P., Wetterich, S., Günther, F., Grigoriev, M. N., Grosse, G., Schirrmeister, L., et al. (2016). Coastal Dynamics and Submarine Permafrost in Shallow Water of the central Laptev Sea, East Siberia. *The Cryosphere* 10, 1449–1462. doi:10.5194/tc-10-1449-2016

Pedrazas, M. N., Cardenas, M. B., Demir, C., Watson, J. A., Connolly, C. T., and McClelland, J. W. (2020). Absence of Ice-Bonded Permafrost beneath an Arctic Lagoon Revealed by Electrical Geophysics. *Sci. Adv.* 6 (43), eabb5083. doi:10.1126/sciadv.abb5083

Ran, Y., Jorgenson, M. T., Li, X., Jin, H., Wu, T., Li, R., et al. (2021). Biophysical Permafrost Map Indicates Ecosystem Processes Dominate Permafrost Stability in the Northern Hemisphere. *Environ. Res. Lett.* 16 (9), 095010. doi:10.1088/1748-9326/ac20f3

Rekant, P., Cherkashev, G., Vanstein, B., and Krinitsky, P. (2005). Submarine Permafrost in the Nearshore Zone of the Southwestern Kara Sea. *Geo-mar. Lett.* 25 (2–3), 183–189. doi:10.1007/s00367-004-0199-5

Shi, Y., Niu, F., Lin, Z., and Luo, J. (2019). Freezing/thawing index Variations over the Circum-Arctic from 1901 to 2015 and the Permafrost Extent. *Sci. Total Environ.* 660, 1294–1305. doi:10.1016/j.scitotenv.2019.01.121

Sjöberg, Y., Marklund, P., Pettersson, R., and Lyon, S. W. (2015). Geophysical Mapping of Palsa Peatland Permafrost. *The Cryosphere* 9, 465–478. doi:10.5194/tc-9-465-2015

Smith, M. W. (1988). The Significance of Climatic Change for the Permafrost Environment *Permafrost. Fifth International Conference*, 3. Trondheim: Tapir Pub., 18–23.

Streletskiy, D., Anisimov, O., and Vasiliev, A. (2015). "Permafrost Degradation," in *Snow And Ice-Related Hazards, Risks, and Disasters*. Editors W. Haeberli and C. Whiteman (Elsevier), 303–344. doi:10.1016/B978-0-12-394849-6.00010-X

Strzelecki, M. C., Kasprzak, M., Lim, M., Swirad, Z. M., Jaskólski, M., Pawłowski, Ł., et al. (2017). Cryo-conditioned Rocky Coast Systems: A Case Study from Wilczekodden, Svalbard. *Sci. Total Environ.* 607-608, 443–453. doi:10.1016/j.scitotenv.2017.07.009

Sun, Z., Zhao, L., Hu, G., Qiao, Y., Du, E., Zou, D., et al. (2020). Modeling Permafrost Changes on the Qinghai-Tibetan Plateau from 1966 to 2100: A Case Study from Two Boreholes along the Qinghai-Tibet Engineering Corridor. *Permafrost and Periglac Process* 31, 156–171. doi:10.1002/ppp.2022

Szafraniec, J. E., and Dobiński, W. (2020). Deglaciation Rate of Selected Nunataks in Spitsbergen, Svalbard-Potential for Permafrost Expansion above the Glacial Environment. *Geosciences* 10 (5), 202. doi:10.3390/geosciences10050202

Szewczyk, J., and Nawrocki, J. (2011). Deep-seated Relict Permafrost in Northeastern Poland. *Boreas* 40, 385–388. doi:10.1111/j.1502-3885.2011.00218.x

Trofaier, A. M., Westermann, S., and Bartsch, A. (2017). Progress in Space-Borne Studies of Permafrost for Climate Science: Towards a Multi-ECV Approach. *Remote Sensing Environ.* 203, 55–70. doi:10.1016/j.rse.2017.05.021

Vasiliev, A. A., Drozdov, D. S., Gravis, A. G., Malkova, G. V., Nyland, K. E., and Streletskiy, D. A. (2020). Permafrost Degradation in the Western Russian Arctic. *Environ. Res. Lett.* 15, 045001. doi:10.1088/1748-9326/ab6f12

Wang, S., Jin, H., Li, S., and Lin, Z. (2000). Permafrost Degradation on the Qinghai-Tibet Plateau and its Environmental Impacts. *Permafr Periglac Process* 11 (1), 43–53. doi:10.1002/(sici)1099-1530(200001/03)11:1<43:aid-ppp332>3.0.co;2-h

Wawrzyniak, T., and Osuch, M. (2020). A 40-year High Arctic Climatological Dataset of the Polish Polar Station Hornsund (SW Spitsbergen, Svalbard). *Earth Syst. Sci. Data* 12, 805–815. doi:10.5194/essd-12-805-2020

Wawrzyniak, T., Osuch, M., Napiórkowski, J., and Westermann, S. (2016). Modelling of the thermal Regime of Permafrost during 1990-2014 in Hornsund, Svalbard. *Polish Pol. Res.* 37 (2), 219–242. doi:10.1515/popore-2016-0013

Werner, A. D., Ward, J. D., Morgan, L. K., Simmons, C. T., Robinson, N. I., and Teubner, M. D. (2012). Vulnerability Indicators of Sea Water Intrusion. *Groundwater* 50 (1), 48–58. doi:10.1111/j.1745-6584.2011.00817.x

Wu, J., Sheng, Y., Wu, Q., and Wen, Z. (2010). Processes and Modes of Permafrost Degradation on the Qinghai-Tibet Plateau. *Sci. China Ser. D-earth Sci.* 53 (1), 150–158. doi:10.1007/s11430-009-0198-5

Yang, M., Nelson, F. E., Shiklomanov, N. I., Guo, D., and Wan, G. (2010). Permafrost Degradation and its Environmental Effects on the Tibetan Plateau: A Review of Recent Research. *Earth-Science Rev.* 103 (1–2), 31–44. doi:10.1016/j.earscirev.2010.07.002

Yin, G., Luo, J., Niu, F., Lin, Z., and Liu, M. (2021). Thermal Regime and Variations in the Island Permafrost Near the Northern Permafrost Boundary in Xidatan,

Qinghai-Tibet Plateau. *Front. Earth Sci.* 9, 708630. doi:10.3389/feart.2021.708630

You, Y., Yu, Q., Pan, X., Wang, X., and Guo, L. (2013). Application of Electrical Resistivity Tomography in Investigating Depth of Permafrost Base and Permafrost Structure in Tibetan Plateau. *Cold Regions Sci. Tech.* 87, 19–26. doi:10.1016/j.coldregions.2012.11.004

Zhang, Y., Chen, W., and Riseborough, D. W. (2006). Temporal and Spatial Changes of Permafrost in Canada since the End of the Little Ice Age. *J. Geophys. Res.* 111, D22103. doi:10.1029/2006JD007284

Conflict of Interest: The authors declare that the research was conducted in the absence of any commercial or financial relationships that could be construed as a potential conflict of interest.

Publisher's Note: All claims expressed in this article are solely those of the authors and do not necessarily represent those of their affiliated organizations, or those of the publisher, the editors and the reviewers. Any product that may be evaluated in this article, or claim that may be made by its manufacturer, is not guaranteed or endorsed by the publisher.

frontiers in Earth Science

ORIGINAL RESEARCH
published: 28 February 2022
doi: 10.3389/feart.2021.797928

Phenological Changes in Alpine Grasslands and Their Influencing Factors in Seasonally Frozen Ground Regions Across the Three Parallel Rivers Region, Qinghai-Tibet Plateau

Chun-Ya Wang[1,2,3], *Jin-Niu Wang*[1,4]*, *Xu-Feng Wang*[3], *Dong-Liang Luo*[5], *Yan-Qiang Wei*[6], *Xia Cui*[7], *Ning Wu*[1] *and Priyamvada Bagaria*[1]

[1]*Chengdu Institute of Biology, Chinese Academy of Sciences, Chengdu, China,* [2]*Earth Sciences College, Chengdu University of Technology, Chengdu, China,* [3]*Key Laboratory of Remote Sensing of Gansu Province, Heihe Remote Sensing Experimental Research Station, Northwest Institute of Eco-Environment and Resources, Chinese Academy of Sciences, Lanzhou, China,* [4]*Mangkang Ecological Monitoring Station, Tibet Ecological Security Barrier Ecological Monitoring Network, Qamdo, China,* [5]*State Key Laboratory of Frozen Soil Engineering, Northwest Institute of Eco-Environment and Resources, Chinese Academy of Sciences, Lanzhou, China,* [6]*Northwest Institute of Eco-Environment and Resources, Chinese Academy Sciences, Lanzhou, China,* [7]*School of Resources and Environmental Sciences, Lanzhou University, Lanzhou, China*

OPEN ACCESS

Edited by:
Zhenhua Zhang,
Northwest Institute of Plateau Biology (CAS), China

Reviewed by:
Jianshuang Wu,
Institute of Environment and Sustainable Development in Agriculture (CAAS), China
Nan Jiang,
Institute of Tibetan Plateau Research (CAS), China

***Correspondence:**
Jin-Niu Wang
wangjn@cib.ac.cn

Specialty section:
This article was submitted to Biogeoscience, a section of the journal Frontiers in Earth Science

Received: *19 October 2021*
Accepted: *24 December 2021*
Published: *28 February 2022*

Citation:
Wang C-Y, Wang J-N, Wang X-F, Luo D-L, Wei Y-Q, Cui X, Wu N and Bagaria P (2022) Phenological Changes in Alpine Grasslands and Their Influencing Factors in Seasonally Frozen Ground Regions Across the Three Parallel Rivers Region, Qinghai-Tibet Plateau. Front. Earth Sci. 9:797928. doi: 10.3389/feart.2021.797928

Alpine ecosystems are sensitive and vulnerable to climate change. In this study, we extracted three phonological parameters, viz. the start of the growing season (SOS), the end of the growing season (EOS), and the length of the growing season (LOS) from the moderate resolution imaging spectroradiometer (MODIS) normalized difference vegetation index (NDVI) dataset during 2000–2019 for alpine grasslands across the three parallel rivers region (TPRR), and also examined the spatiotemporal heterogeneity of the three phenological parameters in seasonally frozen ground regions (hereafter referred to as SFGR) in response to climate change. The results showed that the multiyear mean SOS gradually delayed from 100 to 160 days along higher elevation, EOS advanced as a whole (from 320 to 280 days), and LOS shortened (from 210 to 130 days). The multiyear mean spatial distribution of all the three parameters showed significant north-to-south differences in the TPRR. In general, the variation trends in all the phenological parameters were not significant ($p > 0.05$) in the past 20 years, where SOS was advanced by 0.16 days year^{-1}, EOS delayed by 0.08 days year^{-1}, and consequently LOS extended at a rate of 0.07 days year^{-1}, likely due to the warming and drying climate during the study period. In addition, annual mean temperature (AMT) was negatively correlated with SOS (50.26%) and positively correlated with EOS and LOS (72.25 and 60%, respectively). As for the annual mean total precipitation (AMP), it was positively correlated with SOS and EOS (50.77 and 52.97%, respectively) and negatively correlated with LOS (52.07%). Furthermore, a higher freezing index led to a delayed SOS and an advanced EOS and a shortened LOS at the regional scale. Similar to AMT, a higher thawing index advanced the SOS, delayed the EOS, and extended the LOS. Our results confirmed the importance of climate and permafrost status on vegetation phenological processes and also contributed toward understanding the response of cold region ecosystems to global climate change.

Keywords: vegetation phenology, river basin, spatio-temporal changes, climate factors, freezing/thawing index, TIMESAT

INTRODUCTION

Plant phenology has attracted strong scientific attention in recent years for its relationship with different driving factors of climate change (Rauste et al., 2007; Shen et al., 2015b; Zhao et al., 2016; Ganjurjav et al., 2020). Vegetation phenology plays an essential role in the terrestrial ecosystem, as it is indicative of seasonal activities and physiological processes. Traditionally, vegetation phenology is monitored mainly through ground-based visual observation of the seasonal and inter-annual changes in plant phenology (e.g., plant germination, leaf expansion, flowering, fruiting, withering, falling leaves, etc.) (Richardson et al., 2013; Zhai et al., 2015). However, traditional visual observation is time-consuming and is limited by personal bias. It is being gradually replaced by advanced technological methods of remote sensing phenological data acquisition. For example, a near-ground phenological camera has been widely used in recent studies (Klosterman et al., 2014; Weil et al., 2017). Meanwhile, the emergence of remote sensing technology has greatly broadened the scope of vegetation phenological observations due to its virtues of multi-temporal, long time series, and large-scale regional as well as global datasets (Hmimina et al., 2013; Zhao et al., 2015; Piao et al., 2019). Vegetation indices, such as the NDVI, the enhanced vegetation index (EVI), and the leaf area index (LAI), have been used to infer the timing of vegetation phenology (Delbart et al., 2005; Shen et al., 2014a; Wen et al., 2021).

In the past few decades, the phenomena of advanced spring phenology, delayed autumn phenology, and longer growing seasons have been observed in varying degrees due to assessing the impact of climate change. Studies have reported significant regional-specific differences in the phenological timeline of the observed vegetation (Wang et al., 2013a; Zhang et al., 2013; Zhao et al., 2015; Piao et al., 2019). The available vegetation phenological data, which are mainly from the 1980s and 1990s at middle and high latitudes of the northern hemisphere, show weaker trends of changing phenological cycle, in comparison with the studies in the early 2000s (Zeng et al., 2011; Zhao et al., 2015; Cong and Shen, 2016). Most studies present an obvious trend toward early spring and delayed autumn (Richardson et al., 2013; Zhao et al., 2015). A more detailed description also referred that the changes in phenological trends in Eurasia are more significant than in North America, and the greatest change has occurred in Europe (Zhou et al., 2001).

In China, studies of vegetation phenology are mainly focused on the north temperate zone and high-altitude areas (Jiao et al., 2020; Fu et al., 2021), where the "amplifier" of global warming signals demonstrates a greater rate and amplitude of rising temperature (Wang et al., 2014; Ganjurjav et al., 2020). The Qinghai-Tibet Plateau (QTP), as the "third pole" of the world, has been considered as one of the most sensitive regions to global climate change. In recent years, different views have been declared on vegetation phenological trends in the QTP. Spring phenology of vegetation has advanced in most areas of the QTP, whereas delayed in a few other areas (e.g., the southwest part of the Plateau) (Chen et al., 2015; Shen et al., 2015b; Shen et al., 2016). However, the trend of vegetation phenology in the QTP has been debated in recent studies, likely due to their differences in data sources, methodologies, and study periods (Piao et al., 2011; Shen et al., 2013). The alpine grassland in the QTP shows regional heterogeneity and plays a crucial role in ecosystem functioning and services and is highly sensitive to climatic changes (Ganjurjav et al., 2020; Fu et al., 2021). It has been concluded that temperature and precipitation play important roles in phenological changes in the QTP (Zhou et al., 2001; Yu et al., 2010; Wang et al., 2015). Temperature is the main climatic factor regulating vegetation phenology across the QTP, whereas in a few areas, precipitation and sunshine duration (alternatively, radiation) become more important than temperature (Shen et al., 2011; Che et al., 2014; Shen et al., 2014b). Vegetation phenology in humid areas is more sensitive to the preseason temperature than to the preseason precipitation, and the relatively arid western regions of QTP are divergent or on the contrary. In conclusion, vegetation spring phenology in all these areas has been implicated interactively to covariance control of altitude gradient (Shen et al., 2015a; Liu et al., 2020b).

In the alpine grassland ecosystem, variation in frozen soil can drive vegetation phenology, including abiotic physical factors such as climate and photoperiod (Gao et al., 2020a; Wen et al., 2021). After the Arctic and the Antarctic, the QTP has the largest permafrost and seasonally frozen ground region in the world (Cheng and Jin, 2013; Zou et al., 2017; Jiang et al., 2018). Global warming has already induced significant changes in permafrost and seasonally frozen ground regions throughout most of the Arctic and alpine regions (e.g., increasing active layer thickness, decreasing freezing depth, degradation of permafrost, etc.) (Sazonova and Romanovsky, 2003; Zhao et al., 2004; Jones et al., 2016). Frozen soil, as the sentinel, integrator, and regulator of climate change, may affect ecological and hydrological processes *via* variations in water and heat exchange between the ground and atmosphere in alpine regions (Jiang et al., 2018). These variations can regulate the growth and phenology of vegetation significantly (Hayashi, 2014; Liu et al., 2021) and also indicate that the periodic physiological activities of plants in response to climate change influence the surface-energy flux and carbon budget over a large area (Morisette et al., 2009; Qiao et al., 2021). Therefore, it is essential to monitor the spatiotemporal patterns of vegetation phenology in the SFGR and explore its responses to climatic factors, frozen soil changes, and other such parameters to elucidate the role of vegetation phenology in alpine ecosystems.

The three parallel rivers region (TPRR) is in the transitional zone from the QTP to the Yunnan-Guizhou Plateau, where the typical longitudinal valleys of the Hengduan Mountains are located. The TPRR has attracted much attention as a famous scenic spot and world natural heritage site, global biodiversity, and cultural hotspot at home and abroad (Wang et al., 2013a; Lin et al., 2018). The TPRR is experiencing unprecedented eco-environmental challenges with urbanization and road construction as well as a series of tourism developments (Li et al., 2012). Only a few current studies have been reported on vegetation growth conditions and phenological changes, but without integration of the physical and spatial dynamics of the alpine grasslands in the SFGR (Cheng et al., 2018; Gao et al.,

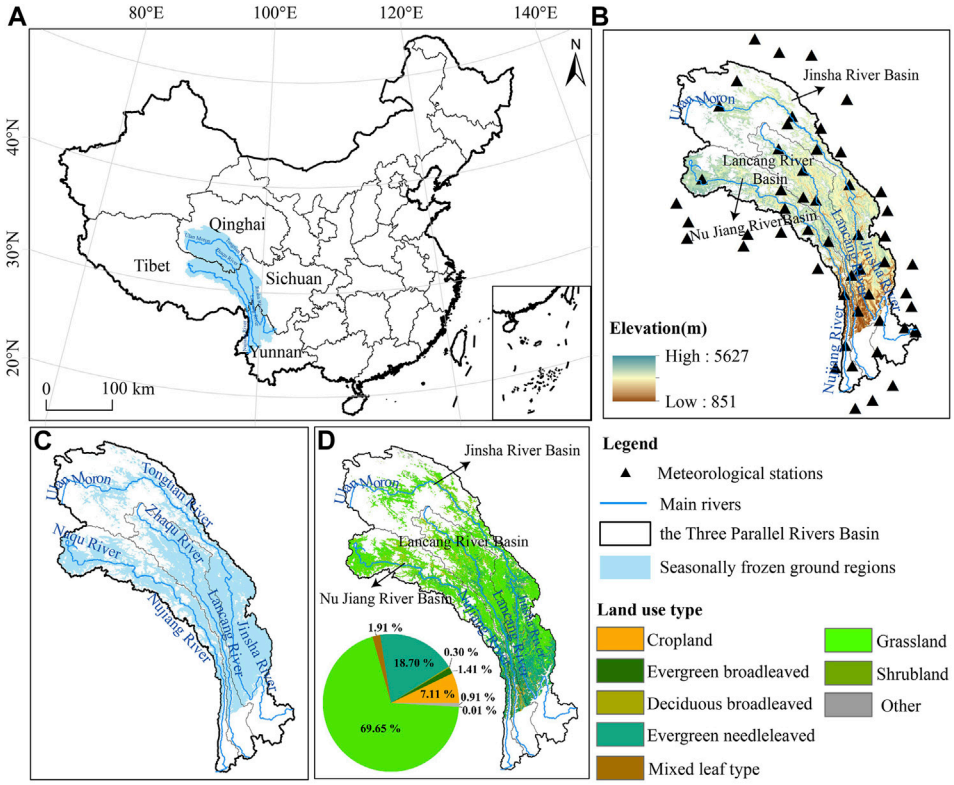

FIGURE 1 | Location and vegetation type of the study area. **(A)** The location of TPRR in China; **(B)** elevation gradients and meteorological sites across the TPRR; **(C)** seasonally frozen ground regions in the TPRR; and **(D)** land-use types of TPRR.

2020b; Yao et al., 2020). The underlying mechanism linkages between seasonally frozen ground and vegetation phenology largely remain understudied in this region.

Thus, we used MODIS NDVI data from 2000 to 2019 for the SFGR, extracted three key phenological parameters (SOS, EOS, and LOS), and established the datasets. We further analyzed the spatiotemporal pattern of regional vegetation phenology with the relevant driving factors and explored the following objectives: 1) investigate the pixel-scale spatiotemporal pattern of the alpine grassland phenology in the SFGR; 2) detect if there are significant trends of vegetation phenological parameters in the alpine grasslands using the time series data; 3) assess the characteristics and linkages of climatic factors and permafrost with vegetation phenology. Our results are expected to provide a scientific reference in the TPRR for the restoration and conservation of regional vegetation ecosystems.

MATERIALS AND METHODS

Study Area

The TPRR (24°00′~36°00′N, 90°20′~102°20′E) is located in the southern part of the QTP in the longitudinal mountains and valleys of the Hengduan Mountains, spanning Qinghai, Tibet, Sichuan, and Yunnan provinces of China, with a total area of approximately 500,670 km^2 (Gao et al., 2020a; Yao et al., 2020) (**Figure 1**). Its upper sections consist of three major rivers of Asia: Nujiang River (the upper reach of the Salween River down in Burma), Lancang River (the upper reach of the Mekong River extending to Vietnam), and Jinsha River (the major upper reach of the Yangtze River) (Wang et al., 2013b; Liang et al., 2014; Cheng et al., 2018). They flow almost parallelly from the Qamdo Prefecture, southeastern Tibet, to northwestern Yunnan and then gradually take separate routes. Hence, the region is named the "Three Parallel Rivers Region" (Kingdon Ward, 1923; Xiao and Xiang, 2017).

The TPRR is characterized by high mountains and longitudinal valleys, with an elevation ranging from 562 to 6,717 m a.s.l., with generally higher elevations in the northwestern parts and lower elevations in the southeastern parts. Due to its unique geographical location and long-term historical evolution, it is well recognized as global biodiversity and cultural hotspot (Lin et al., 2018). The region is influenced by the southwest monsoon and southeast monsoon and is characterized by warm and humid summers and cold and dry winters. Our study area boundaries were extracted from DEM data, combined with watershed data from the Resource and Environment Science and Data Center of the Chinese Academy of Sciences (https://www.resdc.cn) and relevant references (Li and Hao, 2003; Wu et al., 2011).

Data Sources and Preprocessing

Remote Sensing Data

The MOD13Q1 dataset was used to obtain the NDVI during 2000–2019 and conduct a phenological analysis of the TPRR,

which was provided by the National Aeronautics and Space Administration (NASA, available from https://ladsweb.modaps.eosdis.nasa.gov/search/order/) with a spatial resolution of 250 m, corresponding to a maximum synthetic reflectance for 16 days. The dataset has been corrected through a variety of methods, including calibration and removal of atmospheric disturbances and other effects (Khare et al., 2019; Wen et al., 2021). Firstly, we used NASA's MODIS Reprojection Tool (MRT) for data format conversion, image mosaicking, reprojection, mask extraction, and other operations to extract regional NDVI data. To facilitate spatial analysis, we resampled the NDVI data and obtained a 300-m NDVI time-series dataset. Then, the Savitzky–Golay (S-G) filtering method was used to smoothen and reduce noise in the original NDVI data.

Meteorological Data

Daily air temperature, ground surface temperature, and precipitation during 2000–2019 in this study were derived from the China Meteorological Data Service Centre (http://data.cma.cn/) for 52 meteorological stations in the TPRR and nearby. The meteorological data interpolated by ANUSPLINE can better reflect the spatial heterogeneity of each variable (Tan et al., 2016; Liu et al., 2020b), so we used ANUSPLINE for spatial interpolation and obtained meteorological gridded data with a spatial resolution of 300 m, matching the resolution of NDVI data. Finally, we obtained two major datasets: 1) the annual long time-series dataset of annual mean temperature and precipitation; 2) the regional interannual freezing/thawing index dataset, from which we calculated air freezing index (AFI), air thawing index (ATI), ground surface freezing index (GFI), and ground surface thawing index(GTI). The specific calculation process is mentioned later in *Methods*.

Additional Data

ESA CCI-LC land cover types during 2000–2015 were provided by the European Space Agency (http://maps.elie.ucl.ac.be/CCI/viewer/) with a spatial resolution of 300 m, which has been widely used in land use/land cover dynamic monitoring around the world because of its high overall accuracy (Yang et al., 2017; Gang et al., 2018). **Figure 1** shows that the vegetation type in this area was mainly alpine grassland, accounting for nearly 70% of the total area. To minimize the impact of land-use changes on the distribution of vegetation types, we referred to the research methods by Liu et al. (2020a). In this study, areas with no change in vegetation types during 2000–2015 were extracted to represent each vegetation type cover status of this region in recent years. Besides, DEM data at a spatial resolution of 90 × 90 m here were collected from the Earth Science Data Cloud (http://www.gscloud.cn).

In this paper, we resampled all remote sensing data at a 300-m resolution using the nearest neighbor method to facilitate correlation analysis based on pixel scale.

Methods

Extraction of Phenological Parameters

The common methods for phenological parameters extraction include threshold, moving average, maximum slope method, etc. We referred to the research method by Wen et al. (2021) and used the dynamic threshold method to extract three key phenological parameters of alpine grassland in the TIMESAT 3.2 (Jonsson and Eklundh, 2004).

Firstly, we used the S-G filter function to smoothen the NDVI series, which has been considered to be the most effective and widely used method (Zhao et al., 2015; Stanimirova et al., 2019; Liu et al., 2020b). Here, we adopted the adaptation strength of 2.0, the seasonal parameter of 0.5, and the window size of 4 for the S-G filter. Next, we defined NDVI thresholds for identifying the dates of major phenological events by referring to the relevant literature on the phenological characteristics of alpine grassland in the QTP (Ding et al., 2013; Guan et al., 2019; Huang et al., 2019). Given the low vegetation cover in this region, our study sets the relative thresholds of the growing season, which starts and ends at approximately 20 and 50% of the annual amplitude of NDVI, respectively (Chen et al., 2012; Zhang et al., 2013; Ma et al., 2016). Finally, we used EOS minus SOS to obtain LOS and extracted vegetation phenological parameters for alpine grassland in the SFGR for each year and pixel over the last 20 years. In addition, this study also used Julian days to convert the phenological period, i.e., the phenological period was expressed as the actual number of days from January 1 [also expressed as the day of the year (DOY)].

Calculating the Freezing/Thawing Variables

The annual freezing/thawing index was calculated with the daily observed temperature data, including AFI, ATI, GFI, and GTI. The freezing/thawing index is the cumulative value of temperature less than (greater than) 0°C in the specified period, respectively. To ensure the temperature data of the same freezing (thawing) period used in the calculation of the freezing/thawing index, the freezing index was specified to be calculated from July 1 of each year to June 30 of the following year, and the thawing index was calculated from January 1 to December 31 of each year. The specific principles and calculation methods are mentioned in the references (Luo et al., 2014; Shi et al., 2019).

Trend and Correlation Analysis

Sen slope is a nonparametric estimation method, which can be used to calculate the variability of data, and the results of the Mann–Kendall (M-K) test are largely uninterrupted by outliers (Wen et al., 2021). A combination of them has been widely used in vegetation trend analysis and long-term series data analysis in recent years (Gocic and Trajkovic, 2013). In this paper, we classified regional sen slope value into the following main categories: if $sen > 0$, it indicates delayed or extended; conversely, $sen < 0$ indicates advanced or shortened. Meanwhile, M-K test with a 95% confidence level was conducted by Che et al. (2014) and Zhu et al. (2019). The trends could be estimated by combining Sen's slope and the M-K test in light of the phenological parameters. Given confidence level $\alpha = 0.05$, whether the trend changed significantly depended on the $|Z|$ score, which the following categories are available: 1) significantly advanced or shortened ($sen < 0$, $|Z| > 1.96$); 2) insignificantly advanced or shortened (*sen*

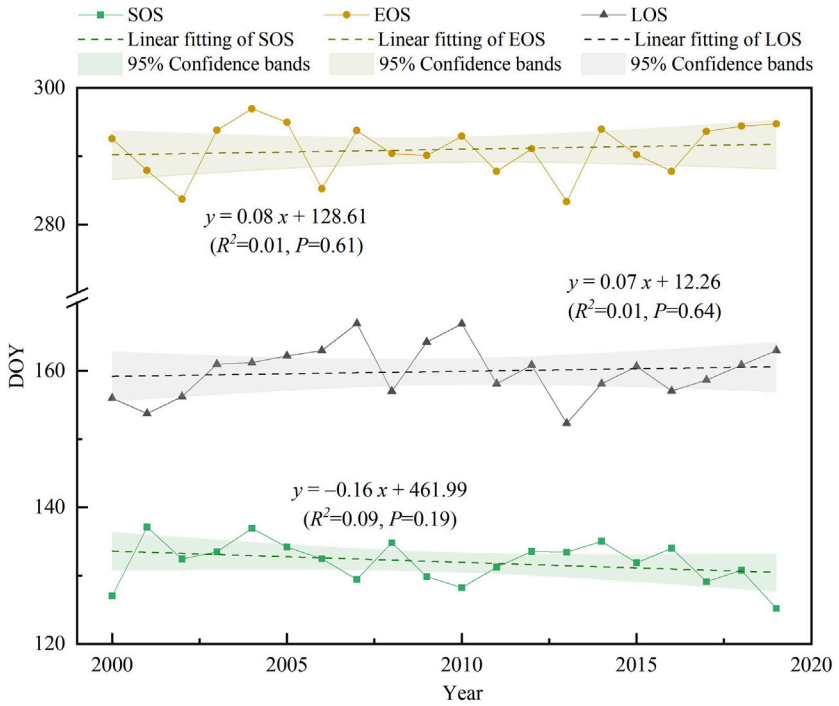

FIGURE 2 | Inter-annual changes of vegetation phenology from 2000 to 2019.

< 0, $|Z| \leq 1.96$); 3) insignificantly delayed or extended ($sen > 0$, $|Z| \leq 1.96$); 4) significantly delayed or extended ($sen > 0$, $|Z| > 1.96$).

We calculated the pixel-by-pixel correlation coefficients (r) and p-values (P) of phenology with climate factors and freezing/thawing indices using Matlab 2015b and analyzed the relationships between them. The calculation formula is as follows (Che et al., 2014):

$$r_{xy} = \frac{\sum_{i=1}^{n}(x_i - \bar{x})(y_i - \bar{y})}{\sqrt{\sum_{i=1}^{n}(x_i - \bar{x})^2}\sqrt{\sum_{i=1}^{n}(y_i - \bar{y})^2}} \quad (1)$$

where x is the independent variable (climate factor, freezing/thawing index), and y is the phenological parameter (SOS, EOS, and LOS). We tested the significance of the correlation coefficients with P-values. The correlation coefficients in this study were mainly divided into three levels (Che et al., 2014): strong correlation ($0.8 < r \leqslant 1$), medium correlation ($0.3 < r \leqslant 0.8$), and weak correlation ($0 < r \leqslant 0.3$). Here $\alpha = 0.05$.

RESULTS

Spatial and Temporal Patterns of Vegetation Phenology

The temporal trends results of the vegetation phenology in this region showed that there was an advanced SOS trend at a rate of 1.64 days per decade ($p > 0.05$) and a delayed EOS trend at a rate of 0.81 days per decade. No significant changes were found for LOS, which extended by an average of 0.74 days per decade (**Figure 2**). Our results also showed a significant spatial difference in phenological trends (**Figure 3**).

The multiyear mean SOS of alpine grasslands in this region ranged from 90 to 170 days (approximately 80% of the overall pixels), i.e., from the end of March to the end of May (**Figure 3A**). However, the variation in SOS is not obvious across space. From northwest to southeast, the overall trend of the multiyear mean SOS showed advancement. However, there was delayed SOS in the TPRR at the junction of Yunnan and Tibet, where the multiyear mean SOS was around 130–150 days.

Compared with SOS, EOS showed an opposite trend in spatial distribution, i.e., EOS was gradually delayed from the northwest to the southeast (**Figure 3B**), and the spatial variation of EOS was much more pronounced than that of SOS. Specifically, the multiyear average EOS mainly appeared in 260–340 days per year, among which the EOS in most of the northern regions was generally concentrated in the range of 270–300 days (82.05%), i.e., from September to October. On the other hand, the overall EOS in the south was later, basically after 300 days, i.e., later than October, over less than 20% of the area.

Most of the LOS varied from 130 to 210 days, and the multiyear mean LOS gradually extended from the northwest to the southeast, showing a vertical divergence pattern more consistent with SOS (**Figure 3C**). The LOS in most areas is between 130 and 170 days (more than 50% of the area), which is mainly distributed in the northwestern high mountains and deep valleys of the TPRR, such as the river source areas of each basin and the middle reaches of the basins.

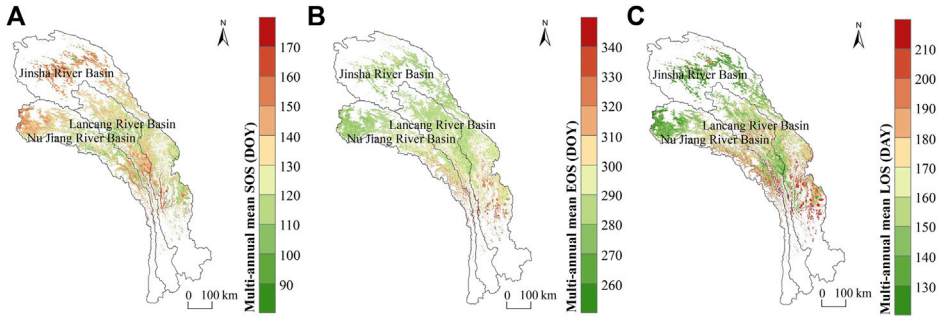

FIGURE 3 | Spatial distribution of multi-annual mean vegetation phenology. **(A)** SOS; **(B)** EOS; and **(C)** LOS.

Trends of Vegetation Phenology

We calculated the linear trends of SOS, EOS, and LOS at a 95% confidence level (**Figure 4**). The results showed an advanced trend in the SOS of alpine grasslands in most areas. There was an advancing trend in the northwestern part of the study area, but the degree of advancement was modest (33.92%), of which less than 2% was significantly advanced, mainly in the upper reaches of the Lancang River basin. A few areas in the southern part of the region showed a trend of insignificantly delayed SOS, especially in the TPRR, whereas significantly delayed areas only accounted for 2.89% (**Figures 4A,B**; **Table 1**).

EOS, on the other hand, mainly showed a trend of extension. The area of significantly delayed EOS accounted for 8.24% and was mainly distributed in the central part of the basin, such as in the middle reaches of the two major areas, the Lancang River basin and Jinsha River basin. The areas with insignificantly delayed EOS accounted for most parts of the study area (47.47%) and were almost distributed in the source area and the central part of the basin. In addition, the areas with EOS advancement were scattered in the midstream of the basin, whereas the regions with significant advancement accounted for less than 1% (**Figures 4C,D**; **Table 1**).

In the past 20 years, the LOS showed a trend of lengthening, with 50.44 and 29.41% of the areas showing insignificantly extended and shortened LOS, respectively (**Figures 4E,F**; **Table 1**). A relatively similar distribution concentrated in the source area of the basin and the central part of the study area was observed. For the pixel points with significant changes, the extended areas were mainly concentrated in a few areas in the upper reaches of the Lancang River basin and the middle reaches of the Jinsha River basin.

Relationships Between Vegetation Phenology and Climate Factors

From the spatial distribution of the multiyear mean values of the climate factors, the annual precipitation in the region gradually decreased from the south to the north during 2000–2019. The distribution of temperature had typical mountainous characteristics due to the special geographical location, i.e., the temperature was higher in the river valley. In addition, as the AMT and AMP gradually decreased with the increasing altitude, the trend was more significant ($p < 0.05$), reflecting strong dependence of climate factors on altitude (**Supplementary Figures S1, S2**).

The correlation coefficient between SOS and temperature ranged from approximately −0.78 to 0.83 (**Figure 5**), where SOS was negatively correlated with AMT in approximately 50.26% of areas. Out of these areas, 6.05% of the areas showed a significant correlation ($p < 0.05$), mainly at the junction of the Jinsha river basins and Lancang River basins, as well as the TPRR at the junction of Yunnan and Tibet. Also, the correlation coefficient between EOS and temperature ranged from −0.78 to 0.80, and EOS was mainly positively correlated with AMT (72.25%), and only 3.05% passed the significance test at 95% level, which was mainly sporadically distributed in the three major basins and more concentrated in the middle reaches of the basin. However, the correlation coefficients between LOS and temperature varied from −0.81 to 0.76, and there was a positive correlation between LOS with AMT for more than 60% of areas, and 3.63% of the areas were significantly correlated in the upper and middle reaches of Nujiang River and the source areas of the Lancang and Jinsha Rivers (**Figure 5**, **Table 2**).

The positive correlation between SOS and precipitation was more common, which ranged from −0.86 to 0.82. Only 3.86% of the areas were significantly correlated (mostly negative), mainly in the source areas of the Nujiang River basin and Jinsha River basin, and also in the midstream areas of the basins but were more scattered. EOS, with correlation coefficients between −0.82 and 0.86, was positively correlated with precipitation (52.97% of the area), and 7.47% of the areas were significantly correlated (mainly positive). These areas were mainly located in the source areas of the Nujiang River basin and the junction of the upper reaches of the Lancang River and Jinsha River basins. Furthermore, there was a negative correlation between LOS and precipitation, with 5.89% of the regions significantly correlated. It was scattered at the source of the Nujiang River basin, the upper reaches of the Lancang River basin and the Jinsha River basin, and the narrowest part of the TPRR (**Figure 6**).

Effects of Freezing/Thawing Index on Vegetation Phenology

The spatial distribution of the multiyear mean freezing/thawing index showed that FI increased from the southeast to the northwest with increasing elevation. The range of AFI was higher than that of the GFI, whereas the thawing index showed a diametrically opposite trend, and the FI/TI varied

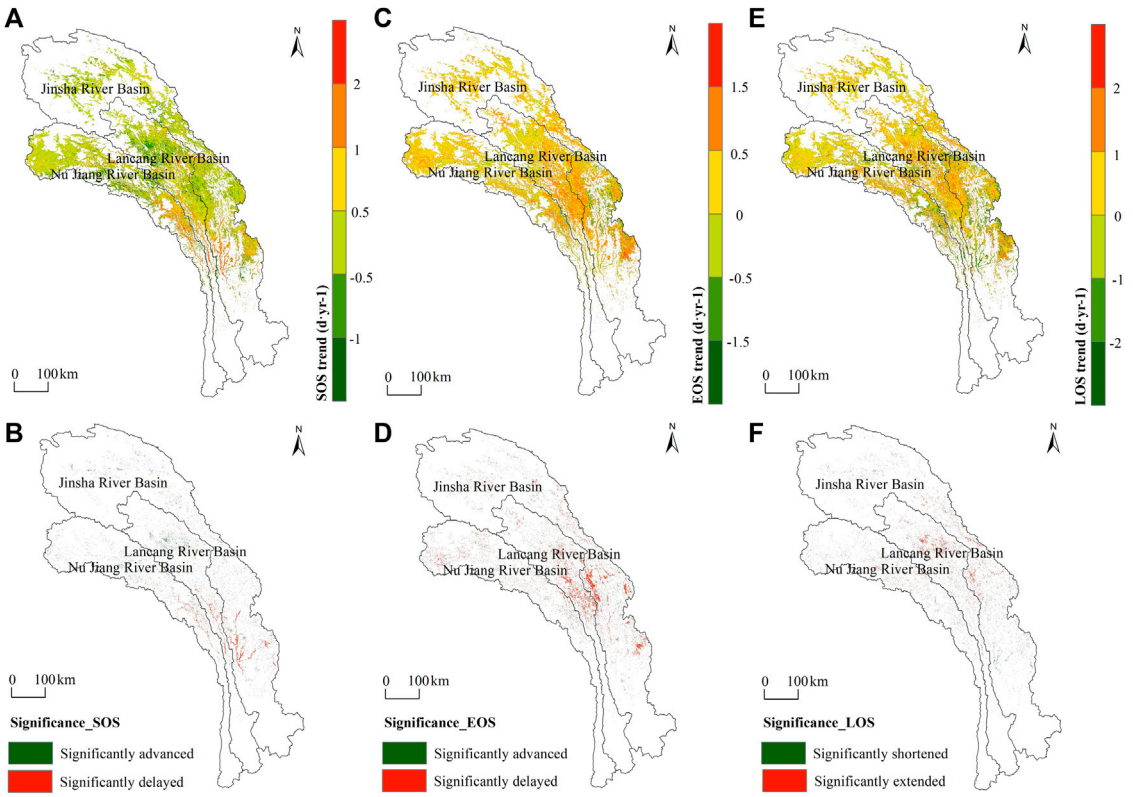

FIGURE 4 | Inter-annual variation [SOS **(A)**, EOS **(B)**, and LOS **(C)**] and significant changes **(D–F)** of vegetation phenology during 2000–2019 in study area. Significant trend corresponds to a $p < 0.05$.

TABLE 1 | Overall trend and proportion of different phenological trends from 2000 to 2019 in SFGR.

	Significantly advanced/ Shortened (%)	Insignificantly advanced/ Shortened (%)	No changes (%)	Insignificantly delayed/ Lengthened (%)	Significantly delayed/ Lengthened (%)
SOS	1.55	33.92	25.45	36.19	2.89
EOS	0.72	14.68	28.89	47.47	8.24
LOS	1.03	29.41	15.35	50.44	3.77

greatly with elevation (**Supplementary Figure S3**). Besides, freezing/thawing indices variation trends indicated that FI showed a decreasing trend with significant north–south differences, whereas both GTI and ATI showed an increasing trend year by year, where ATI had a greater dependence on elevation (**Supplementary Figure S4**).

SOS showed a negative correlation with the freezing/thawing index (**Figure 7**; **Table 3**). Specifically, AFI was negatively correlated in more than 80% of the areas, which were mainly distributed in the two basin areas of the Lancang River and Jinsha River, whereas there is a positive correlation in the source area of the Nujiang River. However, SOS and GFI were somewhat negatively correlated (51.07% of the area) in the river source areas of the Jinsha River basin, the junction of the upper reaches of the Lancang River and Jinsha River basins, and a few areas in the valley zones of the three rivers. The positive correlation was more pronounced in the river source areas of the Nujiang and Lancang Rivers. In addition, the negative correlations between SOS and the two major thawing indices, ATI and GTI (51.21 and 59.09% of the area, respectively), were mainly found in the upstream areas of the three major basins, whereas positive correlations existed in the TPRR and the source area of the Lancang River.

Furthermore, more than 60% of the areas also demonstrated a negative correlation between EOS and the freezing index, in which the negative correlation between EOS and AFI (61.02%) was well reflected in the source areas of the Nujiang and Jinsha rivers and the middle reaches of the Lancang and Jinsha rivers. In 73.35% of the areas, such as the source areas of the basins and the typical regions of the TPRR, i.e., the middle reaches of the three major basins, a negative correlation between EOS and GFI was observed. Relative to the thawing index, EOS had a good positive correlation with ATI and GTI (the area proportion was 73.96 and

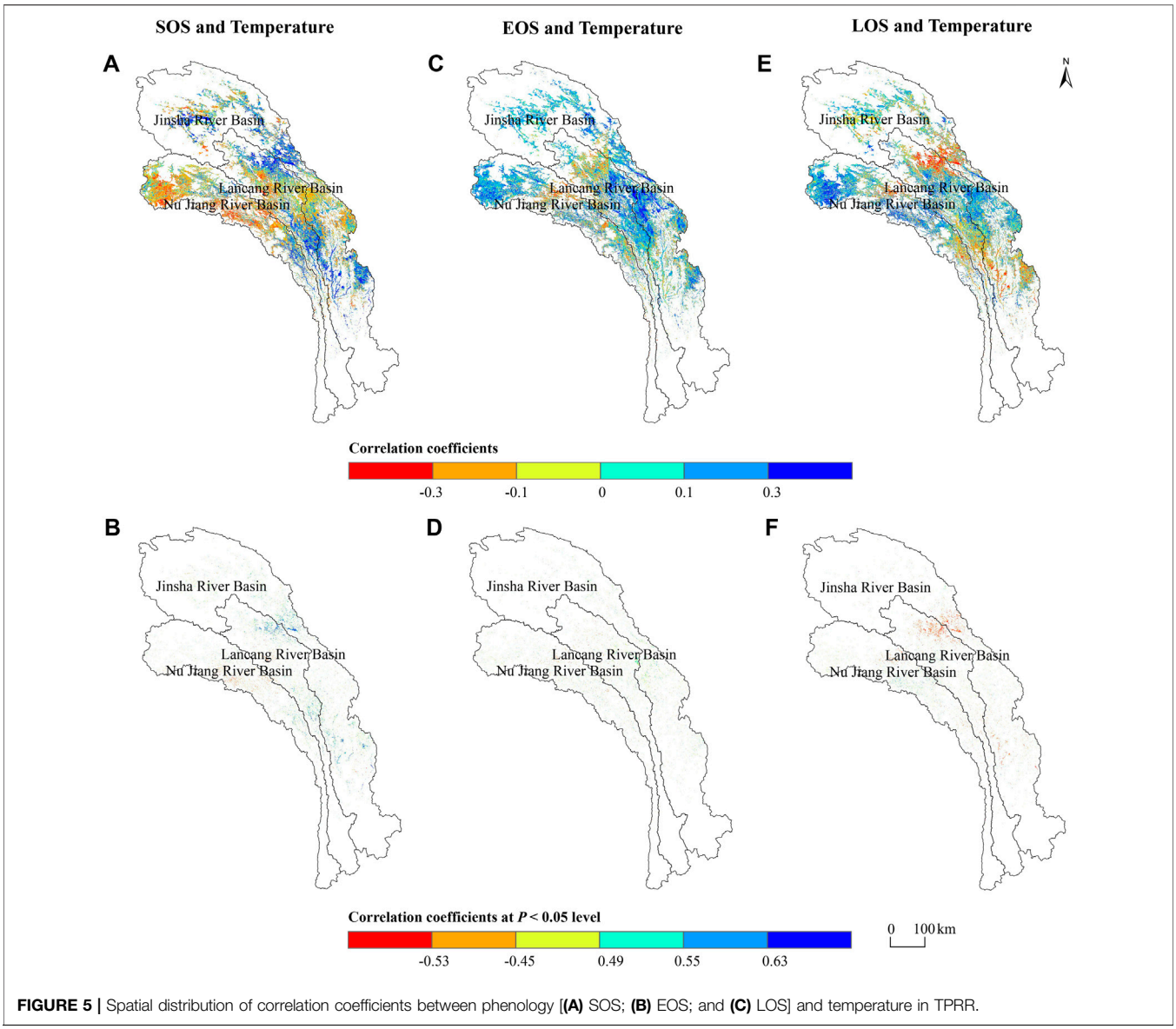

FIGURE 5 | Spatial distribution of correlation coefficients between phenology [**(A)** SOS; **(B)** EOS; and **(C)** LOS] and temperature in TPRR.

TABLE 2 | Area statistics of correlation analysis between phenology and climate factors from 2000 to 2019.

Climate factors	Correlation coefficient level	SOS (%)	EOS (%)	LOS (%)
Temperature	<–0.3	7.33	3.16	6.45
	–0.3 ~ -0.15	26.62	11.84	17.22
	–0.15 ~ 0	16.31	12.75	15.31
	0 ~ 0.15	14.49	19.98	18.45
	0.15 ~ 0.3	21.20	39.00	32.09
	>0.3	14.06	13.27	10.49
Precipitation	<-0.3	9.26	9.42	12.12
	–0.3 ~ -0.15	23.97	23.10	24.23
	–0.15 ~ 0	16.00	14.50	15.72
	0 ~ 0.15	16.69	14.63	14.85
	0.15 ~ 0.3	25.35	22.97	21.71
	>0.3	8.74	15.37	11.37

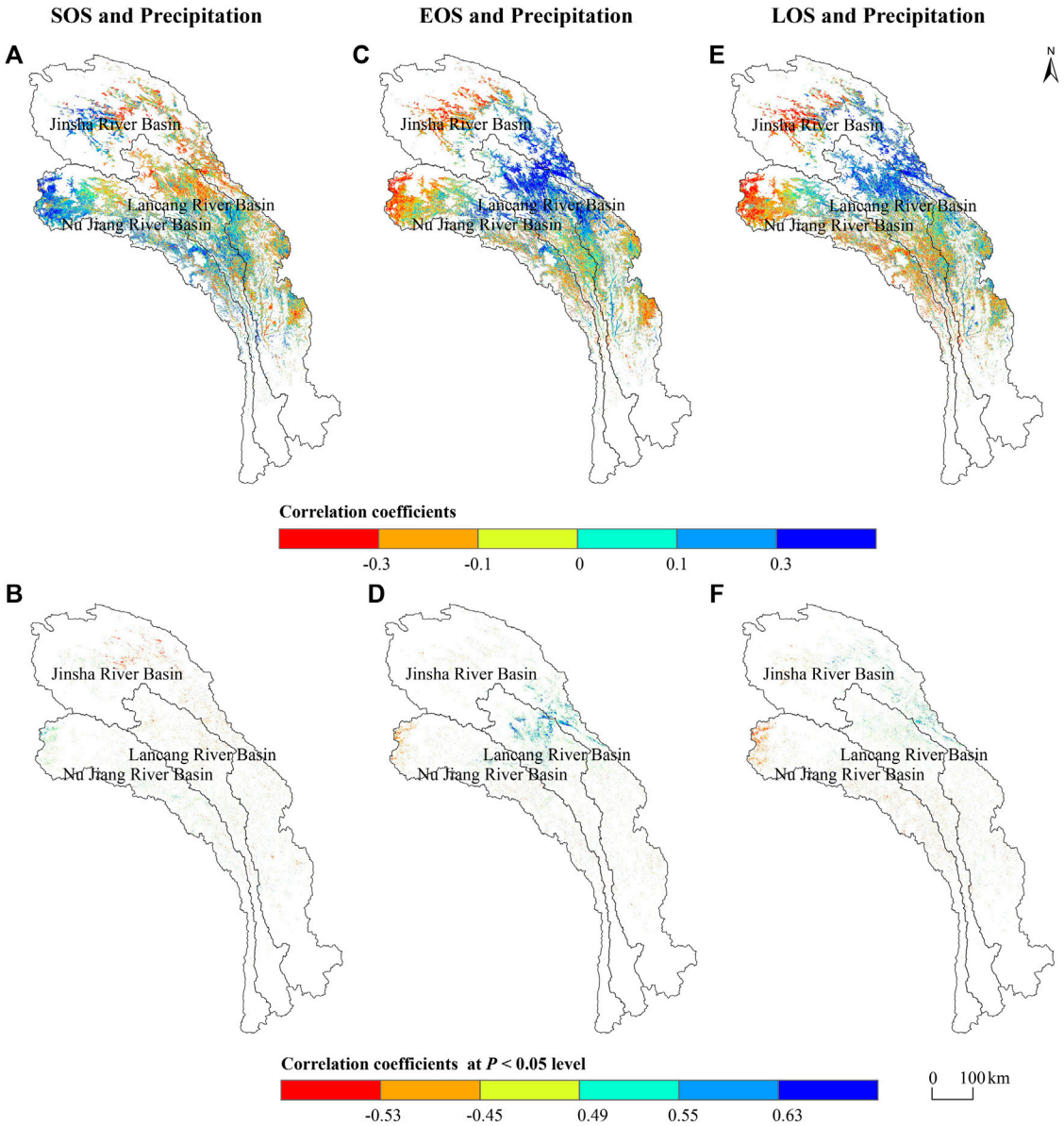

FIGURE 6 | Spatial distribution of correlation coefficients between phenology [**(A)** SOS; **(B)** EOS; and **(C)** LOS] and precipitation in TPRR.

69.41%, respectively), which was well reflected in the source area of the Nujiang River basin and the middle reaches of Lancang River and Jinsha River basin.

Finally, there were certain differences in the correlation between LOS and the freezing index, i.e., LOS was positively correlated with AFI, accounting for approximately 71.32% of the area, which was mainly concentrated in the middle reaches of the three major river basins. However, the positive correlation was more obvious in the source area of the Nujiang River basin, whereas it was negatively correlated with GFI, with a wider distribution in the basin, and the proportion was approximately 63.70%. The area of positive correlation between LOS and thawing index accounted for approximately 65%, and the spatial distribution of correlation coefficients among LOS, ATI, and GTI was relatively consistent, mainly in the core area of the TPRR and the source area of the Nujiang River basin.

DISCUSSION

Spatial and Temporal Patterns of Vegetation Phenology

The results indicated that vegetation phenology of alpine grasslands in the SFGR during 2000–2019 showed a trend of advancement in spring phenology, postponement of autumn phenology, and longer growing season length. In the past 20 years, SOS was advanced by approximately 0.16 days year^{-1}, whereas EOS was delayed at a rate of 0.08 days year^{-1}, leading to an extension of LOS (slope = 0.07 days

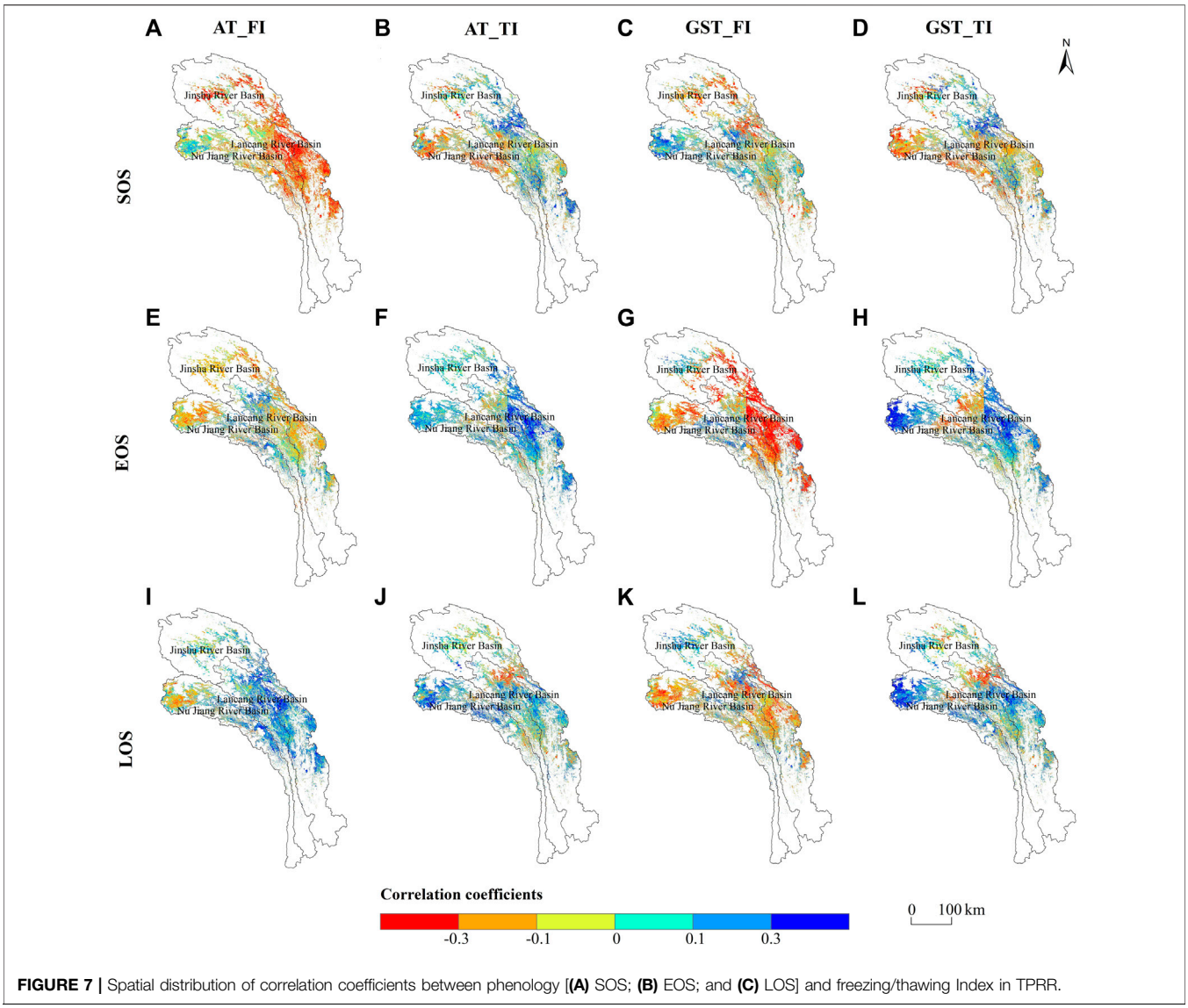

FIGURE 7 | Spatial distribution of correlation coefficients between phenology [**(A)** SOS; **(B)** EOS; and **(C)** LOS] and freezing/thawing Index in TPRR.

year^{-1}). The multiyear mean values of the phenological parameters showed significant spatial differences from the southeast to the northwest as the elevation increased. The greening period in the south was earlier than that in the north, and the withering period was relatively late due to higher temperatures. This resulted in a longer growing season length in the south as compared with the north. Although there were differences in the change ranges of phenology, the general trend and spatial distribution pattern were consistent with the findings by Guan et al. (2019), which may be related to the selection of data sources, time scale, and different methods of phenology extraction (Che et al., 2014; Ganjurjav et al., 2020).

Relationship Between Vegetation Phenology and Climatic Factors

Our results showed that with the regional climate warming and drying, vegetation phenology showed a trend of advanced SOS and delayed EOS. This shift in phenological trend led to a certain extension of the vegetation growing season length. Temperature and precipitation are the main factors influencing vegetation phenology, but their effects are different from each other. Specifically, the higher the average annual temperature, the earlier the vegetation returns to green. On the other hand, the later it enters the wilting period, the longer is the growing season. There is a good positive correlation between the total annual precipitation and SOS as well as EOS. The increase of precipitation will affect the beginning and the end of the vegetation growing season to a certain extent, leading to the shortening of the growing season length (**Table 1**). Some studies have shown that the interaction between climate warming and increased precipitation will affect the SOS of alpine grasslands in the QTP (Ganjurjav et al., 2020; Qiao et al., 2021). An increase in preseason temperature will lead to an earlier SOS and a delay in EOS, thus, indicating that the increase of temperature can accelerate the thawing of soil and the awakening of vegetation, leading to the advance of SOS, which is exactly consistent with

TABLE 3 | Area statistics of correlation analysis between phenology and freezing/thawing indexes from 2000 to 2019.

	Correlation coefficient level	AFI (%)	ATI (%)	GFI (%)	GTI (%)
SOS	<-0.3	33.20	9.00	11.51	13.17
	–0.3 ~ -0.15	27.10	24.69	23.35	28.76
	–0.15 ~ 0	20.32	17.52	16.84	17.16
	0 ~ 0.15	12.74	16.44	18.02	14.99
	0.15 ~ 0.3	5.27	22.22	24.36	17.94
	>0.3	1.36	10.13	5.93	7.98
EOS	<–0.3	7.96	2.75	33.94	5.07
	–0.3 ~ –0.15	32.39	10.55	28.46	13.37
	–0.15 ~ 0	20.84	12.74	10.95	12.15
	0 ~ 0.15	16.20	19.50	9.18	16.44
	0.15 ~ 0.3	17.43	37.68	12.10	33.62
	>0.3	5.18	16.78	5.36	19.35
LOS	<–0.3	2.22	5.09	14.16	5.64
	–0.3 ~ –0.15	12.97	16.03	32.74	14.93
	–0.15 ~ 0	13.49	15.97	16.81	14.29
	0 ~ 0.15	17.26	19.59	13.31	17.11
	0.15 ~ 0.3	35.43	30.96	17.14	31.49
	>0.3	18.63	12.36	5.85	16.55

our results (Ganjurjav et al., 2020; Qiao et al., 2021). However, most studies have demonstrated that vegetation phenology changes may be more strongly correlated with the preseason accumulated temperature or the temperature of the growing season, and the effect of preseason precipitation on vegetation phenology is much greater than that of seasonal or annual precipitation (Shen et al., 2011). In our study, we only analyzed the effects of annual mean temperature and total annual precipitation on phenology. These variables did not reflect a strong response of the phenological parameters to climate and need further analysis.

Impacts of Frozen Soil Changes on Vegetation Phenology

In the past 20 years, the FI/TI of the study area has shown significant geospatial differences due to altitude. There is a certain correlation between the FI and the TI, which showed an obvious decreasing trend from north to south. Specifically, a higher FI caused SOS and EOS delays and a shortened corresponding LOS, whereas the TI was the opposite. Generally speaking, the increase of FI was not conducive to vegetation growth, whereas the TI was different. In the alpine grassland ecosystem, the freezing–thawing state of soil in the frozen area will affect soil moisture and temperature, and the increase of freezing–thawing index can further provide the required hydrothermal conditions for vegetation growth and phenological change (Gao et al., 2020b). Studies on the QTP phenology suggested that degradation of frozen soil caused by warming can negatively affect vegetation spring phenology due to evaporation of soil water, which validates the findings of our study (Jiang et al., 2018). However, Jiang et al. (2018) also noted a positive correlation between SOS and thawing index, which is not quite consistent with our findings, probably because some interaction between changes in soil freezing/thawing state and soil moisture in the permafrost region would have different effects on the spring phenology of vegetation. The results of Wen et al. (2021) also further suggested that frozen soil degradation due to global warming will further affect the length of the vegetation growing season, which is consistent with our findings. A decreasing annual FI and an increasing TI in the frozen soil region indirectly indicate that the region is on a warming trend. This will directly cause the vegetation to enter the growing stage earlier and delay the wilting and yellowing period, resulting in a longer growing season length.

CONCLUSION

In this study, we used the NDVI dataset estimated by remote sensing to retrieve the vegetation phenological parameters of alpine grasslands and their divergent correlations with different climatic factors in the SFGR of the TPRR during 2000–2019. Due to regional warming and drying, the growing season length had been extended due to the advance in spring phenology and delay in autumn phenology. The effects of annual mean temperature and annual total precipitation had spatiotemporal heterogeneous effects on the three phenological parameters. Obvious positive correlations existed between the total annual precipitation with SOS and EOS, and the increasing precipitation shortened the length of the growing season to a certain extent. Furthermore, increased AFI/GFI led to delayed SOS and advanced EOS. In contrast, shorter the growing season length, the opposite was true for the ATI/FTI. Because vegetation phenology of alpine grasslands plays a critical role in the functioning processes of alpine ecosystems and relevant ecosystem services, there is an urgent need to figure out the dynamic balance of carbon source and sink, coupled water and thermal transfer, the interaction between vegetation and soil, and the biogeochemical cycles at local, regional, and global scales. More efforts should be focused on mechanism studies that include not just surficial phenomena, in particular, interfaces of gas, liquid, and solid multiphase flow in the frozen soil region under global climate change and human disturbances (Xiao, 2019).

DATA AVAILABILITY STATEMENT

The raw data supporting the conclusions of the study are included in the article/**Supplementary Material**; further inquiries can be directed to the corresponding author.

AUTHOR CONTRIBUTIONS

C-YW: Conceptualization, methodology, software, validation, formal analysis, investigation, resources, data curation, writing—original draft preparation, writing—review and editing, and visualization; J-NW: Conceptualization, validation, writing—review and editing, supervision, project administration,

and funding acquisition; X-FW and D-LL: Conceptualization, methodology, and writing—review and editing; Y-QW, XC, NW, and PB: writing—review and editing.

FUNDING

This research was funded by the National Science Foundation of China (nos. 31971436 and 41661144045), State Key Laboratory of Cryospheric Science, Northwest Institute of Eco-Environment and Resources, Chinese Academy Sciences (SKLCSOP-2018-07), and China Biodiversity Observation Networks (Sino BON)".

ACKNOWLEDGMENTS

Kind suggestions provided by the Chief Editor are greatly acknowledged. Critical comments from the reviewers greatly improved the initial manuscript.

SUPPLEMENTARY MATERIAL

The Supplementary Material for this article can be found online at: https://www.frontiersin.org/articles/10.3389/feart.2021.797928/full#supplementary-material

REFERENCES

Che, M., Chen, B., Innes, J. L., Wang, G., Dou, X., Zhou, T., et al. (2014). Spatial and Temporal Variations in the End Date of the Vegetation Growing Season throughout the Qinghai-Tibetan Plateau from 1982 to 2011. *Agric. For. Meteorology* 189-190, 81–90. doi:10.1016/j.agrformet.2014.01.004

Chen, S., Liu, W., Sun, Z., Zhao, L., and Liu, Y. (2012). A Quantitative Study on the Plant Population Phenology of Alpine Meadow in the Permafrost Regions of Qinghai-Tibetan Plateau. *J. Glaciology Geocryology* 34 (5), 1142–1148. (in Chinese with English abstract).

Chen, X., An, S., Inouye, D. W., and Schwartz, M. D. (2015). Temperature and Snowfall Trigger alpine Vegetation green-up on the World's Roof. *Glob. Change Biol.* 21 (10), 3635–3646. doi:10.1111/gcb.12954

Cheng, G., and Jin, H. (2013). Permafrost and Groundwater on the Qinghai-Tibet Plateau and in Northeast China. *Hydrogeol J.* 21, 5–23. doi:10.1007/s10040-012-0927-2

Cheng, Z., Weng, C., Guo, J., Dai, L., and Zhou, Z. (2018). Vegetation Responses to Late Quaternary Climate Change in a Biodiversity Hotspot, the Three Parallel Rivers Region in Southwestern China. *Palaeogeogr. Palaeoclimatol. Palaeoecol.* 491, 10–20. doi:10.1016/j.palaeo.2017.11.032

Cong, N., and Shen, M. G. (2016). Variation of Satellite-Based spring Vegetation Phenology and the Relationship with Climate in the Northern Hemisphere over 1982 to 2009. *Ying Yong Sheng Tai Xue Bao* 27 (9), 2737–2746. doi:10.13287/j.1001-9332.201609.028(in Chinese with English abstract)

Delbart, N., Le Toan, T., Kergoat, L., and Fedotova, V. (2006). Remote Sensing of spring Phenology in Boreal Regions: A Free of Snow-Effect Method Using NOAA-AVHRR and SPOT-VGT Data (1982-2004). *Remote Sensing Environ.* 101 (1), 52–62. doi:10.1016/j.rse.2005.11.012

Ding, M., Zhang, Y., Sun, X., Liu, L., Wang, Z., and Bai, W. (2013). Spatiotemporal Variation in alpine Grassland Phenology in the Qinghai-Tibetan Plateau from 1999 to 2009. *Chin. Sci. Bull.* 58 (3), 396–405. doi:10.1007/s11434-012-5407-5(in Chinese with English abstract)

Fu, Y. H., Zhou, X., Li, X., Zhang, Y., Geng, X., Hao, F., et al. (2021). Decreasing Control of Precipitation on Grassland spring Phenology in Temperate China. *Glob. Ecol. Biogeogr.* 30, 490–499. doi:10.1111/geb.13234

Gang, C., Zhao, W., Zhao, T., Zhang, Y., Gao, X., and Wen, Z. (2018). The Impacts of Land Conversion and Management Measures on the Grassland Net Primary Productivity over the Loess Plateau, Northern China. *Sci. Total Environ.* 645, 827–836. doi:10.1016/j.scitotenv.2018.07.161

Ganjurjav, H., Gornish, E. S., Gao, Q. Z., Hu, G. Z., Li, Y., Schwartz, M. W., et al. (2020). Warming and Precipitation Addition Interact to Affect Plant spring Phenology in alpine Meadows on the central Qinghai-Tibetan Plateau. *Agric. For. Meteorology* 287, 107943. doi:10.1016/j.agrformet.2020.107943

Gao, B., Li, J., and Wang, X. (2020a). Impact of Frozen Soil Changes on Vegetation Phenology in the Source Region of the Yellow River from 2003 to 2015. *Theor. Appl. Climatol* 141, 1219–1234. doi:10.1007/s00704-020-03266-5

Gao, Y., Zhao, S., and Deng, J. (2020b). Developing Law of Damming Landslide and Challenges for Disaster Prevention and Mitigation in the Three-River-Parallel Territory in the Tibetan Plateau. *Adv. Eng. Sci.* 52 (5), 50–61. (in Chinese with English abstract). doi:10.15961/j.jsuese.202000283

Gocic, M., and Trajkovic, S. (2013). Analysis of Changes in Meteorological Variables Using Mann-Kendall and Sen's Slope Estimator Statistical Tests in Serbia. *Glob. Planet. Change* 100, 172–182. doi:10.1016/j.gloplacha.2012.10.014

Guan, Q., Ding, M., and Zhang, H. (2019). Spatiotemporal Variation of Spring Phenology in Alpine Grassland and Response to Climate Changes on the Qinghai-Tibet, China. *Mountain Res.* 37 (5), 639–648. (in Chinese with English abstract). doi:10.16089/j.cnki.1008-2786.000455

Hayashi, M. (2014). The Cold Vadose Zone: Hydrological and Ecological Significance of Frozen-Soil Processes. *Vadose Zone J.* 13, vzj2013 03 0064er. doi:10.2136/vzj2013.03.0064er

Hmimina, G., Dufrêne, E., Pontailler, J.-Y., Delpierre, N., Aubinet, M., Caquet, B., et al. (2013). Evaluation of the Potential of MODIS Satellite Data to Predict Vegetation Phenology in Different Biomes: An Investigation Using Ground-Based NDVI Measurements. *Remote Sensing Environ.* 132, 145–158. doi:10.1016/j.rse.2013.01.010

Huang, W., Zeng, T., and Huang, X. (2019). Spatiotemporal Dynamics of alpine Grassland Phenology on the Tibetan Plateau. *Pratacultural Sci.* 36 (4), 1032–1043. (in Chinese with English abstract). doi:10.11829/j.issn.1001-0629.2019-0048

Jiang, H., Zhang, W., Yi, Y., Yang, K., Li, G., and Wang, G. (2018). The Impacts of Soil Freeze/thaw Dynamics on Soil Water Transfer and spring Phenology in the Tibetan Plateau. *Arctic, Antarctic, Alpine Res.* 50, e1439155. doi:10.1080/15230430.2018.1439155

Jiao, F., Liu, H., Xu, X., Gong, H., and Lin, Z. (2020). Trend Evolution of Vegetation Phenology in China during the Period of 1981-2016. *Remote Sensing* 12, 572. doi:10.3390/rs12030572

Jones, B. M., Baughman, C. A., Romanovsky, V. E., Parsekian, A. D., Babcock, E. L., Stephani, E., et al. (2016). Presence of Rapidly Degrading Permafrost Plateaus in South-central Alaska. *The Cryosphere* 10, 2673–2692. doi:10.5194/tc-10-2673-2016

Jönsson, P., and Eklundh, L. (2004). TIMESAT-a Program for Analyzing Time-Series of Satellite Sensor Data. *Comput. Geosciences* 30, 833–845. doi:10.1016/j.cageo.2004.05.006

Khare, S., Drolet, G., Sylvain, J.-D., Paré, M. C., and Rossi, S. (2019). Assessment of Spatio-Temporal Patterns of Black Spruce Bud Phenology across Quebec Based on MODIS-NDVI Time Series and Field Observations. *Remote Sensing* 11, 2745. doi:10.3390/rs11232745

Kingdon Ward, F. (1923). *Mystery Hivers of Tibet*. London: Seeley Service and Co.

Klosterman, S. T., Hufkens, K., Gray, J. M., Melaas, E., Sonnentag, O., Lavine, I., et al. (2014). Evaluating Remote Sensing of Deciduous forest Phenology at Multiple Spatial Scales Using PhenoCam Imagery. *Biogeosciences* 11, 4305–4320. doi:10.5194/bg-11-4305-2014

Li, H., Yao, W. J., Wang, S. Q., Su, P. F., Duan, Q. C., Wang, W. X., et al. (2012). Three Parallel Rivers World Natural Heritage Site Ecological Safety Protection Research. *Adv. Mater. Res.* 599, 278–281. doi:10.4028/www.scientific.net/amr.599.278

Li, L., and Hao, Z. (2003). The Automated Extraction of Catchment Properties from Digital Elevation Models. *Adv. Earth Sci.* 18 (2), 251–256. (in Chinese with English abstract).

Liang, J., Liu, Y., Ying, L., Li, P., Xu, Y., and Shen, Z. (2014). Road Impacts on Spatial Patterns of Land Use and Landscape Fragmentation in Three Parallel

Rivers Region, Yunnan Province, China. *Chin. Geographical Sci.* 24, 15–27. doi:10.1007/s11769-014-0652-y

Lin, S., Wu, R., Yang, F., Wang, J., and Wu, W. (2018). Spatial Trade-Offs and Synergies Among Ecosystem Services within a Global Biodiversity Hotspot. *J. Ecol. Indicators* 84, 371–381. doi:10.1016/j.ecolind.2017.09.007

Liu, J., Wen, Z., and Gang, C. (2020a). Normalized Difference Vegetation index of Different Vegetation Cover Types and its Responses to Climate Change in the Loess Plateau. *Acta Ecologica Sinica* 40 (2), 678–691. (in Chinese with English abstract). doi:10.5846/stxb201901090082

Liu, Y., Wang, J., Dong, J., Wang, S., and Ye, H. (2020b). Variations of Vegetation Phenology Extracted from Remote Sensing Data over the Tibetan Plateau Hinterland during 2000-2014. *J. Meteorol. Res.* 34, 786–797. doi:10.1007/s13351-020-9211-x

Liu, Z., Wang, S., and Chen, B. (2021). Spatial and Temporal Variations of Frozen Ground and its Vegetation Response in the Eastern Segment of China-Mongolia-Russia Economic Corridor from 2000 to 2015. *Acta Geographica Sinica* 76 (5), 1231–1244. (in Chinese with English abstract). doi:10.11821/dlxb202105014

Luo, D., Jin, H., Jin, R., Yang, X., and Lü, L. (2014). Spatiotemporal Variations of Climate Warming in Northern Northeast China as Indicated by Freezing and Thawing Indices. *Quat. Int.* 349, 187–195. doi:10.1016/j.quaint.2014.06.064

Ma, X., Chen, S., Deng, J., Feng, Q., and Huang, X. (2016). Vegetation Phenology Dynamics and its Response to Climate Change on the Tibetan Plateau. *Acta Prataculturae Sinica* 25 (1), 13–21. (in Chinese with English abstract). doi:10.11686/cyxb2015089

Morisette, J. T., Richardson, A. D., Knapp, A. K., Fisher, J. I., Graham, E. A., Abatzoglou, J., et al. (2009). Tracking the Rhythm of the Seasons in the Face of Global Change: Phenological Research in the 21st century. *Front. Ecol. Environ.* 7, 253–260. doi:10.1890/070217

Piao, S., Liu, Q., Chen, A., Janssens, I. A., Fu, Y., Dai, J., et al. (2019). Plant Phenology and Global Climate Change: Current Progresses and Challenges. *Glob. Chang Biol.* 25, 1922–1940. doi:10.1111/gcb.14619

Piao, S., Cui, M., Chen, A., Wang, X., Ciais, P., Liu, J., et al. (2011). Altitude and Temperature Dependence of Change in the spring Vegetation green-up Date from 1982 to 2006 in the Qinghai-Xizang Plateau. *Agric. For. Meteorology* 151, 1599–1608. doi:10.1016/j.agrformet.2011.06.016

Qiao, C., Shen, S., Cheng, C., Wu, J., Jia, D., and Song, C. (2021). Vegetation Phenology in the Qilian Mountains and its Response to Temperature from 1982 to 2014. *Remote Sensing* 13, 286. doi:10.3390/rs13020286

Rauste, Y., Astola, H., Hame, T., Berglund, R., Sirro, L., Veijonen, T., et al. (2007). Automatic Monitoring of Autumn Colours Using MODIS Data. *IGARSS: 2007 IEEE Int. Geosci. Remote Sensing Symp.* 1–12, 1295–1298. doi:10.1109/IGARSS.2007.4423043

Richardson, A. D., Keenan, T. F., Migliavacca, M., Ryu, Y., Sonnentag, O., and Toomey, M. (2013). Climate Change, Phenology, and Phenological Control of Vegetation Feedbacks to the Climate System. *Agric. For. Meteorology* 169, 156–173. doi:10.1016/j.agrformet.2012.09.012

Sazonova, T. S., and Romanovsky, V. E. (2003). A Model for Regional-Scale Estimation of Temporal and Spatial Variability of Active Layer Thickness and Mean Annual Ground Temperatures. *Permafrost Periglac. Process.* 14, 125–139. doi:10.1002/ppp.449

Shen, M., Piao, S., Chen, X., An, S., Fu, Y. H., Wang, S., et al. (2016). Strong Impacts of Daily Minimum Temperature on the green-up Date and Summer Greenness of the Tibetan Plateau. *Glob. Change Biol.* 22 (9), 3057–3066. doi:10.1111/gcb.13301

Shen, M., Piao, S., Cong, N., Zhang, G., and Jassens, I. A. (2015a). Precipitation Impacts on Vegetation spring Phenology on the Tibetan Plateau. *Glob. Change Biol.* 21, 3647–3656. doi:10.1111/gcb.12961

Shen, M., Piao, S., Dorji, T., Liu, Q., Cong, N., Chen, X., et al. (2015b). Plant Phenological Responses to Climate Change on the Tibetan Plateau: Research Status and Challenges. *Natl. Sci. Rev.* 2 (4), 454–467. doi:10.1093/nsr/nwv058

Shen, M., Sun, Z., Wang, S., Zhang, G., Kong, W., Chen, A., et al. (2013). No Evidence of Continuously Advanced green-up Dates in the Tibetan Plateau over the Last Decade. *Proc. Natl. Acad. Sci.* 110, E2329. doi:10.1073/pnas.1304625110

Shen, M., Tang, Y., Chen, J., Zhu, X., and Zheng, Y. (2011). Influences of Temperature and Precipitation before the Growing Season on spring Phenology in Grasslands of the central and Eastern Qinghai-Tibetan Plateau. *Agric. For. Meteorology* 151, 1711–1722. doi:10.1080/01431161.2013.87563610.1016/j.agrformet.2011.07.003

Shen, M., Tang, Y., Desai, A. R., Gough, C., and Chen, J. (2014a). Can EVI-Derived Land-Surface Phenology Be Used as a Surrogate for Phenology of Canopy Photosynthesis? *Int. J. Remote Sensing* 35, 1162–1174. doi:10.1080/01431161.2013.875636

Shen, M., Zhang, G., Cong, N., Wang, S., Kong, W., and Piao, S. (2014b). Increasing Altitudinal Gradient of spring Vegetation Phenology during the Last Decade on the Qinghai-Tibetan Plateau. *Agric. For. Meteorology* 189-190, 71–80. doi:10.1016/j.agrformet.2014.01.003

Shi, Y., Niu, F., Lin, Z., and Luo, J. (2019). Freezing/thawing index Variations over the Circum-Arctic from 1901 to 2015 and the Permafrost Extent. *Sci. Total Environ.* 660, 1294–1305. doi:10.1016/j.scitotenv.2019.01.121

Stanimirova, R., Cai, Z. Z., Melaas, E. K., Gray, J. M., Eklundh, L., Jönsson, P., et al. (2019). An Empirical Assessment of the MODIS Land Cover Dynamics and TIMESAT Land Surface Phenology Algorithms. *Remote Sensing* 11, 2201. doi:10.3390/rs11192201

Tan, J., Li, A., and Lei, G. (2016). Contrast on Anusplin and Cokriging Meteorological Spatial Interpolation in Southeastern Margin of Qinghai-Xizang Plateau. *Plateau Meteorology* 35 (4), 875–886. (in Chinese with English abstract). doi:10.7522/j.issn.1000-0534.2015.00037

Wang, C., Guo, H., Zhang, L., Liu, S., Qiu, Y., and Sun, Z. (2015). Assessing Phenological Change and Climatic Control of alpine Grasslands in the Tibetan Plateau with MODIS Time Series. *Int. J. Biometeorol.* 59, 11–23. doi:10.1007/s00484-014-0817-5

Wang, Q., Fan, X., and Wang, M. (2014). Recent Warming Amplification over High Elevation Regions across the globe. *Clim. Dyn.* 43, 87–101. doi:10.1007/s00382-013-1889-3

Wang, T., Peng, S., Lin, X., and Chang, J. (2013a). Declining Snow Cover May Affect spring Phenological Trend on the Tibetan Plateau. *Proc. Natl. Acad. Sci.* 110 (31), E2854–E2855. doi:10.1073/pnas.1306157110

Wang, W., Körner, C., Zhang, Z., Wu, R., Geng, Y., Shi, W., et al. (2013b). No Slope Exposure Effect on alpine Treeline Position in the Three Parallel Rivers Region, SW China. *Alpine Bot.* 123, 87–95. doi:10.1007/s00035-013-0118-3

Weil, G., Lensky, I. M., and Levin, N. (2017). Using Ground Observations of a Digital Camera in the VIS-NIR Range for Quantifying the Phenology of Mediterranean Woody Species. *Int. J. Appl. Earth Observations Geoinformation* 62, 88–101. doi:10.1016/j.jag.2017.05.016

Wen, L., Guo, M., Yin, S., Huang, S., Li, X., and Yu, F. (2021). Vegetation Phenology in Permafrost Regions of Northeastern China Based on MODIS and Solar-Induced Chlorophyll Fluorescence %J Chinese Geographical Science. *Chin. Geographical Sci.* 31, 459–473. doi:10.1007/s11769-021-1204-x

Wu, J., Guo, K., Wang, M., and Xu, B. (2011). "Research and Extraction of the Hydrological Characteristics Based on GIS and DEM," in Proceeding of the 2011 IEEE 2nd International Conference on Computing, Control and Industrial Engineering, Wuhan, China, Aug. 2011 (IEEE), 4.

Xiao, C. (2019). Available From: http://www.dili360.com/cng/article/p5350c3d7a012056.htm (Accessed, , 10).

Xiao, P., and Xiang, Y. (2017). Francis Kingdon-Ward' S Investigation in Khams-Tibetan and His Achievements and Influence. *J. Yunnan Minzu Univ. (Social Science)* 34 (1), 147–153. doi:10.13727/j.cnki.53-1191/c.2017.01.019(in Chinese with English abstract)

Yang, Y., Xiao, P., Feng, X., and Li, H. (2017). Accuracy Assessment of Seven Global Land Cover Datasets over China. *Isprs J. Photogrammetry Remote Sensing* 125, 156–173. doi:10.1016/j.isprsjprs.2017.01.016

Yao, X., Deng, J., Liu, X., Zhou, Z., Yao, J., Dai, F., et al. (2020). Primary Recognition of Active Landslides and Development Rule Analysis for Pan Three-River-Parallel Territory of Tibet Plateau. *Adv. Eng. Sci.* 52 (5), 16–37. (in Chinese with English abstract). doi:10.15961/j.jsuese.202000529

Yu, H., Luedeling, E., and Xu, J. (2010). Winter and spring Warming Result in Delayed spring Phenology on the Tibetan Plateau. *Proc. Natl. Acad. Sci.* 107 (51), 22151–22156. doi:10.1073/pnas.1012490107

Zeng, H., Jia, G., and Epstein, H. (2011). Recent Changes in Phenology over the Northern High Latitudes Detected from Multi-Satellite Data. *Environ. Res. Lett.* 6, 045508. doi:10.1088/1748-9326/6/4/045508

Zhai, J., Yuan, F., and Wu, J. (2015). Research Progress on Vegetation Phenological Changes. *Chin. J. Ecol.* 34 (11), 3237–3243. (in Chinese with English abstract). doi:10.13292/j.1000-4890.20151023.030

Zhang, G., Zhang, Y., Dong, J., and Xiao, X. (2013). Green-up Dates in the Tibetan Plateau Have Continuously Advanced from 1982 to 2011. *Proc. Natl. Acad. Sci. United States America* 110, 4309–4314. doi:10.1073/pnas.1210423110

Zhao, J., Wang, Y., Zhang, Z., Zhang, H., Guo, X., Yu, S., et al. (2016). The Variations of Land Surface Phenology in Northeast China and its Responses to Climate Change from 1982 to 2013. *Remote Sensing* 8, 400. doi:10.3390/rs8050400

Zhao, J., Zhang, H., Zhang, Z., Guo, X., Li, X., and Chen, C. (2015). Spatial and Temporal Changes in Vegetation Phenology at Middle and High Latitudes of the Northern Hemisphere over the Past Three Decades. *Remote Sensing* 7, 10973–10995. doi:10.3390/rs70810973

Zhao, L., Ping, C.-L., Yang, D., Cheng, G., Ding, Y., and Liu, S. (2004). Changes of Climate and Seasonally Frozen Ground over the Past 30 Years in Qinghai-Xizang (Tibetan) Plateau, China. *Glob. Planet. Change* 43, 19–31. doi:10.1016/j.gloplacha.2004.02.003

Zhou, L., Tucker, C. J., Kaufmann, R. K., Slayback, D., Shabanov, N. V., and Myneni, R. B. (2001). Variations in Northern Vegetation Activity Inferred from Satellite Data of Vegetation index during 1981 to 1999. *J. Geophys. Res.* 106 (D17), 20069–20083. doi:10.1029/2000JD000115

Zhu, W., Zhang, X., Zhang, J., and Zhu, L. (2019). A Comprehensive Analysis of Phenological Changes in forest Vegetation of the Funiu Mountains, China. *J. Geogr. Sci.* 29 (1), 131–145. doi:10.1007/s11442-019-1588-z(in Chinese with English abstract)

Zou, D., Zhao, L., Sheng, Y., Chen, J., Hu, G., Wu, T., et al. (2017). A New Map of Permafrost Distribution on the Tibetan Plateau. *The Cryosphere* 11, 2527–2542. doi:10.5194/tc-11-2527-2017

Conflict of Interest: The authors declare that the research was conducted in the absence of any commercial or financial relationships that could be construed as a potential conflict of interest.

Publisher's Note: All claims expressed in this article are solely those of the authors and do not necessarily represent those of their affiliated organizations or those of the publisher, the editors, and the reviewers. Any product that may be evaluated in this article, or claim that may be made by its manufacturer, is not guaranteed or endorsed by the publisher.

frontiers in Earth Science

ORIGINAL RESEARCH
published: 11 March 2022
doi: 10.3389/feart.2022.837062

Type Classification and Engineering Stability Evaluation of Permafrost Wetlands on the Qinghai–Tibet Plateau

Xuesong Mao[1], Ying Zhao[1], Qian Wu[1], Wanjun Huang[1] and Liangqing Han[2]*

[1]School of Highway, Chang'an University, Xi'an, China, [2]Jiangsu Zhongshe Group Co.,Ltd., Wuxi, China

On the Qinghai–Tibet Plateau area, the permafrost and the wetlands are interdependent to form a symbiotic system, called permafrost wetlands (PWs). Due to the extremely complex hydrothermal conditions, the PWs greatly impact road stability. Thus, it is necessary to classify PWs in terms of engineering characteristics and evaluate their engineering stability. In this study, the typical diseases of subgrade in permafrost wetland areas are analyzed based on field investigation. Then, the permafrost type, waterlogged area ratio, and meadow development degree are used as the main indicators for classifying PWs by a three-level division method. Finally, a scheme for the engineering stability evaluation of PWs was established based on the fuzzy comprehensive theory and used for the pre-evaluation of the engineering stability for the proposed Qinghai 224 highway. The results indicate that the longitudinal cracks and uneven deformation are the main road diseases in this area, caused by the combined effect of permafrost, waterlogged areas, and meadow development. The PWs are divided into 15 types according to the engineering characteristics. Waterlogged area ratio and meadow development degree are proven to represent the development of underlying permafrost. The influencing factors include climatic environment, permafrost property, and wetland conditions, which have decreased influence on the engineering stability of PWs. The engineering stability of k230 + 100 and k255 + 400 is evaluated as basically stable and less stable, and the corresponding measures are adopted. At present, no significant damage occurred on the two road sections. The results suggest that the evaluation model in this article can be used to pre-evaluate the engineering stability of PWs.

Keywords: permafrost wetlands, typical diseases, type classification, engineering stability, evaluation model

OPEN ACCESS

Edited by:
Dongliang Luo,
Northwest Institute of Eco-Environment and Resources (CAS), China

Reviewed by:
Yanhui You,
Northwest Institute of Eco-Environment and Resources (CAS), China
Yao Xiaoliang,
Xi'an University of Technology, China
Zhaohui Yang,
University of Alaska Anchorage, United States

****Correspondence:***
Ying Zhao
2017021007@chd.edu.cn

Specialty section:
This article was submitted to Cryospheric Sciences, a section of the journal Frontiers in Earth Science

Received: *16 December 2021*
Accepted: *18 January 2022*
Published: *11 March 2022*

Citation:
Mao X, Zhao Y, Wu Q, Huang W and Han L (2022) Type Classification and Engineering Stability Evaluation of Permafrost Wetlands on the Qinghai–Tibet Plateau. Front. Earth Sci. 10:837062. doi: 10.3389/feart.2022.837062

INTRODUCTION

The Qinghai–Tibet Plateau is a typical region of high-altitude permafrost distribution in China and even the world. Due to the water blocking effect of the permafrost layer, rainfall, snowmelt, and surface runoff cannot infiltrate into the permafrost, resulting in the accumulation of water on the surface to form wetlands. The natural environment, vegetation characteristics, and permafrost combine to create the environmental sensitivity of permafrost wetlands (Bai et al., 2004; Wang et al., 2015), which significantly affects the stability of roads (Wang et al., 2004; Chai et al., 2017). On the Qinghai–Tibet Plateau, the road pavement instead of the original vegetation has disrupted the original hydrothermal balance of the wetlands and blocked surface runoff, thus exacerbating the degradation of the permafrost, which has led to a series of road disease problems, especially uneven

settlement and longitudinal cracks (Wen et al., 2009; Mu et al., 2014; Li et al., 2015; Peng et al., 2015; Chang et al., 2016; Chai et al., 2017; Yang et al., 2019). Some scholars also pointed out that the thaw settlement of the permafrost beneath the roadway is one of the sources of the subgrade settlement (Qi et al., 2012; Yu et al., 2013). In addition, the wetlands features are also conducive to the development of road diseases. The accumulation of water in the soil layer leads to water migration to the subgrade, causing road diseases with seasonal freezing and thawing (Mao et al., 2010). Meantime, the low temperature of PWs promotes the formation of a peat layer with high compressibility. The settlement caused by the compression of the peat layer is also part of the subgrade settlement. It can be found that these road diseases are closely related to the type and stability of the permafrost and wetlands conditions. The permafrost state is not only influenced by road constructions but also closely related to the wetland conditions (Liu et al., 2009; Chang et al., 2012). It can be seen from the above analysis that the permafrost and wetlands both interact and contribute to each other, and together they affect road stability. Thus, the engineering characteristics of PWs on the Qinghai–Tibet Plateau require attention.

In order to better understand the characteristics of wetlands on the Qinghai–Tibet Plateau, many researchers proposed the classification system in terms of causes or features (Ni et al., 1998; Sun, 2003). Meantime, several scholars proposed classification systems at different spatial scales. Li et al. (1998) classified the wetlands in the Three-River Source region into moor, lake, river, and riverbed. Zhao (1999) classified the alpine wetlands into peat marshes and submerged marshes based on the presence or absence of peat accumulation and then divided them into 11 marsh subtypes based on geomorphological conditions and water recharge types. Sun (2003) classified the wetlands of the Qinghai–Tibet Plateau into grass wetlands, forested wetlands, river wetlands, and lake wetlands according to the Ramsar Convention. Chen et al. (2002) added artificial wetlands on the basis of 3 basic natural wetland types—lake wetland, swamp wetland, and river wetland—according to the basic hydrological, biological, and soil characteristics of plateau wetlands. Zhang et al. (2010) proposed a revised 4-class classification system of alpine wetlands based on remote sensing and classified the wetlands into 13 subcategories, such as river, weedy wet meadow, hippophae rhamnoides, beach gravel, lake, and *Phragmites australis* marsh. Although the classification systems considering the causes, features, and space of wetlands on the Qinghai–Tibet Plateau have been widely documented, little information exists paying attention to the engineering characteristics of wetlands.

The engineering characteristics of wetlands significantly affect the stability of permafrost wetlands. The traditional road safety assessment system mainly adopts the safety factor as the evaluation criterion. The evaluation results have great inaccuracy due to the uncertainty of geotechnical parameters. In order to overcome this problem, Qi et al. (2006) proposed a calculation method to calculate the reliability index and failure probability based on a genetic algorithm for the thawing settlement of the permafrost subgrade. However, road stability is related to geological and climatic conditions, regulation measures, and so on. Huo et al. (2010) selected the annual ground temperature, permafrost type, artificial permafrost table, drainage condition of subgrade, and method of special adjustment as the key factors and established the linguistic variables and fuzzy membership function to describe the relationship between the factors and the road diseases. Meanwhile, Qi et al. (2007) and Miao et al. (2018) established a prediction model of subgrade deformation considering ground temperature, subgrade height, and permafrost table using a BP neural network. For the special engineering measures for subgrade in permafrost areas, the treatment effect was evaluated using fuzzy theory and catastrophe progression method considering the natural environment, frozen soil properties, and engineering measures (Cao et al., 2015; Zhao et al., 2019; Luo et al., 2021). It can be seen that the current research mostly focuses on the evaluation of subgrade stability in permafrost areas and rarely considers the impact of permafrost wetlands on road stability. Therefore, it is necessary to evaluate the engineering stability of the PWs in order to take appropriate treatment measures to strengthen the wetland foundation.

This study proposes the classification system of permafrost wetlands according to engineering characteristics. Furthermore, the engineering stability of permafrost wetlands is evaluated based on the fuzzy comprehensive evaluation model. The results provide an important reference to understanding the role of permafrost wetlands in engineering construction.

PERMAFROST WETLANDS AND TYPICAL DISEASES OF SUBGRADE IN STUDY AREA

The study area is located in the center of the Qinghai–Tibet Plateau and the Midwest of Yushu, with an average altitude of 4179.1 m, belonging to a typical alpine climate. The road traverses many wetlands with meadows covering the surface, waterlogged

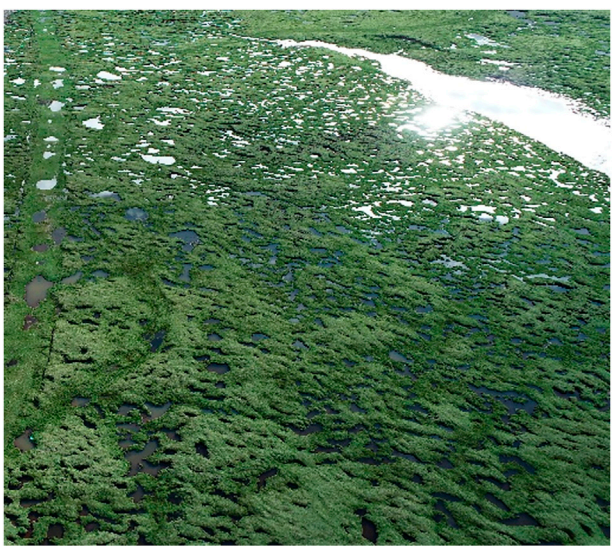

FIGURE 1 | Permafrost wetlands on the Qinghai–Tibet Plateau.

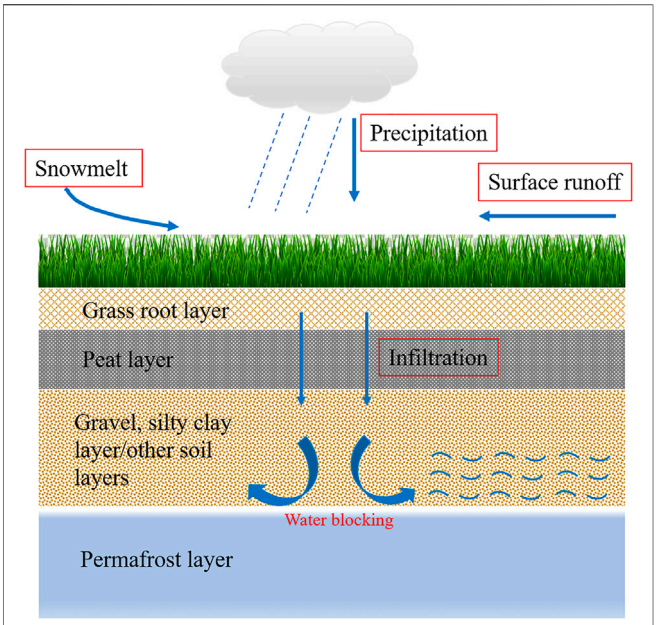

FIGURE 2 | Schematic of PWs profile.

areas, and permafrost existing underground, which can be called permafrost wetland (PWs), as shown in **Figure 1**. The developed modern glaciers and glacial landforms, dense rivers and lakes, abundant ice-snow meltwater, alpine climate, and the prevalence of the permafrost have contributed to the formation and development of wetlands on the Qinghai–Tibet Plateau.

Based on field investigation, the strata of PWs are composed of the grass layer with grass roots, peat layer with an inadequate decomposition of plant residues, powdered clay interspersed with gravel, and permafrost layer, as shown in **Figure 2**. The wetlands and the permafrost underneath constitute a symbiotic system (Sun, 2000; Sun et al., 2008), which is mainly manifested in two aspects: the protection and enhancement of peat and grass layer to permafrost and the promotion of permafrost to peat and grass layer. Vegetation has been found to strongly protect frozen soil from incoming radiation, thereby insulating the soil from ambient conditions (Kudelyacev et al., 1977; Kelly et al., 2004; Cannone and Guglielmin, 2009; Anderson et al., 2019; Fedorov et al., 2019). Moreover, the grass-root layer can reduce the surface heat transfer into a deep stratum due to the poor thermal conductivity. Meantime, the role of ground-hugging vegetation and plant roots in water absorption and retention enables the frozen soil to reach a material-energy balance and ecological equilibrium (Niu et al., 2019). When the temperature rises, the peat layer consumes heat by evaporating water to slow down the transmission of the cold storage of permafrost to the surface. When the temperature drops to negative temperature, the peat layer in a frozen state, due to its higher thermal conductivity, can transfer the cold energy deeper into the soil to promote cold storage of the permafrost (Sun, 2000). The permafrost layer can effectively block water infiltration, allowing snowmelt, precipitation, and river water to accumulate on the surface, forming a waterlogging area, which facilitates the continuity of the soil swampy process. Instead, when the surface vegetation is destroyed, its functions of heat insulation, heat preservation, and water storage are weakened or disappear (Iwahana et al., 2003; Wang et al., 2008), causing heat and water to enter directly into the subsurface, which is manifested by enhanced vertical transport of water and heat. Eventually, the underlying permafrost degrades or disappears, which affects the existence of wetlands leading to the degradation or disappearance (He et al., 2009; Luo et al., 2012). The symbiotic mechanism existing between wetlands and permafrost is a key factor in forming the special geological environment of the Tibetan Plateau. It was found that permafrost on the Qinghai–Tibet Plateau is degrading year by year due to climate warming and construction of ground engineering (Luo et al., 2012; Han et al., 2018; Sheng et al., 2020), which in turn affects the development of wetlands (Wang et al., 2010; Liu et al., 2019).

Based on the above analysis, it is clear that the complex characteristics of permafrost wetlands are the main challenge to be overcome for road construction, which leads to a series of road disease problems. In this study area, the longitudinal cracks and the uneven deformation are the main forms of road diseases according to the field investigation (**Figure 3**). The black asphalt pavement breaks the original hydrothermal equilibrium of the wetlands, and the input of a large amount of heat energy makes the permafrost under the subgrade in a state of degradation. The thawing of the permafrost layer leads to the uneven compression deformation of the subgrade, which is the main internal cause of the uneven settlement and longitudinal cracks. In addition, the developed permafrost wetlands have lush grass, and the soil is wet or overwet all year-round, which leads to the active migration of moisture to the subgrade. The surface water infiltrated by the road shoulder and slope foot carries much heat, resulting in a relative decrease of the permafrost table. Furthermore, water gathers near the permafrost table to form a thick ice layer under the road shoulder (Mao et al., 2010). Finally, the longitudinal cracks and uneven settlement are generated in the subgrade under the coupling action of heat and water. It indicates that the combination of the permafrost, waterlogged area, and meadow development contributes to road diseases.

TYPE CLASSIFICATION OF PERMAFROST WETLANDS

Determination of Classification Index

For the actual engineering project, the classification of PWs should comprehensively consider and analyze the various elements that affect road stability. Based on a field investigation, the permafrost type, waterlogged area ratio, and meadow development degree were selected to be the classification indexes, which considered the effects of permafrost, meadow, and water on the project construction. The permafrost type was identified by the field drilling method. The waterlogged area ratio was obtained by the aerial survey and micro-geomorphology extraction technology. The thickness of the vegetation layer was determined by field measurement.

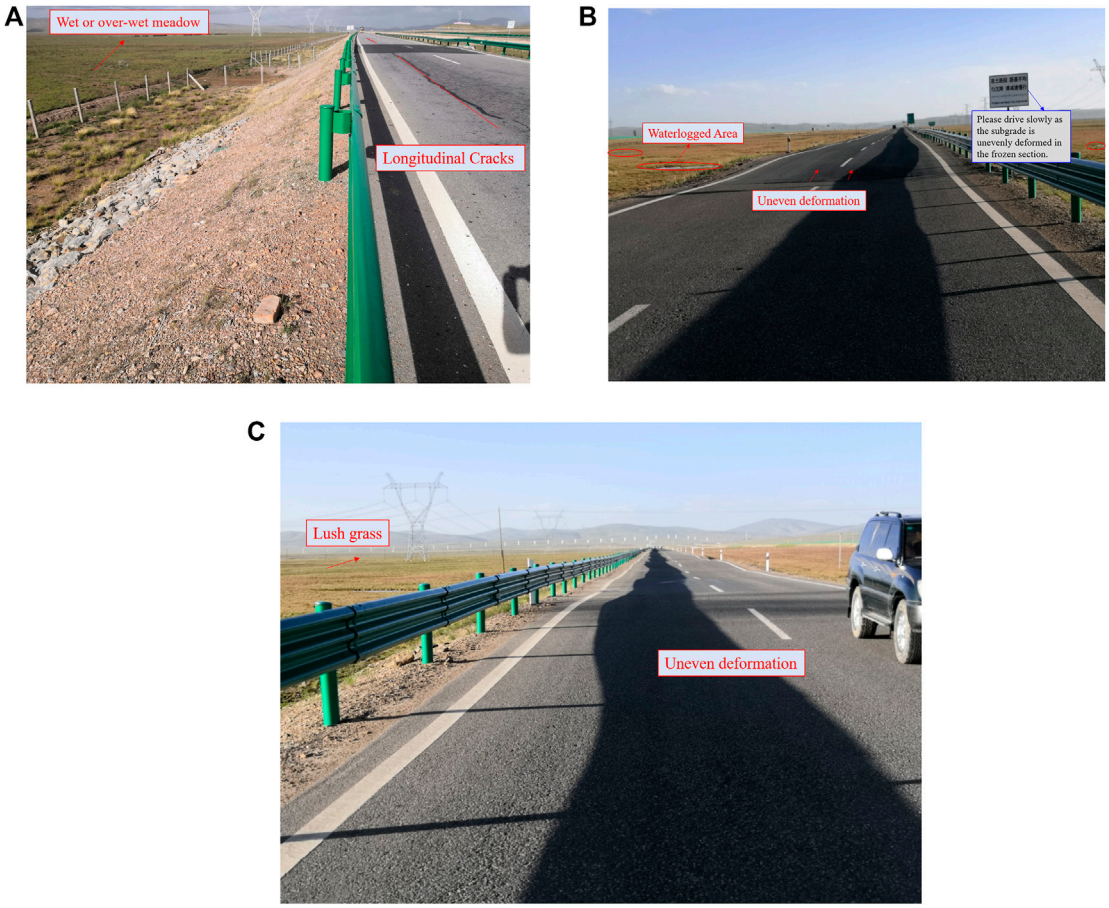

FIGURE 3 | Diseases of the road in the permafrost wetland area. **(A)** Longitudinal cracks. **(B)** Uneven deformation in frozen section. **(C)** Uneven deformation in developed meadow areas.

TABLE 1 | Classification of permafrost by volume ice content.

Permafrost type	Ice-poor soil	Icy soil	Ice-rich soil	Saturated frozen soil	Ice layer interspersed with soil
Ice content (%)	<0.1	0.1–0.2	0.2–0.3	0.3–0.5	>0.5

Permafrost Type

The types of permafrost are the products of the comprehensive action of various natural conditions, reflecting the characteristics of seasonal thaw layer and permafrost, which are the main factor for subgrade design in the permafrost area. Some scholars take permafrost type and ground temperature as the main zoning index (Cheng and Wang, 1982). In addition, the stability of the subgrade in the permafrost region depends on the ice content of the permafrost under the roadway (Wen et al., 2009; Xu, 2014). In China, "Specifications for Design of Highway Subgrades" classifies permafrost according to the volume ice content, which can be divided into ice-poor soil, icy soil, ice-rich soil, saturated frozen soil, and ice layer interspersed with soil, as shown in **Table 1**.

Waterlogged Area Ratio

In the permafrost area, the permafrost layer hinders the infiltration of surface water. Combined with the low-lying terrain and poor drainage conditions, this often increases the water in the soil and forms the waterlogged areas in severe cases. However, the water on both sides of the road infiltrates into the subgrade, and with the freeze-thaw process, it is easy to form a thick pure ice layer inside the subgrade leading to disease problems (Mao et al., 2010). Furthermore, the upper soil layer in the waterlogged area is in an oversaturated state, which can lead to a reduction in its bearing capacity. The consolidation of the upper soil layer is a key factor causing the subgrade settlement. Therefore, it is necessary to pay attention to water accumulation along the road during the road design,

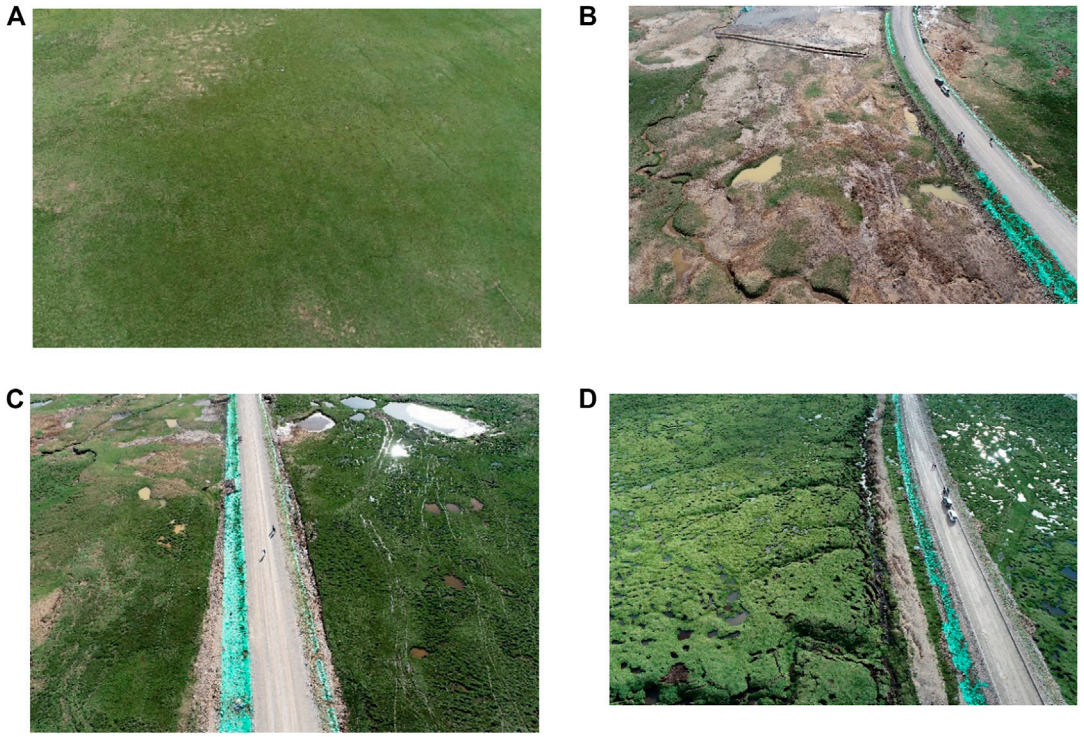

FIGURE 4 | Different waterlogged areas in permafrost wetlands along the road. **(A)** Almost no waterlogging. **(B)** Less waterlogging. **(C)** More waterlogging. **(D)** Severe waterlogging.

construction, and operation and set up drainage facilities or intercept facilities in advance.

Figure 4 shows different waterlogging conditions of wetlands along the road in the study area. It can be seen that the road crosses PWs with different waterlogging conditions. Moreover, the percentage of waterlogged areas is positively correlated with vegetation development; that is, the larger the percentage, the more developed the vegetation. The reason is that water can promote vegetation growth, which shows that the occurrence and development of surface vegetation, water, and permafrost are interdependent and mutually influential relationships. The waterlogging condition of the PWs was evaluated according to the percentage of waterlogged area n_s: almost no waterlogging (n_s <5%), less waterlogging (5% ≤ n_s <25%), more waterlogging (25% ≤ n_s <55%), and severe waterlogging (n_s ≥ 55%).

Meadow Development Degree

Vegetation has a significant influence on the hydrothermal processes of permafrost (Wu et al., 2003; Kelly et al., 2004), although the permafrost restricts the growth of some plants owing to low temperature, water isolation, and other restricts. For a long time, an ecological balance has been established between vegetation and permafrost, and vegetation is often used as an indicator of underlying permafrost and thawing soil (Chang et al., 2012). In this study, the meadow development degree is expressed by the thickness of vegetation h, measured from the top of vegetation to the bottom of grass root. According to the field survey findings, the meadow development degree can be divided into four cases: undeveloped (h < 8 cm), basically developed (8 cm ≤ h < 15 cm), developed (15 cm ≤ h < 40 cm), and fairly developed (h ≥ 40 cm), as shown in **Figure 5**. It can be seen that the more developed the meadow, the higher the ice content of the permafrost. This result indicates that the meadow development degree can be used as an indicator of the permafrost type on the Qinghai–Tibet Plateau wetlands.

Extraction of Waterlogged Areas

Based on the field survey and exploration data, the typical road sections with different permafrost types and waterlogged areas were selected. Then, aerial surveys are conducted on typical road sections to extract the waterlogged areas of specific areas.

The unmanned aerial vehicle (UAV) used for this study is a DJI Genie 4 pro v2.0 with a 20-megapixel FC6310 digital camera. The topographic data of the wetlands along the road are collected by shooting at an altitude of 60 m above the study area. The aerial photography area was a rectangle of 150 m on each side perpendicular to the roadbed centerline and 300 m along the roadbed centerline. In the flight, the ground resolution (GSD) of 1.64 cm/pixel was applied according to the requirements of 1:500 mapping scale. In order to get better results during the flight, the fore-and-aft overlap was set to 80% and the side overlap was set to 70% to facilitate image stitching and generation of elevation points.

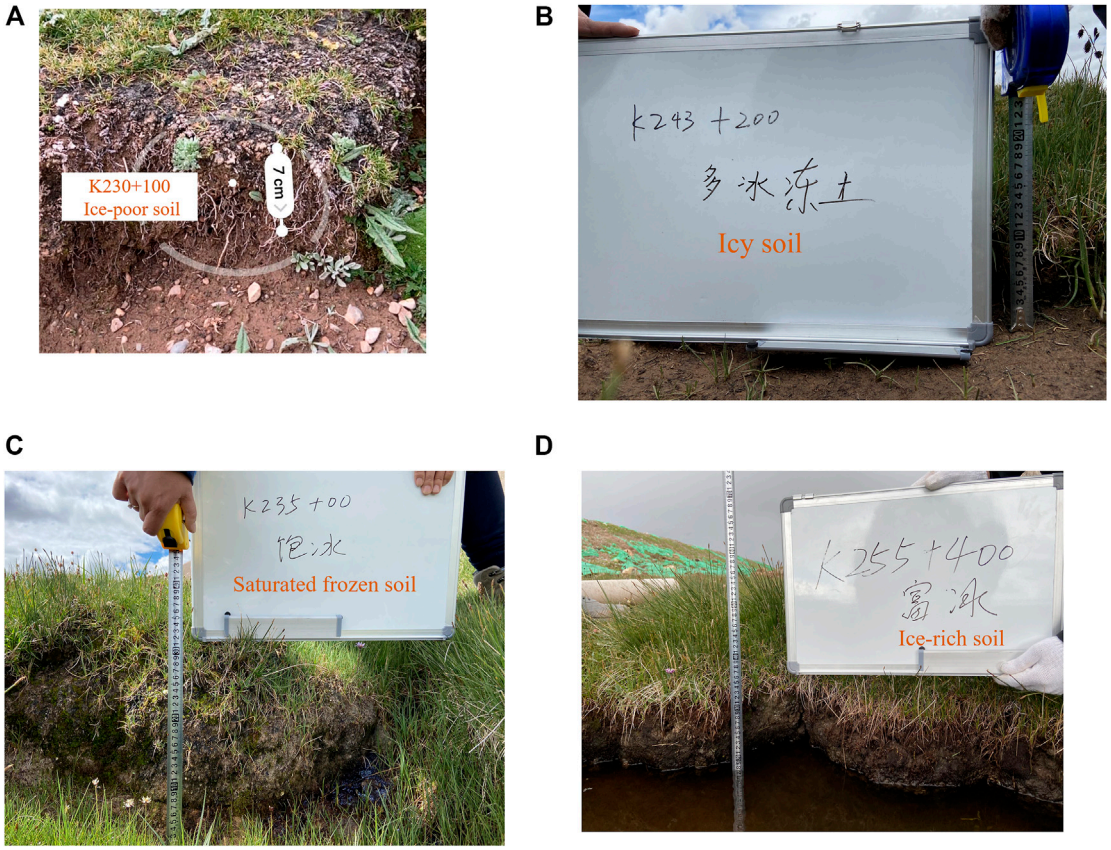

FIGURE 5 | Meadow development degree of different areas along the road. **(A)** Undeveloped (h = 7 cm). **(B)** Basically developed (h = 21 cm). **(C)** Developed (h = 39 cm). **(D)** Fairly developed (h = 55 cm).

The orthophotos taken by the UAV were calibrated by Global Mapper and then imported into Image-Pro Plus for micro-geomorphology extraction, as shown in **Figure 6**. The waterlogged area ratio n_s can be computed by the following equation:

$$n_s = \frac{\sum_{i=1}^{n} s_i}{s} = \frac{s_w}{s}, \quad (1)$$

where s_i is the area of a single waterlogged area, $i = 1, 2, \ldots, n$; n is the number of identified waterlogged areas; s is the total area of the selected area, m^2; s_w is the waterlogged area of the selected area, m^2.

The calculation of n_s is mainly done by extracting the micro-geomorphology from the actual captured 2D model images, identifying the waterlogged area in the specified area, and then counting the proportion of waterlogged area in the specific area. According to the image recognition results, the waterlogged area ratio near the typical road sections was calculated, as shown in **Table 2**. The analysis found a spatial correlation between the waterlogged area ratio and the type of permafrost. The larger the waterlogged area ratio, the higher the ice content of the underlying permafrost, which indicates that the waterlogged area ratio can be used as an indicator of different permafrost types.

Classification of Permafrost Wetlands

This classification system belonging to the small-scale classification model integrates the effect of permafrost, moisture, and vegetation on the engineering characteristics of permafrost wetlands. The permafrost wetlands are divided into 15 types using the three-level division, composed of the permafrost type, waterlogged area ratio, and meadow development degree, as shown in **Table 3**. The permafrost wetlands' characteristics are quantitatively reflected by a combination of letters and numbers. The first letter represents the classfication index, such as W represents the waterlogged area ratio, P represents the permafrost type, and M represents the meadow development degree. The numbers represent the development degree of each index. For waterlogged area ratio, 1~4 represent n_s<5%, 5%≤n_s <25%, 25%≤n_s<55% and n_s≥55%, respectively. For permafrost type, 1~5 represent ice-poor soil, icy soil, ice-rich soil, saturated frozen soil, and ice layer interspersed with soils, respectively. For meadow development degree, 1~4 represent h<8 cm, 8 cm≤ h<15 cm, 15 cm≤h<40 cm, and h≥ 40 cm, respectively. For example, W3 means the proportion of the waterlogged area is 25~55%, P4 means the permafrost type is saturated frozen soil,

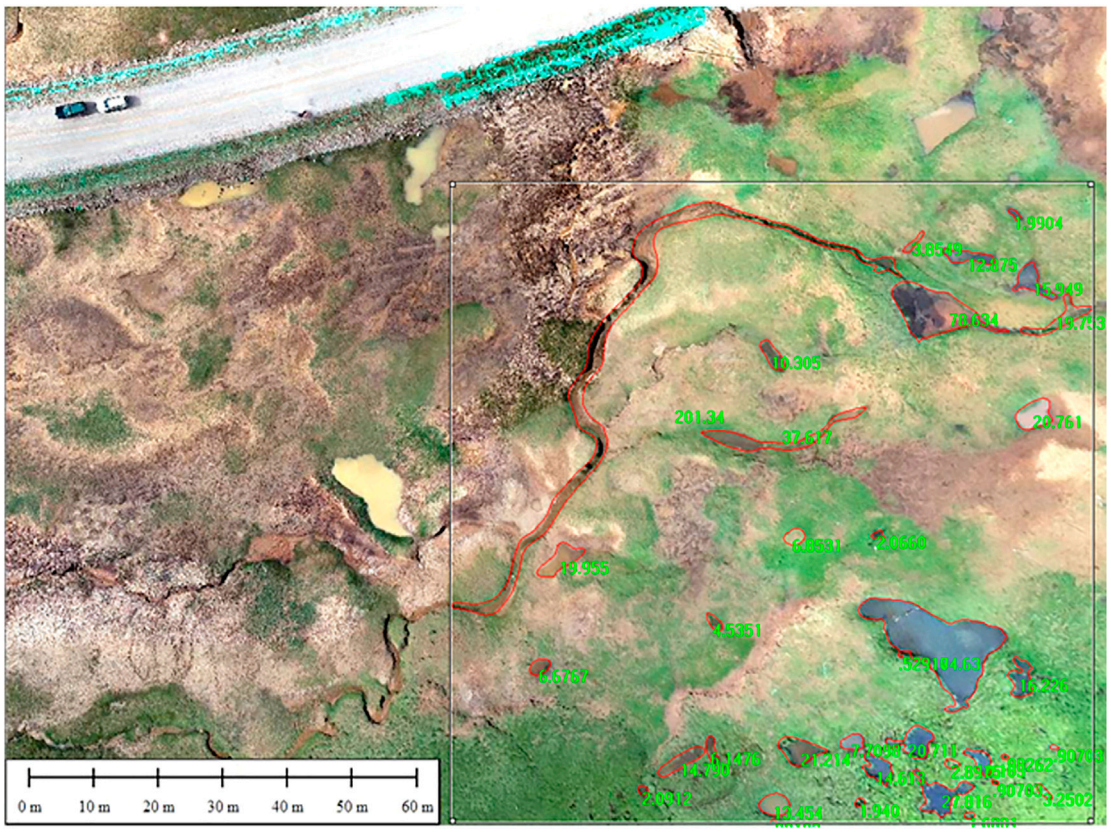

FIGURE 6 | Micro-geomorphological recognition of waterlogged areas.

TABLE 2 | Waterlogged area ratio of PWs near typical road sections.

Stake number	Permafrost type	Waterlogged area ratio n_s (%)	Evaluation results
K230 + 100	Ice-poor soil	2.34, 3.39	Almost no waterlogging
K227 + 400	Icy soil	4.15	Almost no waterlogging
K251 + 000	Icy soil	7.87	Less waterlogging
K251 + 185	Icy soil	18.45	Less waterlogging
K225 + 400	Ice-rich soil	30.13	More waterlogging
K255 + 400	Ice-rich soil	26.35	More waterlogging
K235 + 000	Saturated frozen soil	42.12, 56.35	More waterlogging/severe waterlogging
K228 + 400	Ice layer interspersed with soil	58.37	Severe waterlogging

and M3 means the degree of meadow development is 15~40 cm. Thus, W3-P4-M3 represents the permafrost wetlands having more waterlogging and the developed meadows, and the underlying permafrost is saturated frozen soil. The larger number indicates the greater degree of influence of a factor on the wetland's formation. Correspondingly, the more susceptible the permafrost wetlands are to weakness and less carrying capacity.

EVALUATION OF ENGINEERING STABILITY OF PERMAFROST WETLANDS BASED ON FUZZY THEORY

For evaluating the engineering stability of permafrost wetlands, the analytic hierarchy process (APH) and fuzzy comprehensive evaluation are applied to appropriately reduce the randomness of subjective judgment and improve the reliability of the evaluation results.

TABLE 3 | Classification of permafrost wetlands types.

Permafrost wetlands type	Waterlogged area ratio n_s (%)	Permafrost type	Meadow development degree h (cm)
W1-P1-M1	<5%	Ice-poor soil	<8
W1-P1-M2	<5%	Ice-poor soil	8–15
W1-P2-M1	<5%	Icy soil	<8
W1-P2-M2	<5%	Icy soil	8–15
W2-P1-M1	5–25%	Ice-poor soil	<8
W2-P1-M2	5–25%	Ice-poor soil	8–15
W2-P2-M1	5–25%	Icy soil	<8
W2-P2-M2	5–25%	Icy soil	8–15
W3-P3-M3	25–55%	Ice-rich soil	15–40
W3-P3-M4	25–55%	Ice-rich soil	>40
W3-P4-M3	25–55%	Saturated frozen soil	15–40
W3-P4-M4	25–55%	Saturated frozen soil	>40
W4-P4-M3	>55%	Saturated frozen soil	15–40
W4-P4-M4	>55%	Saturated frozen soil	>40
W4-P5-M4	>55%	Ice layer interspersed with soil	>40

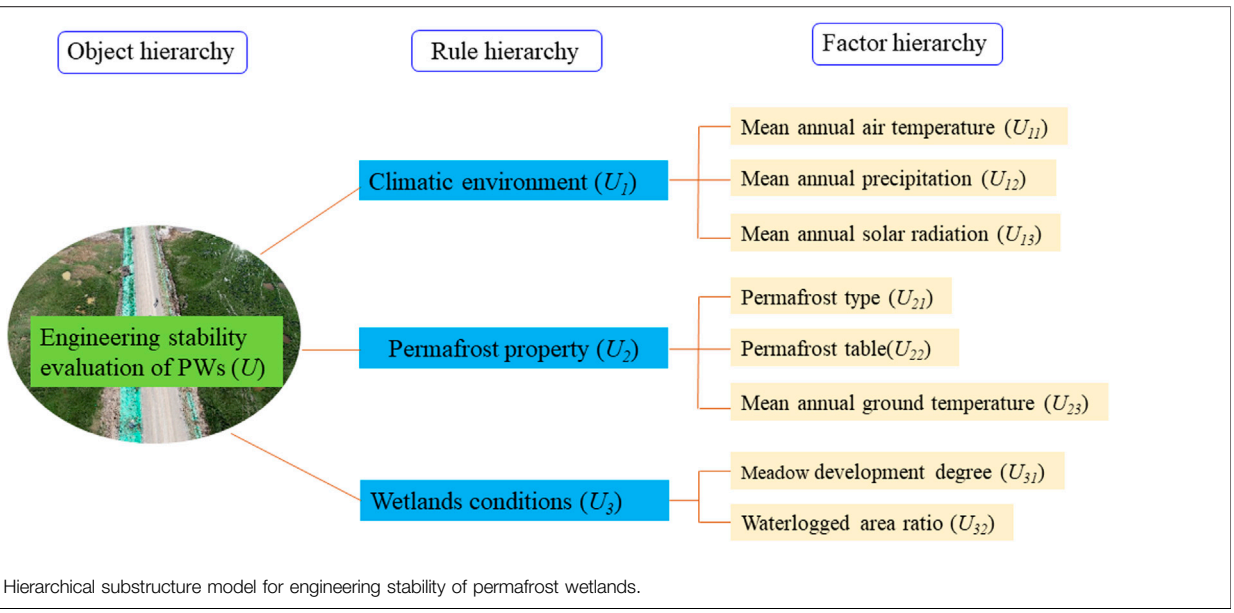

FIGURE 7 | Hierarchical substructure model for engineering stability of permafrost wetlands.

Construction of Index System of the Foundation Stability

The construction of the index system needs to meet the systematic, scientific, operable, and practical principles. Firstly, the index system can accurately and fully reflect the situation of the evaluation object through qualitative or quantitative methods. In addition, the difficulty of quantifying the indicators should be considered. It is required that the scoring methods and standards should be clear and easy to operate while ensuring that the evaluation results are as objective, comprehensive, and fair as possible. Based on the above analysis of factors affecting PWs formation, the hierarchical substructure model for PWs stability is established, as shown in **Figure 7**. This hierarchical substructure model consists of three levels: object hierarchy, rule hierarchy, and factor hierarchy. Rule hierarchy includes climatic environment, permafrost property, and wetlands conditions, controlled by the elements in factor hierarchy. The elements in the factor hierarchy are the evaluation indexes of the engineering stability for PWs.

Establishment of Fuzzy Comprehensive Evaluation Model

Determination of Weight

The reasonableness of weight determination directly affects the accuracy and scientificity of the evaluation results. Firstly, the judgment matrix should be established, which is the evaluation for objective factors. Each value in the matrix was marked by a number from 1 to 9 or its reciprocal and characterized the relative importance of each element. The larger the number, the more

important this factor is relative to other factors. Assume that A_i denotes the kth element in the rule hierarchy ($i = 1, 2, \ldots, n$), and the element in factor hierarchical is B_{ij} ($j = 1, 2, \ldots, m$). The relative importance of elements $B_{i1}, B_{i2}, \ldots, B_{im}$ is determined by pairwise comparison and is quantified as b_{lk} ($l = 1, 2, \ldots, m$; $k = 1, 2, \ldots, m$). The relative importance of each element is determined by an expert questionnaire survey. The judgment matrix can be expressed as

$$B_m = \begin{bmatrix} b_{11} & b_{12} & \cdots & b_{1m} \\ b_{21} & b_{22} & \cdots & b_{2m} \\ \vdots & \vdots & \ddots & \vdots \\ b_{m1} & b_{m2} & \cdots & b_{mm} \end{bmatrix}_{m\times m}, \quad (2)$$

where b_{lk} represents the importance of factor B_{il} relative to B_{ik} and b_{lk} is determined as

$$b_{lk} = \begin{cases} 1, l = k \\ 1/b_{kl}, l \neq k \end{cases}. \quad (3)$$

The judgment matrix is built to make the judgment process and conclusion mathematical and quantifiable. Then, the weight value of each factor is calculated based on the judgment matrix. The calculation steps are as follows:

First, the judgment matrix B_m is normalized to obtain matrix $\overline{B_m}$:

$$\overline{b_{lk}} = b_{lk} \Big/ \sum_{l=1}^{m} b_{lk}, l, k = 1, 2, \ldots, m. \quad (4)$$

And then, each line of the normalized matrix $\overline{B_m}$ is summed to obtain the vector $W = [W_1, W_2, \cdots, W_m]$:

$$W_i = \sum_{k=1}^{m} \overline{b_{lk}}. \quad (5)$$

The vector W is normalized to obtain the eigenvector vector $\bar{W} = [\overline{W_1}, \overline{W_2}, \cdots, \overline{W_m}]$:

$$\overline{W_i} = W_i \Big/ \sum_{i=1}^{m} W_i. \quad (6)$$

Finally, each value in the eigenvector vector $\bar{W}$ is the weight value of each factor.

Consistency Checking of the Judgment Matrix

The consistency checking of the judgment matrix is performed to ensure the rationality of weight value. The consistency index of the judgment matrix can be written as

$$CI = \frac{\lambda_{max} - m}{m - 1}, \quad (7)$$

where λ_{max} is the maximum eigenvalue and $\lambda_{max} = \frac{1}{m}\sum_{i=1}^{m} \frac{(B\bar{W})_i}{\overline{W_i}}$. m is the number of factors. Then, the consistence proportional factor CR is proposed for consistent checking, and the calculation formula is as follows:

$$CR = \frac{CI}{RI}, \quad (8)$$

where RI is the mean random consistency index, as shown in **Table 4**. When $CR < 0.1$, it indicates that the degree of inconsistency of judgment matrix B_m is within the allowed range and the weight value is reasonable. Thus, the weight value of factors can be applied in the stability evaluation calculations.

Establishment of Multi-Level Fuzzy Comprehensive Evaluation Model

The fuzzy comprehensive evaluation method belongs to the category of fuzzy mathematics. Based on the principle of affiliation of fuzzy mathematics, the qualitative problem is transformed into a quantitative problem to make an overall evaluation of the complex system. The steps are as follows:

(1) Determine the influencing factor set and evaluation set.

Assume that $U = \{U_1, U_2, \cdots, U_n\}$ is the influencing factors set of the object to be evaluated. $V = \{V_1, V_2, \cdots, V_m\}$ is the m evaluation levels describing the state of each factor.

(2) Construct the single factor evaluation matrix R.

The membership degree r_{ij} ($0 \le r_{ij} \le 1$) of each factor U_i ($i = 1, 2, \cdots, n$) to the evaluation level V_j ($j = 1, 2, \cdots, m$) was solved by membership function to form a single-factor evaluation matrix R as follows:

$$R = \begin{bmatrix} r_{11} & r_{12} & \cdots & r_{1m} \\ r_{21} & r_{22} & \cdots & r_{2m} \\ \vdots & \vdots & \ddots & \vdots \\ r_{n1} & r_{n2} & \cdots & r_{nm} \end{bmatrix}_{n\times m}. \quad (9)$$

In this study, the value limit of each factor evaluation can be uniformly expressed as $< v_1$, $v_1 \sim v_2$, $v_2 \sim v_3$, $> v_4$, and the membership functions are shown in the following equations:

$$r_{i1} = \begin{cases} 1 & x < v_1 \\ \dfrac{(v_1 + v_2) - 2x}{v_2 - v_1} & v_1 \le x < \dfrac{v_1 + v_2}{2} \\ 0 & x \ge \dfrac{v_1 + v_2}{2} \end{cases}, \quad (10)$$

$$r_{i2} = \begin{cases} 0 & x < v_1, x \ge \dfrac{v_2 + v_3}{2} \\ \dfrac{(v_1 + v_2) - 2x}{v_2 - v_1} & v_1 \le x < \dfrac{v_1 + v_2}{2} \\ \dfrac{(v_2 + v_3) - 2x}{v_3 - v_1} & \dfrac{v_1 + v_2}{2} \le x < \dfrac{v_2 + v_3}{2} \end{cases}, \quad (11)$$

$$r_{i3} = \begin{cases} 0 & x \ge v_3, x < \dfrac{v_2 + v_3}{2} \\ \dfrac{2x - (v_1 + v_2)}{v_3 - v_1} & \dfrac{v_1 + v_2}{2} \le x < \dfrac{v_2 + v_3}{2} \\ \dfrac{2(v_3 - x)}{v_3 - v_2} & x \ge \dfrac{v_2 + v_3}{2} \end{cases}, \quad (12)$$

TABLE 4 | Values of mean random consistency index *RI*.

m	1	2	3	4	5	6	7	8	9	10	11
RI	0	0	0.58	0.90	1.12	1.24	1.32	1.41	1.45	1.49	1.51

TABLE 5 | Evaluation standard for swamp wetland.

Stable level	Stable	Basically stable	Less stable	Unstable
Stability index	(87.5, 100]	(62.5, 87.5]	(37.5, 62.5]	(0, 37.5]

$$r_{i4} = \begin{cases} 0 & x < \dfrac{v_2 + v_3}{2} \\ \dfrac{2x - (v_2 + v_3)}{v_3 - v_2} & \dfrac{v_1 + v_2}{2} \le x < v_3 \\ 1 & x \ge v_3 \end{cases}. \quad (13)$$

(3) Determine the weight vector of evaluation factors.

In fuzzy evaluation, the weight vector $W = [w_1, w_2, \cdots, w_n]$ can be used to express the relative importance among the factors $U_i (i = 1, 2, \cdots, n)$ because

TABLE 6 | Evaluation standard for engineering stability of permafrost wetlands.

Rule hierarchy	Factor hierarchy	Stable	Basically stable	Less stable	Unstable
Climatic environment (U_1)	Mean annual air temperature/°C (U_{11})	<–4.5	–4.5 ~ –3.5	–3.5 ~ –2.5	>–2.5
	Mean annual precipitation/mm (U_{12})	<50	50–150	150–300	>300
	Mean annual solar radiation/MJ/m^2 (U_{13})	<5500	550–6,000	6,000–7,000	>7,000
Permafrost property (U_2)	Permafrost type (U_{21})	Ice-poor	Icy soil	Ice-rich soil	Saturated frozen soil
	Permafrost table/m (U_{22})	<1	1–3	3–5	>5
	Mean annual ground temperature/°C (U_{23})	<–2	–2 ~ –1	–0.5 ~ –1	>–0.5
Wetlands conditions (U_3)	Meadow development degree/cm (U_{31})	<8	8–15	15–40	>40
	Waterlogged area ratio (U_{32})	<5%	5–25%	25–55%	>55%

TABLE 7 | PWs type and permafrost property.

Stake number	Type of PWs	Waterlogged area ratio n_s/%	Meadow development degree *h*/cm	Permafrost type	Permafrost table/m	Mean annual air temperature/°C	Mean annual ground temperature/°C
k230 + 100	W1-M1-P1	3.39	7	Ice-poor soil (3.80%)	5.3	–4.1	–0.2
k255 + 400	W3-M4-P4	26.35	55	Ice-rich soil (16.41%)	1.5	–5.1	–0.4

TABLE 8 | Single factor evaluation matrix for factor set.

Rule set	Factor set	k230 + 100				k235 + 000			
		Stable	Basically stable	Less stable	Unstable	Stable	Basically stable	Less stable	Unstable
Climatic environment	Mean annual air temperature	0.2	0.8	0	0	1	0	0	0
	Mean annual precipitation	0	0	0	1	0	0	0	1
	Mean annual solar radiation	0	0.4	0.6	0	0	0.4	0.6	0
Permafrost property	Permafrost type	1	0	0	0	0.859	0.141	0	0
	Permafrost table	0	0	0	1	0.5	0.5	0	0
	Mean annual ground temperature	0	0	0	1	0	0	0	1
Wetlands conditions	Meadow development degree	1	0	0	0	0	0	0	1
	Waterlogged area ratio	1	0	0	0	0	0.55	0.45	0

TABLE 9 | Judgment matrix of evaluation index for rule set.

Index	Climatic environment	Permafrost property	Wetlands conditions
Climatic environment	1	2/3	1/2
Permafrost property	3/2	1	2/3
Wetlands conditions	2	3/2	1

Note: the consistency index for judgment matrix CR, *0.0008 < 0.1.*

TABLE 10 | Judgment matrix of climatic environment.

Index	Mean annual air temperature	Mean annual precipitation	Mean annual solar radiation
Mean annual air temperature	1	1/2	3
Mean annual precipitation	2	1	4
Mean annual solar radiation	1/3	1/4	1

Note: the consistency index for judgment matrix CR, *0.0091 < 0.1.*

TABLE 11 | Judgment matrix of permafrost property.

Index	Permafrost type	Permafrost table	Mean annual ground temperature
Permafrost type	1	2	1/2
Permafrost table	1/2	1	1/3
Mean annual ground temperature	2	3	1

Note: the consistency index for judgment matrix CR, *0.0046 < 0.1.*

TABLE 12 | Judgment matrix of wetlands conditions.

Index	Permafrost type	Permafrost table
Meadow development degree	1	1/2
Waterlogged area ratio	2	1

Note: the consistency index for judgment matrix CR, *0.*

different factors have different positions and different roles in the evaluation object. In this study, the weight of each factor is determined according to the AHP method described above.

(4) Single-level fuzzy comprehensive evaluation.

For the weight vector W and the single-factor judgment matrix R, the fuzzy operation $F = WR$ is performed:

$$F = WR = [w_1, w_2, \cdots, w_n] \begin{bmatrix} r_{11} & r_{12} & \cdots & r_{1m} \\ r_{21} & r_{22} & \cdots & r_{2m} \\ \vdots & \vdots & \ddots & \vdots \\ r_{n1} & r_{n2} & \cdots & r_{nm} \end{bmatrix}. \quad (14)$$

(5) Multi-level fuzzy comprehensive evaluation.

In this study, the index system has three levels: the object set U, the rule set U_i $(i = 1, 2, \cdots, n)$, and the factor set U_{ij} $(j = 1, 2, \cdots, k)$. Thus, a two-level fuzzy comprehensive evaluation is required to obtain the evaluation results of the object set U. The evaluation level $V = \{V_1, V_2, \cdots, V_m\}$ consists of m evaluation levels. For rule set U_i, the weight factor $W_i = [w_{i1}, w_{i2}, \cdots, w_{ik}]$ is introduced. For object set U, the weight factor $W = [w_1, w_2, \cdots, w_n]$ is introduced. According to the single-level fuzzy comprehensive evaluation method, the weight factor W_i and the single-factor judgment matrix R_i are subject to fuzzy operation $F_i = W_i R_i$ to obtain the secondary fuzzy comprehensive evaluation matrix $F = [F_1, F_2, \cdots, F_n]^T$. Then, the same fuzzy operation is applied on the weight factor W and the secondary fuzzy comprehensive evaluation matrix F:

$$P = WF = \{p_1, p_2, \cdots, p_n\}. \quad (15)$$

Evaluation of Engineering Stability of Permafrost Wetlands

The evaluation set V = {stable, basically stable, less stable, unstable} is established based on the engineering stability of permafrost wetlands in alpine and high-altitude areas. Further, quantify the evaluation set and assign the value to $V = \{100, 75, 50, 25\}$. In order to make the evaluation results easy to understand, the wetlands' stability grades are divided

TABLE 13 | Weight value of engineering stability of PWs.

Rule set	Weight *W*	Factor set	Weight W_i	Relative weight
Climatic environment	0.1638	Mean annual air temperature	0.3202	0.0524
		Mean annual precipitation	0.5572	0.0913
		Mean annual solar radiation	0.1226	0.0201
Permafrost property	0.2973	Permafrost type	0.2973	0.0884
		Permafrost table	0.1638	0.0487
		Mean annual ground temperature	0.5389	0.1602
Wetlands conditions	0.5389	Meadow development degree	0.3333	0.1796
		Waterlogged area ratio	0.6667	0.3593

TABLE 14 | Evaluation results.

Stake number	Type of PWs	Stable level	Evaluation results				Stability index
			Stable	Basically stable	Less stable	Unstable	
k230 + 100	W1- M1-P1	Basically stable	0.6378	0.1141	0.1082	0.1400	81.27
k255 + 400	W3-M4-P4	Less stable	0.1527	0.2424	0.1737	0.4311	52.92

by the stability index. The stability index is obtained by $Q = PV^T$. The larger the stability index, the more stable the wetlands. The range of stability index values corresponding to each level is shown in **Table 5**. In order to ensure the long-term stability of road engineering built on the permafrost wetlands, the underlying permafrost should be protected from degeneration first. Then, some measures should be taken to strengthen the foundation of wetlands due to the existence of the peat layer, which is symbiotic with vegetation.

Based on the field investigation, many references, and experts' opinions, the evaluation standards for the grading of each evaluation index in engineering stability of PWs are given in **Table 6**.

Case Study

The k230 + 100 and k255 + 400 are selected from the study's road—the Qinghai 224 highway—for the engineering stability evaluation of the permafrost wetlands. In this area, precipitation is mainly concentrated from late May to late September, accounting for more than 80% of the total annual precipitation. The annual average precipitation is 409 mm, the annual average evaporation is 1401.8 mm, and the annual solar radiation is about 6200 MJ/m^2 (Wang et al., 2015; Bao et al., 2017). The engineering stability of the wetlands passed through by the selected sections is evaluated. Meantime, the corresponding treatment measures are proposed. The type of wetlands and the property of permafrost are shown in **Table 7**.

The fuzzy evaluation method is used to evaluate the factors affecting the engineering stability of PWs. According to the above survey results and the calculation method for membership degree, the single factor evaluation matrix for each factor set is determined, as shown in **Table 8**.

The judgment matrix for each set can be determined by expert questionnaire survey and reference; refer to **Tables 9–12**. The weight value can be obtained by a judgment matrix to indicate the relative importance of each factor. The weight values are given in **Table 13**. According to the results obtained by the AHP method, the weight values of the climatic environment, permafrost property, and wetlands conditions are 0.1638, 0.2973, and 0.5389, respectively. In the factor set, the relative weights of waterlogged area ratio, meadow development degree, mean annual ground temperature, mean annual precipitation, and permafrost type are 0.3593, 0.1796, 0.1602, 0.0913, and 0.0884, respectively, and the impact on the engineering stability of PWs is reduced in turn.

Through the fuzzy comprehensive evaluation model, the evaluation results of PWs near the two stake numbers are obtained, as shown in **Table 14**. According to the stability index, the engineering stability of PWs near stake numbers k230 + 100 and k255 + 400 is basically stable and less stable, respectively. The area near stake number k230 + 100 belongs to the ice-poor soil area. Foundation soil has weak frost heaving and weak thawing characteristics. The surface was directly impacted by the impact compaction roller without removing the vegetation. Then, backfill the sand gravel to the original surface elevation. After settlement stabilization, fill the sand gravel to the bottom of the pavement layer. The area near stake number k255 + 400 belongs to the ice-rich soil area, with a wet and soft layer thickness of about 0.5 m. Due to its poor bearing characteristics, this layer was reinforced by riprap with a thickness of 0.5 m. Then, the impact compaction technology was applied to squeeze the silt out. Finally, the gravel with 1.0 m thickness was filled with heavy rolling. The engineering stability of the foundation has been enhanced after the treatments. Therefore, the fuzzy comprehensive evaluation model used to evaluate the engineering stability of permafrost wetlands has certain reliability.

CONCLUSION

In this study, the permafrost type, waterlogged area ratio, and meadow development degree were selected to quantify the engineering characteristics of permafrost wetlands. A three-level classification system was applied to classify the types of permafrost wetlands. Based on these analyses and field investigation, a fuzzy comprehensive evaluation model for engineering stability of permafrost wetlands was established, and a case study was conducted to verify the rationality of the evaluation model. The following conclusions can be drawn:

(1) Field investigation indicates that the permafrost layer and the wetlands constitute a symbiotic system on the Qinghai–Tibet Plateau. The permafrost layer facilitates the formation and development of wetlands due to the water isolation effect of the permafrost layer. Under the combined effect of permafrost, waterlogged area, and meadow development, the longitudinal cracks and the uneven deformation are the main forms of road diseases.
(2) The permafrost wetlands can be divided into 15 types using a three-level division considering the engineering characteristics. The permafrost type, meadow development degree, and waterlogged area ratio were selected as the classification indexes.
(3) According to the results obtained by the AHP method, the degree of impact on wetland stability is wetlands conditions > permafrost property > climatic environment, and the waterlogged area ratio, meadow development degree, mean annual ground temperature, mean annual precipitation, and permafrost type are the main factors that affect wetland stability.
(4) The method of combining AHP and fuzzy comprehensive evaluation can effectively evaluate the engineering stability of the permafrost wetlands and can be used to pre-evaluate the engineering stability of permafrost wetlands.

DATA AVAILABILITY STATEMENT

The raw data supporting the conclusions of this article will be made available by the authors without undue reservation.

AUTHOR CONTRIBUTIONS

XM and QW conceived this research. XM and LH contributed to conception and field investigation. WH and YZ contributed to data analysis and methodology. YZ wrote the first draft of the manuscript. All authors contributed to manuscript revision and read and approved the submitted version.

FUNDING

This research was supported by the reconstruction project of Qinghai Provincial Highway 224, the Annual Science and Technology Plan of Inner Mongolia Transportation Department–Research on Key Technologies of Island Frozen Soil Composite Foundation at High-Latitude and Low-Altitude, and the Science and Technology Project of Shaanxi Province (2021JQ-244).

REFERENCE

Anderson, J. E., Douglas, T. A., Barbato, R. A., Saari, S., Edwards, J. D., and Jones, R. M. (2019). Linking Vegetation Cover and Seasonal Thaw Depths in interior Alaska Permafrost Terrains Using Remote Sensing. *Remote Sensing Environ.* 233, 111363. doi:10.1016/j.rse.2019.111363

Bai, J. H., Ouyang, H., Xu, H. F., Zhou, C. P., and Gao, J. Q. (2004). Advances in Studies of Wetlands in Qinghai-Tibet Plateau. *Prog. Geogr.* 23 (04), 1–9. doi:10.11820/dlkxjz.2004.04.001

Bao, G. Y., Zhang, J., Zhou, D., Ma, S. C., and Liu, W. (2017). Analysis of the Spatiotemporal Characteristics of Solar Radiation Intensity in Qinghai Province. *J. Glaciology Geocryology* 03, 563–571. doi:10.7522/j.issn.1000-0240.2017.0063

Cannone, N., and Guglielmin, M. (2009). Influence of Vegetation on the Ground thermal Regime in continental Antarctica. *Geoderma* 151 (3-4), 215–223. doi:10.1016/j.geoderma.2009.04.007

Cao, W., Chen, J., Zhang, B., Wu, J. C., Li, J., and Sheng, Y. (2015). Fuzzy Evaluation of the Effect of Rubble Roadbed Engineering in Permafrost Regions along the Chaidaer-Muli Railway in Qinghai Province. *J. Glaciology Geocryology* 37 (6), 1555–1562. doi:10.7522/j.isnn.1000-0240.2015.0172

Chai, M. T., Zhang, J. M., Mu, Y. H., Liu, G., and Zhou, G. Q. (2017). Probability Model for Subgrade Hazards Susceptibility of Qinghai-Tibet Highway in Permafrost Regions. *J. Chang'an Univ. (Natural Sci. Edition)* 37 (04), 76–83. doi:10.19721/j.cnki.1671-8879.2017.04.010

Chang, X. L., Jin, H. J., Wang, Y. P., Zhou, G. Y., Che, F. Q., and Zhao, Y. M. (2012). Influences of Vegetation on Permafrost: a Review. *Acta Eco Sin* 32 (24), 7981–7990. doi:10.5846/stxb201202120181

Chang, Y. T., Chen, Z. D., Zhang, Z., and Chen, D. G. (2016). Analysis on Influencing Factors of Typical Subgrade Diseases of Qinghai Tibet Highway. *J. China Foreign Highw.* 01, 19–22. doi:10.14048/j.issn.1671-2579.2016.01.005

Chen, G. C., Huang, Z. W., Lu, X. F., and Peng, M. (2002). Characteristics of Wetland and its Conservation in the Qinghai Plateau. *J. Glaciology Geocryology* 03, 254–259. doi:10.3969/j.issn.1000-0240.2002.03.005

Cheng, G. D., and Wang, S. L. (1982). On the Zonation of High-Altitude Permafrost in China. *J. Glaciology Geocryology* 02, 1–17. http://www.bcdt.ac.cn/CN/Y1982/V4/I2/1.

Fedorov, A. N., Konstantinov, P. Y., Vasilyev, N. F., and Shestakova, A. A. (2019). The Influence of Boreal forest Dynamics on the Current State of Permafrost in Central Yakutia. *Polar Sci.* 22, 100483. doi:10.1016/j.polar.2019.100483

Guo, D. X., Ma, S. M., Ding, D. W., and Liu, J. R. (1992). *Translated*. Lanzhou, China: Lanzhou University Press, 96–131.

Han, L. W., Yang, Y. H., Dai, L. S., Zhang, F., and Cheng, J. (2018). Variation of Permafrost on Fill Embankments along Qinghai-Tibet Railway. *China Saf. Sci. J.* S2, 6–10. doi:10.16265/j.cnki.issn1003-3033.2018.S2.002

He, R. X., Jin, H. J., Lv, L. Z., Yu, S. P., Chang, X. L., et al. (2009). Recent Changes of Permafrost and Cold Regions Environments in the Northern Part of Northeastern China. *J. Glaciology Geocryology* 31 (03), 525–531. http://www.bcdt.ac.cn/CN/Y2009/V31/I3/524.

Huo, M., Chen, J. B., Zhu, D. P., and Zhang, J. Z. (2010). Study of Early Warning on Roadbed Diseases of Qinghai-Tibet Highway in Permafrost Regions. *Rock Soil Mech.* 31 (01), 331–336. doi:10.16285/j.rsm.2010.01.012

Iwahana, G., Fukuda, M., Kobayashi, Y., and Fedorow, A. N. (2003). "A Comparative Study of the Surface and Active Layer Conditions at Disturbed forest Site Near Yakutsk," in Proceedings of the 8th International Conference on Permafrost, London, June 16, 2003 (Taylor and Francis Group publication), 483–488.Vol. 1

Kelley, A. M., Epstein, H. E., and Walker, D. A. (2004). Role of Vegetation and Climate in Permafrost Active Layer Depth in Arctic Tundra of Northern Alaska and Canada. *J. Glaciology Geocryology* (s1), 269–274.

Kudelyacev, V. A., Garagulya, L. S., and Melamed, V. (1977). *Fundamentals of Frost Forecasting in Geological Engineering Investigations*. Nauka, Moscow: CRREL, Hanover, NH, 489.

Li, J. P., Wang, Z., Zhang, Y., and Yuan, K. (2015). Cause Analysis on Uneven Deformation of Embankment in Permafrost Regions. *China J. Highw. Transport* 28 (12), 78–85+91. doi:10.19721/j.cnki.1001-7372.2015.12.011

Li, L. X., Zhou, X. M., Wang, Q. J., and Zhou, Z. J. (1998). Jiangheyuan diqu de shidi jiqi zhuyao shengwu leiqun. *J. Qinghai Environ.* 8 (3), 108–114.

Liu, G. S., Wang, G. X., Hu, H. C., Li, T. B., Wang, J. F., et al. (2009). Influence of Vegetation Coverage on Water and Heat Processes of the Active Layer in Permafrost Regions of the Tibetan Plateau. *J. Glaciology Geocryology* 31 (001), 89–095. http://www.bcdt.ac.cn/CN/Y2009/V31/I1/89.

Liu, Z. W., Li, S. N., Wei, W., and Song, X. J. (2019). Research Progress on Alpine Wetland Changes and Driving Forces in Qinghai-Tibet Plateau during the Last Three Decades. *Chin. J. Ecol.* 03, 856–862. doi:10.13292/j.1000-4890.201903.002

Luo, D. L., Jin, H. J., Lin, L., He, R. X., Yang, S. Z., and Chang, X. L. (2012). Degradation of Permafrost and Cold-Environments on the Interior and Eastern Qinghai Plateau. *J. Glaciology Geocryology* 03, 538–546. http://www.bcdt.ac.cn/CN/Y2012/V34/I3/538.

Luo, X. -x., Ma, Q. -g., and Jiang, H. -q. (2021). Pre-evaluation on Stability of Proposed Expressway Embankment with Existing Geothermal Regulation Measures in Permafrost Regions. *J. Cent. South. Univ.* 28 (01), 264–283. doi:10.1007/S11771-021-4601-5

Mao, X. S., Hou, Z. J., Wang, W. N., and Lu, L. (2010). Formation Mechanism and Numerical Simulation of Longitudinal Cracks in Wetland Section of Qinghai-Tibet Highway. *Chin. J. Rock Mech. Eng.* 09, 1915–1921. http://rockmech.whrsm.ac.cn/CN/abstract/abstract26688.shtml.

Miao, J. L., Chen, X., Lv, Y. N., and Wang, D. Y. (2018). Prediction on Deformation and Reliability of Subgrade of Qinghai-Tibet Railway Based on BP Neural Network Method. *J. Nat. Disasters* 27 (04), 81–87. doi:10.13577/j.jnd.2018.0411

Mu, Y. H., Ma, W., Niu, F. J., Liu, G., and Zhang, Q. L. (2014). Study on Geotechnical Hazards to Roadway Engineering in Permafrost Regions. *J. Disaster Prev. Mitigation Eng.* 03, 259–267. doi:10.13409/j.cnki.jdpme.2014.03.005

Ni, J. R., Yin, K. Q., and Zhao, Z. J. (1998). Comprehensive Classification for Wetlands I. Classification. *J. od Nat. Resour.* 03, 22–29.

Niu, F., Gao, Z., Lin, Z., Luo, J., and Fan, X. (2019). Vegetation Influence on the Soil Hydrological Regime in Permafrost Regions of the Qinghai-Tibet Plateau, China. *Geoderma* 354, 113892. doi:10.1016/j.geoderma.2019.113892

Peng, H., Ma, W., Mu, Y. H., Jin, L., and Zhu, D. P. (2015). Analysis of Disease Investigation and Long-Term Deformation Characteristics of Common Fill Embankment of the Qinghai-Tibet Highway. *Rock Soil Mech.* 36 (07), 2049–2056. doi:10.16285/j.rsm.2015.07.029

Qi, C. Q., Wu, Q. B., Shi, B., and Tang, C. S. (2006). Reliability Analysis of Thawing Settlement of Permafrost Subgrade Based on Genetic Algorithm. *Rock Soil Mech.* 27 (08), 1429–1432+1436. doi:10.16285/j.rsm.2006.08.042

Qi, C. Q., Wu, Q. B., Shi, B., Wu, J. M., and Yu, J. (2007). Application of BP Neural Network on Deformation Prediction for Permafrost Embankment. *Hydrogeology Eng. Geology.* 34 (04), 27–30. doi:10.3969/j.issn.1000-3665.2007.04.008

Qi, J., Yao, X., Yu, F., and Liu, Y. (2012). Study on Thaw Consolidation of Permafrost under Roadway Embankment. *Cold Regions Sci. Technol.* 81, 48–54. doi:10.1016/j.coldregions.2012.04.007

Sheng, Y., Wu, J. C., Cao, W., Fang, J. H., Xu, A. H., and Peng, E. X. (2020). Characteristics and Changes of Permafrost along the Engineering Corridor of National Highway 214 in the Eastern Qinghai-Tibet Plateau. *Sci. Cold Arid Regions* 12 (6), 503–516. doi:10.3724/SP.J.1226.2020.00503

Sun, G. Y. (2000). Discussion on the Symbiotic Mechanisms of Swampy with Permafrost-Taking Da-Xiao Hinggan Mountains as Examples. *J. Glaciology Geocryology* 04, 309–316. doi:10.3969/j.issn.1000-0240.2000.04.003

Sun, G. Y., Jin, H. J., and Yu, S. P. (2008). The Symbiotic Models of Marshes and Permafrost – A Case Study in Daxing'an and Xiaoxing'an Mountain in Range. *Wetland Sci.* 04, 479–485. doi:10.13248/j.cnki.wetlandsci.2008.04.009

Sun, S. Y. (2003). Characteristic of Ecological Environment and its Protection along the Qinghai-Tibet Railway. *J. Glaciology Geocryology* S1, 181–185. doi:10.3969/j.issn.1000-0240.2003.z1.042

The Professional Standards Compilation Group of People's Republic of China (2015). *Specifications for Design of Highway Subgrades JTG D30-2015*. Beijing: People's Communications Press.

Wang, C. L., Zhang, Y. L., Wang, Z. F., and Bai, W. Q. (2010). Changes of Wetland Ecosystem Service Value in the Lhasa River Basin of Tibetan Plateau. *Resour. Sci.* 10, 2038–2044. http://www.resci.cn/CN/Y2010/V32/I10/2036.

Wang, C. T., Wang, Q. L., Jing, Z. C., Feng, B. F., Du, Y. G., et al. (2008). Vegetation Roots and Soil Physical and Chemical Characteristic Changes in Kobresia Pygmaca Meadow Under Different Grazing Gradients. *Acta Prataculturae Siniva* 17 (5), 9–15. doi:10.11686/cyxb20080502

Wang, S. J., Huo, M., and Zhou, W. J. (2004). Subgrade Failure of Qinghai-Tibet Highway in Permafrost Area. *Highway* 49 (05), 22–26. doi:10.3969/j.issn.0451-0712.2004.05.006

Wang, S. J., Wang, Z., Yuan, K., and Zhao, Y. G. (2015). Qinghai-Tibet Highway Engineering Geology in Permafrost Regions: Review and Prospect. *China J. Highw. Transport* 28 (12), 1–8+32. doi:10.19721/j.cnki.1001-7372.2015.12.001

Wang, Z. H., Huang, Z. F., Chen, Y., Xiao, H. B., and Guan, Q. (2015). Research on Variation of Solar Radiation over Yushu Region of Qinghai Province from 1961 to 2010. *J. Glaciology Geocryology* 03, 692–700. doi:10.4236/wjet.2015.33c010

Wen, Z., Sheng, Y., Wu, Q. B., Huang, B., Xu, A. H., and Li, H. Q. (2009). Ground Temperature and Deformation Laws of Highway Embankments in Degenerative Permafrost Regions. *Chin. J. Rock Mech. Eng.* 28 (07), 1477–1483. doi:10.3321/j.issn:1000-6915.2009.07.022

Wu, Q. B., Shen, Y. P., and Shi, B. (2003). Relationship between Frozen Soil Together with its Water-Heat Process and Ecological Environment in the Tibetan Plateau. *J. Glaciology Geocryology* 25 (03), 250–255. doi:10.3969/j.issn.1000-0240.2003.03.002

Xu, A. H. (2014). Analysis of the Sensitivity of Highway Diseases in Permafrost Regions to Ground Temperatures and Ice Contents. *J. Glaciology Geocryology* 36 (03), 622–625. doi:10.7522/j.issn.1000-0240.2014.007

Yang, K. F., Mu, Y. H., Bi, G. Q., Li, G. Y., and Chen, T. (2019). Recent Research Progress and Prospect of the South-And North-facing Slope Effect in the Roadway Engineering along the Qinghai-Tibet Engineering Corridor. *J. Disaster Prev. Mitigation Eng.* 39 (01), 180–190. doi:10.13409/j.cnki.jdpme.2019.01.02

Yu, F., Qi, J., Yao, X., and Liu, Y. (2013). *In-situ* Monitoring of Settlement at Different Layers under Embankments in Permafrost Regions on the Qinghai-Tibet Plateau. *Eng. Geology.* 160, 44–53. doi:10.1016/j.enggeo.2013.04.002

Zhang, Y., Wang, C., Bai, W., Wang, Z., Tu, Y., and Yangjaen, D. G. (2010). Alpine Wetlands in the Lhasa River Basin, China. *J. Geogr. Sci.* 20 (03), 375–388. doi:10.1007/s11442-010-0375-7

Zhao, H. T., Wu, Q. B., Zhang, Z. Q., and Huo, Y. D. (2019). Assessment of Cooling Effect of the Crushed Rock Embankment Based on Catastrophe Progression Method. *Chin. J. Rock Mech. Eng.* 38 (08), 1686–1695. doi:10.13722/j.cnki.jrme.2018.1273

Zhao, K. Y. (1999). *Zhongguo Zhaoze Zhi*. Beijing, China: Science press.

Conflict of Interest: LH was employed by the company Jiangsu Zhongshe Group Co., Ltd.

The remaining authors declare that the research was conducted in the absence of any commercial or financial relationships that could be construed as a potential conflict of interest.

Publisher's Note: All claims expressed in this article are solely those of the authors and do not necessarily represent those of their affiliated organizations or those of the publisher, the editors, and the reviewers. Any product that may be evaluated in this article, or claim that may be made by its manufacturer, is not guaranteed or endorsed by the publisher.

frontiers in Earth Science

ORIGINAL RESEARCH
published: 15 March 2022
doi: 10.3389/feart.2022.845824

Impacts of Permafrost Degradation on Hydrology and Vegetation in the Source Area of the Yellow River on Northeastern Qinghai-Tibet Plateau, Southwest China

Xiaoying Jin[1,2], Huijun Jin[1,2,3], Dongliang Luo[3], Yu Sheng[3], Qingbai Wu[3], Jichun Wu[3], Wenhui Wang[1], Shuai Huang[1], Xiaoying Li[4], Sihai Liang[5], Qingfeng Wang[3], Ruixia He[3], Raul D. Serban[3,6], Qiang Ma[3], Shuhui Gao[3,7] and Yan Li[3]*

[1]School of Civil Engineering, Northeast Forestry University, Harbin, China, [2]Institute of Cold Regions Science and Engineering, Northeast Forestry University, Harbin, China, [3]State Key Laboratory of Frozen Soils Engineering, Northwest Institute of Eco-Environment and Engineering, Chinese Academy of Sciences, Lanzhou, China, [4]School of Forestry, Northeast Forestry University, Harbin, China, [5]School of Water Resources and Environment, China University of Geosciences, Beijing, China, [6]Institute for Alpine Environment, Eurac Research, Bozen-Bolzano, Italy, [7]School of Civil Engineering, Lanzhou Jiaotong University, Lanzhou, China

OPEN ACCESS

Edited by:
Fahu Chen, Institute of Tibetan Plateau Research (CAS), China

Reviewed by:
Jing Luo, Northwest Institute of Eco-Environment and Resources (CAS), China
Zhanju Lin, Lanzhou Branch of Chinese Academy of Sciences, China

***Correspondence:**
Huijun Jin
hjjin@lzb.ac.cn

Specialty section:
This article was submitted to Cryospheric Sciences, a section of the journal Frontiers in Earth Science

Received: *30 December 2021*
Accepted: *31 January 2022*
Published: *15 March 2022*

Citation:
Jin X, Jin H, Luo D, Sheng Y, Wu Q, Wu J, Wang W, Huang S, Li X, Liang S, Wang Q, He R, Serban RD, Ma Q, Gao S and Li Y (2022) Impacts of Permafrost Degradation on Hydrology and Vegetation in the Source Area of the Yellow River on Northeastern Qinghai-Tibet Plateau, Southwest China. Front. Earth Sci. 10:845824. doi: 10.3389/feart.2022.845824

Under a persistent warming climate and increasing human activities, permafrost in the Source Area of the Yellow River (SAYR) has been degrading regionally, resulting in many eco-environmental problems. This paper reviews the changes in air temperature and precipitation over the past 60 years and presents the distribution and degradation of alpine permafrost in the SAYR. The review is focused on the permafrost degradation–induced changes in hydrology, wetlands, thermokarst lakes, ponds, and vegetation. Mean annual air temperatures have been rising at an average rate of 0.4°C/10a over the past 60 years, while precipitation has increased only slightly (16 mm/10a). Borehole temperature monitoring at the depth of 15 m shows the permafrost warming rates of 0.01–0.21°C/10a in the Headwater Aera of the Yellow River. As a result of permafrost thaw, the amount of surface waters has declined while groundwater storage has increased. Due to permafrost degradation, the supra-permafrost water table lowers gradually, resulting in a reduction in areal extents of wetlands and lakes in the SAYR. We further renamed the concept of the burial depth of the ecologically-safe supra-permafrost water table, the minimum depth of the groundwater table for sustaining the normal growth of alpine grassland vegetation, for the SAYR to describe the relationship between the lowering permafrost table and succeeding alpine vegetation. Furthermore, we recommended more studies focusing on snow cover and carbon stock and emissions related to permafrost degradation under a warming climate. We also advised to timely establish the long-term monitoring networks for the rapidly changing mountain cryosphere, alpine ecology, alpine hydrology, eco-hydrology, cryo-hydrogeology, and carbon fluxes. Moreover, process-based models should be developed and improved to better simulate and predict the responses of alpine ecosystem changes to the interacting cryospheric and other environmental variables and their ecological and ecohydrological impacts in the SAYR and downstream Yellow River basins. This study can help better manage the ecological

and hydrological environments in the Upper Yellow River that are sensitive to changes in the alpine climate and cryosphere.

Keywords: permafrost degradation, ecological impacts, alpine permafrost ecosystems, burial depth of ecologically-safe groundwater table, source area of the Yellow River

INTRODUCTION

Observations from meteorological stations and results from simulations have demonstrated that the climate is warming and this warming will continue (Intergovernmental Panel of Climate Change (IPCC), 2014), with enlarged amplitudes at higher elevations (Pepin et al., 2015). The climate warming has produced changes to the cryosphere, including alpine permafrost (Haeberli, 2013; Zhao et al., 2020). The Qinghai-Tibet Plateau, with an average elevation of more than 4,000 m, has 70% of the world's elevational permafrost, which is warm and sensitive to climate warming (Jin et al., 2000; Yang et al., 2010; Bockheim 2015). Permafrost thawing on the Qinghai-Tibet Plateau has produced changes to the alpine environment, including the dynamics of hydrological and ecological conditions and other physical, chemical, and biogeochemical processes (Yang et al., 2010; Latif et al., 2019). Understanding the ecological impacts of the climate-induced permafrost degradation is essential for predicting changes in ecosystem, as well as for the development and implementation of management action plans for alpine ecosystems (Wrona et al., 2016; Zhao et al., 2020).

The Source Area of the Yellow River (SAYR) above the Tanag (35°30′N, 100°09′E; 2,691 m a. s. l), with a catchment area of 123,690 km^2 in Qinghai Province, China, is on the northeastern Qinghai-Tibet Plateau (**Figure 1**). As an important part of China's Water Towers, the SAYR provides approximately 38% of the total annual runoff of the Yellow River (Wu et al., 2018). It is characterized by the world's richest biodiversity of alpine grasslands and is one of the core areas of the recently established Sanjiangyuan (The Source Area of the Three Rivers: Yellow, Yangtze and Lancang-Mekong) National Park as well (He et al., 2021). However, the alpine ecosystem here is sensitive and fragile to external disturbances associated with climate changes and human activities (Wang et al., 2001; Yuan et al., 2021).

Since the 1950s, the SAYR has undergone significant warming and this warming will continue in coupling with more and frequent extreme weather events (Wang et al., 2021). Permafrost in the SAYR is warm (≥−1°C) and discontinuous (<90% in areal extent of permafrost), and occupies an areal extent of 25,000 km^2, or 85%, of the areal extent of the SAYR above the Tanag hydrological station, Qinghai Province, China (Li J. et al., 2016; Sheng et al., 2020; Cao H. et al., 2021). Since the 1990s, under the dual influence of a warming climate and anthropogenic activities, permafrost has been degrading, as typically evidenced by decreases in permafrost extent, increases in the active layer thickness (ALT), warming of the ground, and melting of ground ice (Jin et al., 2000; Jin et al., 2009; Luo et al., 2020a; Sheng et al., 2020). These changes have induced a series of ecological and environmental problems, such as the lowered water table, blackened soil spots, and reduced near-surface water resources (Jin et al., 2009). Consequently, the ecological successions from alpine paludal meadows to alpine steppes and deserts are always

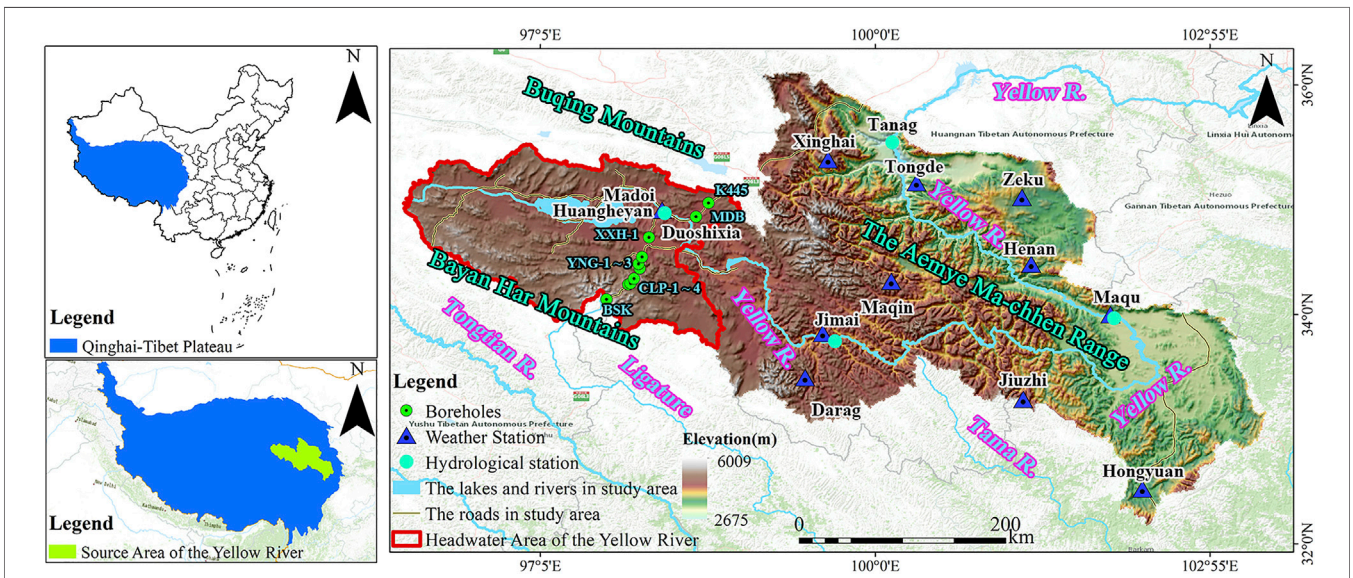

FIGURE 1 | Location, mountains and water systems of the Source Area of the Yellow River on the northeastern Qinghai-Tibet Plateau in Southwest China.

TABLE 1 | Climate changes at the meteorological stations scale in the Source Area of the Yellow River on the northeastern Qinghai-Tibet Plateau in Southwest China from 1961 to 2020.

Meteorological station	Longitude (°E)	Latitude (°N)	Elevation (m.a.s l)	Multi-year average of mean annual air temperature (MAAT,°C)	Changing trend for MAAT (°C/10a)	Multi-year average of annual precipitation (AP in mm)	Changing trend for AP (mm/10a)
Madoi	98.13	34.55	4,272.3	−3.5	0.4*	328.2	16.0*
Maqin	100.14	34.29	3,719.0	−0.1	0.4*	521.9	8.0
Darag	99.39	33.45	3,967.5	−0.6	0.4*	560.3	9.8
Banma	100.45	32.56	3,530.0	3.0	0.3*	663.7	4.8
Jiuzhi	101.29	33.26	3,628.5	0.9	0.4*	759.2	0
Hongyuan	102.33	32.48	3,491.6	1.7	0.3*	763.2	9.0
Maqu	102.05	34.00	3,471.4	1.8	0.4*	611.5	6.5
He'nan	101.36	34.44	3,500.0	0.4	0.0	586.8	−6.1
Zeku	101.28	35.02	366.3	−1.6	0.5*	487.0	13.6*
Tongde	100.36	35.15	3,148.2	1.5	0.8*	444.0	12.7
Xinghai	99.59	35.35	3,323.2	1.5	0.3*	372.7	15.0

*Note: Multi-year averaged of mean annual air temperature and multi-year average of annual precipitation were obtained from the average/sum of monthly data. All data were from 1961 to 2020, except data from He'nan meteorological station, which was from 1967 to 2020. Linear fitting was used to obtain the trend for mean annual air temperature and annual precipitation. The symbol of asterisk * indicates a significant trend at 0.05 level.*

coupled with grassland degradation and desertification, shrinkage of wetlands and lakes, and drying up of some rivers (Wang et al., 2011; Yuan et al., 2021).

There is a growing recognition that environmental changes associated with permafrost degradation may have profound implications for alpine grasslands (Wang et al., 2001; Jin et al., 2009; Wang et al., 2019; Jin et al., 2020; Jin X.-Y. et al., 2021). With the accelerated degradation of alpine permafrost in the SAYR, its eco-environment degradation and the causation have been given much attention and have been lively discussed (e.g., Feng et al., 2006; Qin et al., 2017; Cao H. et al., 2021). However, responses and feedbacks of alpine ecosystems to a warming climate and subsequently degrading permafrost remain poorly understood in the SAYR. Systematic data are needed to understand the responses of hydrological conditions and alpine grasslands to climate change, permafrost degradation, and human intervention in order to better interpret and predict the feedback between climate warming and alpine ecosystems (Cao et al., 2003; Li et al., 2008; Jin et al., 2009; Jin et al., 2020; Jin X.-Y. et al., 2021).

The multi-year average of mean annual air temperature ranges from −3.5°C at Madoi meteorological station to 1.8°C at Maqu meteorological station, and it decreases with the rising elevation. In our study, meteorological data were obtained from the National Meteorological Information Centre (http://data.cma.cn/). Air temperature in the SAYR has been rising during the last 6 decades. During 1961–2020, the mean annual air temperature over the SAYR increased at a rate of 0.4°C/10a, and the increasing rate did not show a clear elevational trend (**Table 1**). In addition, mean annual maximum and minimum air temperatures rose in a fluctuating way at a rate of 0.3 and 0.4°C/10a, respectively (Liu et al., 2021). The rise in the mean annual minimum temperature was the most prominent in winter, resulting in a rising mean annual air temperature (Hu et al., 2012; Luo et al., 2016). The patterns of air temperature rise in the SAYR display strong spatial heterogeneity. The overall rising in air temperature was generally slower in the west than that in the east (Iqbal et al., 2018; Liu et al., 2021).

Unlike the rapidly-rising air temperature, regional average of annual precipitation in the SAYR was 554.4 mm (**Table 1**). Annual precipitation in the SAYR was increasing, but only that at Madio and Zeku slightly increased at a rate of 16 and 13.6 mm/10a, respectively. Seasonally, precipitation increased markedly in spring (47 mm/10a), summer (15 mm/10a), and winter (12 mm/10a), while it declined slightly in autumn (−0.5 mm/10a) (Li Q. et al., 2016; Liu et al., 2021). Spatially, precipitation increased significantly in the northwestern SAYR (Tian et al., 2015). In summary, the climate in the SAYR has exhibited a warming-wetting trend and the extreme weather events have become more frequent (Han et al., 2018; Jiang et al., 2019).

Our research groups have conducted many field surveys and investigations, mapping, and long-term observations of permafrost ecology and hydrology in the SAYR. Here, based on our findings and other research results, we have systemically reviewed the impacts of permafrost degradation on hydrology and plant ecology in the SAYR. We have summarized the changes in climate and permafrost, and we have focused on the alterations and interactions in hydrological regimes and vegetation succession. Finally, research priorities are identified. This study helps provide scientific support for the land, water, ecological management, and establishment of the Sanjiangyuan National Park.

DISTRIBUTION AND DEGRADATION OF PERMAFROST

The distribution of permafrost in the SAYR is mainly controlled by elevation, as well as local environmental variables, such as topography, surface vegetation, water bodies, soil texture, and

TABLE 2 | Frozen ground temperatures in boreholes along the National Highway G214 in the Headwater Area of the Yellow River on the northeastern Qinghai-Tibet Plateau in Southwest China during 2010–2016 (modified from Luo et al., 2018).

Boreholes	Longitude (°E)	Latitude (°N)	Elevation (m a. s l)	Mean annual Ground temperature (MAGT, °C)	Average change rate of MAGT (°C/a)	Vegetation type
BSK	97.66	34.13	4,833	–1.60	–0.016	Alpine marsh meadow
CLP-1	97.85	34.26	4,721	–1.74	0014	Alpine marsh meadow
CLP-2	97.85	34.26	4,724	–1.66	0.0027	Alpine marsh meadow
CLP-3	97.87	34.27	4,663	–1.13	0.0091	Alpine meadow
CLP-4	97.90	34.31	4,564	–0.60	0.0194	Alpine meadow
YNG-1	97.95	34.40	4,446	–0.10	0.0014	Alpine meadow
YNG-2	97.94	34.44	4,395	1.23	0.017	Alpine steppe
YNG-3	97.97	34.50	4,324	1.09	0.028	Alpine steppe
XXH-1	98.03	34.67	4,221	0.90	0.19	Alpine marsh meadow
MDB	98.44	34.85	4,225	–0.66	0.0071	Alpine steppe
K445	98.55	34.97	4,282	–0.93	0.014	Alpine steppe

Notes: Borehole data are from July 2010 to September 2017, and those for boreholes YNG-2 and YNG-3 are from July 2010 to December 2016. MAGT is generally measured at 15 m in depth.

snow-cover regime (Li J. et al., 2016; Luo et al., 2018). Simulations have shown that permafrost zones, seasonal frost zone, and other land types (rivers, reservoirs, and others) comprise approximately 85.1% (2.53×10^4 km^2), 9.7% (0.3×10^4 km^2), and 5.2% of the Headwater Area of the Yellow River (HAYR), and upstream of Duoshixia (Stony Gorge), respectively, (Li J. et al., 2016). The central HAYR around the Sisters' Lakes (Gyaring and Ngöring lakes) (4,250–4,350 m. a. s. l) is found in the vicinity of the lower limit of alpine permafrost, and;alpine permafrost there is on the verge of thawing (Jin et al., 2009; Sheng et al., 2020). Above 4,250 m. a. s. l on north-facing slopes, permafrost generally develops better while there is generally no permafrost on south-facing slopes (Li J. et al., 2016). Permafrost begins to occur on all slopes above 4,350–4,500 m. a. s. l. (Jin et al., 2009). The lower limit of alpine permafrost on south-facing slopes is at least 100 m higher than that on north-facing slopes.

According to the data of ground temperatures measured in boreholes, the thickness of permafrost in the HAYR is generally less than 40 m, and the thickest measured permafrost is 74 m, as observed in the Chalaping boreholes near the National Highway G214 on the north-facing slope of the Bayan Har Mountains. Ground temperatures at the depth of zero annual amplitude are generally higher than −2°C, and the regional average of the ALT in the HAYR is 2.3 m (Luo et al., 2014; Luo et al., 2018; Wang et al., 2019). The total storage of ground ice is 51.68 ± 18.81 km^3 at depths of 3.0–10.0 m in permafrost based on the data of landform types, lithology, and soil moisture content (Wang S. et al., 2018). Generally, on the Qinghai-Tibet Plateau ground ice is stored at depths close to the permafrost table and declines downwards with increasing depth.

Many studies have shown a degrading permafrost in the SAYR, which has been accelerating since the 1990s (e.g., Jin et al., 2000; Jin et al., 2009). The simulation results have shown a reduction in the areal extent of permafrost from 2.4×10^4 km^2 in 1980 to 2.2×10^4 km^2 in 2016 (Luo et al., 2014). Model reconstruction results have shown a decline in permafrost extent by 1,056 km^2 from 1972 to 2012 and will decline by 2,224, 2,347, and 2,559 km^2 (accounting for 7.5%, 7.9%, and 8.6% of the current total permafrost extent in the SAYR) under the climate warming scenarios of RCP2.6, RCP6.0, and RCP8.5, respectively, by 2050 (Sheng et al., 2020).

Ground temperatures, including mean ground surface temperature and mean annual ground temperature (MAGT), are rising and the active layer is thickening in the SAYR (Luo et al., 2018; Qin et al., 2020). According to the data measured at meteorological stations and observational sites from 2010 to 2016, the regional average of mean annual ground surface temperature in the SAYR increased by 1.1°C/10a, and that of MAGT by 0.01–0.21°C/10a (**Table 2**) (Luo et al., 2018; Luo et al., 2020b). Temperature of warm permafrost (MAGT≥ −1°C) increased significantly, accompanied by the recent disappearance of permafrost with the temperature of 0.5°C, while the warming trends were relatively high for permafrost located in the open terrains with dense vegetation (Luo et al., 2018). In addition, model simulation results of the temperature at the top of permafrost (TTOP) based on the Stefan equation showed that the ALT in the HAYR increased at an average rate of 34.7 cm/10a from 1980 to 2018, while the maximum depth of seasonal frost penetration decreased at an average rate of 9.3 cm/10a (Wang R. et al., 2020). More recently, the maximum seasonal frost depth decreased at a rate of 3.1–7.0 cm/10a from 2003 to 2015 (Gao B. et al., 2020) and the most significant declines occurred in the transitional zone between permafrost and seasonal frost (Wang et al., 2019).

ECOLOGICAL IMPACTS OF PERMAFROST DEGRADATION

Hydrological Regimes

As an aquitard, permafrost weakens the downward infiltration from precipitation, glacier, and snow-cover melt-water and raises the supra-permafrost water table, influencing the streamflow and soil water content in the active layer. Surface waters and near-

surface soil water availability are important for the growth and survival of alpine vegetation (Li et al., 2020a; Cao W. et al., 2021). Meanwhile, the melting of ground ice could release more water to soil, impacting the groundwater and the water cycle at a local scale, and even at a regional and global scale (Walvoord and Kurylyk, 2016; Schuur and Mack, 2018; Yang et al., 2019). Permafrost degradation has significant implications on alpine ecosystems through alterations in soil hydrological regimes (Wrona et al., 2016; Zhao et al., 2020). Coupled with lowering permafrost table and thickening active layer, regional permafrost degradation may result in lowering supra-permafrost water table and declining water-holding capacity of near-surface soils in the aeration zone (Jin X.-Y. et al., 2021; Jin H.-J. et al., 2021; Lv et al., 2022). As a result, the capillary water cannot move upward to the shallower soil layer where the roots of herbaceous and aquatic plants concentrate. Thus, near-surface soil could salinize by the enhanced evaporation, thereby restricting the growth of most vegetation (Wang et al., 2006; Qin et al., 2017; Sun et al., 2020).

Water resources in the SAYR are mainly recharged by precipitation, snow- and ice-melt, and groundwater of various types. Under a warming climate with permafrost degradation, mean annual evaporation increased and surface runoff have decreased (Lan et al., 2013; Wu et al., 2018; Yan et al., 2020). The mean annual runoff volume was approximately 2.02×10^{10} m^3 and decreased by 5.5×10^9 m^3 from 1960 to 2007 as recorded at the Tanag and/or Jimai hydrological stations, mainly due to the reduced runoff from mid-June to late October, i.e., the growth season (Wang T. et al., 2018; Wu et al., 2018). However, for the entire SAYR, the annual runoff exhibited a decreasing trend (6.51 mm/10a), while the annual precipitation increased (6.48 mm/10a), suggesting that other factors may influence the change trend of runoff, such as the potential evapotranspiration and more importantly permafrost degradation (Wang T. et al., 2018). The analysis of stable isotopes (δ^{18}O and δD) in a representative watershed of the HAYR show a contribution ratio of precipitation of the surface runoff at 52.2–53.5% and that of ground ice melting at 13.2–16.7% (Ma et al., 2019; Yang et al., 2019). Water from melted ground ice directly contributes approximately 4.8% to the annual runoff of the Yellow River in of the SAYR, whereas the recharge from melted ground ice cannot completely offset the increase in land surface evapotranspiration under a persistently warming climate, hence resulting in a decrease in surface runoff, but otherwise an increase in groundwater storage ($11.4 \pm 13.9 \times 10^8$ m^3/a from 2003 to 2009) (Xiang et al., 2016; Lin et al., 2019). However, little is known about the moving trajectories of water from ice melting, total volume water from the melting ground ice, and the magnitudes of melt-water of this ground ice to contribute to surface and subsurface water.

According to the observations in the past 30 years, the local groundwater table in the Yellow River valley plain near the Madoi county town continuously lowered by 0.8–1.5 m, with a maximum lowering decreased depth of 1.8 m, with an average annual lowering rate of approximately 0.5 m/10a (Cheng and Jin, 2013). In the meantime, this lowering groundwater table may also be associated with good soil drainage due to a high percentage of sandy and gravely constituents of soil texture (Gao et al., 2018; Lv et al., 2022). According to the model results of the percentage reduction of the single-spring runoff modulus, the recharge amount of the supra-permafrost water in the SAYR decreased by 15×10^8 m^3 during the 14 years from 1989 to 2003, with an average annual decrease rate of 1.1×10^7 m^3/a (Jin et al., 2009; Cheng and Jin, 2013). Together with a slight wetting and an enhanced evapotranspiration, the sharp decrease in recharge to the supra-permafrost layer resulted in a lower level of the supra-permafrost water table, thus causing water tables in the HAYR to continuously decline (Wang T. et al., 2018; Wu et al., 2018).

Although the melting of ground ice may replenish water resources and increase the total groundwater storage—though probably at a very limited magnitude or rate— warming climate, increasing evaporation, and changing land surface processes have reduced runoff generation, resulting in a lower groundwater table (Wu et al., 2018; Lin et al., 2019; Sun et al., 2020). The main source of soil water is precipitation and with the continuous temperature rise, the evaporation of soil water increases, while the annual precipitation has been fluctuating with a minor increase trend of 16 mm/10a (Qin et al., 2017; Xie et al., 2021). As a result, near-surface soil moisture, the key to maintaining the long-term growth of herbaceous plants, is depleting continuously and is on the decline. As a result, the regional water table lowers as well. In arid regions on the Qinghai-Tibet Plateau, this kind of groundwater table for sustaining the long-term growth of herbaceous plants is called the "the burial-depth of ecologically safe groundwater table" (Liang et al., 2007; Wang et al., 2012). In permafrost regions, we can thus rename it as the "burial-depth of ecologically safe supra-permafrost table" (BESST).

Field surveys have found that the deepening permafrost table leads to a lowering BESST (Wang et al., 2006; Yang et al., 2013). When the groundwater table is less than 2 m, soil water content may suffice plant growth and accordingly maintain high vegetation cover (Wang et al., 2012; Jin et al., 2020). When the burial depth of groundwater table is lower than 2 m, most of alpine plants with a shallow root system suffer the drought stress, and only a few types of drought-tolerant plants with well-developed root systems may access the limited available soil water for survival (Jin et al., 2020). Therefore, the vegetation coverage decreases. When the burial depth of the groundwater table is greater than 5 m, herbaceous plants often wither and eventually die from drought and only shrubs with deep roots can be occasionally observed (Wang et al., 2006). This indicates that changes or variations in the permafrost table control the BESST and the unfrozen water content of near-surface soils, thereby affecting the growth of plants (Wang et al., 2012). In cold and arid regions, a burial depth of 2 m of the groundwater table can thus be regarded as the threshold of the ecologically safe groundwater table (Liang et al., 2007; Wang et al., 2012), or the BESST. At a BESST deeper than 2 m and with slow replenishment by surface water infiltration, the capillary water cannot rise to the shallow soil layer, where the roots of most plants are concentratively distributed, so most plants are subjected to long-term drought stress from the growth environment, leading adverse successions and perpetual degradation of alpine grasslands (Liang et al., 2007; Li et al.,

2020a; Li et al., 2020b; Jin X.-Y. et al., 2021, Jin H.-J. et al., 2021). However, the mechanisms for this depth control of the alpine vegetation growth remains poorly understood.

Shrinking of Wetlands and Lakes

As an aquitard, permafrost help enrich soil water above the bottom of the active layer or above the permafrost table in the presence of the supra-permafrost subaerial talik, which increases evaporation and runoff, but reduces downward infiltration, thus favoring the formation of thermokarst lakes and ponds, shallow rivers, and wetlands in lowlands (Walvoord and Kurylyk, 2016; Schuur and Mack, 2018). There are numerous rivers and lakes in the HAYR and wetlands are widely distributed. There are more than 5,300 lakes in the SAYR with a total area of more than 1,270.77 km^2 (Luo et al., 2020c). These lakes, which are characterized as small and densely distributed, are close to the main streams along the Yellow River, and low-lying flat marshes. According to the remote sensing data, the area and number of lakes greater than 0.01 km^2 both experienced four stages from 1986 to 2019: reduction (1986–2004), increase (2004–2012), reduction (2012–2017), and increase again (2017–2019) (Luo et al., 2020c). The number of lakes greater than six hectares (>0.06 km^2) decreased from 405 to 261 in Madoi County from 1990 to 2000 (Dong et al., 2009). Small lakes were extremely unstable because of their small area, shallow water depths, and high susceptibility to disturbances (Watts et al., 2014; Luo et al., 2020c; Şerban et al., 2020; Şerban et al., 2021). Since the 21st century, especially after 2004, the area and number of lakes have begun to increase, possibly due to the increased water resources replenished by ground ice meltwater (Li et al., 2008). To date, there is an urgent need to develop and improve the methods for mapping the distribution and changes of medium and small water bodies using the remote sensing in permafrost regions. Furthermore, we also need to have in-depth understanding of influences of permafrost degradation on water-heat dynamics of thermokarst lakes (Şerban et al., 2020; Şerban et al., 2021).

The main types of alpine wetlands are lacustrine wetlands, alpine peat bogs, and marshlands. The areal extent of wetlands is about 2,126.33 km^2, accounting for approximately 10% of the total catchment area of the HAYR (Niu, 2020). The lacustrine wetlands in this region, as represented by those in the peripheries of the Gyaring and Ngöring lakes, are mainly distributed in lowlands, while the marshes are mostly close to rivers and lakes and are on the low-lying shadowy slopes (Li et al., 2016c; Luo et al., 2020a). Under the influence of climate warming, strong evaporation, and permafrost degradation, wetlands are shrinking (Gao et al., 2013; Dong et al., 2009). From 1990 to 2004, wetlands were continuously shrinking at a rate of 2,864.48 km^2/a, resulting in a total areal reduction of 40,102.65 km^2 during this 14-year period, including a decrease of 23,298.09 km^2 in the first 10 years and a decrease of 16,804.56 km^2 years in the last 4 years (Li et al., 2009). After 2004, the wetland shrinkage and degradation began to slow down (Li et al., 2009). The area of wetlands near Madoi town decreased by 570 km^2 from 1990 to 2013, including a decrease of 1,481 km^2 from 1990 to 2001, and an increase of 911 km^2 from 2002 to 2013 (Li et al., 2016c). At present, these wetlands are very unstable, with a high rate of conversion from wetlands to other land types (Dong et al., 2009; Wang J. et al., 2020).

Under a warming climate, annual precipitation in the SAYR has fluctuated and increased slightly. Rising temperature has led to an increase in the ALT and land surface evaporation. Every 1 cm increase in the ALT may result in a 1.3 mm decrease in annual runoff and a 0.9 mm increase in annual evapotranspiration in the SAYR (Wang Y. et al., 2018). In addition, the thawing of permafrost resulted in an increase in the downward permeability of soil water, further reducing the surface runoff (Wang Y. et al., 2018; Wu et al., 2018). Under a warming climate, precipitation in the SAYR has fluctuated and increased only slightly. If this situation continues, the water balance in the SAYR will negatively feed back to the warming climate, eventually leading to the shrinkage and degradation of marshes.

Changes in precipitation, runoff, and permafrost degradation are the main influencing factors for wetland hydrothermal dynamics in the SAYR (Wang et al., 2001; Wu et al., 2018; Wu et al., 2021). Persistent climate warming has enhanced land surface evaporation, lowered the burial depth of the permafrost table, and has deepened the active layer and the aeration/vadose zone, resulting in a deeper groundwater table, causing the continuously distributed wetlands to become fragmented or even completely disappear (drained) (Li et al., 2016c; Li G. et al., 2020c). With shrinking wetlands, alpine vegetation coverage declined, in turn, resulting in the bare patches of ground surface (blackened soil spots) in grasslands (Yi et al., 2011). In addition, the increased rodent activity and wind erosion reduced the area of marsh meadows and further increased the area of bare ground patches, leading to the degradation of moist and paludal alpine meadows dominated by *Artemisia wellbyi* into alpine steppes dominated by constructive species *Artemisia absinthium* and *Stipa capillata*. Furthermore, the water conservation capacity may have declined considerably (Wang et al., 2001; Feng et al., 2006; Qin et al., 2017). These hydrothermal processes are interactive, interdependent, and produce extensive and profound eco-hydrological impacts.

There is a recognition that permafrost degradation (melt of ground ice or presence of taliks) may have important implications for changes in wetlands and lakes (Jin et al., 2009; Wang Y. et al., 2018; Shi et al., 2020; Cao W. et al., 2021). These changes, in turn, are accelerating the permafrost thaw by transferring more thermal energy *via* heat convection and advection (Sjöberg et al., 2016; Luo et al., 2018). An electrical resistivity tomography study shows that sbu- permafrost groundwater moves towards to talik zones and this brings the heat to the surrounding permafrost as well, and hence, a further thaw of permafrost (Gao et al., 2019).

Impacts of Permafrost Degradation on Alpine Vegetation Succession

The plant ecosystem in the SAYR is fragile due to its simple structure. Main vegetation types here include alpine paludal meadows, alpine meadows, and alpine steppes. Borehole

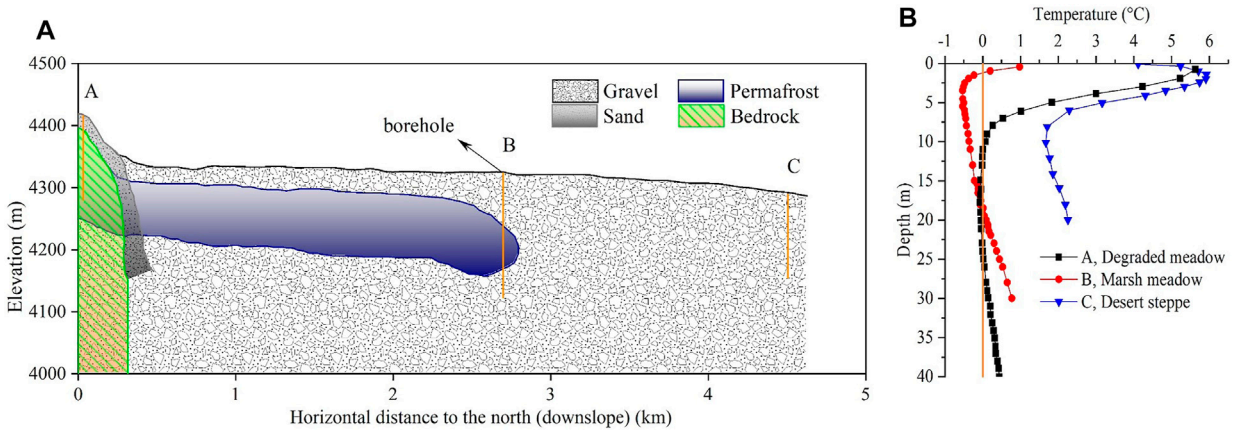

FIGURE 2 | Borehole locations and vegetation types **(A)** and the corresponding soil temperature **(B)**. Ground temperatures in Panel 2B were measured on 30 September 2016.

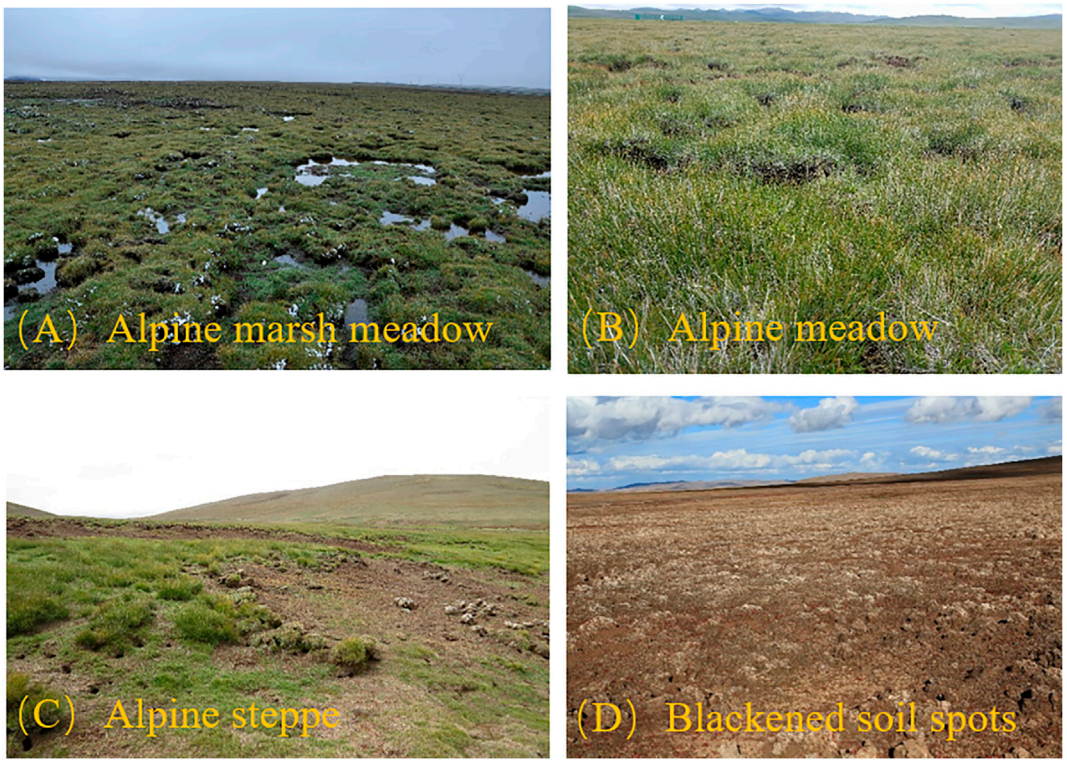

FIGURE 3 | Degradation of alpine meadows into blackened soil spots in the Headwater Area of Yellow River on the northeastern Qinghai-Tibet Plateau, Southwest China. **(A)** Alpine marsh meadow with high sedge cover and saturated soil, **(B)** alpine meadow with high sedge cover but less soil water content, **(C)** Alpine steppe with a lower sedge cover and weeds, and **(D)** blackened soil spots without sedge and with dry soil.

temperatures and other data have revealed a good correlation between vegetation distribution and permafrost development (**Figure 2**). Positions of these boreholes are shown in **Figure 2A** and their corresponding ground temperature curves are shown in **Figure 2B**. Borehole A is located at the edge of a degrading alpine meadow with positive temperature at depths of 0–12 m. The zero curtain phenomenon has been observed at depths of 12–24 m. Stable positive temperatures are recorded at depths greater than 24 m. Thus, this borehole site is underlain by degrading permafrost on the margin of thawing. Borehole B is located in a paludal meadow underlain by 18-m-thick, very warm (−0.5°C) permafrost. Borehole C is set in an alpine desert steppe

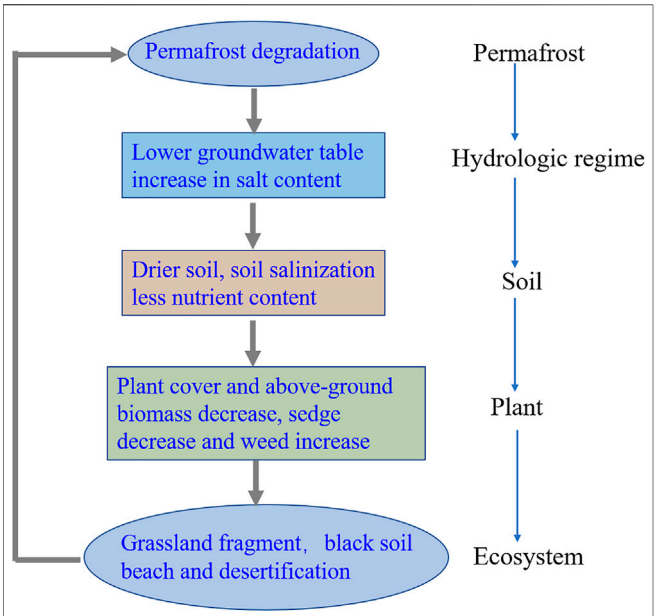

FIGURE 4 | Interactions between permafrost degradation and vegetation degradation in the Headwater Area of Yellow River on northeastern Qinghai-Tibet Plateau, Southwest China.

and ground temperature here is always positive, indicating a site of talik.

In the SAYR, as illustrated in **Figure 2**, paludal and alpine meadows are generally areas where permafrost develops and desert steppes are generally underlain by seasonal frost or talik. With permafrost degradation, the zone of alpine meadows retreated while alpine desert steppes expanded into the former ground of alpine meadows. Additionally, alpine desert steppes are dry and covered by a thin layer of steppe soil (crust), under which, are glaciofluvial sand, pebbles, and gravel. In the severely cold, dry, and windy environment, the sparse and cushion-like vegetation is often disrupted, so land desertification processes are prone to occur, resulting in land desertification as evidenced by mobilizing sand dunes or drifting sand (Hu et al., 2013; Li et al., 2016d).

Climate warming and permafrost degradation have changed the distributive features of surface waters and deepened and elongated the flow paths of groundwater, resulting in a series of vegetation successions from alpine marsh meadows to alpine meadows, and further to alpine steppes, resulting in the blackened soil spots, or even alpine deserts (**Figure 3**) (Mu et al., 2018; Jin et al., 2020; Jin X.-Y. et al., 2021). Permafrost, as an aquitard, blocks the downward movement of water from infiltration and stores water at the bottom of the active layer, generally at depths of about 1–2 m, which could be utilized by plants (Gao Z. et al., 2020). With a thickening of the active layer and the deepening of the permafrost table, water moves further downward, and the surface layer of soil becomes drier (Wang et al., 2006; Jin et al., 2020). This may accelerate the grassland degradation, especially in low-lying valley zones underlain by the isolated patches of alpine permafrost, where the soil water infiltration is dominated by lateral flow and downward movements (Sun et al., 2019; Jin et al., 2020; Cao H. et al., 2021). These land surface changes, furthermore, have resulted in the reduction of vegetation coverage.

As the active layer deepens progressively, the plant species richness, vegetation coverage, and underground biomass in alpine paludal meadows and the coverage of Cyperaceae decreases, but the coverage of forbs species increases (Jin et al., 2020). With further degradation of alpine steppes, the similarity index among communities decreases, and aboveground biomass significantly decreases in grasses, while it first increases and then decreases in forbs (Wang et al., 2012). In addition to ALT, an acceleration of ground freeze–thaw cycles (at 5 cm in depth) under the changing climate, could reduce the activity of root cells of plants and even leads to the death of plant root and rhizospheric microorganisms, thereby lowering the nitrogen fixation ability (Man et al., 2019). Moreover, ground thaw at a depth of 5 cm has advanced at rates of 0.1–1.5 days/year (2003–2015), and the maximum depth of frost penetration has decreased at rates of 0.7–3.1 cm/year, resulting in an earlier start date of the vegetation growing season (Gao B. et al., 2020).

All these aspects have led to the stresses of alpine vegetation from physiological droughts, accelerating grassland degradation. If effective measures are not taken in time to mitigate further grassland degradation, the imbalance between the permafrost environment and alpine vegetation in this region will result in positive feedback between permafrost degradation and grassland degradation (**Figure 4**). The consequence will be the extensive, persistent, and intensifying deterioration of the ecological environment, such as the degradation of grasslands and land desertification. These changes will lead to an increase in surface albedo, a decrease in the convection effect of the near-surface air flows, and an increase in near-surface ground temperatures. In addition, the patterns of atmospheric circulations over the Qinghai-Tibet Plateau will change, resulting in extensive environmental impacts.

Recent remote sensing studies have found increasing normalized difference vegetation index (NDVI) and plant productivity in the SAYR on the northeastern Qinghai-Tibet Plateau, Southwest China (Ge et al., 2018; Bai et al., 2020; Wang M. et al., 2020). Using the TTOP model simulations and remote sensing data, a recent study has showed that from 1980 to 2018, half of the areal extent of alpine permafrost in the SAYR (where permafrost accounts for 20.37% in areal extent) has been converted to seasonal frost, but the NDVI in the growing season has been increasing at an average rate of 0.002/10a, and; the increase in NDVI mainly occurred in the transitional zone between permafrost and seasonal frost (Wang R. et al., 2020). However, this does not necessarily signal the recovery of vegetation upon permafrost thaw in the HAYR. First, changes in vegetation species are difficult to determine based on the increase in NDVI, and the increased NDVI is likely due to the increase in weeds. In addition, the increase in NDVI is likely to be a short-term effect of permafrost degradation. In a long run, under a weak increase in precipitation, permafrost thaw will eventually lead to aridification of the environment, resulting in the degradation of alpine grasslands. However, the timely and

proper implementation of ecological protection programs and establishment and prudent operation of national parks may have mitigated the vegetation degradation to some extents (e.g., Zhao et al., 2018).

RESEARCH PRIORITIES

In the SAYR, undergoing changes in alpine vegetation are closely related to the complex interactions of climate warming, permafrost degradation, soil hydrological regimes, soil texture, and other environmental factors (Jin et al., 2020; Shi et al., 2020). However, more studies are needed on the moving trajectories of water from ice melting, total volume of the melt-water from the ground ice, and how the magnitudes of this melt-water contribute to surface water and groundwater. In addition, although it has been observed that snowfall accounts for 8.8% of annual precipitation, it has substantial implication for the occurrence of permafrost and the overlying alpine plants (Li et al., 2021). However, not much research, except for some studies from remote sensing, focus on the snow cover in this region, its changes, and its ecological, hydrological and engineering impact. This is mainly due to the area's harsh environment and the challenge to establish and sustain longer term ground-based measurements and observation stations. More monitoring networks of snow cover, glaciers and frozen ground should be built and improved in the SAYR. In addition to the mountain cryosphere observational networks, long-term ecosystem and flow-system monitoring sites and networks should also be established and progressively improved in this region to study the vegetation succession trajectories coupled with the rapidly and extensively changing cryospheric components and their profound and extensive impacts. The impacts of permafrost degradation on carbon storage and stability, as well as greenhouse gases emissions and dissolved organic and inorganic carbon and nitrogen, in the SAYR, especially those in the extensively distributed alpine wetlands, meadows and peatlands and peat plateaus, are also critical for future climate change due to their positive feedback to climate warming through an enhanced carbon and nitrogen cycling.

All these environmental attributes have collectively structured the alpine plant ecosystem and changes in any individual driver can interact with other interwoven and interdependent variables. These complex and dynamically changing processes and mechanisms are the prompting challenges for the current scientific research and ecological management. Future research should build and improve the process-based model to better understand and predict how alpine vegetation may respond to permafrost/cryosphere-related hydrological and cryopedological changes, which is based on more systematic and integrated observational networks.

CONCLUSION

Research based on historical and contemporary data and simulations showed that alpine ecosystems in the SAYR, one of the cores of the Asian Water Towers and niches and refuges, for alpine species diversity, were, are, and will be affected by many environmental factors related to climate warming and permafrost degradation. According to the observational data from meteorological stations during the last 60 years, regional average air temperature in the SAYR has been rising at a multi-year average rate of 0.4°C/10a, while annual precipitation has been fluctuating with a slight wetting trend. As a result, from 1980 to 2016, permafrost extent shrank by about 2,000 km^2; the ground warmed at a rate of 0.01–0.21°C/10a and the ALT enlarged at a rate of 35 cm/10a. These changes in permafrost features have produced substantial changes in surface and subsurface hydrologic regimes and flow dynamics. Under a warming climate, mean annual evaporation increased, while the surface runoff decreased, possibly due to the imbalance of only slightly increased annual precipitation, much enhanced evaporation, and extensively degrading permafrost. Moreover, the regional groundwater table in the Yellow River valleys declines simultaneously with the lowering permafrost table. This cannot be offset by the appreciably added water from the melting of ground ice and/or slightly increased precipitation. Field surveys have found a close association of grassland expansion and the lowering of groundwater table. Alpine vegetation cover is generally high when the burial depth of the supra-permafrost water table is less than 2 m, which is a critical value for alpine plants, and thus dubbed as the burial-depth of the ecologically safe supra-permafrost water table (BESST).

Temperature rise and permafrost degradation have been linked to the shrinkage of wetlands and marsh/paludal meadows, a decline in water conservation capacity, driving the adverse successions of alpine grassland ecosystems in the SAYR, and resulting in severe degradation of grasslands and reduced grassland productivity, diversity, and vegetation coverage. Moreover, blackened soil spots and land desertification have arisen with severe grassland degradation, seriously threatening the ecological and water security of the SAYR and surrounding areas. The growth of short-rooted herbaceous plants will be restricted if the BESST becomes deeper than 2 m. The long-term effect of a deeper ecological water table will promote a change in vegetation species, regional evolution of plant life, the overall evolution from hygrophytes to xerophytes, as well as the degradation and even desertification of alpine grasslands.

DATA AVAILABILITY STATEMENT

The original contributions presented in the study are included in the article/Supplementary Material, further inquiries can be directed to the corresponding author.

AUTHOR CONTRIBUTIONS

XJ and HJ conceived the project and organized the draft. DL, YS, and JW collected the boreholes data and offered the pictures. WW, SH, YL, and QM helped plot the figures. SL, QW, RH, RDS,

and SG helped improve the manuscript. HJ, QW, and YS provided the funding for research activities.

FUNDING

This research was funded by the Chinese Academy of Sciences (CAS) Strategic Priority Research Program "Changing permafrost hydrology in the Qilian Mountains and the Source Area of the Yellow River and its impacts on water supplies and security" (Grant No. XDA20100103), National Natural Science Foundation of China (Grant Nos U20A2082 and 41871052), and Consulting Project of Ministry of Natural Resources "Impacts of shrinking glaciers and degrading permafrost on ecosystems, Yellow River discharge and carbon sources and sinks in the Source Area of Yellow River on northeastern Qinghai-Tibet Plateau, China".

ACKNOWLEDGMENTS

The authors thank the reviewers for their review work to improve this manuscript.

REFERENCES

Bai, Y., Guo, C., Degen, A. A., Ahmad, A. A., Wang, W., Zhang, T., et al. (2020). Climate Warming Benefits alpine Vegetation Growth in Three-River Headwater Region, China. *Sci. Total Environ.* 742, 140574. doi:10.1016/j.scitotenv.2020.140574

Bockheim, J. G. (2015). Global Distribution of Cryosols with Mountain Permafrost: an Overview. *Permafrost Periglac. Process.* 26, 1–12. doi:10.1002/ppp.1830

Cao, W., Wan, L., Zhou, X., Hu, F., Li, Z., and Liang, S. (2003). A Study of the Geological Environmental of Suprapermafrost Water in the Headwater Area of the Yellow River. *Hydrogeol. Eng. Geol.* 6, 6–10. (In Chinese with English abstract). doi:10.16030/j.cnki.issn.1000-3665.2003.06.002

Cao, H., Gao, B., Gong, T., and Wang, B. (2021a). Analyzing Changes in Frozen Soil in the Source Region of the Yellow River Using the MODIS Land Surface Temperature Products. *Remote Sensing* 13 (2), 180. doi:10.3390/rs13020180

Cao, W., Sheng, Y., Wu, J., and Peng, E. (2021b). Differential Response to Rainfall of Soil Moisture Infiltration in Permafrost and Seasonally Frozen Ground in Kangqiong Small basin on the Qinghai-Tibet Plateau. *Hydrological Sci. J.* 66, 525–543. doi:10.1080/02626667.2021.1883619

Cheng, G., and Jin, H. (2013). Groundwater in the Permafrost Regions on the Qinghai-Tibet Plateau and it Changes. *Hydrogeol. Eng. Geol.* 40, 1–11. doi:10.16030/j.cnki.issn.1000-3665.2013.01.017

Dong, L., Wang, W., Ma, M., Kong, J., and Veroustraete, F. (2009). The Change of Land Cover and Land Use and its Impact Factors in Upriver Key Regions of the Yellow River. *Int. J. Remote Sensing* 30, 1251–1265. doi:10.1080/01431160802468248

Feng, J., Wang, T., and Xie, C. (2006). Eco-environmental Degradation in the Source Region of the Yellow River, Northeast Qinghai-Xizang Plateau. *Environ. Monit. Assess.* 122, 125–143. doi:10.1007/s10661-005-9169-2

Gao, J., Li, X.-l., Cheung, A., and Yang, Y.-w. (2013). Degradation of Wetlands on the Qinghai-Tibet Plateau: A Comparison of the Effectiveness of Three Indicators. *J. Mt. Sci.* 10, 658–667. doi:10.1007/s11629-013-2562-3

Gao, Z., Niu, F., Wang, Y., Lin, Z., Luo, J., and Liu, M. (2018). Root-induced Changes to Soil Water Retention in Permafrost Regions of the Qinghai-Tibet Plateau, China. *J. Soils Sediments* 18, 791–803. doi:10.1007/s11368-017-1815-0

Gao, S., Jin, H., Bense, V. F., Wang, X., and Chai, X. (2019). Application of Electrical Resistivity Tomography for Delineating Permafrost Hydrogeology in the Headwater Area of Yellow River on Qinghai-Tibet Plateau, SW China. *Hydrogeol. J.* 27 (5), 1725–1737. doi:10.1007/s10040-019-01942-z

Gao, B., Li, J., and Wang, X. (2020a). Impact of Frozen Soil Changes on Vegetation Phenology in the Source Region of the Yellow River from 2003 to 2015. *Theor. Appl. Climatol.* 141, 1219–1234. doi:10.1007/s00704-020-03266-5

Gao, Z., Lin, Z., Niu, F., and Luo, J. (2020b). Soil Water Dynamics in the Active Layers under Different Land-Cover Types in the Permafrost Regions of the Qinghai-Tibet Plateau, China. *Geoderma* 364, 114176. doi:10.1016/j.geoderma.2020.114176

Ge, J., Meng, B., Liang, T., Feng, Q., Gao, J., Yang, S., et al. (2018). Modeling alpine Grassland Cover Based on MODIS Data and Support Vector Machine Regression in the Headwater Region of the Huanghe River, China. *Remote Sensing Environ.* 218, 162–173. doi:10.1016/j.rse.2018.09.019

G., W., J., Q., G., C., and Y., L. (2001). Eco-Environmental Degradation and Causal Analysis in the Source Region of the Yellow River. *Environ. Geology.* 40, 884–890. doi:10.1007/s002540100248

Haeberli, W. (2013). Mountain Permafrost - Research Frontiers and a Special Long-Term challenge. *Cold Regions Sci. Technol.* 96, 71–76. doi:10.1016/j.coldregions.2013.02.004

Han, Y. P., Chen, Z. T., and Xiao, H. (2018). Projection in Extreme Climate Events and Uncertainty Analysis in the Source Area of the Yellow River for the Next Three Decades. *IOP Conf. Ser. Earth Environ. Sci.* 199, 022024. doi:10.1088/1755-1315/199/2/022024

He, X., Yu, Y., Cui, Z., and He, T. (2021). Climate Change and Ecological Projects Jointly Promote Vegetation Restoration in Three-River Source Region of China. *Chin. Geogr. Sci.* 31, 1108–1122. doi:10.1007/s11769-021-1245-1

Hu, Y., Maskey, S., and Uhlenbrook, S. (2012). Trends in Temperature and Rainfall Extremes in the Yellow River Source Region, China. *Climatic Change* 110, 403–429. doi:10.1007/s10584-011-0056-2

Hu, G., Jin, H., Dong, Z., Lu, J., and Yan, C. (2013). Driving Forces of Aeolian Desertification in the Source Region of the Yellow River: 1975-2005. *Environ. Earth Sci.* 70, 3245–3254. doi:10.1007/s12665-013-2389-9

Intergovernmental Panel of Climate Change (IPCC) (2014). *Climate Change 2014: Synthesis Report. Contribution of Working Groups I, II and III to the Fifth Assessment Report of the Intergovernmental Panel on Climate Change*. Geneva, Switzerland: IPCC, 151.

Iqbal, M., Wen, J., Wang, X., Lan, Y., Tian, H., Anjum, M. N., et al. (2018). Assessment of Air Temperature Trends in the Source Region of Yellow River and its Sub-Basins, China. *Asia-Pacific J. Atmos. Sci.* 54, 111–123. doi:10.1007/s13143-017-0064-x

Jiang, P., Yu, Z., Yuan, F., and Acharya, K. (2019). The Multi-Scale Temporal Variability of Extreme Precipitation in the Source Region of the Yellow River. *Water* 11, 92. doi:10.3390/w11010092

Jin, H., Li, S., Cheng, G., Shaoling, W., and Li, X. (2000). Permafrost and Climatic Change in China. *Glob. Planet. Change* 26, 387–404. doi:10.1016/S0921-8181(00)00051-5

Jin, H., He, R., Cheng, G., Wu, Q., Wang, S., Lü, L., et al. (2009). Changes in Frozen Ground in the Source Area of the Yellow River on the Qinghai-Tibet Plateau, China, and Their Eco-Environmental Impacts. *Environ. Res. Lett.* 4, 045206. doi:10.1088/1748-9326/4/4/045206

Jin, X., Jin, H., Wu, X., Luo, D., Yu, S., Li, X., et al. (2020). Permafrost Degradation Leads to Biomass and Species Richness Decreases on the Northeastern Qinghai-Tibet Plateau. *Plants* 9, 1453. doi:10.3390/plants9111453

Jin, X.-Y., Jin, H.-J., Iwahana, G., Marchenko, S. S., Luo, D.-L., Li, X.-Y., et al. (2021). Impacts of Climate-Induced Permafrost Degradation on Vegetation: A Review. *Adv. Clim. Change Res.* 12 (1), 29–47. doi:10.1016/j.accre.2020.07.002

Jin, H.-J., Wu, Q.-B., and Romanovsky, V. E. (2021). Degrading Permafrost and its Impacts. *Adv. Clim. Change Res.* 12 (1), 1–5. doi:10.1016/j.accre.2021.01.007

Lan, C., Zhang, Y., Gao, Y., Hao, Z., and Cairang, L. (2013). The Impacts of Climate Change and Land Cover/use Transition on the Hydrology in the Upper Yellow River Basin, China. *J. Hydrol.* 502, 37–52. doi:10.1016/j.jhydrol.2013.08.003

Latif, A., Ilyas, S., Zhang, Y., Xin, Y., Zhou, L., and Zhou, Q. (2019). Review on Global Change Status and its Impacts on the Tibetan Plateau Environment. *J. Plant Ecol.* 12, 917–930. doi:10.1093/jpe/rtz038

Li, L., Wu, S., Zhu, X., Chang, G., and Li, F. (2008). Response of the Plateau Lakes to Changes of Climate and Frozen Earth Environment in the Headwaters of the

Yellow River since the 21st century. *J. Nat. Resour.* 23, 245–253. (In Chinese with English abstract). doi:10.11849/zrzyxb.2008.02.009

Li, F., Chang, G., Xiao, J., Zhou, B., and Fu, Y. (2009). Relationship between Wetland Changes and Climate Change in the Yellow River Source Region. *J. Nat. Resour.* 24, 683–690. (In Chinese with English abstract). doi:10.11849/zrzyxb.2009.04.014

Li, J., Sheng, Y., Wu, J., Feng, Z., Ning, Z., Hu, X., et al. (2016). Landform-related Permafrost Characteristics in the Source Area of the Yellow River, Eastern Qinghai-Tibet Plateau. *Geomorphology* 269, 104–111. doi:10.1016/j.geomorph.2016.06.024

Li, Q., Yang, M., Wan, G., and Wang, X. (2016). Spatial and Temporal Precipitation Variability in the Source Region of the Yellow River. *Environ. Earth Sci.* 75, 594. doi:10.1007/s12665-016-5583-8

Li, X., Xue, Z., and Gao, J. (2016c). Dynamic Changes of Plateau Wetlands in Madou County, the Yellow River Source Zone of China: 1990-2013. *Wetlands* 36, 299–310. doi:10.1007/s13157-016-0739-6

Li, X., Yao, Z., Dong, Z., and Xiao, J. (2016d). Causes and Processes of sandy Desertification in Guinan County, Qinghai-Tibet Plateau. *Environ. Earth Sci.* 75, 1–12. doi:10.1007/s12665-016-5481-0

Li, G., Li, X., Chen, W., Li, J., Zhu, H., Hu, X., et al. (2020c). Effects of Degradation Severity on the Physical, Chemical and Mechanical Properties of Topsoil in alpine Meadow on the Qinghai-Tibet Plateau, West China. *Catena* 187, 104370. doi:10.1016/j.catena.2019.104370

Li, Z., Ma, J., Song, L., Gui, J., Xue, J., Zhang, B., et al. (2020a). Investigation of Soil Water Hydrological Process in the Permafrost Active Layer Using Stable Isotopes. *Hydrological Process.* 34, 2810–2822. doi:10.1002/hyp.13765

Li, Z., Gao, P., Hu, X., Yi, Y., Pan, B., and You, Y. (2020b). Coupled Impact of Decadal Precipitation and Evapotranspiration on Peatland Degradation in the Zoige basin, China. *Phys. Geogr.* 41, 145–168. doi:10.1080/02723646.2019.1620579

Li, Z., Lyu, S., Chen, H., Ao, Y., Zhao, L., and Wang, S. (2021). Changes in Climate and Snow Cover and Their Synergistic Influence on Spring Runoff in the Source Region of the Yellow River. *Sci. Total Environ.* 799, 149503. doi:10.1016/j.scitotenv.2021.149503

Liang, S., Wan, L., Li, Z., and Cao, W. (2007). The Effect of Permafrost on alpine Vegetation in the Source Regions of the Yellow River. *J. Glaciol. Geocryol.* 29, 45–52. (In Chinese with English abstract). doi:10.3969/j.issn.1000-0240.2007.01.008

Lin, M., Biswas, A., and Bennett, E. M. (2019). Spatio-Temporal Dynamics of Groundwater Storage Changes in the Yellow River Basin. *J. Environ. Manage.* 235, 84–95. doi:10.1016/j.jenvman.2019.01.016

Liu, C., Wang, P., Wen, T., Yu, D., and Bai, W. (2021). Spatio-Temporal Characteristics of Climate Change in the Yellow River Source Area from 1960 to 2019. *Arid Zone Res.* 38, 293–302. (In Chinese with English abstract). doi:10.13866/j.azr.2021.02.01

Luo, D., HuiJun, J., Marchenko, S., and Romanovsky, V. (2014). Distribution and Changes of Active Layer Thickness (ALT) and Soil Temperature (TTOP) in the Source Area of the Yellow River Using the GIPL Model. *Sci. China Earth Sci.* 57, 1834–1845. doi:10.1007/s11430-014-4852-1

Luo, D., Jin, H., Lü, L., and Zhou, J. (2016). Spatiotemporal Changes in Extreme Ground Surface Temperatures and the Relationship with Air Temperatures in the Three-River Source Regions during 1980-2013. *Theor. Appl. Climatol.* 123, 885–897. doi:10.1007/s00704-015-1543-6

Luo, D., Jin, H., Jin, X., He, R., Li, X., Muskett, R. R., et al. (2018). Elevation-Dependent Thermal Regime and Dynamics of Frozen Ground in the Bayan Har Mountains, Northeastern Qinghai-Tibet Plateau, Southwest China. *Permafrost and Periglac Process* 29, 257–270. doi:10.1002/ppp.1988

Luo, D., Jin, H., Bense, V. F., Jin, X., and Li, X. (2020a). Hydrothermal Processes of Near-Surface Warm Permafrost in Response to strong Precipitation Events in the Headwater Area of the Yellow River, Tibetan Plateau. *Geoderma* 376, 114531. doi:10.1016/j.geoderma.2020.114531

Luo, D., Liu, L., Jin, H., Wang, X., and Chen, F. (2020b). Characteristics of Ground Surface Temperature at Chalaping in the Source Area of the Yellow River, Northeastern Tibetan Plateau. *Agric. For. Meteorology* 281, 107819. doi:10.1016/j.agrformet.2019.107819

Luo, D., Jin, H., Du, H., Li, C., Ma, Q., Duan, S., et al. (2020c). Variation of alpine Lakes from 1986 to 2019 in the Headwater Area of the Yellow River, Tibetan Plateau Using Google Earth Engine. *Adv. Clim. Change Res.* 11, 11–21. doi:10.1016/j.accre.2020.05.007

Lv, M., Wang, Y., and Gao, Z. (2022). The Change Process of Soil Hydrological Properties in the Permafrost Active Layer of the Qinghai-Tibet Plateau. *CATENA* 210, 105938. doi:10.1016/j.catena.2021.105938

Ma, Q., Jin, H.-J., Bense, V. F., Luo, D.-L., Marchenko, S. S., Harris, S. A., et al. (2019). Impacts of Degrading Permafrost on Streamflow in the Source Area of Yellow River on the Qinghai-Tibet Plateau, China. *Adv. Clim. Change Res.* 10, 225–239. doi:10.1016/j.accre.2020.02.001

Man, Z., Weng, B., Yang, Y., Gong, X., Li, M., and Yu, Z. (2019). Effects of the Freezing-Thawing Cycle Mode on alpine Vegetation in the Nagqu River Basin of the Qinghai-Tibet Plateau. *Water* 11, 2122. doi:10.3390/w11102122

Mu, C., Li, L., Zhang, F., Li, Y., Xiao, X., Zhao, Q., et al. (2018). Impacts of Permafrost on above- and Belowground Biomass on the Northern Qinghai-Tibetan Plateau. *Arctic, Antarctic, Alpine Res.* 50, e1447192. doi:10.1080/15230430.2018.1447192

Niu, Y. (2020). Wetland Information Extraction of the Yellow River Source Based on Decision Tree Model. Master's thesis. Beijing (China): China University of Geosciences.

Pepin, N., Bradley, R. S., Diaz, H. F., Baraër, M., Caceres, E. B., Forsythe, N., et al. (2015). Elevation-dependent Warming in Mountain Regions of the World. *Nat. Clim Change* 5, 424–430. doi:10.1038/nclimate2563

Qin, Y., Yang, D., Gao, B., Wang, T., Chen, J., Chen, Y., et al. (2017). Impacts of Climate Warming on the Frozen Ground and Eco-Hydrology in the Yellow River Source Region, China. *Sci. Total Environ.* 605-606, 830–841. doi:10.1016/j.scitotenv.2017.06.188

Qin, Y., Zhang, P., Liu, W., Guo, Z., and Xue, S. (2020). The Application of Elevation Corrected MERRA2 Reanalysis Ground Surface Temperature in a Permafrost Model on the Qinghai-Tibet Plateau. *Cold Regions Sci. Technol.* 175, 103067. doi:10.1016/j.coldregions.2020.103067

Schuur, E. A. G., and Mack, M. C. (2018). Ecological Response to Permafrost Thaw and Consequences for Local and Global Ecosystem Services. *Annu. Rev. Ecol. Evol. Syst.* 49, 279–301. doi:10.1146/annurev-ecolsys-121415-032349

Şerban, R.-D., Jin, H., Şerban, M., Luo, D., Wang, Q., Jin, X., et al. (2020). Mapping Thermokarst Lakes and Ponds across Permafrost Landscapes in the Headwater Area of Yellow River on Northeastern Qinghai-Tibet Plateau. *Int. J. Remote Sensing* 41, 7042–7067. doi:10.1080/01431161.2020.1752954

Şerban, R. D., Jin, H., Şerban, M., and Luo, D. (2021). Shrinking Thermokarst Lakes and Ponds on the Northeastern Qinghai-Tibet Plateau over the Past Three Decades. *Permafrost and Periglac Process* 32, 601–617. doi:10.1002/ppp.2127

Sheng, Y., Ma, S., Cao, W., and Wu, J. (2020). Spatiotemporal Changes of Permafrost in the Headwater Area of the Yellow River under a Changing Climate. *Land Degrad. Dev.* 31, 133–152. doi:10.1002/ldr.3434

Shi, R., Yang, H., and Yang, D. (2020). Spatiotemporal Variations in Frozen Ground and Their Impacts on Hydrological Components in the Source Region of the Yangtze River. *J. Hydrol.* 590, 125237. doi:10.1016/j.jhydrol.2020.125237

Sjöberg, Y., Coon, E., Sannel, A. B. K., Harp, D., Frampton, A., Painter, S. L., et al. (2016). Thermal Effects of Groundwater Flow through Subarctic Fens: A Case Study Based on Field Observations and Numerical Modeling. *Water Resour. Res.* 52, 1591–1606. doi:10.1002/2015WR017571

Sun, A., Zhou, J., Yu, Z., Jin, H., Sheng, Y., and Yang, C. (2019). Three-dimensional Distribution of Permafrost and Responses to Increasing Air Temperatures in the Head Waters of the Yellow River in High Asia. *Sci. Total Environ.* 666, 321–336. doi:10.1016/j.scitotenv.2019.02.110

Sun, A., Yu, Z., Zhou, J., Acharya, K., Ju, Q., Xing, R., et al. (2020). Quantified Hydrological Responses to Permafrost Degradation in the Headwaters of the Yellow River (HWYR) in High Asia. *Sci. Total Environ.* 712, 135632. doi:10.1016/j.scitotenv.2019.135632

Tian, H., Lan, Y., Wen, J., Jin, H., Wang, C., Wang, X., et al. (2015). Evidence for a Recent Warming and Wetting in the Source Area of the Yellow River (SAYR) and its Hydrological Impacts. *J. Geogr. Sci.* 25, 643–668. doi:10.1007/s11442-015-1194-7

Walvoord, M. A., and Kurylyk, B. L. (2016). Hydrologic Impacts of Thawing Permafrost-A Review. *Vadose Zone J.* 15, vzj2016.01.0010. doi:10.2136/vzj2016.01.0010

Wang, G., Li, Y., Wu, Q., and Wang, Y. (2006). Impacts of Permafrost Changes on Alpine Ecosystem in Qinghai-Tibet Plateau. *Sci. China Ser. D* 49, 1156–1169. doi:10.1007/s11430-006-1156-0

Wang, G., Bai, W., Li, N., and Hu, H. (2011). Climate Changes and its Impact on Tundra Ecosystem in Qinghai-Tibet Plateau, China. *Climatic Change* 106, 463–482. doi:10.1007/s10584-010-9952-0

Wang, Z., Yang, G., Yi, S., Wu, Z., Guan, J., He, X., et al. (2012). Different Response of Vegetation to Permafrost Change in Semi-Arid and Semi-Humid Regions in Qinghai-Tibetan Plateau. *Environ. Earth Sci.* 66, 985–991. doi:10.1007/s12665-011-1405-1

Wang, S., Sheng, Y., Li, J., Wu, J., Cao, W., and Ma, S. (2018). An Estimation of Ground Ice Volumes in Permafrost Layers in Northeastern Qinghai-Tibet Plateau, China. *Chin. Geogr. Sci.* 28, 61–73. doi:10.1007/s11769-018-0932-z

Wang, T., Yang, H., Yang, D., Qin, Y., and Wang, Y. (2018). Quantifying the Streamflow Response to Frozen Ground Degradation in the Source Region of the Yellow River within the Budyko Framework. *J. Hydrol.* 558, 301–313. doi:10.1016/j.jhydrol.2018.01.050

Wang, Y., Yang, H., Gao, B., Wang, T., Qin, Y., and Yang, D. (2018). Frozen Ground Degradation May Reduce Future Runoff in the Headwaters of an Inland River on the Northeastern Tibetan Plateau. *J. Hydrol.* 564, 1153–1164. doi:10.1016/j.jhydrol.2018.07.078

Wang, R., Dong, Z.-B., and Zhou, Z.-V. C. (2019). Changes in the Depths of Seasonal Freezing and Thawing and Their Effects on Vegetation in the Three-River Headwater Region of the Tibetan Plateau. *J. Mt. Sci.* 16, 2810–2827. doi:10.1007/s11629-019-5450-7

Wang, R., Dong, Z., and Zhou, Z. (2020). Different Responses of Vegetation to Frozen Ground Degradation in the Source Region of the Yellow River from 1980 to 2018. *Chin. Geogr. Sci.* 30, 557–571. doi:10.1007/s11769-020-1135-y

Wang, J., Zhu, Q., Yang, Y., Zhang, X., Zhang, J., Yuan, M., et al. (2020). High Uncertainties Detected in the Wetlands Distribution of the Qinghai-Tibet Plateau Based on Multisource Data. *Landscape Ecol. Eng.* 16, 47–61. doi:10.1007/s11355-019-00402-w

Wang, M., Fu, J. E., Wu, Z., and Pang, Z. (2020). Spatiotemporal Variation of NDVI in the Vegetation Growing Season in the Source Region of the Yellow River, China. *ISPRS Int. J. Geo-inf.* 9, 282. doi:10.3390/ijgi9040282

Wang, X., Chen, D., Pang, G., Gou, X., and Yang, M. (2021). Historical and Future Climates over the Upper and Middle Reaches of the Yellow River Basin Simulated by a Regional Climate Model in CORDEX. *Clim. Dyn.* 56, 2749–2771. doi:10.1007/s00382-020-05617-4

Watts, J. D., Kimball, J. S., Bartsch, A., and McDonald, K. C. (2014). Surface Water Inundation in the Boreal-Arctic: Potential Impacts on Regional Methane Emissions. *Environ. Res. Lett.* 9, 075001. doi:10.1088/1748-9326/9/7/075001

Wrona, F. J., Johansson, M., Culp, J. M., Jenkins, A., Mård, J., Myers-Smith, I. H., et al. (2016). Transitions in Arctic Ecosystems: Ecological Implications of a Changing Hydrological Regime. *J. Geophys. Res. Biogeosci.* 121, 650–674. doi:10.1002/2015JG003133

Wu, X., Zhang, X., Xiang, X., Zhang, K., Jin, H., Chen, X., et al. (2018). Changing Runoff Generation in the Source Area of the Yellow River: Mechanisms, Seasonal Patterns and Trends. *Cold Regions Sci. Technol.* 155, 58–68. doi:10.1016/j.coldregions.2018.06.014

Wu, J., Li, M., Zhang, X., Fiedler, S., Gao, Q., Zhou, Y., et al. (2021). Disentangling Climatic and Anthropogenic Contributions to Nonlinear Dynamics of alpine Grassland Productivity on the Qinghai-Tibetan Plateau. *J. Environ. Manage.* 281, 111875. doi:10.1016/j.jenvman.2020.111875

Xiang, L., Wang, H., Steffen, H., Wu, P., Jia, L., Jiang, L., et al. (2016). Groundwater Storage Changes in the Tibetan Plateau and Adjacent Areas Revealed from GRACE Satellite Gravity Data. *Earth Planet. Sci. Lett.* 449, 228–239. doi:10.1016/j.epsl.2016.06.002

Xie, J., Xu, Y.-P., Guo, Y., and Wang, Y. (2021). Detecting the Dominant Contributions of Runoff Variance across the Source Region of the Yellow River Using a New Decomposition Framework. *Hydrol. Res.* 52, 1015–1032. doi:10.2166/nh.2021.179

Yan, D., Lai, Z., and Ji, G. (2020). Using Budyko-type Equations for Separating the Impacts of Climate and Vegetation Change on Runoff in the Source Area of the Yellow River. *Water* 12, 3418. doi:10.3390/w12123418

Yang, M., Nelson, F. E., Shiklomanov, N. I., Guo, D., and Wan, G. (2010). Permafrost Degradation and its Environmental Effects on the Tibetan Plateau: A Review of Recent Research. *Earth-Science Rev.* 103, 31–44. doi:10.1016/j.earscirev.2010.07.002

Yang, Z.-p., Gao, J.-x., Zhao, L., Xu, X.-l., and Ouyang, H. (2013). Linking Thaw Depth with Soil Moisture and Plant Community Composition: Effects of Permafrost Degradation on alpine Ecosystems on the Qinghai-Tibet Plateau. *Plant Soil* 367, 687–700. doi:10.1007/s11104-012-1511-1

Yang, Y., Wu, Q., Jin, H., Wang, Q., Huang, Y., Luo, D., et al. (2019). Delineating the Hydrological Processes and Hydraulic Connectivities under Permafrost Degradation on Northeastern Qinghai-Tibet Plateau, China. *J. Hydrol.* 569, 359–372. doi:10.1016/j.jhydrol.2018.11.068

Yi, S., Zhou, Z., Ren, S., Xu, M., Qin, Y., Chen, S., et al. (2011). Effects of Permafrost Degradation on alpine Grassland in a Semi-arid basin on the Qinghai-Tibetan Plateau. *Environ. Res. Lett.* 6, 045403. doi:10.1088/1748-9326/6/4/045403

Yuan, Q., Yuan, Q., and Ren, P. (2021). Coupled Effect of Climate Change and Human Activities on the Restoration/degradation of the Qinghai-Tibet Plateau Grassland. *J. Geogr. Sci.* 31, 1299–1327. doi:10.1007/s11442-021-1899-8

Zhao, X., Zhao, L., Li, Q., Chen, H., Zhou, H., Xu, S., et al. (2018). Using Balance of Seasonal Herbage Supply and Demand to Inform Sustainable Grassland Management on the Qinghai-Tibetan Plateau. *Front. Agr. Sci. Eng.* 5, 1–8. doi:10.15302/J-FASE-2018203

Zhao, L., Zou, D., Hu, G., Du, E., Pang, Q., Xiao, Y., et al. (2020). Changing Climate and the Permafrost Environment on the Qinghai-Tibet (Xizang) Plateau. *Permafrost and Periglac Process* 31, 396–405. doi:10.1002/ppp.2056

Conflict of Interest: The authors declare that the research was conducted in the absence of any commercial or financial relationships that could be construed as a potential conflict of interest.

Publisher's Note: All claims expressed in this article are solely those of the authors and do not necessarily represent those of their affiliated organizations, or those of the publisher, the editors and the reviewers. Any product that may be evaluated in this article, or claim that may be made by its manufacturer, is not guaranteed or endorsed by the publisher.

frontiers in Earth Science

ORIGINAL RESEARCH
published: 24 March 2022
doi: 10.3389/feart.2022.846456

Spatio-Temporal Patterns of Carbon Storage Derived Using the InVEST Model in Heilongjiang Province, Northeast China

Xiaoying Li[1,2], Chensheng Huang[1], Huijun Jin[2,3], Yilun Han[1], Siqi Kang[1], Jing Liu[1], Huiying Cai[1], Tongxin Hu[1], Guang Yang[1], Hongzhou Yu[1] and Long Sun[1]**

[1]Key Laboratory of Sustainable Forest Ecosystem Management-Ministry of Education, School of Forestry, Northeast Forestry University, Harbin, China, [2]State Key Laboratory of Frozen Soils Engineering, Da-Xing'anling Observatory and Research Station of Permafrost Engineering and Environment, Northwest Institute of Eco-Environment and Resources, Chinese Academy of Sciences, Lanzhou, China, [3]School of Civil Engineering, Institute of Cold-Regions Science and Engineering, Northeast-China Observatory and Research-Station of Permafrost Geo-Environment (Ministry of Education PRC), Northeast Forestry University, Harbin, China

OPEN ACCESS

Edited by:
Sizhong Yang,
GFZ German Research Centre for Geosciences, Germany

Reviewed by:
Shuying Zang,
Harbin Normal University, China
Chuanyu Gao,
Northeast Institute of Geography and Agroecology (CAS), China

***Correspondence:**
Xiaoying Li
lixiaoying@nefu.edu.cn
Long Sun
sunlong365@126.com

Specialty section:
This article was submitted to Cryospheric Sciences, a section of the journal Frontiers in Earth Science

Received: 31 December 2021
Accepted: 02 March 2022
Published: 24 March 2022

Citation:
Li X, Huang C, Jin H, Han Y, Kang S, Liu J, Cai H, Hu T, Yang G, Yu H and Sun L (2022) Spatio-Temporal Patterns of Carbon Storage Derived Using the InVEST Model in Heilongjiang Province, Northeast China. Front. Earth Sci. 10:846456. doi: 10.3389/feart.2022.846456

Carbon storage is an important component of ecosystem services. Under climate warming and human activities, land use/land cover (LULC) have been undergoing tremendous change, leading to spatio-temporal variations in carbon storage. Based on seven series of LULC data and combined with carbon module of Integrated Valuation of Ecosystem Services and Tradeoffs (InVEST) model, spatial-temporal changes in LULC types and carbon storage were analyzed and estimated for Heilongjiang Province, Northeast China. Results show varied carbon storage among different types of LULC. Forest and cropland are the dominant LULC types in Heilongjiang Province, Northeast China, accounting for 46–49% (20.90×10^4–22.12×10^4 km^2) and 30–37% (13.56×10^4–16.70×10^4 km^2) of the total area. Areal extents of forest, grassland, and unused land declined from 1980 to 2015, by 1.22, 0.84, and 1.11×10^4 km^2, respectively; while those of cropland and construction land expanded, by 3.14 and 0.08×10^4 km^2, respectively. From 1980 to 2015, carbon storage displayed consistent change trends with those of LULC types: carbon storage of forest, grassland, and unused land decreased by 236.22, 116.61 and 21.82×10^6 Mg C, respectively; and those of cropland and construction land increased by 414.65 and 0.99×10^6 Mg C, respectively. The total carbon storage in the study region was $6{,}863.06 \times 10^6$–$6{,}907.64 \times 10^6$ Mg C, for which the forest, cropland, and grassland were the major contributor ($6{,}778.75 \times 10^6$–$6{,}840.57 \times 10^6$ Mg C). Due to the conversion of large extents of forest, grassland, and unused land to cropland, which facilitated the formation of carbon sinks and thus enlarged the carbon storage by 45.36×10^6 Mg C from 1980 to 2015. Frequent forest fires, urban expansion, farmland reclamation, and engineering construction were the important factors of changes in the LULC, accelerating permafrost degradation and leading to obvious changes in the total carbon storage in the Heilongjiang Province, Northeast China. Therefore, the estimation of carbon storage in different LULC types can provide important data support and have important implications for evaluation of ecosystem services and carbon cycle.

Keywords: carbon storage, LULC types, InVEST model, spatio-temporal changes, permafrost degradation, ecosystem services

INTRODUCTION

Ecosystem services refer to the benefits that derive from the structure and function of ecosystems and are major contributors to human well-being (Adelisardou et al., 2021). However, these services are currently under great pressure due to anthropogenic activities and climate change, such as continuous growth of population, industrialization, urbanization, and wildfire (Tolessa et al., 2017; Xie et al., 2017; Li et al., 2020a). Thus, protecting natural ecosystems and enhancing their services have become an urgent global challenge (Ouyang et al., 2016). Carbon storage is a key indicator of ecosystem services function since its closely related with climate regulation and productivity of terrestrial ecosystems (Houghton, 2003; Zhao et al., 2019). Climate and land use/land cover (LULC) changes are the major influencing factors for ecosystem carbon storage, due to fundamental changes in the structure and functions of ecosystems over time (Adelisardou et al., 2021). Climate change alters ecosystem carbon storage by controlling the balance between carbon inputs from plant productivity and carbon outputs from soil carbon decomposition (Wang et al., 2019). Under a warming climate, boreal ecosystems are experiencing continuous and severe LULC changes, affecting the environment, biodiversity, and human health (Viana et al., 2019; Serban et al., 2021). Changes in LULC types are usually accompanied by a large amount of carbon exchange and alter the carbon cycle process by modifying the ecosystem's structure and function. (Noble et al., 2000; Chen and Tian, 2007).

The Integrated Valuation of Ecosystem Services and Tradeoffs (InVEST) model is a suite of free, open-source software used to map and assess the changes in carbon storage due to LULC changes (Zhao et al., 2019). Carbon storage module of InVEST is a simplified carbon cycle that maps and quantifies how much carbon is stored in a landscape, as well as how much is sequestered or lost over time (Dida et al., 2021). The InVEST model is more effective in assessing and studying the impact of climate and LULC change on ecosystem carbon storage (Nie et al., 2020). Under a warming climate, understanding the relationship between LULC systems and carbon stock is essential since every LULC system has either a positive or negative impact on the carbon balance (Toru and Kibret, 2019). Carbon dynamics are highly influenced by the alteration of forest cover and different land cover types that store varying amounts of carbon (Dida et al., 2021).

In permafrost regions, the LULC change has significant consequences on ecological environment and engineered systems (Serban et al., 2021). The area of all soils in the northern circumpolar permafrost region is approximately 1.8782×10^7 km^2, or approximately 16% of the global soil area (Tarnocai et al., 2009). However, this region contains approximately 1,672 Pg C, of which 1,466 Pg C is stored in permafrost terrains (Tarnocai et al., 2009). This 1,672 Pg C accounts for approximately 50% of the estimated global belowground organic carbon pool (Tarnocai et al., 2009). Heilongjiang Province in Northeast China is on the southern margin of both the boreal coniferous forest and the Eurasia permafrost body, which is more sensitive to the LUCC and climate change. Moreover, Heilongjiang Province is a major province of agriculture, industry and forestry in China, and an important grain production base and primary forest distribution region. It has the largest natural forest in China, with strong carbon sink reserves and carbon sink production capacity (Guo, 2011), and has the highest plant carbon storage and carbon density in China (Wang et al., 2001). Heilongjiang Province is located in the mid-high latitude region, with low temperature all the year round, and vegetation grows slowly. However, the increase in population and human activity (e.g., deforestation) had led to significant changes in LULC before 2000s. Therefore, this study aims at exploring the changes of LULC and their effects on carbon storage in Heilongjiang Province in Northeast China during the past 35 years (1980–2015) under a changing climate and human activities. The quantitative assessment of ecosystem carbon storage is vital for sustainable development and utilization of natural resources and proper management of ecological environment. The main objectives were: 1) to analyze the spatio-temporal patterns of LULC and carbon storage; 2) to evaluate the impact of climate change, forest fire and human activities on the LULC and the response characteristics of carbon storage to LULC changes.

STUDY REGION AND METHODS

Study Region

This study region (Heilongjiang Province) (43.4167°—53.05°N; 121.1833°—135.0833°E; 0-1,692 m a. s. l.), Northeast China (**Figure 1**) is rich in water resources, with four water systems: the Heilongjiang-Amur River and tis three tributaries (Songhua, Suifen and Ussuri rivers). The Songhua River is the largest tributary of the Heilongjiang-Amur River. The Wudalianchi and Xingkai lakes are the main inland lakes. Heilongjiang Province is bestowed with the most important state-owned forest area and largest timber production base in China. The rich forest vegetation types mainly include *Larix gmelinii* (Rupr.) Kuzen, *Pinus koraiensis* Sieb. *et* Zucc., *Pinus sylvestris var. mongolica* Litv., *Picea asperata* Mast., *Abies fabri* (Mast.) Craib, *Betula platyphylla* Suk., *Quercus mongolica* Fisch. ex Ledeb., *Acer saccharum* Marsh, and *Fraxinus mandshurica* Rupr. The soil type in the study region is brown coniferous forest soil.

The region is characterized by a cold temperate continental monsoon climate with mean annual air temperature (MAAT) of 2.22°C (from 1961 to 2019), at a rising rate of 0.25°C/10a, and with a mean annual precipitation of 518 mm, at a rate of 8.3 mm/10a (**Figure 2**). Compared with the MAAT during 1961–1987 (1.67°C), the MAAT increased by 1.01°C during 1988–2019 (2.68°C). The increasing trend of MAAT is very significant ($p < 0.001$).

Data Sources

The meteorological data were obtained from the National Meteorological Information Center of China (http://www.nsmc.cma.gov.cn). The LULC data were downloaded from the Resource and Environment Science and Data Center (https://

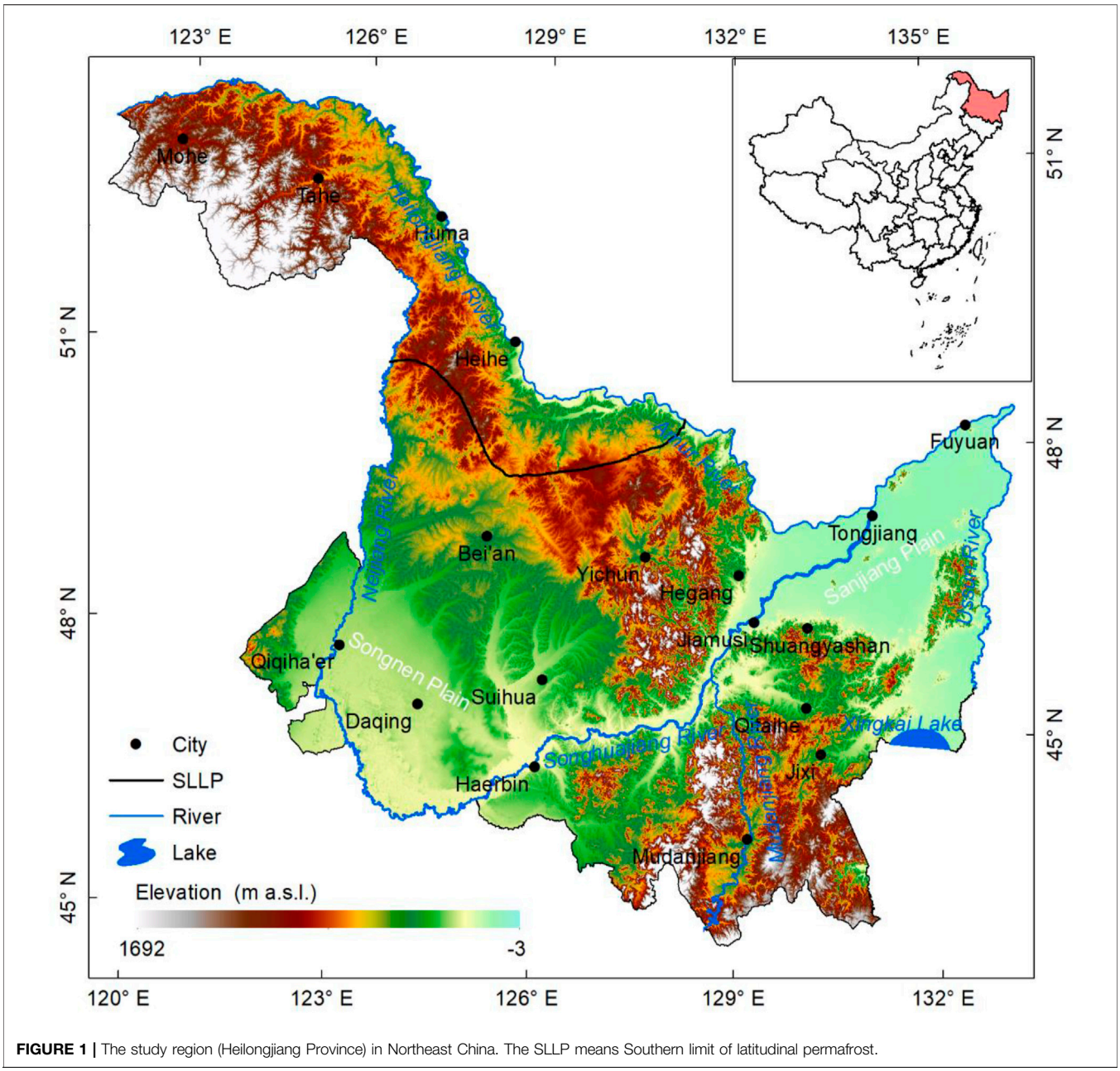

FIGURE 1 | The study region (Heilongjiang Province) in Northeast China. The SLLP means Southern limit of latitudinal permafrost.

www.resdc.cn/?aspxerrorpath=/Datalist1.aspx), with the resolution of 1 km. The digital elevation map (DEM) was collected from Geospatial Data Cloud (http://www.gscloud.cn/home), and the resolution is 90 m.

Carbon Module of InVEST Model

The InVEST model is based on the ArcGIS or as a stand-alone to transformed into software tools using Python as the scripting language (Liu. et al., 2018). The carbon module of InVEST uses a simplified carbon cycle to estimate the amount of static carbon storage and dynamic sequestration for each cell in a specific region (Tallis et al., 2013; He et al., 2016; Adelisardou et al., 2021). The carbon module consists of four carbon pools: aboveground carbon, belowground carbon, dead biological carbon (litter carbon), and soil carbon. The calculation formula is as follows:

$$C_i = C_{i-above} + C_{i-below} + C_{i-soil} + C_{i-dead} \quad (1)$$

$$C_{total} = \sum_{i=1}^{m} C_i \times A_i \quad (2)$$

where $C_{i-above}$, $C_{i-below}$, C_{i-soil}, and C_{i-dead} are the carbon density of aboveground carbon, belowground carbon, soil carbon and dead biological carbon for the i^{th} LULC type,

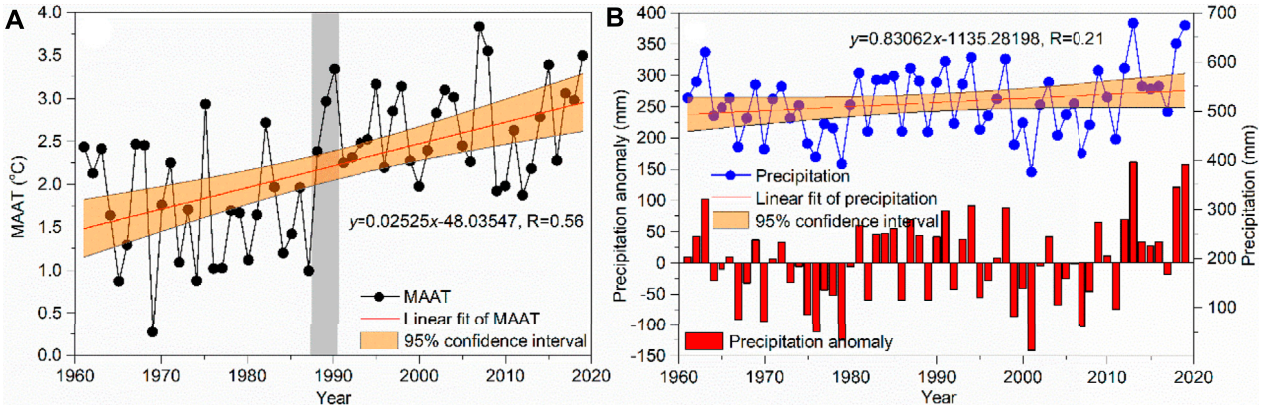

FIGURE 2 | Changes in the mean annual air temperature (MAAT) and mean annual precipitation during 1961–2019 in Heilongjiang Province, Northeast China during 1961–2019.

TABLE 1 | Carbon density of different LULC type (Yang et al., 2021).

LULC type	Aboveground carbon density (Mg/hm^2)		Belowground carbon density (Mg/hm^2)		Dead organic matter carbon density (Mg/hm^2)		Soil organic carbon density (Mg/hm^2)	
	Before revised	After revised	Before revised	After revised	Before revised	After revised	Before revised	After revised
Cropland	17	5.72	80.7	27.17	9.82	3.31	108.4	99.37
Forest	42.4	14.28	115.9	39.02	14.11	4.75	158.8	145.57
Grassland	35.3	11.89	86.5	29.12	7.28	2.45	99.9	91.58
Water	0.3	0.1	0	0	0	0	0	0
Construction land	2.5	0.84	27.5	9.26	0	0	0	0
Unused land	1.3	0.44	0	0	0	0	21.6	19.8

respectively; C_i is the carbon density for the i^{th} LULC type; and A_i is the area of the i^{th} LULC type; m is the total number of LULC types.

Carbon density data at depths of 0–1 m were obtained from literature and National Science and Technology Infrastructure (**Table 1**) (Li et al., 2003; Xie et al., 2004; Chuai et al., 2013; Yang et al., 2021).

Biomass carbon density (aboveground and belowground carbon) and soil carbon density are closely related to air temperature and precipitation (Raich and Nadelhoffer, 1989). Therefore, we use the MAAT and mean annual precipitation (MAP) during 1980–2019 in Heilongjiang Province and in China to revise the carbon density. The revised formula is as follows (Giardina and Ryan, 2000; Chen et al., 2007; Alam et al., 2013; Yang et al., 2021):

$$C_{SP} = 3.3968 \times MAP + 3996.1 \ (R^2 = 0.11) \quad (3)$$

$$C_{BP} = 6.798 \times e^{0.0054 \times MAP} \ (R^2 = 0.70) \quad (4)$$

$$C_{BT} = 28 \times MAAT + 398 \ (R^2 = 0.47, \ p < 0.01) \quad (5)$$

$$K_{BP} = \frac{C'_{BP}}{C''_{BP}} \quad (6)$$

$$K_{BT} = \frac{C'_{BT}}{C''_{BT}} \quad (7)$$

$$K_B = K_{BP} \times K_{BT} \quad (8)$$

$$K_S = \frac{C'_{SP}}{C''_{SP}} \quad (9)$$

where C_{SP} is soil carbon density (Mg/hm^2) based on MAP; C_{BP} and C_{BT} are biomass carbon densities (aboveground and belowground carbon) based on the MAP and MAAT, respectively; K_{BP} and K_{BT} are the correction coefficients of MAP and MAAT factors of biomass carbon density; C'_{BP} and C''_{BP} are biomass carbon density data (Mg/hm^2) based on MAP in the Heilongjiang Province and China, respectively. C'_{BT} and C''_{BT} are the biomass carbon density data (Mg/hm^2) based on MAAT in the Heilongjiang Province and China, respectively; C'_{SP} and C''_{SP} are soil carbon density data (Mg/hm^2) based on MAAT in the Heilongjiang Province and the China, respectively. K_B and K_S are the correction coefficients of biomass carbon density and soil carbon density, respectively. The revised carbon density data (0–1 m) are listed in **Table 1**.

RESULTS

Changes in LULC Types From 1980 to 2015

In Heilongjiang Province, forest was the main LULC type, accounting for 46–49% of the total area (**Figure 3**, **Supplementary Figure S1** and **Table 2**). It was followed by

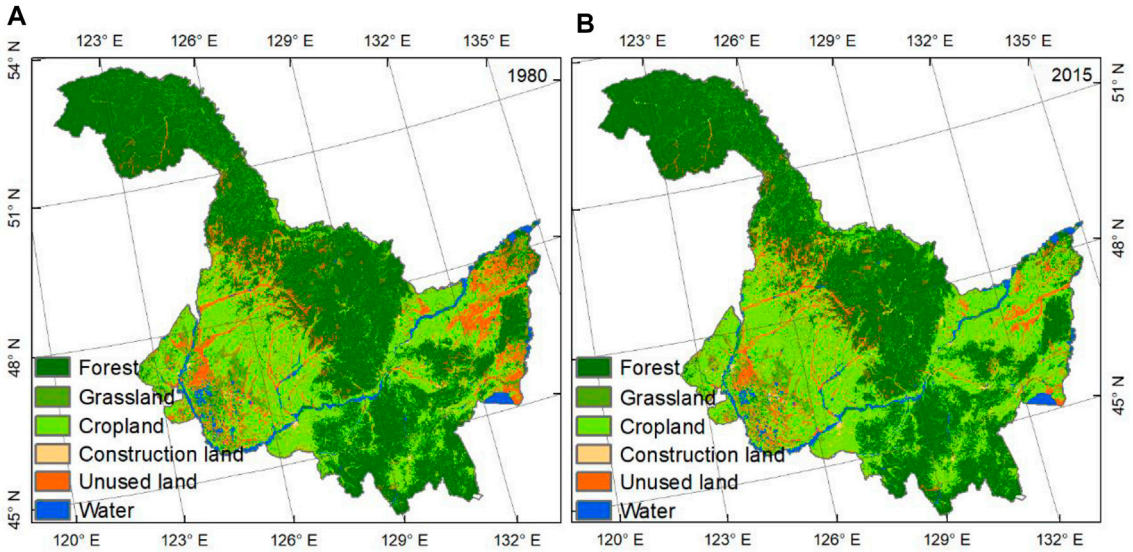

FIGURE 3 | Changes in LULC types in Heilongjiang Province, Northeast China in 1980 and 2015.

TABLE 2 | LULC and carbon storage transfer matrix during 1980–2015 in Heilongjiang Province, Northeast China ($10^4 km^2$, 10^6 Mg).

	1980 (LULC)							
2015	LULC type	Forest	Grassland	Cropland	Construction land	Unused land	Water	Total
	Forest	20.49	0.19	0.15	0.00	0.06	0.01	20.90
	Grassland	0.23	2.40	0.07	0.00	0.13	0.03	2.86
	Cropland	1.30	0.99	13.14	0.05	1.13	0.09	16.70
	Construction land	0.02	0.02	0.09	0.59	0.01	0.00	0.73
	Unused land	0.07	0.08	0.07	0.00	2.30	0.05	2.56
	Water	0.01	0.02	0.04	0.00	0.04	1.31	1.42
	Total	22.12	3.70	13.56	0.65	3.67	1.47	45.17
				1980 (Carbon storage)				
2015	LULC type	Forest	Grassland	Cropland	Construction land	Unused land	Water	Total
	Forest		13.25	9.83	0.76	10.41	1.27	35.52
	Grassland	−15.96		−0.04	0.49	14.34	4.27	3.1
	Cropland	−88.06	0.53		5.90	130.27	11.58	60.22
	Construction land	−3.07	−1.98	−11.39		−0.09	0.01	−16.52
	Unused land	−11.90	−9.07	−8.35	0.00		0.92	−28.4
	Water	−2.36	−0.09	−5.29	−0.01	−0.81		−8.56
	Total	−121.35	2.63	−15.24	7.15	154.12	18.05	45.36

cropland, accounting for 30–37% of the total area. Grassland and unused land accounted for 6–8% of the total area. The area of water (3%) and construction land (1–2%) were less than 3% of the total area. From 1980 to 2015, the areal extents of forest, grassland, unused land, and water decreased by 1.22×10^4, 0.84×10^4, 1.11×10^4 and $0.05 \times 10^4 km^2$, respectively. Cropland and construction land increased by 3.14×10^4 and $0.08 \times 10^4 km^2$, respectively (**Tables 2** and **3**).

From 1980 to 2015 (**Table 2**), forest was mainly converted to cropland and grassland. Grassland and unused land were mainly converted to cropland. Water was mainly converted to unused land. The increase in cropland was mainly due to the conversion from forest, grassland, and unused land. The increased construction land was mainly due to the conversion from cropland. During 1980 to 2000, the decreasing areas of forest, grassland, and unused land were the largest. The increasing areas of water and cropland were the largest (**Table 3**).

Changes of Carbon Storage From 1980 to 2015

From **Figure 4**, **Supplementary Figure S2** and **Table 4**, carbon was mainly stored in forest, cropland, and grassland. Changes in LULC have led to increases or decreases in carbon storage of different LULC types. From 1980 to 2015, the carbon

TABLE 3 | Changes in LULC types during 1980–1990, 1990–1995, 1995–2000, 2000–2005, 2005–2010, 2010–2015 in Heilongjiang Province, Northeast China (10^4 km^2).

Year LULC type	1980–1990	1990–1995	1995–2000	2000–2005	2005–2010	2010–2015	1980–2015
Forest	−0.20	−0.43	−0.45	−0.02	−0.21	−0.09	−1.22
Grassland	−0.26	−0.47	−0.08	0.00	0.01	−0.04	−0.84
Cropland	0.92	1.21	0.62	0.12	0.05	0.22	3.14
Construction land	0.03	0.00	0.00	0.01	0.01	0.03	0.08
Unused land	−0.52	−0.23	−0.12	−0.09	−0.04	−0.11	−1.11
Water	0.03	0.08	0.03	−0.04	0.02	−0.01	−0.05

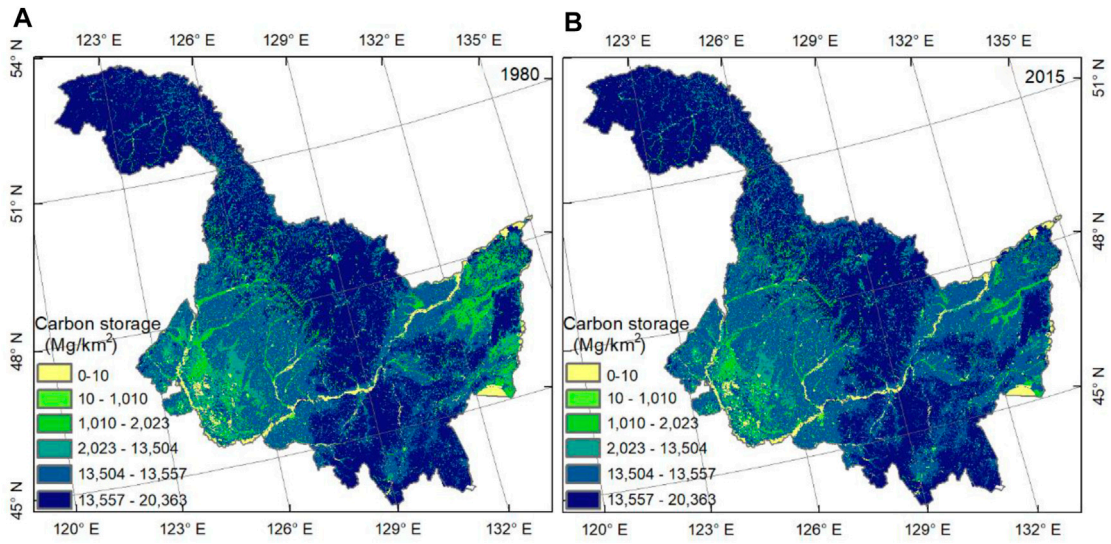

FIGURE 4 | Changes in carbon storage of Heilongjiang Province, Northeast China in 1980 and 2015.

TABLE 4 | Carbon storage in different LULC type from 1980 to 2015 in Heilongjiang Province, Northeast China (×10^6 Mg).

LULC types	1980	1990	1995	2000	2005	2010	2015
Forest	4,425.06	4,389.51	4,305.84	4,220.46	4,213.86	4,206.07	4,188.84
Grassland	545.20	508.60	440.89	429.22	431.67	433.57	428.59
Cropland	1,808.49	1,928.20	2,090.93	2,173.79	2,188.14	2,195.31	2,223.14
Construction land	8.09	8.56	8.61	8.68	8.75	8.78	9.08
Unused land	76.07	65.76	61.23	58.77	57.21	56.31	54.25
Water	0.15	0.15	0.15	0.15	0.15	0.15	0.15
Total	6,863.06	6,900.79	6,907.64	6,891.08	6,899.78	6,900.19	6,904.05

storage of forest, grassland, and unused land decreased gradually, while that of cropland and construction land increased gradually. The total carbon storage of Heilongjiang Province increased from 1980 to 2015, with the lowest in 1980 and the highest in 1995.

From 1980 to 2015, the total carbon storage of Heilongjiang Province increased by 45.36 × 10^6 Mg C (**Table 2**), since the conversion of large areas of forest, grassland, and unused land to cropland. Due to the low carbon density of the unused land, the conversion to cropland facilitated the formation of carbon sinks and thus increases carbon storage. However, the change of carbon storage varied with changes in different LULC types: the carbon storage in forest and cropland types decreased after transformation, and those of grassland, water, construction land, and unused land increased (**Table 2**).

DISCUSSIONS

Impacts on the LULC Types

There are many driving factors of LULC changes, which can be divided into anthropogenic and natural factors. With rising global temperatures, the belt of boreal forest is moving northward, and temperate forests would continue to migrate closer or into the positions of current boreal forests, and possibly at an unprecedented moving rate (Leithead et al.,

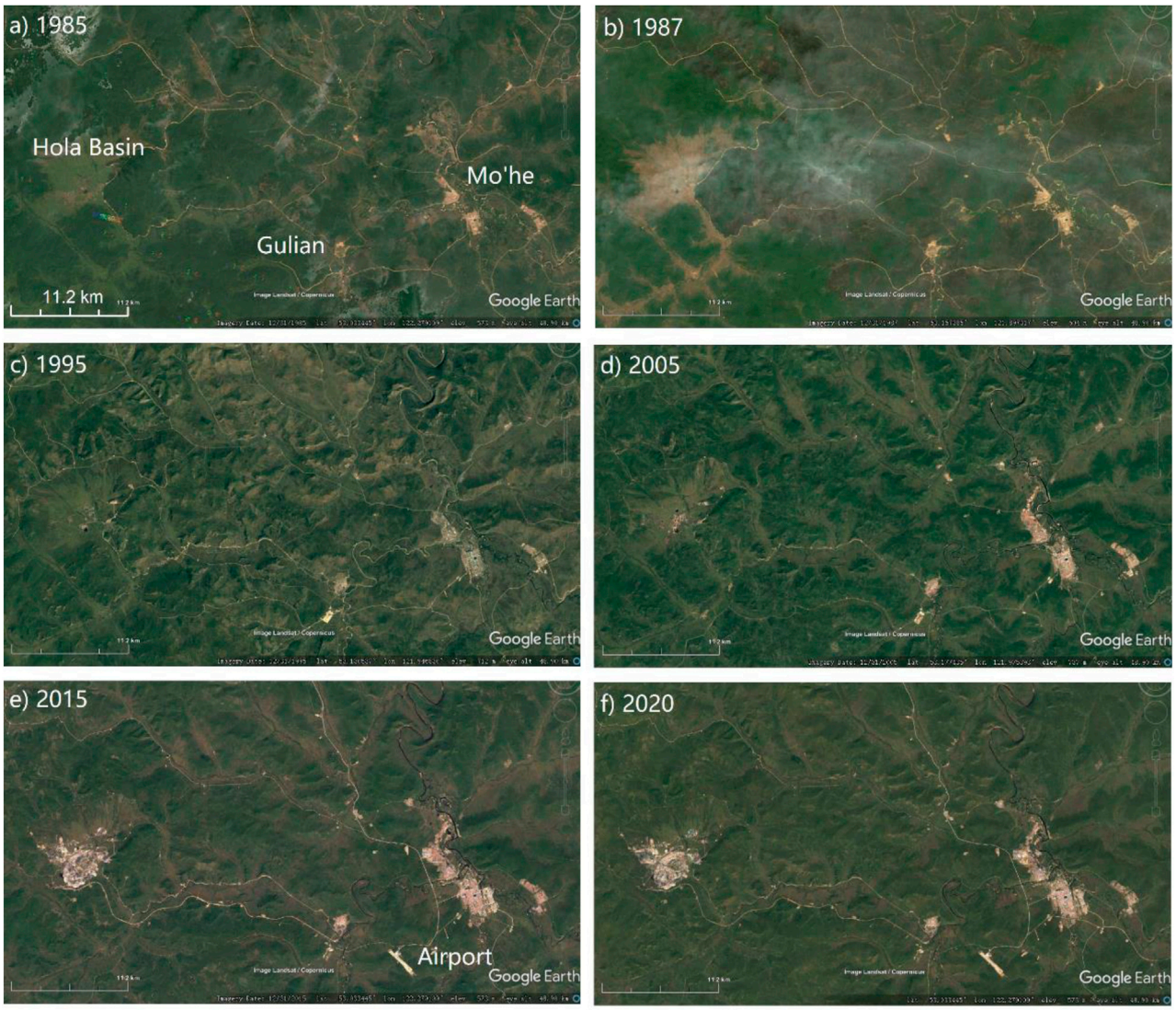

FIGURE 5 | Landscape changes in Mo'he, Gulian and Hola basins in Mo'he County in northern Heilongjiang Province, Northeast China from 1985 to 2020. Panel **(A–F)** is the expansion of Mo'he and Gulian towns, panel **(A–D)** is the expansion of coal mines at Hola and basins and roads, panel **(E,F)** represents the construction of airport, and panel **(B)** represents the forest fire in 1987.

2010). Then, the coniferous forest would transfer to broadleaf forest, shrubs, grassland, or even wetlands. Due to its marginal location at the southern edge of the boreal forest, the LULC in Northeast China are more sensitive to climate warming (Serban et al., 2021). Moreover, Northeast China underwent the largest increase in air temperature and a significant decline in summer-autumn precipitation (Zhang et al., 2020; Li X. et al., 2021). In Heilongjiang Province, Northeast China, persistent climate warming was recorded from 1961 to 2019, especially after 1988 (**Figure 2**). The MAAT during 1988–2019 was 1.01°C higher than that during 1961–1987, and; it rose by 1.06°C from 1961 to 2019 at an average rate of 0.25°C/10a. However, the average rising rate of global MAAT was 0.12°C/10a from 1951 to 2012 (Zhang et al., 2018). Under a climate change, the permafrost in northeast China was undergoing large-scale degradation and the southern limit of permafrost was moving northward significantly (Li X. et al., 2021). And compared with that in the 1960s, the extent of Xing'an permafrost in Northeast China had decreased by 40.6% by the 2010s (Li X. et al., 2021). And the permafrost degradation had caused large areas of coniferous forest moved northward significantly (Jin et al., 2007). Consequently, the pronounced shrub expansion was occurring in the circumpolar Arctic tundra driven by climate warming and permafrost degradation (Myers-Smith et al., 2011).

The increases in cropland and construction land were mainly concentrated around roads and major settlements. Thus, the main causes for unused land, grassland, and forest disturbances were deforestation and clearing for agricultural cultivation, construction of public facilities, resource exploitation, lumbering, airport construction, and others. Since

1893, a large number of people emigrated from the south to northeast China, the population grew exponentially and land was reclaimed and cultivated on a large scale. LULC had undergone significant changes, and which of Heilongjiang Province has the most intense (Jiang, 2017). After 1904, the implementation of the open-land reclamation policy and the construction of the Middle-East railway in Heilongjiang Province, as well as the activities of going and working in the countryside and mountainous areas in 1949, resulted in drastic changes to LULC, which mainly focused on the expansion of cropland and the reclamation of grassland and wetland (Cheng and Fang, 2010). For example, in **Figure 3**, the areas of cropland in Sanjiang Plain and Songnen Plain increased significantly from 1980 to 2015. In Mo'he County in northern Heilongjiang Province, rapid population growth and the demand for residence and factories forced the clearance of natural vegetation, resulting in the expansion of urbanization area and increase of road from 1985 to 2020 (**Figures 5A–F**). Changes of LULC types were concentrated in the Hola Basin for coal mining, airport construction, and along the roads in the south for transporting coal after 2005 (**Figures 5A–F**); those all contributed to the rapid expansion of the anthropic class (Serban et al., 2021). From **Table 3**, compared with that during 1980–1990, 1990–1995 and 1995–2000, the forest decreased and cropland increased significantly during 2000–2005, 2005–2010 and 2010–2015, and the grassland conversion area was 0 km^2 during 2000–2005. This may be explained by the implementation of policy of returning the cultivated croplands to forest and grasslands in 2003.

Wildfires is also an important driver for changes in the LULC types. Under a warming climate and human activities, the fire frequency, magnitude, and severity gradually increase, influencing the ecosystem. Importantly, wildfires were caused not only by climatic factors, but also by Anthropocene changes in landscape (Bowman et al., 2020). In the western United States, sedimentary charcoal records showed a primary control of fire activity by temperature and drought over the last 3,000 years (Marlon et al., 2012). Moreover, the effect of climate change is becoming apparent in the increasing numbers of extreme fire events (Cruz et al., 2012; Bowman et al., 2017; Ndalila et al., 2018). Such as in Australia, a globally anomalous fire season in 2019–2020 burned over 5×10^6 hm^2 of *Eucalyptus* forests (Boer et al., 2020). The wildfire occurred in the northern Da Xing'anling (Hinggan) Mountains, Northeast China, burned more than 1×10^6 hm^2 of forests on 6 May-2 June 1987 (Li X. et al., 2021). Wildfires could result in an irreversible permafrost degradation, successions of vegetation, rapid losses of soil carbon, and formation and development of thermokarst (Cong et al., 2020; Li X. et al., 2021). After wildfires, ground temperatures and active layer thickness increase; the release of soil carbon enhances, and; vegetation changes from coniferous forests to broad-leaved forests, shrublands or grasslands. It may take decades or even centuries for the fire-disturbed ecosystems and permafrost environment to return to pre-fire conditions (Holloway et al., 2020; Li X. et al., 2021). For example, in **Figure 5B**, the black and brown areas showed the burned area causing by the fire in 1987, which resulted in extensive vegetation destruction. The high fire frequency and severity could cause the conversion of coniferous forest to meadow, shrub, deciduous broadleaf forest, or tundra, and expansion of shrubs across the Arctic tundra, it may even take hundreds of years to recover to the pre-fire conditions (Li X. et al., 2021; Chen et al., 2021).

Changes in LULC and Effects on Carbon Storage

Under a warming climate, more severe and frequent boreal forest fires had driven and shifted boreal ecosystem into a positive net carbon balance (from a net carbon sink to a net carbon source over a fire cycle), resulting in a positive climate feedback (Bond-Lamberty et al., 2007; Walker et al., 2019). It is mainly manifested in increasing emissions of CO_2 directly through the combustion of forest biomass (LULC changes) and soil carbon stocks (e.g., wetlands and peatlands) and emissions of CH_4 and N_2O indirectly through thawing of permafrost and changing thermokarst hydrology (O'Connor et al., 2010; Gibson et al., 2018; Loranty et al., 2018; Walker et al., 2019; Bowman et al., 2020). Boreal forests store 30–40% of terrestrial carbon; 70–80% of which is stored in organic soil, and; consequently, this shift from a net carbon sink to a carbon source could impact the global carbon cycle (Lorenz and Lal, 2010). In the northern permafrost region, organic soils (peatlands) and cryoturbated permafrost-affected mineral soils have the highest mean soil organic carbon contents (32.2–69.6 kg/m^2) (Tarnocai et al., 2009).

The change of LULC after fire (removal of vegetation and organic layer) increases exposure to solar radiation, result in the diminishing or even disappearance of thermal insulation and reducing of surface albedo, while the ground heat influx increases (Nossov et al., 2013; Holloway et al., 2020). Furthermore, because of heat accumulation, permafrost degrades rapidly in the form of deepening active layer and rising soil temperature (Brown et al., 2015; Li X. et al., 2021). In addition to forest fires and climate warming directly induced soil carbon emissions, permafrost degradation can alter microbial activity and result in more carbon being released into the atmosphere in the form of CH_4 and CO_2 effluxes that contribute to further warming (Loranty et al., 2018). The thawing of ice-rich permafrost could lead to the occurrence of thermokarst phenomenon, such as thermokarst lakes and ponds, surface subsidence, and thaw slumps (Holloway et al., 2020). Thermokarst development can lead to landscape wetting by promoting the transition from permafrost plateau forest to wetlands (Baltzer et al., 2014). Thermokarst lakes in permafrost regions are sources of the strong CH_4 emissions and their expansion may have significantly contributed to the rise of the atmospheric CH_4 concentrations (van Huissteden et al., 2011).

Heilongjiang Province is located at the southern edge of boreal forest and Eurasian permafrost, with forest area accounting for 46.3–49.0% of the province area from 1980 to 2015, and permafrost area accounting for 21.6% of the province area (**Figure 1**). The research at the Xiao Xing'anling Mountains in Heilongjiang Province, Northeast China, also showed the rapidly degrading permafrost under marsh-wetlands since 2004. The

organic matter and CH_4 stored in the permafrost soil were gradually released to the atmosphere (Shan et al., 2020). The studies in Northeast China show that forest fire and permafrost degradation not only lead to the change of LULC, but also to the reduction of carbon storage (Li et al., 2020b; Li et al., 2022). Furthermore, in Northeast China, a more rapid permafrost degradation has been occurring under the expanding urban regions and engineering infrastructures, such as the Mo'he County and airport and in the right-of-way along the China-Russia Crude Oil Pipeline (Li et al., 2018; Mao et al., 2019). Under a warming climate and thermal disturbances of airport construction and operation, the warming rate of permafrost at depth of 10 m reached by 0.03–0.15°C/a; the permafrost table lowered by 7.5 m from depths of 4.5–12 m in ten year (Mao et al., 2019). Due to the construction of the China-Russia Crude Oil Pipeline and the removal of vegetation, active layer thickness increased by 2.7 m and permafrost temperature at depth of 15–20 m rose by 0.2°C from 2014 to 2017 (Li et al., 2018). Under the influence of urbanization, the area of construction land in Mo'he County increased by 39.3% in the last decade. From the edge of the urban area to the center of Mo'he County, ground temperature increased from −0.9 to 3.0°C at the depth of 15 m and the permafrost table lowered from 6.1 to 22.3 m (Lu, 2018). In Northeast China, a severe burn led to a rising of soil temperatures (2.3°C) and substantial reduction of soil carbon (67.5%) in the active layer, which were not recovered seven years after forest fire (Li et al., 2020b).

Therefore, under the combined effects of climate warming, urbanization expansion, high frequency forest fires, rapid permafrost degradation, and engineering construction, significant changes in LULC and soil carbon storage have occurred in Heilongjiang Province, Northeast China.

CONCLUSIONS

The changes of LULC types and soil carbon storages were analyzed based on InVEST modeling from 1980 to 2015 in Heilongjiang Province, Northeast China, with the following conclusions:

Forest and cropland are the dominant LULC types in Heilongjiang Province, Northeast China, accounting for 46%-49%and 30–37% of the total area. From 1980 to 2015, forest, grassland, unused land, and water decreased by 1.22×10^4, 0.84×10^4, 1.11×10^4, and 0.05×10^4 km^2, respectively. Cropland and construction land increased by 3.14×10^4 and 0.08×10^4 km^2, respectively. This was due to the conversion of forest to cropland and grassland, that of grassland and unused land to cropland, and that of water surfaces to unused land from 1980 to 2015. The changes of LULC types were the most obviously during 1980–2000. The carbon storage of forest, grassland, and unused land decreased gradually by 236.22, 116.61 and 21.82 $\times$ 10^6 Mg C, respectively, while those of cropland and construction land increased gradually by 414.65 and 0.99 $\times$ 10^6 Mg C, respectively. From 1980 to 2015, due to the conversion of large areas of forest, grassland, and unused land to cropland. The unused land has a low carbon density, and the conversion of the unused land to cropland facilitated the formation of carbon sinks and thus increased carbon storage. Therefore, the total carbon storage of Heilongjiang Province increased by 45.36×10^6 Mg C from 1980 to 2015.

Under a warming climate and human activities, such as frequent wildfires, urban expansion, farmland reclamation, and engineering construction had led to changes in LULC, accelerating permafrost degradation. Under the combined action of these factors, soil carbon storages were significantly changed. Forest and grassland areas and their carbon storage decreased obviously, even though the total carbon storage of Heilongjiang Province increased. However, forest and grassland are important component of ecosystem service function and carbon pools in Northeast China. Therefore, evaluation of ecosystem carbon storage in boreal forest and permafrost regions are of great significance for decision-making in ecosystem service, ecological environmental protection and sustainable development.

DATA AVAILABILITY STATEMENT

The original contributions presented in the study are included in the article/**Supplementary Material**, further inquiries can be directed to the corresponding authors.

AUTHOR CONTRIBUTIONS

XL and HJ contributed to the conceptualization and writing of the manuscript. XL, LS and CH contributed to the theory and methodology. CH, HC, TH, GY, HY, YH, SK and JL contributed to the resources and field data collection and data compilation. All authors contributed to the article and approved the submitted version.

FUNDING

This research is funded by the Natural Science Foundation of China (Grant No. 42001052); Startup Fund of Northeast Forestry University for Chengdong Outstanding Youth Scholarship (YQ 2020-10); the State Key Laboratory of Frozen Soils Engineering Open Fund (Grant No. SKLFSE202008), and; Fundamental Research Fund for the Central Universities (Grant No. 2572021BA03).

SUPPLEMENTARY MATERIAL

The Supplementary Material for this article can be found online at: https://www.frontiersin.org/articles/10.3389/feart.2022.846456/full#supplementary-material

REFERENCES

Adelisardou, F., Zhao, W., Chow, R., Mederly, P., Minkina, T., and Schou, J. S. (2021). Spatiotemporal Change Detection of Carbon Storage and Sequestration in an Arid Ecosystem by Integrating Google Earth Engine and InVEST (The Jiroft plain, Iran). *Int. J. Environ. Sci. Technol.* 71, 1279–1290. doi:10.1007/s13762-021-03676-6

Alam, S. A., Starr, M., and Clark, B. J. F. (2013). Tree Biomass and Soil Organic Carbon Densities across the Sudanese woodland savannah: A Regional Carbon Sequestration Study. *J. Arid Environments* 89, 67–76. doi:10.1016/j.jaridenv.2012.10.002

Baltzer, J. L., Veness, T., Chasmer, L. E., Sniderhan, A. E., and Quinton, W. L. (2014). Forests on Thawing Permafrost: Fragmentation, Edge Effects, and Net forest Loss. *Glob. Change Biol.* 20, 824–834. doi:10.1111/gcb.12349

Boer, M. M., Resco de Dios, V., and Bradstock, R. A. (2020). Unprecedented Burn Area of Australian Mega forest Fires. *Nat. Clim. Chang.* 10, 171–172. doi:10.1038/s41558-020-0716-1

Bond-Lamberty, B., Peckham, S. D., Ahl, D. E., and Gower, S. T. (2007). Fire as the Dominant Driver of central Canadian Boreal forest Carbon Balance. *Nature* 450 (7166), 89–92. doi:10.1038/nature06272

Bowman, D. M. J. S., Kolden, C. A., Abatzoglou, J. T., Johnston, F. H., van der Werf, G. R., and Flannigan, M. (2020). Vegetation Fires in the Anthropocene. *Nat. Rev. Earth Environ.* 1, 500–515. doi:10.1038/s43017-020-0085-3

Bowman, D. M. J. S., Williamson, G. J., Abatzoglou, J. T., Kolden, C. A., Cochrane, M. A., and Smith, A. M. S. (2017). Human Exposure and Sensitivity to Globally Extreme Wildfire Events. *Nat. Ecol. Evol.* 1, 58. doi:10.1038/s41559-016-0058

Brown, D. R. N., Jorgenson, M. T., Douglas, T. A., Romanovsky, V. E., Kielland, K., Hiemstra, C., et al. (2015). Interactive Effects of Wildfire and Climate on Permafrost Degradation in Alaskan lowland Forests. *J. Geophys. Res. Biogeosci.* 120, 1619–1637. doi:10.1002/2015jg003033

Chen, G., and Tian, H. (2007). Land Use/cover Change Effects on Carbon Cycling in Terrestrial Ecosystems. *Chin. J. Plant Ecol.* 31, 189–204 [in Chinese]. doi:10.1111/gcb.15069

Chen, G., Yang, Y., Liu, L., Li, X., Zhao, Y., and Yuan, Y. (2007). Research Review on Total Belowground Carbon Allocation in Forest Ecosystems. *J. Subtrop. Res. Environ.* 2, 34–42 [in Chinese]. doi:10.19687/j.cnki.1673-7105.2007.01.005

Chen, Y., Hu, F. S., and Lara, M. J. (2021). Divergent Shrub-cover Responses Driven by Climate, Wildfire, and Permafrost Interactions in Arctic Tundra Ecosystems. *Glob. Change Biol.* 27, 652–663. doi:10.1111/gcb.15451

Cheng, Y., and Fang, Y. (2010). Morphology Change and its Influencing Factors of Agricultural Terrain Structure in Northeast China. *Econ. Geogr.* 30 (8), 1349–1353. doi:10.15957/j.cnki.jjdl.2010.08.017

Chuai, X., Huang, X., Lai, L., Wang, W., Peng, J., and Zhao, R. (2013). Land Use Structure Optimization Based on Carbon Storage in Several Regional Terrestrial Ecosystems across China. *Environ. Sci. Pol.* 25, 50–61. doi:10.1016/j.envsci.2012.05.005

Cong, J., Gao, C., Han, D., Li, Y., and Wang, G. (2020). Stability of the Permafrost Peatlands Carbon Pool under Climate Change and Wildfires during the Last 150 Years in the Northern Great Khingan Mountains, China. *Sci. Total Environ.* 712, 136476. doi:10.1016/j.scitotenv.2019.136476

Cruz, M. G., Sullivan, A. L., Gould, J. S., Sims, N. C., Bannister, A. J., Hollis, J. J., et al. (2012). Anatomy of a Catastrophic Wildfire: The Black Saturday Kilmore East Fire in Victoria, Australia. *For. Ecol. Manag.* 284, 269–285. doi:10.1016/j.foreco.2012.02.035

Dida, J. J. V., Tiburan, C. L., Jr, Tsutsumida, N., and Saizen, I. (2021). Carbon Stock Estimation of Selected Watersheds in Laguna, Philippines Using InVEST. *Philippine J. Sci.* 150, 501–513.

Giardina, C. P., and Ryan, M. G. (2000). Evidence that Decomposition Rates of Organic Carbon in mineral Soil Do Not Vary with Temperature. *Nature* 404, 858–861. doi:10.1038/35009076

Gibson, C. M., Chasmer, L. E., Thompson, D. K., Quinton, W. L., Flannigan, M. D., and Olefeldt, D. (2018). Wildfire as a Major Driver of Recent Permafrost Thaw in Boreal Peatlands. *Nat. Commun.* 9, 3041. doi:10.1038/s41467-018-05457-1

Guo, S. (2011). Analysis on Carbon Stock and Potential Carbon Sequestration in Heilongjiang Province. *For. Eng.* 27 (3), 9–16. doi:10.16270/j.cnki.slgc.2011.03.022

He, C., Zhang, D., Huang, Q., and Zhao, Y. (2016). Assessing the Potential Impacts of Urban Expansion on Regional Carbon Storage by Linking the LUSD-Urban and InVEST Models. *Environ. Model. Softw.* 75, 44–58. doi:10.1016/j.envsoft.2015.09.015

Holloway, J. E., Lewkowicz, A. G., Douglas, T. A., Li, X., Turetsky, M. R., Baltzer, J. L., et al. (2020). Impact of Wildfire on Permafrost Landscapes: A Review of Recent Advances and Future Prospects. *Permafrost and Periglac Process* 31, 371–382. doi:10.1002/ppp.2048

Houghton, R. A. (2003). Revised Estimates of the Annual Net Flux of Carbon to the Atmosphere from Changes in Land Use and Land Management 1850-2000. *Tellus B* 55, 378–390. doi:10.1034/j.1600-0889.2003.01450.x

Jiang, L. (2017). Effect and Mechanism of Land Cover Change on Climate Change in Heilongjiang Province during 1900s-2010s. Doctoral Dissertation. Heilongjing (China): Harbin Normal University.

Jin, H., Yu, Q., Lü, L., Guo, D., He, R., Yu, S., et al. (2007). Degradation of Permafrost in the Xing'anling Mountains, Northeastern China. *Permafrost Periglac. Process.* 18, 245–258. doi:10.1002/ppp.589

Leithead, M. D., Anand, M., and Silva, L. C. R. (2010). Northward Migrating Trees Establish in Treefall Gaps at the Northern Limit of the Temperate-Boreal Ecotone, Ontario, Canada. *Oecologia* 164, 1095–1106. doi:10.1007/s00442-010-1769-z

Li, G., Wang, F., Ma, W., Fortier, R., Mu, Y., Zhou, Z., et al. (2018). Field Observations of Cooling Performance of Thermosyphons on Permafrost under the China-Russia Crude Oil Pipeline. *Appl. Therm. Eng.* 141, 688–696. doi:10.1016/j.applthermaleng.2018.06.005

Li, K., Wang, S., and Cao, M. (2003). Carbon Storage of Vegetation and Soil in China. *Sci. China (Series D).* 33, 72–80. doi:10.1002/ecs2.3341

Li, X., Jin, H., Wang, H., Marchenko, S. S., Shan, W., Luo, D., et al. (2021b). Influences of forest Fires on the Permafrost Environment: A Review. *Adv. Clim. Change Res.* 12, 48–65. doi:10.1016/j.accre.2021.01.001

Li, X., Jin, H., He, R., and Huang, Y. (2020a). Effects of forest Fires on Ecological Service in Permafrost Regions. *Clim. Chang. Res.* 16, 545–554 [in Chinese]. doi:10.12006/j.issn.1673-1719.2020.019

Li, X., Jin, H., Sun, L., Wang, H., He, R., Huang, Y., et al. (2021a). Climate Warming over 1961-2019 and Impacts on Permafrost Zonation in Northeast China. *J. For. Res.* doi:10.1007/s11676-021-01403-y

Li, X., Jin, H., Wang, H., Jin, X., Bense, V. F., Marchenko, S. S., et al. (2022). Effects of Fire History on thermal Regimes of Permafrost in the Northern Da Xing'anling Mountains, NE China. *Geoderma* 410, 115670. doi:10.1016/j.geoderma.2021.115670

Li, X., Jin, H., Wang, H., Wu, X., Huang, Y., He, R., et al. (2020b). Distributive Features of Soil Carbon and Nutrients in Permafrost Regions Affected by forest Fires in Northern Da Xing'anling (Hinggan) Mountains, NE China. *Catena* 185, 104304. doi:10.1016/j.catena.2019.104304

Liu, S., Hu, N., Zhang, J., and Lv, Z. (2018). Spatiotemporal Change of Carbon Storage in the Loess Plateau of Northern Shaanxi, Based on the InVEST Model. *Sci. Cold Arid Reg.* 10, 0240–0250. doi:10.3724/SP.J.1226.2018.00240

Loranty, M. M., Abbott, B. W., Blok, D., Douglas, T. A., Epstein, H. E., Forbes, B. C., et al. (2018). Reviews and Syntheses: Changing Ecosystem Influences on Soil thermal Regimes in Northern High-Latitude Permafrost Regions. *Biogeosciences* 15, 5287–5313. doi:10.5194/bg-15-5287-2018

Lorenz, K., and Lal, R. (2010). "Carbon Dynamics and Pools in Major Forest Biomes of the World", in *Carbon sequestration in Forest Ecosystems* (Dordrecht: Springer), 159–205.

Lu, Y. (2018). Study on the Change of Permafrost in Urban Environment: A Case Study of Mohe County. *Northwest Institute of Eco-Environmental and Resources Chinese Academy of Sciences*, Doctoral thesis. (Lanzhou, China: University of Chinese Academy of Sciences), 1–141 (in Chinese).

Mao, Y., Li, G., Ma, W., Mu, Y., Wang, F., Miao, J., et al. (2019). Field Observation of Permafrost Degradation under Mo'he Airport, Northeastern China from 2007 to 2016. *Cold Regions Sci. Tech.* 161, 43–50. doi:10.1016/j.coldregions.2019.03.004

Marlon, J. R., Bartlein, P. J., Gavin, D. G., Long, C. J., Anderson, R. S., Briles, C. E., et al. (2012). Long-term Perspective on Wildfires in the Western USA. *Proc. Natl. Acad. Sci.* 109, E535–E543. doi:10.1073/pnas.1112839109

Myers-Smith, I. H., Forbes, B. C., Wilmking, M., Hallinger, M., Lantz, T., Blok, D., et al. (2011). Shrub Expansion in Tundra Ecosystems: Dynamics, Impacts and

Research Priorities. *Environ. Res. Lett.* 6, 045509. doi:10.1088/1748-9326/6/4/045509

Ndalila, M. N., Williamson, G. J., and Bowman, D. M. J. S. (2018). Geographic Patterns of Fire Severity Following an Extreme Eucalyptus Forest Fire in Southern Australia: 2013 Forcett-Dunalley Fire. *Fire* 1, 40. doi:10.3390/fire1030040

Nie, X., Lu, B., Chen, Z., Yang, Y., Chen, S., Chen, Z., et al. (2020). Increase or Decrease? Integrating the CLUMondo and InVEST Models to Assess the Impact of the Implementation of the Major Function Oriented Zone Planning on Carbon Storage. *Ecol. Indicators* 118, 106708. doi:10.1016/j.ecolind.2020.106708

Noble, I. R., Bolin, B., Ravindranath, N. H., Verardo, D. J., and Dokken, D. J. (2000). Land Use, Land Use Change, and Forestry. *Environ. Conserv.* 28, 284–293.

Nossov, D. R., Torre Jorgenson, M., Kielland, K., and Kanevskiy, M. Z. (2013). Edaphic and Microclimatic Controls over Permafrost Response to Fire in interior Alaska. *Environ. Res. Lett.* 8, 035013. doi:10.1088/1748-9326/8/3/035013

O'Connor, F. M., Boucher, O., Gedney, N., Jones, C. D., Folberth, G. A., Coppell, R., et al. (2010). Possible Role of Wetlands, Permafrost, and Methane Hydrates in the Methane Cycle under Future Climate Change: A Review. *Rev. Geophys.* 48, RG4005. doi:10.1029/2010rg000326

Ouyang, Z., Zheng, H., Xiao, Y., Polasky, S., Liu, J., Xu, W., et al. (2016). Improvements in Ecosystem Services from Investments in Natural Capital. *Science* 352, 1455–1459. doi:10.1126/science.aaf2295

Raich, J. W., and Nadelhoffer, K. J. (1989). Belowground Carbon Allocation in forest Ecosystems: Global Trends. *Ecology* 70, 1346–1354. doi:10.2307/1938194

Serban, R.-D., Serban, M., He, R., Jin, H., Li, Y., Li, X., et al. (2021). 46-Year (1973-2019) Permafrost Landscape Changes in the Hola Basin, Northeast China Using Machine Learning and Object-Oriented Classification. *Remote Sensing* 13, 1910. doi:10.3390/rs13101910

Shan, W., Xu, Z., Guo, Y., Zhang, C., Hu, Z., and Wang, Y. (2020). Geological Methane Emissions and Wildfire Risk in the Degraded Permafrost Area of the Xiao Xing'an Mountains, China. *Sci. Rep.* 10, 21297. doi:10.1038/s41598-020-78170-z

Tallis, H. T., Ricketts, T., Guerry, A. D., Wood, S. A., Sharp, R., Nelson, E., et al. (2013). *Capital Project: Stanford. InVEST 2.5.6 User's Guide*. Stanford, CA, USA: Nat. Cap. Proj.

Tarnocai, C., Canadell, J. G., Schuur, E. A. G., Kuhry, P., Mazhitova, G., and Zimov, S. (2009). Soil Organic Carbon Pools in the Northern Circumpolar Permafrost Region. *Glob. Biogeochem. Cycles* 23, GB2023. doi:10.1029/2008gb003327

Tolessa, T., Senbeta, F., and Kidane, M. (2017). The Impact of Land Use/land Cover Change on Ecosystem Services in the central highlands of Ethiopia. *Ecosystem Serv.* 23, 47–54. doi:10.1016/j.ecoser.2016.11.010

Toru, T., and Kibret, K. (2019). Carbon Stock under Major Land Use/land Cover Types of Hades Sub-watershed, Eastern Ethiopia. *Carbon Balance Manage* 14, 7. doi:10.1186/s13021-019-0122-z

van Huissteden, J., Berrittella, C., Parmentier, F. J. W., Mi, Y., Maximov, T. C., and Dolman, A. J. (2011). Methane Emissions from Permafrost Thaw Lakes Limited by lake Drainage. *Nat. Clim Change* 1, 119–123. doi:10.1038/nclimate1101

Viana, C. M., Oliveira, S., Oliveira, S. C., and Rocha, J. (2019). Land Use/land Cover Change Detection and Urban Sprawl Analysis. *Spat. Model. GIS R Earth Environ. Sci.* 2019, 621–651. doi:10.1016/b978-0-12-815226-3.00029-6

Walker, X. J., Baltzer, J. L., Cumming, S. G., Day, N. J., Ebert, C., Goetz, S., et al. (2019). Increasing Wildfires Threaten Historic Carbon Sink of Boreal forest Soils. *Nature* 572, 520–523. doi:10.1038/s41586-019-1474-y

Wang, X., Feng, Z., and Ouyang, Z. (2001). Vegetation Carbon Storage and Density of Forest Ecosystems in China. *Chin. J. Appl. Ecol.* 12 (1), 13–16 [in Chinese]. doi:10.13287/j.1001-9332.2001.0003

Wang, X., Li, Y., Gong, X., Niu, Y., Chen, Y., Shi, X., et al. (2019). Storage, Pattern and Driving Factors of Soil Organic Carbon in an Ecologically Fragile Zone of Northern China. *Geoderma* 343, 155–165. doi:10.1016/j.geoderma.2019.02.030

Xie, G., Zhang, C., Zhen, L., and Zhang, L. (2017). Dynamic Changes in the Value of China's Ecosystem Services. *Ecosystem Serv.* 26, 146–154. doi:10.1016/j.ecoser.2017.06.010

Xie, X., Sun, B., Zhou, H., Li, Z., and Li, A. (2004). Organic Carbon Density and Storage in Soils of China and Spatial Analysis. *Acta Pedologica Sin* 41, 35–43 [in Chinese]. doi:10.11766/trxb200301140106

Yang, J., Xie, B., and Zhang, D. (2021). Spatio-temporal Evolution of Carbon Stocks in the Yellow River Basin Based on InVEST and CA-Markov Models. *Chin. J. Eco-agric.* 29, 1018–1029 [in Chinese]. doi:10.13930/j.cnki.cjea.200746

Zhang, X., Liu, X., Wang, W., Zhang, T., Zeng, X., Xu, G., et al. (2018). Spatiotemporal Variability of Drought in the Northern Part of Northeast China. *Hydrological Process.* 32, 1449–1460. doi:10.1002/hyp.11503

Zhang, Y., Liang, S., and Xiao, Z. (2020). Observed Vegetation Greening and its Relationships with Cropland Changes and Climate in China. *Land* 9, 274. doi:10.3390/land9080274

Zhao, M., He, Z., Du, J., Chen, L., Lin, P., and Fang, S. (2019). Assessing the Effects of Ecological Engineering on Carbon Storage by Linking the CA-Markov and InVEST Models. *Ecol. Indicators* 98, 29–38. doi:10.1016/j.ecolind.2018.10.052

Conflict of Interest: The authors declare that the research was conducted in the absence of any commercial or financial relationships that could be construed as a potential conflict of interest.

Publisher's Note: All claims expressed in this article are solely those of the authors and do not necessarily represent those of their affiliated organizations, or those of the publisher, the editors and the reviewers. Any product that may be evaluated in this article, or claim that may be made by its manufacturer, is not guaranteed or endorsed by the publisher.

frontiers in Earth Science

ORIGINAL RESEARCH
published: 24 March 2022
doi: 10.3389/feart.2022.782013

Dissolved Organic Carbon (DOC) in Ground Ice on Northeastern Tibetan Plateau

Yuzhong Yang[1,2], Xiaoyan Guo[3,4,5], Qingfeng Wang[1], Huijun Jin[1], Hanbo Yun[1] and Qingbai Wu[2]**

[1]State Key Laboratory of Frozen Soil Engineering, Northwest Institute of Eco-Environment and Resources, Chinese Academy of Sciences, Lanzhou, China, [2]Beiluhe Observation Station of Frozen Soil Environment and Engineering, Northwest Institute of Eco-Environment and Resource, Chinese Academy of Science, Lanzhou, China, [3]Key Laboratory of Ecohydrology of Inland River Basin, Northwest Institute of Eco–Environment and Resources, Chinese Academy of Sciences, Lanzhou, China, [4]Alax Desert Eco-hydrology Experimental Research Station, Lanzhou, China, [5]Qilian Mountains Eco–Environment Research Center in Gansu Province, Beijing, China

Ground ice in permafrost stores substantial amounts of dissolved organic carbon (DOC) upon thaw, which may perpetuate a carbon feedback in permafrost regions, yet little is known to date about the dynamics of DOC and source variability of ground ice on the Tibetan Plateau. Here, the high-resolution data of DOC in ground ice (4.8 m in depth) from two permafrost profiles on the Northeastern Tibetan Plateau (NETP) were firstly presented. We quantified the DOC concentrations (mean: 9.7–21.5 mg/L) of ground ice and revealed sizeable—by a factor of 7.0–36.0—enrichment of the ground ice relative to the other water elements on the TP. Results indicated remarkable depth differences in the DOC of ground ice, suggestive of diverse sources of DOC and different sequestration processes of DOC into ice during permafrost evolution. Combined with DOC and carbon isotopes (δ13CDOC), we clarified that decomposition of soil organic matter and leaching of DOC from organic layers and surrounding permafrost sediments are the important carbon sources of ground ice. The DOC sequestration of ground ice in the upper layers was related to the active layer hydrology and freeze–thaw cycle. However, the permafrost evolution controlled the decomposition of organic carbon and sequestration of DOC in the deep layers. A conceptual model clearly illustrated the dynamics of DOC in ground ice and suggested a significant impact on the carbon cycle on the NETP. The first attempt to explore the DOC in ground ice on the NETP is important and effective for further understanding of carbon cycle under permafrost degradation on the Tibetan Plateau.

Keywords: ground ice, dissolved organic carbon, permafrost degradation, carbon sources, Tibetan plateau

OPEN ACCESS

Edited by:
Marcia Katharina Phillips, Swiss Federal Institute for Forest, Snow and Landscape Research (WSL), Switzerland

Reviewed by:
Andrea Pain, University of Maryland Center for Environmental Science (UMCES), United States
Weichao Wu, Stockholm University, Sweden

****Correspondence:***
Xiaoyan Guo
guoxy2012@lzb.ac.cn
Qingbai Wu
qbwu@lzb.ac.cn

Specialty section:
This article was submitted to Cryospheric Sciences, a section of the journal Frontiers in Earth Science

Received: *23 September 2021*
Accepted: *14 February 2022*
Published: *24 March 2022*

Citation:
Yang Y, Guo X, Wang Q, Jin H, Yun H and Wu Q (2022) Dissolved Organic Carbon (DOC) in Ground Ice on Northeastern Tibetan Plateau. Front. Earth Sci. 10:782013. doi: 10.3389/feart.2022.782013

INTRODUCTION

Ground ice is substantially preserved in permafrost with an ice volume of 11.8–35.46 × 10^3 km^3 on the northern hemisphere (Zhang et al., 2000). Considerable amounts of dissolved carbon (DOC) locking in different ground ice are reported. For instance, high concentration of DOC (48–1,548 mg/L) is preserved in melting water of segregated ground ice in yedoma permafrost from central Alaska (Ewing et al., 2015a), and as much as 45.2 Tg DOC (with a maximum concentration of 28.6 mg/L) is stored in ice wedges in arctic yedoma permafrost regions (Fritz et al., 2015).

The current continuous global warming has resulted in the degradation of permafrost and subsequent melting of ground ice. The deepening of the active layer, melting of ground ice, and thermokarst processes lead to the decomposition and release of ancient DOC into aquatic systems (Vonk et al., 2015; Tanski et al., 2016). Notably, melting of ground ice accelerates the thawing of surrounding frozen sediments and concurrently brought OC, dissolved solutes, and microorganisms into ice meltwater, which would be an essential source of rivers and lakes (Connolly et al., 2020). Upon entering an aquatic system, DOC can be converted to CO_2 and emitted into the atmosphere, which would exert enormous influence on accelerating climate change and alternation of the biochemical cycle (Fritz et al., 2015; Selvam et al., 2017) in permafrost regions. The majority of studies on DOC mainly focused on ice wedges and massive ground ice (Vonk et al., 2013a; Fritz et al., 2015). Minor concern has been given to the pore ice.

The Tibetan Plateau (TP) is the largest region in a high-altitude setting. The permafrost stores as much as 12,700 km^3 of ground ice (Zhao et al., 2019). During recent decades, remarkable degradative trends of permafrost on the TP have been documented (Stocker et al., 2014; Ran et al., 2018). Decrease in ground ice content due to permafrost degradation facilitates the percolation of more water to deeper soil layers, thus resulting in the reallocation of runoff and water balance (Xu et al., 2008) and carbon distribution in the aquatic system and atmosphere (Guo et al., 2012; Chen et al., 2016; Mu et al., 2017; Ma et al., 2019). However, the current studies on the TP only focused on the soil carbon changes and stocks (Mu et al., 2015) in permafrost soils. Despite the vast amounts of ground ice volumes on the TP, little attention has been paid to the consequences of releasing DOC from melting ground ice, which has greatly underestimated the carbon budget in permafrost regions and could facilitate major ecosystem shifts on the TP. Under continuous warming and resultant permafrost degradation, considerable amounts of DOC in ground ice would release directly into the rivers and lakes to influence water quality of plateau and downstream recharge areas.

In this paper, we select the Source Area of Yellow River (SAYR) as our specific study area, which is often called the water tower of the Yellow River (Tian et al., 2015) and has experienced rapid degradation of permafrost. We aim to 1) expound the depth variations of DOC composition in high-resolution ground ice from two permafrost profiles in the SAYR; 2) trace the possible carbon sources and sequestration processes of DOC in the two profiles; and 3) discuss the consequences of DOC release from melting ice due to permafrost degradation in the SCG basin.

STUDY AREA AND SAMPLING SITES

The source area of the Yellow River (SAYR), defined as the catchment above the Tangnag Hydrological Station, is located on the northeastern TP (**Figure 1**). It provides as much as 34.5% of the total annual runoff with only 16.2% of areal extent (Lan et al., 2010), highlighting its importance for water resources

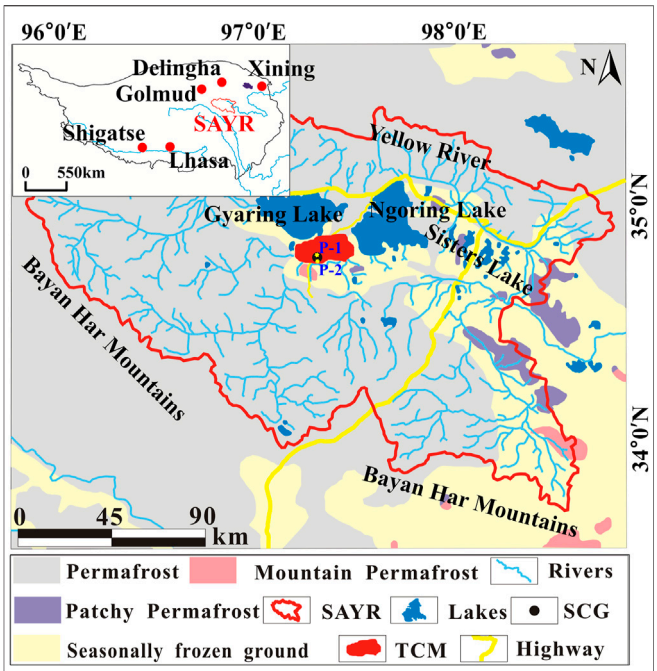

FIGURE 1 | Location of SAYR on the QTP and the sampling sites in the SCG basin.

managements and freshwater supply to the population in the middle and lower reaches of Yellow River. A mosaic of continuous, discontinuous, and sporadic permafrost as well as seasonally frozen ground is extensively distributed in the SAYR (Jin et al., 2009). Recent estimations reported a substantial reserve of ground ice between 3 and 10 m in the SAYR, reaching approximately 49.62 km^3 (Wang et al., 2017). According to field investigations and ground temperature records, permafrost in the SAYR is generally warm (>−1°) (Luo et al., 2014), and therefore vulnerable to thawing under continuous permafrost degradation, resulting in the release of dissolved solutes into surface water (Yang et al., 2019).

The Shuangchagou (SCG) basin was selected as our study site, near the southern bank of Ngoring Lake and Gyaring Lake (**Figure 1**). The landscape transition is remarkable in the SCG, which progresses from a desert steppe to an alpine meadow. Two streams are located in different ecosystems. The South branch is characterized by swampy alpine meadow, and the North branch flows through the desert steppe. Ice-rich permafrost is extensively developed, with ice content exceeding 60% (Yang et al., 2019). From 2014 to 2017, the annual average air temperature at SCG is −2.87°C, the total precipitation amount was 420 mm, and the average evaporation amount was as high as 1,000–1,500 mm. Two profiles (named as P-1 and P-2) with different vegetation and landform (Yang et al., 2019) at the SCG basin are dug to investigate the dissolved organic carbon (DOC) in ground ice. The P-1 (N 97°20′22.05″, E 34°39′14.1″, elevation: 4,455 m) is a palsa-like peat mound (**Figure 2A**), with more than 90% of alpine steppe dominating around this profile. Waters from around the peat mound and

FIGURE 2 | Landscapes for the two permafrost profiles **(A,B)** and sampling pictures **(C,D)**.

the wetland water converge and flow into the Wanlongwoma River (**Figure 2A**), which remarkably influences the regional hydrological processes (Yang et al., 2019). Profile P-2 (N 97°19′44.36″, E 34°34′49.19″, elevation: 4,485 m) is on a flat terrain, exhibiting evident collapse in landscape of thermokarst gullies (**Figure 2B**). The predominant vegetation type is degraded alpine meadow (~90%). Continuous seepage was observed along this gully during our fieldwork, which was inferred to consist of summer rain, snowmelt water, and meltwater from thawing permafrost.

MATERIALS AND METHODS

Sampling Designations and Cryostratigraphic Record

To clarify the DOC distributions in ground ice, two sites presenting different landscapes (**Figure 2**) were designed at the SCG basin to investigate cryostratigraphy and obtain ground ice. Before excavation, the vegetation cover, topography, and hydrological conditions were investigated and photographically recorded (**Figure 2**). Two profiles were excavated manually using a shovel and an electric pick. The P-1 profile was excavated on top of a palsa-like frozen mound (**Figure 2A**; **Figure 2B**) with a height of ~2 m. Moreover, a thermal-erosion gully located 15 km apart from P-1 was chosen, and a profile (P-2) was dug from an exposed slump crack (**Figure 2C**; **Figure 2D**). Two profiles were excavated to a depth of 4.8 m. The lithology, cryostructures, and ice conditions were documented and photographed before sampling. The frozen sediments and ice layers were cut using a chain saw and a chisel (**Figure 2B**; **Figure 2D**). The superficial layer of each sample was discarded to avoid any contamination. The profiles were cut in 5-cm intervals for P-1 (every 10 cm below 3 m) and 3-cm intervals for P-2.62, and 125 samples were collected in P-1 and P-2, respectively. In addition, the soil samples from the active layer and frozen layers were retrieved synchronously. All the samples were numbered in terms of depth, preserved in HDPE bottles, and kept frozen at –4°C in the field. In addition, five sites in the SCG basin were selected to collect the active layer water. Five pits were dug to a depth of 1.0 m, and the laterally and vertically permeated soil water were obtained in September (2014–2015) during our fieldwork.

Data Analysis Methods

The frozen samples were thawed entirely at 4°C, left until sediment settled, and then the liquid water above was filtered with pre-combusted GF/F filters and acidified (HCL, pH < 2) to prevent microbial conversion and to remove the carbonates. The DOC concentrations were measured with the solid and liquid modules of OI Analytical Analyzer (OI-Picarro, CA, United States), with a standard deviation of less than 0.5‰. The $\delta^{13}C_{DOC}$ values were analyzed with a Picarro Isotope

TABLE 1 | DOC and $\delta^{13}C_{DOC}$ in different water components on QTP.

Water components	Permafrost conditions[a]	Sample size	$\delta^{13}C_{DOC}$ (‰)			DOC (mg/L)			References
			Mean	Max	Min	Mean	Max	Min	
P–1	PF	62	–29.8	–27.4	–36.1	9.7	24.6	5.6	This study
P–2	PF	125	–31.6	–28.1	–36.9	21.5	70.1	8.8	This study
ALW	PF	169	–30.2	–26.1	–36.8	6.4	11.3	3.7	This study
LRW	PF	21	–25.6	–23.2	–26.9	2.3	7.1	0.2	1, 2, 3
	SFG	22	–25.8	–25.1	–26.9	1.2	2.6	0.2	2, 3, 4, 5
SSW	PF	26	–12.6	–10.7	–15.0	9.5	13.5	4.7	1, 6, 7, 8
SPW	— —	26	–21	–21	–21	0.6	1.3	0.2	9–12
PW	— —	11	–23	–21	–25	1.0	1.3	0.7	13–14
LLW	SFG	173	–25.6	–22.2	–28.8	2.8	8.1	0.5	4, 15
TLW	PF	9	–16.2	–15.1	–18.4	10.5	35.6	3.0	16
GW	PF	2	n.a.	n.a.	n.a.	11.9	15.0	8.8	2
	SFG	21	n.a.	n.a.	n.a.	1.3	3.8	0.3	2
GMW	— —	263	n.a.	n.a.	n.a.	1.2	2.2	0.2	9, 17, 18

[a]*PF: permafrost; SFG: seasonal frozen ground.*

1: Ma et al., 2018; 2: Hu et al., 2019; 3: Qu et al., 2017; 4: Kai et al., 2019; 5: Gao et al., 2019; 6: Liu et al., 2018; 7: Song et al., 2019; 8: Mu et al., 2017; 9: Yan et al., 2016; 10: Gao et al., 2020; 11: Liu et al., 2016; 12: Li Q. et al., 2018; 13: Li et al., 2017; 14: Li C. et al., 2018; 15: Su et al., 2018; 16: Mu et al., 2016; 17: Zhang et al., 2018; 18: Li X. et al., 2018.

Analyzer (Picarro G1102). Stable isotope results were expressed as δ values relative to the Vienna Peedee belemnite (VPDB) standard. The precision of $\delta^{13}C$ is <0.5‰, and the detection limit of DOC is 0.3 mg/L.

Total organic carbon (TOC) in sediments was measured using an OI Analytical model 1030 TOC analyzer (OI Analytical, United States). Each dry and homogenized sample was put into a small quartz boat after weighing. The 1 M HCl was added to the sample for 12 h to remove the carbonates. Then, the samples were heated to 900°C in the combustion chamber, and the organic matter in the samples was oxidized to CO_2 to measure the carbon contents.

Data Collection From Different Water Components

In order to clarify the potential origins of DOC in ground ice, the published data from different water components over the TP were collected and synthesized. Specifically, thermokarst lake water (TLW), glacial meltwater (GMW), small stream water (SSW), large river water (LRW), large lake water (LLW), precipitation water (PW), snowpit water (SPW), and groundwater (GW) at different sites were comprehensively investigated. The DOC and $\delta^{13}C$ (not available in GMW and GW) data were reanalyzed for comparison (**Table 1**; **Figure 5**).

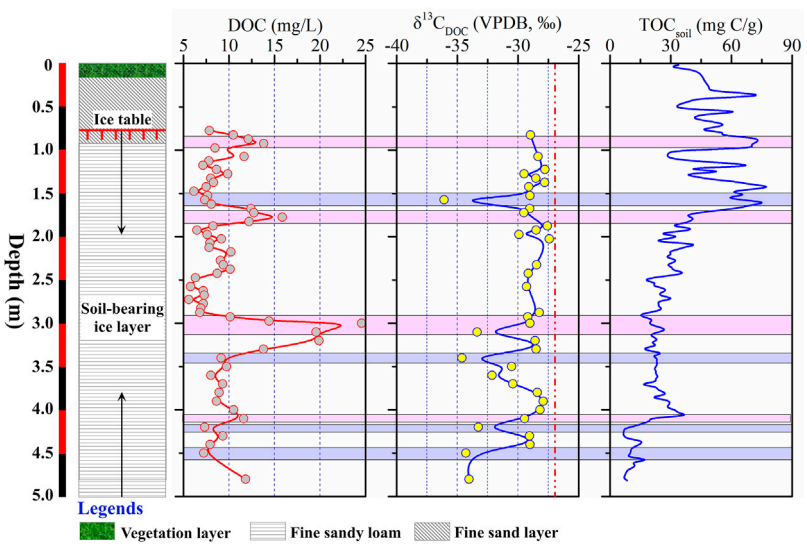

FIGURE 3 | Variations in DOC and $\delta^{13}C_{DOC}$ of ground ice and (total organic carbon) TOC of soil along depth in P-1. The pink bars represent four peaks of DOC in ground ice and the corresponding values of $\delta^{13}C$ and TOC_{soil}. The blue bars denote the lower DOC and more negative $\delta^{13}C$ values.

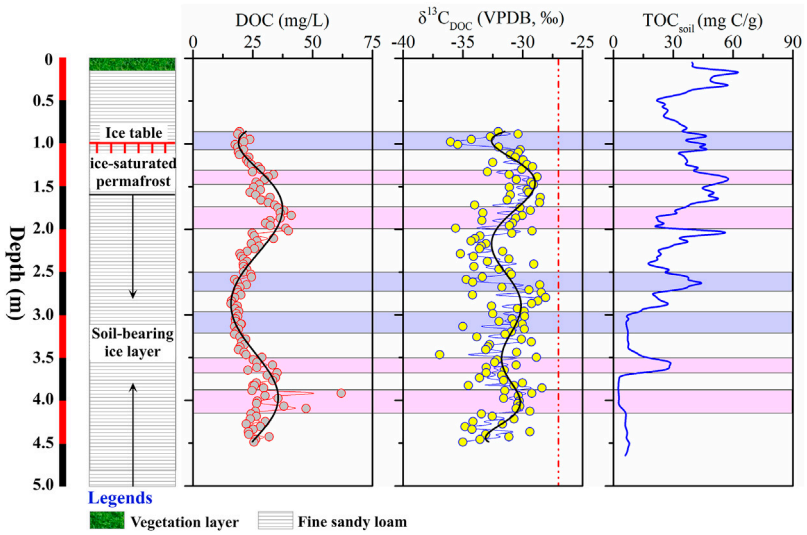

FIGURE 4 | Variations in DOC and $\delta^{13}C_{DOC}$ of ground ice and (total organic carbon) TOC of soil along depth in P-2. The pink bars represent four peaks of DOC in ground ice and the corresponding values of $\delta^{13}C$ and TOC_{soil}. The blue bars denote the lower DOC and more negative $\delta^{13}C$ values.

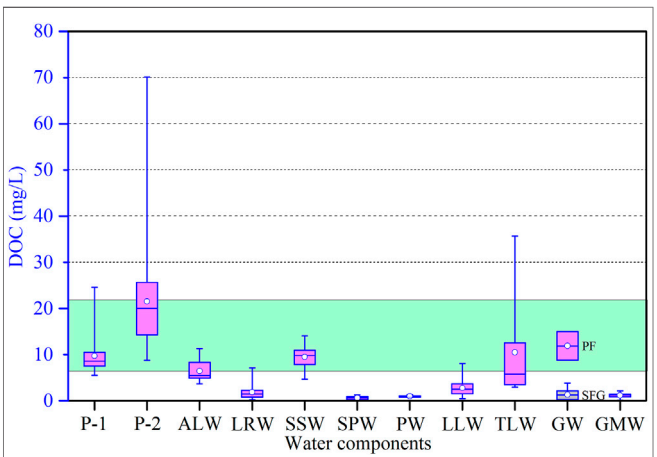

FIGURE 5 | Comparison of DOC in different water components on the QTP.

RESULTS

Cryostratigraphy, Dissolved Organic Carbon and $\delta^{13}C_{DOC}$ of Ground Ice, and Total Organic Carbon of Soil in P-1

According to the field investigations, fine sandy soil is predominant in the upper layer and fine sandy loam dominates in the frozen layer in P-1 (**Figure 3**). Substantial soil-bearing ice layers are identified with volumetric ice contents ranging from 40% to 90% (**Figure 3**). The concentration of DOC ranges between 5.6 mg/L and 24.6 mg/L, with a mean of 9.7 mg/L. The peak DOC (24.6 mg/L) presents at 3.0 m (**Figure 3**). The $\delta^{13}C_{DOC}$ varies from −27.4‰ to −36.1‰. Three higher DOC peaks are present at 0.9 m (13.8 mg/L), 1.8 m (15.8 mg/L), and 3.0 m (24.6 mg/L), corresponding to the relatively enriched $\delta^{13}C_{DOC}$ (pink bars in **Figure 3**). In contrast, the most negative $\delta^{13}C_{DOC}$ peaks appear at 1.6 m (−36.1‰), 3.1 m (−33.3‰), 3.4 m (−34.6‰), and 4.5 m (−34.3‰), which are consistent with the lower DOC contents (purple bars in **Figure 3**). However, higher DOC contents appear at 3.1 m, corresponding to the most negative $\delta^{13}C_{DOC}$ (green bar in **Figure 3**). In addition, the total organic carbon of soil (TOC_{soil}) in different depths was determined for comparison (**Figure 3**), the range of which is between 0.65% and 8.14%, with a mean value of 3.31%. The upper layer (0–1.6 m) contains much higher (mean level of 5.25%) and fluctuating TOC_{soil} than those in the deeper layers (**Figure 3**), suggesting the important influence of freeze–thaw cycle and evolution of permafrost/ground ice.

Cryostratigraphy, Dissolved Organic Carbon and $\delta^{13}C_{DOC}$ of Ground Ice, and Total Organic Carbon of Soil in P-2

For comparison, fine sandy loam layers dominated in the full profile for P-2 (**Figure 4**). Cryostratigraphy in this profile consists of ice-saturated permafrost (0.78–1.6 m) and soil-bearing ice layers (below 1.6 m), with volumetric ice contents ranging between 50% and 90%. The ground ice in P-2 presents higher DOC compared with P-1 (**Figure 4**). The DOC ranges between 8.8 and 70.1 mg/L, with a median of 21.5 mg/L. Moreover, the $\delta^{13}C_{DOC}$ ranges from −28.1‰ to −36.9‰, which is similar to that in P-1. There are three positive DOC peaks, located at 1.8 m, 2.2 m, and 4.1 m, respectively. Furthermore, $\delta^{13}C_{DOC}$ also shows some negative peaks (**Figure 4**). As for the ground ice in P-1, the DOC and $\delta^{13}C_{DOC}$ in P-2 show coincident trends, with higher DOC corresponding to the relatively enriched $\delta^{13}C_{DOC}$ and *vice*

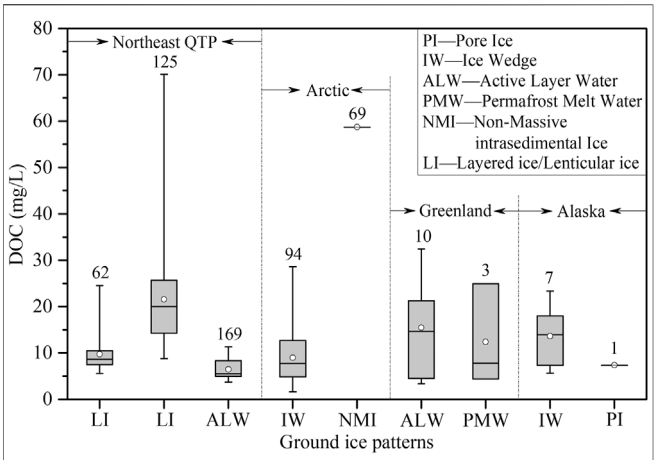

FIGURE 6 | Boxplot of DOC concentrations in different ground-ice types in northern hemisphere permafrost regions. Plot shows minimum, maximum, and median values, and the sample sizes in each category.

versa. However, similarly opposite relations between DOC and $\delta^{13}C_{DOC}$ are identified at approximately 3.0 m, at which the lowest DOC concentrations correspond to the most enriched (median: −28.8‰) value of $\delta^{13}C_{DOC}$. Generally, the contents of TOC_{soil} in this profile exhibit remarkable variations with depth (**Figure 4**), ranging between 0.23% and 6.74%. Higher TOC_{soil} values (mean: 4.11%) appeared in the upper layer (0–1.7 m), which was similar to that in P-1, reflecting repeated freeze–thaw cycles and frequent exchange with external environment, resulting in carbon decomposition by microorganism. The frozen soil in the deep layer presents lower TOC_{soil} (mean: 1.95%).

Comparison of Dissolved Organic Carbon in Ground Ice and Other Water Components on the Tibetan Plateau

In order to determine the possible carbon sources of DOC in ground ice, the DOC data of different water components (including precipitation, snowpit, glacial meltwater, lakes, rivers, and groundwater) on the TP were collected for comparison (**Table 1**).

Remarkably, the ground ice in both profiles exhibits higher DOC concentrations (mean: 9.7–21.5 mg/L) than those in large river water (LRW) (mean: 1.2–2.3 mg/L), LLW (mean: 2.8 mg/L), snowpit water (SPW) (mean: 0.6 mg/L), precipitation water (PW) (mean: 1.0 mg/L), groundwater (GW) in seasonal frozen ground regions (mean: 1.3 mg/L), and glacial meltwater (GMW) (mean: 1.2 mg/L; **Table 1** and **Figure 5**). In comparison, the DOC of active layer water (ALW) (mean: 6.4 mg/L), small stream water (SSW) (mean: 9.5 mg/L), thermokarst lake water (TLW) (mean: 10.5 mg/L), and groundwater (GW) in permafrost regions (mean: 11.9 mg/L) is higher and comparable to that of ground ice (**Figure 5**), indicating connections between them and similar carbon behaviors with regard to the influence of permafrost.

Dissolved Organic Carbon Concentrations of Ground Ice in Different Types of Ground Ice

As shown in **Figure 6**, the highest contents of DOC (from 9.5 to 347.0 mg/L; mean: 58.7 mg/L) appear in the non-massive intrasedimental ice (NMI) in the arctic (Tanski et al., 2016; **Figure 6** and **Table 2**). However, the pore ice (PI) in Alaska (7.3 mg/L; Abbott et al., 2014) exhibited the lowest DOC concentration. Although the higher ice contents and huge volumes are found in ice wedges (IW) in the Arctic and Alaska, the DOC concentrations are not quite high as expected (**Figure 6**). By comparison, the layered ice and lenticular ice (LI) in the SAYR exhibit higher DOC concentrations, which are consistent with those in permafrost meltwater (PMW) and ALW. Specifically, the DOC concentrations in P-1 are consistent with the ice wedges, massive ice, and thermokarst exposed ice in the Arctic regions (Vonk et al., 2013a; Fritz et al., 2015; Tanski et al., 2016). However, the much higher concentrations of DOC in P-2 are close to those found in a localized thermal erosion ice wedge in Alaska (mean: 28.8 mg/L; Douglas et al., 2011).

DISCUSSION

Possible Carbon Origins of Dissolved Organic Carbon in Ground Ice in the Shuangchagou

The carbon sources and accumulation processes of DOC in ground ice exert essential roles in the magnitude and bioavailability of DOC (Fritz et al., 2015). Generally, lower DOC concentrations in these types of ice were probably due to limited carbon inputs (Raymond and Bauer, 2000; Spencer et al., 2015), lower ice contents, and rapid *in situ* freezing (French and Shur, 2010). By contrast, the higher DOC concentrations of these ices are assumed to strongly interact with the higher ice contents and lacustrine origin of host sediments (Tanski et al., 2016). Importantly, the stable carbon isotopes ($\delta^{13}C_{DOC}$) for the initial source water of ground ice vary substantially. It was potentially due to various carbon input, local vegetation conditions, freeze fractionation (Cristea et al., 2014), ice formation patterns (Tanski et al., 2016), and different decomposition processes of organic carbon (Alewell et al., 2011). Accordingly, the $\delta^{13}C_{DOC}$ in ground ice can also be used to infer the carbon sources of ground ice.

As shown in **Figure 5**, the DOC concentrations in ground ice are similar to those of ALW, and the ^{13}C values are alike, indicating that the DOC in ground ice was closely related to the dissolving of organic matter from the active layer (Yu et al., 2017). The previous study also reported a similar DOC concentration of the soil solution in the upper active layer (26.3–39.5 mg/L) on the Northeastern Tibetan Plateau (NETP) (Luo et al., 2009) and substantial input (as high as 70%–94%)

TABLE 2 | Variations in the DOC concentration among different ground ice types.

Ice types	Monitor sites	Sample size	Mean DOC (mg/L)	References
LI	QTP	187	9.6–21.5	This study
IW	Arctic/Alaska	94/7	9.0/13.6	1, 2, 3
NMI	Arctic	69	58.7	2
PI	Alaska	1	7.3	3
PMW	Greenland	3	12.4	4
ALW	QTP/Greenland	169/10	6.4/15.4	This study/4

1: Fritz et al., 2015; 2: Tanski et al., 2016; 3: Abbott et al., 2014; 4: Leman, 2018.

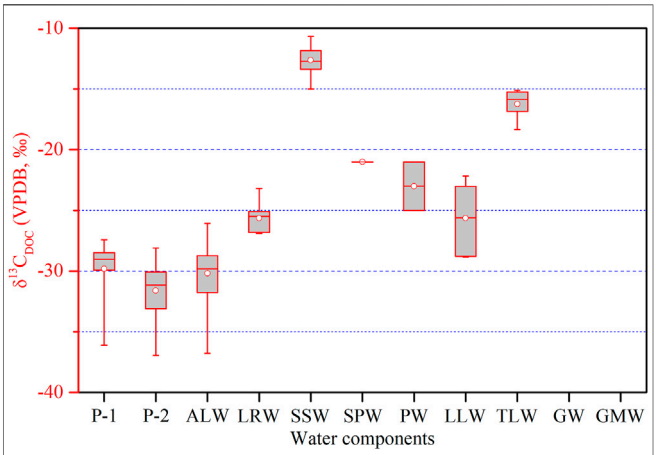

FIGURE 7 | Comparison of $\delta^{13}C_{DOC}$ in different water components on the QTP.

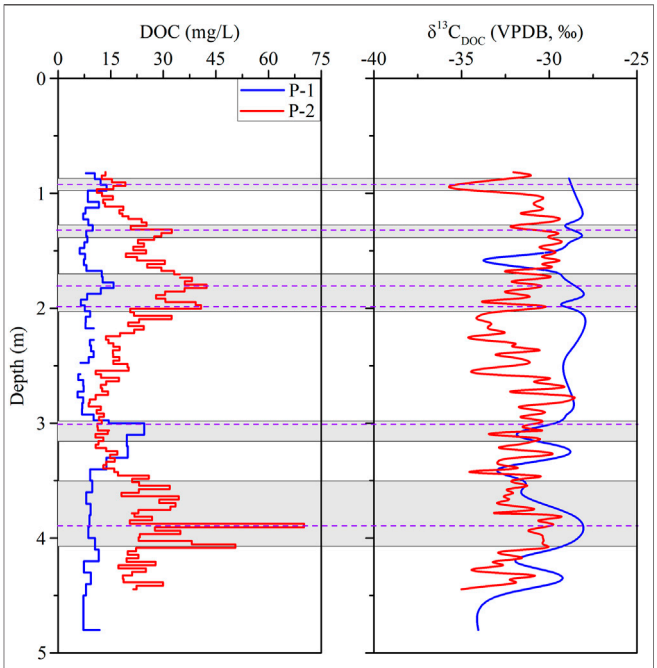

FIGURE 8 | The DOC behaviors of ground ice along depth in both profiles. The gray bars represent the prominent DOC accumulation areas.

of OC from the active layer leachate to the permafrost streams (Wang et al., 2018). These kinds of DOC were usually originated from modern terrestrial biomass and surface organic layers (Guo et al., 2007). Due to the high hydraulic conductivity, low mineral content, and low DOC sorption capacity of the active layer soil (Striegl et al., 2005), the younger and biodegradable DOC (Drake et al., 2015) could migrate quickly to the permafrost table with limited microbial transformation. The DOC was easily sequestrated into the ground ice by freezing.

More depleted $\delta^{13}C_{DOC}$ values of ground ice in the SAYR (**Figure 7**; **Table 1**) are different from those of other water components on the TP. For comparison, the $\delta^{13}C_{DOC}$ values of ground ice (–31.6‰ to –29.8‰) are similar to ALW (–30.2‰), suggesting similar decomposition mechanisms and carbon sources. However, the $\delta^{13}C_{DOC}$ values of ground ice are much lower than the SSW and TLW (**Figure 7**), although melting ground ice was an important source of water for SSW and TLW (Yang et al., 2016; 2019). It suggests differences in carbon sources and decomposition processes under changing environments and distinct freezing conditions, which greatly influenced the stable isotopes of DOC (Krüger et al., 2014).

Notably, the mean values of measured $\delta^{13}C_{DOC}$ in the ground ice lie within the range of plants on the TP (Li et al., 2007) and are similar (slightly depleted) to the values measured in $\delta^{13}C$ for moist soils on the northwestern TP (Mu et al., 2014). This suggests that all of the plants performed C_3 photosynthetic pathways with $\delta^{13}C$ values ranging from approximately −32‰ to −20‰ (Boutton, 1991; Farquhar et al., 1989; Raymond and Bauer., 2001). In addition, the consistent negative $\delta^{13}C_{DOC}$ values of ground ice and ALW (**Figure 7**) also suggest the leaching of organic matter from active layer soil. During water migration through the sediments of the active layer, the organic carbon of sediments and roots of plants melted out and subsequently dissolved into the supra-permafrost water, which sequestrated into ice during cold seasons (Guo and Macdonald, 2006; Guo et al., 2007; Tanski et al., 2016).

We thus conclude that the substantial leaching of DOC from organic layers and surrounding permafrost sediments are the important carbon sources of ground ice in the SAYR. Both freezing–thawing processes and permafrost evolution would

influence the embedding and sequestrating of DOC into ice. In addition, the microorganisms heterogeneously decomposed the organic carbon in permafrost and plants.

Sequestration Mechanisms of Dissolved Organic Carbon Into Ground Ice at Depths

The DOC and $\delta^{13}C_{DOC}$ composition show remarkable variations with depths (**Figure 3**; **Figure 4**), indicating different permafrost evolution processes and the resultant drivers of DOC incorporating into ice (Fritz et al., 2015), and the decomposition processes influenced by climate transition (Krüger et al., 2014). The depths with enriched $\delta^{13}C_{DOC}$ may reflect warm and wet climate conditions; in contrast, the lower $\delta^{13}C_{DOC}$ values reflect dry and cold conditions (Cristea et al., 2014). The higher DOC suggests quick freezing, and the lower DOC points towards the slow segregation, which excluded the solute in the water during ice formation.

As shown in **Figure 8**, the DOC in ground ice exhibits changing trends along depths, indicating different sequestration mechanisms of DOC during ice formation processes. As one of the most effective mechanisms for long-term carbon fixation in permafrost, freezing complicated the sequestrate process of DOC into ground ice. Meanwhile, the active layer properties, vegetation characteristics, and permafrost aggregation rates are also critical factors for DOC sequestration (Fritz et al., 2015).

Generally, the DOC of ground ice in the upper layers (1.6 m) presents gradually increasing DOC in both profiles, suggesting control of the freeze–thaw cycle. Below 1.6 m, the DOC and $\delta^{13}C_{DOC}$ exhibit fluctuating trends, suggesting alternating controls of permafrost evolution and the resultant ice formation mechanism under changing climate conditions (French and Pollar, 1986; Ewing et al., 2015a).

Specifically, the low DOC at P-1 and higher DOC at P-2 at 1.3 m (**Figure 8**) correspond to different ice formation mechanisms. The ice segregation process at P-1 and quick *in situ* freezing processes at P-2 are proposed. However, the second highest DOC peaks and enriched $\delta^{13}C_{DOC}$ at both P-1 and P-2 at approximately 1.8–2.0 m (**Figure 8**) are inferred to be affected by the warmer and wetter climate conditions (Cristea et al., 2014). The subsequent cold events at 1.9 ka (~2.2 m; Wang et al., 2018) promoted the upward aggradation of permafrost and quickly locked the DOC into ground ice. The much higher deposition rate at 2.0 m (Wang et al., 2018) also confirms the quick freezing processes.

At the depth of 3.1 m, the ground ice shows positive DOC peaks in both profiles, which follow depleted $\delta^{13}C_{DOC}$ values (**Figure 8**). As reported in Luo et al. (2018), the mean active layer thickness (ALT) in the SAYR is 2.8 m, and the repeated freeze–thaw cycles and microorganism activities in the active layer could significantly alter the DOC (Yu et al., 2017; Fuss et al., 2016). Also, the diverse carbon input and water availability from the external environment can influence the carbon isotopes in general (Cristea et al., 2014).

Between 3.5 and 4.3 m, the identical $\delta^{13}C_{DOC}$ trends in both profiles (**Figure 8**) suggest similar sequestration processes and climate conditions (Porter et al., 2019). However, a high density of DOC at P-2 and a lower one at P-1 were observed, suggesting distinct ice formation mechanisms and organic carbon behaviors (i.e., decomposition, accumulation, and mixing). The P-1 is a palsa-like frozen mound; it was formed by an aggradation process (Krüger et al., 2014). The slow segregation processes at P-1 excluded the DOC from solid ice due to self-purification (Cheng, 1983). In contrast, P-2 exhibits an open-system feature, which could receive external water and produce a waterlogged and anaerobic environment. Thus, it reveals substantial accumulation of DOC in the ground ice, suggesting quick-freezing and efficiently locking of the DOC into the ice.

Significance of Dissolved Organic Carbon in Ground Ice on the Carbon Cycle Under Permafrost Degradation

As shown, the DOC concentrations of ground ice, TLW, SSW, and GW in permafrost regions are much higher than those of LLW and LRW in seasonal frozen ground regions (**Figure 9**), which may be significantly related to the degradation of permafrost with high-content ground ice. For comparison, the ice contents in the seasonally frozen ground are usually lower (Zhou et al., 2000; Zou et al., 2017) and are commonly surrounded by thick unfrozen sediments, so the influence of thawing permafrost is thus negligible. Previous studies on the TP suggested that the contribution of melting ground ice to thermokarst lakes were as high as 37.75%–51.75% (Yang et al., 2016), and the melting ground ice similarly provided 13.2%–16.7% of total discharges to the streams (Yang et al., 2019). It has been suggested that permafrost thaw has released substantial melt water, bringing massive labile DOC into streams (Gao et al., 2019; Song et al., 2019) and thermokarst lakes (Mu et al., 2016) on the TP.

During recent decades, the SAYR has been undergoing remarkable permafrost degradation due to continuous temperature rise (Jin et al., 2009). A gradual increase in ALT at a rate of 2.2 cm/a in the SAYR was determined (Luo et al., 2014). Note that these rates of permafrost degradation in the SAYR are sizably higher than those in the interior TP (Jin et al., 2009), which resulted in massive melting of ground ice. On the one hand, the excess ground ice would release a large amount of meltwater to recharge the surface runoff and lakes (Lee et al., 2014) and simultaneously release a considerable DOC flux into the freshwater system (Vonk et al., 2015), which can be used by plant roots (Becker et al., 2016; **Figure 9**). On the other hand, the melting of ground ice increased the soil pore (Walvoord and Kurylyk, 2016) and allowed much more supra-permafrost water, precipitation, and surface water to infiltrate into the deep permafrost (Yang et al., 2017). These waters could penetrate deeply through taliks to connect with the sub-permafrost water, and further leached labile carbon from the ambient frozen sediments (**Figure 9**). During this process, the DOC in shallow layers could enter the sub-permafrost water *via* taliks. These activities substantially altered the DOC dynamics in permafrost (ground ice) and aquatic systems (**Figure 9**).

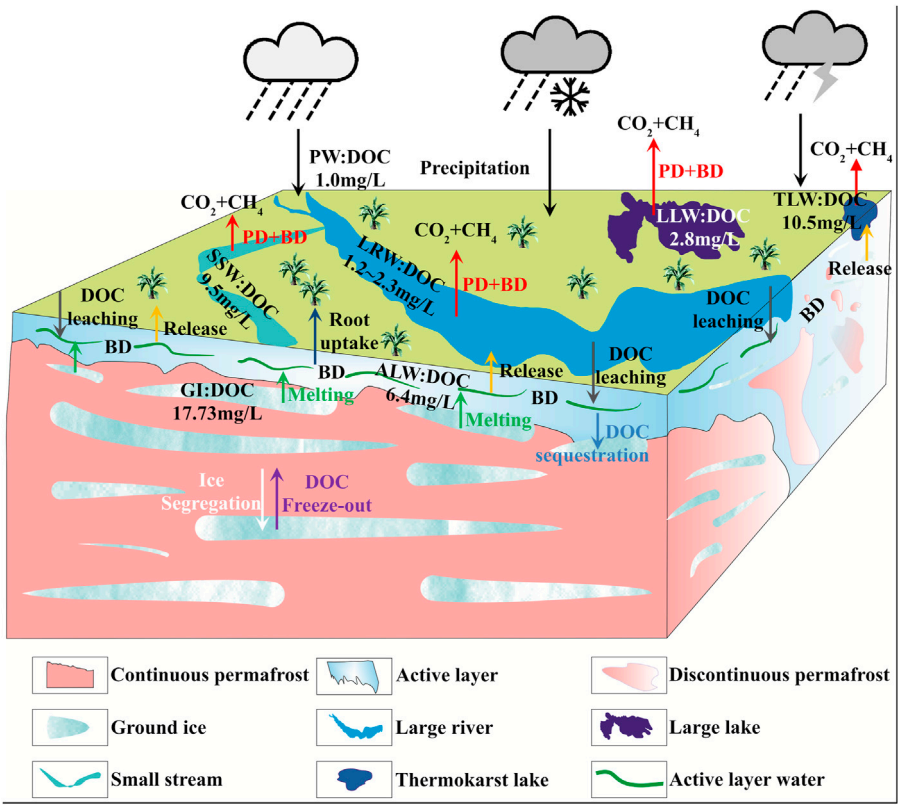

FIGURE 9 | Conceptual diagram of DOC dynamics under permafrost thaw in the SAYR. BD and PD stand for biochemical degradation and photo degradation.

Importantly, continuous permafrost would degrade into discontinuous permafrost and finally change into seasonally frozen ground. The GW in permafrost regions presents higher DOC levels than that in seasonally frozen ground regions (**Figure 5**), which is closely related to the occurrence of ground ice. Accordingly, the transition from permafrost to seasonal frozen ground will greatly influence the thermal regimes of large lakes and large rivers distributing in seasonal frozen ground regions, ultimately leading to a great increase in DOC of LLW and LRW (**Figure 9**). Because the DOC from ground ice is chemically labile (Vonk et al., 2013a), it can be decomposed easily by microbial and photochemical processes after entering into lakes and rivers (Battin et al., 2008; Vonk et al., 2013a) and finally released to the atmosphere (**Figure 9**).

CONCLUSION AND OUTLOOK

In this study, the high-resolution DOC data in ground ice from two permafrost profiles in the SAYR were firstly shown, the origins and sequestrations of DOC in ground ice were investigated, and the potential influence of DOC on the carbon cycle upon permafrost thaw were discussed. The following conclusions can be drawn:

1) Remarkable depth differences in the ground ice DOC and $\delta^{13}C_{DOC}$ were found for both sites. The ground ice in upper layers (0–1.6 m) exhibits higher DOC concentrations rather than those in deeper layers (>1.6 m), which is related to the active layer hydrology and freeze–thaw cycles. However, the origins and sequestration processes of DOC in the deeper ground ice were complex, which is closely related to the evolution of ice, the carbon behaviors of the ambient water (Fritz et al., 2015).
2) Our conceptual model emphasizes the significant contribution of DOC in ground ice to the carbon cycle in the SAYR. Considering the important water conservation area in China and the sensitive regions to climate warming, the release of DOC from ground ice in the SAYR will be significant under continuous permafrost degradation.
3) Due to the limitation of ground ice reserve data and lack of mass investigations of DOC in ground ice on a large scale in the SAYR, accurate evaluation of DOC budgets in ground ice in the SAYR is hard to estimate. Accordingly, future work is indispensable to investigate the general distribution and storage of DOC in ground ice on regional scales on the TP.

This work is the first and preliminary attempt at carrying out a DOC study on ground ice on the TP. These results serve as a call for other studies to include the carbon cycle on the TP as an underpinning to comprehend the behavior of permafrost-related

organic carbon, and incorporate this variation into projections of future climate change.

DATA AVAILABILITY STATEMENT

The original contributions presented in the study are included in the article/Supplementary Material. Further inquiries can be directed to the corresponding authors.

AUTHOR CONTRIBUTIONS

YY and XG: Conceptualization, Methodology, Investigation, and Writing—review and editing. QW: Data analysis. HJ: review and editing. HY: Data analysis. QW: Supervision and editing.

FUNDING

This work was supported by the Key Research Program of Frontier Sciences, CAS (Grant No. ZDBS-LY-DQC026), the National Key R&D Program of China (Grant No. 2017YFC0404306), and the National Natural Science Foundation of China (Grant No. 41871062).

ACKNOWLEDGMENTS

We express our gratitude to Hong Tan and Yadong Huang for their kind help during field sampling. HY thanks the partial support from Scientific Instrument Developing Project of the Chinese Academy of Sciences (Grant No. YJKYYQ20190012).

REFERENCES

Abbott, B. W., Larouche, J. R., Jones, J. B., Bowden, W. B., and Balser, A. W. (2014). Elevated Dissolved Organic Carbon Biodegradability from Thawing and Collapsing Permafrost. *J. Geophys. Res. Biogeosci.* 119 (10), 2049–2063. doi:10.1002/2014jg002678

Alewell, C., Giesler, R., Klaminder, J., Leifeld, J., and Rollog, M. (2011). Stable Carbon Isotopes as Indicators for Environmental Change in Palsa Peats. *Biogeosciences* 8 (7), 1769–1778. doi:10.5194/bg-8-1769-2011

Battin, T. J., Kaplan, L. A., Findlay, S., Hopkinson, C. S., Marti, E., Packman, A. I., et al. (2008). Biophysical Controls on Organic Carbon Fluxes in Fluvial Networks. *Nat. Geosci* 1, 95–100. doi:10.1038/ngeo101

Becker, M. S., Davies, T. J., and Pollard, W. H. (2016). Ground Ice Melt in the High Arctic Leads to Greater Ecological Heterogeneity. *J. Ecol.* 104 (1), 114–124. doi:10.1111/1365-2745.12491

Boutton, T. W. (1991). Stable Carbon Isotope Ratios of Natural Materials: II. Atmospheric, Terrestrial, Marine, and Freshwater Environments. *Carbon Isotope Techniques*. Academic Press Inc., 173–185.

Chen, L., Liang, J., Qin, S., Liu, L., Fang, K., Xu, Y., et al. (2016). Determinants of Carbon Release from the Active Layer and Permafrost Deposits on the Tibetan Plateau. *Nat. Commun.* 7, 1–12. doi:10.1038/ncomms13046

Connolly, C. T., Cardenas, M. B., Burkart, G. A., Spencer, R. G. M., and McClelland, J. W. (2020). Groundwater as a Major Source of Dissolved Organic Matter to Arctic Coastal Waters. *Nat. Commun.* 11 (1), 1–8. doi:10.1038/s41467-020-15250-8

Cristea, G., Cuna, S. M., Fărcaş, S., Tanţău, I., Dordai, E., and Măgdaş, D. A. (2014). Carbon Isotope Composition as Indicator for Climatic Changes during the Middle and Late Holocene in a Peat Bog from Maramureş Mountains (Romania). *The Holocene* 24 (1), 15–23. doi:10.1177/0959683613512166

Douglas, T. A., Fortier, D., Shur, Y. L., Kanevskiy, M. Z., Guo, L., Cai, Y., et al. (2011). Biogeochemical and Geocryological Characteristics of Wedge and Thermokarst-Cave Ice in the CRREL Permafrost Tunnel, Alaska. *Permafrost Periglac. Process.* 22 (2), 120–128. doi:10.1002/ppp.709

Drake, T. W., Wickland, K. P., Spencer, R. G. M., McKnight, D. M., and Striegl, R. G. (2015). Ancient Low-Molecular-Weight Organic Acids in Permafrost Fuel Rapid Carbon Dioxide Production upon Thaw. *Proc. Natl. Acad. Sci. USA* 112, 13946–13951. doi:10.1073/pnas.1511705112

Ewing, S. A., O'Donnell, J. A., Aiken, G. R., Butler, K., Butman, D., Windham-Myers, L., et al. (2015a). Long-term Anoxia and Release of Ancient, Labile Carbon upon Thaw of Pleistocene Permafrost. *Geophys. Res. Lett.* 42 (24), 10730–10738. doi:10.1002/2015gl066296

Farquhar, G. D., Ehleringer, J. R., and Hubick, K. T. (1989). Carbon Isotope Discrimination and Photosynthesis. *Annu. Rev. Plant Physiol. Plant Mol. Biol.* 40 (1), 503–537. doi:10.1146/annurev.pp.40.060189.002443

French, H. M., and Pollard, W. H. (1986). Ground-ice Investigations, Klondike District, Yukon Territory. *Can. J. Earth Sci.* 23 (4), 550–560. doi:10.1139/e86-055

French, H., and Shur, Y. (2010). The Principles of Cryostratigraphy. *Earth-Science Rev.* 101 (3-4), 190–206. doi:10.1016/j.earscirev.2010.04.002

Fritz, M., Opel, T., Tanski, G., Herzschuh, U., Meyer, H., Eulenburg, A., et al. (2015). Dissolved Organic Carbon (DOC) in Arctic Ground Ice. *The Cryosphere* 9, 737–752. doi:10.5194/tc-9-737-2015

Gao, T., Kang, S., Zhang, Y., Sprenger, M., Wang, F., Du, W., et al. (2020). Characterization, Sources and Transport of Dissolved Organic Carbon and Nitrogen from a Glacier in the Central Asia. *Sci. Total Environ.* 725, 138346. doi:10.1016/j.scitotenv.2020.138346

Gao, T., Kang, S., Chen, R., Zhang, T., Zhang, T., Han, C., et al. (2019). Riverine Dissolved Organic Carbon and its Optical Properties in a Permafrost Region of the Upper Heihe River basin in the Northern Tibetan Plateau. *Sci. total Environ.* 686, 370–381. doi:10.1016/j.scitotenv.2019.05.478

Guo, D., Wang, H., and Li, D., 2012. A Projection of Permafrost Degradation on the Tibetan Plateau during the 21st century: Projection of Permafrost Degradation. *J. Geophys. Res.* 117. 16545. doi:10.1029/2011JD016545

Guo, L., and Macdonald, R. W. (2006). Source and Transport of Terrigenous Organic Matter in the Upper Yukon River: Evidence from Isotope ($\delta^{13}C$, $\Delta^{14}C$, and $\delta^{15}N$) Composition of Dissolved, Colloidal, and Particulate Phases. Global Biogeochem. *Cycles* 20, 1–12. doi:10.1029/2005gb002593

Guo, L., Ping, C. L., and Macdonald, R. W. (2007). Mobilization Pathways of Organic Carbon from Permafrost to Arctic Rivers in a Changing Climate. *Geophys. Res. Lett.* 34 (13), L13603. doi:10.1029/2007gl030689

Guodong, C. (1983). The Mechanism of Repeated-Segregation for the Formation of Thick Layered Ground Ice. *Cold Regions Sci. Tech.* 8 (1), 57–66. doi:10.1016/0165-232x(83)90017-4

Hu, Y. L. (2019). *PhD Thesis.Impacts of the Groundwater Flow Path on the Patterns of Dissolved Organic Carbon Export in the Cold Alpine Area*. Wuhan: China University of Geosciences, 1–134

Jin, H., He, R., Cheng, G., Wu, Q., Wang, S., Lü, L., et al. (2009). Changes in Frozen Ground in the Source Area of the Yellow River on the Qinghai–Tibet Plateau, China, and Their Eco-Environmental Impacts. *Environ. Res. Lett.* 4, 045206.

Kai, J. L., Wang, J. B., Huang, L., Wang, Y., Ju, J. T., and Zhu, L. P. (2019). Seasonal Variations of Dissolved Organic Carbon and Total Nitrogen Concentrations in Nam Co and Inflowing Rivers, Tibet Plateau. *J. Lake Sci.* 31 (4), 1099–1108.

Krüger, J. P., Leifeld, J., and Alewell, C. (2014). Degradation Changes Stable Carbon Isotope Depth Profiles in Palsa Peatlands. *Biogeosciences* 11, 3369–3380. doi:10.5194/bg-11-3369-2014

Lan, Y., Zhao, G., Zhang, Y., Wen, J., Liu, J., and Hu, X. (2010). Response of Runoff in the Source Region of the Yellow River to Climate Warming. *Quat. Int.* 226 (1-2), 60–65. doi:10.1016/j.quaint.2010.03.006

Lee, H., Swenson, S. C., Slater, A. G., and Lawrence, D. M. (2014). Effects of Excess Ground Ice on Projections of Permafrost in a Warming Climate. *Environ. Res. Lett.* 9, 124006. doi:10.1088/1748-9326/9/12/124006

Li, C., Chen, P., Kang, S., Yan, F., Tripathee, L., Wu, G., et al. (2018b). Fossil Fuel Combustion Emission from South Asia Influences Precipitation Dissolved Organic Carbon Reaching the Remote Tibetan Plateau: Isotopic and Molecular Evidence. *J. Geophys. Res. Atmos.* 123 (11), 6248–6258. doi:10.1029/2017jd028181

Li, C., Yan, F., Kang, S., Chen, P., Hu, Z., Han, X., et al. (2017). Deposition and Light Absorption Characteristics of Precipitation Dissolved Organic Carbon (DOC) at Three Remote Stations in the Himalayas and Tibetan Plateau, China. *Sci. Total Environ.* 605-606, 1039–1046. doi:10.1016/j.scitotenv.2017.06.232

Li, M., Liu, H., Li, L., Yi, X., and Zhu, X. (2007). Carbon Isotope Composition of Plants along Altitudinal Gradient and its Relationship to Environmental Factors on the Qinghai-Tibet Plateau. *Polish J. Ecol.* 55 (1), 67–78.

Li, Q., Wang, N., Barbante, C., Kang, S., Yao, P., Wan, X., et al. (2018a). Levels and Spatial Distributions of Levoglucosan and Dissolved Organic Carbon in Snowpits over the Tibetan Plateau Glaciers. *Sci. Total Environ.* 612, 1340–1347. doi:10.1016/j.scitotenv.2017.08.267

Li, X., Ding, Y., Xu, J., He, X., Han, T., Kang, S., et al. (2018c). Importance of Mountain Glaciers as a Source of Dissolved Organic Carbon. *J. Geophys. Res. Earth Surf.* 123 (9), 2123–2134. doi:10.1029/2017jf004333

Liu, F., Chen, L., Zhang, B., Wang, G., Qin, S., and Yang, Y. (2018). Ultraviolet Radiation rather Than Inorganic Nitrogen Increases Dissolved Organic Carbon Biodegradability in a Typical Thermo-Erosion Gully on the Tibetan Plateau. *Sci. Total Environ.* 627, 1276–1284. doi:10.1016/j.scitotenv.2018.01.275

Luo, C., Xu, G., Wang, Y., Wang, S., Lin, X., and Hu, Y. (2009). Effects of Grazing and Experimental Warming on DOC Concentrations in the Soil Solution on the Qinghai-Tibet Plateau. *Soil Biol. Biochem.* 41 (12), 2493–2500. doi:10.1016/j.soilbio.2009.09.006

Luo, D., HuiJun, J., Marchenko, S., and Romanovsky, V. (2014). Distribution and Changes of Active Layer Thickness (ALT) and Soil Temperature (TTOP) in the Source Area of the Yellow River Using the GIPL Model. *Sci. China Earth Sci.* 57 (8), 1834–1845. doi:10.1007/s11430-014-4852-1

Ma, Q., Jin, H., Yu, C., and Bense, V. F. (2019). Dissolved Organic Carbon in Permafrost Regions: A Review. *Science China Earth Sciences* 62 (2), 349–364. doi:10.1007/s11430-018-9309-6

Mu, C. C., Abbott, B. W., Wu, X. D., Zhao, Q., Wang, H. J., Su, H., et al. (2017). Thaw Depth Determines Dissolved Organic Carbon Concentration and Biodegradability on the Northern Qinghai-Tibetan Plateau. *Geophys. Res. Lett.* 44 (18), 9389–9399. doi:10.1002/2017gl075067

Mu, C., Zhang, T., Wu, Q., Peng, X., Cao, B., Zhang, X., et al. (2015). Organic Carbon Pools in Permafrost Regions on the Qinghai–Xizang (Tibetan) Plateau. *The Cryosphere* 9 (2), 479–486. doi:10.5194/tc-9-479-2015

Mu, C., Zhang, T., Wu, Q., Zhang, X., Cao, B., Wang, Q., et al. (2014). Stable Carbon Isotopes as Indicators for Permafrost Carbon Vulnerability in Upper Reach of Heihe River basin, Northwestern China. *Quat. Int.* 321, 71–77. doi:10.1016/j.quaint.2013.12.001

Mu, C., Zhang, T., Zhang, X., Li, L., Guo, H., Zhao, Q., et al. (2016). Carbon Loss and Chemical Changes from Permafrost Collapse in the Northern Tibetan Plateau: Permafrost Collapse Caused Carbon Loss. *J. Geophys. Res. Biogeosci* 121, 1781–1791. doi:10.1002/2015jg003235

Qu, B., Sillanpää, M., Li, C., Kang, S., Stubbins, A., Yan, F., et al. 2017. Aged Dissolved Organic Carbon Exported from Rivers of the Tibetan Plateau. *PloS one*, 12.1–11.doi:10.1371/journal.pone.0178166

Ran, Y., Li, X., and Cheng, G. (2018). Climate Warming over the Past Half century Has Led to thermal Degradation of Permafrost on the Qinghai–Tibet Plateau. *The Cryosphere* 12 (2), 595. doi:10.5194/tc-12-595-2018

Raymond, P. A., and Bauer, J. E. (2000). Bacterial Consumption of DOC during Transport through a Temperate Estuary. *Aquat. Microb. Ecol.* 22 (1), 1–12. doi:10.3354/ame022001

Raymond, P. A., and Bauer, J. E. (2001). Riverine export of Aged Terrestrial Organic Matter to the North Atlantic Ocean. *Nature* 409 (6819), 497–500. doi:10.1038/35054034

Selvam, B. P., Lapierre, J. F., Guillemette, F., Voigt, C., Lamprecht, R. E., Biasi, C., et al. (2017). Degradation Potentials of Dissolved Organic Carbon (DOC) from Thawed Permafrost Peat. *Scientific Rep.* 7, 45811. doi:10.1038/srep45811

Song, C., Wang, G., Mao, T., Chen, X., Huang, K., Sun, X., et al. (2019). Importance of Active Layer Freeze-Thaw Cycles on the Riverine Dissolved Carbon export on the Qinghai-Tibet Plateau Permafrost Region. *PeerJ* 7, e7146. doi:10.7717/peerj.7146

Spencer, R. G., Mann, P. J., Dittmar, T., Eglinton, T. I., McIntyre, C., and Holmes, R. M. (2015). Detecting the Signature of Permafrost Thaw in Arctic Rivers. *Geophys. Res. Lett.* 42 (8), 2830–2835. doi:10.1002/2015gl063498

Stocker, T. (2014) Edition. Climate Change 2013: the Physical Science Basis: Working Group I Contribution to the Fifth Assessment Report of the Intergovernmental Panel on Climate Change. Cambridge university press.

Striegl, R. G., Aiken, G. R., Dornblaser, M. M., Raymond, P. A., and Wickland, K. P. (2005). A Decrease in Discharge-Normalized DOC export by the Yukon River during Summer through Autumn. *Geophys. Res. Lett.* 32, 413. doi:10.1029/2005gl024413

Su, Y., Hu, E., Liu, Z., Jeppesen, E., and Middelburg, J. J. (2018). Assimilation of Ancient Organic Carbon by Zooplankton in Tibetan Plateau Lakes Is Depending on Watershed Characteristics. *Limnology and Oceanography* 63 (6), 2359–2371. doi:10.1002/lno.10943

Tanski, G., Couture, N., Lantuit, H., Eulenburg, A., and Fritz, M. (2016). Eroding Permafrost Coasts Release Low Amounts of Dissolved Organic Carbon (DOC) from Ground Ice into the Nearshore Zone of the Arctic Ocean. *Glob. Biogeochem. Cycles* 30 (7), 1054–1068. doi:10.1002/2015gb005337

Tian, H., Lan, Y., Wen, J., Jin, H., Wang, C., Wang, X., et al. (2015). Evidence for a Recent Warming and Wetting in the Source Area of the Yellow River (SAYR) and its Hydrological Impacts. *J. Geographical Sci.* 25 (6), 643–668. doi:10.1007/s11442-015-1194-7

Vonk, J. E., Mann, P. J., Dowdy, K. L., Davydova, A., Davydov, S. P., Zimov, N., et al. (2013a). Dissolved Organic Carbon Loss from Yedoma Permafrost Amplified by Ice Wedge Thaw. *Environ. Res. Lett.* 8, 035023. doi:10.1088/1748-9326/8/3/035023

Vonk, J. E., Tank, S. E., Bowden, W. B., Laurion, I., Vincent, W. F., Alekseychik, P., et al. (2015). Reviews and Syntheses: Effects of Permafrost Thaw on Arctic Aquatic Ecosystems. *Biogeosciences* 12 (23), 7129–7167. doi:10.5194/bg-12-7129-2015

Walvoord, M. A., and Kurylyk, B. L. (2016). Hydrologic Impacts of Thawing Permafrost—A Review. *Vadose Zone J.* 15 (6), 1–20. doi:10.2136/vzj2016.01.0010

Wang, S. T., Sheng, Y., Cao, W., Li, J., Ma, S., and Hu, X. Y. (2017). Estimation of Permafrost Ice Reserves in the Source Area of the Yellow River Using Landform Classification. *Adv. Water Sci.* 28 (6), 801–810.

Wang, Y., Spencer, R. G., Podgorski, D. C., Kellerman, A. M., Rashid, H., and Zito, P. (2018). Spatiotemporal Transformation of Dissolved Organic Matter along an alpine Stream Flow Path on the Qinghai–Tibet Plateau: Importance of Source and Permafrost Degradation. *Biogeosciences* 15 (21), 6637–6648. doi:10.5194/bg-15-6637-2018

Xu, X., Lu, C., Shi, X., and Gao, S. (2008). World Water tower: an Atmospheric Perspective. *Geophys. Res. Lett.* 35, L20815.

Yan, F., Kang, S., Li, C., Zhang, Y., Qin, X., Li, Y., et al. (2016). Concentration, Sources and Light Absorption Characteristics of Dissolved Organic Carbon on a Medium-Sized valley Glacier. *Northern Tibetan Plateau. Cryosphere* 10.

Yang, Y., Wu, Q., Hou, Y., Zhang, Z., Zhan, J., Gao, S., et al. (2017). Unraveling of Permafrost Hydrological Variabilities on Central Qinghai-Tibet Plateau Using Stable Isotopic Technique. *Sci. Total Environ.* 605, 199–210. doi:10.1016/j.scitotenv.2017.06.213

Yang, Y., Wu, Q., Jin, H., Wang, Q., Huang, Y., Luo, D., et al. (2019). Delineating the Hydrological Processes and Hydraulic Connectivities under Permafrost Degradation on Northeastern Qinghai-Tibet Plateau, China. *J. Hydrol.* 569, 359–372. doi:10.1016/j.jhydrol.2018.11.068

Yang, Y., Wu, Q., Yun, H., Jin, H., and Zhang, Z. (2016). Evaluation of the Hydrological Contributions of Permafrost to the Thermokarst Lakes on the Qinghai–Tibet Plateau Using Stable Isotopes. *Glob. Planet. Change* 140, 1–8. doi:10.1016/j.gloplacha.2016.03.006

Yu, S.-Y., He, H., Cheng, P., and Hou, Z. (2017). Depth Heterogeneity of Soil Organic Carbon Dynamics in a Heavily Grazed alpine Meadow on the Northeastern Tibetan Plateau: A Radiocarbon-Based Approach,. *J. Geophys. Res. Biogeosci.* 122, 1775–1788. doi:10.1002/2016JG003567

Zhang, T., Heginbottom, J. A., Barry, R. G., and Brown, J. (2000). Further Statistics on the Distribution of Permafrost and Ground Ice in the Northern Hemisphere. *Polar Geogr.* 24 (2), 126–131. doi:10.1080/10889370009377692

Zhang, Y., Kang, S., Li, G., Gao, T., Chen, P., Li, X., et al. (2018). Dissolved Organic Carbon in Glaciers of the southeastern Tibetan Plateau: Insights into Concentrations and Possible Sources. *PloS one* 13, e0205414.

Zhao, L., Hu, G., Zou, D., Wu, X., Ma, L., Sun, Z., et al. (2019). Permafrost Changes and its Effects on Hydrological Processes on Qinghai-Tibet Plateau. *Bull. Chin. Acad. Sci.* 34 (11), 1233–1246.

Zhou, Y. W., Guo, D. X., Qiu, G. Q., Cheng, G. D., and Li, S. D. (2000). *Geocryology in China*. Beijing: Science Press.

Zou, D., Zhao, L., Yu, S., Chen, J., Hu, G., Wu, T., et al. (2017). A New Map of Permafrost Distribution on the Tibetan Plateau. *The Cryosphere* 11 (6), 2527–2542. doi:10.5194/tc-11-2527-2017

Conflict of Interest: The authors declare that the research was conducted in the absence of any commercial or financial relationships that could be construed as a potential conflict of interest.

frontiers in Earth Science

ORIGINAL RESEARCH
published: 31 March 2022
doi: 10.3389/feart.2022.850220

The Effects of Freeze–Thaw Cycles on Methane Emissions From Peat Soils of a High-Altitude Peatland

Zao Yang[1,2], *Dan Zhu*[1,2]*, *Liangfeng Liu*[1,2], *Xinwei Liu*[1,2] and *Huai Chen*[1,2]

[1]Chengdu Institute of Biology, Chinese Academy of Sciences, Chengdu, China, [2]Zoîgé Wetland Ecosystem Research Station, Chinese Academy of Sciences, Aba, China

The Qinghai– Tibet Plateau (QTP), which embodies the largest area of permafrost at mid–low altitudes of the world, has been experiencing rapid permafrost degradation and changes in freeze–thaw processes for the past decades. However, the responses and potential feedbacks of the methane flux from peatlands on the QTP to changing freeze–thaw cycles (FTCs) remain unknown. In this study, we collected peat soils from the Zoîgé peatlands, the largest peatland complex on the QTP, to examine methane emissions under simulated diurnal FTC scenarios. In incubation experiments of 15 days, two freeze–thaw temperature ranges of −5 to 4°C (mild) and −15 to 4°C (intense) were applied to two sets of peat soil samples, and each of them was characterized by 100% or 80% maximum water holding capacity (MWHC). The results showed that the peak of methane emission from the peat soil occurred after the first freeze–thaw cycle (FTC1), with the highest reaching a value of 0.103 mg kg soil^{-1}·h^{-1}. Generally, the cumulative methane emissions were elevated by FTCs, and relative higher rates of methane emissions were found for the 2nd FTC to the 15th FTC, compared with those from low-altitude peatlands. Methane emissions were significantly correlated to the export of dissolved organic carbon (DOC) and the activities of β-D-cellobiosidase and phenol oxidase in various freeze–thaw conditions. This study highlights the importance of FTCs in stimulating methane emissions and implies that methane emissions during FTCs from high-altitude peatlands would increase under a warmer climate in the future.

Keywords: methane emissions, high-altitude peatlands, freeze–thaw cycles, dissolved organic carbon, enzyme activity

OPEN ACCESS

Edited by:
Huijun Jin,
Northeast Forestry University, China

Reviewed by:
Xinhou Zhang,
Nanjing Normal University, China
Ziming Yang,
Oakland University, United States

***Correspondence:**
Dan Zhu
zhudan_m@cib.ac.cn

Specialty section:
This article was submitted to Biogeoscience, a section of the journal Frontiers in Earth Science

Received: *07 January 2022*
Accepted: *07 March 2022*
Published: *31 March 2022*

Citation:
Yang Z, Zhu D, Liu L, Liu X and Chen H (2022) The Effects of Freeze–Thaw Cycles on Methane Emissions From Peat Soils of a High-Altitude Peatland. Front. Earth Sci. 10:850220. doi: 10.3389/feart.2022.850220

INTRODUCTION

Since the Last Glacial Maximum, peatlands have accumulated more than 600 Pg organic carbon (Yu et al., 2010). Peatlands are an important source of atmospheric methane, accounting for about 10% of the global methane budget (Roulet, 2000; Frolking et al., 2011). However, methane emissions from peatlands are sensitive and vulnerable to environmental variations, and larger methane emissions when peatlands are subject to higher temperatures (Schuur et al., 2015) as the soil organic carbon decomposition would be accelerated (Natali et al., 2011).

Most of the peatlands are distributed in high latitude and high-altitude areas where the seasonal freeze–thaw is a typical surface process (Zhang and Armstrong, 2001). During the seasonal freeze–thaw periods, autumn freeze and spring thaw, with intensive diurnal freeze–thaw cycles

(FTCs), were known as the "shoulder season" (Arndt et al., 2019; Pirket al., 2015). Recent studies from the northern region have reported considerable methane emissions during the periods of spring thaw (e.g., Song et al., 2012; Tokida et al., 2007) and autumn freeze (Bao et al., 2021; Raz-Yaseef et al., 2017; Pirk et al., 2015; Mastepanov et al., 2008). A significant increase of methane emissions during freeze–thaw periods has been observed from a peatland of the Sanjiang Plain, Northeast China (Yang W. et al., 2006). A large amount of methane was found to be released during the spring thaw period with great spatiotemporal heterogeneity from a peatland in Hokkaido, Japan (Tokida et al., 2007). One study even found that methane emissions during spring thaw accounted for 80% of the annual budget (Song et al., 2012). On the contrary, three to four times higher contributions of methane emissions during the autumn freeze than that of the spring thaw were observed from a tundra ecosystem in Alaska, United States (Bao et al., 2021). Another study found a methane emission burst in the early winter from tundra regions as well (Mastepanov et al., 2008). The field monitoring on a peatland of the Qinghai–Tibet Plateau (QTP) showed that methane emissions during FTCs accounted for 11 to 27% of the annual budget, and methane emissions of the autumn freeze period were higher than those of the spring thaw period (Chen et al., 2021), with the underlying mechanism remaining unknown.

The average thickness of peat in the northern region is 2.3 m (Gorham, 1991), and FTCs mainly occur in the surface soil (Jin et al., 1999; Song et al., 2006). Studies show that the FTC primarily changes the physical structure of soil by shifting the thermal and hydrological conditions, and then affects the related biological processes, including changes in plant root activities, soil enzyme activities, and microbial community composition, which consequently affect the methane production and emission (Freeman et al., 2001; Herrmann and Witter, 2002; Wang et al., 2007; Sorensen et al., 2018). Cellulose and lignin are the two most abundant soil organic compounds, and the microbial-mediated decomposition of these substances provides the main substrates for soil respiration. Among them, the hydrolysis of cellulose and hemicellulose is mainly catalyzed by cellulose, such as β-D-cellobiosidase, and the oxidation and degradation of phenolic recalcitrant-like compounds are catalyzed by ligninase, such as phenoloxidase (Chen et al., 2018).

In high altitude regions, due to the stronger diurnal temperature variations in the cold season (Dong and Huang, 2015), the seasonal freeze–thaw processes are characterized by a short period of freeze-up and long shoulder seasons of ground freezing and thawing than their counterparts in high latitudes (Yang M. et al., 2006). Under such conditions, FTCs are expected to have a similar or even stronger impact on methane emissions (Xiang et al., 2009; Wang et al., 2011). Despite the large areal extent of peatlands in the mountain regions of the world (Xu et al., 2018), there have been limited attempts to quantify their methane emissions during FTCs. Therefore, in this study we aimed to test 1) whether FTCs will enhance methane emissions from high-altitude peatlands; 2) the relationships between methane emissions and influencing factors of FTCs.

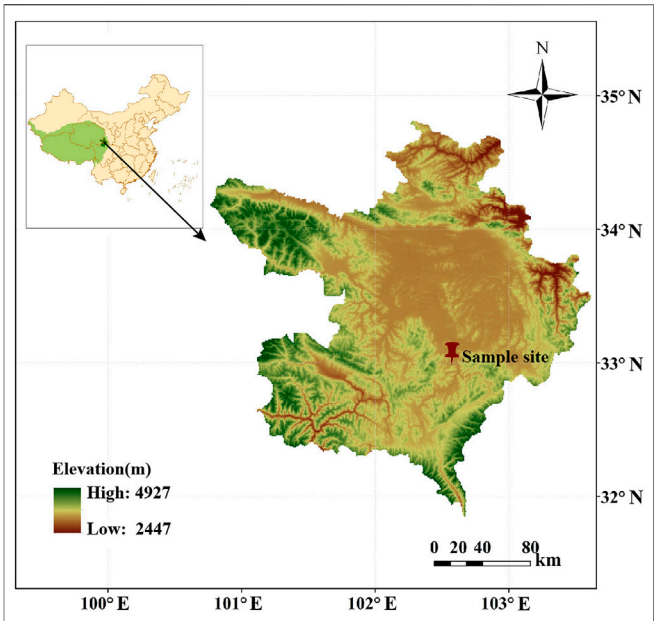

FIGURE 1 | Map of the Zoîgé Plateau with the sample site location in the Ruokeba peatland. The green part of China map is QTP.

MATERIALS AND METHODS

Study Site and Sample Collection

We selected the Zoîgé peatlands on the northeastern QTP as our study site. With an area extent of 4.6×10^3 km^2, the Zoîgé peatlands are the largest high-altitude peatlands of the world and account for about 44% of the total peatland area of China (Liu et al., 2012; Mei Wang et al., 2014). The sampling plot was located at a peatland developed on a fluvial–pluvial fan in the interior of the Zoîgé peatlands (33°04′06″N, 102°34′31″E; 3428 m a.s.l.) (**Figure 1**). The thickness of the peat of the sampling plot was 2–3 m.

The climate in the Zoîgé peatlands belongs to cold temperate continental climate with alternating summer and winter monsoons. During the period of 2013 to 2017, the highest monthly mean air temperature ranged from 9.1 to 11.4°C in July, while the lowest one ranged from −10.9 to −8.2°C in January (Liu, 2021). The range of mean annual precipitation was approximately 656 mm, 86% of which occurred between April and October. According to field observation at 5 cm in soil (Liu, 2021), spring ground surface thawing occurred between February to April, whereas autumn ground surface freezing occurred between September to December. During the autumn ground surface freezing periods, the mean soil freezing temperature was around −5°C, while spring ground surface thawing temperature was around 4°C. Moreover, the minimum daily mean soil temperature was around −15°C. The vegetation plant species of the sampling plot were dominated by *Kobresia tibetica* and *Carex muliensis*.

We collected 20 cylindrical peat blocks (diameter, 9 cm; height, 20 cm) from the surface layer (0–20 cm) in October,

2018. Each peat soil sample was divided into two halves: one was analyzed for physical and chemical properties, while the other for incubation experiments.

Determination of Peat Samples

The pH was measured with an electronic pH meter (Sartorius P10). Total carbon and nitrogen were measured with an element analyzer (Isoprime 100, Elementar). The total organic carbon (TOC) of the soil was measured with a TOC analyzer (Vario TOC). The maximum water holding were calculated according to the procedures described in Rey et al. (2005).

Incubation Experiments

Two freeze–thaw intensities (freezing at −5°C for 12 h, then thawing at 4°C for 12 h, and freezing at −15°C for 12 h, then thawing at 4°C for 12 h. Named as mild FTCs and intense FTCs hereafter, respectively) were introduced into the incubation and two water content gradients, maximum water holding capacity of 100% (100% MWHC) for one half of the soil sample and the other half to 80% (80% MWHC). A set of control samples was incubated at 4°C (control) for reference. Therefore, the 20 peat soil samples that were collected from the field were divided into five groups, i.e., mild+100% MWHC, mild+80% MWHC, intense +100% MWHC, intense+80% MWHC and control, with four replicates in each group. For each replicate, air-dried peat soil (55 g) was placed in 250 mL flasks, all samples were kept at 4°C for 5 days until they were incubated in an adjustable temperature freezer.

The methane flux measurement for headspace gas samples was collected at 10 min intervals after 0, 1st, 3rd, 5th, 10th, and 15th FTCs (FTC0, FTC1, FTC3, FTC5, FTC10, and FTC15, respectively). The gas samples were analyzed for methane concentrations by flame ionization detection (FID) on a gas chromatograph (GC, PE Clarus 500, PerkinElmer, Inc., United States), operating at 350°C and a 2 m porapak 80-100 Q column. The column oven temperature was 35°C and the carrier gas was N_2 with a flow rate of 20 cm^3 min^{-1}. The minimum detectable concentration was 1×10^{-3} μL L^{-1} (ppb) standard with a concentration of 4.9 μL L^{-1} (China National Research Center for Certified Reference Materials, Beijing).

The formula for the gas emission rate is (Liu et al., 2016)

$$F = \frac{dc}{dt} \cdot \frac{V}{V_0} \cdot \frac{P}{P_0} \cdot \frac{T_0}{T} \cdot \frac{M}{m}, \quad (1)$$

where F represents the gas emission rate (mg kg $soil^{-1} \cdot h^{-1}$); dc/dt (mol h^{-1}) represents the rate of change in gas concentration; M (mg mol^{-1}) represents the molar mass of the gas; P (Pa) represents the atmospheric pressure at the sampling site; T (K) represents the absolute room temperature during the sampling time; V (m^3) represents the headspace volume of the culture flask; m (kg) indicates the dry weight of the soil sample; and V_0 (m^3), P_0 (Pa), and T_0 (K) represent the molar volume, atmospheric pressure, and absolute temperature under standard conditions, respectively.

The formula for cumulative gas emissions is (Wang, 2014)

$$CE = \sum_{i=1}^{n} \left(\frac{F_i + F_{i+1}}{2} \right) \cdot (T_{i+1} - T_i) \cdot 24, \quad (2)$$

where CE represents the cumulative gas emission (mg kg $soil^{-1}$); F stands for the gas emission rate (mg kg $soil^{-1} \cdot h^{-1}$); i represents the times of gas collection; T_{i+1}-T_i represents the interval between two adjacent gas collections; n represents the total number of gas collections during the observation period; and *24* means 24 h in 1 day.

Dissolved organic carbon (DOC) measurement fresh peat soil (5 g) was passed through a 100-mesh sieve and was placed in a centrifuge tube. 50 ml of deionized water was added and shaken for 30 min. The supernatant was taken and passed through a 0.45- μm organic filter membrane. The concentration was determined with a TOC analyzer. We adopted the procedures of Zhang et al. (2006).

The formula for cumulative DOC output is (Wang, 2014)

$$CD = \sum_{i=1}^{n} \left(\frac{D_i + D_{i+1}}{2} \right) \cdot (T_{i+1} - T_i), \quad (3)$$

where CD represents the cumulative output of DOC (g kg $soil^{-1}$); D represents the output of DOC (g kg $soil^{-1}$); i represents the number of FTCs; T_{i+1}-T_i represents the time interval between two measurements; and n represents the total number of measurements in the observation period.

β-D-cellobiosidase and phenoloxidase activity measurement fresh peat soil (2 g) was placed in a 250 ml beaker, and 200 ml of acetic acid buffer was added to make a suspension. A fluorescence plate was used for the determination of the β-D-cellobiosidase activity (with 4-MUB-β-d-glucoside and 4-MUB-β-d-cellobiosid as substrates), and a white board was used for the phenoloxidase activity (with L-DOPA as substrates). β-D-cellobiosidase was reacted for four h and the phenoloxidase substrate was reacted for 20 h at 25°C. Finally, 20 μL of sodium hydroxide was added to the fluorescent plate for comparing the color at the absorbance of 365 nm/450 nm and at the absorbance of 460 nm for the white plate (Blagodatskaya et al., 2016; Dunn and Freeman, 2018; Sorensen et al., 2018).

Statistical Analysis

The variations of the methane emission rate and methane cumulative emission, DOC, and enzyme activity under different ground surface freezing and thawing conditions were examined by a one-way analysis of variance (ANOVA). The correlation between DOC, enzyme activity, and the methane emission rate were examined by the Pearson correlation. The effects of the number of FTCs, freeze–thaw intensity, peat water content, and their interactions with the methane emission rate, DOC, and enzyme activity were tested by a multi-factor analysis of variance (MANOVA). The significant difference and extremely significant difference were indicated by $p < 0.05$ and $p < 0.01$, respectively. Statistical analyses were conducted using SPSS 17.0.

RESULTS

Methane Emission

The methane emission rate showed significant peaks ($p < 0.05$) after the first freeze–thaw cycle (FTC1) in all the treatments. In terms of the emission rate of FTC1, the sequence was mild

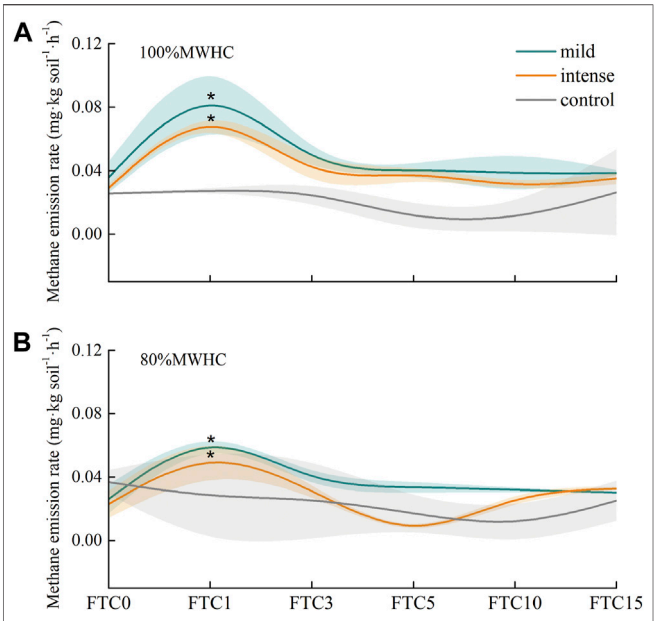

FIGURE 2 | Methane emission rate in freeze–thaw cycles. **(A)** The methane emission rates of 100%MWHC peat; **(B)** the methane emission rates of 80%MWHC peat. Mild means freeze–thaw cycle at −5~4°C; intense means freeze–thaw cycle at −15–4°C; *, there is a significant difference between freeze–thaw peat and control group ($p < 0.05$).

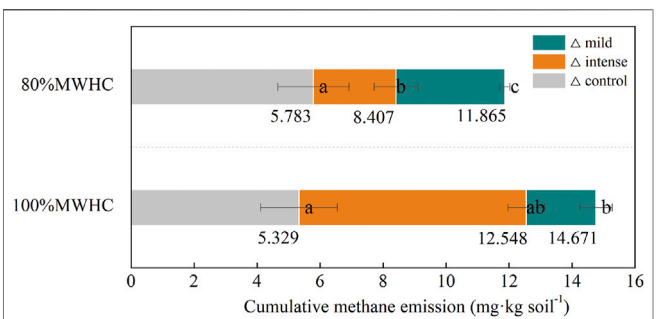

FIGURE 3 | Cumulative methane emission. Mild means freeze–thaw cycle at −5~4°C; intense means freeze–thaw cycle at −15–4°C. Triangles (△) indicate the difference of cumulative methane emission between the target setting condition and next sequence setting condition.

+100% MWHC > intense +100% MWHC > mild +80% MWHC > intense +80% MWHC, with their rates ranged from 0.060 to 0.103 mg kg soil^{-1}·h^{-1}, and mild +100% MWHC was approximately 2.5 times as control, yet FTC0, 3, 5, 10, and 15 showed no significant differences with control (**Figure 2**).

The cumulative methane emissions increased after all the FTCs compared with the control (△> 0). Similar to the emission rate of FTC1, the sequence of cumulative methane emissions was mild +100%MWHC > intense +100%MWHC > mild +80%MWHC > intense +80%MWHC, with their amounts ranged from 8.407 to 14.671 mg kg soil^{-1}. Notably, under the 80% MWHC condition, the difference between mild and intense FTCs was significant ($p = 0.031$). The cumulative methane emission under 100% MWHC is higher than that under 80% MWHC, regardless of the freeze–thaw intensity (intense, $p = 0.032$; mild, $p = 0.206$) (**Figure 3**).

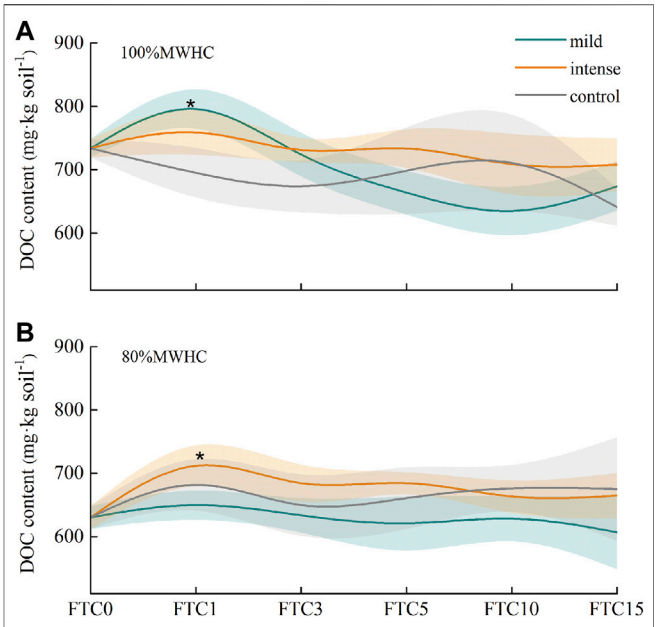

FIGURE 4 | DOC content in freeze–thaw cycles. **(A)** The DOC outputs of 100%MWHC peat; **(B)** the DOC outputs of 80%MWHC peat. Mild means freeze–thaw cycle at −5~4°C; intense means freeze–thaw cycle at −15–4°C; *, there is a significant difference between the freeze–thaw peat and control group ($p < 0.05$).

DOC Output

The DOC content reached its peak at FTC1in all the four treatments. Intense +80% MWHC and mild +100% MWHC showed a significant peak ($p < 0.05$) after FTC1. However, no significant differences were observed among the other two FTC treatments and control groups ($p > 0.05$). Furthermore, the DOC content of mild+80%MWHC decreased after FTC1 (**Figure 4**).

Under intense FTCs, the cumulative DOC output increased by 0.257 and 0.337 g kg soil^{-1} in 80% MWHC and 100% MWHC, respectively (△>0). Under mild FTCs, the cumulative DOC decreased by 0.603 and 0.399 g kg soil^{-1} in 80% MWHC and 100% MWHC, respectively (△<0). The cumulative DOC output under 100% MWHC was higher than that of 80% MWHC, and this was significant under the mild FTC ($p = 0.029$) (**Figure 5**).

Enzyme Activity

The β-D-cellobiosidase activity decreased significantly after FTC1 and remained stable until the end of 15 FTCs under mild freeze–thaw conditions, the mild +80% MWHC decreased significantly compared with FTC0 (**Figure 6A**), and the mild +100%MWHC increased significantly at FTC1 (**Figure 6B**) ($p < 0.05$). Moreover, the β-D-cellobiosidase

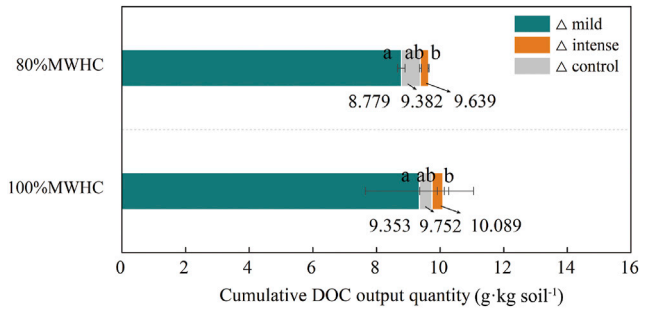

FIGURE 5 | Cumulative DOC output quantity. Mild means freeze–thaw cycle at –5~4°C; intense means freeze–thaw cycle at –15–4°C. Triangles (△) indicate the difference of cumulative DOC output quantity between the target setting condition and next sequence setting condition.

activity fluctuated and reached its minimum in FTC5 under intense FTC (**Figure 6**).

Under intense +80% MWHC, the phenol oxidase activity decreased significantly after FTC1, and dropped to the lowest value after FTC3, whereas it remained stable in mild +80% MWHC (**Figure 7A**). Under intense +100% MWHC, the phenol oxidase activity was the highest in FTC1 while it increased significantly after FTC1 and FTC3, and was the highest after FTC3 under mild +100%MWHC (**Figure 7B**).

Effects of FTCs on Methane Release, DOC Output, and Enzyme Activity

The methane emission rate was significantly affected by FTCs in different freeze–thaw patterns. Under 80% MWHC condition, the number and intensity of FTCs and the interaction between the two significantly affected the methane emission rate (p = 0.003, 0.000, 0.003), while the number of FTCs significantly affected the methane emission rate under 100% MWHC condition (p = 0.000). Furthermore, the number of FTCs and its interaction with water content significantly affected the methane emission rate ($p < 0.05$) under a mild FTC condition, while the number of FTCs and water content had extremely significant impacts under the intense FTC condition (p = 0.001, 0.000).

The intensity of FTCs affected the DOC under 100% MWHC condition (p = 0.000), and the number of FTCs had a significant effect on the DOC (p = 0.003). Under the mild FTC condition, the number of FTCs, water content, and the interaction between the two significantly affected the DOC concentration ($p < 0.05$).

The β-D-cellobiosidase activity was significantly affected by the number of FTCs and their interaction with intensity under 100% MWHC condition (p = 0.000; p = 0.000). Both the β-D-cellobiosidase (p = 0.015) and phenoloxidase (p = 0.025) activities were significantly affected by the interactions between the number of FTCs and intensity under 80%MWHC condition. Moreover, the number of FTCs and their interaction with water content significantly affected the β-D-cellobiosidase activity (p = 0.000; p = 0.001). However, the intense FTC condition did not show obvious effects on the DOC, β-D-cellobiosidase activity, and phenoloxidase activity ($p > 0.05$) (**Table 1**).

Relationship Between Methane Emission Rate and Variables

The methane emission rate was correlated significantly to the DOC content under 100% MWHC condition (p = 0.002), whereas no significant correlation was observed under 80%MWHC condition (p = 0.410). Moreover, the DOC content was found to have significant correlations with the methane emission rate under both mild (p = 0.000) and intense (p = 0.023) FTCs under 100% MWHC condition. Generally, the methane emission rate was significantly correlated with β-D-cellobiosidase and phenoloxidase activities, regardless of the freeze–thaw intensity and soil water content (**Table 2**).

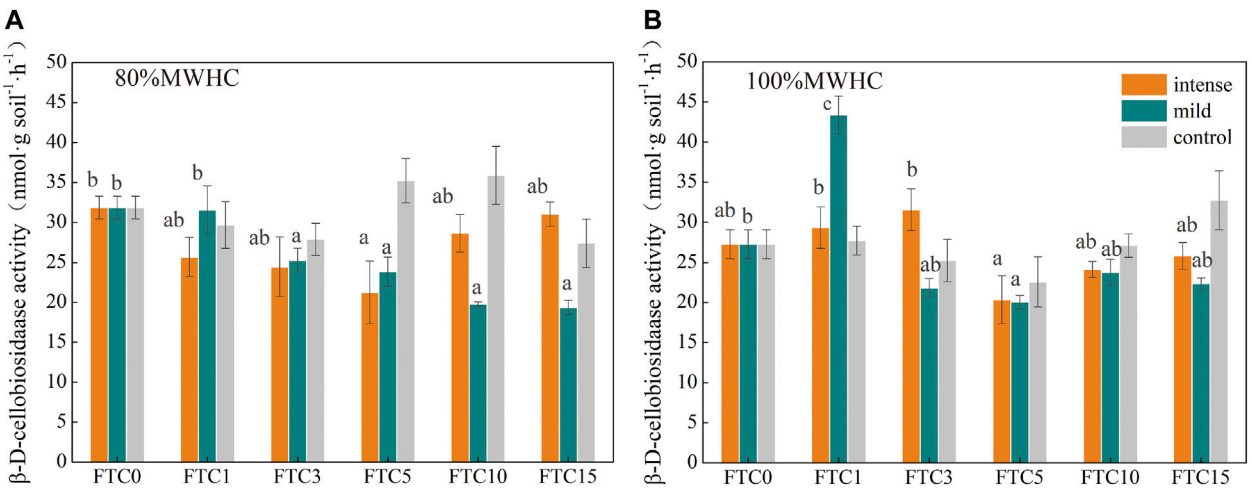

FIGURE 6 | β-D-cellobiosidase activity changes during the freeze–thaw cycles. **(A)** the β-D-cellobiosidase activity of 80%MWHC peat; **(B)** the β-D-cellobiosidase activity of 100%MWHC peat; mild means freeze–thaw cycle at –5~4°C; intense means freeze–thaw cycle at –15~4°C.

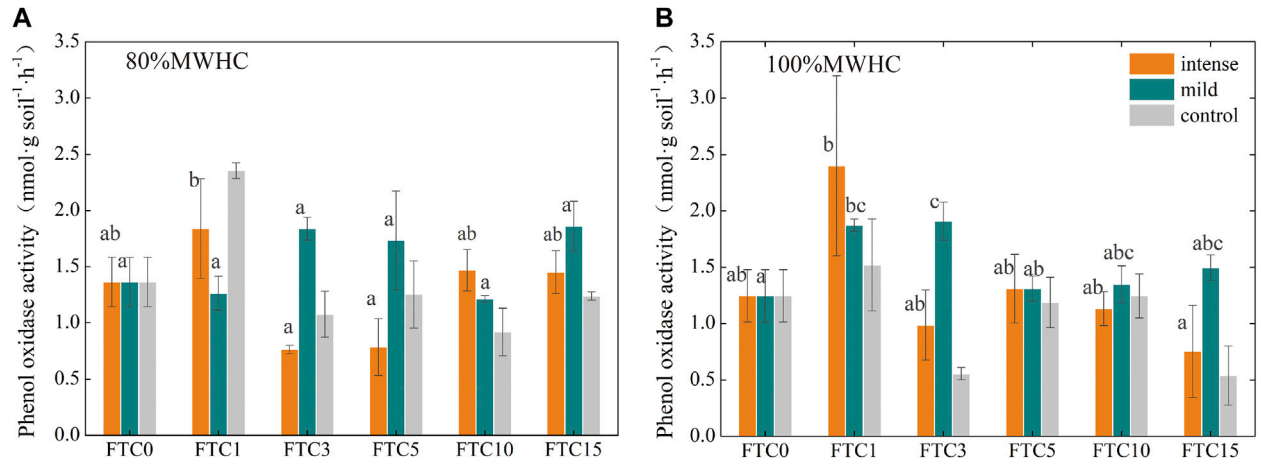

FIGURE 7 | Phenol oxidase activity changes during the freeze–thaw cycles. **(A)** The phenol oxidase activity of 80%MWHC peat; **(B)** the phenol oxidase activity of 100%MWHC peat. Mild means freeze–thaw cycle at −5~4°C; intense means freeze–thaw cycle at −15~4°C.

TABLE 1 | MANOVA results of enzyme activity in different freeze–thaw patterns.

		Methane emission rate	DOC	β-D-cellobiosidase	Phenoloxidase
Different freeze–thaw intensity(100%MWHC)	I	0.240	0.103	0.978	0.272
	T	**0.000**	**0.000**	**0.000**	0.095
	I×T	0.936	0.087	**0.000**	0.348
Different freeze–thaw intensity(80%MWHC)	I	**0.003**	**0.003**	0.215	0.085
	T	**0.000**	0.488	0.309	0.573
	I×T	**0.003**	0.486	**0.015**	**0.025**
Different water content (−5–4°C)	W	0.064	**0.000**	0.059	0.970
	T	**0.000**	**0.001**	**0.000**	0.123
	W×T	**0.001**	**0.027**	**0.001**	0.147
Different water content (−15–4°C)	W	**0.001**	0.197	0.986	0.840
	T	**0.000**	0.172	0.104	0.052
	W×T	0.633	0.731	0.223	0.503

I, freeze–thaw intensity; T, freeze–thaw times; W, water content. Values are p *values; bold indicates significant levels* (p < *0.05) or extremely significant levels* (p < *0.01).*

TABLE 2 | The correlation between methane emission rate and DOC content.

Freeze–thaw condition		DOC	β-D-cellobiosidase	Phenoloxidase
Different freeze–thaw intensity(100%MWHC)	Pearson correlation	0.432[a]	0.518[a]	0.327[b]
	p value	0.002	0.000	0.024
Different freeze–thaw intensity(80%MWHC)	Pearson correlation	0.122	0.322[b]	0.345[b]
	p value	0.410	0.042	0.016
Different water content (−5~4°C)	Pearson correlation	0.497[a]	0.627[a]	0.017
	p value	0.000	0.000	0.909
Different water content(−15–4°C)	Pearson correlation	0.328[b]	0.046	0.470[a]
	p value	0.023	0.756	0.001

[a]*Extremely significant correlation* (p< *0.01).*
[b]*Significant correlation* (p< *0.05).*

DISCUSSION

Methane Emissions During the FTCs

It has already been shown that methane emissions are more significant at the beginning of continuous FTCs (Wang, 2014; Kurganova et al., 2007). As the number of FTCs increases, methane emission rate tends to decrease (Wang, 2010; Wang, 2015; Hao et al., 2007; Prieme and Christensen, 2001). Our result was consistent with the aforementioned studies. When soil freezing and thawing occurs, the water phase changes, ice

crystal grows, and water migrates on soil particles and pores, thus soil structure is damaged (Xie et al., 2015; Wang et al., 2013), and gas trapped in soil gaps is squeezed out and contributes to the increasing methane emission (Shindell et al., 2009). As the soil temperature decreased during the autumn freeze period, the thermal conductivity of peat soil increased by 13 times in the process of changing from dryness and positive temperature to ice saturation and freezing (Zhou et al., 2000), resulting in the change in the heat capacity of the soil and the heat exchange flux with the atmosphere. Accompanied by the release of a biological activity compound (Tan et al., 2012) and carbon dioxide (McLain et al., 2002), with the impact of organic carbon (Tveit et al., 2012; Wu et al., 2019) and enzymes (Jiaoyue Wang et al., 2014; Kuttim et al., 2017; Chen et al., 2018) on gas emissions, the methane emissions could be enhanced. In the field observation adjacent to our sampling plot, higher methane emissions during the autumn freeze period than those in the spring thaw period was found with the emission peaks during the early autumn freezing period as well (Chen et al., 2021). Although our study only conducted simulation experiments, it could be helpful for understanding the effects of the intensity and number of FTCs on *in situ* high methane emissions in the early autumn freezing period.

In terms of the source strength of the methane emission induced by FTCs, our results were much lower than those found from a low-altitude peatland, where the methane emission peak ranged from 13.40 to 55.02 mg $m^{-2}{\cdot}h^{-1}$, and it was 4–19 times of the control (Wang, 2014). The incubation of peat soil from the low latitude area set the FTCs as freezing at −6°C for 2 days and thawing at 6°C for 5 days, resulting in high emissions due to longer-term ground surface freezing and thawing processes. Our incubation followed the FTCs in the field and thus has more frequent daily FTCs (Chen et al., 2021). Therefore, lower methane emission rates from this study could be attributed to the different experimental settings.

Our study also showed the impact of the number of FTCs on methane emissions in various freeze–thaw treatments. Generally, the gas emission tends to decrease after the initial emission peak (Prieme and Christensen, 2001; Hao et al., 2007; Wang, 2010, 2015). In our study, the cumulative methane emission under mild+100%MWHC condition was 2.469 mg kg $soil^{-1}$ during FTC1 and 12.202 mg kg $soil^{-1}$ from FTC2 to FTC15, which were 3.74 and 2.61 times their counterparts in the control group, respectively. Even under intense +80%MWHC condition, the lowest increments among the four FTC conditions, the cumulative methane emission was 1.430 mg kg $soil^{-1}$ during FTC1 and 6.977 mg kg $soil^{-1}$ from FTC2 to FTC15, which were 2.21 and 1.36 times of their counterparts in the control group, respectively. In summary, under a variety of freeze–thaw environmental conditions, the methane emission induced by the whole FTCs was 1.45–2.75 times of that without FTCs; The cumulative effect of the number of FTCs in our study was stronger to that of the low-altitude areas (Wang, 2014; Zhang et al., 2018). Jiaoyue Wang et al. (2014) found that the cumulative methane emission was about 1.35 times of that without FTCs under mild FTCs (−6~6°C), whereas Zhang et al. (2018) found that it was about 1.19 times and 2.85 times under mild FTCs (−5~5°C) and intense FTCs (−15–5°C), respectively. Therefore, our finding highlights the profound effect of the number or duration of FTCs on methane emissions on the peatlands, at least during the autumn freezing period at the high altitudes. Furthermore, it indicates higher methane emissions during shoulder seasons from those high-altitude peatlands in the context of warmer climate and longer shoulder seasons.

In contrast to other studies (e.g., Zhang et al., 2018; Wang, 2014; Goldberg et al., 2008; Gao et al., 2015), this study found the greater cumulative methane emission under mild FTC than that under intense FTCs. Although a large amount of organic carbon is released from the aggregates because of freezing damage to the soil structure and more greenhouse gases will be released in a more intense freezing state, soil biological changes that induced by a higher temperature were more effective for enhancing methane emissions in the mild freezing-thawing mode. Furthermore, as plant roots have degenerated during the autumn freeze period, substrates retained in the soil for methanogenesis, whereas ammonium and nitrate components were accumulated in the soil, inhibiting methane oxidation (Groffman et al., 2006), resulting in greater methane emissions. This indicated a potential higher methane emission from high-altitude peatlands under the mild FTCs in future climate scenarios.

Effect of DOC Content and Enzyme Activity on Methane Emission

The DOC content first increased and then decreased throughout the FTCs. Similar dynamics have also been presented in other studies (Hao et al., 2007; Zhou et al., 2008; Wang, 2014). In addition, the methane emission rate was significantly positively correlated with the DOC in a variety of freeze–thaw environments. The microbial community composition can adjust the carbon utilization efficiency to the freeze–thaw processes (Herrmann and Witter, 2002; Chen et al., 2018). At FTC1, the microbial community composition changed significantly, and then gradually returned to the state before FTCs. Moreover, the active organic carbon in the aggregates was gradually released at the beginning of FTCs (Groffman et al., 2001; Bechmann et al., 2005; Wang et al., 2013), whereas the original DOC in the soil was constantly being decomposed and consumed by living microorganisms. Therefore, the DOC content decreased after multiple FTCs (Herrmann and Witter, 2002; Wang et al., 2011), and this process is compatible with the methane production.

Our study showed that the number of FTCs had significantly impact on the β-D-cellobiosidase activity, which was consistent with the results from an analysis on a low-altitude peatland (Li et al., 2019). As a catalytic enzyme in the final stage of glucose production, the activity of β-D-cellobiosidase was greatly affected by the concentration of the substrate from cellulose decomposition (Brouns et al., 2016). Moreover, in the early stage of organic matter decomposition, cellulose with a higher content was

decomposed by FTCs preferentially, producing more biodegradable substrates for eutrophic bacteria, such as *Pedobacter*, a predominant bacterium in eutrophic water (Zheng et al., 2015). Therefore, the β-D-cellobiosidase activity was higher at the early stage of FTCs.

Phenol oxidase was the limiting factor for the decomposition of soil organic carbon in peat soil (Chen et al., 2018). The activity of phenol oxidase in peatlands is found to be related to carbon storage and DOC release (Freeman et al., 2001). The increase of phenolic compounds will inhibit the decomposition of organic carbon in soil, thus reduce the amount of substrates for methane production. Therefore, the accumulation of phenolic compounds inhibited the decomposition of DOC, resulting in the increased cumulative release of DOC this ultimately leaded to a declined methane emission, particularly under intense FTCs. As the phenol oxidase activity is thought to be enhanced under warmer climate in the future (Chen et al., 2018), the effect of altered FTCs on methane emissions from peatlands would be complicated. Therefore, more insights are needed to obtain a better understanding on methane emissions during FTCs.

CONCLUSION

Increased methane emissions were found after the simulated FTCs from peat soils of a high-altitude peatland on the QTP. Similar to other studies, the methane emission peak occurred after the first FTC. The longer duration of the FTCs seems to have a profound effect on elevating methane emissions in our study compared with those from low-altitude peatlands. The incubated soils with mild freeze–thaw intensity and higher water content had a higher cumulative methane emission than that of their counterparts. Furthermore, DOC, β-D-cellobiosidase, and phenol oxidase were significantly correlated to methane emissions in a variety of freeze–thaw environments. These results have suggested a higher methane emission during the seasonal freeze–thaw process from high-altitude peatlands under the projected future climate scenarios, as both longer and warmer shoulder seasons could be expected.

DATA AVAILABILITY STATEMENT

The original contributions presented in the study are included in the article/Supplementary Material, further inquiries can be directed to the corresponding author.

AUTHOR CONTRIBUTIONS

Conceptualization: DZ. Methodology: ZY, XL, LL, and DZ. Investigation: ZY, XL, and DZ. Funding acquisition: DZ and HC. Writing—original draft: DZ, ZY, and HC.

FUNDING

This study was partially supported by the National Natural Science Foundation of China (41571220), West Light Foundation of the Chinese Academy of Sciences (2021XBZG_XBQNXZ_A_008), and Sichuan Science and Technology Program (2019YFH0041).

ACKNOWLEDGMENTS

Our sincere thanks are due to Sunita Chaudhary for her great efforts on improving the manuscript.

REFERENCES

Arndt, K. A., Oechel, W. C., Goodrich, J. P., Bailey, B. A., Kalhori, A., Hashemi, J., et al. (2019). Sensitivity of Methane Emissions to Later Soil Freezing in Arctic Tundra Ecosystems. *J. Geophys. Res. Biogeosci.* 124 (8), 2595–2609. doi:10.1029/2019jg005242

Bao, T., Xu, X., Jia, G., Billesbach, D. P., and Sullivan, R. C. (2021). Much Stronger Tundra Methane Emissions during Autumn Freeze Than spring Thaw. *Glob. Change Biol.* 27, 376–387. doi:10.1111/gcb.15421

Bechmann, M. E., Kleinman, P. J. A., Sharpley, A. N., and Saporito, L. S. (2005). Freeze-Thaw Effects on Phosphorus Loss in Runoff from Manured and Catch-Cropped Soils. *J. Environ. Qual.* 34, 2301–2309. doi:10.2134/jeq2004.0415

Blagodatskaya, E., Blagodatsky, S., Khomyakov, N., Myachina, O., and Kuzyakov, Y. (2016). Temperature Sensitivity and Enzymatic Mechanisms of Soil Organic Matter Decomposition along an Altitudinal Gradient on Mount Kilimanjaro. *Sci. Rep.* 6 (1), 22240–22311. doi:10.1038/srep22240

Brouns, K., Keuskamp, J. A., Potkamp, G., Verhoeven, J. T. A., and Hefting, M. M. (2016). Peat Origin and Land Use Effects on Microbial Activity, Respiration Dynamics and Exo-Enzyme Activities in Drained Peat Soils in the Netherlands. *Soil Biol. Biochem.* 95, 144–155. doi:10.1016/j.soilbio.2015.11.018

Chen, H., Liu, X. W., Xue, D., Zhu, D., Zhan, W., Li, W., et al. (2021). Methane Emissions during Different Freezing-Thawing Periods from a Fen on the Qinghai-Tibetan Plateau: Four Years of Measurements. *Agric. For. Meteorology* 297, 1–13. doi:10.1016/j.agrformet.2020.108279

Chen, J., Luo, Y., García-Palacios, P., Cao, J., Dacal, M., Zhou, X., et al. (2018). Differential Responses of Carbon-Degrading Enzyme Activities to Warming: Implications for Soil Respiration. *Glob. Change Biol.* 24, 4816–4826. doi:10.1111/gcb.14394

Dong, D. H., and Huang, G. (2015). Relationship between Altitude and Variation Characteristics of the Maximum Temperature, Minimum Temperature, and Diurnal Temperature Range in China. *Chin. J. Atmos. Sci.* 39 (05), 1011–1024. (in Chinese). doi:10.3878/j.issn.1006-9895.1501.14291

Dunn, C., and Freeman, C. (2018). The Role of Molecular Weight in the Enzyme-Inhibiting Effect of Phenolics: the Significance in Peatland Carbon Sequestration. *Ecol. Eng.* 114, 162–166. doi:10.1016/j.ecoleng.2017.06.036

Freeman, C., Evans, C. D., Monteith, D. T., Reynolds, B., and Fenner, N. (2001). Export of Organic Carbon from Peat Soils. *Nature* 412, 785. doi:10.1038/35090628

Frolking, S., Talbot, J., Jones, M. C., Treat, C. C., Kauffman, J. B., Tuittila, E.-S., et al. (2011). Peatlands in the Earth's 21st century Climate System. *Environ. Rev.* 19, 371–396. doi:10.1139/a11-014

Gao, Y., Zeng, X., Xie, Q., and Ma, X. (2015). Release of Carbon and Nitrogen from Alpine Soils during Thawing Periods in the Eastern Qinghai-Tibet Plateau. *Water Air Soil Pollut.* 226 (7), 209–218. doi:10.1007/s11270-015-2479-2

Goldberg, S. D., Muhr, J., Borken, W., and Gebauer, G. (2008). Fluxes of Climate-Relevant Trace Gases between a Norway spruce forest Soil and Atmosphere during Repeated Freeze-Thaw Cycles in Mesocosms. *Z. Pflanzenernähr. Bodenk.* 171, 729–739. doi:10.1002/jpln.200700317

Gorham, E. (1991). Northern Peatlands: Role in the Carbon Cycle and Probable Responses to Climatic Warming. *Ecol. Appl.* 1, 182–195. doi:10.2307/1941811

Groffman, P. M., Driscoll, C. T., Fahey, T. J., Hardy, J. P., Fitzhugh, R. D., and Tierney, G. L. (2001). Effects of Mild winter Freezing on Soil Nitrogen and Carbon Dynamics in a Northern Hardwood forest. *Biogeochemistry* 56, 191–213. doi:10.1023/a:1013024603959

Groffman, P. M., Hardy, J. P., Driscoll, C. T., and Fahey, T. J. (2006). Snow Depth, Soil Freezing, and Fluxes of Carbon Dioxide, Nitrous Oxide and Methane in a Northern Hardwood forest. *Glob. Change Biol.* 12 (9), 1748–1760. doi:10.1111/j.1365-2486.2006.01194.x

Hao, R. J., Li, Z. P., and Che, Y. P. (2007). Effect of Freeze-Thaw Alternation on Water-Soluble Organic Carbon Content and Organic Carbon Mineralization in Paddy Soil. *Soil Bull.* 38, 1052–1057. doi:10.19336/j.cnki.trtb.2007.06.003

Herrmann, A., and Witter, E. (2002). Sources of C and N Contributing to the Flush in Mineralization upon Freeze-Thaw Cycles in Soils. *Soil Biol. Biochem.* 34, 1495–1505. doi:10.1016/s0038-0717(02)00121-9

Jiaoyue Wang, J., Song, C., Hou, A., Miao, Y., Yang, G., and Zhang, J. (2014). Effects of Freezing-Thawing Cycle on Peatland Active Organic Carbon Fractions and Enzyme Activities in the Da Xing'anling Mountains, Northeast China. *Environ. Earth Sci.* 72, 1853–1860. doi:10.1007/s12665-014-3094-z

Jin, H., Wu, J., Cheng, G., Nakano, T., and Sun, G. (1999). Methane Emissions from Wetlands on the Qinghai-Tibet Plateau. *Chin.Sci.Bull.* 44 (24), 2282–2286. doi:10.1007/bf02885940

Kurganova, I., Teepe, R., and Loftfield, N. (2007). Influence of Freeze-Thaw Events on Carbon Dioxide Emission from Soils at Different Moisture and Land Use. *Carbon Balance Manage* 2, 2–11. doi:10.1186/1750-0680-2-2

Kuttim, M., Hofsommer, M. L., Robroek, B. J. M., Signarbieux, C., Jassey, V. E. J., Laine, A. M., et al. (2017). Freeze-thaw Cycles Simultaneously Decrease Peatland Photosynthetic Carbon Uptake and Ecosystem Respiration. *Boreal Environ. Res.* 22, 267–276.

Li, F., Zang, S. Y., Liu, Y. N., Wu, X. W., and Ni, H. W. (2019). Effects of Freezing and Thawing on Soil Active Organic Carbon and Enzyme Activity in the Sanjiang Plain Wetlands. *Chin. J. Ecol.* 39 (21), 7938–7949. (in Chinese). doi:10.5846/stxb201809121962

Liu, L. F., Chen, H., Peng, C. H., Zhu, Q. A., and Li, B. X. (2016). CH_4 Release from Peat at Different Depths on the Zoîgé Plateau under Increasing Temperature. *Chin. J. Appl. Environ. Biol.* 22 (1), 1–7. doi:10.3724/SP.J.1145.2015.05022

Liu, Z., Wang, M., and Ma, X. (2012). Estimation of Storage and Density of Organic Carbon in Peatlands of China. *Chin. Geogr. Sci.* 22, 637–646. doi:10.1007/s11769-012-0572-7

Liu, X. W. (2021). *Research on Carbon Dynamics and Model Simulation of Typical Peatland in Qinghai-Tibet Plateau*. dissertation. Beijing, China: The University of Chinese Academy of Sciences. (in Chinese).

Mastepanov, M., Sigsgaard, C., Dlugokencky, E. J., Houweling, S., Ström, L., Tamstorf, M. P., et al. (2008). Large Tundra Methane Burst during Onset of Freezing. *Nature* 456, 628–630. doi:10.1038/nature07464

McLain, J. E. T., Kepler, T. B., and Ahmann, D. M. (2002). Belowground Factors Mediating Changes in Methane Consumption in a forest Soil under Elevated CO_2. *Glob. Biogeochem. Cycles* 16 (3), 2301–2314. doi:10.1029/2001gb001439

Mei Wang, M., Chen, H., Wu, N., Peng, C., Zhu, Q., Zhu, D., et al. (2014). Carbon Dynamics of Peatlands in China during the Holocene. *Quat. Sci. Rev.* 99, 34–41. doi:10.1016/j.quascirev.2014.06.004

Natali, S. M., Schuur, E. A. G., Trucco, C., Hicks Pries, C. E., Crummer, K. G., and Baron Lopez, A. F. (2011). Effects of Experimental Warming of Air, Soil and Permafrost on Carbon Balance in Alaskan Tundra. *Glob. Change Biol.* 17 (3), 1394–1407. doi:10.1111/j.1365-2486.2010.02303.x

Pirk, N., Santos, T., Gustafson, C., Johansson, A. J., Tufvesson, F., Parmentier, F. J. W., et al. (2015). Methane Emission Bursts from Permafrost Environments during Autumn Freeze-In: New Insights from Ground-Penetrating Radar. *Geophys. Res. Lett.* 42 (16), 6732–6738. doi:10.1002/2015gl065034

Priemé, A., and Christensen, S. (2001). Natural Perturbations, Drying-Wetting and Freezing-Thawing Cycles, and the Emission of Nitrous Oxide, Carbon Dioxide and Methane from Farmed Organic Soils. *Soil Biol. Biochem.* 33, 2083–2091. doi:10.1016/s0038-0717(01)00140-7

Raz-Yaseef, N., Torn, M. S., Wu, Y., Billesbach, D. P., Liljedahl, A. K., Kneafsey, T. J., et al. (2017). Large CO2 and CH4 Emissions from Polygonal Tundra during spring Thaw in Northern Alaska. *Geophys. Res. Lett.* 44, 504–513. doi:10.1002/2016gl071220

Rey, A., Petsikos, C., Jarvis, P. G., and Grace, J. (2005). Effect of Temperature and Moisture on Rates of Carbon Mineralization in a Mediterranean oak forest Soil under Controlled and Field Conditions. *Eur. J. Soil Sci.* 56, 589–599. doi:10.1111/j.1365-2389.2004.00699.x

Roulet, N. T. (2000). Peatlands, Carbon Storage, Greenhouse Gases, and the Kyoto Protocol: Prospects and Significance for Canada. *Wetlands* 20, 605–615. doi:10.1672/0277-5212(2000)020[0605:pcsgga]2.0.co;2

Schuur, E. A. G., McGuire, A. D., Schädel, C., Grosse, G., Harden, J. W., Hayes, D. J., et al. (2015). Climate Change and the Permafrost Carbon Feedback. *Nature* 520, 171–179. doi:10.1038/nature14338

Shindell, D. T., Faluvegi, G., Koch, D. M., Schmidt, G. A., Unger, N., and Bauer, S. E. (2009). Improved Attribution of Climate Forcing to Emissions. *Science* 326 (5953), 716–718. doi:10.1126/science.1174760

Song, C., Wang, Y., Wang, Y., and Zhao, Z. (2006). Emission of CO2, CH4 and N2O from Freshwater Marsh during Freeze-Thaw Period in Northeast of China. *Atmos. Environ.* 40 (35), 6879–6885. doi:10.1016/j.atmosenv.2005.08.028

Song, C. C., Xu, X. F., Sun, X. X., Tian, H. Q., Sun, L., MiaoY, Q., et al. (2012). Large Methane Emission upon spring Thaw from Natural Wetlands in the Northern Permafrost Region. *Environ. Res. Lett.* 7 (3), 1–8. doi:10.1088/1748-9326/7/3/034009

Sorensen, P. O., Finzi, A. C., Giasson, M.-A., Reinmann, A. B., Sanders-DeMott, R., and Templer, P. H. (2018). Winter Soil Freeze-Thaw Cycles lead to Reductions in Soil Microbial Biomass and Activity Not Compensated for by Soil Warming. *Soil Biol. Biochem.* 116, 39–47. doi:10.1016/j.soilbio.2017.09.026

Tan, B., Wu, F. Z., Yang, W. Q., Wang, A., and Yang, Y. L. (2012). Soil Biochemical Dynamics at Three Elevations during the Soil Thawing Period, Eastern Tibetan Plateau: Nutrient Availabilities, Microbial Properties and Enzyme Activities. *Afr. J. Microbiol. Res.* 6, 4712–4721. doi:10.5897/ajmr11.1537

Tokida, T., Mizoguchi, M., Miyazaki, T., Kagemoto, A., Nagata, O., and Hatano, R. (2007). Episodic Release of Methane Bubbles from Peatland during spring Thaw. *Chemosphere* 70, 165–171. doi:10.1016/j.chemosphere.2007.06.042

Tveit, A., Schwacke, R., Svenning, M. M., and Urich, T. (2012). Organic Carbon Transformations in High-Arctic Peat Soils: Key Functions and Microorganisms. *ISME J.* 7 (2), 299–311. doi:10.1038/ismej.2012.99

Wang, X. W. (2010). *Analysis of Freezing and Thawing Laws and Simulation of Hydrological Characteristics of Seasonal Frozen Soil in Northern China*. Heilongjiang, China: Northeastern Agricultural University. (in Chinese).

Wang, J. Y. (2014). *Effects of Freezing and Thawing on Soil Organic Carbon of Peatland in Permafrost Region of Da Xing' Anling Mountains*. dissertation. Beijing, China: The University of Chinese Academy of Sciences. (in Chinese).

Wang, X. L. (2015). *Research on Methane Emission Characteristics of Zoîgé Alpine Peat Wetland*. Yangling, Shanxi, China: Northwest A & F University. (in Chinese).

Wang, Y., Liu, J. S., Wang, G. P., and Zhou, W. M. (2007). Study on the Relationship between Freeze-Thaw Effects and Soil Physical and Chemical Effects. *Geographical Inf. Sci.* 2, 91–96. (in Chinese). doi:10.16258/j.cnki.1674-5906.2013.07.012

Wang, J. Y., Song, C. C., Wang, X. W., and Wang, L. L. (2011). Research Progress in the Studies of Effects of Freezing and Thawing on Soil Organic Carbon Pool and Microorganisms. *J. Glaciology Geocryology* 33, 442–452. (in Chinese).

Wang, Y., Liu, J. S., and Wang, Q. Y. (2013). The Effects of Freezing and Thawing on Soil Aggregates and Organic Carbon Components. *J. Ecol. Environ.* 22, 1269–1274. (in Chinese).

Wu, H., Xingkai, X., Cheng, W., and Lin, H. (2019). Dissolved Organic Matter and Inorganic N Jointly Regulate Greenhouse Gases Fluxes from forest Soils with Different Moistures during a Freeze-Thaw Period. *Soil Sci. Plant Nutr.* 66 (1), 163–176. doi:10.1080/00380768.2019.1667212

Xiang, S., Guo, R., Wu, N., and Sun, S. (2009). Current Status and Future Prospects of Zoige Marsh in Eastern Qinghai-Tibet Plateau. *Ecol. Eng.* 35, 553–562. doi:10.1016/j.ecoleng.2008.02.016

Xie, S.-b., Jian-jun, Q., Yuan-ming, L., Zhi-wei, Z., and Xiang-tian, X. (2015). Effects of Freeze-Thaw Cycles on Soil Mechanical and Physical Properties in the Qinghai-Tibet Plateau. *J. Mt. Sci.* 12, 999–1009. doi:10.1007/s11629-014-3384-7

Xu, J., Morris, P. J., Liu, J., and Holden, J. (2018). PEATMAP: Refining Estimates of Global Peatland Distribution Based on a Meta-Analysis. *Catena* 160, 134–140. doi:10.1016/j.catena.2017.09.010

Yang, M. X., Ya, T. D., Hirose, N., and Hideyuki, F. (2006a). The Daily Freeze-Thaw Cycle of the Surface Soil on the Qinghai-Tibet Plateau. *Chin. Sci. Bull.* 51, 1974–1976.

Yang, W., Song, C., and Zhang, J. (2006b). Dynamics of Methane Emissions from a Freshwater Marsh of Northeast China. *Sci. total Environ.* 371, 286–292. doi:10.1016/j.scitotenv.2006.08.034

Yu, R., Kampschreur, M. J., Loosdrecht, M. C. M. v., and Chandran, K. (2010). Mechanisms and Specific Directionality of Autotrophic Nitrous Oxide and Nitric Oxide Generation during Transient Anoxia. *Environ. Sci. Technol.* 44, 1313–1319. doi:10.1021/es902794a

Zhang, J. B., Song, C. C., and Yang, W. Y. (2006). Land Use Effects on the Distribution of Labile Organic Carbon Fractions through Soil Profiles. *Soil Sci. Soc. America J.* 70, 660–667. doi:10.2136/sssaj2005.0007

Zhang, C. F., Sheng, L. X., Gong, C., He, C. G., and Zhang, J. (2018). Effects of Freezing and Thawing on Soil Carbon Emissions and Soil Microbes in Wetlands in Northeast China. *Chin. J. Ecol.* 37, 304–311. (in Chinese). doi:10.13292/j.1000-4890.201802.035

Zhang, T., and Armstrong, R. L. (2001). Soil Freeze/thaw Cycles over Snow-free Land Detected by Passive Microwave Remote Sensing. *Geophys. Res. Lett.* 28, 763–766. doi:10.1029/2000gl011952

Zheng, Y. K., Liu, K., Xiong, Z. J., Miao, C. P., Chen, Y. W., Xu, L. H., et al. (2015). Effect of Large-Scale Planting Water Hyacinth on Cultivable Bacterial Community Structure in the Eutrophic lake. *Microbiol. China* 42 (1), 42–53. (in Chinese). doi:10.13344/j.microbiol.china.140385

Zhou, Y. W., Guo, D. X., and Cheng, G. D. (2000). *Geocryology in China*. Beijing: Science Press. (in Chinese).

Zhou, W. M., Wang, J. D., Liu, J. S., Qin, S. J., and Wang, Y. (2008). The Effects of Freezing and Thawing on the Soluble Carbon, Nitrogen and Nitrogen Mineralization of Wetland Soil. *J. Ecol. Rural Environ.* 24 (3), 1–6. (in Chinese).

Conflict of Interest: The authors declare that the research was conducted in the absence of any commercial or financial relationships that could be construed as a potential conflict of interest.

Publisher's Note: All claims expressed in this article are solely those of the authors and do not necessarily represent those of their affiliated organizations, or those of the publisher, the editors, and the reviewers. Any product that may be evaluated in this article, or claim that may be made by its manufacturer, is not guaranteed or endorsed by the publisher.

frontiers | Frontiers in Earth Science

ORIGINAL RESEARCH
published: 08 April 2022
doi: 10.3389/feart.2022.845873

Quantifying the Relationship Between Human Activities Intensity and Thawing Hazards of the Frozen Ground on the Qinghai–Tibet Plateau

Jie Ni[1,2], Tonghua Wu[1], Xiaofan Zhu[1], Jie Chen[1], Xiaodong Wu[1], Guojie Hu[1], Defu Zou[1], Ren Li[1] and Yizhen Du[2]*

[1]Cryosphere Research Station on the Qinghai–Tibet Plateau, State Key Laboratory of Cryospheric Science, Northwest Institute of Eco-Environment and Resources, Chinese Academy of Sciences, Lanzhou, China, [2]College of Tourism, Resources, and Environment, Zaozhuang University, Zaozhuang, China

Climate warming could accelerate frozen ground degradation on the Qinghai–Tibet Plateau (QTP). Quantitative analysis of the impacts of thaw-induced hazards of the frozen ground on human activities in cold regions has become one of the most important issues in current research. To identify adverse impacts of these thawing hazards on human activities, this study explores a spatially explicit, temporally consistent and quantitative method to map human activity intensity (HAI). Four categories of variables are selected to represent some of the most important human activities on the QTP, including land use, road distribution, population density, and grazing density. By improving the human footprint index method, HAI maps of the QTP in 1995, 2005, and 2015 are created, and then quantitative analysis of the HAI under different thawing hazard levels in the frozen ground of QTP is done. The results show that, for the above three periods, the mean HAI values on the QTP are 0.10, 0.11, and 0.12, respectively. Moreover, during 1995–2015, the intensity and extent of human activities increase by 15.35% and 40.64%, respectively. The superposition results of the HAI and frozen ground thawing hazard maps show that a seasonally frozen ground region has relatively larger HAI, and its mean value is more than twice that of the permafrost region. For permafrost regions, the medium-hazard area has the highest HAI (0.09), which possibly has great impacts on the linear infrastructure. The establishment of a thawing disaster warning map can effectively shield high thaw settlement hazard areas without human activities and thus can present a more accurate early warning. These results can provide important scientific references for the disaster prevention and mitigation work in frozen ground regions, including risk assessment and infrastructure maintenance.

Keywords: frozen ground, human activity intensity, climate warming, thaw-induced hazard, Qinghai–Tibet plateau

OPEN ACCESS

Edited by:
Guo Donglin,
Institute of Atmospheric Physics (CAS), China

Reviewed by:
Ping Lu,
Tongji University, China
Bo Su,
Beijing Normal University, China

***Correspondence:**
Tonghua Wu
thuawu@lzb.ac.cn

Specialty section:
This article was submitted to Cryospheric Sciences, a section of the journal Frontiers in Earth Science

Received: *30 December 2021*
Accepted: *21 February 2022*
Published: *08 April 2022*

Citation:
Ni J, Wu T, Zhu X, Chen J, Wu X, Hu G, Zou D, Li R and Du Y (2022) Quantifying the Relationship Between Human Activities Intensity and Thawing Hazards of the Frozen Ground on the Qinghai–Tibet Plateau. Front. Earth Sci. 10:845873. doi: 10.3389/feart.2022.845873

INTRODUCTION

Frozen ground is an important part of the cryosphere, which plays a critical role in ecohydrological processes, climate regulation, and engineering construction in cold regions (Qin et al., 2018; Karjalainen et al., 2019; Neill et al., 2020). At present, climate warming has led to widespread thawing of permafrost, which is mainly manifested in a rising ground temperature, a thickening active layer, an emergence and expansion of taliks, and a shrinking area of permafrost (Qin et al., 2017; Wang et al., 2018; Ni et al., 2020). The Qinghai–Tibet Plateau (QTP) has the largest areas of

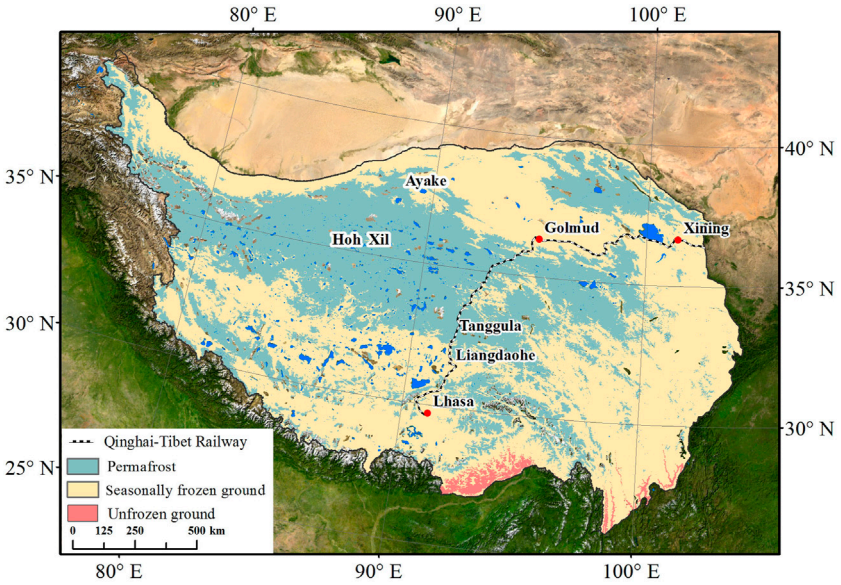

FIGURE 1 | The location of the study area.

permafrost in the mid- and low-latitude regions. The area of permafrost and seasonally frozen ground covers approximately 1.06×10^6 and 1.46×10^6 km^2, respectively, accounting for approximately 96% of the total area of the QTP (**Figure 1**, Zou et al., 2017). Compared with high-latitude regions, the permafrost on the QTP shows a higher ground temperature and a poorer hydrothermal stability (Cheng et al., 2019; Obu et al., 2019; Qin et al., 2020). These characteristics further exacerbate the degradation of permafrost in the QTP. It is noteworthy that, currently, thaw-induced hazards caused by frozen ground degradation are increasingly frequent and complex on the QTP (Ni et al., 2020; Wei et al., 2021). This poses a great threat to the ecological environment and related infrastructure (Wu et al., 2012; Hjort et al., 2018; Ni et al., 2021). Meanwhile, with the opening of the Qinghai–Tibet Railway/Highway (QTR/QTH) and the rapid development of urbanization, human activities on the QTP have been increasing (Xu et al., 2020). The impact of the rapidly degrading frozen ground on human activities has drawn considerable attention.

In recent years, considerable research on the negative effects of frozen ground degradation has been carried out. Wu and Niu (2013) found that thaw-induced hazards would cause huge economic losses to infrastructure engineering. Since the 21st century, the damage rate of the QTH has reached more than 30% due to freeze–thaw-related disasters in permafrost regions (Yao et al., 2013). Compared with road infrastructures, the stability of transmission lines and gas/oil pipelines with their buried foundations is more severely affected by thermal disturbances (Wang et al., 2014). With future increases in load and foundation size, the safe operation of power facilities and gas/oil pipelines will face greater threats (He and Jin, 2010). Similar evidence from recent studies based on interferometric synthetic aperture radar (In-SAR) technology suggests that the engineering corridor in the central QTP is experiencing widespread seasonal deformation and long-term subsidence due to the degradation of frozen ground (Chen et al., 2022). In addition, permafrost degradation also leads to lower groundwater levels and drying topsoil and consequently affects vegetation biomass (Fang et al., 2011a; Teufel and Sushama, 2019). The grassland is the basis for the survival of herdsmen on the QTP. Slight variations in grassland productivity will have a greater impact on the herdsmen's livelihood (Fang et al., 2011a; 2019). Relevant research showed that due to permafrost degradation, the carrying capacity of theoretical livestock was reduced by 11% in the source regions of the Yangtze and Yellow Rivers during 1980–2007 (Fang et al., 2011a; 2011b). More and more studies showed that lake outburst also may accelerate permafrost degradation around the lake and threaten the safety of linear projects (Niu et al., 2011; Lu et al., 2020). Although the investigations above have been conducted on the impact of thaw-induced hazards on the frozen ground, most of them focus on local areas or a single category of impact, such as roads, transmission lines, grasslands and animal husbandry, etc. These studies are not sufficient to reflect the comprehensive impacts on human activities under the expansion and aggravation of thaw-induced hazards (Zhang and Wu, 2012; Hjort et al., 2018). Therefore, it is necessary to conduct a comprehensive risk assessment on this scientific issue.

As a kind of human activity intensity (HAI) measurement, human footprint data were first proposed by Sanderson et al. (2002). The generation of this dataset provides an important means to study the interaction between human beings and the natural environment (Sanderson et al., 2002; Duan and Luo, 2020). The original version of the human footprint map was drawn based on nine variables as proxies for human activity;

however, this version was static and time-limited (Venter et al., 2016a). Subsequently, this method was improved at regional and global scales. Etter et al. (2011) incorporated temporality and biophysical vulnerability to quantify the spatial footprint of humans on the ecosystem. Venter et al. (2016b) reintegrated human activity data and finally selected eight variables to draw a global human footprint map in 1993 and 2009. Ayram et al. (2017) adjusted the human footprint index in terms of habitat loss and fragmentation in Mexico. By considering the regional characteristics of the QTP, Li et al. (2018) ultimately selected four types of human activity data to illustrate the human influence intensity data for the three periods of 1990, 2000, and 2010. Duan and Luo (2020) extended and refined the datasets of Li et al. (2018) from 1990 to 2015 (every 5 years). Based on the above analyses, the human footprint map was mainly used to study the negative impacts of human activities on the ecological environment. However, to some extent, the human footprint dataset can reflect the importance of the region. As we all know, while using and transforming nature, human beings are inevitably threatened by natural disasters (Sanderson et al., 2002). Based on these characteristics, this study revised the human footprint map to objectively reflect the importance of human activities in a given area and further provide empirical support for the quantitative analysis of the impact of frozen ground thawing on human activities.

As mentioned above, frozen ground degradation and consequential thaw-induced hazards have become widespread during recent decades. Therefore, it is necessary to quantitatively analyze the intensity of human activities under the thawing hazards of the frozen ground in the QTP. As such, the objectives of this study are 1) to select and assign human activity data, 2) to draw multiperiod human footprint maps and analyze change trends on the QTP, and 3) to quantitatively analyze the intensity of human activities under different thawing hazard levels in the frozen ground and assess their impacts. The created warning map can specifically highlight areas with intense human activities and great thawing hazards. This study can provide a scientific reference for preventing the losses caused by the thawing of frozen ground and is of great significance to regional sustainable development.

DATA AND METHOD

In this study, the human footprint is called the HAI, which represents the importance of a given region in terms of the intensity of human activity. Compared with previous studies, we chose four categories of data as proxies for human activity, which represent some of the most important actions taken by humans, including land use, road distribution, population density, and grazing density (**Figure 2**, step 1). To more objectively reflect the HAI, we assigned a score to each type of HAI dataset; the higher the score was, the greater the importance. Then, we normalized the scores within a 0–1 scale (**Figure 2**, step 2). The normalized data were weighted and summed to create the standardized HAI map for the QTP in 1995, 2005, and 2015 (**Figure 2**, step 3). The four categories of HAI are not mutually exclusive, and some co-occurred in the same location. Finally, according to the results of the frozen ground thawing hazards, we analyzed the human activities in the QTP (**Figure 2**, step 4). To intuitively display the HAI under different thawing hazard levels on the frozen ground of the QTP to achieve an early warning effect, we normalized the thawing hazard levels and then multiplied them with the HAI layer to obtain the thawing disaster warning index. Based on the Jenks Natural Breaks algorithm (Jenks, 1967), the warning index was divided into four risk levels, from low to high risk, as low, medium, high, and warning zones. During the above research, all layers were resampled to a matching spatial resolution (~1 km) using Albers conical equal-area projection. It should be noted that this study analyzes the HAI under different thawing hazard levels in the frozen ground. The thawing hazards do not occur in the unfrozen ground area. Hence, the region of unfrozen ground is excluded in the study.

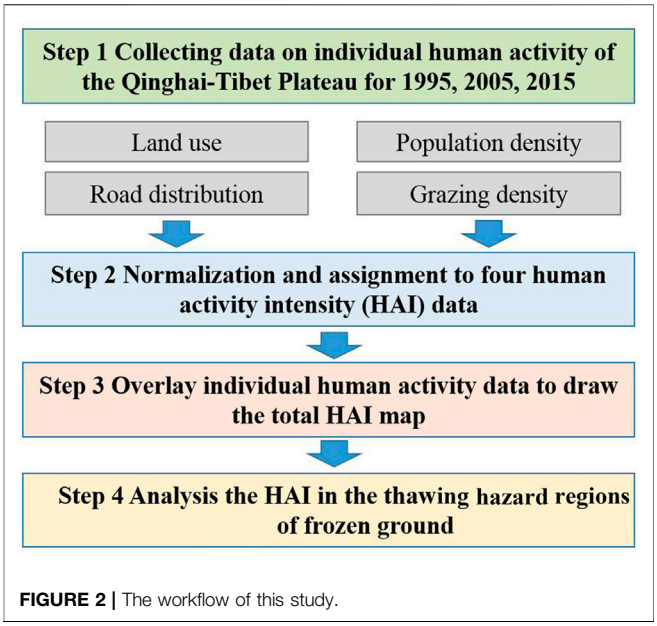

FIGURE 2 | The workflow of this study.

Data Source

(1) Land use

Land use is an important manifestation of human activities, and its changes reflect the magnitude of human activities (Otto et al., 2016; Zhang et al., 2020). The land use data on the QTP were obtained from the Resource and Environment Science and Data Center (available at http://www.resdc.cn/), which covers the years 1995, 2005, and 2015. The dataset includes six land use classes and 25 subclasses. Based on the HAI, recent studies have reclassified the initial land use types and then assigned scores to each new type (**Table 1**) (Zhao et al., 2015; Li et al., 2018). A maximum score of 10 was assigned to built-up land, which means that this type of land use was the most important area for human activities, while lower scores (8, 8, and 7) were allocated to rural settlements, reservoirs/ponds, and croplands, respectively. The traditional nomadic lifestyle of Tibetan herdsmen enables dense grasslands to have the best grazing potential, followed by

TABLE 1 | Land use types and their human influence scores (Li et al., 2018).

Land use type	Descriptions	Score
Built-up land	Lands used for urban, factories, quarries, mining, transportation facilities, and airport	10
Rural settlements	Lands used for settlements in villages	8
Reservoir/ponds	Man-made facilities for water reservation	8
Cropland	Cultivated lands for crops, including paddy land and dry land	7
Dense grassland	Grassland with canopy coverage greater than 50%	2
Moderate grassland	Grassland with canopy coverage between 20% and 50%	1
Sparse grassland	Grassland with canopy cover between 5% and 20%	0
Woodland	Lands growing trees including arbor, shrub, and bamboo	0
Stream, rivers, lakes, permanent ice, snow	Lands covered by natural water bodies	0
Unused land	Lands that are not put into practical use or difficult to use, including sandy land, Gobi, salina, swampland, and others	0

TABLE 2 | Human activity intensity scores for roads and railways revised from Li et al. (2018).

Road type	0–1 km	1–3 km	3–5 km	5–7 km
Expressway	10	8	7	5
National level highway	10	8	4	2
Provincial level highway	8	6	2	0
County level highway	6	4	1	0
Rural level road	4	2	0	0
Railway	9	9	5	3

moderate grasslands (Fang et al., 2011a; Li et al., 2018). Therefore, scores of 2 and 1 were assigned to these grasslands, respectively. A minimum score of 0 was assigned to all other land cover types, which had the lowest intensity of human activities.

(2) Roads and railways

As some of the most prolific linear infrastructures, roads/railways are important drivers of habitat conversion by humans (Trombulak and Frissell, 2000), especially on the QTP. The data for 2005 and 2015 on the QTP were vectorized from road traffic maps and combined with OpenStreetMap (OSM, http://download.geofabrik.de/). Since the data for 1995 were not available, we used the global roads open access dataset (Center for International Earth Science Information Network Columbia University, and Information Technology Outreach Services University of Georgia, 2013) from 2000 instead. Detailed information can be found in Table S1. The data for the above three periods all included expressways; national-, provincial-, county-, and rural-level highways; and railways. Since the thermal disturbance of frozen ground threatens the surrounding infrastructure within a certain distance, this study added a buffer analysis to the road importance assignment. The further away from the road, the less harmful and less important the impact. The buffer range was ultimately set as 7 km in this study, instead of the 10 km used in previous studies (Li et al., 2018), and the intensity score diminished gradually to either side of the road (**Table 2**). A detailed explanation is provided in the *Discussion* section.

(3) Population density

Population density is a direct reflection of the importance of a region (Ellis and Ramankutty, 2008). The 1 km population density datasets of the QTP for 1995, 2005, and 2015 were obtained from the Resource and Environment Science and Data Center (Table S1). The population density was established based on the land use type, nighttime light, and the population distribution weight of residential density (Xu, 2017). Compared with the cities on the east coast, the QTP was extremely sparsely populated (Fang, 2013). To reasonably reflect the distribution of population density in this study, we modified the formula proposed by Venter et al. (2016a). For locations with more than 100 people per square kilometer, we assigned an intensity score of 10. For more sparsely populated areas, we logarithmically scaled the intensity score using the following formula:

$$Intensity\ score = 2.214 \times log(population\ density + 1) \quad (1)$$

(4) Grazing density

The QTP is a major pastoral area of China (Li et al., 2018). Although long-term grazing activities affect the grassland vegetation biomass, they can also stimulate plant growth and improve soil fertility through excrement (Lin et al., 2010; Zhao et al., 2019). Therefore, grazing activities in the QTP were considered a key indicator in this study. The grazing density data were acquired from the United Nations Food and Agricultural Organization (UN FAO, https://data.apps.fao.org/). We overlaid the cattle and sheep densities to represent the grazing density. Since only the grazing data from 2010 were obtained, a trend extrapolation method (Duan and Luo, 2020) was used to obtain the grazing density data for 1995, 2005, and 2015. First, we calculated the change rates of cattle and sheep production from 1995 to 2015 based on the statistical yearbooks of the Qinghai Province and the Tibet Autonomous Region. Then, we used the cattle and sheep density layer from 2010 to calculate the cattle and sheep density data in these two areas for 1995, 2005, and 2015. Considering the impact of different herds on the ecological environment in this calculation, the grazing intensity of one cattle was regarded as equivalent to that of five sheep (Ouyang, et al., 2016). Finally, we converted the cattle data into the equivalent intensity of sheep and overlaid them together. Referring to the conversion method of population density, we also logarithmically scaled the intensity score using the following formula:

$$Intensity\ score = 2.453 \times log(grazing\ density + 1) \quad (2)$$

(5) Thawing hazard regions of frozen ground

Frozen ground degradation poses a huge threat to human activities on the QTP. However, the value of the HAI varies with different thawing hazard levels of the frozen ground. The data of the thawing hazard regions of the frozen ground were derived from our previous research results (**Supplementary Figure S1**; Ni et al., 2021). It should be noted that the seasonally frozen ground only experiences a periodic seasonal thaw settlement that has a lower hazard. However, in addition to seasonal settlement, permafrost also experiences a long-term, absolute ground settlement (due to the thawing of ground ice, **Supplementary Figure S2**) that has a relatively large hazard. Therefore, we classified seasonally frozen ground as a minimal hazard region. We divided the permafrost regions into low-, medium-, and high-hazard areas (the low hazard area in this study included the stable area) according to the hazard level of the thawing settlement.

Method

(1) Normalization method

To eliminate the impact of the dimensions and magnitudes of each factor (various physical properties and conditions) and to effectively overlay the four types of data, we normalized the intensity score of the human activity in each type to 0–1. The following standardized processing formula was performed:

$$x_i^{'} = (x_i - x_{imin}) \Big/ (x_{imax} - x_{imin}) \quad (3)$$

where i is the factor number, x_i and $x_i^{'}$ are the initial intensity assignment and actual calculated value, respectively, and x_{imin} and x_{imax} are the minimum and maximum values of the factors in the study area, respectively. The higher the index value is, the greater the intensity.

(2) The analytic hierarchy process

The analytic hierarchy process (AHP) is a multiobjective, multicriteria decision-making approach that is used to analyze complex problems (Saaty and Kearns, 1985; Niu et al., 2011). This model requires the creation of a reciprocal pairwise comparison matrix used to determine weighted coefficients for the computation of HAI scores. Generally, the pairwise comparison is subjective, and the quality of the results is dependent on the experts' judgment. Hence, a consistency ratio was proposed to evaluate the accuracy of the results (Saaty and Kearns, 1985; Niu et al., 2015). In a successful expert judgement, the consistency ratio should be <0.1. In our AHP model, the consistency ratio was 0.04, indicating an acceptable assessment. The weight coefficients obtained by this method are shown in Table S2. Subsequently, we computed the total HAI on the QTP based on the AHP method:

$$\begin{aligned} HAI = {} & (Land\ use \times 0.11) + (Road\ distribution \times 0.26) \\ & + (Population\ density \times 0.41) \\ & + (Grazing\ density \times 0.22) \end{aligned} \quad (4)$$

RESULT

The Four Categories of Human Activity Intensity

Based on the above methods, we obtained the individual HAI maps of four categories of variables (**Figure 3**). The statistical results showed that the mean values of land use, road distribution, population density, and grazing density were 0.06, 0.08, 0.10, and 0.18, respectively (**Table 3**), which indicated that the HAI values of the four variables were low on the QTP during the study period. The high values of these individual HAIs were mainly distributed in the eastern and southern QTP. Two regions with high HAI values could be easily identified in Xining, Lhasa, and the surrounding areas (**Figures 1**and **3**). Low HAI values were mainly distributed in the western QTP.

The Total Human Activity Intensity on the QTP

Through the weighted average of the four categories of individual HAI datasets, we obtained the total HAI map of the QTP for 1995, 2005, and 2015 (**Figure 4**). The statistical results showed that the mean HAI values were 0.10, 0.11, and 0.12, respectively. Since the theoretical maximum was 1.00, the QTP had a relatively low HAI for 1995–2015. In addition, during the study period, the percentages of grids where the HAI value was lower than the mean value were 59.12%, 58.89%, and 58.85%, respectively. These conclusions can be seen in **Figure 3**.

In terms of the spatial patterns of the HAI, the largest value was mainly located around the city of Xining, followed by Lhasa (city locations can be seen in **Figure 1**). Overall, the eastern and southeastern QTP had high HAI values for all 3 years studied. In the central part of the QTP, the extent of human activities was mainly concentrated in the QTH/QTR and other transportation corridors. In the western QTP, the HAI value was low. The main reason for this was that the region is one of the least populated regions of China due to high altitude, thin air, and permafrost. Relatively wilder areas existed on the Hoh Xil and Changtang Plateau, which were once known as "no-man's land" (**Figure 1**).

From 1995 to 2015, the mean value of the HAI increased by 15.35%. Grids with an increased HAI value accounted for 40.64% of the total grids, while grids with decreased HAI values accounted for 10.09%. The increased HAI regions were mostly located in the eastern and southern QTP. The detailed reasons for the increase in HAI can be obtained from **Table 3**. During the study period, roads and railways had the largest growth rate

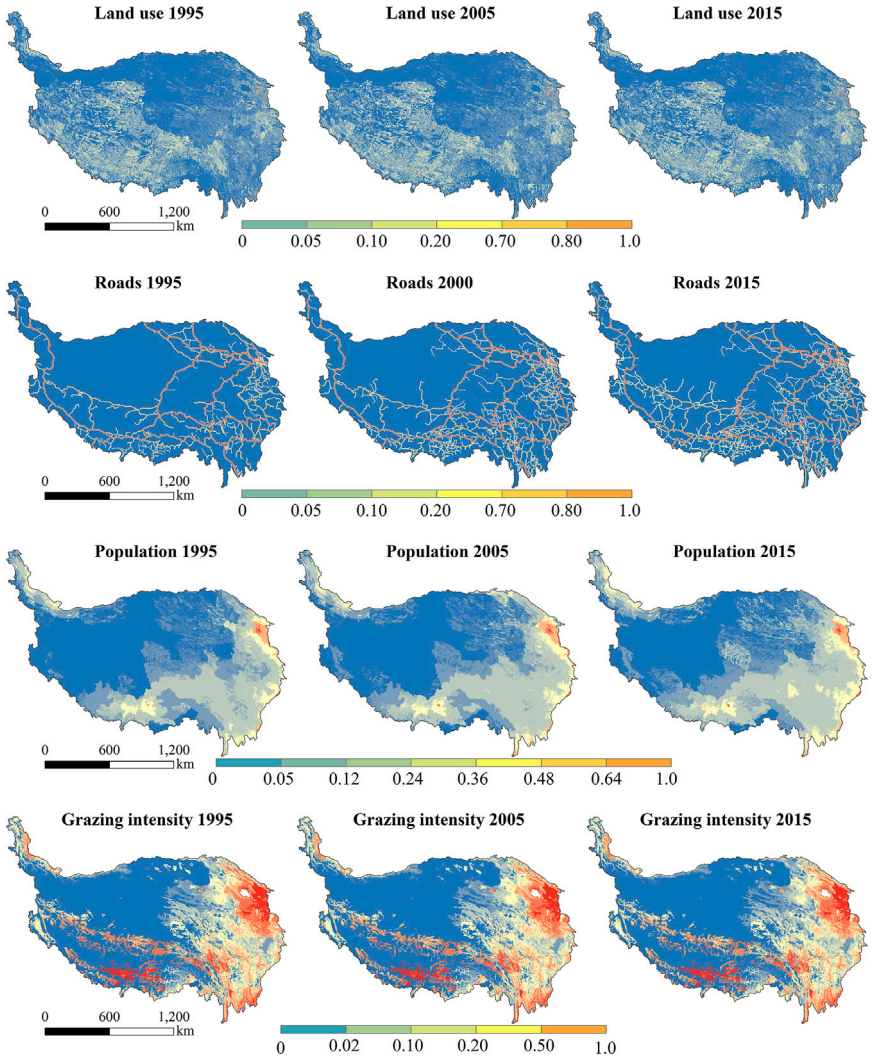

FIGURE 3 | Spatial distribution of four individual human activity intensity datasets in 1995, 2005, and 2015 on the Qinghai–Tibet Plateau.

TABLE 3 | The mean values of four individual human activity intensity datasets in 1995, 2005, and 2015 on the Qinghai–Tibet Plateau.

Factors\Year	1995	2005	2015	Mean
Land use	0.06	0.06	0.06	0.06
Roads and railways	0.07	0.08	0.09	0.08
Population density	0.09	0.10	0.10	0.10
Grazing density	0.18	0.18	0.19	0.18

(28.6%); followed by population density with a growth rate of 11.1%; the smallest change was the land use, and its value remained basically stable from 1995 to 2015. No obvious HAI changes were detected in the mid-western QTP. The changes in the above data illustrated the development trend of human activities in the different areas of the QTP, and the new human footprint map can well illustrate these characteristics.

Human Activity Intensity Within the Thawing Hazard Regions of Frozen Ground

The spatial overlay of the frozen ground map and HAI map (**Figure 5**) showed that the permafrost region generally occurs in the hinterland and northwest of the QTP with an average altitude of more than 4,000 m. Its distribution corresponds well with the low-value regions of the HAI, except for the G219 and G109 highways and the surrounding areas. The HAI statistical results under the different thaw settlement hazard levels in the permafrost regions showed higher value of 0.09 in medium-hazard areas, while the HAIs of low-hazard areas and high-hazard areas were 0.06 and 0.03, respectively (**Table 4**). In contrast, seasonally frozen ground regions had relatively large HAIs, and their mean values were more than twice that of the permafrost area.

According to **Figure 6**, the mean value of the HAI in seasonally frozen ground areas was not only the highest but also the most dispersed. This indicated that the overall level of development in the

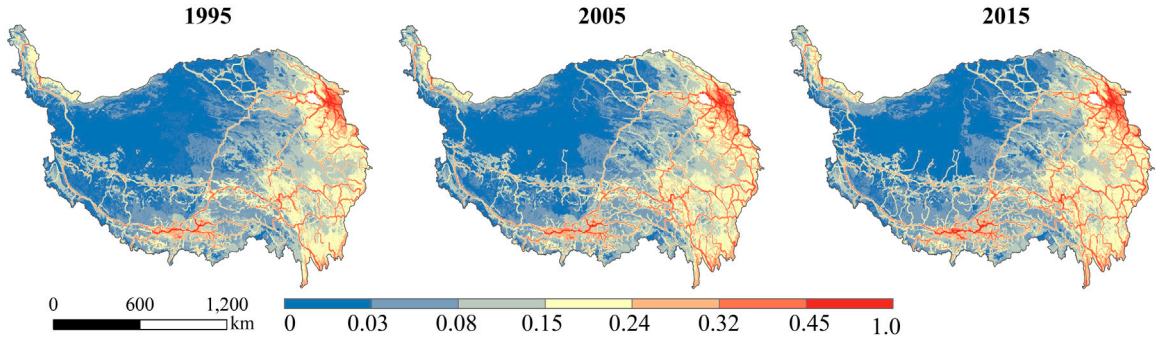

FIGURE 4 | Spatial distribution of total human activity intensity in 1995, 2005, and 2015 on the Qinghai–Tibet Plateau.

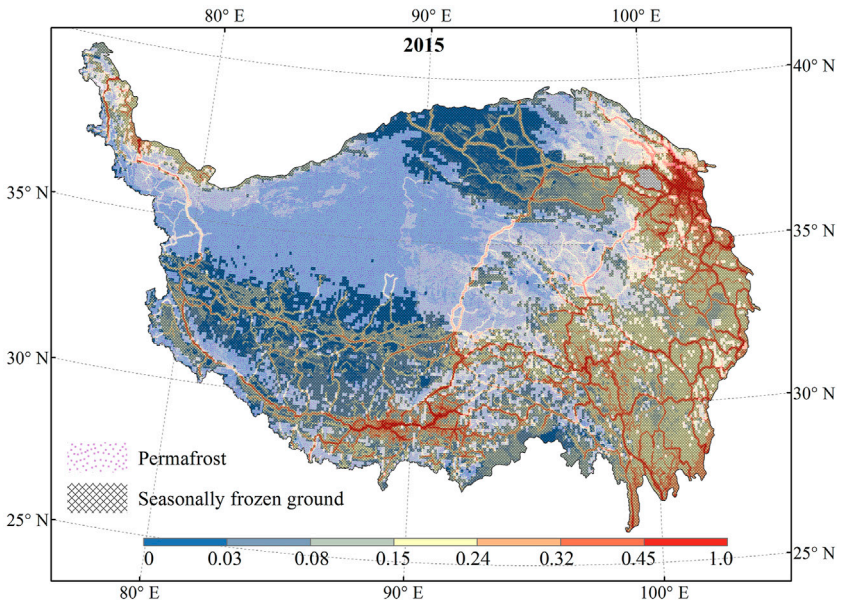

FIGURE 5 | Human activity intensity within the frozen ground in 2015.

TABLE 4 | Mean human activity intensity (HAI) in different thaw settlement risk regions of frozen ground in 2015.

	Risk type	Area (×10^4 km^2)	Mean HAI	Mean HAI
Permafrost region	High risk	10.80	0.03	0.07
	Medium risk	35.64	0.09	
	Low risk	66.11	0.06	
Seasonally frozen ground region	Minimum risk	141.71	0.15	0.15

region was relatively high but unevenly distributed. The main reason for this is that the region has favorable natural conditions and is suitable for human habitation, working, grazing, and farming compared with other parts of the QTP (Li et al., 2018). In the different thaw settlement hazard levels of the permafrost, the HAI in the high-hazard areas was the lowest, while that of the medium-hazard areas was the highest, which was mainly because most sections of the roads and railways pass through the medium-hazard areas. Overall, the HAI in the seasonally frozen ground areas was higher; however, this region only experienced periodic seasonal thaw settlement, and the hazard was relatively lower. For the permafrost areas, although the HAI value was relatively low, the roads and railways were more affected because they were more sensitive to permafrost thawing.

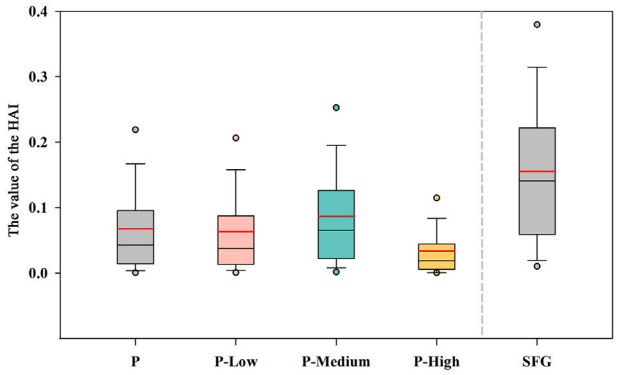

FIGURE 6 | The boxplots depict the human activity intensity (HAI) under different thawing hazard levels in the frozen ground of the Qinghai–Tibet Plateau. The gray boxes represent the HAI statistics of the permafrost (P) and seasonally frozen ground (SFG) regions, the colored boxes represent the HAI statistics under different thawing hazard in the permafrost regions, and the red line shows the average.

Risk Assessment of Thawing Hazards of Frozen Ground

The map (**Figure 7**) of the thawing disaster warning index of the frozen ground of the QTP integrates two kinds of information: the location information related to the thawing hazard of the frozen ground and the intensity information related to human activities. We can see that the warning index in the eastern part of the QTP was obviously higher than that in the western part. The warning areas in the permafrost region were mainly distributed in the Qilian Mountains, the G219 section in the northwest, and the G109 section from Xidatan to Tanggula in the central part. Among these three typical areas, the warning indices varied between different road sections, but the main levels were high risk and warning area. In addition, the Qilian Mountains had a high or warning risk level due to the higher grazing density and road density (**Figure 3**). It should be noted that the previous study on thawing risk by Ni et al. (2021) was aimed at permafrost regions, so this study focused on those regions. Moreover, the warning map considered seasonally frozen ground regions due to the high intensity of human activity in these regions. However,

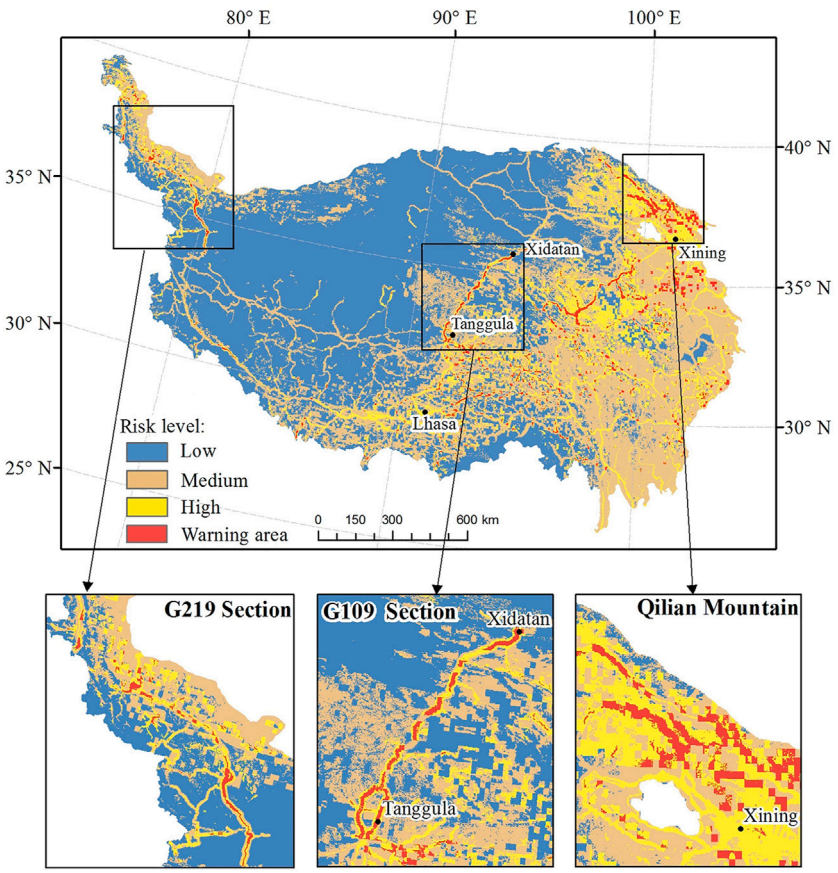

FIGURE 7 | The thawing disaster warning map of the frozen ground of the QTP.

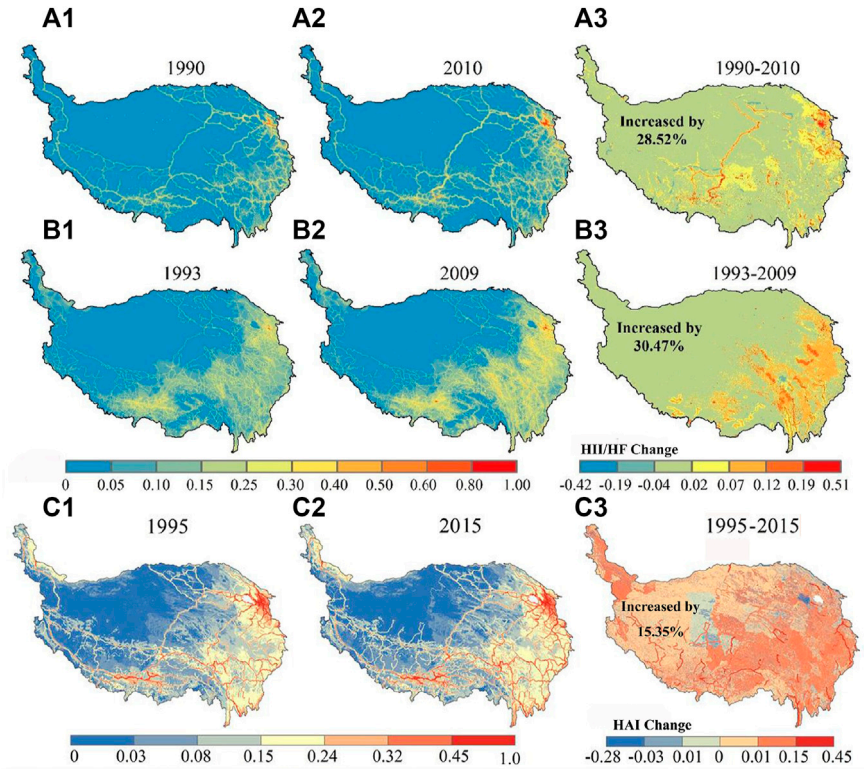

FIGURE 8 | Comparison of the human activity intensity results of different studies on the QTP. **(A)** The results of the global human footprint on the QTP (HF, 2009; Venter et al., 2016b); **(B)** the results of the human influence intensity (HII, 2010; Li et al., 2018); **(C)** the results of the HAI map in this study.

the accuracy of the warning index in seasonally frozen ground regions needs to be further verified.

DISCUSSION

Comparisons With Previous Results

To ensure the accuracy of our results, we compared our results of the HAI map of the QTP to those of previous studies, including the global human footprint (HF, 2009; Venter et al., 2016b) and the human influence intensity (HII, 2010; Li et al., 2018) maps of the QTP. Since these two results were cumulative HAI measures, normalization was undertaken before comparison. The results revealed that the distribution patterns of the three maps were basically consistent, with high values in the eastern QTP and low values in the western QTP (**Figure 8**).

However, there were still some region-specific differences among the three results. In terms of our results, the mean HAI on the QTP increased by 15.35% in 1995–2015, while the corresponding increases in the HF and HII on the QTP were 30.47% and 28.52% in the 1990s to 2010s, respectively. The main reasons for these differences were the following factors: 1) The results of previous studies were a direct summation of individual layers of human activities. We comprehensively analyzed the impact of different human activity factors on the QTP and ultimately used the AHP model to assign weights to each layer, which inevitably led to different results. 2) There was a gap between the research periods. In our study, the human activity variables we considered were updated at different time scales. 3) The pasture, road, and railway data in the previous studies were static and could not reflect the dynamic information well. However, in our study, all the datasets were dynamic, which was more likely to reflect changes in human activity over time. 4) For the grazing intensity data, our study used the cattle and sheep density. Based on the statistical yearbook, we found that the grazing intensity on the QTP increased slowly (with an annual change rate of 0.45%) from 1995 to 2015. However, the 2010 HII dataset used the county-scale statistical data to represent pixel-scale data, and the 2009 HF dataset used the percentage of the pasture area in the unit pixel to represent the grazing intensity. In fact, the grazing intensity in the 2009 HF dataset was not a good representation of the grazing density, which may have led to a large bias in the results.

Accurate understanding of the spatial distribution of human activities and their changes over time is the first step to protecting human beings from natural threats. The above comparison showed that our methodology and results were reliable. This approach can be applied in other case studies as long as their characteristics are considered at a regional scale that is consistent with previous studies (Li et al., 2018).

Implications and New Discoveries

(1) The implications of thawing disaster warning map

In a previous study, the high-hazard areas of thawing frozen ground were mainly distributed in the northwest and central parts of the QTP (**Supplementary Figure S1**) and were mainly affected by the distribution pattern of the ground ice content, ground temperature levels, and changes in the active layer thickness (Ni et al., 2021). However, these areas generally had low HAI values, and the potentially high-hazard areas would not cause much trouble for human activities. Therefore, the potential thaw settlement hazard map still has certain limitations for actual risk management. In this study, the thawing disaster warning map can shield high-hazard areas of thawing frozen ground without human activities and can provide a more accurate early warning. The analysis of the four individual HAI maps, combined with the thawing of frozen ground, can provide important decision support for different departments. The results from *Result* section showed that permafrost thawing had the greatest impact on roads and railways. Hence, early warning is needed to take effective measures, such as air-cooled ripraps, rubble slopes, ventilated pipes, and thermosyphons, to reduce economic losses (Wu and Niu, 2013).

(2) The new discovery of human activity intensity data

The updated HAI map in this study more clearly showed the location information and activity intensity. It helps to track economic development and provides more useful information for science-based protection of human activities. This study also found a series of additional uses for the HAI dataset. It can serve as an important input for ecosystem models to assess human-induced losses of ecosystem services. In addition, it can be used as a proxy for human disturbance, species extinction risk and distribution analyses, and conservation science and decision-making, among others (Venter et al., 2016a). In fact, one of the interesting uses of the HAI map may be to identify places where sensitive species thrive despite high levels of human activities and determine which human behaviors permit coexistence. The HAI map provides an important foundation for understanding conservation work at regional and global scales.

In summary, climate warming will aggravate the occurrence of thawing settlement hazards in the frozen ground regions of the QTP, which would cause detrimental effects on human activities. Research on the impacts of frozen ground degradation on human activities is a topic worthy of consideration. Collaboration among permafrost scientists, hazard specialists, and policy experts is critical for a timely and effective response to the problems associated with a thawing frozen ground. As a preliminary research, this study only considered the thawing hazard of the frozen ground brought by the slow warming of the climate and did not consider some disaster incidents. The sudden thawing of permafrost and the outburst of lakes will pose a huge threat to human activities, although they may not be common and may rarely occur (Lu et al., 2020). The results provide basic data for the study of the impact of thawing frozen ground on human activities. However, the relationship between humans and nature is mutually reinforcing. While developing the economy, humans have also caused damage to the natural environment, which has exacerbated the thawing risk of frozen ground. Nevertheless, the consequences of long-term impacts of human activities on any particular location are complex, positive or negative, benign or catastrophic, depending on the history of the location, the current type of impacts, and our willingness to shoulder responsibility for our stewardship (Sanderson, et al., 2002; Redford and Richter, 1999).

Uncertainty Analysis

There are some uncertainties in the results that need to be understood to improve HAI assessments in the QTP in future studies. First, poor data availability on the QTP is the main reason for the limited reliability of the results. For example, the road vector data for 1995 was not available, so we had no choice but to use the data from 2000 as an alternative. For some rural roads, due to the limitation of the dataset, there are still some missing data. The grazing intensity data for 1995, 2005, and 2015 were also unavailable. In this study, these data were interpolated using data from 2010, but the impacts of subsequent policy interventions were not considered. Due to the implementation of ecological restoration projects (e.g., the Grain for Green Project and the Grazing Withdrawal Program) and the establishment of nature reserves (Fang, 2013; Ren et al., 2016; Zhang et al., 2018), grazing intensity has changed locally. To some extent, the above factors may have weakened the reliability of the results at the local scale.

In addition, we did not account for all human activity data, including wind power stations, transmission lines, and gas/oil pipelines. In general, this type of infrastructure is always distributed on the periphery of the roads. To make the results more realistic, we added a buffer analysis to the road and set the maximum distance to 7 km for a conservative estimation (in *Data* section). Meanwhile, traffic volumes can also represent different intensities of human activity, but the unavailability of these data forced us to omit this indicator, which may lead to a conservative assessment of activity intensity. Therefore, the QTP may have a greater HAI than we have demonstrated. More human activity datasets need to be considered in future works. Additionally, with the development of new technologies such as big data, mobile internet, and crowdsourcing platforms, data acquisition means will be effectively increased. Compared with the traditional GIS (Geographic Information System)-based mapping method, these approaches have obvious advantages.

Third, the weight assignment method also requires refinement. The semiquantitative method based on the AHP is subjective, and more accurate evaluation models need to be used in the future. In addition, more evidence shows that a reasonable allocation of activity intensity within a local scale would improve the accuracy of the results (Li et al., 2018). We treated the land surface as a blank slate, but we know that is not the case in reality. The overlay of multiple layers and the omission of some intensity data result in the same HAI region not representing the same degree of importance. Therefore, we suggest that the HAI in different areas should be interpreted with caution. In general, although the abovementioned factors may affect the accuracy of the

assessment, the basic pattern of HAI will not change, and our results are representative in the current study.

CONCLUSION

In this study, four categories of HAI data were selected as key indicators in a HAI map for 1995, 2005, and 2015. The dataset provided a cumulative measure of HAI with a resolution of 1 km on the QTP. We also analyzed the HAI in the thaw settlement hazard area of frozen ground and discussed the impacts of thawing settlement of frozen ground on human activities.

The results showed that except for in Lhasa and Xining, the mean values of the HAI in the QTP were very low for 1995, 2005, and 2015, which were 0.10, 0.11, and 0.12, respectively. In total, the HAI in the eastern QTP was higher than that in the west, which means that more suitable natural conditions facilitated more human activities. Moreover, during the period from 1995 to 2015, the intensity and extent of human activities increased by 15.35% and 40.64%, respectively.

The seasonally frozen ground region of the QTP had the highest HAI, and the value was twice that of the permafrost region. In the permafrost regions, the HAI in medium-risk areas was the highest (0.09), which mainly had a great impact on linear infrastructures such as roads and railways. The newly established thawing disaster warning map can effectively shield the high thaw settlement hazard areas without human activities, for more accurate warnings.

DATA AVAILABILITY STATEMENT

The raw data supporting the conclusion of this article will be made available by the authors, without undue reservation.

AUTHOR CONTRIBUTIONS

TW and XW designed the study. JN led the manuscript writing. XZ, GH, RL, and JC contributed to data analysis. YD and DZ produced the figures.

FUNDING

This work was financially supported by the National Natural Science Foundations of China (41771076, 41690142, and 42001072), the CAS "Light of West China" Program, and the State Key Laboratory of Cryospheric Science (SKLCS-OP-2021-04). The logistical support from the Cryosphere Research Station on the Qinghai–Tibet Plateau are especially appreciated.

SUPPLEMENTARY MATERIAL

The Supplementary Material for this article can be found online at: https://www.frontiersin.org/articles/10.3389/feart.2022.845873/full#supplementary-material

REFERENCES

Ayram, C. A., Mendoza, M. E., Etter, A., and Pérez Salicrup, D. R. (2017). Anthropogenic Impact on Habitat Connectivity: A Multidimensional Human Footprint index Evaluated in a Highly Biodiverse Landscape of Mexico. *Ecol. Indicators* 72, 895–909. doi:10.1016/j.ecolind.2016.09.007

Center for International Earth Science Information Network Columbia University, and Information Technology Outreach Services University of Georgia (2013). *Global Roads Open Access Data Set, Version 1 (gROADSv1)*. Palisades, NY: NASA Socioeconomic Data and Applications Center SEDAC. doi:10.7927/H4VD6WCT

Chen, J., Wu, T., Zou, D., Liu, L., Wu, X., Gong, W., et al. (2022). Magnitudes and Patterns of Large-Scale Permafrost Ground Deformation Revealed by Sentinel-1 InSAR on the central Qinghai-Tibet Plateau. *Remote Sensing Environ.* 268, 112778. doi:10.1016/j.rse.2021.112778

Duan, Q., and Luo, L. (2020). A Dataset of Human Footprint over the Qinghai-Tibet Plateau during 1990–2015. *Chin. Sci. Data* 5 (3), 303–321. doi:10.11922/csdata.2019.0082.zh

Ellis, E. C., and Ramankutty, N. (2008). Putting People in the Map: Anthropogenic Biomes of the World. *Front. Ecol. Environ.* 6 (8), 439–447. doi:10.1890/070062

Etter, A., Mcalpine, C. A., Seabrook, L., and Wilson, K. A. (2011). Incorporating Temporality and Biophysical Vulnerability to Quantify the Human Spatial Footprint on Ecosystems. *Biol. Conservation* 144 (5), 1585–1594. doi:10.1016/j.biocon.2011.02.004

Fang, Y. (2013). Managing the Three-Rivers Headwater Region, China: From Ecological Engineering to Social Engineering. *Ambio* 42 (5), 566–576. doi:10.1007/s13280-012-0366-2

Fang, Y., Qin, D., and Ding, Y. (2011b). Frozen Soil Change and Adaptation of Animal Husbandry: a Case of the Source Regions of Yangtze and Yellow Rivers. *Environ. Sci. Pol.* 14 (5), 555–568. doi:10.1016/j.envsci.2011.03.012

Fang, Y., Qin, D., Ding, Y., Yang, J., and Xu, K. (2011a). The Impacts of Permafrost Change on NPP and Implications: A Case of the Source egions of Yangtze and Yellow Rivers. *J. Mt. Sci.* 8, 437–447. doi:10.1007/s11629-011-1004-3

He, R., and Jin, H. (2010). Permafrost and Cold-Region Environmental Problems of the Oil Product Pipeline from Golmud to Lhasa on the Qinghai-Tibet Plateau and Their Mitigation. *Cold Regions Sci. Techn.* 64 (3), 279–288. doi:10.1016/j.coldregions.2010.01.003

Hjort, J., Karjalainen, O., Aalto, J., Westermann, S., Romanovsky, V. E., Nelson, F. E., et al. (2018). Degrading Permafrost Puts Arctic Infrastructure at Risk by Mid-century. *Nat. Commun.* 9 (1), 1–9. doi:10.1038/s41467-018-07557-4

Jenks, G. F. (19671967). The Data Model Concept in Statistical Mapping. *Int. Yearb. Cartography* 7, 186–190.

Karjalainen, O., Aalto, J., Luoto, M., Westermann, S., Romanovsky, V. E., Nelson, F. E., et al. (2019). Circumpolar Permafrost Maps and Geohazard Indices for Near-Future Infrastructure Risk Assessments. *Sci. Data* 6 (1), 190037. doi:10.1038/sdata.2019.37

Li, R., Wu, Q., Li, X., Sheng, Y., Hu, G., Cheng, G., et al. (2019). Characteristic, Changes and Impacts of Permafrost on Qinghai-Tibet Plateau. *Chin. Sci. Bull.* 64 (27), 2783–2795. (in Chinese). doi:10.1360/TB-2019-0191

Li, S., Zhang, Y., Wang, Z., and Li, L. (2018). Mapping Human Influence Intensity in the Tibetan Plateau for Conservation of Ecological Service Functions. *Ecosystem Serv.* 30, 276–286. doi:10.1016/j.ecoser.2017.10.003

Lin, Y., Hong, M., Han, G., Zhao, M., Bai, Y., and Chang, S. X. (2010). Grazing Intensity Affected Spatial Patterns of Vegetation and Soil Fertility in a Desert Steppe. *Agric. Ecosyst. Environ.* 138 (4), 282–292. doi:10.1016/j.agee.2010.05.013

Lu, P., Han, J., Li, Z., Xu, R., Li, R., Hao, T., et al. (2020). Lake Outburst Accelerated Permafrost Degradation on Qinghai-Tibet Plateau. *Remote Sensing Environ.* 249, 112011. doi:10.1016/j.rse.2020.112011

Ni, J., Wu, T., Zhu, X., Hu, G., Zou, D., Wu, X., et al. (2021). Simulation of the Present and Future Projection of Permafrost on the Qinghai-Tibet Plateau with

Statistical and Machine Learning Models. *Geophys. Res. Atmos.* 126, e2020JD033402. doi:10.1029/2020JD033402

Ni, J., Wu, T., Zhu, X., Wu, X., Pang, Q., Zou, D., et al. (2021). Risk Assessment of Potential Thaw Settlement hazard in the Permafrost Regions of Qinghai-Tibet Plateau. *Sci. Total Environ.* 776, 145855. doi:10.1016/j.scitotenv.2021.145855

Niu, F., Lin, Z., Liu, H., and Lu, J. (2011). Characteristics of Thermokarst Lakes and Their Influence on Permafrost in Qinghai-Tibet Plateau. *Geomorphology* 132 (3), 222–233. doi:10.1016/j.geomorph.2011.05.011

Niu, F., Lin, Z., Lu, J., and Wang, H. N. (2015). Assessment of Terrain Susceptibility to Thermokarst lake Development along the Qinghai–Tibet Engineering Corridor, China. *Environ. Earth Sci.* 73, 5631. doi:10.1007/s12665-014-3818-0

Obu, J., Westermann, S., Bartsch, A., Berdnikov, N., Christiansen, H. H., Dashtseren, A., et al. (2019). Northern Hemisphere Permafrost Map Based on TTOP Modelling for 2000-2016 at 1 Km2 Scale. *Earth-Science Rev.* 193, 299–316. doi:10.1016/j.earscirev.2019.04.023

O'Neill, H. B., Burn, C. R., Allard, M., Arenson, L. U., Bunn, M. I., Connon, R. F., et al. (2020). Permafrost Thaw and Northern Development. *Nat. Clim. Chang.* 10, 722–723. doi:10.1038/s41558-020-0862-5

Otto, C. R. V., Roth, C. L., Carlson, B. L., and Smart, M. D. (2016). Land-use Change Reduces Habitat Suitability for Supporting Managed Honey Bee Colonies in the Northern Great Plains. *Proc. Natl. Acad. Sci. USA* 113 (37), 10430–10435. doi:10.1073/pnas.1603481113

Ouyang, Z., Zheng, H., Xiao, Y., Polasky, S., Liu, J., Xu, W., et al. (2016). Improvements in Ecosystem Services from Investments in Natural Capital. *Science* 352 (6292), 1455–1459. doi:10.1126/science.aaf2295

Qin, D., Ding, Y., Xiao, C., Kang, S., Ren, J., Yang, J., et al. (2018). Cryospheric Science: Research Framework and Disciplinary System. *Natl. Sci. Rev.* 5 (02), 255–268. doi:10.1093/nsr/nwx108

Qin, Y., Wu, T., Zhao, L., Wu, X. D., Li, R., Xie, C. W., et al. (2017). Numerical Modeling of the Active Layer Thickness and Permafrost thermal State across Qinghai-Tibetan Plateau. *J. Geophys. Res. Atmos.* 122 (21), 11604–11620. doi:10.1002/2017jd026858

Qin, Y., Zhang, P., Liu, W., Guo, Z., and Xue, S. (2020). The Application of Elevation Corrected MERRA2 Reanalysis Ground Surface Temperature in a Permafrost Model on the Qinghai-Tibet Plateau. *Cold Regions Sci. Techn.* 175, 103067. doi:10.1016/j.coldregions.2020.103067

Redford, K. H., and Richter, B. D. (1999). Conservation of Biodiversity in a World of Use. *Conservation Biol.* 13 (6), 1246–1256. doi:10.1046/j.1523-1739.1999.97463.x

Ren, Y., Lü, Y., and Fu, B. (2016). Quantifying the Impacts of Grassland Restoration on Biodiversity and Ecosystem Services in China: A Meta-Analysis. *Ecol. Eng.* 95, 542–550. doi:10.1016/j.ecoleng.2016.06.082

Saaty, T. L., and Kearns, K. P. (1985). Systems Characteristics and the Analytic Hierarchy Process. *Anal. Plann.*, 63–86. doi:10.1016/B978-0-08-032599-6.50008-810.1016/b978-0-08-032599-6.50009-x

Sanderson, E. W., Jaiteh, M., Levy, M. A., Redford, K. H., Wannebo, A. V., and Woolmer, G. (2002). The Human Footprint and the Last of the Wild. *BioScience* 52 (10), 891–904. doi:10.1641/0006-3568(2002)052[0891:thfatl]2.0.co;2

Teufel, B., and Sushama, L. (2019). Abrupt Changes across the Arctic Permafrost Region Endanger Northern Development. *Nat. Clim. Chang.* 9 (11), 858–862. doi:10.1038/s41558-019-0614-6

Trombulak, S. C., and Frissell, C. A. (2000). Review of Ecological Effects of Roads on Terrestrial and Aquatic Communities. *Conservation Biol.* 14 (1), 18–30. doi:10.1046/j.1523-1739.2000.99084.x

Venter, O., Sanderson, E. W., Magrach, A., Allan, J. R., Beher, J., Jones, K. R., et al. (2016a). Global Terrestrial Human Footprint Maps for 1993 and 2009. *Sci. Data* 3, 160067. doi:10.1038/sdata.2016.67

Venter, O., Sanderson, E. W., Magrach, A., Allan, J. R., Beher, J., Jones, K. R., et al. (2016b). Sixteen Years of Change in the Global Terrestrial Human Footprint and Implications for Biodiversity Conservation. *Nat. Commun.* 7 (1), 1–11. doi:10.1038/ncomms12558

Wang, S., Yu, Q. H., Guo, L., You, Y. H., Wang, S. J., and Yu, Y. (2014). Prevention and Control of Freezing and Thawing Disasters in Electric Transmission Lines Constructed in Permafrost Regions. *J. Glaciology Geocryology* 36 (01), 137–143. doi:10.7522/j.issn.1000-0240.2014.0017

Wang, W., Wu, T., Zhao, L., Li, R., Zhu, X., Wang, W., et al. (2018). Exploring the Ground Ice Recharge Near Permafrost Table on the central Qinghai-Tibet Plateau Using Chemical and Isotopic Data. *J. Hydrol.* 560, 220–229. doi:10.1016/j.jhydrol.2018.03.032

Wei, Z., Du, Z., Wang, L., Lin, J., Feng, Y., Xu, Q., et al. (2021). Sentinel-Based Inventory of Thermokarst Lakes and Ponds across Permafrost Landscapes on the Qinghai-Tibet Plateau. *Earth Space Sci.* 8 (11), e2021EA001950. doi:10.1029/2021EA001950

Wu, Q., and Niu, F. (2013). Permafrost Changes and Engineering Stability in Qinghai-Xizang Plateau. *Chin. Sci. Bull.* 58 (02), 1079–1094. (in Chinese). doi:10.1007/s11434-012-5587-z

Wu, Q., Zhang, T., and Liu, Y. (2012). Thermal State of the Active Layer and Permafrost along the Qinghai-Xizang (Tibet) Railway from 2006 to 2010. *The Cryosphere* 6 (3), 607–612. doi:10.5194/tc-6-607-2012

Xu, T., Zhao, X., Zhang, X., Wang, X., Geng, Q. Y., Hu, L. Y., et al. (2020). Sustainable Development of Ecological Grass-Based Livestock Husbandry in Qinghai-Tibet Plateau Alpine Area: Principle, Technology and Practice. *Acta Ecol. Sin.* 40 (18), 6324–6337. doi:10.5846/stxb201912142705

Xu, X. L. (2017). *A Dataset of Population Spatial Distribution of the People's Republic of China*. Beijing: Data Center for Resources and Environmental Sciences, Chinese Academy of Sciences.

Yao, T., Qin, D., Shen, Y., Zhao, L., Wang, N., and Lu, A. (2013). Cryospheric Changes and Their Impacts on Regional Water Cycle and Ecological Conditions in the Qinghai-Tibetan Plateau. *Chin. J. Nat.* 35 (03), 179–186. (in Chinese). doi:10.3969/j.issn.0253-9608.2013.03.004

Zhang, H., Fan, J., Cao, W., Zhong, H., Harris, W., Gong, G., et al. (2018). Changes in Multiple Ecosystem Services between 2000 and 2013 and Their Driving Factors in the Grazing Withdrawal Program, China. *Ecol. Eng.* 116, 67–79. doi:10.1016/j.ecoleng.2018.02.028

Zhang, X. R., Zhou, J., and Li, M. M. (2020). Analysis on Spatial and Temporal Changes of Regional Habitat Quality Based on the Spatial Pattern Reconstruction of Land Use. *Acta Geographica Sinica* 75 (01), 160–178. (in Chinese). doi:10.11821/dlxb202001012

Zhang, Z., and Wu, Q. (2012). Thermal Hazards Zonation and Permafrost Change over the Qinghai-Tibet Plateau. *Nat. Hazards* 61 (2), 403–423. doi:10.1007/s11069-011-9923-4

Zhao, G., Liu, J., Kuang, W., Ouyang, Z., and Xie, Z. (2015). Disturbance Impacts of Land Use Change on Biodiversity Conservation Priority Areas across China: 1990-2010. *J. Geogr. Sci.* 25, 515–529. doi:10.1007/s11442-015-1184-9

Zhao Wanglin, 赵., Luo Tianxiang, 罗., and Zhang Lin, 张. (2019). Relative Impact of Climate Change and Grazing on NDVI Variations in Typical alpine Desert Grasslands in Tibet. *Acta Eco Sin* 39 (22), 8494–8503. (in Chinese). doi:10.5846/stxb201811192509

Zou, D., Zhao, L., Sheng, Y., Chen, J., Hu, G., Wu, T., et al. (2017). A New Map of Permafrost Distribution on the Tibetan Plateau. *The Cryosphere* 11 (6), 2527–2542. doi:10.5194/tc-11-2527-2017

Conflict of Interest: The authors declare that the research was conducted in the absence of any commercial or financial relationships that could be construed as a potential conflict of interest.

Publisher's Note: All claims expressed in this article are solely those of the authors and do not necessarily represent those of their affiliated organizations, or those of the publisher, the editors and the reviewers. Any product that may be evaluated in this article, or claim that may be made by its manufacturer, is not guaranteed or endorsed by the publisher.

frontiers | Frontiers in Earth Science

ORIGINAL RESEARCH
published: 08 June 2022
doi: 10.3389/feart.2022.892524

Distributive Features of Dissolved Organic Carbon in Aquatic Systems in the Source Area of the Yellow River on the Northeastern Qinghai–Tibet Plateau, China

Qiang Ma[1], Huijun Jin[1,2,3], Qingbai Wu[1]*, Yuzhong Yang[1], Qingfeng Wang[1], Dongliang Luo[1], Yadong Huang[1], Yan Li[1], Xiaoying Li[3], Raul D. Serban[4], Sihai Liang[5], Shuhui Gao[1,6] and Sergey S. Marchenko[1,7]*

[1]State Key Laboratory of Frozen Soil Engineering, Northwest Institute of Eco-Environment and Resources, Chinese Academy of Sciences, Lanzhou, China, [2]School of Civil Engineering, Ministry of Education Observational and Research Station of Permafrost Geo-Environment in Northeast China, Institute of Cold-Regions Science and Engineering, Northeast Forestry University, Harbin, China, [3]Key Laboratory of Sustainable Forest Ecosystem Management-Ministry of Education, School of Forestry, Northeast Forestry University, Harbin, China, [4]Institute for Alpine Environment, Eurac Research, Bolzano, Italy, [5]School of Water Resources and Environment, China University of Geosciences, Beijing, China, [6]School of Civil Engineering, Lanzhou Jiaotong University, Lanzhou, China, [7]Geophysical Institute, University of Alaska Fairbanks, Fairbanks, AK, United States

OPEN ACCESS

Edited by:
Tommaso Tesi,
National Research Council (CNR), Italy

Reviewed by:
Chunlin Song,
Sichuan University, China
Xiaofan Yang,
Beijing Normal University, China

***Correspondence:**
Huijun Jin
hjjin@lzb.ac.cn
Qingbai Wu
qbwu@lzb.ac.cn

Specialty section:
This article was submitted to Cryospheric Sciences, a section of the journal Frontiers in Earth Science

Received: *09 March 2022*
Accepted: *19 April 2022*
Published: *08 June 2022*

Citation:
Ma Q, Jin H, Wu Q, Yang Y, Wang Q, Luo D, Huang Y, Li Y, Li X, Serban RD, Liang S, Gao S and Marchenko SS (2022) Distributive Features of Dissolved Organic Carbon in Aquatic Systems in the Source Area of the Yellow River on the Northeastern Qinghai–Tibet Plateau, China. Front. Earth Sci. 10:892524. doi: 10.3389/feart.2022.892524

Dissolved organic carbon (DOC) is the main participant in carbon cycles through water pathways. Recent studies have highlighted the roles of aquatic systems in landscape and watershed carbon budgets. This study is based on 261 samples collected between 2016 and 2017, from individual water types (e.g., river/stream, lake/pond, icing/spring, snow/rain, groundwater/ice, and others) in the source area of the Yellow River (SAYR). These samples were analyzed for examining the distributive features of DOC in aquatic systems, especially in relation to environmental factors. It shows that: 1) DOC concentrations in permafrost-related waters (7.2–234.4 mg $C{\cdot}L^{-1}$) were often the highest among all aquatic DOC sources (lakes/ponds: 21.3 ± 34.1 mg $C{\cdot}L^{-1}$, rivers/streams: 4.3 ± 3.7 mg $C{\cdot}L^{-1}$, and groundwater: 1.8 ± 1.4 mg $C{\cdot}L^{-1}$); 2) the seasonality of riverine DOC showed declining features in 2016 and high in summer/autumn, followed by a spring freshet in 2017, and a close association with intra-annual precipitation modes; 3) the main controls of aquatic DOC are permafrost presence, precipitation, and NDVI, and they contribute to 38% of variances of environmental variables in affecting variations in aquatic DOC in the SAYR; and 4) a literature review on biodegradable DOC (BDOC) of varied aquatic DOC pools indicates the highest DOC concentrations (48–1,548 mg $C{\cdot}L^{-1}$) and BDOC (23–71%) of ground-ice meltwater. Thus, we suggest that in the SAYR, permafrost dynamics dominate aquatic DOC distribution, and permafrost thaw may alter aquatic DOC budgets, eventually becoming an additional source for atmospheric carbon emissions.

Keywords: alpine permafrost, source area of the Yellow River, dissolved organic carbon, DOC distribution, aquatic systems

1 INTRODUCTION

Soils in permafrost regions store ~60% organic carbon all over the globe, despite the limited areal extents of permafrost occupying less than 15% of currently exposed global land area (Hugelius et al., 2014; Schuur et al., 2015). Permafrost regions are globally important organic carbon reservoirs and play a key role in global carbon cycling (Schuur et al., 2008; Strauss et al., 2017; Jin and Ma, 2021). The Qinghai–Tibet Plateau (QTP) is underlain by the most extensive alpine and plateau permafrost (1.15×10^6 km^2) in the world, and the warm and thin high-elevational permafrost is very sensitive to climate change (Ran et al., 2020).

Aquatic ecosystems are important pathways of carbon cycling in permafrost regions (Frey and McClelland, 2009). Dissolved organic carbon (DOC) is the major organic carbon pool in aquatic ecosystems and an active participant in freshwater ecology, biogeochemistry, and carbon cycles in permafrost regions through lateral pathways (Hope et al., 1994; Eimers et al., 2008). Under a warming climate, DOC dynamics in aquatic systems (e.g., rivers/streams, lakes/ponds, groundwater, among many others) have been substantially shifted and have been frequently reported in permafrost regions (Schindler et al., 1997; Vonk et al., 2015a; Tank et al., 2016; Ma, 2020). A multi-decadal observation (1972–2012) of in-stream DOC dynamics in the Mackenzie River basin reported a general increasing trend of DOC flux (+39.9%) at the outlet and suggests the important roles of permafrost thaw in DOC fluxes according to seasonal and sub-catchment trends (Tank et al., 2016). Climate change, droughts, and forest fires have already caused a 15–20% decrease in DOC concentrations in boreal lakes, northeastern Ontario (Schindler et al., 1997). Thermokarst lakes formed by the thawing of ice-rich permafrost are generally characterized by high DOC concentrations (Shirokova et al., 2013; Matheus Carnevali et al., 2015; Matveev et al., 2016; Mu et al., 2016). Groundwater is projected to become an increasing source of freshwater and DOC to the Arctic Basin as permafrost thaws (Connolly et al., 2020). However, the distributive features of DOC in aquatic systems and individual water types (rivers/streams, lakes/ponds, groundwater, and others) are less investigated in permafrost regions, especially on the QTP.

Aquatic organic carbon pools are also sources of atmospheric carbon emissions (Cole et al., 2007; Serikova et al., 2018; Dean et al., 2020; Zhang et al., 2020; Rosentreter et al., 2021). Half of the global methane emissions originate from aquatic ecosystems, such as those in lakes/ponds, reservoirs, rivers/streams, wetlands, coastal regions, and oceans, among many others (Rosentreter et al., 2021). The Arctic, on average with a 16% areal extent of water bodies in all landscapes (Vonk et al., 2015a), may become a region of net carbon emission under a warming climate (Serikova et al., 2018). The QTP is also a water-abundant domain, originating from 13 major rivers in Eastern and Southern Asia (e.g., Yellow, Yangtze, and Mekong rivers), annually discharging about 6.56 trillion m^3 (6,560 km^3) of water, or 13% of global total annual discharge (Wang et al., 2021). In-stream average methane emission rates from the eastern QTP were also reported as high as 11.9 mmol $CH_4 \cdot m^{-2} \cdot d^{-1}$, six times higher than the concurrent global average (Zhang et al., 2020). Therefore, aquatic DOC pools are potentially important sources for atmospheric carbon emissions.

Extensively (34% of the areal extent of the catchment) underlain by permafrost, the source area of the Yellow River (SAYR) above the Tanag hydrological station on northeastern QTP presents various water types, such as rivers/streams, tectonic and thermokarst lakes, wetlands, icings, and springs. Aquatic systems are crucial pathways for regional carbon budgets, while distributive features of aquatic DOC and its regulators have been seldomly systematically explored. In this study, a total of 261 water samples from various waters across the SAYR were collected and analyzed for investigating the distribution of DOC concentrations in aquatic systems. Then, by employing principal component analysis (PCA), influencing environmental factors of DOC concentrations in individual water types are examined. In the end, by synthesizing globally published data on biodegradable DOC in varied water types, the release potentials of aquatic DOC to the atmosphere are briefly discussed.

2 STUDY AREA AND METHODS

2.1 Study Area

The SAYR (32.2°–36.1°N, 95.9°–103.4°E; 2,629–6,235 m a. s. l.) is the up-reach catchment of the Yellow River basin above the Tanag hydrological station (35.5°N, 100.2°E; 2,629 m a. s. l.), on the northeastern QTP, China (**Figure 1**), covering an area of 1.212×10^5 km^2. The climate in the SAYR is characterized by long winters (November–April) and short summers (June–August). Mean annual air temperature (MAAT) and annual precipitation in the SAYR are 0.2°C and 507.7 mm (1960–2012), respectively (Lan et al., 2013). The climate in the up-reach SAYR above the Huanghe'yan hydrological station (34.9°N, 98.2°E; 4,215 m a. s. l.) is characterized by a dry–cold climate with a MAAT less than −3.5°C and annual precipitation of 300–400 mm (Jin et al., 2010). The growing season varies with elevation but mainly concentrates from May to September. With an areal extent of permafrost at 34% in the SAYR, permafrost occurs extensively (86%) in the up-reach SAYR, with rich manifestations in periglacial landforms and MAAT (1961–2019) varying from −3.5 to about 0°C. Alpine permafrost can be as thick as up to about 360 m on very high mountain tops on the peak of Mt. Maqên Gangri (6,235 m a. s. l.) in the Anye Maqên Mountains (Wang and French, 1995; Jin et al., 2009, 2020; Luo et al., 2020; Sheng et al., 2020). The lower reaches/basins of the SAYR between Huanghe'yan and Tanag hydrological stations are dominated by a relatively warm–wet climate, particularly in the southeastern SAYR (mainly on the Zoîgé Peat Plateau), where MAAT is at about 7.5°C and annual precipitation, about 654 mm (Yu et al., 2017). The snow-melt season generally extends from April to October in the lower reaches/basins of the SAYR. Glaciers are minimally presented in the SAYR (mainly in the Anye Maqên Mountains) (126.7 km^2), or 2% of the SAYR in the areal extent (Blue et al., 2013; Jin et al., 2019).

The SAYR is characterized by a high-mountain surrounded by flat valleys and plains. The baseflow accounts for a large portion

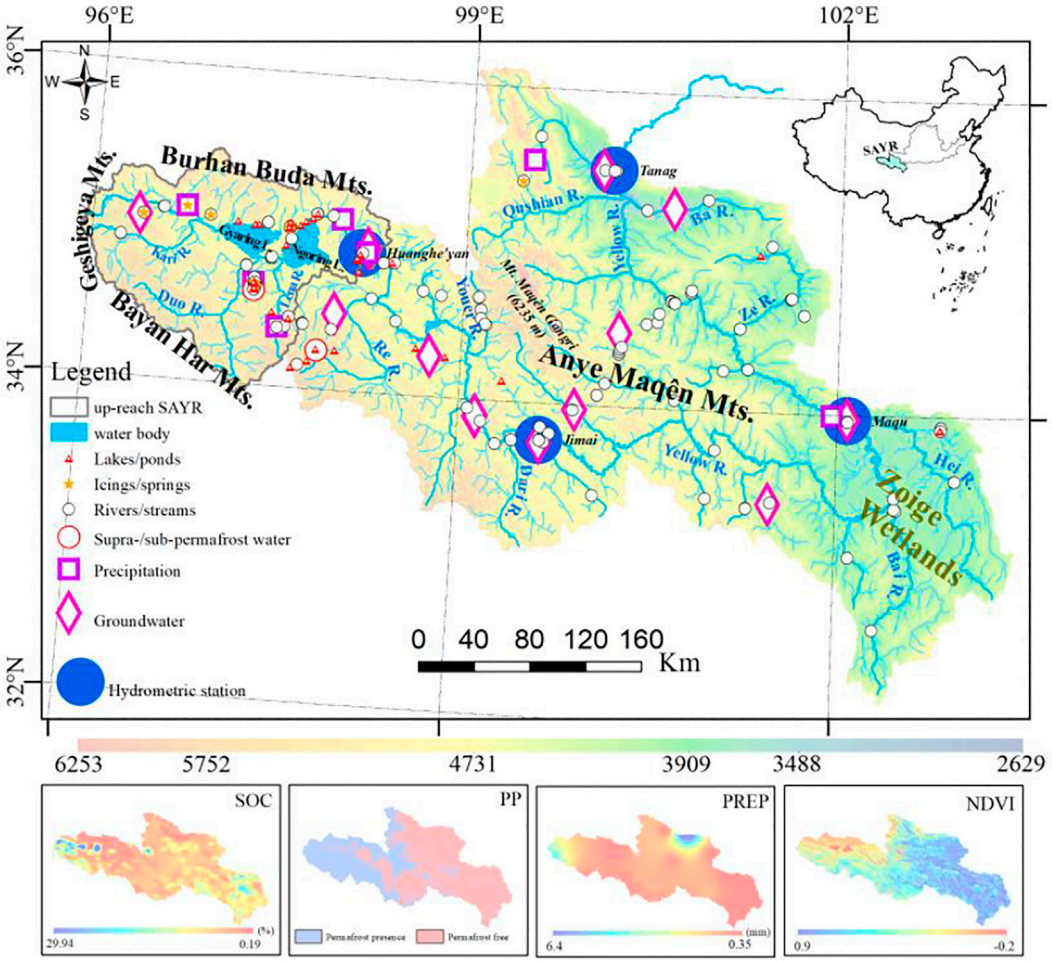

FIGURE 1 | Map of sampling locations in the source area of the Yellow River (SAYR) on the northeastern Qinghai–Tibet Plateau, SW China. Notes: Sub-panel SOC shows the spatial distribution of soil organic carbon (SOC) content; sub-panel PP shows the distribution of permafrost presence; sub-panel PREP is the distribution of daily precipitation on 12 August 2016; and sub-panel NDVI is the normalized difference vegetation index on 12 August 2016.

of annual streamflow (~50% or more) (Ma et al., 2019a). Numerous meandering rivers in the valleys on the Zoîgé Peat Plateau, which are conducive to water conservancy, in addition to rich precipitation, have facilitated the accumulation of thick peat layers (0.5~10.5 m) in the Holocene (mainly since 11.7 ka B.P.), particularly in the Megathermal period in the mid-Holocene at 8.5–4.0 ka B. P. (Yu et al., 2017; Jin et al., 2019, 2020). Alpine steppes and alpine meadows dominate alpine vegetation in the up-reach SAYR and the lower reaches/basins of SAYR; The SAYR is sporadically dotted with shrubs and forests at lower elevations. In alpine wetlands on the Zoîgé Peat Plateau, aquatic vegetation (e.g., *Kobresia pygmaea* and *K. tibetica*) is extensively observed (Brierley et al., 2016).

2.2 Methods

2.2.1 Sample Collection and Laboratory Analyses

The field data were collected from April 2016 to December 2017 in rivers/streams, lakes/ponds, commercial wells, precipitation, aufeis, and springs in the SAYR (**Figure 1**). A total of 261 water samples were collected during the sampling periods. The river/stream samples were mainly collected in the up-reach SAYR, such as the mainstream Yellow River and its tributaries (Kari Qu, Duo Qu, Lena Qu, Ze Qu, You'er Qu, and Hei'he and Bai'he rivers on the Zoîgé Peat Plateau) in the snow-melt season (April–May), summer–autumn season (July–October), and the freezing season (November–next March). The water samples of lakes/ponds were collected from thermokarst lakes, large-size tectonic lakes (e.g., Gyaring and Ngoring lakes), and lakes on the Zoîgé Plateau, among many others. Groundwater samples were collected from multiple commercial wells in villages and towns across the SAYR. A borehole was drilled on the northern shore of the Wanlong Worma Lake to the south of Ngöring Lake in the up-reach SAYR and the samples of supra- and sub-permafrost waters were collected during the field-work season of 29 April to 2 May 2017. In the lower reaches/basins of SAYR, a 25-m-deep borehole was drilled on 22 October 2017 near Maqu County, and the water samples were collected and labeled as phreatic groundwater. Precipitation samples were collected in both solid

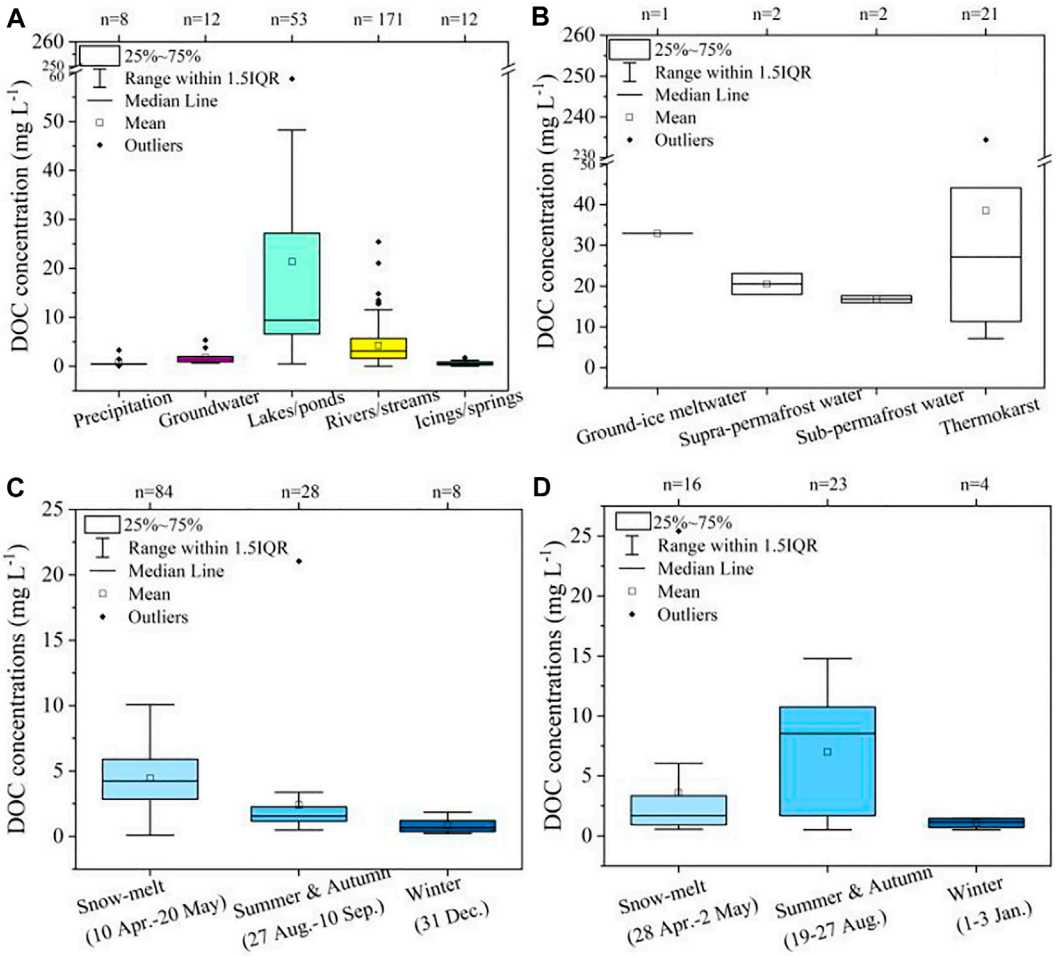

FIGURE 2 | Dissolved organic carbon concentrations (mg C·L^{-1}) in aquatic systems in the source area of the Yellow River (SAYR) above the Tanag hydrological station in Qinghai Province, SW China. Notes: "***n***" indicates the number of field samples. **(A)** DOC concentrations in individual water type (hail/snow/rain, groundwater, lakes/ponds, river/stream, and icing/spring); **(B)** permafrost-related aquatic DOC concentrations; **(C)** seasonal variations of in-stream DOC concentrations in 2016; **(D)** seasonal variations of in-stream DOC concentrations in 2017.

precipitation (snow/hail) and rain. Aufeis/icings were mainly collected in the up-reach SAYR in the winter of 2016 and 2017 (**Figure 2**). Detailed information on water sampling is provided in **Table S1**.

The water samples were taken to the State Key Laboratory of Frozen Soils Engineering, Lanzhou, China, after collection and kept at 4°C before laboratory pre-processing and analyses. The water samples were first filtered through the mixed cellulose ester (MCE) filters (0.45 μm pore size), and the content of DOC was determined using a total organic carbon analyzer (TOC analyzer, I. O. Corporation; precision: ± 0.5‰).

2.2.2 Statistical Analyses

To evaluate the environmental controllers for aquatic DOC concentrations, we employed the principal component analysis (PCA) (Kotz and Nadarajah, 2004). The presence of permafrost, SOC content, normalized difference vegetation index (NDVI), and precipitation were taken as the environmental controllers for aquatic DOC concentrations (**Figure 1**). Data information and sources are presented in **Table 1**.

Daily precipitation data were measured using the Chinese standard precipitation gauge without discriminating between liquid and solid precipitation forms. An error validation (wetting and evaporation losses, trace precipitation, and wind) was implemented for liquid and solid precipitation forms, respectively, by employing daily air temperature and wind speed data (Ye et al., 2004; Yang et al., 2005). The validated daily precipitation was then interpolated using the empirical Bayesian kriging method to obtain the spatial distribution of daily precipitation in the SAYR. Winter precipitation was calculated by accumulating daily solid precipitation in winter. Spring precipitation was calculated by accumulating winter snowfall, due to spring freshet was mainly impacted by melting accumulated snow in winter (Ma et al., 2019a). The site-specific data of the environmental variables were extracted from spatial data at the sampling sites (**Figure 1**). PCA was used

TABLE 1 | List of environmental controllers for aquatic DOC concentrations in the source area of the Yellow River (SAYR) above the Tanag hydrological station in Qinghai Province, Southwest China.

Data type	Abbreviation	Temporal span	Temporal resolution (d)	Data source
Precipitation	PREP	2016–2017	1	National Meteorological Information Center (http://data.cma.cn)
Permafrost presence	PP	—	—	Ran et al. (2022)
Normalized difference vegetation index	NDVI	2016–2017	16	National Earth System Science Data Center (http://www.geodata.cn)
Soil organic carbon content	OC	—	—	Wieder et al. (2014)

TABLE 2 | List of minimum, average, median, and maximum values of dissolved organic carbon (DOC) concentrations in each water type in the source area of the Yellow River (SAYR) above the Tanag hydrological station in Qinghai Province, China.

Water type	Region	DOC (mg C·L^{-1})				Reference
		Minimum	Average ± SD	Median	Maximum	
Streams/rivers	SAYR	0.7	4.2 ± 3.7	3.1	21.0	This study
	Permafrost regions	1.0	—	—	32.0	Ma et al. (2019b)
	QTP	0.4	—	—	30.8	Chen et al. (2021)
Spring streamflows	SAYR	0.1	4.3 ± 3.1	3.8	25.4	This study
	Upper Yukon	—	36.12	—	—	Guo and Macdonald (2006)
Summer–autumn streamflows	SAYR	0.5	4.5 ± 4.8	2.1	21.0	This study
	Upper Yukon	—	7.3	—	—	Guo and Macdonald (2006)
Winter streamflows	SAYR	0.5	0.9 ± 0.6	0.8	1.5	This study
	Yukon Basin	1.0	3.9 ± 0.5	—	20.0	O'Donnell et al. (2012)
	YZR	—	0.5 ± 0.2	—	—	Chen et al. (2021)
Lakes/ponds	SAYR	0.5	21.3 ± 34.1	9.4	234.4	This study
	Permafrost regions	0.0	—	10.8	1,130.0	Stolpmann et al. (2021)
Springs/icings	SAYR	0.2	0.6 ± 0.5	0.5	1.7	This study
Precipitation (rain, snow, and others)	SAYR	0.4	0.8 ± 1.0	0.4	1.8	This study
	Permafrost regions	1.0	—	—	2.4	Ma et al. (2019b)
Groundwater	SAYR	0.6	1.8 ± 1.4	1.4	5.3	This study
	Permafrost regions	—	~0.7	—	—	Ma et al. (2019b)
Supra-permafrost water	SAYR	17.9	20.5 ± 3.6	—	23.1	This study
	Alaskan Arctic NE coast	—	33 ± 2	—	—	Connolly et al. (2020)
Sub-permafrost water	SAYR	15.9	16.8 ± 1.2	—	17.6	This study
Ground-ice meltwater	SAYR	—	32.94	—		This study
	Interior Alaska	48	—	—	1,548	Ewing et al. (2015)
Thermokarst lakes/ponds	SAYR	7.2	38.5 ± 48.5	27.1	234.4	This study
	QTP	1.2	—	—	49.6	Mu et al. (2016)

Note: YZR stands for the Yarlung Zangbo River in the southern Tibet Autonomous Region, Southwest China.

to summarize the rescaled variables (PREP, PP, SOC, and NDVI) by reducing the dimensionality of the data while retaining most of the variability in the dataset to determine impacting environmental variables at aquatic DOC sampling sites and to find linear relationships between environmental variables. All statistical analyses were implemented in the Origin Pro 2021b.

2.2.3 Literature Synthesis

A meta-analysis of results of both seasonally in-stream dynamics and concentrations of DOC in various water types was implemented to compare DOC concentrations in various water types in the SAYR with those in other alpine/high-plateau and northern/Arctic permafrost regions to have a comprehensive understanding of aquatic DOC distributions. A synthesis of published data on biodegradable DOC in various water types in northern permafrost regions, in combination with the distribution of aquatic DOC concentrations, was analyzed to determine the releasing potentials of aquatic DOC to atmospheric carbon emissions. DOC concentrations and BDOC data were gathered by synthesizing relevant studies on the ISI Web of Science^{TM}, as well as previous compilations on DOC in permafrost regions and the biodegradability of aquatic DOC (such as Vonk et al., 2015b; Ma et al., 2019b). A total of 19 studies on DOC concentrations and aquatic BDOC with experimental data were referred (Finlay et al., 2006, 2009; Guo and Macdonald, 2006; Petrone et al., 2006; Holmes et al., 2008; Balcarczyk et al., 2009; O'Donnell et al., 2012; Wickland et al., 2012; Olefeldt and Roulet, 2014; Abbott et al., 2014; Vonk et al., 2013; Ewing et al., 2015; Mann et al., 2015; Mu et al., 2016; Selvam et al., 2017; Textor et al., 2019; Connolly et al., 2020; Payandi-Rolland et al., 2020; Chen et al., 2021; Stolpmann et al., 2021). Among these results, we collect DOC concentrations and BDOC in literature works by following the criteria, as: 1) located in the alpine (e.g., QTP) or

TABLE 3 | Correlations between multi-environmental variables and aquatic DOC concentrations for each principal component in a PCA analysis.

	Snow-melt season				Summer/autumn				Winter		
	1	**2**	**3**		**1**	**2**	**3**		**1**	**2**	**3**
PP	**0.59**	0.04	0.09	PP	**0.65**	0.10	−0.06	PP	0.46	**0.51**	0.07
PREP	**0.61**	−0.01	−0.07	PREP	−0.27	0.46	**0.80**	PREP	−0.07	**0.77**	0.28
SOC	0.09	**−0.69**	**0.71**	SOC	0.40	−0.46	**0.55**	SOC	**0.57**	−0.27	−0.04
NDVI	−0.42	0.37	**0.52**	NDVI	**−0.57**	−0.27	−0.11	NDVI	0.49	0.16	**−0.65**
DOC	0.32	**0.63**	0.46	DOC	0.13	**0.71**	−0.19	DOC	0.47	0.23	**0.70**
Variance explained	41	22	18	Variance explained	33	27	17	Variance explained	42	28	14
	Groundwater				**Lakes/ponds**				**Aquatic systems**		
	1	**2**			**1**	**2**	**3**		**1**	**2**	**3**
PP	**0.56**	0.22	—	PP	0.43	0.44	−0.12	PP	**0.52**	0.22	0.17
PREP	0.13	**−0.66**	—	PREP	**0.63**	−0.06	−0.16	PREP	**0.59**	−0.06	−0.11
SOC	0.39	0.46	—	SOC	−0.16	**0.60**	**−0.68**	SOC	0.03	**0.82**	0.46
NDVI	−0.33	**0.55**	—	NDVI	−0.40	**0.57**	**0.50**	NDVI	**−0.52**	−0.10	0.49
DOC	**0.64**	−0.06	—	DOC	0.49	0.34	**0.50**	DOC	0.31	**−0.52**	**0.71**
Variance explained	42	33	—	Variance explained	36	23	19	Variance explained	38	22	18

Notes: According to the practice of Vonk et al. (2015b), the correlation coefficients of above 0.7 are considered strong, and those at 0.5–0.7, moderate.

Arctic permafrost regions, 2) ranges of DOC concentrations and BDOC were adopted, and 3) using incubation experiments or chemical proxies to access BDOC.

3 RESULTS AND DISCUSSIONS

3.1 Patterned DOC Concentrations in Aquatic Systems in the SAYR

DOC concentrations in aquatic systems show strong variations among individual water types in the SAYR (**Figure 2A**). The highest DOC concentration was found in thermokarst lakes with an average of 38.4 ± 48.5 mg C·L^{-1} (n = 171 samples; data are expressed as average ± one standard deviation) and a maximum of 234.4 mg C·L^{-1}. Permafrost-related water types showed similarly high DOC concentrations (ground-ice meltwater: 32.94 mg C·L^{-1}, supra-permafrost water: 20.54 ± 3.6 mg C·L^{-1}, and sub-permafrost water: 16.8 ± 1.2 mg C·L^{-1}) (**Figure 2B**). Thermokarst lakes/ponds (21.3 ± 34.1 mg C·L^{-1}) were characterized by almost five times higher average DOC concentrations than those of rivers/streams (4.3 ± 3.7 mg C·L^{-1}) and with a wide DOC range of ~0.5–234.4 mg C·L^{-1}. Other water types (hail/snow/rain, springs/icings, and groundwater) had low average DOC concentrations between 0.8 ± 1.0 and 1.8 ± 1.4 mg C·L^{-1}, and their ranges were much narrower than those lakes/ponds and rivers/streams (**Table 2**). There are marked seasonal variations in in-stream DOC concentrations in the SAYR. The SAYR-average of DOC concentrations in winter is generally lower than those in spring (snow-melt season), summer, and autumn. In 2016, the greatest in-stream DOC concentration (4.5 ± 2.2 mg C·L^{-1}) occurred during the spring snow-melt season, and decreased into summer–autumn (2.4 ± 3.7 mg C·L^{-1}), and winter (0.8 ± 0.6 mg C·L^{-1}) (**Figure 2C**). In 2017, DOC concentrations were the greatest in summer–autumn (7.0 ± 4.8 mg C·L^{-1}), with a range of 0.5–13.4 mg C·L^{-1}, followed by those of the snow-melt season (3.6 ± 6.0 mg C·L^{-1}) and the winter season (1.1 ± 0.5 mg C·L^{-1}) (**Figure 2D**).

In the SAYR, in-stream DOC concentrations are averaged at 4.2 ± 3.7 mg C·L^{-1}, with a range of 0.7–21.0 mg C·L^{-1}, comparable to DOC ranges in northern permafrost regions (1–32 mg C·L^{-1}) and some other catchments on the QTP (0.4–30.8 mg C·L^{-1}). In the SAYR, in-stream DOC concentrations were characterized by the greatest values (4.5 ± 2.2 mg C·L^{-1}) during the spring snow-melt season, and decreased in summer–autumn (2.4 ± 3.7 mg C·L^{-1}) and declined further in winter (0.8 ± 0.6 mg C·L^{-1}) in 2016 (**Figure 2C**). In 2017, DOC concentrations were the greatest in summer–autumn (7.0 ± 4.8 mg C·L^{-1}), followed by those in the snow-melt season (3.6 ± 6.0 mg C·L^{-1}) and winter season (1.1 ± 0.5 mg C·L^{-1}) (**Figure 2D**). In northern permafrost regions, such as the upper Yukon River Basin, seasonal DOC concentrations are characterized by the greatest average in-stream DOC (36.12 mg C·L^{-1}) in the snow-melt season and decreased to that in summer–autumn (7.3 mg C·L^{-1}) (Guo and Macdonald, 2006; Guo et al., 2018). It is generally proven that in-stream DOC concentrations are positively related with discharge. In the upper Yukon River, the yearly peak flow occurs in spring freshet and the discharge declines in the following seasons (Guo and Macdonald, 2006; Guo et al., 2018).

The Yellow River flow in the SAYR is dominated by the monsoonal climate and mainly recharged by summer precipitation from July to September. In 2017, the summer peak flow induced high in-stream DOC concentrations from July to September. However, in 2016, the SAYR underwent a dryer summer, and no peak flow was observed from July to September. Therefore, accumulated snowfall in winter merely induced a small spring freshet and relatively high snow-melt DOC concentrations. In winter, in-stream DOC concentrations in the SAYR were smaller than those in the summer–autumn and snow-melt season in both 2016 and 2017. They are consistent with those existing observations in northern permafrost regions. However, winter in-stream DOC concentrations in the SAYR

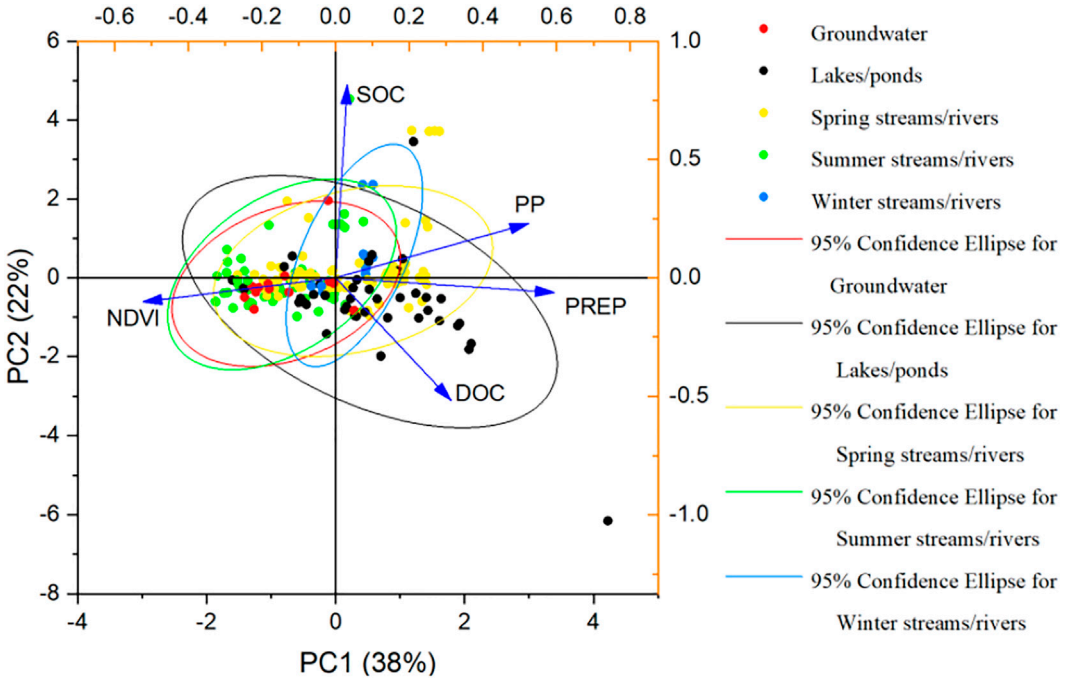

FIGURE 3 | Biplot of the PCA of various water types in the source area of the Yellow River (SAYR) and variable correlation plot (blue arrow).

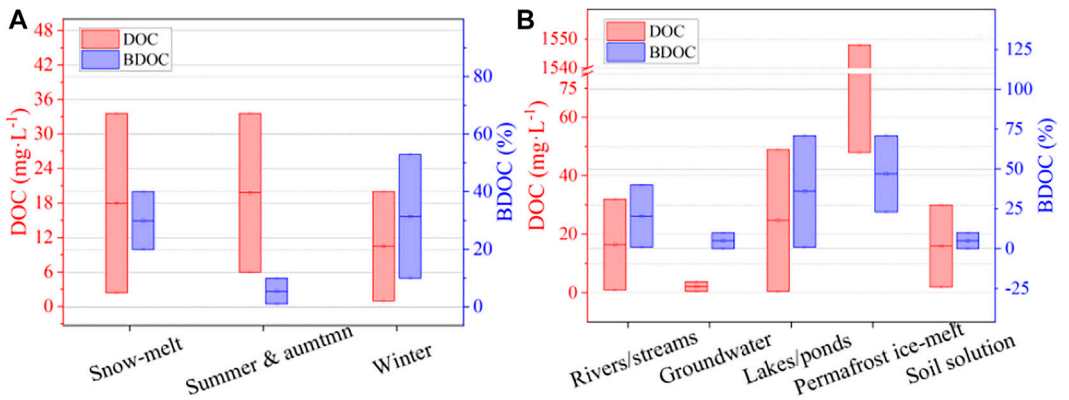

FIGURE 4 | DOC concentrations and biodegradable DOC (BDOC) in aquatic systems in permafrost domains. **(A)** Seasonal distribution of in-stream DOC and BDOC (Finlay et al., 2006, 2009; Petrone et al., 2006; Holmes et al., 2008; O'donnell et al., 2012; Wickland et al., 2012; Olefeldt and Roulet, 2014; Abbott et al., 2014), and **(B)** DOC and BDOC in varied water types (Vonk et al., 2013, 2015b; Abbott et al., 2014; Mann et al., 2015; Selvam et al., 2017; Textor et al., 2019; Payandi-Rolland et al., 2020); Notes: BDOC can be calculated by either incubation experiment (7–40 d) (Holmes et al., 2008; Vonk et al., 2013; Abbott et al., 2014; Selvam et al., 2017; Textor et al., 2019) or proxies of chemical compositions, for example, hydrophilic compounds as a labile fraction of DOC mineralization (O'Donnell et al., 2012) and tyrosine- and tryptophan-like fluorophores (Finlay et al., 2006; Guo and Macdonald, 2006; Petrone et al., 2006; Balcarczyk et al., 2009).

(0.9 ± 0.6 mg C·L^{-1}), comparable with those of the upper Yarlung Zangbo River (0.5 ± 0.2 mg C·L^{-1}) on the southern Tibet Plateau, are smaller than those in northern permafrost regions (e.g., Yukon: 3.9 ± 0.5 mg C·L^{-1}). Lacustrine DOC concentrations (0.5–234.4 mg C·L^{-1}) in the SAYR are generally lower than those in northern permafrost regions (0–1,130 mg C·L^{-1}), while comparable to those on the QTP (21.3 ± 34.1 mg C·L^{-1}). DOC concentrations in the supra-permafrost water (20.5 ± 3.6 mg C·L^{-1}) are higher than those in the sub-permafrost water (16.8 ± 1.2 mg C·L^{-1}) ($n = 4$; north bank of the Wanlong Worma Lake in the Wanlong Worma River Basin of the Duo Qu River in the south-central SAYR). Along the Alaska Arctic coast, DOC concentrations of supra-permafrost water are reported as 33 ± 2 mg C·L^{-1} (Connolly et al., 2020), which is higher than those observed in the SAYR. DOC concentrations in ground-ice melt-water in the up-reach SAYR are much lower

than those in northern permafrost regions, which may be resulted from the limited dataset. DOC concentrations in springs/icings waters, precipitation, and groundwater are generally low (~1 mg C·L^{-1}), with DOC in groundwater a bit higher than the other two water types.

3.2 Environmental Controllers for Aquatic DOC Concentrations in the SAYR

The site-specific data of environmental elements (PREP, NDVI, SOC, and PP) were extracted and the principle environmental controllers for aquatic DOC concentrations were examined by employing the standard PCA method. Data were binned into in-stream water samples collected in the snow-melt season, summer/autumn and winter, groundwater samples, lacustrine samples, and altogether binning of various aquatic samples for the PCAs (**Table 3**; **Figure 3**). In different water types, the sources and formations of DOC may differ, such as seasonally hydrological processes bringing in different DOC sources into streams/rivers. By binning environmental variables and DOC concentrations in different water types, the key environmental controllers can be determined for each water type.

PC1, PC2, and PC3 together explained 81% of the variance among all environmental factors in the snow-melt season (**Table 3**). PC1 was moderately correlated with PREP (r = 0.61) and PP (r = 0.59), PC2 was moderately correlated with DOC (r = 0.63) and SOC (r = −0.69), and PC3 was strongly correlated with SOC (r = 0.71) and moderately with NDVI (r = 0.52) (**Table 3**). Due to the fact that we took accumulated solid precipitation in winter as precipitation in the snow-melt season, the positive correlation between PP and PREP illustrates higher accumulated snow in winter in permafrost regions than that in areas of seasonal frost or talik. In-stream DOC concentrations were negatively correlated with the SOC content, obviously inconsistent with those previous observations (Prokushkin et al., 2009; Kindler et al., 2011; Kicklighter et al., 2013). When the ground surface starts to thaw in the snow-melt season, SOC and litterfalls dominate the in-stream DOC (Prokushkin et al., 2010; Guo et al., 2018), possibly due to representativeness of sampling locations. Three components (PC1, PC2, and PC3) together (**Table 3**) explained 77% variance of all environmental factors in summer–autumn. PC1 was moderately correlated with PP (r = 0.65) and negatively correlated with NDVI (r = −0.57); PC2 was strongly correlated with DOC (r = 0.71); and PC3 was strongly correlated with PREP (r = 0.80) and moderately with SOC (r = 0.55). PP was negatively correlated with NDVI, possibly due to warmer climate and higher NDVI in the downstream SAYR compared to alpine steppes and meadows in upstream SAYR extensively underlain by alpine permafrost. PC1, PC2, and PC3 explained 84% of the variance of environmental factors in winter (**Table 3**). PC1 was moderately correlated with SOC (r = 0.57). PC2 was closely correlated with PREP (r = 0.77) and moderately with PP (r = 0.51). PC3 was closely correlated with DOC (r = 0.70) and moderately with NDVI (r = −0.65). The negative correlation of winter DOC with NDVI demonstrates relatively higher NDVI in downstream SAYR characterized by lower winter in-stream DOC concentrations.

Two principal components explained 75% of the variance in environmental factors in groundwater sampling sites (**Table 3**). PC1 was moderately correlated with DOC (r = 0.64) and negatively with PP (r = 0.56). PC2 was moderately correlated with PREP (r = −0.66) and NDVI (r = 0.55). The correlation of groundwater DOC with PP proves that groundwater has become an increasing source of DOC upon permafrost thaw (Moore, 2010). The negative correlation of PREP with NDVI disagrees with the environmental characteristics in the SAYR, likely due to specific sampling locations. PC1, PC2, and PC3 together explained 78% variations of environmental factors in lacustrine sampling sites (**Table 3**). PC1 was moderately correlated with PREP (r = 0.63), PC2 was moderately correlated with SOC (r = 0.60) and NDVI (r = 0.57), and PC3 was negatively correlated with SOC (r = -0.68) and moderately with NDVI (r = 0.50) and DOC (r = 0.50). Correlations between SOC and NDVI illustrate that a higher NDVI can accumulate more SOC. The correlation of NDVI and lacustrine DOC indicates that sampling plots with higher NDVI are likely to have higher DOC concentrations in lakes/ponds, similar to that reported in earlier studies (Schindler et al., 1997). However, the fact that they were negatively correlated with SOC contradicted those previous observations (De March et al., 1975; Schindler et al., 1997). This might have resulted from samples mostly collected in the up-reach SAYR and lower reaches of SAYR around the Zoîgé wetlands, where SOC was negatively correlated with PP and lacustrine DOC. PC1 explained 38% of the variation of all aquatic samples, with important contributions of PP (r = 0.52), PREP (r = 0.59), and NDVI (r = −0.52) (**Table 3**). The PC2 explained 22% of the variations, correlated with SOC (r = 0.82) and DOC (r = −0.52) (**Table 3**). SOC appeared to be grouped with PP, whereas NDVI was on the opposite side of the plot (**Figure 3**), implying the positive and negative correlations between SOC and NDVI, respectively, with PP. DOC and PREP were grouped together in the down-right quadrant of the plot, indicating the positive correlation between DOC and PREP among all aquatic types. Groundwater and summer streams/rivers were clustered on the left side of the plot, while other water types showed no clear separation.

3.3 Potentials of DOC Decomposition in Aquatic Systems

Aquatic organic carbon is also an important atmospheric carbon source. A meta-analysis of results for decomposability of DOC in varied aquatic systems (e.g., rivers/streams, groundwater, lakes/ponds, and soil solutions) and seasonal rivers/streams was performed for identifying the potentials of transformation from aquatic DOC into atmospheric carbon. Combined with results of DOC concentrations of varied water types and seasonal rivers/streams in northern and other permafrost regions through the method of literature synthesis, hotspots of atmospheric carbon emission from aquatic systems were preliminarily explored (**Figure 4**).

The ranges of in-stream DOC concentrations are similar in the snow-melt season (2.4–33.6 mg C·L^{-1}) and summer–autumn (6–44.0 mg C·L^{-1}) across 10 sampling sites, in the Yukon River Basin and northeastern Siberia (Finlay et al., 2006, 2009; Guo and

Macdonald, 2006; Petrone et al., 2006; Olefeldt and Roulet, 2014) (**Figure 4A**). In the SAYR, ranges of in-stream DOC concentrations in the snow-melt season (0.1–25.4 mg C·L^{-1}) and summer/autumn (0.5–21.0 mg C·L^{-1}) fell in the existing ranges. In-stream biodegradable DOC (BDOC) in the snow-melt season is 20–40% (Abbott et al., 2014), yet in-stream BDOC in summer–autumn is much smaller ranging from 1 to 10% (Wickland et al., 2012) (**Figure 4A**). In-stream DOC concentrations in winter range from 1 to 20 mg C·L^{-1}, relatively lower than those in both the snow-melt seasons and summer–autumn (O'Donnell et al., 2012) (**Figure 4A**). Winter in-stream DOC concentrations in the SAYR ranged from 0.5 to 1.5 mg C·L^{-1} were also smaller than those in other seasons. In the winter season, in-stream BDOC reported across the Yukon River Basin ranges from 10 to 53%, higher than in-stream BDOC in other seasons (O'Donnell et al., 2012; Wickland et al., 2012) (**Figure 4A**). Thus, in-stream BDOC in the spring snow-melt season and winter with relatively higher DOC concentrations or BDOC are potentially important sources of atmospheric carbon emissions from aquatic systems. DOC concentrations in different water types have shown featured distributions. The ranges of DOC concentrations are the lowest in groundwater (0.5–3.9 mg C·L^{-1}), and the highest in ground-ice melt-water (48–1,548 mg C·L^{-1}) (Ma et al., 2019b) (**Figure 4B**). DOC ranges in lakes/ponds (0.5–49 mg C·L^{-1}) are generally higher than those in rivers/streams (1–32 mg C·L^{-1}) and soil solutions (2–30 mg C·L^{-1}) (Abbott et al., 2014; Ma et al., 2019b). The distributive features of aquatic DOC in the SAYR are consistent with existing and latest research results. Correspondingly, the BDOC of ground-ice meltwater is the highest among all water types (23–71%), followed by lakes/ponds (1–71%), rivers/streams (1–40%), and soil solutions (0–10%) (Mann et al., 2015; Payandi-Rolland et al., 2020; Selvam et al., 2017; Textor et al., 2019; Vonk et al., 2013, 2015b) (**Figure 4B**). Therefore, DOC associated with ground-ice melt-water, lakes/ponds, and rivers/streams are relatively labile and potentially a major atmospheric carbon source among other aquatic water types in permafrost regions.

4 CONCLUSION

In permafrost regions, aquatic systems are important pathways of carbon cycling, and potentially acted as major atmospheric carbon sources. DOC concentrations in aquatic systems show strong variations among individual water types in the SAYR. Permafrost-related water types show higher DOC concentrations (ground-ice meltwater, 32.94 mg C·L^{-1}; supra-permafrost water, 20.54 ± 3.6 mg C·L^{-1}; and sub-permafrost water, 16.8 ± 1.2 mg C·L^{-1}) than other water types (lakes/ponds, 21.3 ± 34.1 mg C·L^{-1}; rivers/streams, 4.3 ± 3.7 mg C·L^{-1}; and groundwater, 1.8 ± 1.4 mg C·L^{-1}). Seasonal features of in-stream DOC concentrations were characterized by declining features in 2016 (snow-melt season: 4.5 ± 2.2 mg C·L^{-1} > summer–autumn: 2.4 ± 3.7 mg C·L^{-1} > winter: 0.8 ± 0.6 mg C·L^{-1}) and the greatest in-stream DOC concentrations (7.0 ± 4.8 mg C·L^{-1}) in summer–autumn, and they decreased in the spring snow-melt season (3.6 ± 6.0 mg C·L^{-1}) and winter (1.1 ± 0.5 mg C·L^{-1}) in 2017, and they were associated with intra-annual variations in precipitation modes. Aquatic DOC concentrations and their ranges in the SAYR are consistent with those observed in northern permafrost regions and other QTP sub-basins. PP, PREP, and NDVI explained 38% variance of environmental variables in aquatic DOC distribution in the SAYR, and the PCA analysis reveals that the presence of permafrost is correlated with groundwater DOC, which suggests that groundwater is becoming an additional source of DOC with progressive permafrost thaw in the SAYR. Relatively higher in-stream DOC concentrations in the snow-melt season and winter in combination with higher BDOC and higher DOC concentrations in ground-ice meltwater, lakes/ponds, and rivers/streams are potentially major sources of atmospheric carbon emission from aquatic systems in the SAYR.

DATA AVAILABILITY STATEMENT

The original contributions presented in the study are included in the article/Supplementary Material, further inquiries can be directed to the corresponding authors.

AUTHOR CONTRIBUTIONS

Conceptualization, QM and HJ; methodology, QM; software, RS and SM; validation, YY and SL; formal analysis, QM; investigation, DL, YH, XL, and SG; resources, HJ and QW; data curation, QM; writing—original draft preparation, QM; writing—review and editing, HJ; visualization, QM; supervision, project funding, and administration, HJ and QW. All authors have read and agreed to the published version of the manuscript.

FUNDING

This work was funded by the Chinese Academy of Sciences (CAS) Strategic Priority Research Program (Grant No. XDA20100103) and Consulting Project of Ministry of Natural Resources "Impacts of shrinking glaciers and degrading permafrost on ecosystems, Yellow River discharge and carbon sources and sinks in the Source Area of Yellow River on northeastern Qinghai–Tibet Plateau, China." The article processing charges (APC) are funded by the CAS Strategic Priority Research Program (Grant No. XDA20100103).

ACKNOWLEDGMENTS

The authors would like to express the sincere gratitude to the five unidentified reviewers for their kind comments and generous efforts in reviewing and improving the manuscript.

SUPPLEMENTARY MATERIAL

The Supplementary Material for this article can be found online at: https://www.frontiersin.org/articles/10.3389/feart.2022.892524/full#supplementary-material.

REFERENCES

Abbott, B. W., Larouche, J. R., Jones, J. B., Jr., Bowden, W. B., and Balser, A. W. (2014). Elevated Dissolved Organic Carbon Biodegradability from Thawing and Collapsing Permafrost. *J. Geophys. Res. Biogeosci.* 119, 2049–2063. doi:10.1002/2014JG002678

Balcarczyk, K. L., Jones, J. B., Jr., Jaffé, R., and Maie, N. (2009). Stream Dissolved Organic Matter Bioavailability and Composition in Watersheds Underlain with Discontinuous Permafrost. *Biogeochemistry* 94, 255–270. doi:10.1007/s10533-009-9324-x

Blue, B., Brierley, G., and Yu, G.-a. (2013). Geodiversity in the Yellow River Source Zone. *J. Geogr. Sci.* 23, 775–792. doi:10.1007/s11442-013-1044-4

Brierley, G. J., Li, X. L., Cullum, C., and Gao, J. (2016). "Introduction: Landscape and Ecosystem Diversity in the Yellow River Source Zone," in *Landscape and Ecosystem Diversity, Dynamics and Management in the Yellow River Source Zone*. Editors G. J. Brierley, X. Li, C. Cullum, and J. Gao (New York: Springer). doi:10.1007/978-3-319-30475-5_1

Chen, M., Li, C., Spencer, R. G. M., Maie, N., Hur, J., McKenna, A. M., et al. (2021). Climatic, Land Cover, and Anthropogenic Controls on Dissolved Organic Matter Quantity and Quality from Major Alpine Rivers across the Himalayan-Tibetan Plateau. *Sci. Total Environ.* 754, 142411. doi:10.1016/j.scitotenv.2020.142411

Cole, J. J., Prairie, Y. T., Caraco, N. F., McDowell, W. H., Tranvik, L. J., Striegl, R. G., et al. (2007). Plumbing the Global Carbon Cycle: Integrating Inland Waters into the Terrestrial Carbon Budget. *Ecosystems* 10, 171–184. doi:10.1007/s10021-006-9013-8

Connolly, C. T., Cardenas, M. B., Burkart, G. A., Spencer, R. G. M., and McClelland, J. W. (2020). Groundwater as a Major Source of Dissolved Organic Matter to Arctic Coastal Waters. *Nat. Commun.* 11, 1479. doi:10.1038/s41467-020-15250-8

De March, L. (1975). *Nutrient Budgets and Sedimentation in Char Lake, N. W. T., 72°42′N; 94°50′W*. Winnpeg: University of Manitoba.

Dean, J. F., Meisel, O. H., Martyn Rosco, M., Marchesini, L. B., Garnett, M. H., Lenderink, H., et al. (2020). East Siberian Arctic Inland Waters Emit Mostly Contemporary Carbon. *Nat. Commun.* 11, 1627. doi:10.1038/s41467-020-15511-6

Eimers, M. C., Watmough, S. A., and Buttle, J. M. (2008). Long-term Trends in Dissolved Organic Carbon Concentration: a Cautionary Note. *Biogeochemistry* 87, 71–81. doi:10.1007/s10533-007-9168-1

Ewing, S. A., O'Donnell, J. A., Aiken, G. R., Butler, K., Butman, D., Windham-Myers, L., et al. (2015). Long-term Anoxia and Release of Ancient, Labile Carbon upon Thaw of Pleistocene Permafrost. *Geophys. Res. Lett.* 42, 710–730. doi:10.1002/2015gl066296

Finlay, J., Neff, J., Zimov, S., Davydova, A., and Davydov, S. (2009). Impacts of Permafrost Degradation on Arctic River Biogeochemistry. *Hydrol. Process.* 23, 169–182. doi:10.1002/hyp.7196

Finlay, J., Neff, J., Zimov, S., Davydova, A., and Davydov, S. (2006). Snowmelt Dominance of Dissolved Organic Carbon in High-Latitude Watersheds: Implications for Characterization and Flux of River DOC. *Geophys. Res. Lett.* 33, a–n. doi:10.1029/2006GL025754

Guo, L., and Macdonald, R. W. (2006). Source and Transport of Terrigenous Organic Matter in the Upper Yukon River: Evidence from Isotope (δ13C, Δ14C, and δ15N) Composition of Dissolved, Colloidal, and Particulate Phases. *Glob. Biogeochem. Cycles* 20, a–n. doi:10.1029/2005GB002593

Guo, L., and Macdonald, R. W. (2006). Source and Transport of Terrigenous Organic Matter in the Upper Yukon River: Evidence from Isotope (δ13C, Δ14C, and δ15N) Composition of Dissolved, Colloidal, and Particulate Phases. *Glob. Biogeochem. Cycles* 20 (2), a–n. doi:10.1029/2005gb002593

Guo, Y., Song, C., Tan, W., Wang, X., and Lu, Y. (2018). Hydrological Processes and Permafrost Regulate Magnitude, Source and Chemical Characteristics of Dissolved Organic Carbon Export in a Peatland Catchment of Northeastern China. *Hydrol. Earth Syst. Sci.* 22, 1081–1093. doi:10.5194/hess-22-1081-2018

Holmes, R. M., McClelland, J. W., Raymond, P. A., Frazer, B. B., Peterson, B. J., and Stieglitz, M. (2008). Lability of DOC Transported by Alaskan Rivers to the Arctic Ocean. *Geophys. Res. Lett.* 35, L03402. doi:10.1029/2007GL032837

Hope, D., Billett, M. F., and Cresser, M. S. (1994). A Review of the Export of Carbon in River Water: Fluxes and Processes. *Environ. Pollut.* 84, 301–324. doi:10.1016/0269-7491(94)90142-2

Hugelius, G., Strauss, J., Zubrzycki, S., Harden, J. W., Schuur, E. A. G., Ping, C.-L., et al. (2014). Estimated Stocks of Circumpolar Permafrost Carbon with Quantified Uncertainty Ranges and Identified Data Gaps. *Biogeosciences* 11, 6573–6593. doi:10.5194/bg-11-6573-2014

Jin, H., He, R., Cheng, G., Wu, Q., Wang, S., Lü, L., et al. (2009). Changes in Frozen Ground in the Source Area of the Yellow River on the Qinghai-Tibet Plateau, China, and Their Eco-Environmental Impacts. *Environ. Res. Lett.* 4 (4), 045206. doi:10.1088/1748-9326/4/4/045206

Jin, H., Jin, X., He, R., Luo, D., Chang, X., Wang, S., et al. (2019). Evolution of Permafrost in China during the Last 20 Ka. *Sci. China Earth Sci.* 62 (8), 1207–1223. doi:10.1007/s11430-018-9272-0

Jin, H., and Ma, Q. (2021). Impacts of Permafrost Degradation on Carbon Stocks and Emissions under a Warming Climate: A Review. *Atmosphere* 12, 1425. doi:10.3390/atmos12111425

Jin, H., Vandenberghe, J., Luo, D., Harris, S. A., He, R., Chen, X., et al. (2020). Quaternary Permafrost in China: Framework and Discussions. *Quaternary* 3, 32. doi:10.3390/quat3040032

Jin, H., Wang, S., Lü, L., He, R., Chang, X., and Luo, D. (2010). Features and Degradation of Frozen Ground in the Sources Area of the Yellow River, China. *J. Glociol. Geocryol.* 32, 10–17. (In Chinese with English abstract).

Kicklighter, D. W., Hayes, D. J., Mcclelland, J. W., Peterson, B. J., Mcguire, A. D., and Melillo, J. M. (2013). Insights and Issues with Simulating Terrestrial DOC Loading of Arctic River Networks. *Ecol. Appl.* 23, 1817–1836. doi:10.1890/11-1050.1

Kindler, R., Siemens, J., Kaiser, K., Walmsley, D. C., Bernhofer, C., Buchmann, N., et al. (2011). Dissolved Carbon Leaching from Soil Is a Crucial Component of the Net Ecosystem Carbon Balance. *Glob. Change Biol.* 17, 1167–1185. doi:10.1111/j.1365-2486.2010.02282.x

Kotz, S., and Nadarajah, S. (2004). *Multivariate T-distributions and Their Applications*. Cambridge: Cambridge University Press.

Lan, Y., Jin, H., Lu, C., La, C., Shen, Y., Song, J., et al. (2013). The Fact of Climate Shift to Warm-Humid in the Source Regions of the Yellow River and its Hydrologic Response. *J. Glociol. Geocryol.* 35, 920–928. (In Chinese with English abstract). doi:10.7522/j.issn.1000-0240.2013.0104

Luo, D., Liu, L., Jin, H., Wang, X., and Chen, F. (2020). Characteristics of Ground Surface Temperature at Chalaping in the Source Area of the Yellow River, Northeastern Tibetan Plateau. *Agric. For. Meteorology* 281, 107819. doi:10.1016/j.agrformet.2019.107819

Ma, Q., Jin, H.-J., Bense, V. F., Luo, D.-L., Marchenko, S. S., Harris, S. A., et al. (2019a). Impacts of Degrading Permafrost on Streamflow in the Source Area of Yellow River on the Qinghai-Tibet Plateau, China. *Adv. Clim. Change Res.* 10, 225–239. doi:10.1016/j.accre.2020.02.001

Ma, Q., Jin, H., Yu, C., and Bense, V. F. (2019b). Dissolved Organic Carbon in Permafrost Regions: A Review. *Sci. China Earth Sci.* 62 (2), 349–364. doi:10.1007/s11430-018-9309-6

Ma, Q. (2020). *Research on In-Stream Dissolved Organic Carbon Dynamics and Mechanisms in the Source Area of the Yellow River on the Northeastern Qinghai-Tibet Plateau, Southwest China*. Lanzhou, China: Chinese Academy of Sciences. (In Chinese with English abstract).

Mann, P. J., Eglinton, T. I., McIntyre, C. P., Zimov, N., Davydova, A., Vonk, J. E., et al. (2015). Utilization of Ancient Permafrost Carbon in Headwaters of Arctic Fluvial Networks. *Nat. Commun.* 6, 7856. doi:10.1038/ncomms8856

Matheus Carnevali, P. B., Rohrssen, M., Williams, M. R., Michaud, A. B., Adams, H., Berisford, D., et al. (2015). Methane Sources in Arctic Thermokarst Lake Sediments on the North Slope of Alaska. *Geobiology* 13, 181–197. doi:10.1111/gbi.12124

Matveev, A., Laurion, I., Deshpande, B. N., Bhiry, N., and Vincent, W. F. (2016). High Methane Emissions from Thermokarst Lakes in Subarctic Peatlands. *Limnol. Oceanogr.* 61, S150–S164. doi:10.1002/lno.10311

Moore, W. S. (2010). The Effect of Submarine Groundwater Discharge on the Ocean. *Annu. Rev. Mar. Sci.* 2, 59–88. doi:10.1146/annurev-marine-120308-081019

Mu, C., Zhang, T., Wu, Q., Peng, X., Zhang, P., Yang, Y., et al. (2016). Dissolved Organic Carbon, CO2, and CH4 Concentrations and Their Stable Isotope Ratios in Thermokarst Lakes on the Qinghai-Tibetan Plateau. *J. Limnol.* 75 (2), 313–319. doi:10.4081/jlimnol.2016.1346

O'Donnell, J. A., Aiken, G. R., Walvoord, M. A., and Butler, K. D. (2012). Dissolved Organic Matter Composition of Winter Flow in the Yukon River Basin:

Implications of Permafrost Thaw and Increased Groundwater Discharge. *Glob. Biogeochem. Cycles* 26, GB0E06. doi:10.1029/2012GB004341

Olefeldt, D., and Roulet, N. T. (2014). Permafrost Conditions in Peatlands Regulate Magnitude, Timing, and Chemical Composition of Catchment Dissolved Organic Carbon Export. *Glob. Change Biol.* 20, 3122–3136. doi:10.1111/gcb.12607

Panneer Selvam, B., Lapierre, J.-F., Guillemette, F., Voigt, C., Lamprecht, R. E., Biasi, C., et al. (2017). Degradation Potentials of Dissolved Organic Carbon (DOC) from Thawed Permafrost Peat. *Sci. Rep.* 7, 45811. doi:10.1038/srep45811

Payandi-Rolland, D., Shirokova, L. S., Tesfa, M., Bénézeth, P., Lim, A. G., Kuzmina, D., et al. (2020). Dissolved Organic Matter Biodegradation along a Hydrological Continuum in Permafrost Peatlands. *Sci. Total Environ.* 749, 141463. doi:10.1016/j.scitotenv.2020.141463

Petrone, K. C., Jones, J. B., Hinzman, L. D., and Boone, R. D. (2006). Seasonal Export of Carbon, Nitrogen, and Major Solutes from Alaskan Catchments with Discontinuous Permafrost. *J. Geophys. Res.* 111, a–n. doi:10.1029/2005JG000055

Prokushkin, A. S., Hobara, S., and Prokushkin, S. G. (2010). "Behavior of Dissolvedorganiccarbon in Larch Ecosystems," in *Permafrost Ecosystems Siberian Larch Forests*. Editors A. Osawa, O. A. Zyryanova, Y. Matsuura, T. Kajimoto, and R. W. Wein (Springer). doi:10.1007/978-1-4020-9693-8_11

Prokushkin, A. S., Hobara, S., and Prokushkin, S. G. (2009). "Global Warming and Dissolved Organic Carbon Release from Permafrost Soils," in *Permafrost Soils*. Editor R. Margesin (Berlin: Springer-Verlag).

Ran, Y., Li, X., Cheng, G., Che, J., Aalto, J., Karjalainen, O., et al. (2022). New High-Resolution Estimates of the Permafrost Thermal State and Hydrothermal Conditions over the Northern Hemisphere. *Earth Syst. Sci. Data* 14, 865–884. doi:10.5194/essd-14-865-2022

Ran, Y., Li, X., Cheng, G., Nan, Z., Che, J., Sheng, Y., et al. (2020). Mapping the Permafrost Stability on the Tibetan Plateau for 2005-2015. *Sci. China Earth Sci.* 64 (1), 62–79. doi:10.1007/s11430-020-9685-3

Rosentreter, J. A., Borges, A. V., Deemer, B. R., Holgerson, M. A., Liu, S., Song, C., et al. (2021). Half of Global Methane Emissions Come from Highly Variable Aquatic Ecosystem Sources. *Nat. Geosci.* 14, 225–230. doi:10.1038/s41561-021-00715-2

Schindler, D. W., Curtis, P. J., Bayley, S. E., Parker, B. R., Beaty, K. G., and Stainton, M. P. (1997). Climate-induced Changes in the Dissolved Organic Carbon Budgets of Boreal Lakes. *Biogeochemistry* 36, 9–28. doi:10.1023/a:1005792014547

Schuur, E. A. G., Bockheim, J., Canadell, J. G., Euskirchen, E., Field, C. B., Goryachkin, S. V., et al. (2008). Vulnerability of Permafrost Carbon to Climate Change: Implications for the Global Carbon Cycle. *Biosciences* 58, 701–714. doi:10.1641/b580807

Schuur, E. A. G., McGuire, A. D., Schädel, C., Grosse, G., Harden, J. W., Hayes, D. J., et al. (2015). Climate Change and the Permafrost Carbon Feedback. *Nature* 520, 171–179. doi:10.1038/nature14338

Serikova, S., Pokrovsky, O. S., Ala-Aho, P., Kazantsev, V., Kirpotin, S. N., Kopysov, S. G., et al. (2018). High Riverine CO2 Emissions at the Permafrost Boundary of Western Siberia. *Nat. Geosci.* 11, 825–829. doi:10.1038/s41561-018-0218-1

Sheng, Y., Ma, S., Cao, W., and Wu, J. (2020). Spatiotemporal Changes of Permafrost in the Headwater Area of the Yellow River under a Changing Climate. *Land Degrad. Dev.* 31 (1), 133–152. doi:10.1002/ldr.3434

Shirokova, L. S., Pokrovsky, O. S., Kirpotin, S. N., Desmukh, C., Pokrovsky, B. G., Audry, S., et al. (2013). Biogeochemistry of Organic Carbon, CO2, CH4, and Trace Elements in Thermokarst Water Bodies in Discontinuous Permafrost Zones of Western Siberia. *Biogeochemistry* 113, 573–593. doi:10.1007/s10533-012-9790-4

Stolpmann, L., Coch, C., Morgenstern, A., Boike, J., Fritz, M., Herzschuh, U., et al. (2021). First Pan-Arctic Assessment of Dissolved Organic Carbon in Lakes of the Permafrost Region. *Biogeosciences* 18, 3917–3936. doi:10.5194/bg-18-3917-2021

Strauss, J., Schirrmeister, L., Grosse, G., Fortier, D., Hugelius, G., Knoblauch, C., et al. (2017). Deep Yedoma Permafrost: A Synthesis of Depositional Characteristics and Carbon Vulnerability. *Earth-Science Rev.* 172, 75–86. doi:10.1016/j.earscirev.2017.07.007

Tank, S. E., Striegl, R. G., McClelland, J. W., and Kokelj, S. V. (2016). Multi-decadal Increases in Dissolved Organic Carbon and Alkalinity Flux from the Mackenzie Drainage Basin to the Arctic Ocean. *Environ. Res. Lett.* 11, 054015. doi:10.1088/1748-9326/11/5/054015

Textor, S. R., Wickland, K. P., Podgorski, D. C., Johnston, S. E., and Spencer, R. G. M. (2019). Dissolved Organic Carbon Turnover in Permafrost-Influenced Watersheds of Interior Alaska: Molecular Insights and the Priming Effect. *Front. Earth Sci.* 7, 275. doi:10.3389/feart.2019.00275

Vonk, J. E., Mann, P. J., Davydov, S., Davydova, A., Spencer, R. G. M., Schade, J., et al. (2013). High Biolability of Ancient Permafrost Carbon upon Thaw. *Geophys. Res. Lett.* 40, 2689–2693. doi:10.1002/grl.50348

Vonk, J. E., Tank, S. E., Bowden, W. B., Laurion, I., Vincent, W. F., Alekseychik, P., et al. (2015a). Reviews and Syntheses: Effects of Permafrost Thaw on Arctic Aquatic Ecosystems. *Biogeosciences* 12, 7129–7167. doi:10.5194/bg-12-7129-2015

Vonk, J. E., Tank, S. E., Mann, P. J., Spencer, R. G. M., Treat, C. C., Striegl, R. G., et al. (2015b). Biodegradability of Dissolved Organic Carbon in Permafrost Soils and Aquatic Systems: a Meta-Analysis. *Biogeosciences* 12, 6915–6930. doi:10.5194/bg-12-6915-2015

Wang, B., and French, H. M. (1995). Permafrost on the Tibet Plateau, China. *Quat. Sci. Rev.* 14, 255–274. doi:10.1016/0277-3791(95)00006-b

Wang, L., Yao, T., Chai, C., Cuo, L., Su, F., Zhang, F., et al. (2021). TP-river: Monitoring and Quantifying Total River Runoff from the Third Pole. *Bull. Am. Meteorol. Soc.* 102 (5), E948–E965. doi:10.1175/bams-d-20-0207.1

Wickland, K. P., Aiken, G. R., Butler, K., Dornblaser, M. M., Spencer, R. G. M., and Striegl, R. G. (2012). Biodegradability of Dissolved Organic Carbon in the Yukon River and its Tributaries: Seasonality and Importance of Inorganic Nitrogen. *Glob. Biogeochem. Cycles* 26 (4), GB0E03. doi:10.1029/2012GB004342

Wieder, W. R., Boehnert, J., Bonan, G. B., and Langseth, M. (2014). *Regridded Harmonized World Soil Database v1.2*. Oak Ridge, Tennessee, USA: ORNL DAAC.

Yang, D., Kane, D., Zhang, Z., Legates, D., and Goodison, B. (2005). Bias Corrections of Long-Term (1973-2004) Daily Precipitation Data over the Northern Regions. *Geophys. Res. Lett.* 32, a–n. doi:10.1029/2005GL024057

Ye, B., Yang, D., Ding, Y., Han, T., and Koike, T. (2004). A Bias-Corrected Precipitation Climatology for China. *J. Hydrometeorol.* 5, 1147–1160. doi:10.1175/jhm-366.1

Yu, K.-f., Lehmkuhl, F., and Falk, D. (2017). Quantifying Land Degradation in the Zoige Basin, NE Tibetan Plateau Using Satellite Remote Sensing Data. *J. Mt. Sci.* 14, 77–93. doi:10.1007/s11629-016-3929-z

Zhang, L., Xia, X., Liu, S., Zhang, S., Li, S., Wang, J., et al. (2020). Significant Methane Ebullition from Alpine Permafrost Rivers on the East Qinghai-Tibet Plateau. *Nat. Geosci.* 13, 349–354. doi:10.1038/s41561-020-0571-8

Conflict of Interest: The authors declare that the research was conducted in the absence of any commercial or financial relationships that could be construed as a potential conflict of interest.

Advantages of publishing in Frontiers

OPEN ACCESS
Articles are free to read for greatest visibility and readership

FAST PUBLICATION
Around 90 days from submission to decision

HIGH QUALITY PEER-REVIEW
Rigorous, collaborative, and constructive peer-review

TRANSPARENT PEER-REVIEW
Editors and reviewers acknowledged by name on published articles

Frontiers
Avenue du Tribunal-Fédéral 34
1005 Lausanne | Switzerland

Visit us: www.frontiersin.org
Contact us: frontiersin.org/about/contact

REPRODUCIBILITY OF RESEARCH
Support open data and methods to enhance research reproducibility

DIGITAL PUBLISHING
Articles designed for optimal readership across devices

FOLLOW US
@frontiersin

IMPACT METRICS
Advanced article metrics track visibility across digital media

EXTENSIVE PROMOTION
Marketing and promotion of impactful research

LOOP RESEARCH NETWORK
Our network increases your article's readership